For Official Use **NEA/CSNI/R(2004)11**

Organisation de Coopération et de Développement Economiques
Organisation for Economic Co-operation and Development **20-Jul-2004**

English - Or. English

NUCLEAR ENERGY AGENCY
COMMITTEE ON THE SAFETY OF NUCLEAR INSTALLATIONS

NEA/CSNI/R(2004)11
For Official Use

INTERNATIONAL STANDARD PROBLEM NO.48

Containment Capacity. Phase 2 Report - Results of Pressure Loading Analysis

The complete version of this document is only available in PDF format.

English - Or. English

JT00167590

ORGANISATION FOR ECONOMIC CO-OPERATION AND DEVELOPMENT

Pursuant to Article 1 of the Convention signed in Paris on 14th December 1960, and which came into force on 30th September 1961, the Organisation for Economic Co-operation and Development (OECD) shall promote policies designed:

- to achieve the highest sustainable economic growth and employment and a rising standard of living in member countries, while maintaining financial stability, and thus to contribute to the development of the world economy;
- to contribute to sound economic expansion in member as well as non-member countries in the process of economic development; and
- to contribute to the expansion of world trade on a multilateral, non-discriminatory basis in accordance with international obligations.

The original member countries of the OECD are Austria, Belgium, Canada, Denmark, France, Germany, Greece, Iceland, Ireland, Italy, Luxembourg, the Netherlands, Norway, Portugal, Spain, Sweden, Switzerland, Turkey, the United Kingdom and the United States. The following countries became members subsequently through accession at the dates indicated hereafter: Japan (28th April 1964), Finland (28th January 1969), Australia (7th June 1971), New Zealand (29th May 1973), Mexico (18th May 1994), the Czech Republic (21st December 1995), Hungary (7th May 1996), Poland (22nd November 1996), Korea (12th December 1996) and the Slovak Republic (14 December 2000). The Commission of the European Communities takes part in the work of the OECD (Article 13 of the OECD Convention).

NUCLEAR ENERGY AGENCY

The OECD Nuclear Energy Agency (NEA) was established on 1st February 1958 under the name of the OEEC European Nuclear Energy Agency. It received its present designation on 20th April 1972, when Japan became its first non-European full member. NEA membership today consists of 28 OECD member countries: Australia, Austria, Belgium, Canada, the Czech Republic, Denmark, Finland, France, Germany, Greece, Hungary, Iceland, Ireland, Italy, Japan, Luxembourg, Mexico, the Netherlands, Norway, Portugal, Republic of Korea, the Slovak Republic, Spain, Sweden, Switzerland, Turkey, the United Kingdom and the United States. The Commission of the European Communities also takes part in the work of the Agency.

The mission of the NEA is:

- to assist its member countries in maintaining and further developing, through international co-operation, the scientific, technological and legal bases required for a safe, environmentally friendly and economical use of nuclear energy for peaceful purposes, as well as
- to provide authoritative assessments and to forge common understandings on key issues, as input to government decisions on nuclear energy policy and to broader OECD policy analyses in areas such as energy and sustainable development.

Specific areas of competence of the NEA include safety and regulation of nuclear activities, radioactive waste management, radiological protection, nuclear science, economic and technical analyses of the nuclear fuel cycle, nuclear law and liability, and public information. The NEA Data Bank provides nuclear data and computer program services for participating countries.

In these and related tasks, the NEA works in close collaboration with the International Atomic Energy Agency in Vienna, with which it has a Co-operation Agreement, as well as with other international organisations in the nuclear field.

COMMITTEE ON THE SAFETY OF NUCLEAR INSTALLATIONS

The Committee on the Safety of Nuclear Installations (CSNI) of the OECD Nuclear Energy Agency (NEA) is an international committee made up of senior scientists and engineers. It was set up in 1973 to develop and co-ordinate the activities of the Nuclear Energy Agency concerning the technical aspects of the design, construction and operation of nuclear installations insofar as they affect the safety of such installations. The Committee's purpose is to foster international co-operation in nuclear safety among the OECD Member countries.

The CSNI constitutes a forum for the exchange of technical information and for collaboration between organizations, which can contribute, from their respective backgrounds in research, development, engineering or regulation, to these activities and to the definition of the programme of work. It also reviews the state of knowledge on selected topics on nuclear safety technology and safety assessment, including operating experience. It initiates and conducts programmes identified by these reviews and assessments in order to overcome discrepancies, develop improvements and reach international consensus on technical issues of common interest. It promotes the co-ordination of work in different Member countries including the establishment of co-operative research projects and assists in the feedback of the results to participating organizations. Full use is also made of traditional methods of co-operation, such as information exchanges, establishment of working groups, and organisation of conferences and specialist meetings.

The greater part of the CSNI's current programme is concerned with the technology of water reactors. The principal areas covered are operating experience and the human factor, reactor coolant system behaviour, various aspects of reactor component integrity, the phenomenology of radioactive releases in reactor accidents and their confinement, containment performance, risk assessment, and severe accidents. The Committee also studies the safety of the nuclear fuel cycle, conducts periodic surveys of the reactor safety research programmes and operates an international mechanism for exchanging reports on safety related nuclear power plant accidents.

In implementing its programme, the CSNI establishes co-operative mechanisms with NEA's Committee on Nuclear Regulatory Activities (CNRA), responsible for the activities of the Agency concerning the regulation, licensing and inspection of nuclear installations with regard to safety. It also co-operates with NEA's Committee on Radiation Protection and Public Health and NEA's Radioactive Waste Management Committee on matters of common interest

FOREWORD

At the CSNI meeting in June 2002, the proposal for an International Standard Problem on containment integrity (ISP 48) based on the NRC/NUPEC/Sandia test was approved. Objectives are to extend the understanding of capacities of actual containment structures based on results of the recent PCCV Model test and other previous research.

The ISP is sponsored by the USNRC, and results have been made available thanks to NUPEC and to the USNRC. Sandia National Laboratory was contracted to manage the technical aspects of the ISP.

This report presents the pretest analysis results of the calculation of the Limit State Test (LST), i.e. static pressure loading, provided by the ISP48 participants.

A second report to be published in 2005 will present results of calculations of response to both thermal and mechanical loadings. This second report will also include a thorough analysis of the results to draw conclusions and recommendations with regard to the modeling and performance of capacities of containment structures.

The complete list of CSNI reports, and the text of reports from 1993 onwards, is available on

http://www.nea.fr/html/nsd/docs/

ACKNOWLEDGMENTS

This effort would not have been possible without the cooperation and support of many individuals and groups. The Committee on the Safety of Nuclear Installations (CSNI), the U.S. Nuclear Regulatory Commission (NRC), the Japan Nuclear Energy Safety Organization (JNES) (formerly the Nuclear Power Engineering Corporation, NUPEC), and Sandia National Laboratories (SNL) are pleased to have had the participation of the following organizations in this International Standard Problem on Containment Capacity. While there were many other individuals who contributed to this effort, the principal correspondents are listed below:

BE/HSE/NNC	British Energy Nuclear Installations Inspectorate/Health & Safety Executive NNC Ltd.	Graham Doughty David Shepherd Nawal Prinja
EGP	Energoprojekt Praha, UJV Rez. Div.	Jan Maly Jan Stepan
GRS	Gesellschaft für Anlagen und Reaktorsicherheit mbH	Jurgen Sievers Hans Grebner
IRSN/CEA	Institut de Radioprotection et de Sûreté Nucléaire Commisssariat a l'Energie Atomique	Georges Nahas Thierry Charras
KAERI	Korea Atomic Energy Research Institute	Sang-jin Lee Jeong-Moon Seo Hong-Po Lee
KOPEC	Korea Power Engineering Company	Nam-Ho Lee
NRC/SNL/DEA	US Nuclear Regulatory Commission Sandia National Laboratories David Evans and Associates	Bret A. Tegler Michael F. Hessheimer Robert A. Dameron
SCANSCOT	Scanscot Technology	Ola Jovall

While not formally participating in Phase 2 of this ISP, the support and contributions of the following organizations and individuals is also recognized:

EDF	Électricité de France	Jean-Pierre Touret Jean-Luc Valfort
JNES	Japan Nuclear Energy Safety Organization	Satoru Shibata
JPRG	Japan PCCV Research Group	Takeshi Kawasoto
VÚEZ	Vúez Levice	Milan Prandorfy

These organizations received no financial support from CSNI, NRC, or SNL, and their efforts are gratefully acknowledged.

The author also wishes to acknowledge the guidance, support, and encouragement of the CSNI's Eric Mathet; and Dr. James F. Costello (retired), formerly of the NRC's Engineering and Research Applications Branch, Division of Engineering Technology, Office of Reactor Research.

EXECUTIVE SUMMARY

At the CSNI meeting in June 2002, the proposal for an International Standard Problem on containment integrity (ISP 48) based on the NRC/NUPEC/Sandia test was approved. Objectives are to extend the understanding of capacities of actual containment structures based on results of the recent PCCV Model test and other previous research. Sandia National Laboratories (SNL) conducted a Cooperative Containment Integrity Program under the joint sponsorship of the Nuclear Power Engineering Corporation (NUPEC) of Japan, and the NRC Office of Nuclear Regulatory Research. The purpose of the program was to investigate the response of representative models of nuclear containment structures to pressure loading beyond the design basis accident and to compare analytical predictions to measured behavior. A uniform 1:4-scale model of a prestressed concrete containment vessel (PCCV) was constructed and tested at SNL from 1997 through 2001. This model was representative of the containment structure of an actual pressurized-water reactor plant in Japan.

The first meeting of the ISP48 members was held on November 20 & 21, 2002 in Stockholm, Sweden to define the scope and the schedule for the ISP. It was agreed that the ISP would consist of four phases:

- Phase 1: Data Collection and Identification
- Phase 2: Calculation of the Limit State Test (LST), i.e. static pressure loading
- Phase 3: Calculation of response to both Thermal and Mechanical Loadings
- Phase 4: Reporting Workshop

Under Phase 1, Sandia National Laboratories (SNL) was tasked with providing the data on the model design/construction and testing to complete the calculations in Phases 2 and 3. A detailed test report was published by the US Nuclear Regulatory Commission. A condensed version of this report was prepared to meet the requirements of Phase 1 of the ISP.

This report also presents the results of the Phase 2 analyses of the PCCV model for the static pressure loading. Thirteen organizations (or teams) accepted the invitation to participate in the ISP and the majority of these performed calculations to predict the structural response of the PCCV model to static overpressurization. Teams are listed at the beginning of the report.

This report presents the pretest analysis results provided by the ISP48 participants. These results include predictions of the response of the PCCV model in terms of 55 measurements (strain, displacement, force) at specified locations throughout the model, the pressure capacity of the PCCV model, and the failure mode and mechanisms. Section 2 summarizes the design/, construction and instrumentation of the PCCV model. Section 3 summarizes the procedures and results of the overpressure tests. Section 4 presents the Phase 2 calculations and the composite plots presented in Appendix A. Section 5 summarizes the Phase 2 effort and provides some observations from the comparison of results. Appendices B through I are the individual participant reports.

The work reported herein represents, arguably, the state of the art in the numerical simulation of the response of a prestressed concrete containment vessel (PCCV) model to pressure loads up to failure. Results are presented in this report as well as considerations on the approach.

Most of the calculations show results beyond the maximum pressure achieved in the LST. These results were used to estimate the failure pressures for the liner, the tendons and the rebar. Although 3D-models are necessary for simulation of local behavior in the vicinity of perturbations, the global deformations and strains of the model containment are simulated quite well by axisymmetric models. The most accurate estimates of the global hoop strain are obtained from the average radial displacements at a given elevation. The rebar strains compare less favorably (than the displacements) with analyses. Nevertheless the meridional rebar strains at the wall-base junction appear to capture the bending response and, the rebar strains at the mid-height of cylinder are consistent with displacement based strains. Liner strain comparisons with analysis are generally inconsistent primarily due to local perturbations in the structure. In general the calculated change (increase) in tendon strain/force resulting from pressurization of the model are consistent and in agreement with test results. As to cracking, most of the analyses demonstrate that the formation of cracking in the concrete starts at about 1.5 Pd. One of the consequences is that the dependence of radial displacement on pressure becomes nonlinear. This effect is in agreement with measured results.

By performing the ISP and comparing the different methodologies presented by participants, questions were raised as to the most appropriate criteria for failure and modeling hypothesis to calibrate models and validate methodologies. This is actually the essence of such ISP and consensus on best approaches will try to be achieved.

The next phase of ISP48 will combine thermal and pressure loading using two scenarios: (1) Saturated Steam Conditions (mandatory for all Phase 3 participants), and (2) Station Blackout Scenario. Results will be presented in April 2005.

CONTENTS

FIGURES

TABLES

INTRODUCTION

Background

At the CSNI meeting in June 2002, the proposal for an International Standard Problem on containment integrity (ISP 48) based on the NRC/NUPEC/Sandia test was approved (Ref. IAGE_CONC/ISP48/(03)2). Objectives are to extend the understanding of capacities of actual containment structures based on results of the recent PCCV Model test and other previous research. Sandia National Laboratories (SNL) conducted a Cooperative Containment Integrity Program under the joint sponsorship of the Nuclear Power Engineering Corporation (NUPEC) of Japan, and the NRC Office of Nuclear Regulatory Research. The purpose of the program was to investigate the response of representative models of nuclear containment structures to pressure loading beyond the design basis accident and to compare analytical predictions to measured behavior. A uniform 1:4-scale model of a prestressed concrete containment vessel (PCCV) was constructed and tested at SNL from 1997 through 2001. This model was representative of the containment structure of an actual pressurized-water reactor plant in Japan.

Scope of ISP48

The first meeting of the ISP48 members was held on November 20 & 21, 2002 in Stockholm, Sweden to define the scope and the schedule for the ISP. It was agreed that the ISP would consist of four phases:

Phase 1: Data Collection and Identification

Phase 2: Calculation of the Limit State Test (LST), i.e. static pressure loading

Phase 3: Calculation of response to both Thermal and Mechanical Loadings

Phase 4: Reporting Workshop

Under Phase 1, Sandia National Laboratories (SNL) was tasked with providing the data on the model design/construction and testing to complete the calculations in Phases 2 and 3. A detailed test report was published by the US Nuclear Regulatory Commission [1]. A condensed version of this report was prepared to meet the requirements of Phase 1 of the ISP.

This report also presents the results of the Phase 2 analyses of the PCCV model for the static pressure loading. Thirteen organizations (or teams) accepted the invitation to participate in the ISP and the majority of these performed calculations to predict the structural response of the PCCV model to static overpressurization. The participating organizations are:

BE/HSE/NNC	British Energy Nuclear Installations Inspectorate/Health & Safety Executive NNC Ltd.	UK
EGP	Energoprojekt Praha, UJV Rez. Div.	Czech Rep.
GRS	Gesellschaft für Anlagen und Reaktorsicherheit mbH	Germany
IRSN/CEA	Institut de Radioprotection et de Sûreté Nucléaire Commisssariat a l'Energie Atomique	France
KAERI	Korea Atomic Energy Research Institute	Korea
KOPEC	Korea Power Engineering Company	Korea
NRC/SNL/DEA	US Nuclear Regulatory Commission Sandia National Laboratories David Evans and Associates	US
SCANSCOT	Scanscot Technology	Sweden

Some of these organizations participated in the Pretest Round Robin Analysis organized by SNL in 1995 to predict the response of the PCCV model prior to testing [2] while for other participants this was a new problem. Each participating organization was provided with the model and loading data and was asked to perform independent analyses to simulate the response of the PCCV model. Written reports summarizing the Phase 2 calculations were submitted to SNL and are included in the appendices.

In order to provide an initial basis for comparison of the Phase 2 calculations with the test data, each participant was asked to submit response time histories at the same 55 Standard Output Locations (SOLs) used in the PCCV Pretest Round Robin Analysis. Each participant was also asked to specify the pressure at which they calculated key structural milestones, such as cracking, liner yield and failure. These results are summarized in this report and were reviewed at a Phase 2 meeting held in conjunction with the 8th meeting of the CSNI Working Group on the Integrity and Ageing of Components and Structures on March 19, 2004 in Madrid, Spain.

At the same workshop, plans for the Phase 3 combined thermal and mechanical analysis were finalized and each participant was requested to complete their calculations and submit their summary reports and results by December, 2004. These results will be compiled and a final summary report on the ISP will be prepared and is tentatively scheduled to be presented at the June 2005 CSNI meeting.

Report Organization

This report presents the pretest analysis results provided by the ISP48 participants. These results include predictions of the response of the PCCV model in terms of 55 measurements (strain, displacement, force) at specified locations throughout the model, the pressure capacity of the PCCV model, and the failure mode and mechanisms. Section 2 summarizes the design, construction and instrumentation of the PCCV model. Section 3 summarizes the procedures and results of the overpressure tests. Section 4 presents the Phase 2 calculations and the composite plots presented in Appendix A. Section 5 summarizes the Phase 2 effort and provides some observations from the comparison of results. Appendices B through I are the individual participant reports.

PRESTRESSED CONCRETE CONTAINMENT VESSEL MODEL

The PCCV model was a 1:4-scale model of the prestressed concrete containment vessel (PCCV) of an actual nuclear poser plant in Japan, Ohi-3 (Figure 2.1). Ohi-3 is an 1127 MWe Pressurized Water Reactor (PWR) unit, one of four units comprising the Ohi Nuclear Power Station located in Fukui Prefecture, owned and operated by Kansai Electric Power Company.

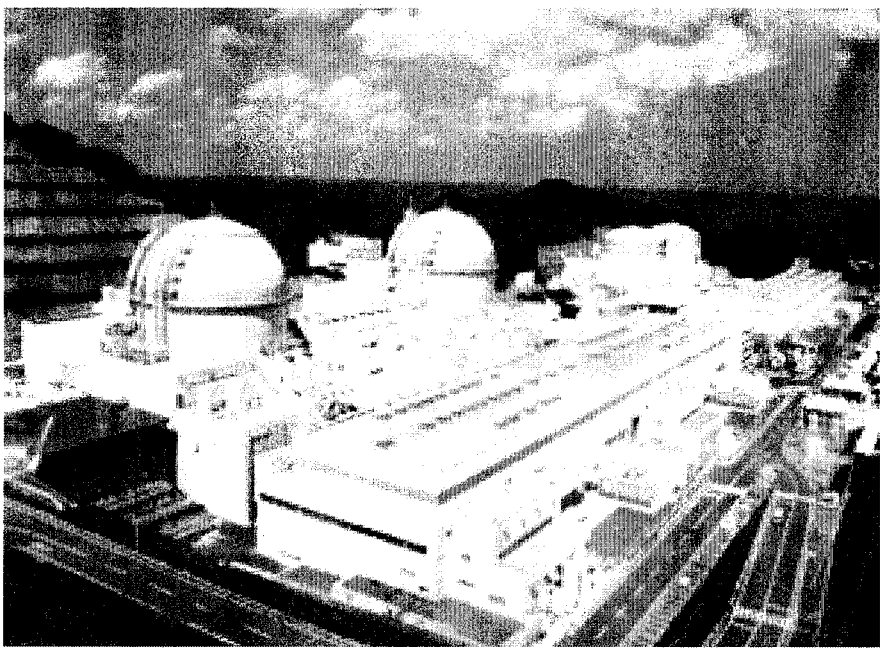

Figure 2.1 Ohi Nuclear Power Station, Ohi-cho, Fukui, Japan

Model Features and Scale

The Ohi-3 containment is a thin prestressed concrete cylindrical shell with a hemispherical dome and a continuous steel liner anchored to a reinforced concrete basemat which extends beyond the containment to support other plant structures. Consistent with the objectives of the sponsoring organizations, the features and scale of the PCCV model were chosen so that the response of the model would mimic the global behavior of the prototype and local details, particularly those around penetrations, would be represented. One of the primary considerations in determining the scale of the model was the desire to utilize construction materials that were identical, or nearly so, to the material used in the construction of the prototype. Preliminary design studies, conducted to determine the appropriate scale of the model, initially focused on a mixed scale model where the scale on the overall geometry would be 1:6, while the scale on the liner thickness would be 1:3. These preliminary studies indicated, however, that use of this mixed scale might upset the relationship between failure modes which might be expected in the prototype. In particular, the use of a steel liner which was twice as thick, relative to the prestressed concrete shell, as the prototype might retard the onset of liner tearing (leakage) failure modes and increase the likelihood of a structural failure mode occurring. As a result, it was decided that the scale of the model would be a uniform 1:4, with minor exceptions to

accommodate fabrication and construction concerns. This was judged to be the minimum scale that would allow the steel liner to be constructed from prototypical materials and fabricated with details and procedures that were representative of the prototype. The overall geometry and dimensions of the PCCV model are shown in Figure 2.2.

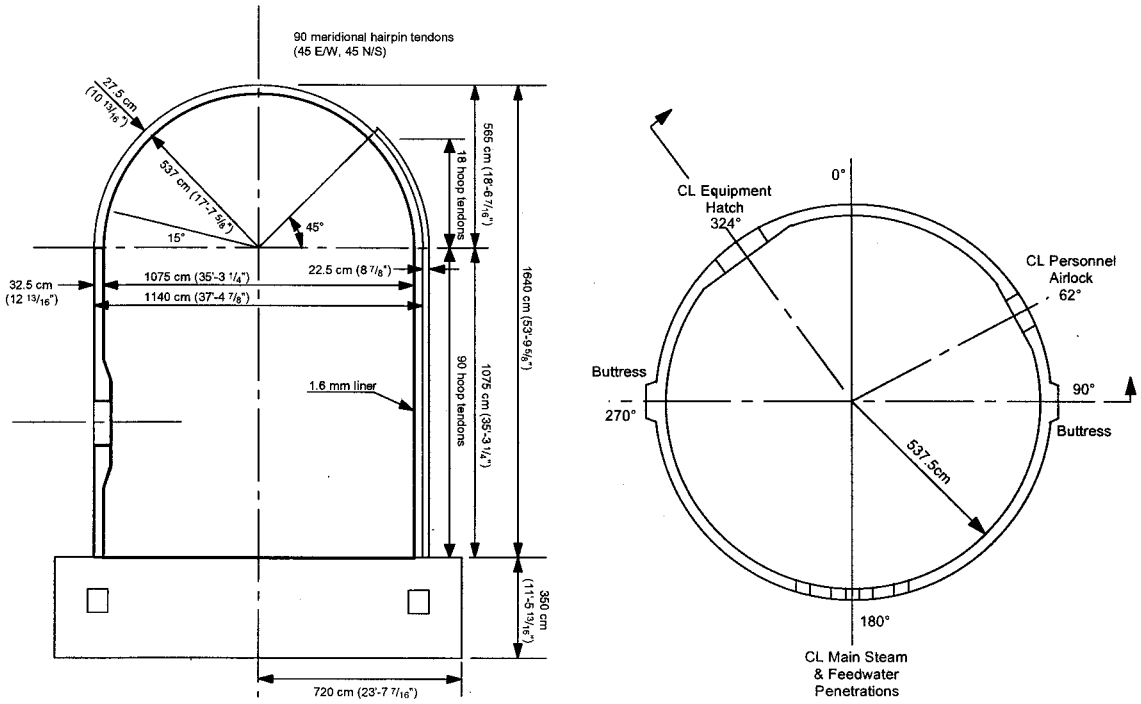

Figure 2.2 PCCV Model Elevation and Cross-Section

Although both NUPEC and SNL (under NRC sponsorship) had conducted component tests of both full-size and scaled penetrations, it was decided that PCCV model would include both functional representation of the major penetrations, namely the equipment hatch (E/H) and the personnel air lock (A/L), and non-functional representation of the main steam (M/S) and feed water (F/W) penetrations. The E/H and A/L penetrations were fully-functional, one-fourth scale models of the penetrations in the prototype, while only the penetration sleeves of the M/S and F/W penetrations, terminated with pressure seating blind flanges, were included in the model. The liner and concrete reinforcing details around these penetrations were also retained in the model.

During construction and instrumentation of the model, primary access to the interior was through the E/H, while the A/L was used to provide heating, cooling and ventilation for personnel working inside the model. The M/S and F/W penetrations provided portals for interior instrumentation cabling, power and, during testing, the pressurization medium. Prior to testing, after the E/H cover was installed and sealed, the A/L provided the means for final egress and sealing of the model with a specially designed pressure seating cover which could be closed from the outside of the model.

Project Schedule

The NUPEC/NRC Cooperative Containment Research Program commenced in June 1991. The tests were conducted at the Containment Technology Test Facility-West at Sandia National Laboratories, Albuquerque, New Mexico. Construction of the PCCV model commenced January 3, 1997 with initial site preparation. Milestones in the construction and testing of the PCCV model include the following:

12 February 1997	First Basemat Pour (F1)
19 June 1997	First Liner Panel Installed
15 April 1999	Final Dome Pour (D3)
12-14 October 1999	Pretest Round Robin Meeting
8 March-3 May 2000	Prestressing
25 June 2000	PCCV Construction Completed
12-14 September 2000	Structural Integrity and Integrated Leak Rate Test
27-28 September 2000	Limit State Test
22 August 2001	Posttest Round Robin Meeting
14 November 2002	Structural Failure Mode Test
3 May 2002	PCCV Demolition and Site Restoration Completed

Design

The Prestressed Concrete Containment Vessel model design was directed by NUPEC with overall responsibility for the design and construction contracted to Mitsubishi Heavy Industries, Ltd. (MHI), Tokyo. Responsibility for the design of the liner and penetrations was assigned to MHI's Kobe Shipyard and Machinery Works while the design of the concrete portions of the model were subcontracted to Obayashi Corp., Tokyo.

The basic philosophy guiding the design of the PCCV model was agreed upon very early in the program. Key elements of this design philosophy included:

- The PCCV model would be a uniform 1:4-scale model of the prototype prestressed concrete containment vessel of Ohi Unit 3.
- Elements of the model which would affect the ultimate strength would be equivalent to the prototype. The model liner would be one-fourth the thickness of the prototype liner. Reinforcing ratios would be maintained and the number and arrangement of the prestressing tendons would, to the extent possible, be identical to the prototype.
- The model should be capable of reproducing the failure modes postulated for the prototype, including

  a) Hoop Tensile failure of the cylinder wall

  b) Bending-Shear failure at the junction of the cylinder wall with the basemat

  c) Shear failure in the basemat above the tendon gallery

  d) Bearing failure at the tendon anchors

  e) Bending-Shear failure at the large penetrations

  f) Bending-Shear at the small penetrations

  g) Liner tearing due to strain concentrations at local discontinuities (stiffeners/anchors, thickened reinforcing plates at penetrations and embedments)

  h) Leakage at penetration seals due to ovalization or distortion of the sealing surfaces.

  Furthermore, to the extent possible, introduction of non-representative failure modes, as a result of scaling or other modeling artifacts, was to be avoided.

The general arrangement of the prototype and representative failure mode locations are shown in Figure 2.3.

While the PCCV model was not 'designed' in the conventional sense, its features were scaled directly from the Ohi-3 design with some simplification to facilitate construction without compromising the objectives of the test. The prototype, Ohi-3 was designed in accordance with the "Draft Technical Code for Concrete Containment Vessels in Nuclear Power Plants" issued by MITI/ANRE in November, 1981. This draft code was formally adopted in 1993 as MITI Notification No. 452. The code is not identical to the ASME/ACI code which governs the design of concrete containments in the US, however, the basic design philosophies are similar, i.e. to ensure that all elements of the containment structure respond essentially elastically (with some minor exceptions for secondary stresses) to the specified design loading conditions.

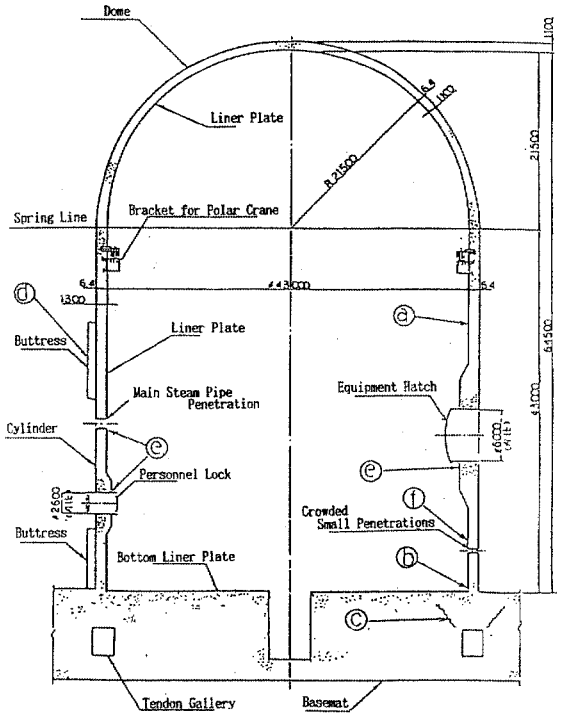

Figure 2.3 Elevation of PCCV Prototype and Potential Failure Locations

Construction of the prototype was also governed by Japanese Architectural Standard Specifications No. 5 and 5N for Reinforced Concrete Work at Nuclear Power Plants. Construction specifications for the PCCV model also followed these standards to the extent possible, however, modifications were made to adapt the specifications to US construction practices.

It is beyond the scope of this report to include all the details of the design and construction specifications. Those details are provided in the test report [1].

The completed PCCV model is shown in Figure 2.4.

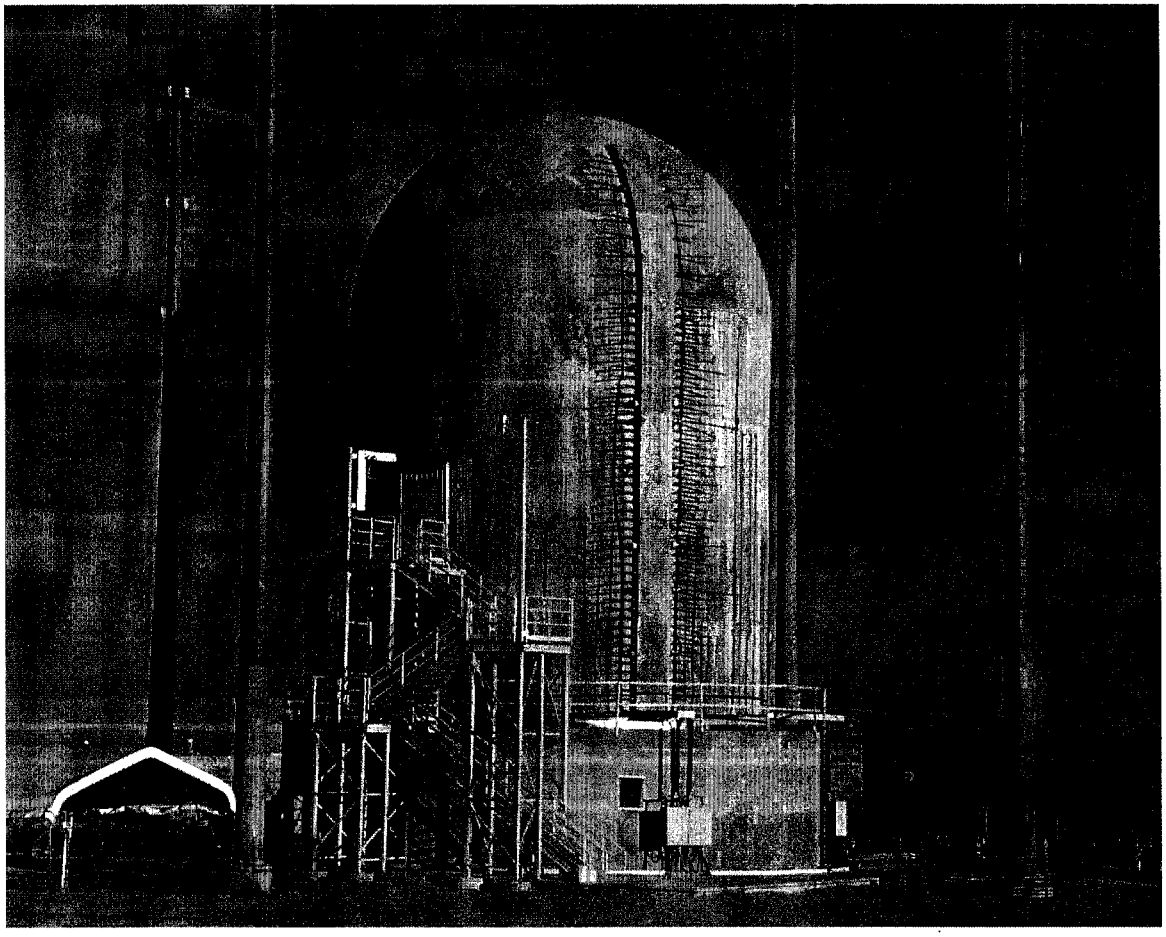

Figure 2.4 Completed PCCV Model

Instrumentation

The basic instrumentation plan was outlined by NUPEC in early 1992 during the initial planning for the PCCV model test. Considering the basic design philosophy, described in Section 2.3, the basic instrumentation plan identified the following measurements to be taken during the PCCV pressure tests:

1. load (internal pressure),
2. displacement,
3. rebar strain,
4. concrete strain,
5. concrete crack mapping,
6. liner and liner anchor strain,
7. tendon force, and
8. temperature

These parameters were to be measured at a number of locations to be able to characterize both the global and local response of the model.

The basic instrumentation plan also specified a grid of azimuths and elevations which would form the basis for the instrumentation layout and provide a scheme for incorporating the nominal gage locations in the individual gage ID's. This basic grid of cardinal lines is shown in Figure 2.6.

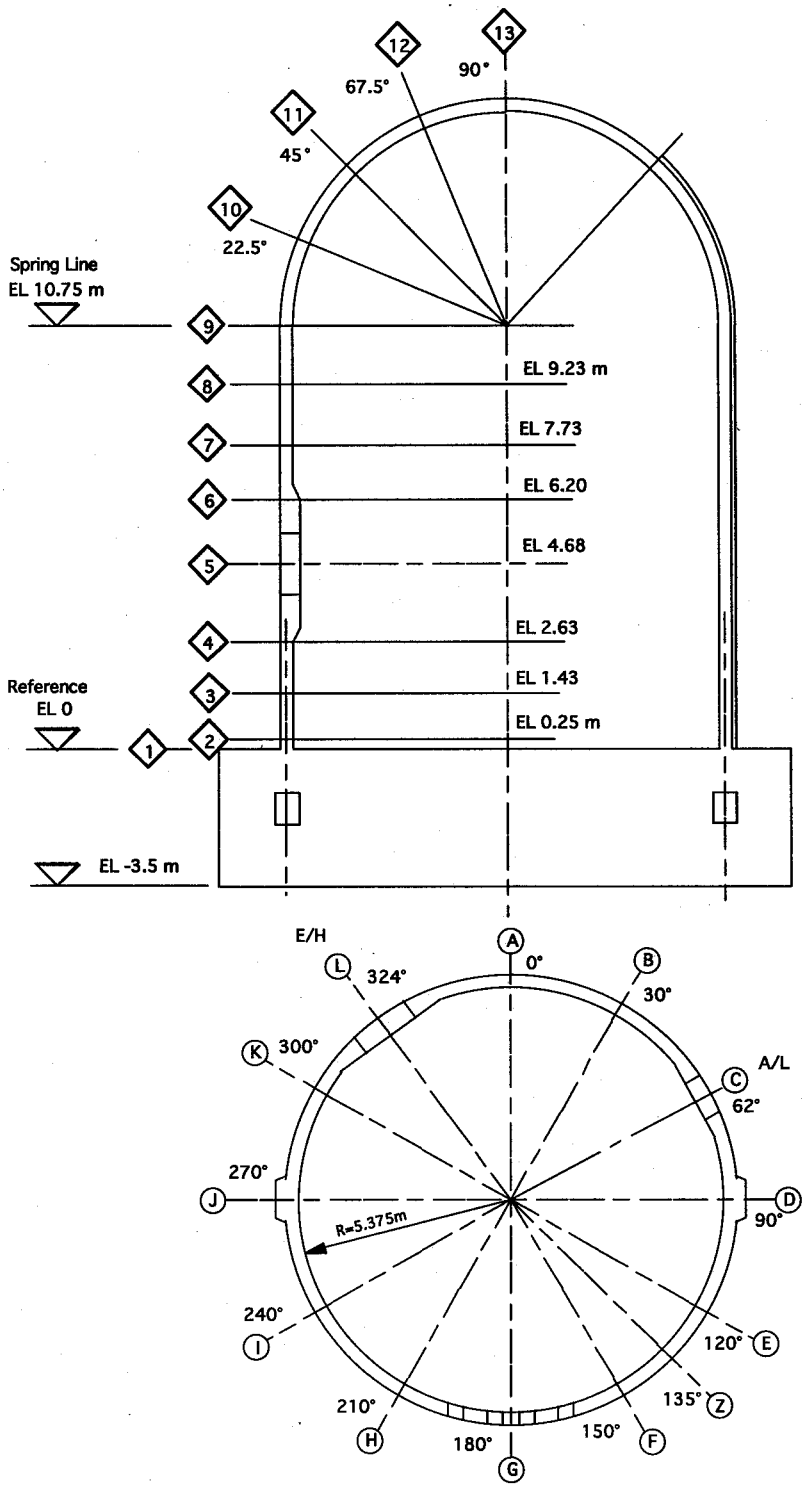

Figure 2.6 Cardinal Instrumentation Layout Lines

Thirteen cardinal elevations were established, from 1 at the top of the basemat (El. 0.00) to 13 at the dome apex. Twelve cardinal azimuths, spaced roughly 30° apart, were established with A at 0° (or 360°) to L at 324°. A thirteenth cardinal azimuth was established at 135° and designated Z. This azimuth was selected as representative of the global axisymmetric response of the containment, based on preliminary analysis results. While the PCCV model is not axisymmetric in terms of geometry and stiffness, Azimuth Z is reasonably distant from any major structural discontinuities and the net hoop prestressing force is close to the average.

Acoustic monitoring was not specified in the basic instrumentation plan but it was agreed to incorporate it into the final instrumentation plan to allow monitoring of the entire structure since it was likely that damage could occur at locations which were not monitored via other methods. The specific goals of the acoustic monitoring system were to:

- detect tendon wire breaks
- detect rebar breaks
- detect concrete cracking and crushing
- detect liner tearing and leakage

Acoustic monitoring of the PCCV model during both the prestressing and low and high pressure tests was performed Pure Technologies Inc. of Calgary, Canada under a turn-key contract. Pure Technologies developed the SoundPrint® acoustic monitoring system and has extensive experience in acoustically monitoring structures, especially prestressed concrete structures such as parking garages and bridges. This system was run independently of the main DAS. The system consisted of the acoustic sensors, essentially piezo-electric accelerometers bonded to the structure and connected to a separate data acquisition system. One of the unique features of this system is the capability to perform real-time data processing and analysis to identify event types and locations. Thirty-two sensors were glued the external surface of the model to monitor and 16 sensors were placed inside the model.

The nominal locations of the gages are shown in Figures 2.7 to 2.12. A detailed description of the instrumentation is provided in the test report [1]. The total number of each type of instrument installed on the PCCV Model is shown in Table 2.1.

Table 2.1 PCCV Instrument Summary

Instrument Type		**Number of Gages**
Strain	Liner	559
	Rebar	391
	Tendons (Tensmeg)	37
	Tendons (wire)	156
	Concrete	94
Displacements		101
Load Cells (1/3 of Tendons)		68
Temperature and Pressure		100
Acoustic		54
Total		**1560**

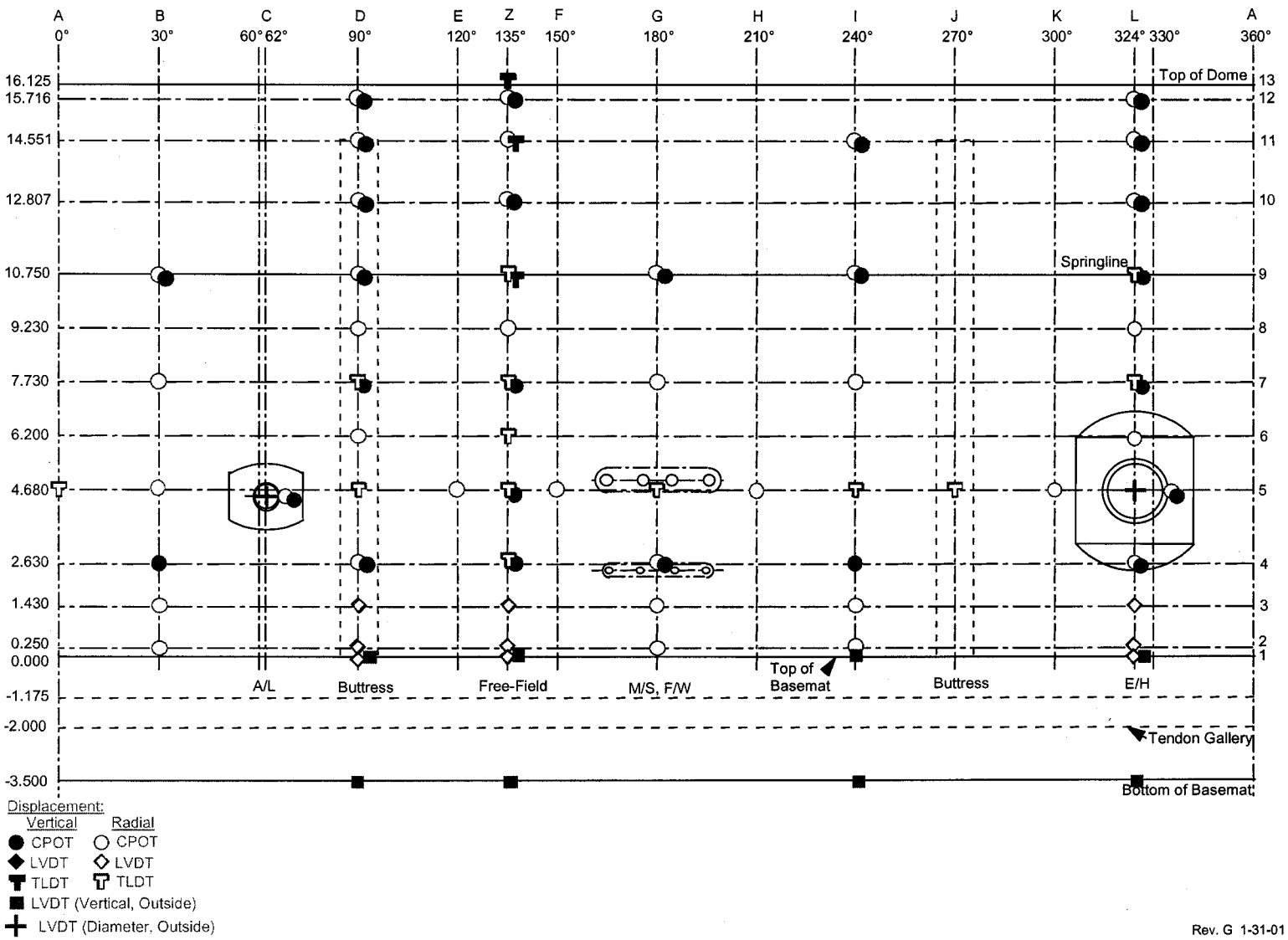

Figure 2.7 Displacement Instrumentation Locations

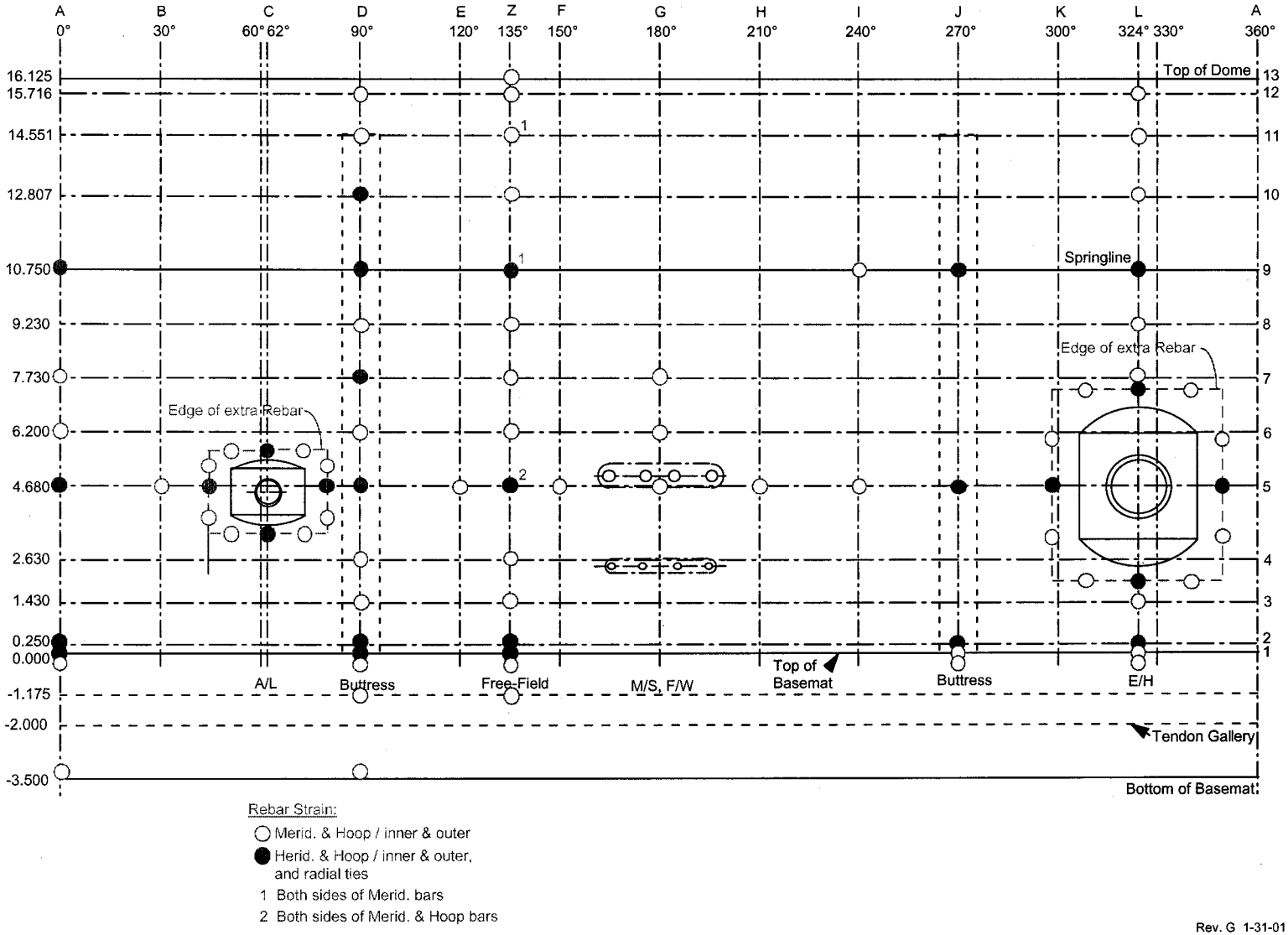

Figure 2.8 Rebar Instrumentation Locations

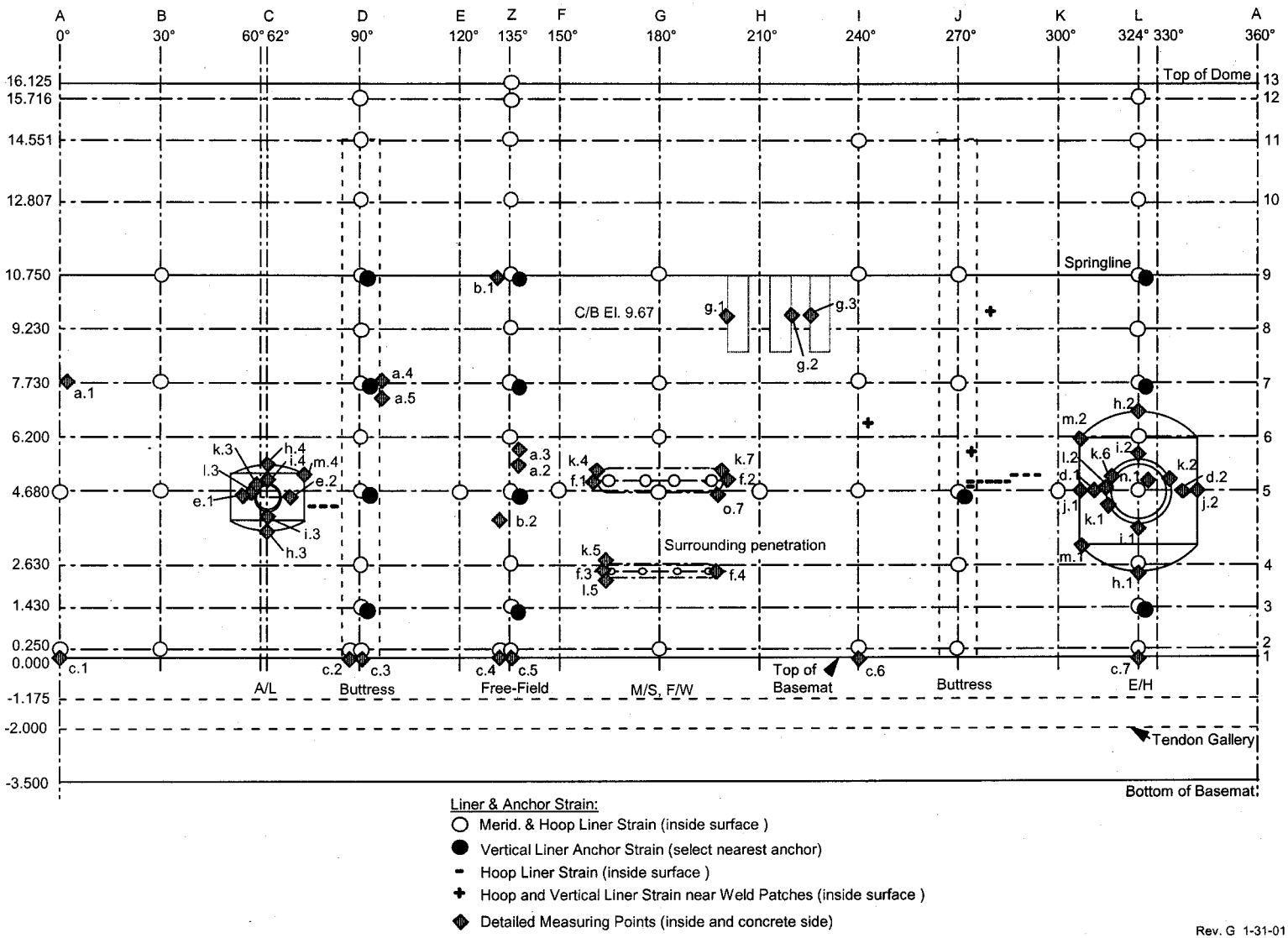

Figure 2.9 Liner and Liner Anchor Instrumentation Locations

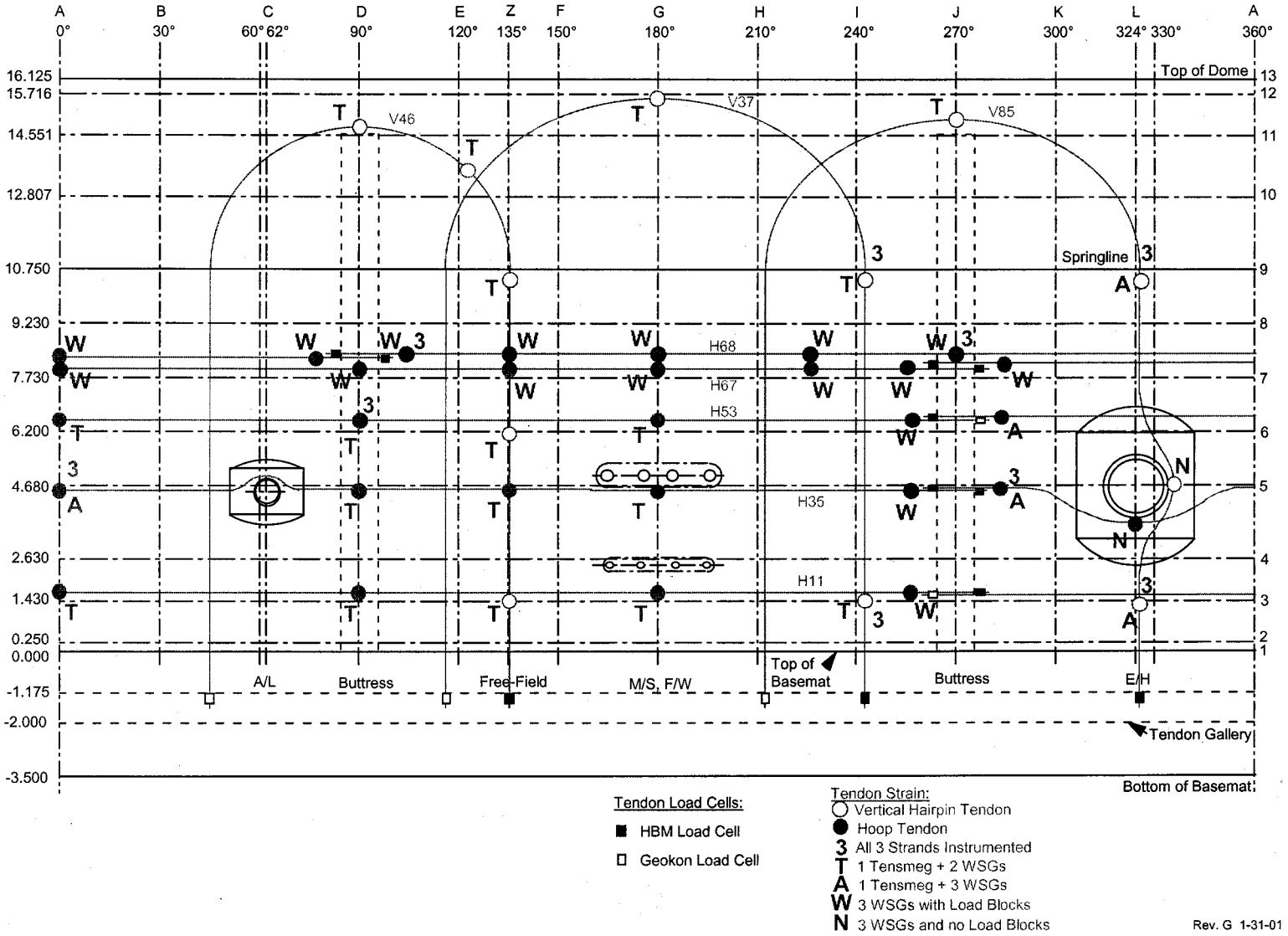

Figure 2.10 Tendon Instrumentation Locations

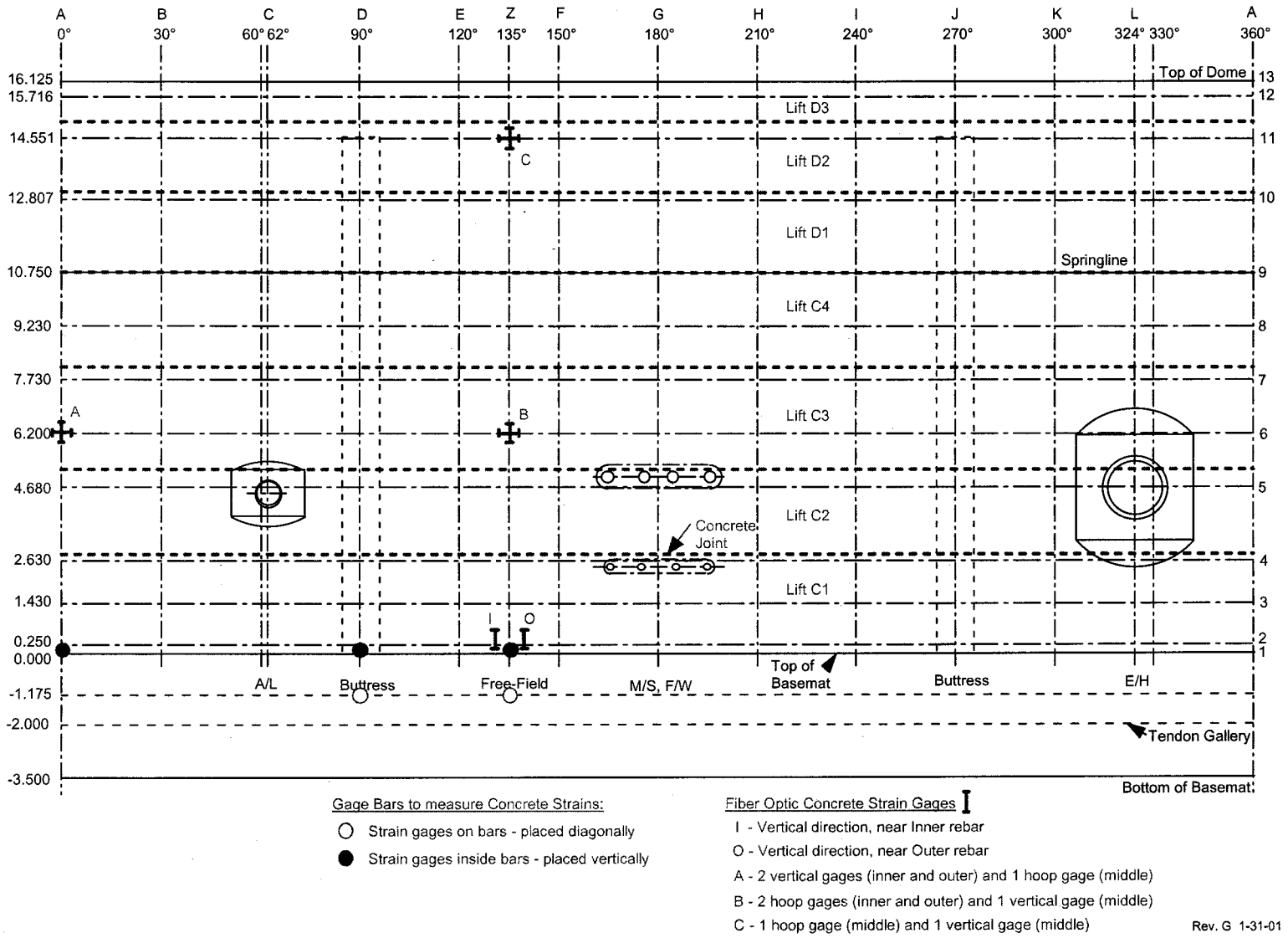

Figure 2.11 Concrete Instrumentation Locations

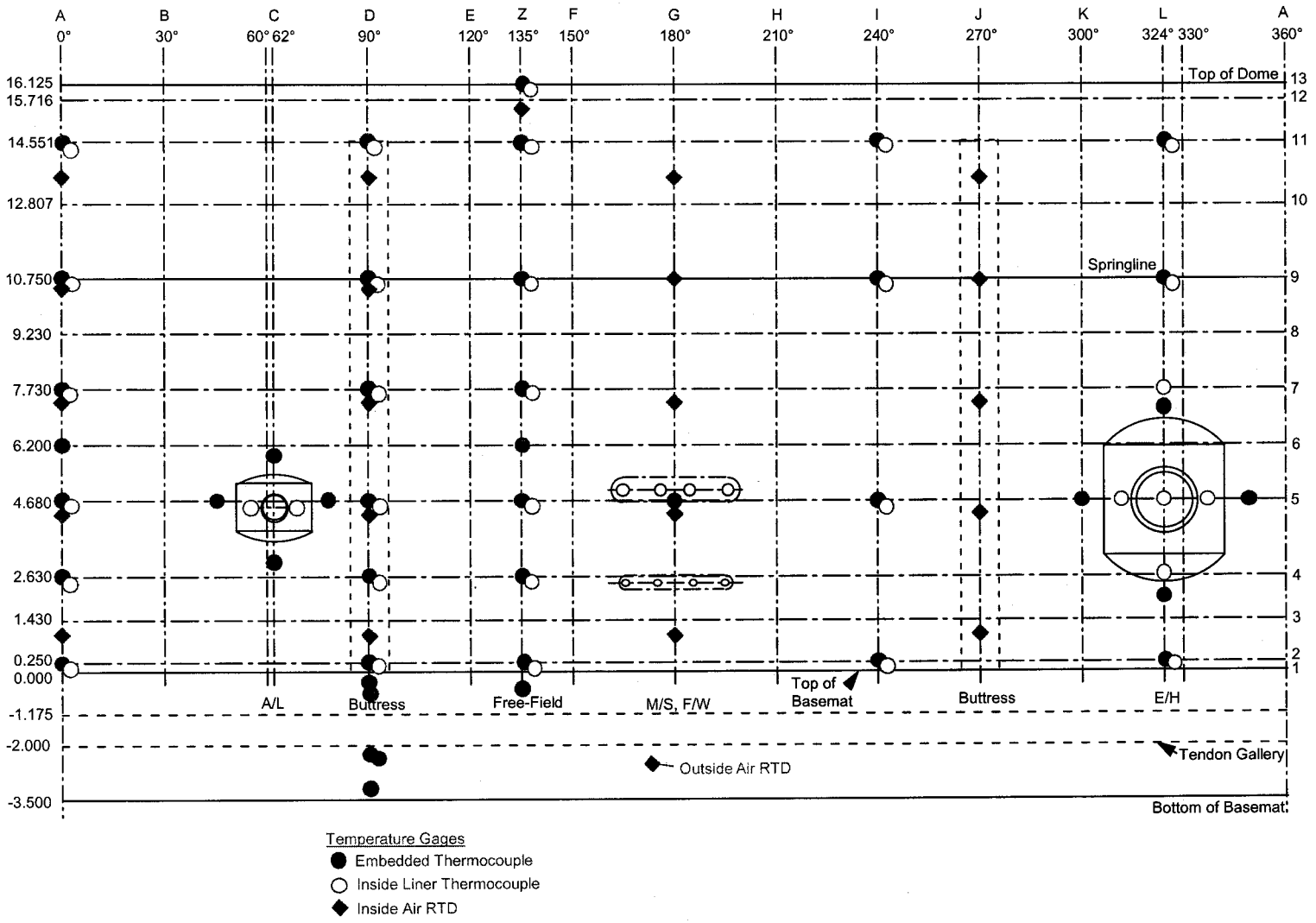

Figure 2.12 Temperature Instrumentation Locations

PCCV TESTING

For the test program, it was necessary to decide whether both thermal and pressure loads would be applied to the model, either separately or simultaneously, what the pressurization medium should be, and whether the transient characteristics of these loads should be considered. Programmatically, the decision to perform a **static, pneumatic** overpressurization test at **ambient temperature** was dictated by risk and cost considerations and previous experience.

It should be noted that the **pneumatic** Limit State Test was the final test in the original program plan. This test was terminated following a functional failure, i.e. a leak, in the PCCV model, with only limited structural damage occurring. Subsequently, it was decided to re-pressurize the PCCV model, prior to demolition, in an attempt to observe larger inelastic response and, possibly, a global structural failure. This test was a combined **pneumatic-hydrostatic** test, where the PCCV model was sealed inside with an elastomeric membrane and filled nearly full with water, to reduce the volume of gas to be pressurized, and nitrogen gas was used to generate the overpressure.

The effect of elevated temperatures will be considered in Phase 3 of the ISP.

Test Planning

The basic objectives of the PCCV test were specified by NUPEC in the Master Project Plan. The stated objective of this plan was to... "investigate the ultimate behavior of PCCV under pressure beyond the design basis accident and to prove the pressure retaining capacity of PCCV". After extensive discussions between NUPEC, the NRC and SNL, a series of three tests were agreed upon. These tests are defined as follows and are illustrated in Figure 3.1.

- A leak check and System Functionality Test (SFT) @ 0.5 Pd (2.0 kgf/cm2 or 28.4 psig)
- A Structural Integrity Test (SIT) @1.125 Pd followed by an Integrated Leak Rate Test (ILRT) @ 0.9 Pd
- A Limit State Test (LST) to the static pressure capacity of the PCCV model (or the pressurization system, whichever comes first)

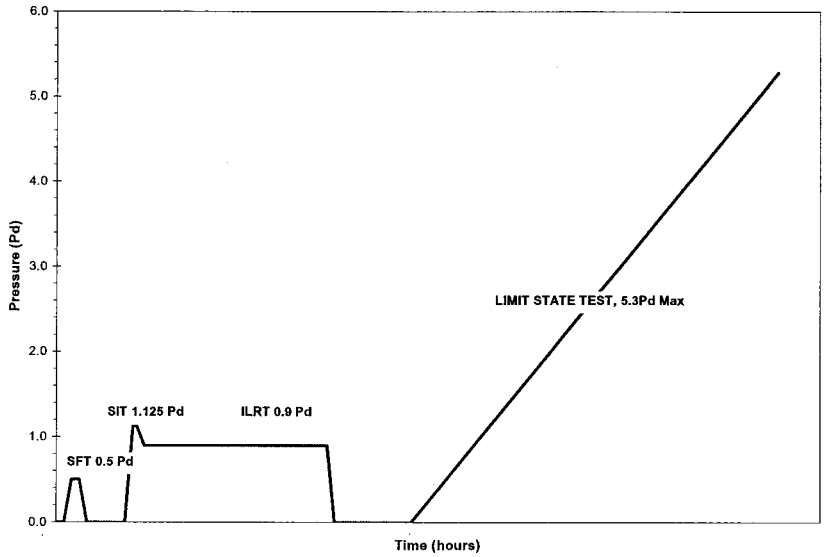

Figure 3.1 Pressurization Plan

A fourth test was added to the test program after the conclusion of the LST. After careful evaluation of the LST results, NUPEC, the NRC, SNL and their technical advisors concluded that all of the objectives of the test program were not fully met. SNL was tasked with designing and conducting a test which would allow the PCCV model to be pressurized beyond the level reached during the LST in an attempt to observe greater inelastic response of the model and, hopefully, generate a structural failure mode. This Structural Failure Mode Test (SFMT) is described in Section 3.2.2.

Test Operations

For purposes of ISP48, only the Limit State Test and, secondarily, the Structural Failure Mode Test are of interest. Details and results of the low pressure tests are provided in the test report [1].

Limit State Test

The Limit State Test (LST) was designed to fulfill the primary objectives of the PCCV test program, i.e. to investigate the response of representative models of nuclear containment structures to pressure loading beyond the design basis accident and to compare analytical predictions to measured behavior. The LST was conducted after the SIT and ILRT were completed and the data from these tests evaluated. The PCCV model was depressurized between the SIT/ILRT and the LST. The LST began at 10:00 AM, Tuesday, September, 26, 2000 and continued, without depressurization, until the test was terminated just before 5:00 PM on Wednesday, September 27.

The pressure and average temperature time histories during the LST, including depressurization, are plotted in Figure 3.2. The LST followed the planned pressurization sequence up to the point where the model began leaking.

Initially, the model pressurization sequence matched the pressurization steps followed for the SIT to allow for comparison of the model response to two identical cycles of loading. Pressurization continued in increments of approximately 0.2Pd until a pressure of 1.5 Pd (6.0 kgf/cm2 or 85.3 psig) was reached at approximately 4:30 PM. At this pressure, the first planned leak check was conducted by isolating the model and monitoring the temperature and pressure. After approximately 3 hours, a leak rate of 0.48% mass/day was calculated. Considering previous experience from the ILRT, which demonstrated that thermal expansion of the model during the day yielded apparent leak rates in this range, the results were interpreted to indicate that the PCCV model was leak-tight.

Pressurization of the model continued in increments of approximately 0.1Pd until a pressure of 2.0Pd (8.0 kgf/cm2 or 113.8 psig) was reached at approximately 11:00 PM. At this pressure the model was again isolated to perform a planned leak check. This leak check was also planned to be held for 8 hours to allow the test team to partially stand down for a rest period. A 'skeleton crew' consisting of the Test Conductor (TC), Data Acquisition System Operator (DO) and Nitrogen Supply Operator (NO) continued to monitor the response of the model and all other systems until approximately 7:00 AM on September 27. This pressure hold and leak check was also selected below the lower bound prediction for the onset of structural yielding (i.e. yielding of the rebar or tendons) to ensure that the model would remain relatively stable during this period. After approximately 8 hours, the calculated leak rate was 0.003%, i.e. essentially zero. This confirmed the interpretation of the leak check results at 1.5 Pd and also demonstrated the greater accuracy of the leak rate results when the model is thermally stable.

Pressurization of the model resumed at 7:00 AM in increments of 0.1Pd, with increasing dwell time between pressure steps, ~30 minutes, required to meet the gage stability criteria. As the pressure was increased to the next planned leak check at 2.5Pd, liner strain gages in the vicinity of the E/H (LSI-C-K5-12) began registering rapidly increasing strains in excess of 1%. At 2.4Pd, the acoustic system operator (AO) reported hearing a change in the acoustic output which might indicate that "something had happened". At approximately 10:00 AM at a pressure of 2.5Pd (10.0 kgf/cm2 or 142.2 psig), the

model was isolated for the third planned leak check. After approximately 1-1/2 hours, a fairly stable leak rate of 1.628% mass per day was calculated. The leak rate calculations at 1.5, 2.0 and 2.5Pd are plotted in Figure 3.3. Coupled with the confirmation from the AO that the acoustic data continued to confirm that some new event had occurred, it became clear that the model was leaking, most likely from a tear in the liner in the vicinity of the E/H. Plots of the output of the four internal acoustic sensors surrounding the E/H at 2.3, 2.4 and 2.5 Pd are shown in Figure 3.4.

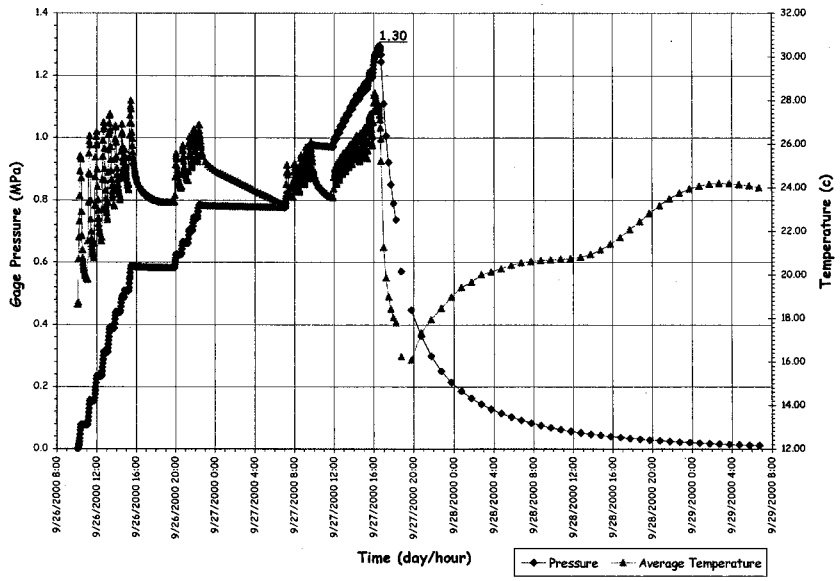

Figure 3.2 Limit State Test Pressure and Average Temperature

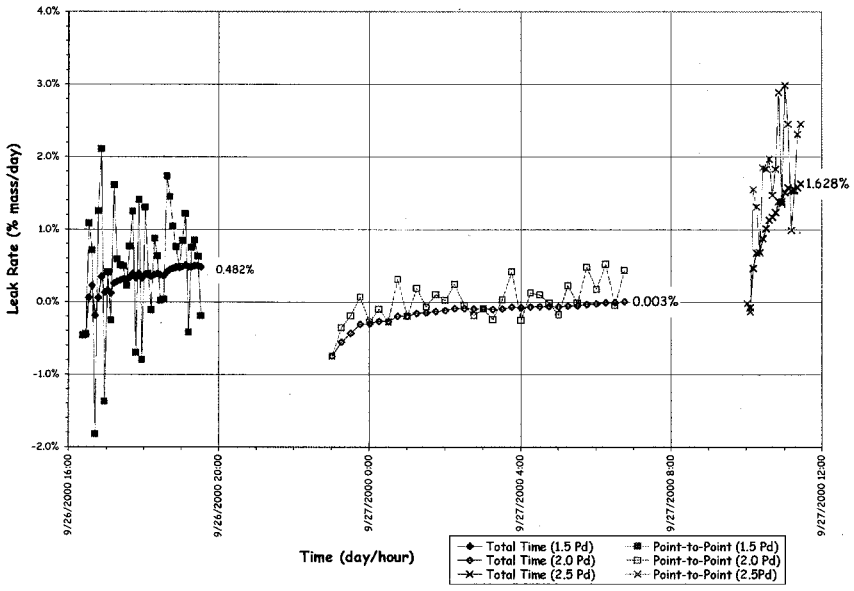

Figure 3.3 LST Calculated Leak Rates at 1.5, 2.0 and 2.5 Pd

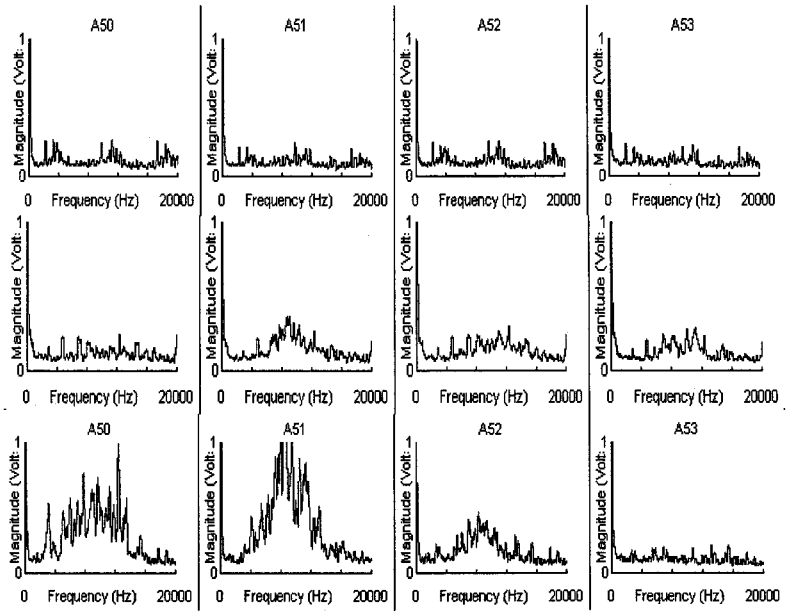

Figure 3.4 Internal Acoustic Sensor Signals @ the Equipment Hatch

After consulting with NUPEC and the NRC, the Test Conductor concluded that the model had functionally failed between 2.4 and 2.5 Pd and directed a change in the pressurization plan. Since the model was leaking, the next goal was to pressurize the model as high as possible to collect data on the inelastic response of the structure and to observe, if possible, a structural failure mode. Pressurization continued in increments of 0.05 Pd, as planned, however, the gage stability criterion was abandoned and the hold time at each pressure step was reduced to less than 10 minutes.

The PCCV model was pressurized to approximately 3.0Pd with increasing evidence of leakage and increasing liner strains. At 3.0Pd it became increasingly difficult to pressurize the model, and the nitrogen flow rate was increased to 99 std.m3/min (3500 scfm). At this flow rate, the pressure in the model was increase to 3.1Pd, however the pressure dropped steadily after reaching this pressure. The leak rate at this point was estimated to be 100% mass/day

The nitrogen flow rate was increased to the maximum capacity of the pressurization system, 142 std.m3/min (5000 scfm), and the pressure was increased to slightly over 3.3 Pd before the leak rate exceeded the capacity of the pressurization system. The pressure time history and flow rates during the final phase of the test are shown in Figures 3.5 and 3.6. Since it was no longer possible to increase the pressure in the model and the supply of nitrogen was nearly exhausted, the TC made the decision to begin terminating the test.

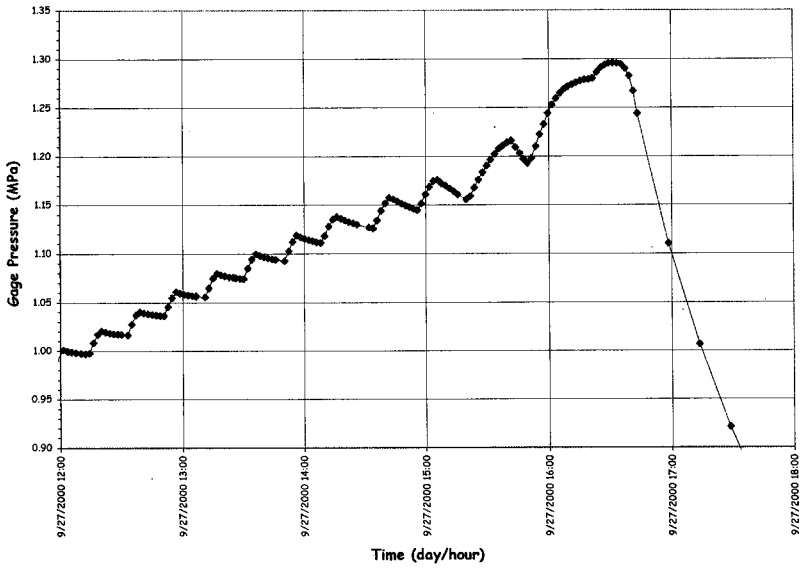

Figure 3.5 LST Pressure Time History, 2.5 to 3.3 Pd

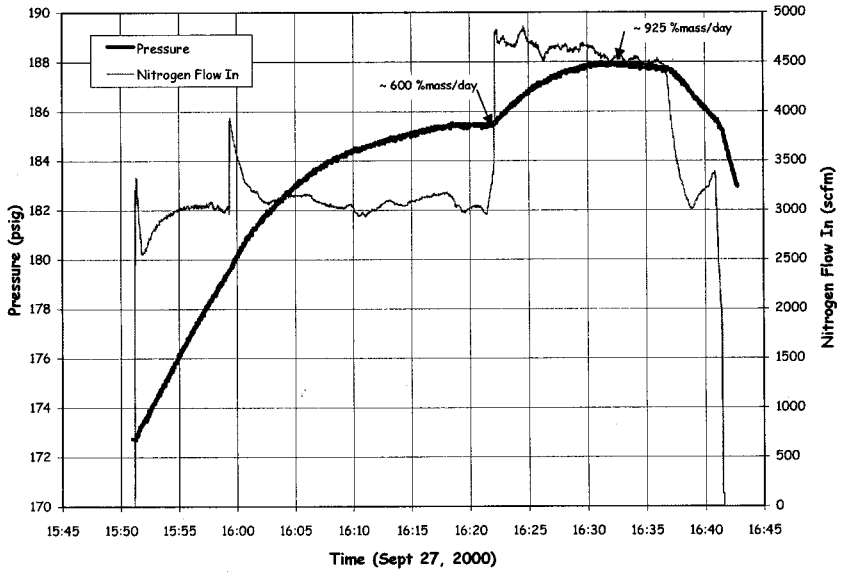

Figure 3.6 LST Pressure and Flow Rates @ Maximum Pressure

The isolation valve was closed and the model was allowed to depressurize on its own. The terminal leak rate was estimated to be on the order of 900% mass/day. (The maximum flow rate of nitrogen, 5000 scfm, is equivalent to a leak rate of 1000% mass/day.) Estimated leak rates during the final pressurization and depressurization phases are shown in Figures 3.7 and 3.8.

After the model pressure was reduced to 1.0 Pd, test personnel were able to enter the test site to inspect the model close-up. Nitrogen gas was observed (heard and felt) escaping through many small cracks in the concrete, around the penetration sleeves and at the tendon anchors. It was speculated that the liner acted as a leak chase, allowing nitrogen gas escaping through a tear or tears in the liner to travel between the liner and the concrete until it found an exit path through a crack in the concrete or a conduit in the tendon duct.

At maximum pressure, local liner strains of up to 6.5% were recorded and global hoop strains (computed from the radial displacement) at the mid-height of the cylinder averaged 0.4%. While large liner strains were observed and it was suspected that the liner might have torn in several locations, the remainder of the structure appeared to have suffered very little damage with the exception of more extensive concrete cracking at some locations. The largest crack was observed to the left of the E/H, shown in Figure 3.9.

After the model had completely depressurized, the model was purged with fresh air, the E/H was removed and detailed posttest inspection of the inside of the model began. A cursory inspection of the model identified 26 discrete tears at 18 separate locations.

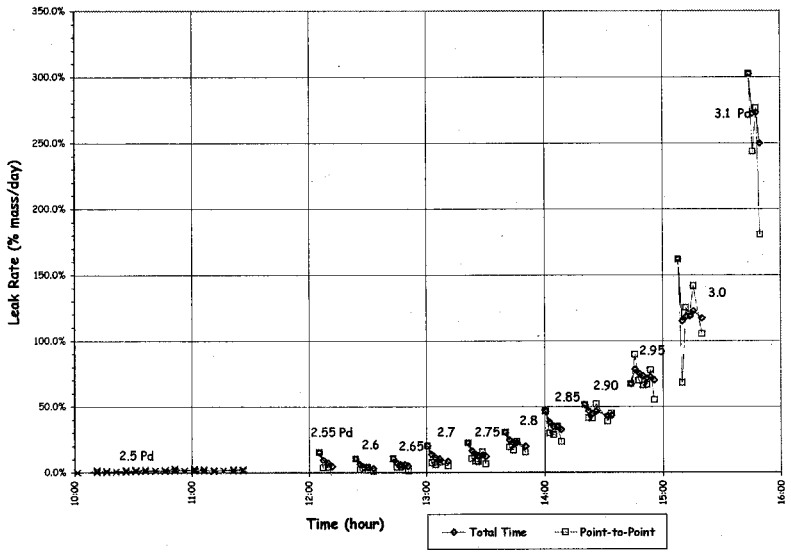

Figure 3.7 LST - Estimated Leak Rates (2.5-3.1 Pd)

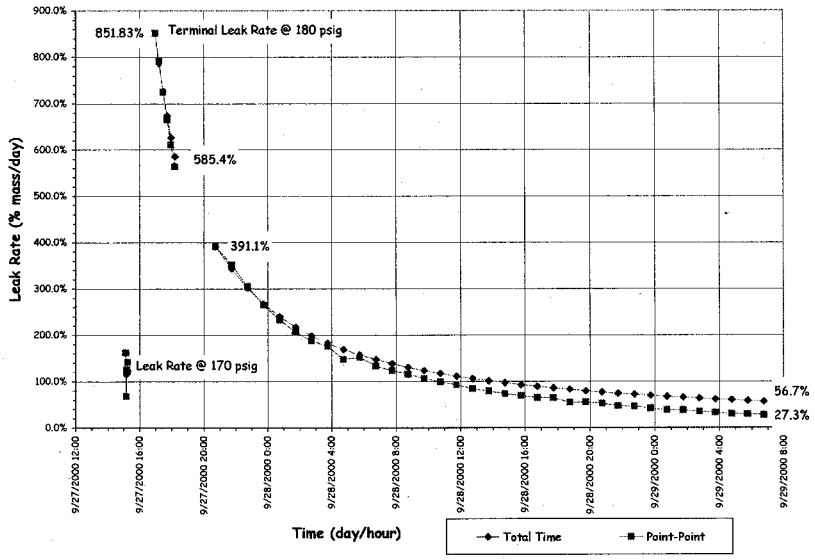

Figure 3.8 LST Estimated Terminal Leak Rates

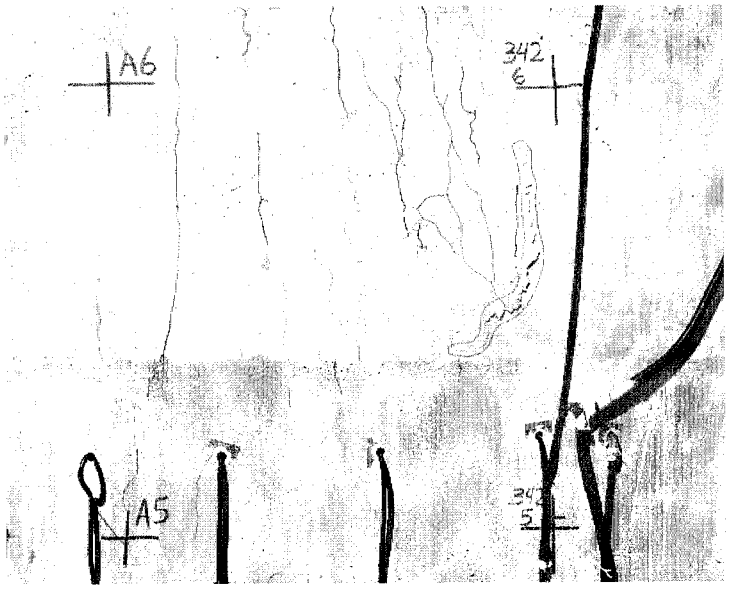

Figure 3.9 Post-LST Cracks @ Az. 350°, El 4680 to 6200 (Grid 45)

Structural Failure Mode Test

Almost immediately after the completion of the LST, there was a recognition that while the PCCV model had demonstrated its capacity to resist pressures well above the design pressure and confirmed, arguably, liner tearing and leaking as the functional failure mode. The test objectives were not, however, fully met with respect to observing large inelastic deformations, for comparison with analyses, and witnessing the structural failure mode of the PCCV model. SNL was tasked by NUPEC and the NRC with investigating the possibility of conducting a second limit state test.

Two issues needed to first be addressed to determine the technical feasibility of reloading the PCCV model. First was the question of whether the LST had caused sufficient damage to the structure such that any data obtained by reloading the structure would be compromised and of limited value for comparison with analytical results. The LST data was thoroughly reviewed and, with the exception of the liner and cracking of the concrete, there was no evidence of excessive structural damage. There was also no indication that the tendons had been strained beyond their yield limit and, except for a few isolated measurements, the same was true for the rebar. (Only 27 of the rebar gages registered strains in excess of 0.4%, with a maximum of 1.7%-which likely reflects the local perturbation caused by the presence of the gage.) Considering the radial displacement at the mid-height of the cylinder, compared to the pretest Round Robin predictions in Figure 3.10, clearly illustrates that the structure was on the verge of global yielding but had not undergone a significant amount of inelastic deformation. (In this context, only the yielding of the steel and rebar is being addressed. Obviously, the loss in stiffness that occurs with global concrete cracking at approximately 1.5Pd, cannot be recovered.) This was a positive finding for the prospect of reloading the model since most, if not all, of the capacity of the rebar and tendons was still available. Another important conclusion from the consideration of the LST data was that, if in fact, the model was on the verge of global structural yielding, the additional pressure required to cause larger inelastic deformations was not very large, perhaps only on the order of a few tenths to half the design pressure, i.e. an additional 1.0 to 2.0 kgf/cm2 (14 to 30 psig).

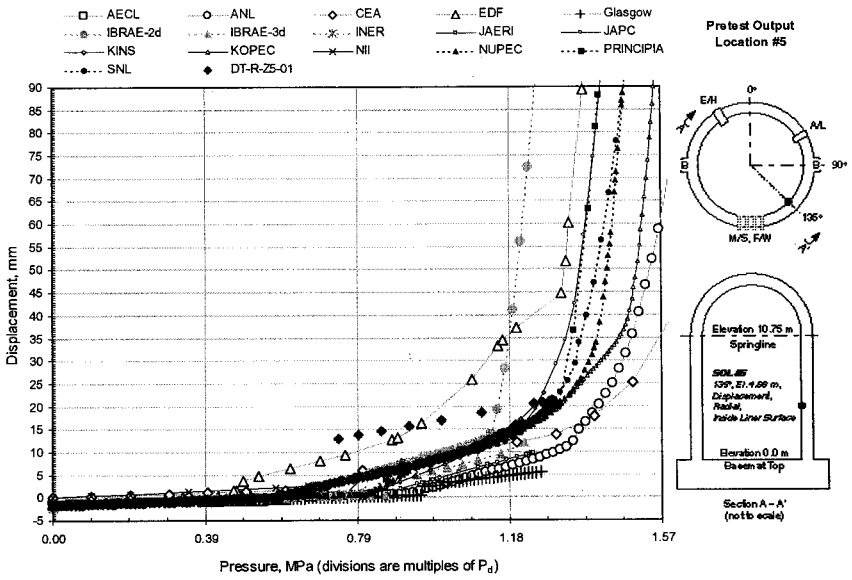

Figure 3.10 LST Radial Displacement @ Az. 135°, El. 4680

The second issue was the requirement to re-seal the model in order to re-pressurize it. Since large sections of the liner were removed as part of the post-LST inspection, the liner was no longer capable of providing an effective membrane to prevent premature leakage. Furthermore, even if the liner tears and cutouts were locally repaired or sealed, it was clear that other areas of the liner were susceptible to tearing at the same pressures (or perhaps even at lower pressures) which caused the liner to tear during the LST. It was necessary, therefore, to devise a cost-effective method of completely replacing the liner function in order to proceed with plans to re-pressurize the PCCV. The replacement 'liner' was also required to ensure that the model could be re-pressurized to a level beyond the maximum pressure achieved during the LST. (A corollary of this conclusion was that there was no further need to investigate the response of the liner and the instrumentation applied to the liner could be abandoned.)

Furthermore, the SFMT had to be completed within the current program budget and schedule for completing the project. The concept that was developed to re-pressurize the PCCV model is illustrated in Figure 3.11.

The concept consists of sealing the interior surface of the liner with an elastomeric membrane after removing all interior transducers on the liner. After closing the E/H and A/L, the model would be filled with water to 1.5m (5 ft.) from the dome apex, approximately 97% of the interior volume 1,591,000 ltr (350,000 gal). Filling the model with water would provide several advantages:

- The leak rate of water through any tears in the liner is much less than the corresponding leak rate of gas. Therefore, even if a leak path developed, the flow rate capacity of the pressurization system should be adequate to compensate for the leak.
- By maintaining a gas pocket in the model, the pressurization system used for the LST, using nitrogen gas as the pressurization medium, could be used for the SFMT without any major modifications. The only modification required was the installation of additional piping inside the model to allow the gas to be introduced at the dome apex and a pipe to fill (and drain, if necessary) the model. Reducing the volume of gas to be pressurized reduced the demand on the pressurization system in the event of a leak and also reduced the volume of gas required to conduct the test. In the case of the SFMT, a pressurized tube trailer could be used instead of the more expensive liquid nitrogen source required for the LST.

- Since the pressurization system could compensate for small leaks, it was not essential that the elastomeric liner be completely leak tight, only that the leaks were small enough to allow the model to be pressurized to the desired level.
- Leaks of water would be readily visible compared to gas leaks.
- In the event of a catastrophic rupture of the PCCV model, the energy stored in the model nearly filled with water was much less than the stored energy if pressurized to the same level with only gas. As a result, the safety exclusion zone around the model could be reduced if necessary.

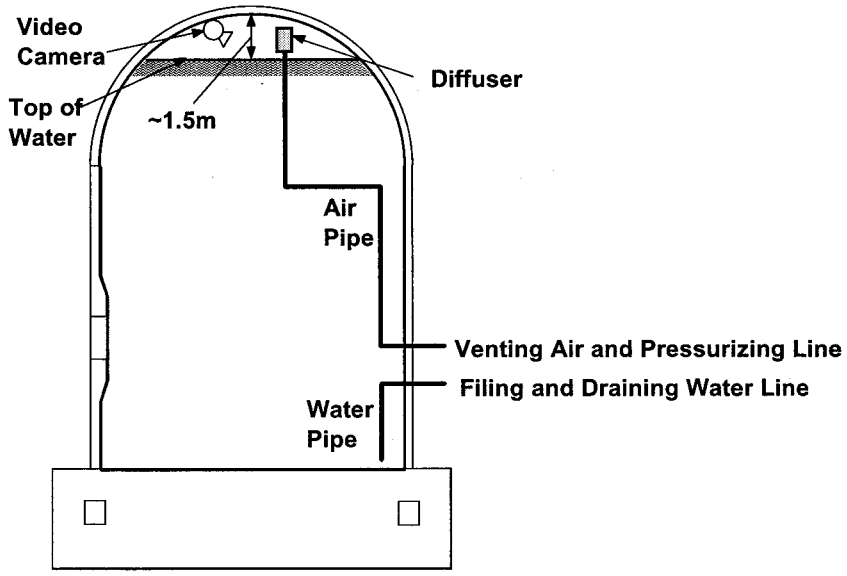

Figure 3.11 PCCV Structural Failure Mode Test Concept

At the same time, filling the model with water had some disadvantages:

- Any instruments or other electrically powered components (lights, cameras, etc.) inside the model had to be removed or completely sealed.
- The internal pressure would not be uniform due to the hydrostatic head, approximately 1.4 kgf/cm2 (20 psig).

These disadvantages, however, were not deemed to be significant, and efforts were then focused on selection of a suitable liner. A number of vendors were contacted and two proposals for sealing the liner were considered. One proposal was to prefabricate a 5 mm (200 mil) PVC sheet liner which would be installed inside the model by heat welding the seams and sealing around the penetrations using ring clamps. The second proposal was to apply a sprayed-on two-part polyurea coating, also a minimum of 5 mm (200 mil) thick. After considering both proposals, the sprayed-on lining was selected since it could be more readily adapted to the irregular liner surface and had significant cost and schedule advantages. The elastomeric liner was installed by Ershigs Corporation in August, 2001 after the interior model inspection was completed and all the surface instrumentation was removed.

After the elastomeric liner was installed the interior instrumentation for the SFMT was installed. A reduced set of instruments was selected to allow one data acquisition computer to scan all the gages in less than 60 seconds to support 'rapid' pressurization of the model. The instrumentation suite for the SFMT consisted of the following:

- All interior gages used for the LST were removed or abandoned. These were replaced by 20 water proof displacement transducers (LVDTs), 17 radial and 3 vertical, located as shown in Figure 3.12.
- Five interior pressure transducers, three below water at the base, cylinder mid-height and springline, two to measure the gas pressure.
- Two interior video cameras and lights to monitor the E/H and the water surface
- 18 Exterior Liner Strain Gages:
    - 14 @ Meridional @ Wall-Base junction
    - 4 @ Hoop stiffener details
- 82 Rebar Strain Gages (Standard Output Locations):
    - 35 rebar gages (all 22 SOL plus 13 meridional at Wall-Base)
    - 47 Gage bars (all surviving)
- All surviving Tendon strain gages and all Load Cells
- Soundprint® acoustic monitoring (external sensors only)
- Concrete Strain (6 SOFO gages)
- Four external digital video cameras at 0°, 90°, 270° and 360°, completely covering the PCCV cylinder wall.

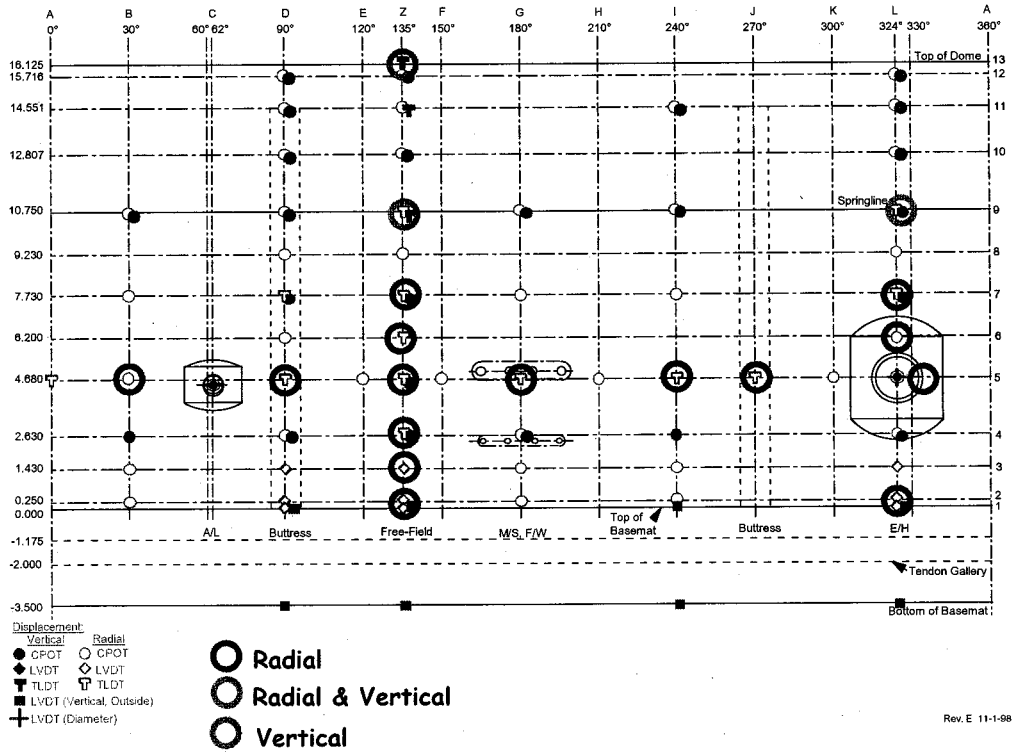

Figure 3.12 SFMT Displacement Transducer Layout

After completing the installation and completing all test-readiness checks, the equipment hatch cover was installed and after sealing the airlock, a low pressure pneumatic test was conducted to check for leaks on October 3, 2001. The leak test began at approximately 09:30 and a leak was detected (via the

acoustic system) at approximately 0.2 Pd (~12 psig). Pressure was increased to the target pressure of 0.5Pd (30 psig) at which time the vessel was isolated and monitored for a 24 hour leak test. The acoustic system (multiple sensors) continued to output signals consistent with a leak in the model and several potential leak locations were identified.

Once it was determined that the model was stable, the nitrogen supply was isolated and close inspection of the model was conducted. Through a combination of visual/auditory inspection, hand-held acoustic monitoring and application of soap-water solution, a number of locations where nitrogen gas was leaking from the model were discovered:

- The largest apparent leak was from a crack on the left-hand side of the 90-degree buttress at an elevation of approximately 6 meters (20 ft.) above the top of the basemat (Level 6 in our cardinal coordinate system). This leak was the first detected by the acoustic system and was immediately confirmed during the close-up inspection
- Secondary leaks, identified by the acoustic system, were confirmed at 150-degrees/3 and 6 meters (10 and 20 ft) and 210-degrees/4.5 meters (15 ft). These leaks appeared to be through previously existing cracks in the concrete. The leak at 150-degrees was along the horizontal construction joints between C1, C2 and C3 as well as along a vertical crack extending between C2 and C3. The leak at 210-dergrees also appeared to be through a previous crack.
- The acoustic system also suggested leaks at 300-degrees/1 to 2 meters (3 to 6-1/2 ft) and 360-degrees/0 meters, but close-up examination could not confirm leakage at either of these locations.
- During the close-up inspection, we also detected a leak at 30-degrees/5 meters (16 ft) which was not initially identified by the acoustic system.
- Close-up inspection of the penetrations also revealed leakage at the feedwater penetrations. There was no evidence of leakage at the E/H, A/L or M/S penetrations.

These results indicated that, in spite of the manufacturer's quality control procedures coupled with detailed visual inspection (individual locations which appeared suspect were also sealed with RTV prior to closing the model), the sprayed-on liner was not impermeable and once the gas escaped through the sprayed-on and steel liners, it migrated between the steel and concrete until it was able to find an exit path. It did not appear that the pressure was high enough to tear the sprayed-on liner when a leak was first detected.

The calculated leak rate was initially 70% mass/day at the maximum pressure of 2.1 kgf/cm2 (30 psi) decaying to 45% at 0.77 kgf/cm2 (11 psi) over 24 hours. The sound levels as detected by the SoundPrint system, which are roughly proportional to the rate of gas escaping, indicated a stable leak rate which was, to a large extent, independent of the pressure.

Based on these results, it was concluded that the leak was most likely due to a pre-existing hole(s) in the sprayed on liner which did not increase (or decrease) significantly during pressurization or during the leak test. (The equivalent orifice size reduced from about 6mm (0.25") at 2.1 kgf/cm2 (30 psi) to 5mm (0.20") at 0.8 kgf/cm2 (12 psi), based on the calculated leak rates.) As a result, it was decided that the SFMT could be conducted without repairing the sprayed-on liner and still have a reasonable chance that the leak would not grow significantly and overwhelm the capacity of the pressurization system. (Nevertheless, during an un-scheduled one-month postponement of the SFMT, the surface was re-tested with a 'spark-tester' and a few small holes were discovered and sealed with RTV. The model was then resealed and readied for filling with water.)

Filling of the PCCV with water and the SFMT began at approximately 09:00 November 6, after the initial data scan was taken, and continued until November 8, 2001. Slow leaks of water were initially observed late November 6, after the model was about one-fourth full, however, the amount of water

leaking was not significant. The pressure time histories at various elevations in the model from the start of filling up to the SFMT are shown in Figure 3.13. This figure illustrates the hydrostatic head and also reflects the slight loss of water due to leaks. The water level was 'topped off' on November 12, prior to the start of the SFMT.

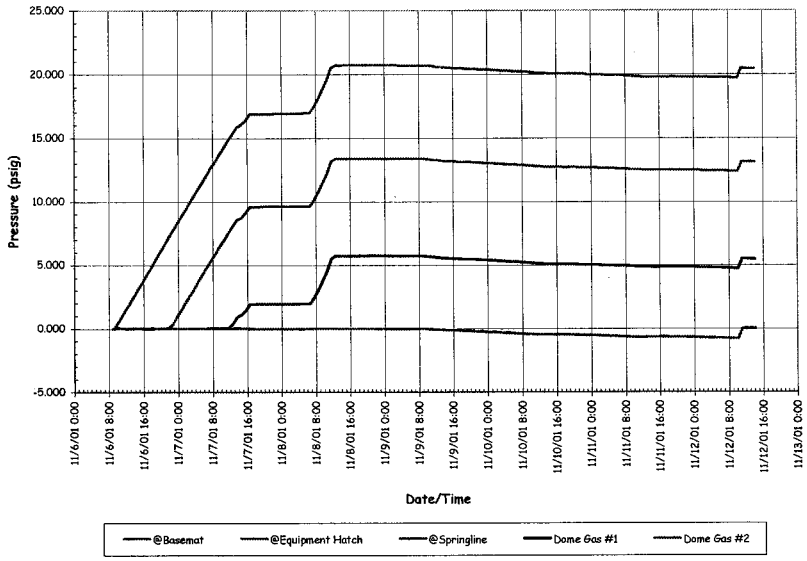

Figure 3.13 Pre-SFMT Hydrostatic Pressures

The test sequence planned for the SFMT was to 'rapidly' pressurize the model using nitrogen gas to compensate for the known leaks in the model. The minimum flow rate capacity of pressurization system, 14 std.m3/min (500 scfm), would increase pressure in the reduced void space at a rate of about 0.35 kgf/cm2 (5 psi) every minute. At this rate, the model could be pressurized to failure in less than an hour.

The SFMT began shortly after 10:00 AM on Wednesday, November 14, 2001. The pressure time histories are shown in Figure 3.14. The pressure time history of all 5 gages are shown along with the effective model pressure, which is calculated as a volume-weighted average. Any references to the SFMT pressures are to the effective pressure, unless noted otherwise.

The model was continuously pressurized at a rate of approximately 0.35 kgf/cm2 (5psi)/min. All active sensors were continuously scanned at intervals of approximately 30 seconds and the video cameras were continuously recording the response of the model. As the pressure was increased, evidence of leakage was visible as increasing wetting of the concrete surface. At 10:38 AM, the effective pressure in the model equaled the peak pressure achieved during the LST, 3.3 Pd (1.29 MPa or 188 psig). At approximately 10:39 AM, the acoustic system recorded a very high noise level event which was interpreted as the breaking of a tendon wire. At this point in the test, events occurred very quickly. Shortly after detecting the wire break, a small spray of water was observed at approximately 0° azimuth and additional tendon wire breaks were detected by the acoustic system with increasing frequency. The wire break events are plotted in Figure 3.15, along with the effective pressure and the radial displacement at Az. L (324°), Elevation 6 (6280), as a function of time.

The rate of pressurization was decreasing and the nitrogen flow rate was increased to maintain the pressurization rate. The gas pressure and flow rates are shown in Figure 3.16. The water surface inside the model, viewed through the internal video camera, was observed to be dropping slowly, but it was unclear if this was due to leakage or radial expansion of the vessel.

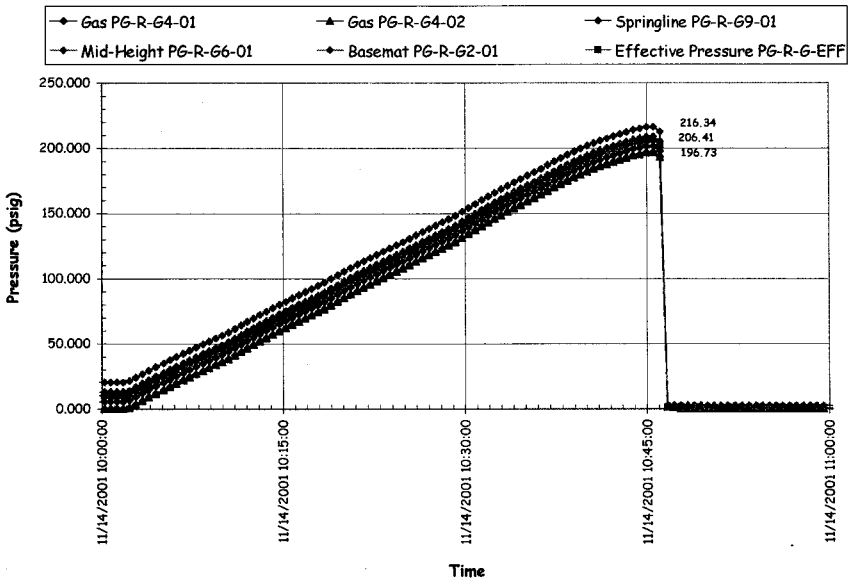

Figure 3.14 SFMT Pressure Time Histories

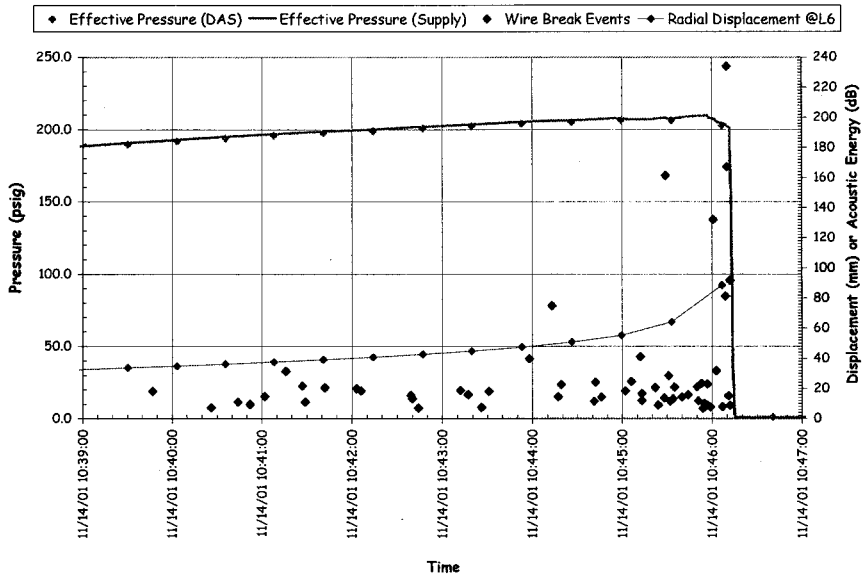

Figure 3.15 SFMT Wire Break Events vs. Pressure vs. Displacement

Pressurization of the model continued until a second spray of water was observed and then, suddenly, at 10:46:12.3, at an effective pressure of 3.63 Pd (1.42 MPa or 206.4 psig) the PCCV model ruptured violently at ~6° azimuth near the mid-height of the cylinder. The rupture propagated vertically in both directions and then radiated circumferentially about 2 meters above the top of the basemat, shearing off the cylinder wall. The dome and cylinder wall then came to rest on the instrumentation frame which appears to have prevented the model from toppling over. The entire collapse was over in slightly more than one second. The entire SFMT, including the sequence of rupture and collapse was recorded by the digital video cameras. A short movie (.mpg) file showing the rupture of the model is included on the data CD enclosed. The moment of rupture is shown from all four angles in Figure 3.17. The video recorded failure of the tendons including ejection of tendon anchors. The condition of the model after the SFMT is shown in Figure 3.18.

Because of program schedule constraints, demolition of the PCCV model commenced in December, 2001 and was completed in April 2002. During this period, attempts were made to further inspect the model and characterize the damage caused by the SFMT, however, these efforts were of limited value due to the difficulty of discriminating the damage caused during the SFMT from the demolition process. A few specimens from the model were retrieved, however, more for sentimental value than for providing any further technical insight into the behavior of the model.

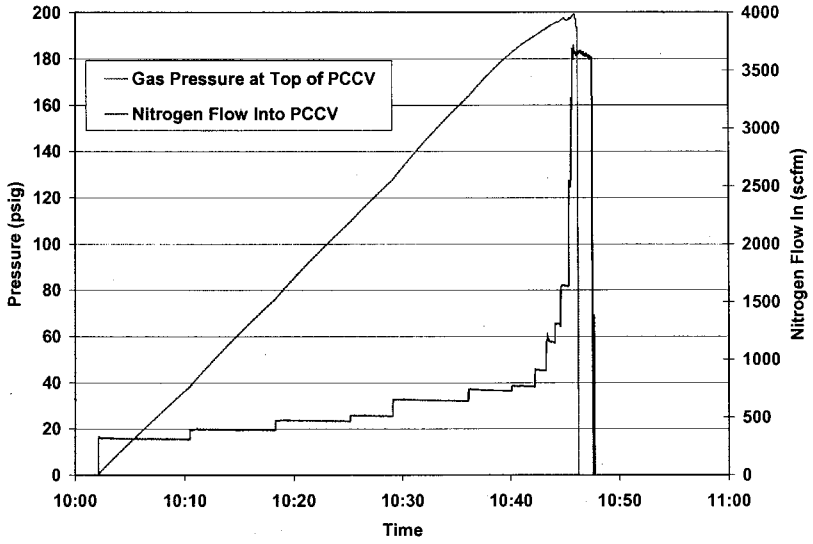

Figure 3.16 SFMT Pressurization System Data

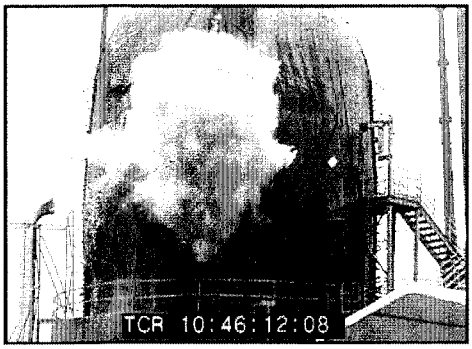

(a) 0° Azimuth

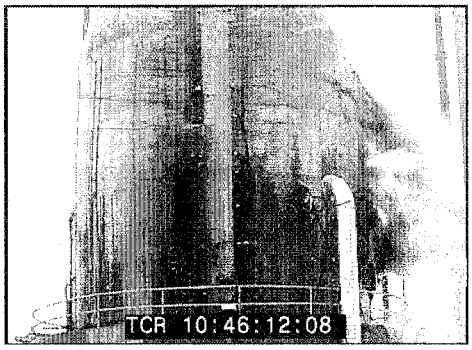

(b) 90° Azimuth

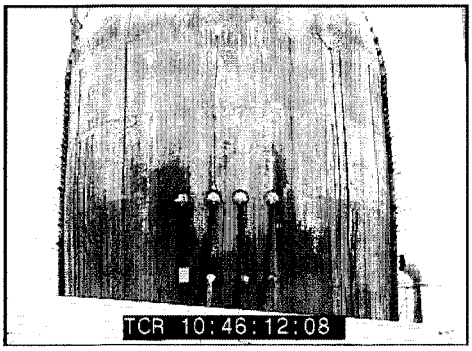

(a) 180° Azimuth

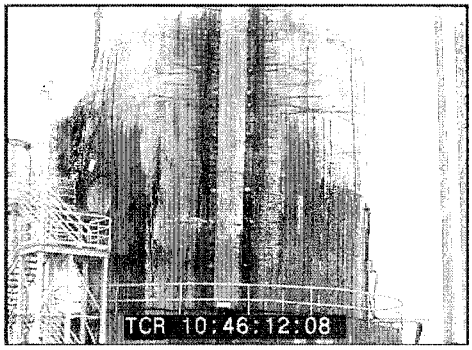

(b) 270° Azimuth

Figure 3.17 SFMT: Rupture of the PCCV Model

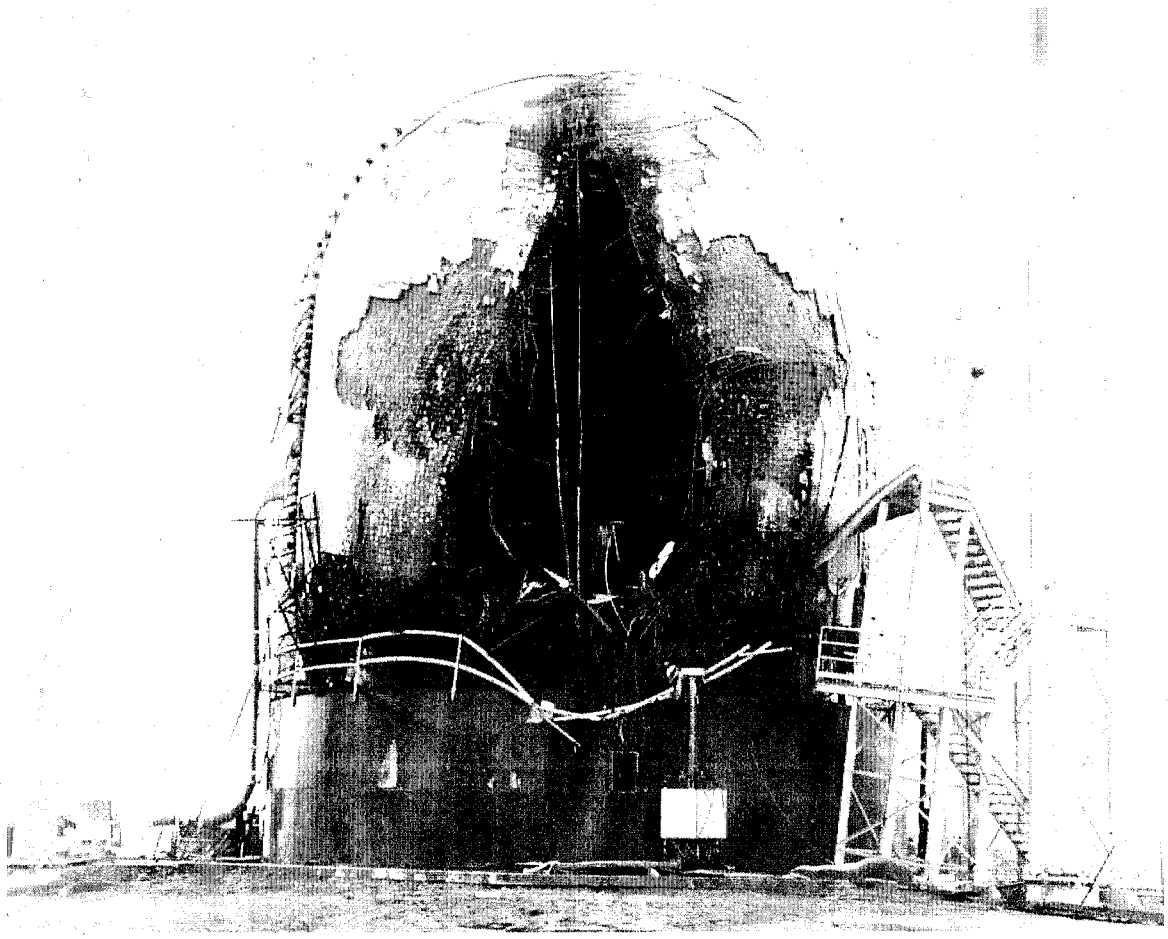

Figure 3.18 PCCV Model after the Structural Failure Mode Test

Test Results

The response of the model was continuously recorded beginning March 3, 2000, prior to prestressing, through October 11, 2000, following the LST. Additional data was recorded, using a modified instrumentation suite, from November 6 to 14, 2001 for the SFMT. A detailed description of the data file structure and the data were provided in the test report [1].

The basic data was recorded for each instrument at discrete time steps. This basic data is referred to as the DYNAMIC data. It should be noted that the time reported in the data files is the DAS clock time at the start of a data scan. Since it took up to two minutes to complete a data scan (one minute for the SFMT), the actual time the data was recorded may be up to two minutes later than the recorded time. For pseudo-static loading, this is not a significant issue, but it may have some effect on the response recorded near the end of the LST and SFMT.

The Data of Record (DOR) is a subset of the dynamic data. The concept of the DOR was defined to facilitate comparison of the data with analysis results. Typically, the analysis results are described as a function of pressure. The DOR is intended to provide a single, stable response value at each pressure step. The DOR were recorded separately from the dynamic data when the gage stability criteria was met or at the direction of the test conductor.

The concept of DYNAMIC and DOR data is illustrated in Figure 3.19. In this figure the DYNAMIC data during and after the LST is plotted along with the DOR for the radial displacement at the cylinder mid-height at 135°. At lower pressures, the data are essentially identical, however at higher pressures

the drift due to model creep and/or leakage is apparent. Furthermore, the DOR data set does not capture the maximum pressure. In subsequent discussions of the DOR, the response at the maximum pressure from the DYNAMIC data has been appended to the DOR for completeness

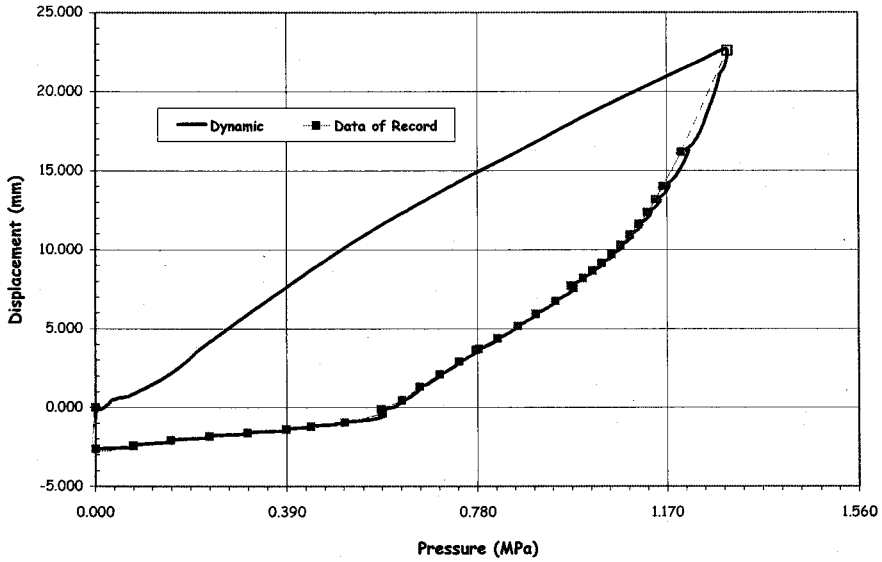

Figure 3.19 Radial Displacement @ AZ 135°, El. 6200

PHASE 2 CALCULATIONS

Each ISP participant was asked to provide a report summarizing their analysis approach and results. Each individual report is reproduced in Appendices B through I.

Fifty-five standard output locations, listed in Table 4.1, were selected to facilitate initial comparison of the Phase 2 calculations with the test results. The selection of these locations was based on the containment experience of the project team at Sandia and the results of preliminary analyses to characterize model responses and identify possible failure modes. The general locations are illustrated in Figure 4.1. This is the same set of variables used for the pretest Round Robin comparison. A gage, or set of gages, were installed at every standard output location for the LST. Due to the practical limitations, the model response was not measured at all these locations during the SFMT. The participants were asked to provide analysis results as a function of gage pressure at these locations. A summary of the results provided by each of the participants is given in Table 4.2. The calculated results were collected into composite plots for comparison with the LST and SFMT results at each SOL. These composite plots are provided in Appendix A.

To facilitate comparison of the calculated results with the pressure response of the model, most, if not all of the participants chose to 'initialize' their analysis results with the test data at the start of the LST. This was done to eliminate the variation in the calculation of the response due to dead load and prestressing as well as the effects of creep, shrinkage and changes in ambient conditions, which were not modeled. As a result, **most of the comparisons are for the change in the response variable due to pressure, not the total response**. Comparisons of analyses before initializing the response variables were much more inconsistent and a similar result would be expected for full-scale containments where the initial conditions might not be known.

In addition to submitting response predictions at the SOLs, each participant was also asked to provide a best estimate of failure pressure and mechanisms of the PCCV model. These are summarized in Table 4.3. Table 4.3 also summarizes predictions of the pressure for various milestones (onset of cracking, yielding, etc.) leading up to failure.

Table 4.1 Standard Output Locations for PCCV Round Robin Analysis

Loc. #	Type	Orientation	Az. (°)	El. (m)	Comments	General Location
1	Displacement	Vertical	135	0.00	Outside Cylinder	Top of Basemat
2	"	Radial	135	0.25	Inside Liner Surface	Base of Cylinder
3	"	Radial	135	1.43	"	"
4	"	Radial	135	2.63	"	"
5	"	Radial	135	4.68	"	E/H elev.
6	"	Radial	135	6.20	"	Approximate Midheight
7	"	Radial	135	10.75	"	Springline
8	"	Vertical	135	10.75	"	"
9	"	Horiz.(Rad)	135	14.55	"	Dome 45 deg
10	"	Vertical	135	14.55	"	"
11	"	Vertical	135	16.13	"	Dome apex
12	"	Radial	90	6.20	"	Midheight @ Buttress
13	"	Radial	90	10.75	"	Springline @ Buttress
14	"	Radial	324	4.675	"	Center of E/H
15	"	Radial	62	4.525	"	Center of A/L
16	Rebar Strain	Meridional	135	0.05	Inner Rebar Layer	Base of Cylinder
17	"	Meridional	135	0.05	Outer Rebar Layer	"
18	"	Meridional	135	0.25	Inner Rebar Layer	"
19	"	Meridional	135	0.25	Outer Rebar Layer	"
20	"	Meridional	135	1.43	Inner Rebar Layer	"
21	"	Meridional	135	1.43	Outer Rebar Layer	"
22	"	Hoop	135	6.20	Outer Rebar Layer	Midheight
23	"	Meridional	135	6.20	Outer Rebar Layer	"
24	"	Hoop	135	10.75	Outer Rebar Layer	Springline
25	"	Meridional	135	10.75	Inner Rebar Layer	"
26	"	Meridional	135	10.75	Outer Rebar Layer	"
27	"	Hoop	135	14.55	Outer Rebar Layer	Dome 45 deg
28	"	Meridional	135	14.55	Inner Rebar Layer	"
29	"	Meridional	135	14.55	Outer Rebar Layer	"
30	"	Meridional	90	0.05	Inner Rebar Layer	Base of Cylinder @ Buttress
31	"	Meridional	90	0.05	Outer Rebar Layer	"
32	"	Hoop	90	6.20	Outer Rebar Layer	Midheight @ Buttress
33	"	Meridional	90	6.20	Outer Rebar Layer	"
34	Liner Strain	Meridional	0	0.010	Inside Liner Surface	Base of Cylinder
35	"	Meridional	0	0.010	Outside Liner Surface	"
36	"	Meridional	135	0.25	Inside Liner Surface	"
37	"	Hoop	135	0.25	"	"
38	"	Meridional	135	6.20	"	Midheight
39	"	Hoop	135	6.20	"	"
40	"	Meridional	135	10.75	"	Springline
41	"	Hoop	135	10.75	"	"
42	"	Meridional	135	16.13	"	Dome apex
43	"	Meridional	90	6.20	"	Midheight @ Buttress
44	"	Hoop	90	6.20	"	"
45	"	Hoop	332	4.675	"	10 mm from thickened plate
46	"	Hoop	59	4.525	"	10 mm from thickened plate
47	Base Liner	Radial	135	0.00	100 mm Inside Cyl.	FF Basemat Liner Strain
48	Tendon Str.	Hairpin	180	15.60	Tendon - V37	Tendon Apex
49	"	Hairpin	135	10.75	Tendon - V46	Tendon Springline
50	"	Hoop	90	6.58	Tendon - H53	Mid Tendon
51	"	Hoop	180	6.58	Tendon - H53	1/4 - Tendon
52	"	Hoop	225	6.58	Tendon - H53	1/8 - Tendon
53	"	Hoop	0	4.57	Tendon - H35	Tendon btwn E/H and A/L
54	Tendon Force	Hairpin	241	-1.16	Tendon - V37	Tendon Gallery
55	"	Hoop	275	6.58	Tendon - H53	@ Buttress

Table 4.2 Results at Standard Output Location

					TEST DATA		BE/HSE/NNC						KAERI				
Loc. #	Type	Orientation	Az. (deg)	El. (m)	LST	SFMT	ABAQUS 6.4	ANAMAT	EGP	GRS	IRSN-CEA	AXISYM	3D	KOPEC	NRC/SNL/DEA	SCANSCOT
1	Displacement	Vertical	135	0												
2	Displacement	Radial	135	0.25												
3	Displacement	Radial	135	1.43												
4	Displacement	Radial	135	2.63												
5	Displacement	Radial	135	4.68												
6	Displacement	Radial	135	6.2												
7	Displacement	Radial	135	10.75												
8	Displacement	Vertical	135	10.75												
9	Displacement	Horiz. (Rad)	135	14.55												
10	Displacement	Vertical	135	14.55												
11	Displacement	Vertical	135	16.13												
12	Displacement	Radial	90	6.2												
13	Displacement	Radial	90	10.75												
14	Displacement	Radial	324	4.675												
15	Displacement	Radial	62	4.525												
16	Rebar Strain	Meridional	135	0.05												
17	Rebar Strain	Meridional	135	0.05												
18	Rebar Strain	Meridional	135	0.25												
19	Rebar Strain	Meridional	135	0.25												
20	Rebar Strain	Meridional	135	1.43												
21	Rebar Strain	Meridional	135	1.43												
22	Rebar Strain	Hoop	135	6.2												
23	Rebar Strain	Meridional	135	6.2												
24	Rebar Strain	Hoop	135	10.75												
25	Rebar Strain	Meridional	135	10.75												
26	Rebar Strain	Meridional	135	10.75												
27	Rebar Strain	Hoop	135	14.55												
28	Rebar Strain	Meridional	135	14.55												
29	Rebar Strain	Meridional	135	14.55												
30	Rebar Strain	Meridional	90	0.05												
31	Rebar Strain	Meridional	90	0.05												
32	Rebar Strain	Hoop	90	6.2												
33	Rebar Strain	Meridional	90	6.2												
34	Liner Strain	Meridional	0	0.01												
35	Liner Strain	Meridional	0	0.01												
36	Liner Strain	Meridional	135	0.25												
37	Liner Strain	Hoop	135	0.25												
38	Liner Strain	Meridional	135	6.2												
39	Liner Strain	Hoop	135	6.2												
40	Liner Strain	Meridional	135	10.75												
41	Liner Strain	Hoop	135	10.75												
42	Liner Strain	Meridional	135	16.13												
43	Liner Strain	Meridional	90	6.2												
44	Liner Strain	Hoop	90	6.2												
45	Liner Strain	Hoop	334	4.675												
46	Liner Strain	Hoop	58	4.525												
47	Base Liner	Radial	135	0												
48	Tendon Strain	Hairpin	180	15.6												
49	Tendon Strain	Hairpin	135	10.75												
50	Tendon Strain	Hoop	90	6.58												
51	Tendon Strain	Hoop	180	6.58												
52	Tendon Strain	Hoop	280	6.58												
53	Tendon Strain	Hoop	0	4.57												
54	Tendon Force	Hairpin	241	-1.16												
55	Tendon Force	Hoop	275	6.58												

Table 4.3 Summary of Results: Calculated Pressures (MPa) and Strains (%)

Participant	Concrete Cracking		Liner Yield	Hoop Tendon		Failure Modes		
	Hoop	Meridonal		Yield	2%	Pressure @ Failure	Free Field Hoop Strain	Mode
LST	**0.59-0.78**	**?**	**1.10**	**1.17**	**-**	**0.98** **1.294**	**0.17%** **0.42%**	**Liner tear, 1% mass/day leak** **Max. pressure @ 1000% mass/day leak**
BE / NNC	0.60	0.60	1.2 - 1.4			1.50	3.00%	Linear tear with extensive concrete cracking at buttress
EGP	0.60 0.44	0.96 0.44	0.98	1.25	1.53	aprox. 1.0	0.14%	cracking around EH
GRS	0.74-0.75	1.10	0.76	1.25	1.44	1.30 1.50	0.43%	Estimated tendon failure based on uniaxial measured failure strain of 3.25%
IRSN-CEA	0.68		0.84	0.94				
KAERI	0.59-0.62	0.59-0.62			1.47			
KOPEC	0.60	0.58	0.84	1.43	1.47	1.52		Tendon Failure Strain 3.5%
NRC/SNL/DEA	0.62	1.14	0.85	1.15	-	1.26	0.35%	Liner Tear, leakage
SCANSCOT	0.55-0.7	0.8-1.0	0.8	1.12	1.35			More detailed model(s) needed to predict overpressure at liner rupture.

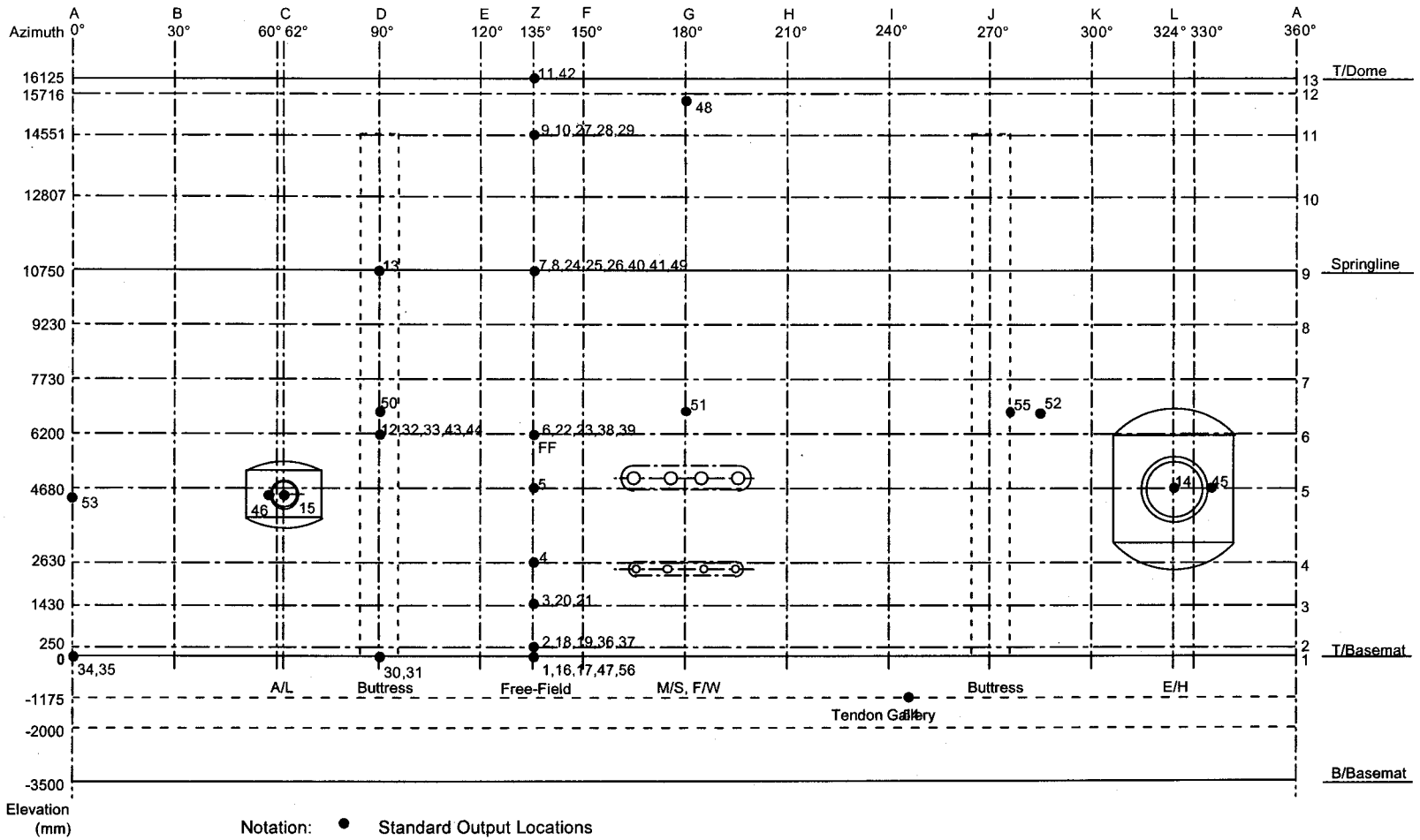

Notation: ● Standard Output Locations
A/L: Airlock
E/H: Equipment Hatch
M/S: Main Steam Penetration
F/W: Feedwater Penetration

Figure 4.1 Standard Output Locations

SUMMARY

Phase 2 Results

The work reported herein represents, arguably, the state of the art in the numerical simulation of the response of a prestressed concrete containment vessel (PCCV) model to pressure loads up to failure. A significant expenditure of time and money on the part of the sponsors, contractors, and ISP participants was required to meet the objectives. While it is difficult to summarize the results of this extraordinary effort in a few paragraphs, the following observations are offered for the reader's consideration:

(Note: These observations by the ISP coordinator, Sandia National Laboratories, and other participants do not necessarily represent the consensus of all the participants.)

- The figures in Appendix A include the LST post test analysis results in comparison with LST and SFMT results. Most of the calculations show results beyond the maximum pressure achieved in the LST. These results were used to estimate the failure pressures for the liner, the tendons and the rebar, partly summarized in Table 4.3.
- Most of the comparison plots in Appendix A demonstrate that there is good agreement between the calculated and measured response of the model up to approximately twice the design pressure. This is the pressure where extensive hoop cracking has occurred, with the associated loss of stiffness, and yielding of the metallic components (tendons, rebar and liner) is starting to occur. Once generalized non-linear behavior begins to occur, agreement between the analytical results and the experimental data degrades. Some cases which show poor agreement, even at pressures below 2Pd, when the structure is still essentially elastic require further investigation to explain the differences. These may be examined in more detail during Phase 3.
- Displacements:
  - The global deformations and strains of the model containment, especially in regions far away from penetrations, are simulated quite well by axisymmetric models as well as full 3D models. 3D-models are necessary for simulation of local behavior in the vicinity of perturbations like the air lock, the equipment hatch, the main steam, the feedwater penetrations and the buttresses.
  - The most accurate estimates of the global hoop strain are obtained from the average radial displacements at a given elevation (divided by the radius).
- Rebar strains:
  - The rebar strains compare less favorably (than the displacements) with analyses. This is primarily due to the difficulties in making point-to-point comparisons when local perturbations in the structure are not known or accurately modeled. Some differences also result from local perturbations resulting from the installation of the strain gages themselves.
  - The meridional rebar strains at the wall-base junction appear to capture the bending response.
  - The rebar strains at the mid-height of cylinder are consistent with displacement based strains.

- Liner strains:
  - For the locations compared in Appendix A, there is, in general good agreement between the calculated and experimental results, at least up to 2Pd. Beyond this pressure the comparison is less favorable. (Note: Other data [1] not included in this report suggests that near geometric perturbations in the liner, where strain concentrations are present, the comparison between analysis and test results is less favorable, even at low pressures. This may be partially due to the assumptions and level of detail in the modeling of the liner and anchorage.
- Tendon strain/force:
  - In general the calculated change (increase) in tendon strain/force resulting from pressurization of the model are consistent and in agreement with test results.
  - In some cases there is significant variation in the initial tendon strains and forces due to the application of the prestressing. This is likely due to the assumptions and approach to applying the prestressing forces and modeling the interaction between the unbonded tendons and the concrete structure. These differences are hidden, to a large extent, in the comparison plots in Appendix A, since most of the calculated results were initialized to match the data at the onset of pressurization. Nevertheless, since the total response is critical to establishing failure limits, these initial variations are important and should not be ignored.
  - It appears that the effect of the pressure loading has much less influence on the vertical tendons than the hoop tendons and the hoop tendons are more highly stressed by pressure loading up to failure.
- Cracking:
  - Most of the analyses demonstrate that the formation of cracking in the concrete starts at about 1.5 P_d. One of the consequences is that the dependence of radial displacement (e.g. Fig. A-6) on pressure becomes nonlinear. This effect is in agreement with measured results.

Also, as a result of these comparisons, other questions regarding the approach were identified

- Are the SOLs adequate for comparison of results with test data?
  - How do concrete strains compare?
  - What other variables should be compared?
  - Would comparison of displacement profiles be more meaningful than point comparisons
- Should the tendon force distribution be compared instead of strain or force at a 'point'?
- What is the appropriate criteria for the Limit State of the model (or prototype)? Liner rupture, tendon rupture, structural collapse?
- What level of modeling is required to achieve an accurate estimate of capacity? What is the level of uncertainty?
- Are there any scaling effects? Should Phase 3 calculations be done at full scale?
- How can the response of the model be calculated in terms of leak rate? Crack size/width?

- How well do the material models represent the behavior of the structural components? Are standard material property measurement methods adequate for development of non-linear constitutive models?
- Should parametric calculations be performed to understand the relative importance of the various model elements?

Phase 3 Plans

Plans for Phase 3 calculations, for combined thermal and pressure loading, were finalized at the Phase 2 Review Meeting. Two load cases will be considered for Phase 3:

- Case 1: Saturated Steam Conditions (mandatory for all Phase 3 participants)
  - Monotonically increasing static pressure and temperature (saturated steam).
  - Each participant performs heat transfer calculations or uses gradients provided by SNL.

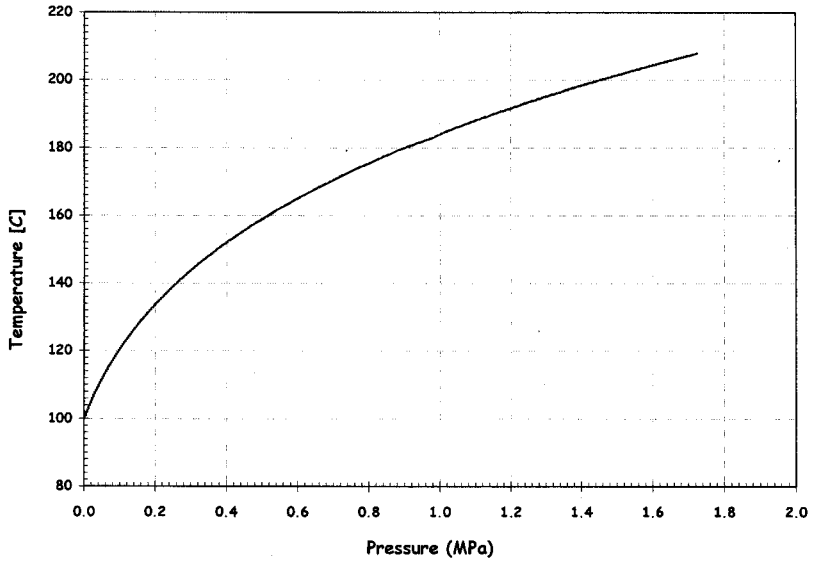

Figure 5.1 Phase 3, Case 1 Temperature-Pressure Loading

- Case 2: Station Blackout Scenario
  - NRC/SNL/DEA proposal plus hydrogen detonation defined by IRSN
  - SNL will perform heat transfer calculation using full-scale axisymmetric model w/ 12 nodes through the thickness.
  - Apply resulting gradients to 1:4-scale model

The thermal and mechanical analyses will be de-coupled with the heat transfer calculations being performed first using a full-scale axisymmetric model with twelve nodes through the thickness in the cylinder and dome. Thermal material properties will be based on typical data. Thermal gradiens will be calculated at several locations and provided to the participants to perform combined temperature-pressure response calculations.

The results of these independent participant calculations are scheduled to be completed by the end of December, 2004. The results will be summarized in the same manner as the Phase 2 results and presented in the final report for the ISP, to be published in June, 2005. A meeting of the participants and workshop will be held in early (March) 2005 to review the results and develop a consensus on issues related to:

- Modeling and analysis methods
- Constitutive models for materials
- Limit state and structural failure criteria

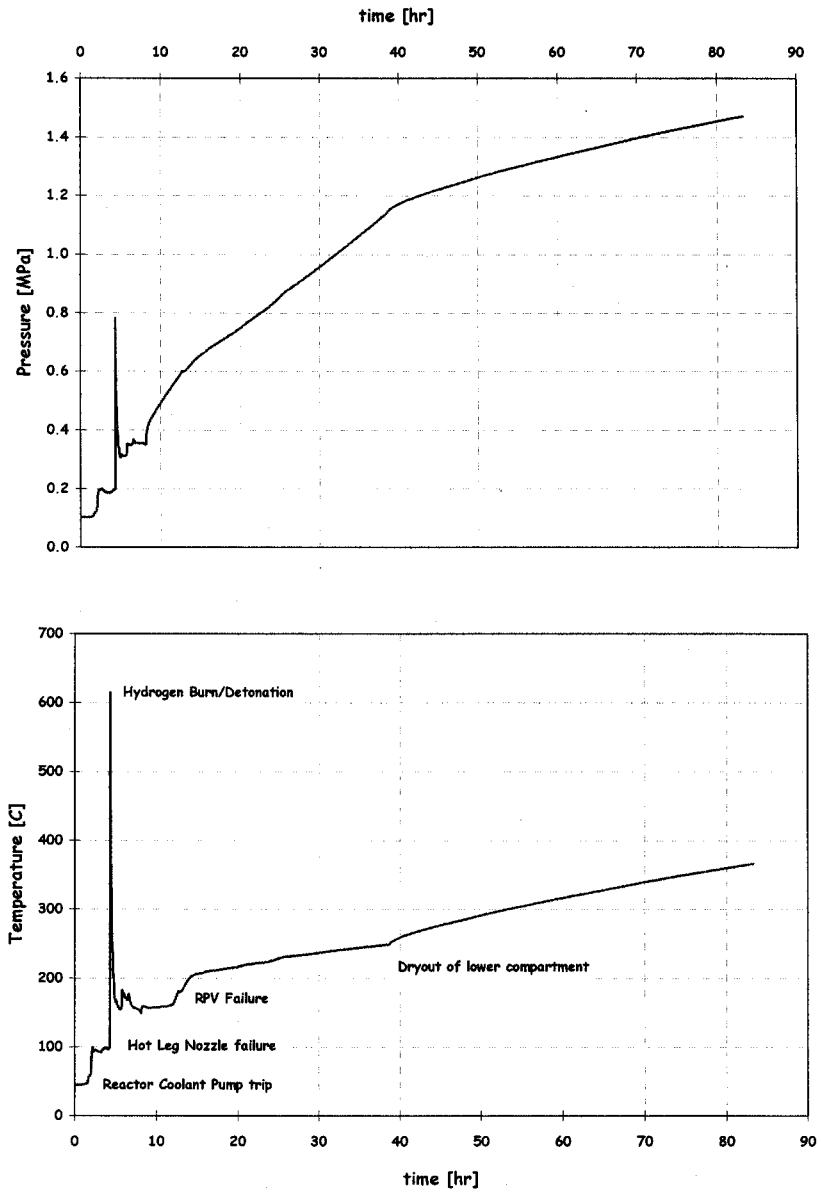

Figure 5.2 Phase 3, Case 2 Pressure and Temperature Time Histories

REFERENCES

1. Hessheimer, M. F., Klamerus, E. W., Rightley, G. S., Lambert, L. D. and Dameron, R. A., "*Overpressurization Test of a 1:4-Scale Prestressed Concrete Containment Vessel Model*", NUREG/CR-6810, SAND2003-0840P, Sandia National Laboratories, Albuquerque NM. March, 2003.

2. Luk, V. K., "*Pretest Round Robin Analysis of a Prestressed Concrete Containment Vessel Model*", NUREG/CR-6678, SAND00-1535, Sandia National Laboratories, Albuquerque, NM, August, 2000.

Appendix A:

Comparison Slots on Standard Output Locations

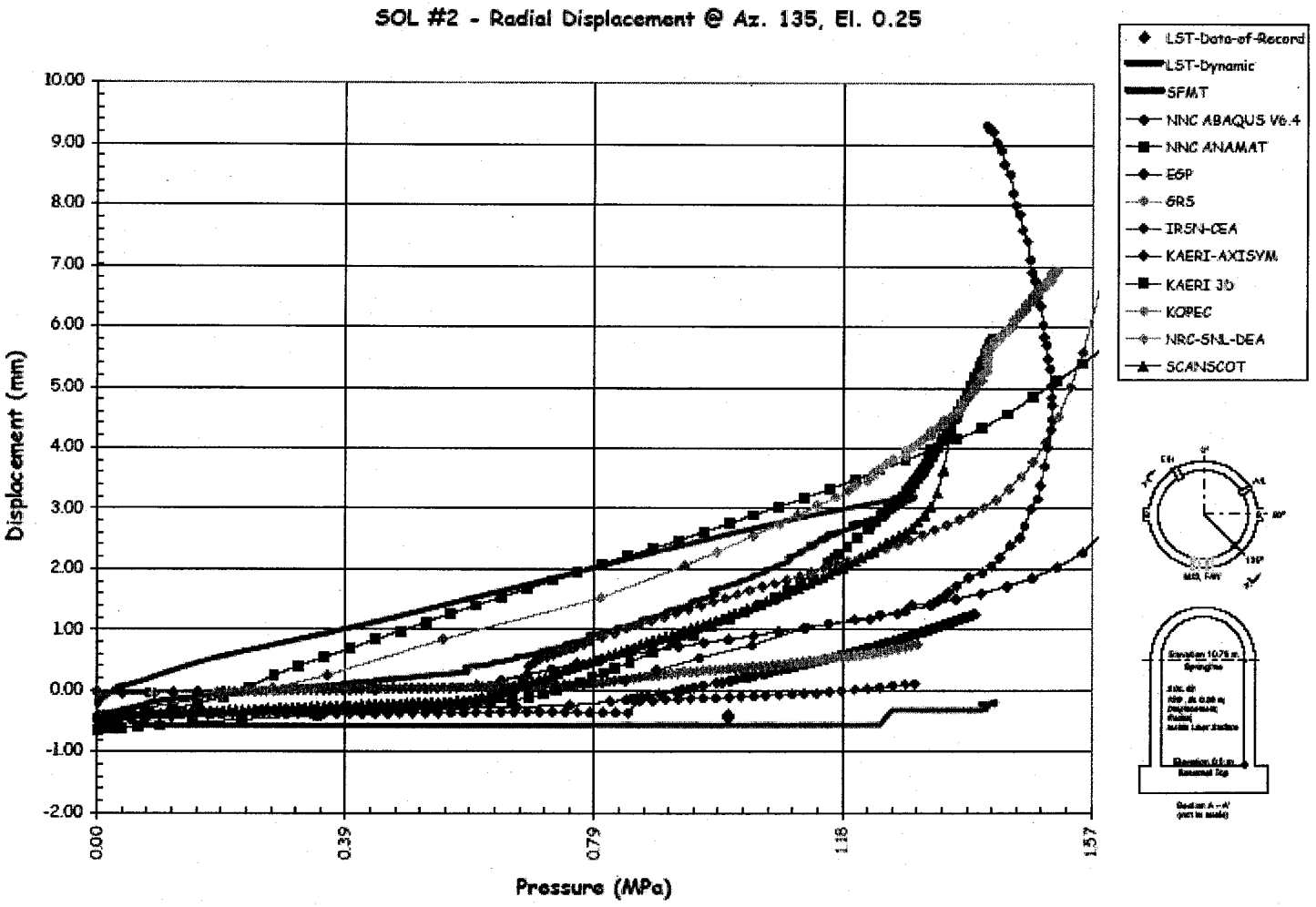
SOL #2 - Radial Displacement @ Az. 135, El. 0.25
Displacement (mm)
10.00
9.00
8.00
7.00
6.00
5.00
4.00
3.00
2.00
1.00
0.00
-1.00
-2.00
0.00
0.39
0.79
1.18
1.57
Pressure (MPa)
LST-Data-of-Record
LST-Dynamic
SFMT
NNC ABAQUS V6.4
NNC ANAMAT
EGP
6R5
IRSN-CEA
KAERI-AXISYM
KAERI 3D
KOPEC
NRC-SNL-DEA
SCANSCOT

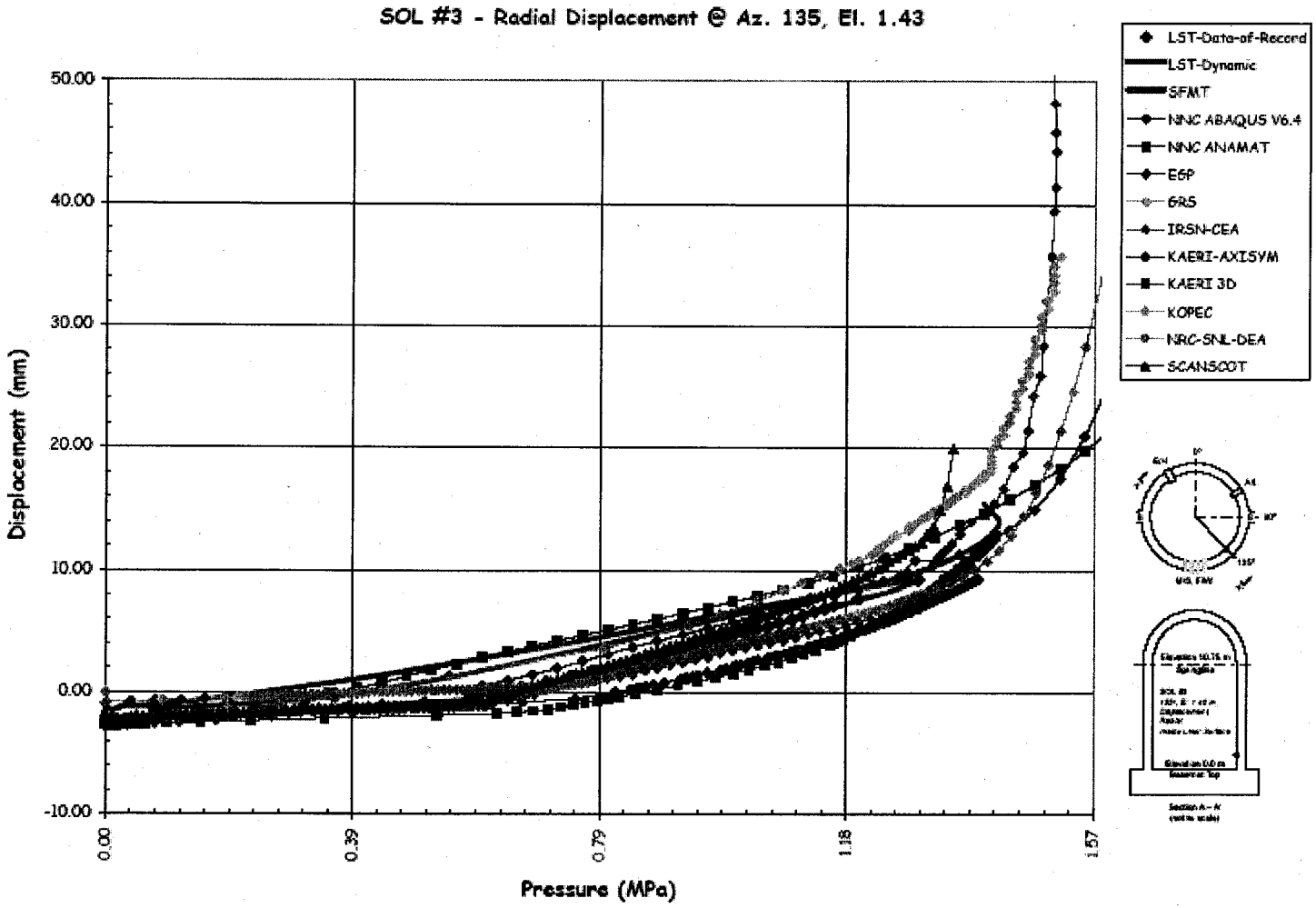
SOL #3 - Radial Displacement @ Az. 135, El. 1.43
Displacement (mm)
50.00
40.00
30.00
20.00
10.00
0.00
-10.00
0.00
0.39
0.79
1.18
1.57
Pressure (MPa)
LST-Data-of-Record
LST-Dynamic
SFMT
NNC ABAQUS V6.4
NNC ANAMAT
E6P
6R5
IRSN-CEA
KAERI-AXISYM
KAERI 3D
KOPEC
NRC-SNL-DEA
SCANSCOT

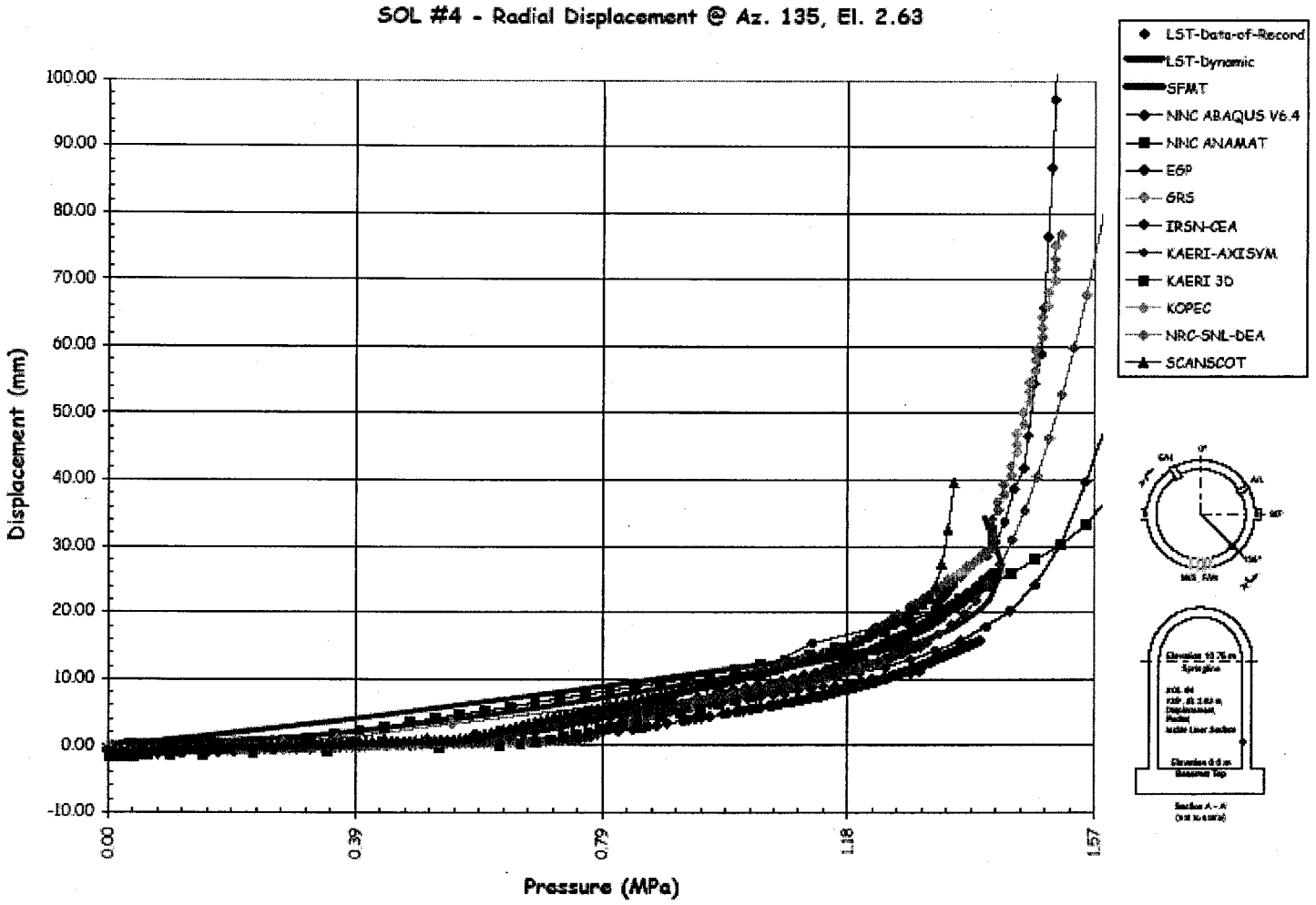
SOL #4 - Radial Displacement @ Az. 135, El. 2.63
Displacement (mm)
100.00
90.00
80.00
70.00
60.00
50.00
40.00
30.00
20.00
10.00
0.00
-10.00
0.00
0.39
0.79
1.18
1.57
Pressure (MPa)
LST-Data-of-Record
LST-Dynamic
SFMT
NNC ABAQUS V6.4
NNC ANAMAT
E6P
GRS
IRSN-CEA
KAERI-AXISYM
KAERI 3D
KOPEC
NRC-SNL-DEA
SCANSCOT

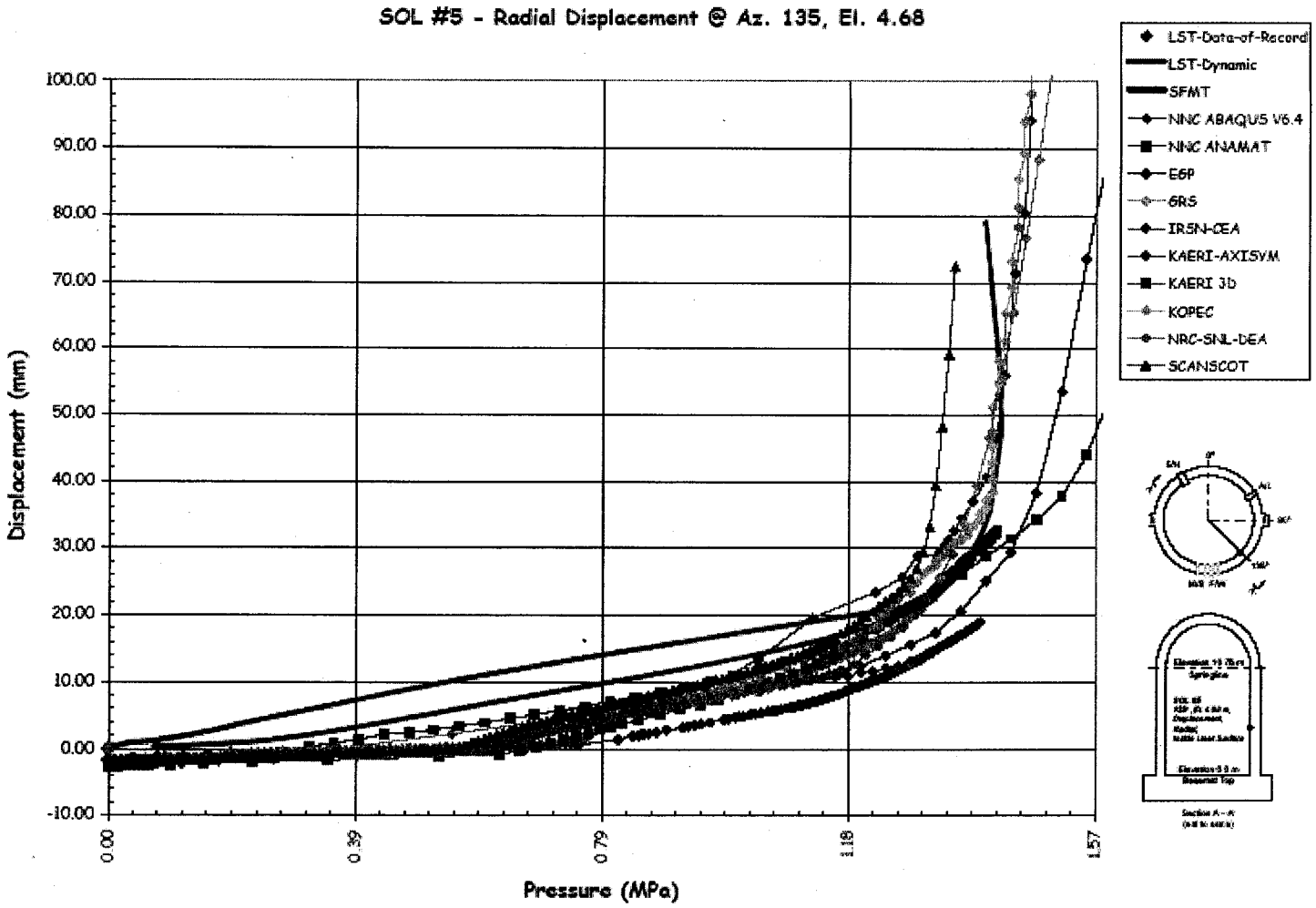
SOL #5 - Radial Displacement @ Az. 135, El. 4.68
Displacement (mm)
100.00
90.00
80.00
70.00
60.00
50.00
40.00
30.00
20.00
10.00
0.00
-10.00
0.00
0.39
0.79
1.18
1.57
Pressure (MPa)
LST-Data-of-Record
LST-Dynamic
SFMT
NNC ABAQUS V6.4
NNC ANAMAT
E6P
6RS
IRSN-CEA
KAERI-AXISYM
KAERI 3b
KOPEC
NRC-SNL-DEA
SCANSCOT

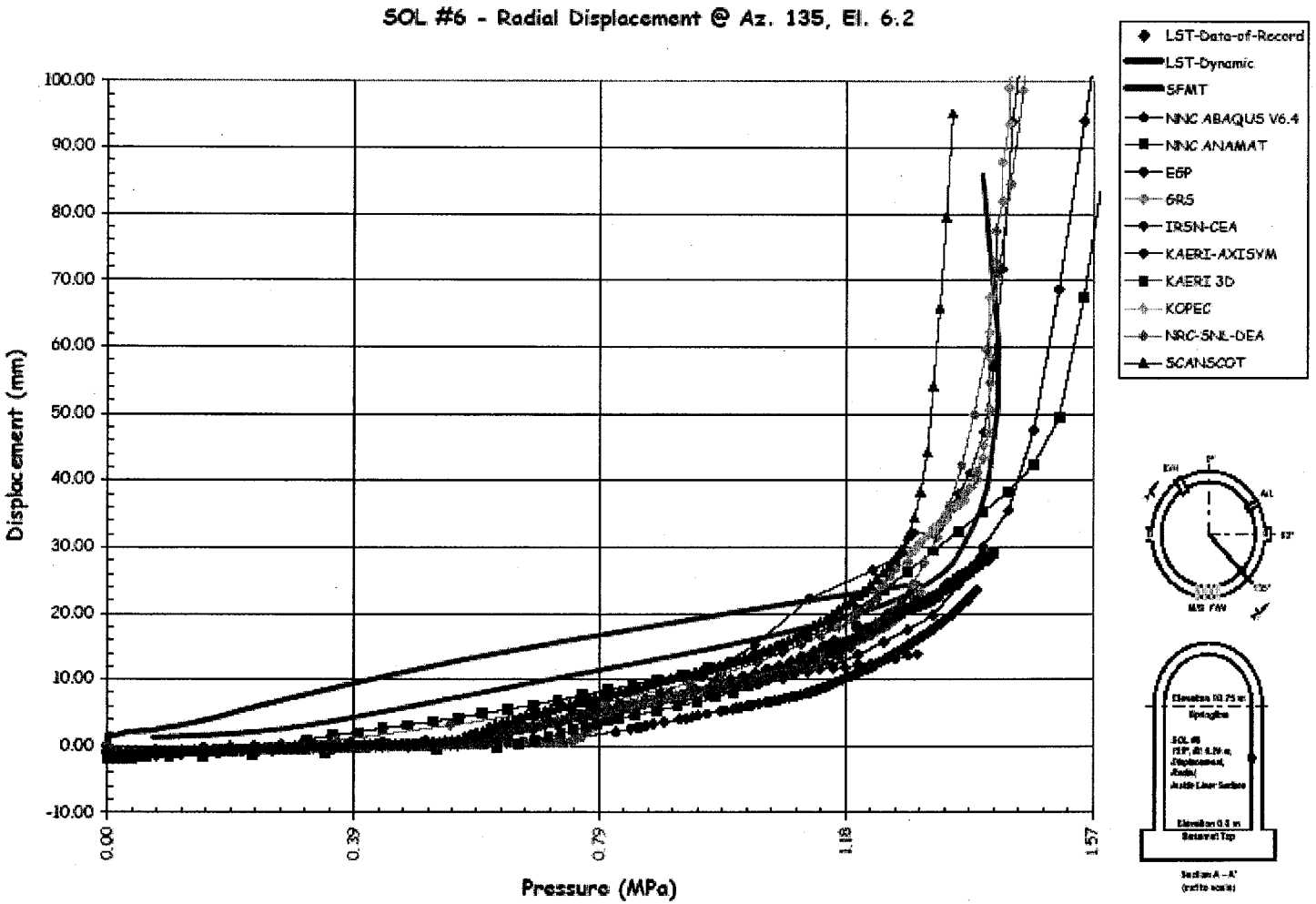
SOL #6 - Radial Displacement @ Az. 135, El. 6.2
Displacement (mm)
100.00
90.00
80.00
70.00
60.00
50.00
40.00
30.00
20.00
10.00
0.00
-10.00
0.00
0.39
0.79
1.18
1.57
Pressure (MPa)
LST-Data-of-Record
LST-Dynamic
SFMT
NNC ABAQUS V6.4
NNC ANAMAT
E6P
6R5
IRSN-CEA
KAERI-AXISYM
KAERI 3D
KOPEC
NRC-SNL-DEA
SCANSCOT

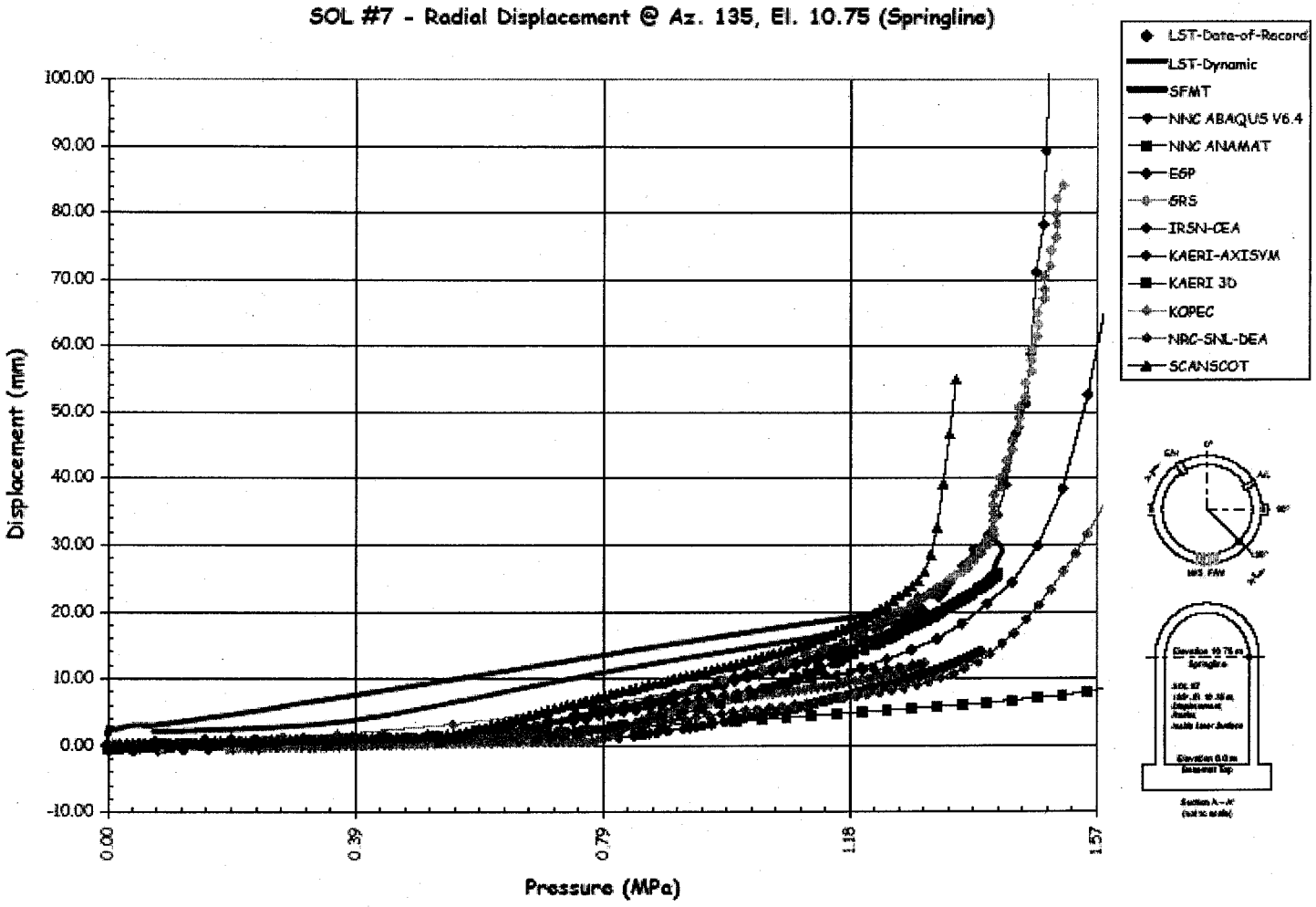
SOL #7 - Radial Displacement @ Az. 135, El. 10.75 (Springline)
Displacement (mm)
100.00
90.00
80.00
70.00
60.00
50.00
40.00
30.00
20.00
10.00
0.00
-10.00
0.00
0.39
0.79
1.18
1.57
Pressure (MPa)
LST-Date-of-Record
LST-Dynamic
SFMT
NNC ABAQUS V6.4
NNC ANAMAT
EGP
SRS
IRSN-CEA
KAERI-AXISYM
KAERI 3D
KOPEC
NRC-SNL-DEA
SCANSCOT

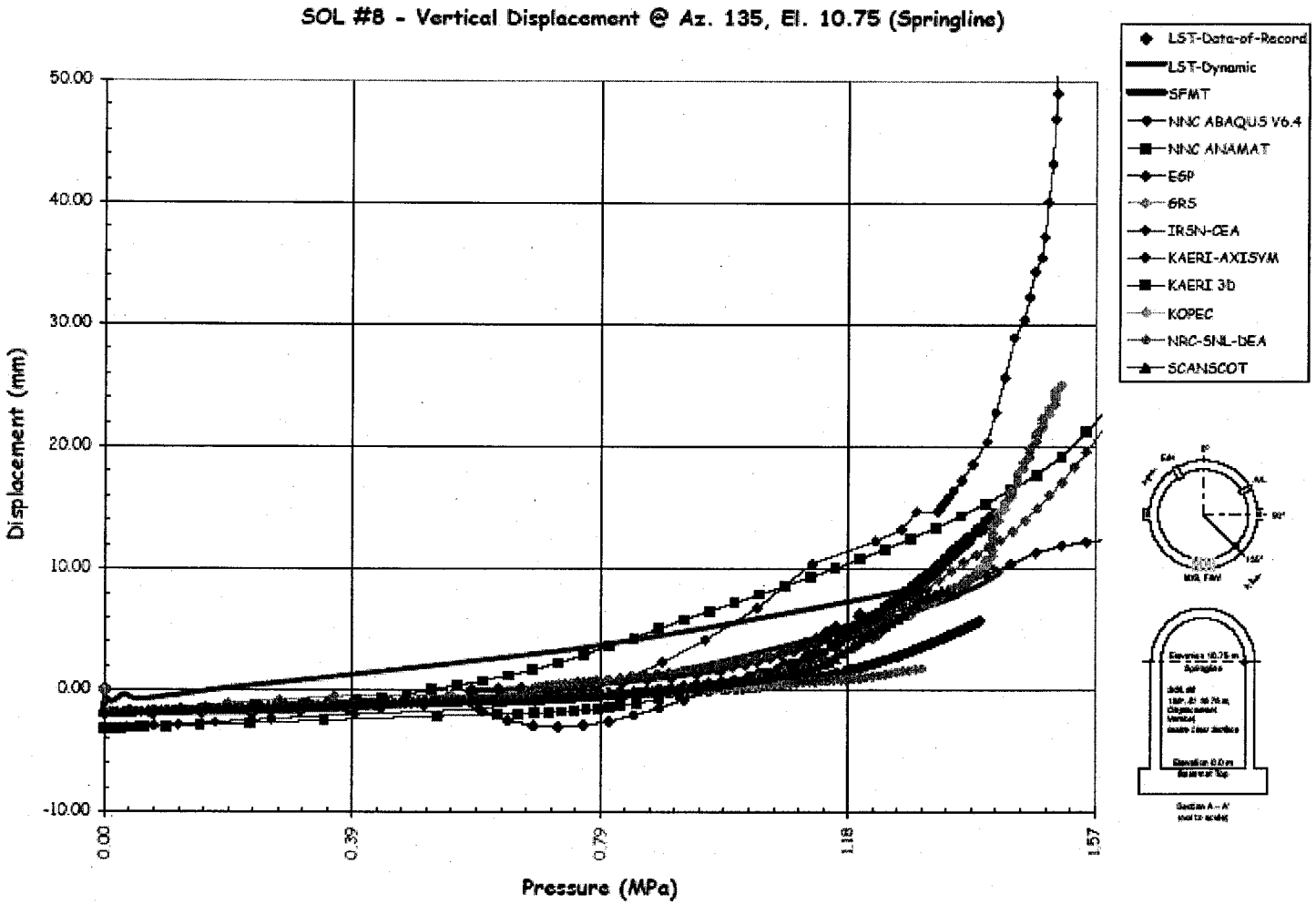
SOL #8 - Vertical Displacement @ Az. 135, El. 10.75 (Springline)
Displacement (mm)
50.00
40.00
30.00
20.00
10.00
0.00
-10.00
0.00
0.39
0.79
1.18
1.57
Pressure (MPa)
LST-Data-of-Record
LST-Dynamic
SFMT
NNC ABAQUS V6.4
NNC ANAMAT
E6P
6R5
IRSN-CEA
KAERI-AXISYM
KAERI 3D
KOPEC
NRC-SNL-DEA
SCANSCOT

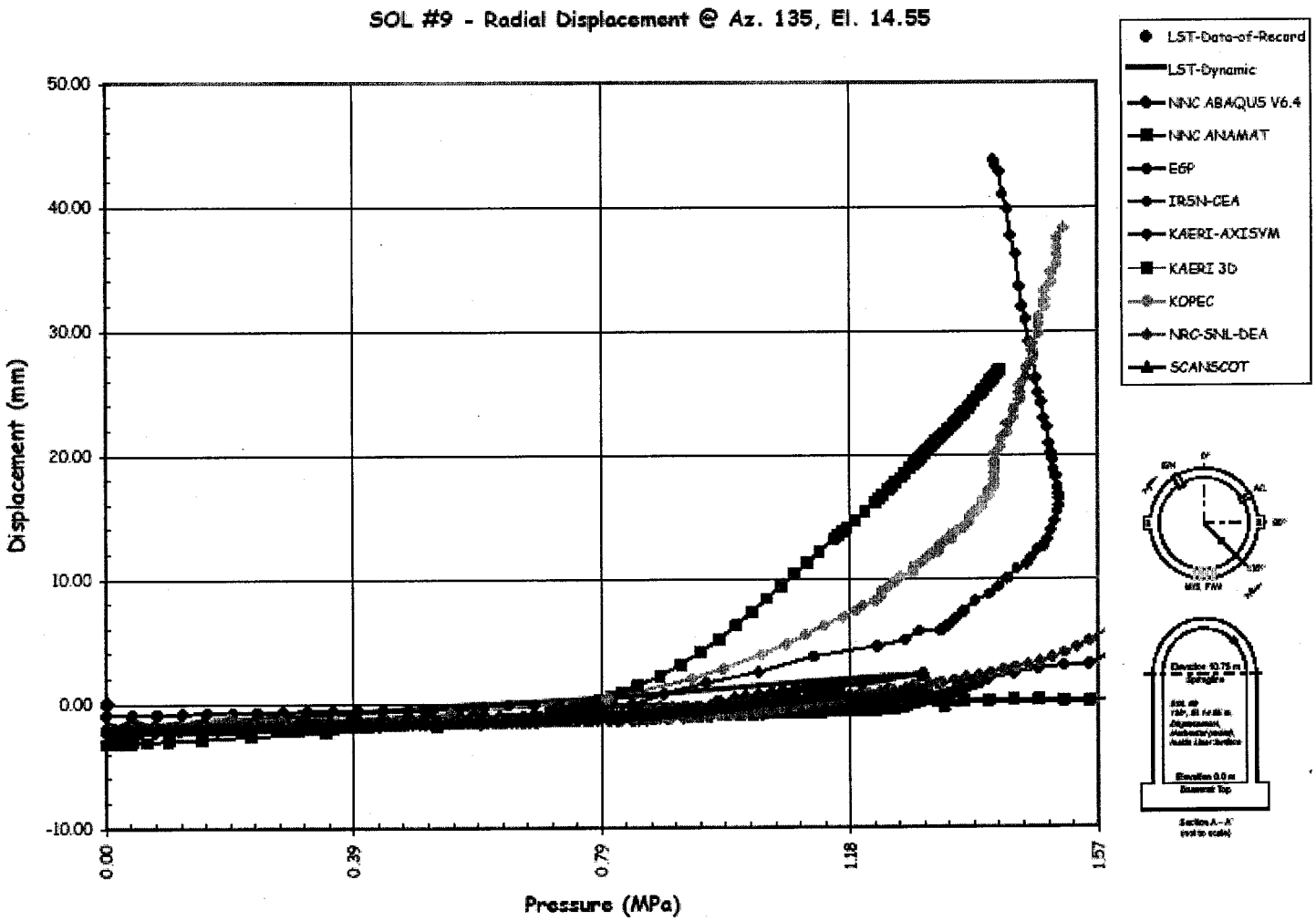
SOL #9 - Radial Displacement @ Az. 135, El. 14.55
LST-Data-of-Record
LST-Dynamic
NNC ABAQUS V6.4
NNC ANAMAT
EGP
IRSN-CEA
KAERI-AXISYM
KAERI 3D
KOPEC
NRC-SNL-DEA
SCANSCOT
Displacement (mm)
50.00
40.00
30.00
20.00
10.00
0.00
-10.00
0.00
0.39
0.79
1.18
1.57
Pressure (MPa)

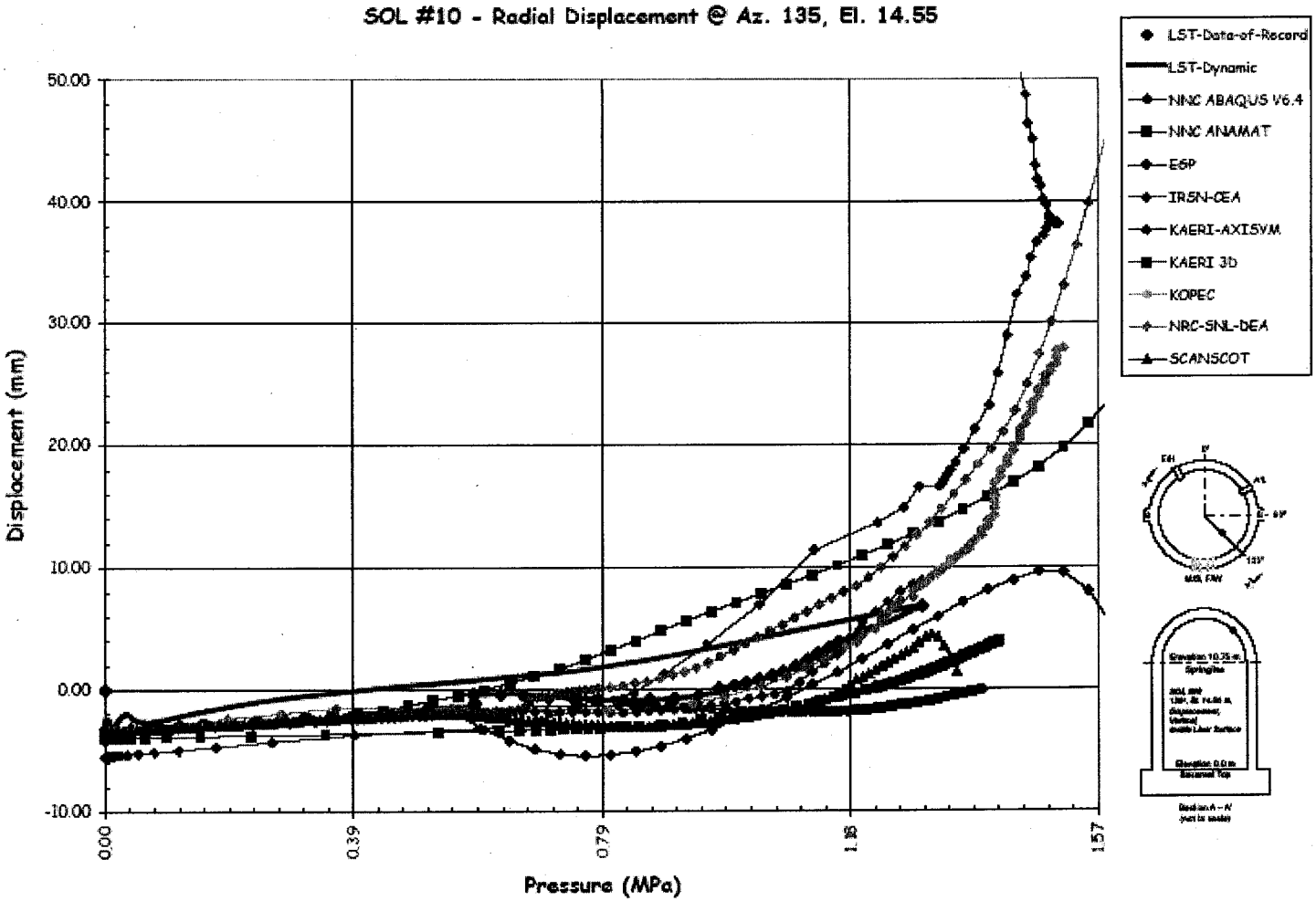
SOL #10 - Radial Displacement @ Az. 135, El. 14.55
LST-Data-of-Record
LST-Dynamic
NNC ABAQUS V6.4
NNC ANAMAT
E6P
IRSN-CEA
KAERI-AXISVM
KAERI 3D
KOPEC
NRC-SNL-bEA
SCANSCOT
Displacement (mm)
50.00
40.00
30.00
20.00
10.00
0.00
-10.00
0.00
0.39
0.79
1.18
1.57
Pressure (MPa)

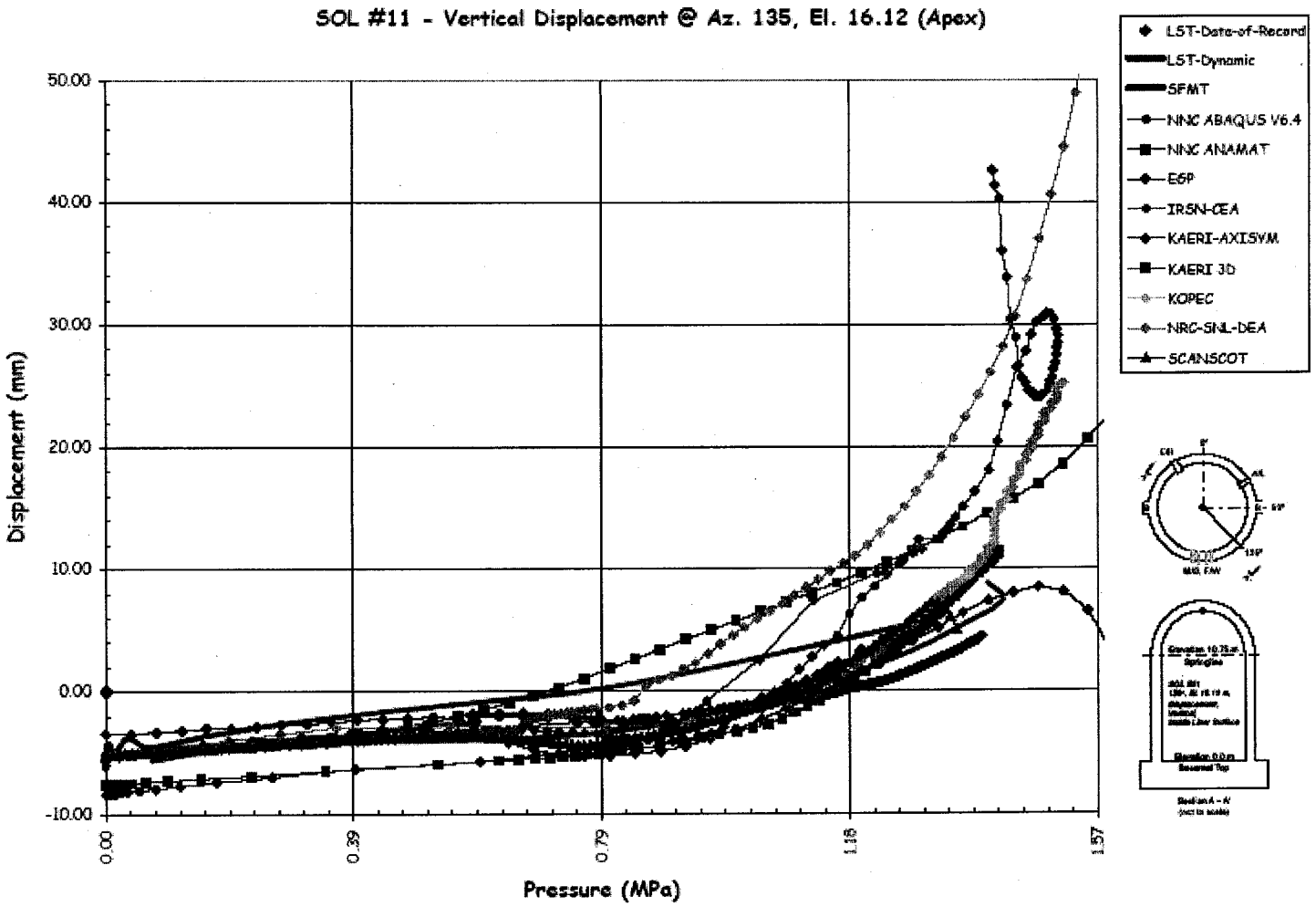
SOL #11 - Vertical Displacement @ Az. 135, El. 16.12 (Apex)
Displacement (mm)
50.00
40.00
30.00
20.00
10.00
0.00
-10.00
0.00
0.39
0.79
1.18
1.57
Pressure (MPa)
L5T-Data-of-Record
L5T-Dynamic
SFMT
NNC ABAQUS V6.4
NNC ANAMAT
E6P
IRSN-CEA
KAERI-AXISYM
KAERI 3D
KOPEC
NRC-SNL-DEA
SCANSCOT

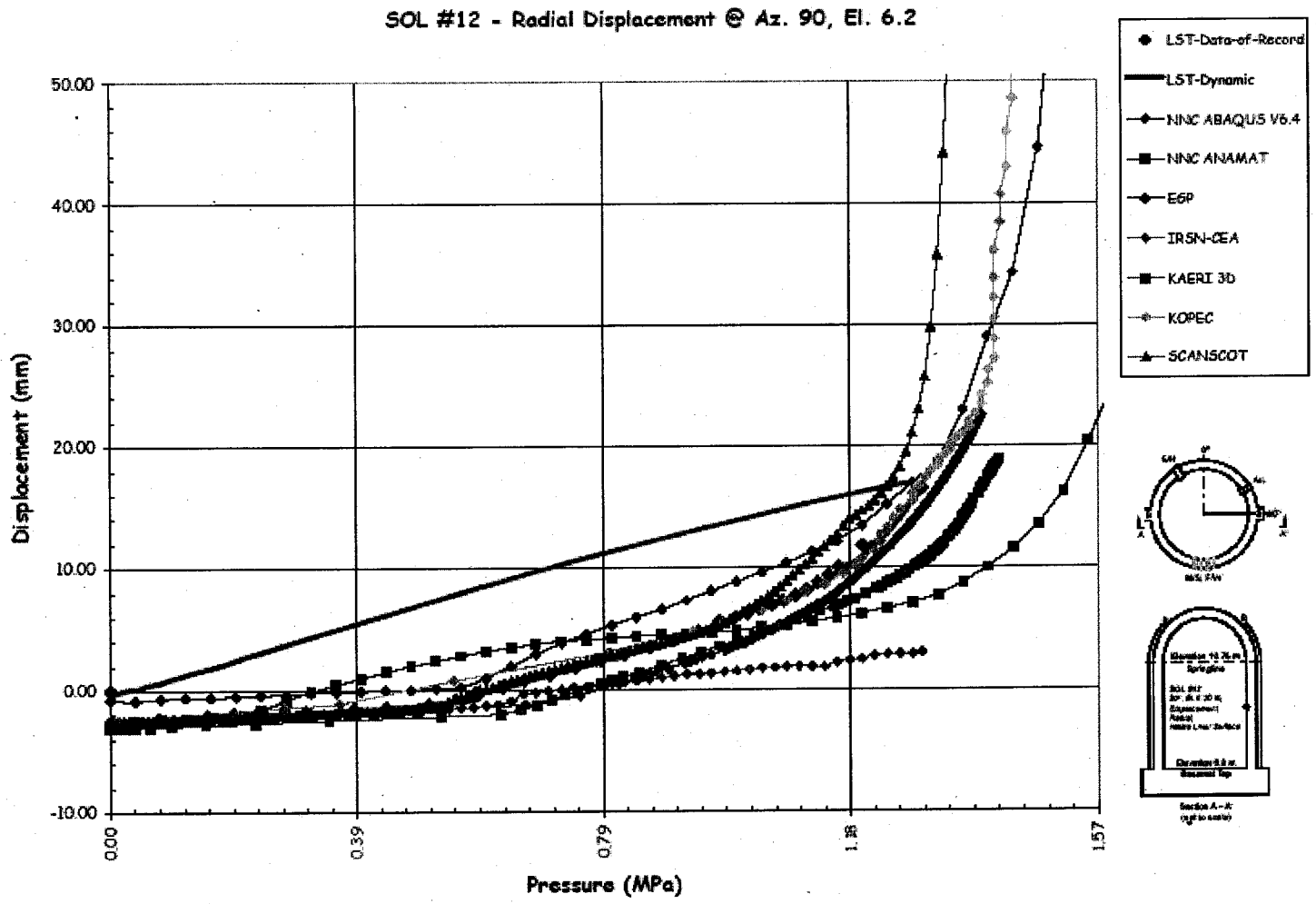
SOL #12 - Radial Displacement @ Az. 90, El. 6.2
Displacement (mm)
50.00
40.00
30.00
20.00
10.00
0.00
-10.00
0.00
0.39
0.79
1.18
1.57
Pressure (MPa)
LST-Data-of-Record
LST-Dynamic
NNC ABAQUS V6.4
NNC ANAMAT
E6P
IRSN-CEA
KAERI 3D
KOPEC
SCANSCOT

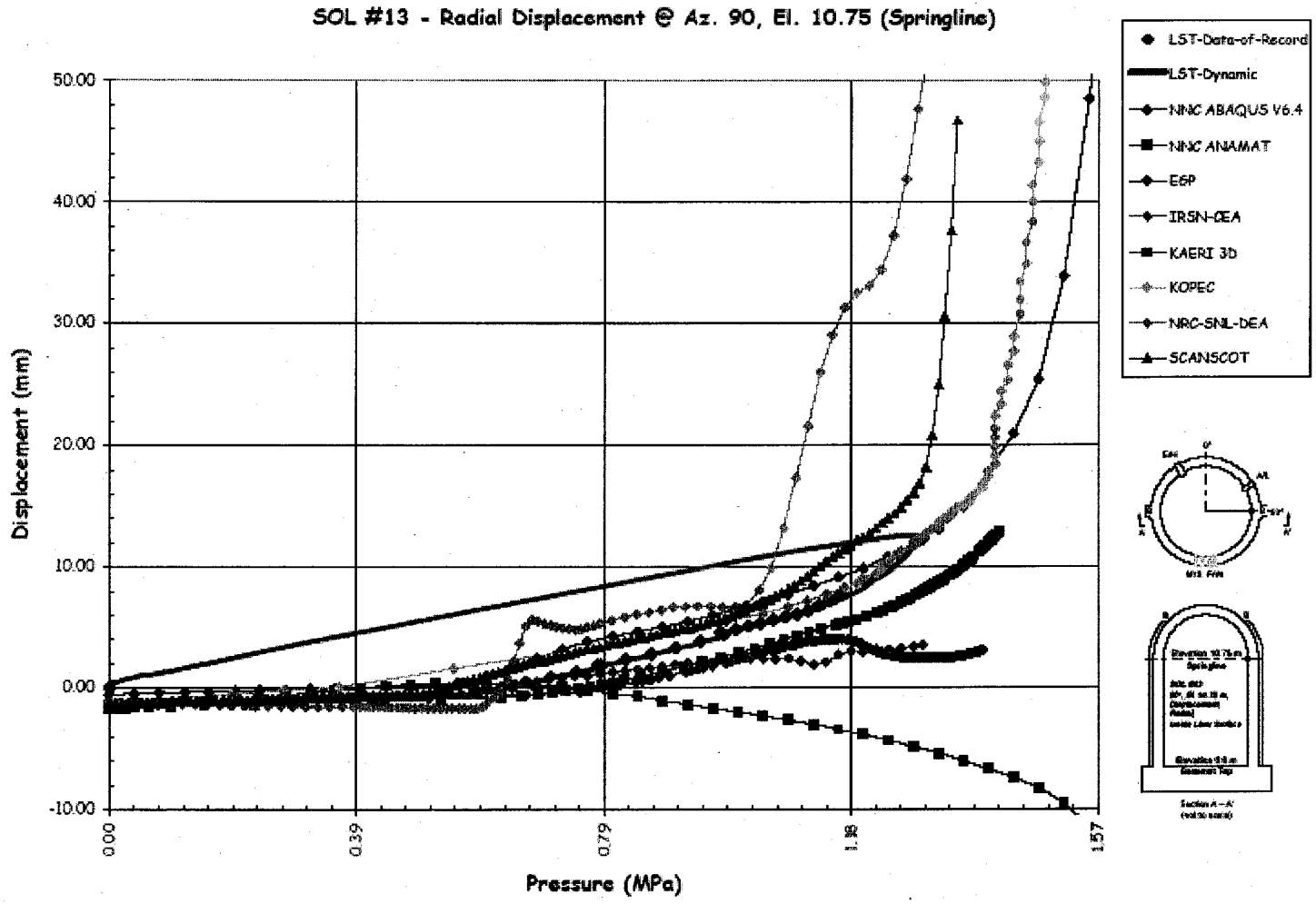
SOL #13 - Radial Displacement @ Az. 90, El. 10.75 (Springline)
Displacement (mm)
50.00
40.00
30.00
20.00
10.00
0.00
-10.00
0.00
0.39
0.79
1.18
1.57
Pressure (MPa)
LST-Data-of-Record
LST-Dynamic
NNC ABAQUS V6.4
NNC ANAMAT
E6P
IRSN-CEA
KAERI 3D
KOPEC
NRC-SNL-DEA
SCANSCOT

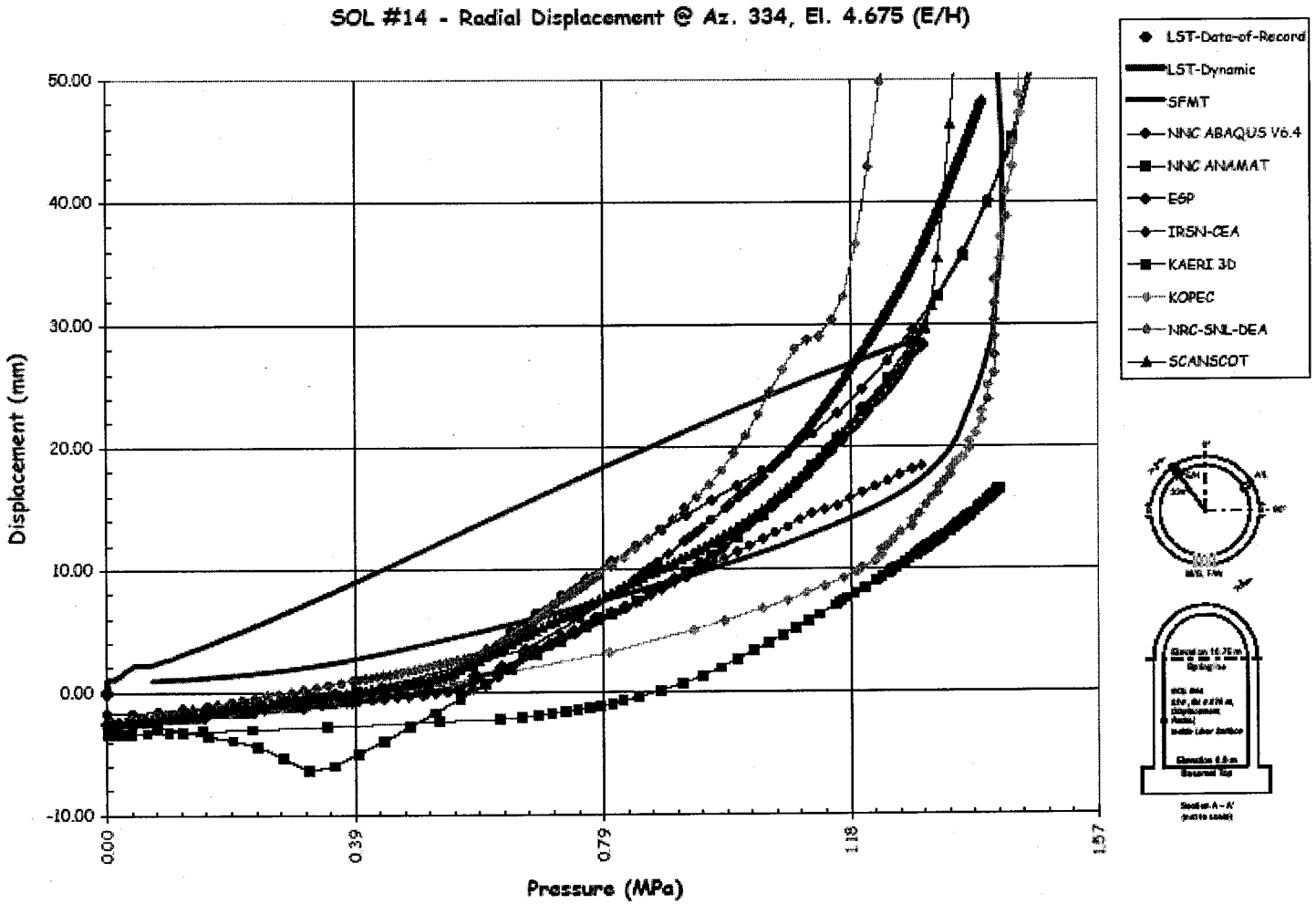
SOL #14 - Radial Displacement @ Az. 334, El. 4.675 (E/H)
Displacement (mm)
50.00
40.00
30.00
20.00
10.00
0.00
-10.00
0.00
0.39
0.79
1.18
1.57
Pressure (MPa)
LST-Data-of-Record
LST-Dynamic
SFMT
NNC ABAQUS V6.4
NNC ANMMAT
EGP
IRSN-CEA
KAERI 3D
KOPEC
NRC-SNL-DEA
SCANSCOT

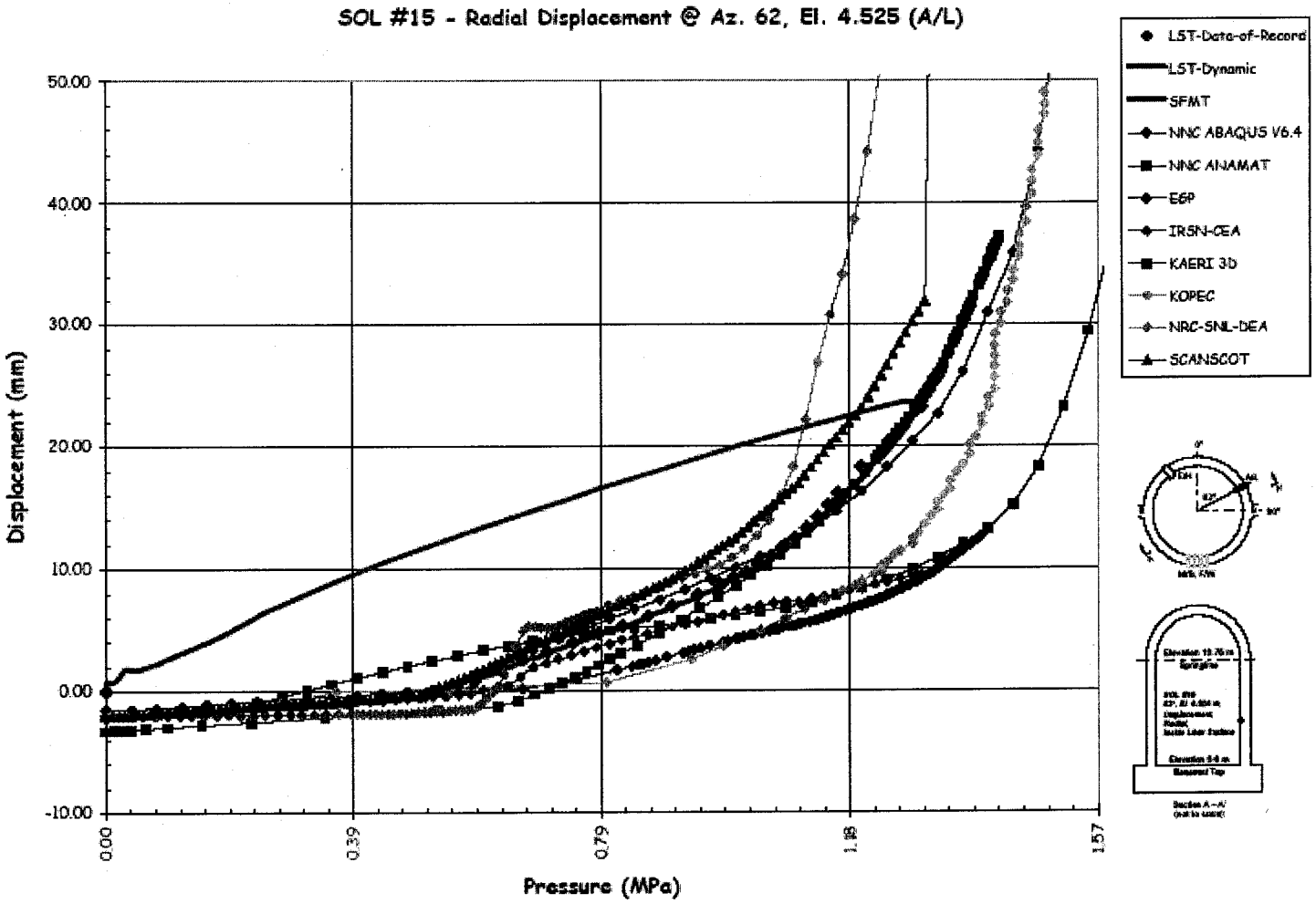
SOL #15 - Radial Displacement @ Az. 62, El. 4.525 (A/L)
Displacement (mm)
50.00
40.00
30.00
20.00
10.00
0.00
-10.00
0.00
0.39
0.79
1.18
1.57
Pressure (MPa)
LST-Data-of-Record
LST-Dynamic
SFMT
NNC ABAQUS V6.4
NNC ANAMAT
E6P
IRSN-CEA
KAERI 3D
KOPEC
NRC-SNL-DEA
SCANSCOT

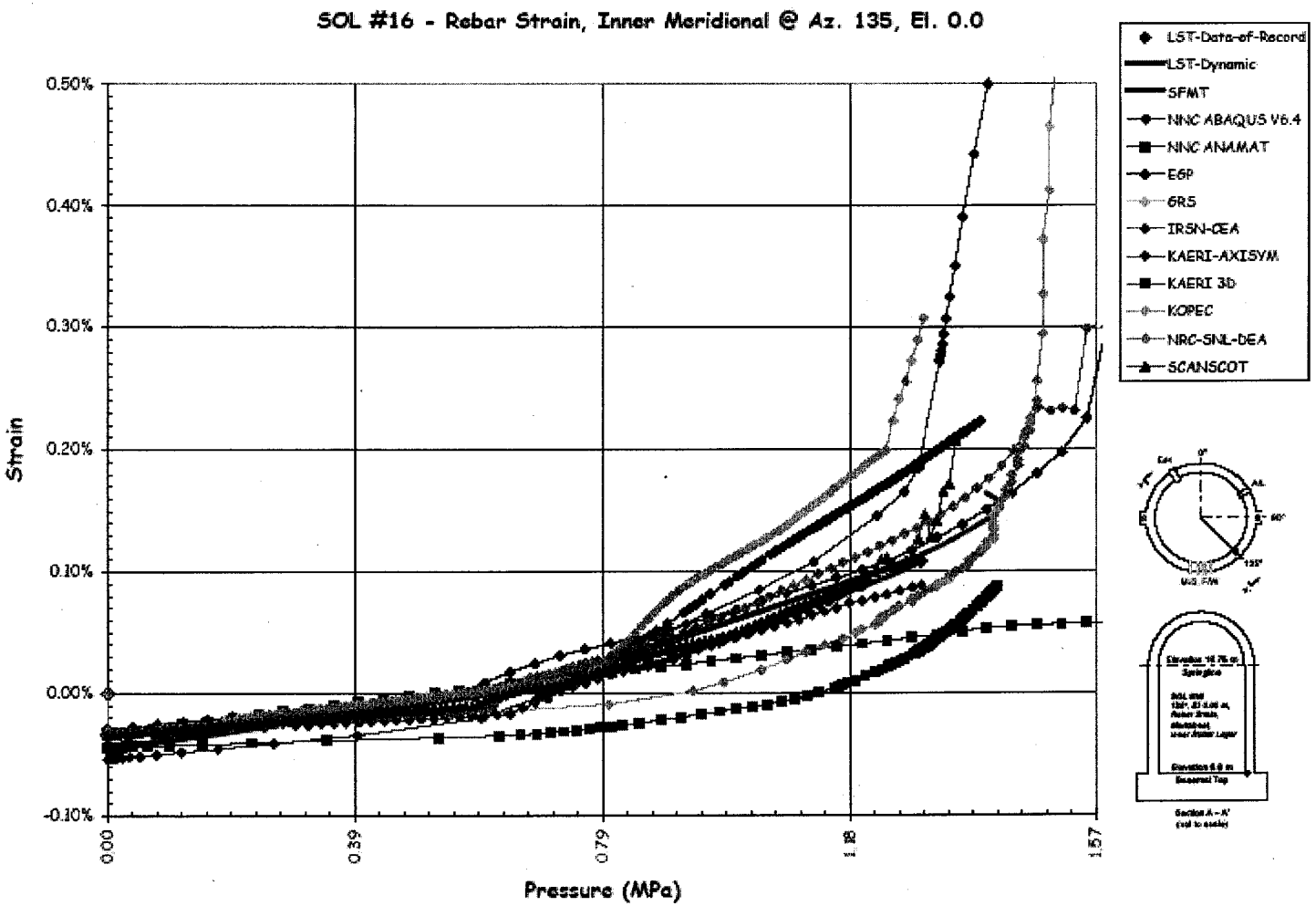
SOL #16 - Rebar Strain, Inner Meridional @ Az. 135, El. 0.0
Strain
0.50%
0.40%
0.30%
0.20%
0.10%
0.00%
-0.10%
0.00
0.39
0.79
1.18
1.57
Pressure (MPa)
LST-Data-of-Record
LST-Dynamic
SFMT
NNC ABAQUS V6.4
NNC ANAMAT
E6P
6R5
IRSN-CEA
KAERI-AXISYM
KAERI 3D
KOPEC
NRC-SNL-DEA
SCANSCOT

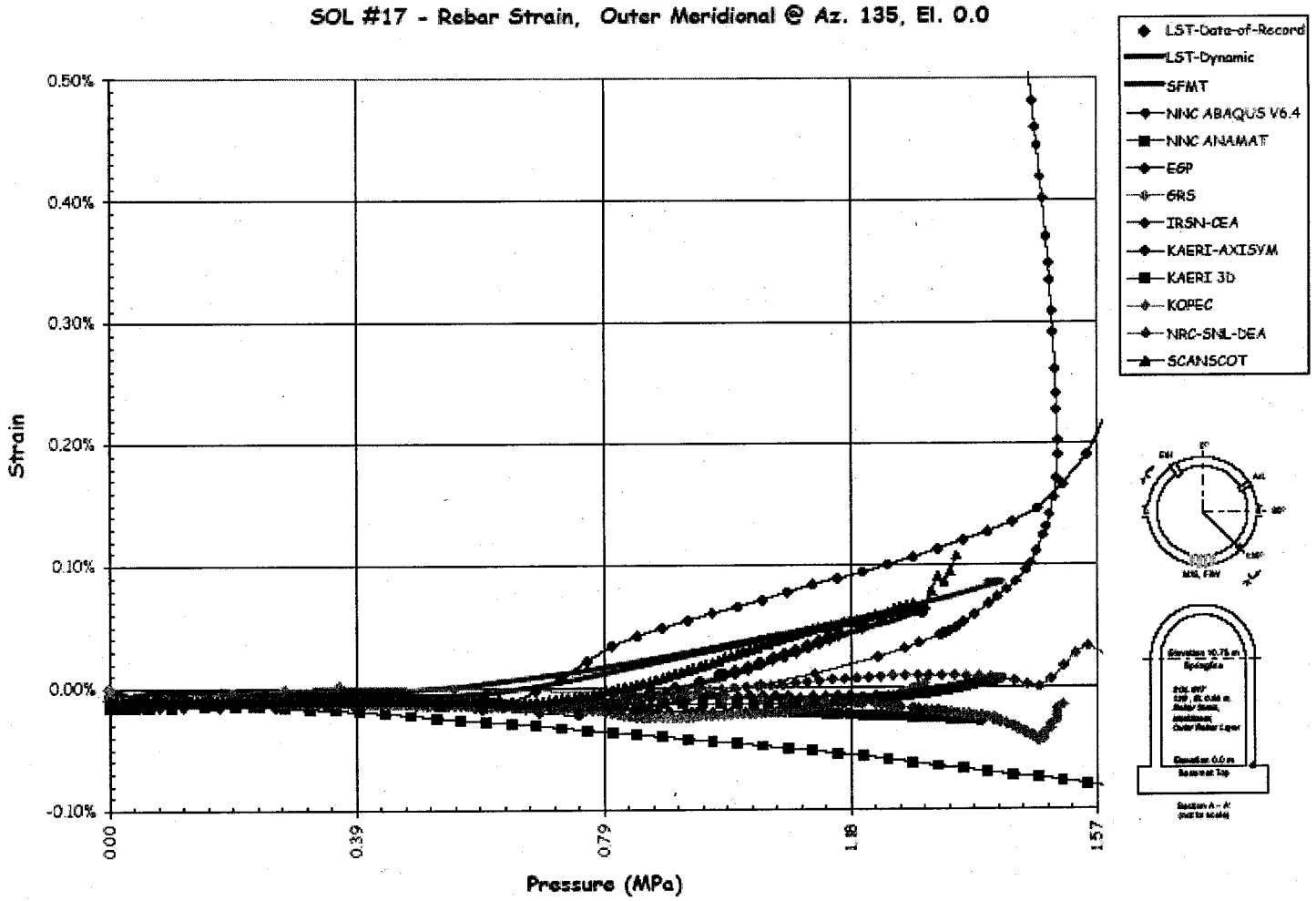
SOL #17 - Rebar Strain, Outer Meridional @ Az. 135, El. 0.0
LST-Data-of-Record
LST-Dynamic
SFMT
NNC ABAQUS V6.4
NNC ANAMAT
EGP
GRS
IRSN-CEA
KAERI-AXISYM
KAERI 3D
KOPEC
NRC-SNL-DEA
SCANSCOT
Strain
0.50%
0.40%
0.30%
0.20%
0.10%
0.00%
-0.10%
0.00
0.39
0.79
1.18
1.57
Pressure (MPa)

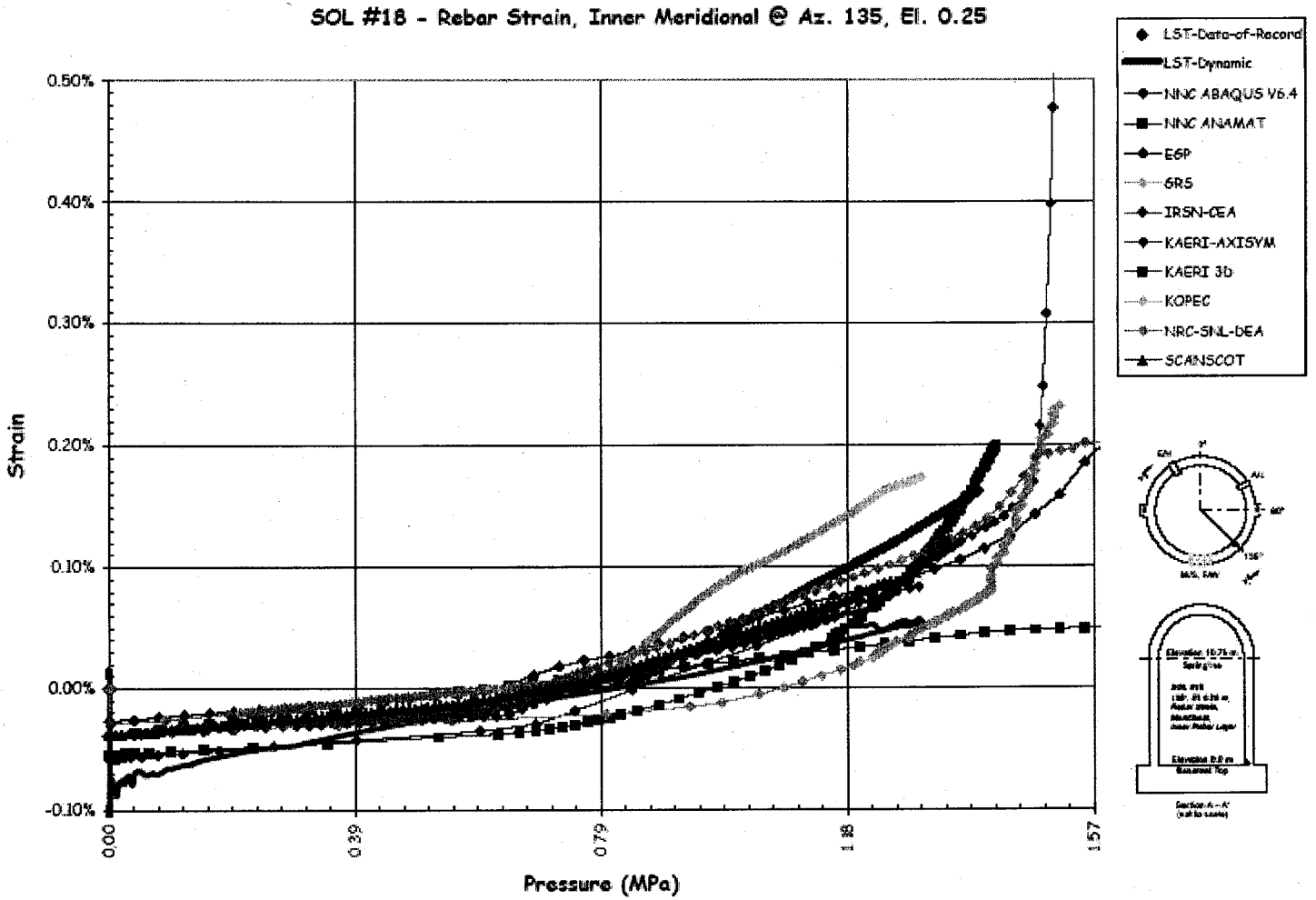
SOL #18 - Rebar Strain, Inner Meridional @ Az. 135, El. 0.25
Strain
0.50%
0.40%
0.30%
0.20%
0.10%
0.00%
-0.10%
0.00
0.39
0.79
1.18
1.57
Pressure (MPa)
LST-Data-of-Record
LST-Dynamic
NNC ABAQUS V6.4
NNC ANAMAT
E6P
GRS
IRSN-CEA
KAERI-AXISYM
KAERI 3D
KOPEC
NRC-SNL-CEA
SCANSCOT

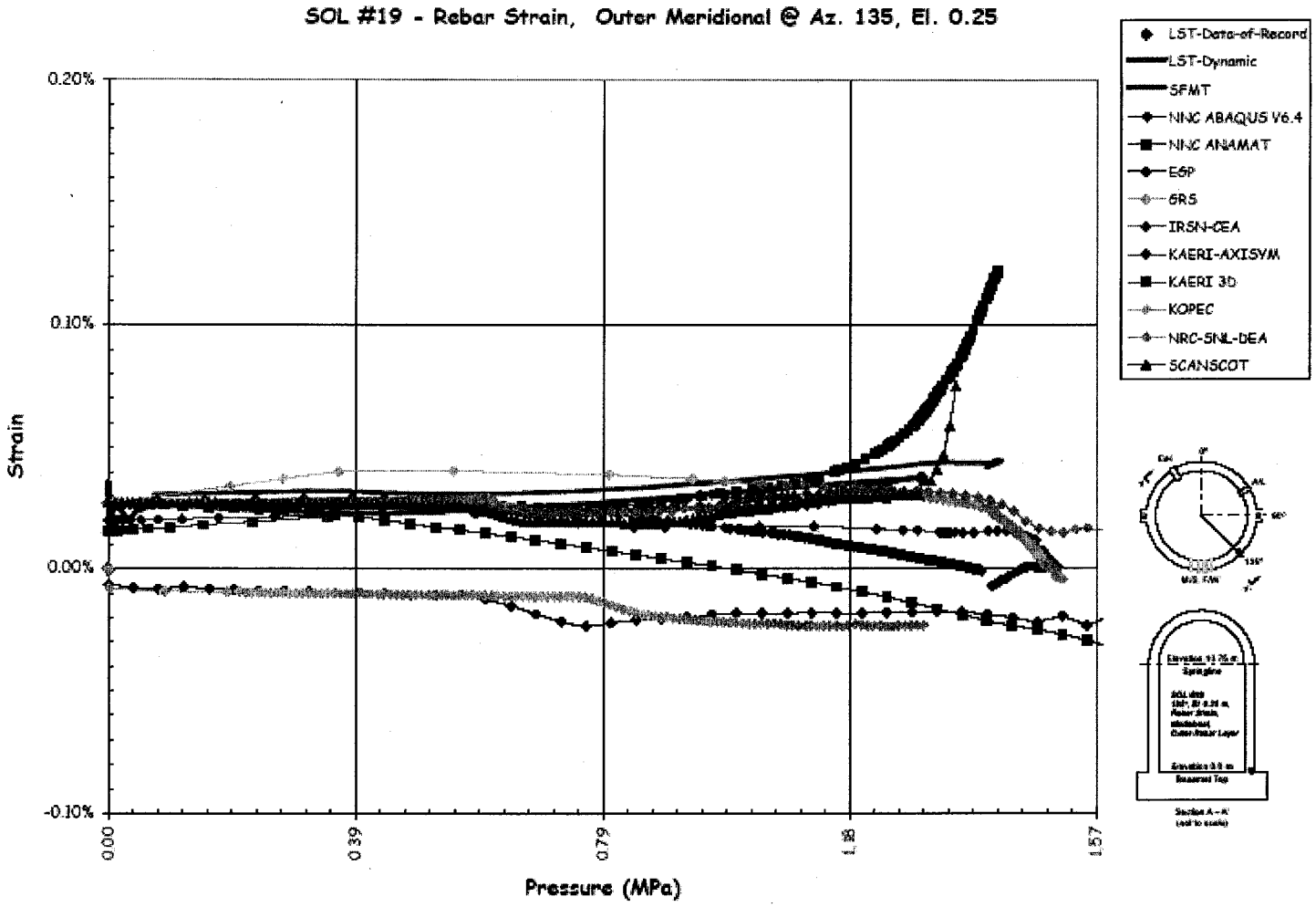
SOL #19 - Rebar Strain, Outer Meridional @ Az. 135, El. 0.25
0.20%
0.10%
0.00%
-0.10%
Strain
0.00
0.39
0.79
1.18
1.57
Pressure (MPa)
LST-Data-of-Record
LST-Dynamic
SFMT
NNC ABAQUS V6.4
NNC ANAMAT
EGP
GRS
IRSN-CEA
KAERI-AXISYM
KAERI 3D
KOPEC
NRC-SNL-DEA
SCANSCOT

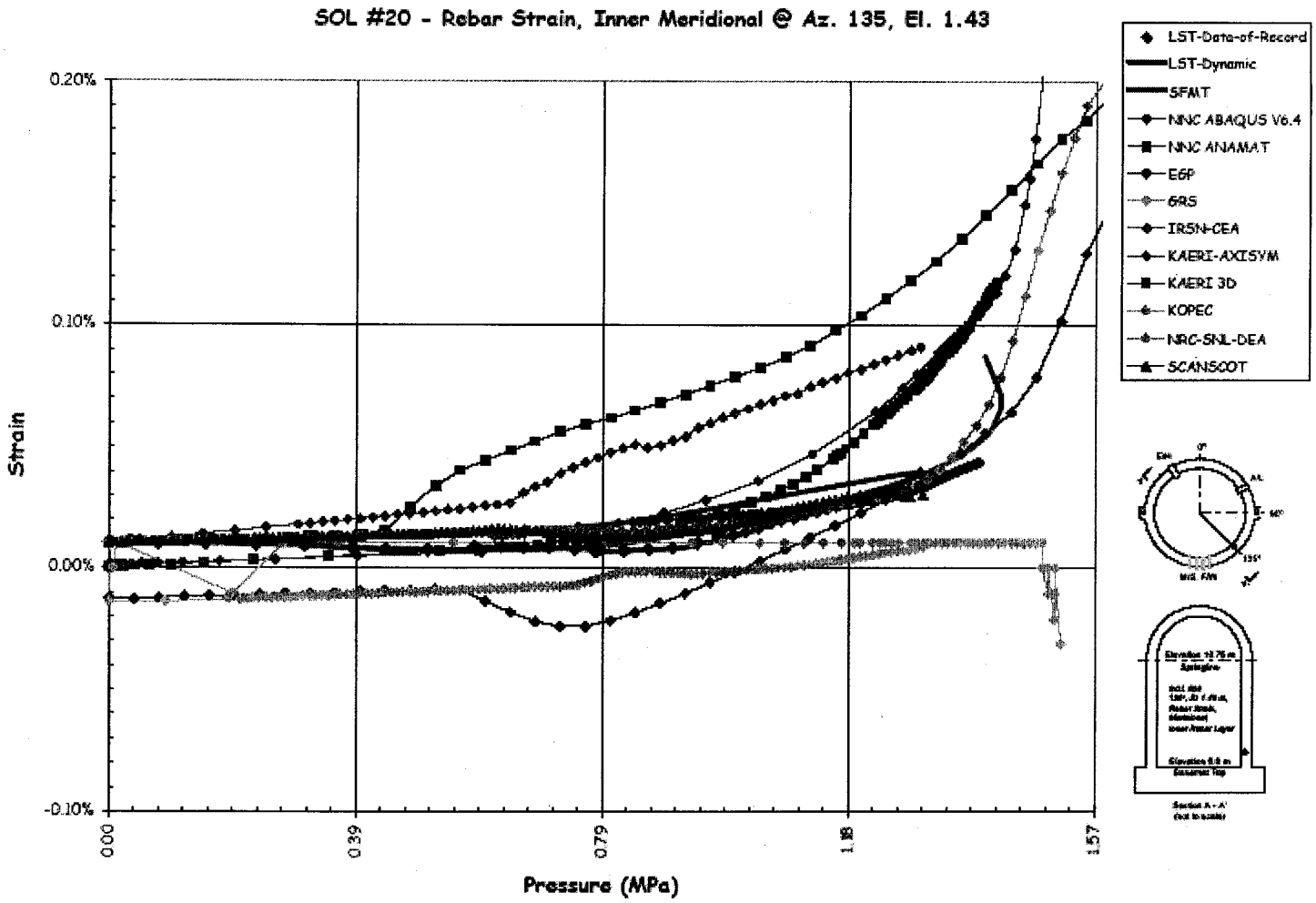
SOL #20 - Rebar Strain, Inner Meridional @ Az. 135, El. 1.43
0.20%
0.10%
0.00%
-0.10%
Strain
0.00
0.39
0.79
1.18
1.57
Pressure (MPa)
LST-Data-of-Record
LST-Dynamic
SFMT
NNC ABAQUS V6.4
NNC ANAMAT
EGP
GRS
IRSN-CEA
KAERI-AXISYM
KAERI 3D
KOPEC
NRC-SNL-DEA
SCANSCOT

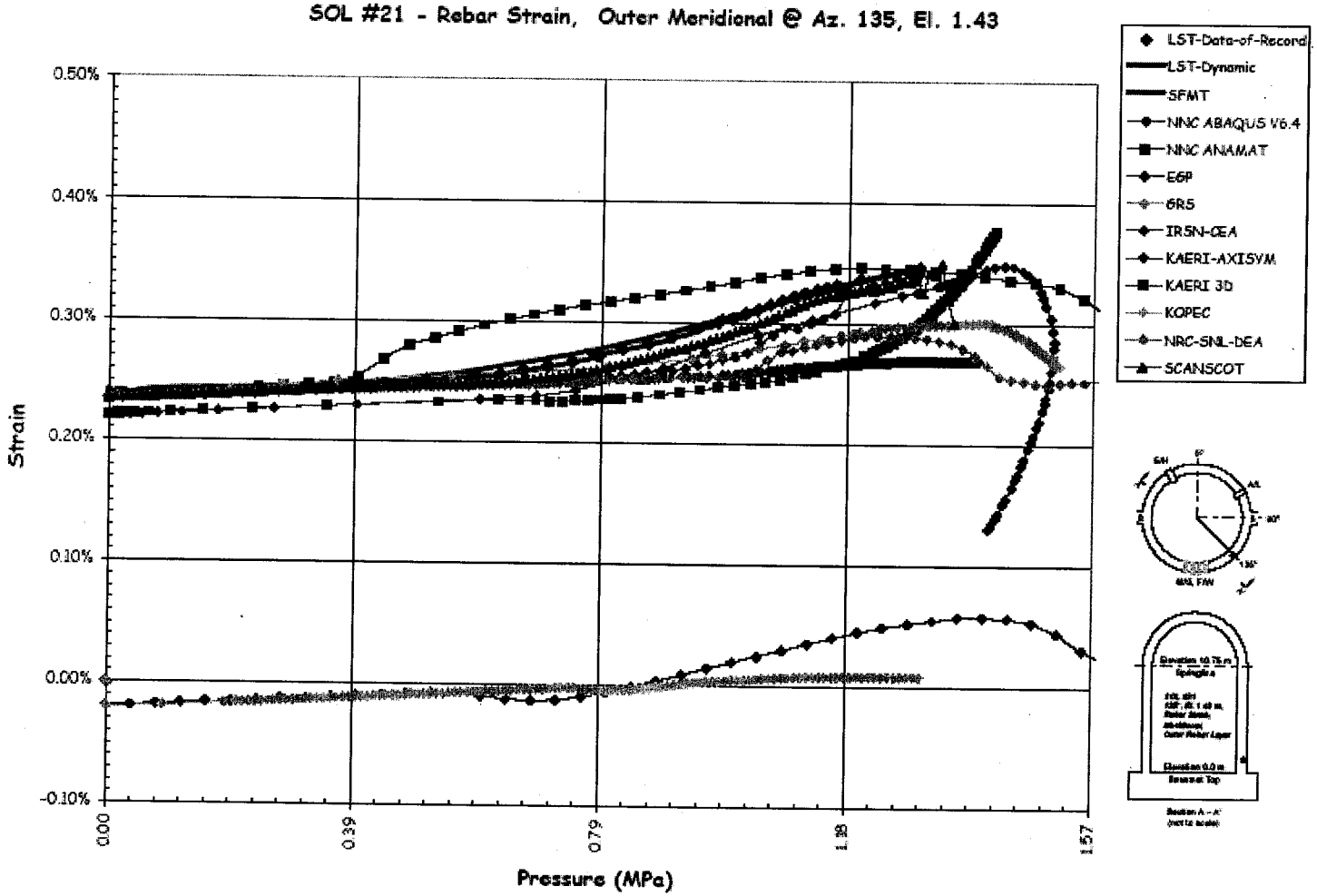
SOL #21 - Rebar Strain, Outer Meridional @ Az. 135, El. 1.43
0.50%
0.40%
0.30%
0.20%
0.10%
0.00%
-0.10%
Strain
0.00
0.39
0.79
1.18
1.57
Pressure (MPa)
LST-Data-of-Record
LST-Dynamic
SFMT
NNC ABAQUS V6.4
NNC ANAMAT
E6P
6R5
IRSN-CEA
KAERI-AXISYM
KAERI 3D
KOPEC
NRC-SNL-bEA
SCANSCOT

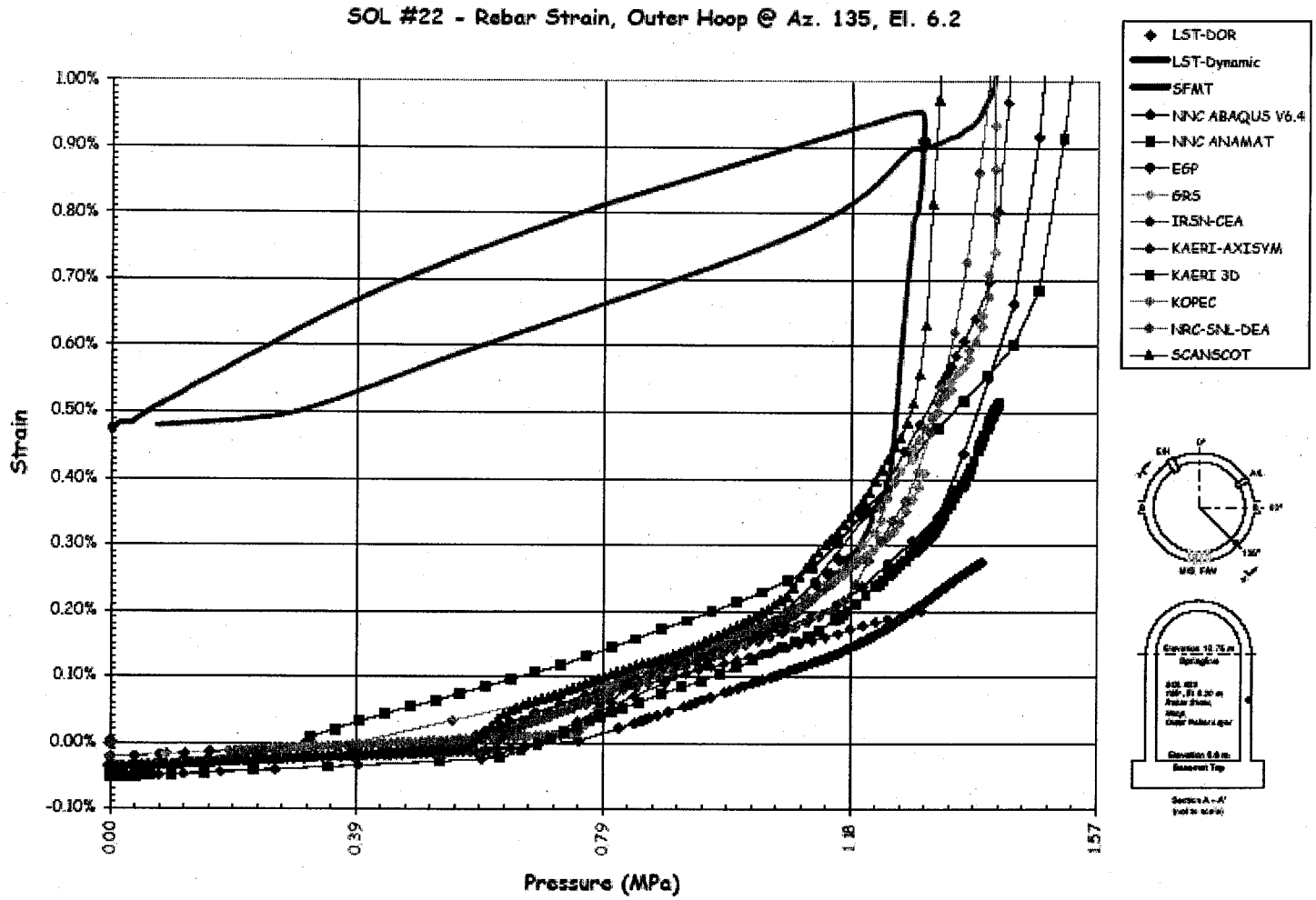
SOL #22 - Rebar Strain, Outer Hoop @ Az. 135, El. 6.2
Strain
1.00%
0.90%
0.80%
0.70%
0.60%
0.50%
0.40%
0.30%
0.20%
0.10%
0.00%
-0.10%
0.00
0.39
0.79
1.18
1.57
Pressure (MPa)
LST-DOR
LST-Dynamic
SFMT
NNC ABAQUS V6.4
NNC ANAMAT
E6P
6R5
IRSN-CEA
KAERI-AXISYM
KAERI 3D
KOPEC
NRC-SNL-DEA
SCANSCOT

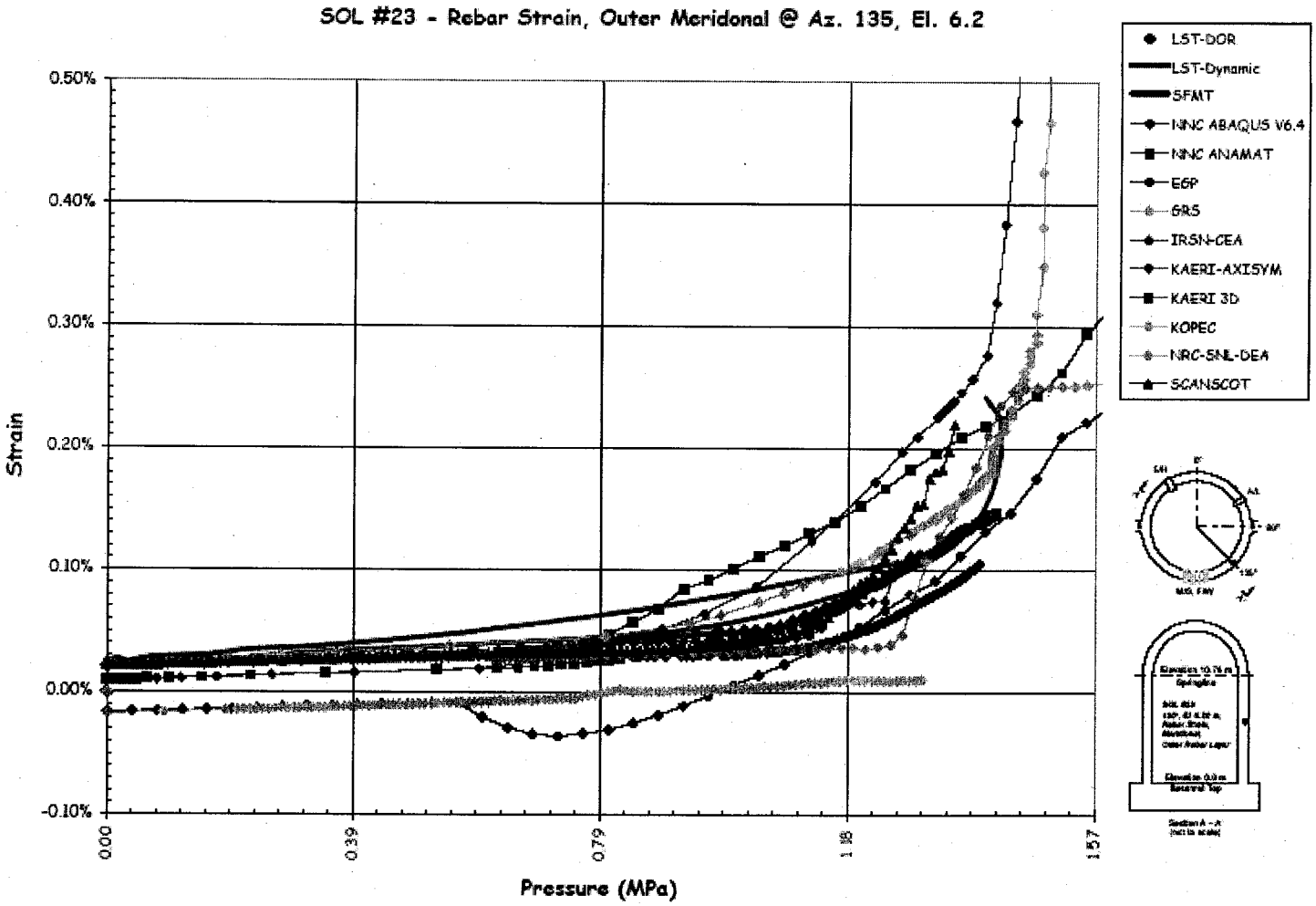
SOL #23 - Rebar Strain, Outer Meridonal @ Az. 135, El. 6.2
Strain
0.50%
0.40%
0.30%
0.20%
0.10%
0.00%
-0.10%
0.00
0.39
0.79
1.18
1.57
Pressure (MPa)
LST-DOR
LST-Dynamic
SFMT
NNC ABAQUS V6.4
NNC ANAMAT
EGP
GRS
IRSN-CEA
KAERI-AXISYM
KAERI 3D
KOPEC
NRC-SNL-DEA
SCANSCOT

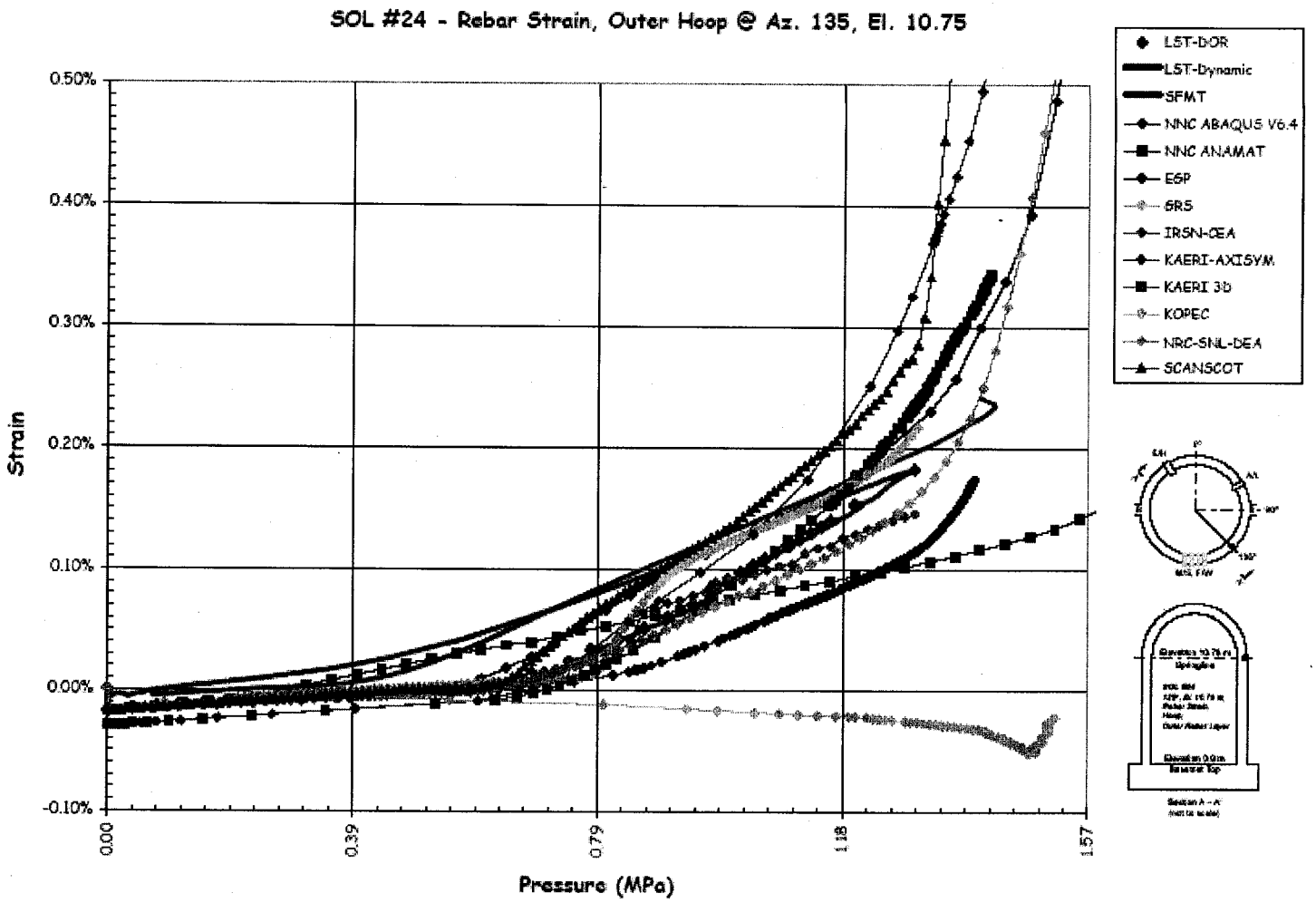
SOL #24 - Rebar Strain, Outer Hoop @ Az. 135, El. 10.75
Strain
0.50%
0.40%
0.30%
0.20%
0.10%
0.00%
-0.10%
0.00
0.39
0.79
1.18
1.57
Pressure (MPa)
LST-DOR
LST-Dynamic
SFMT
NNC ABAQUS V6.4
NNC ANAMAT
ESP
6R5
IRSN-CEA
KAERI-AXISYM
KAERI 3D
KOPEC
NRC-SNL-DEA
SCANSCOT

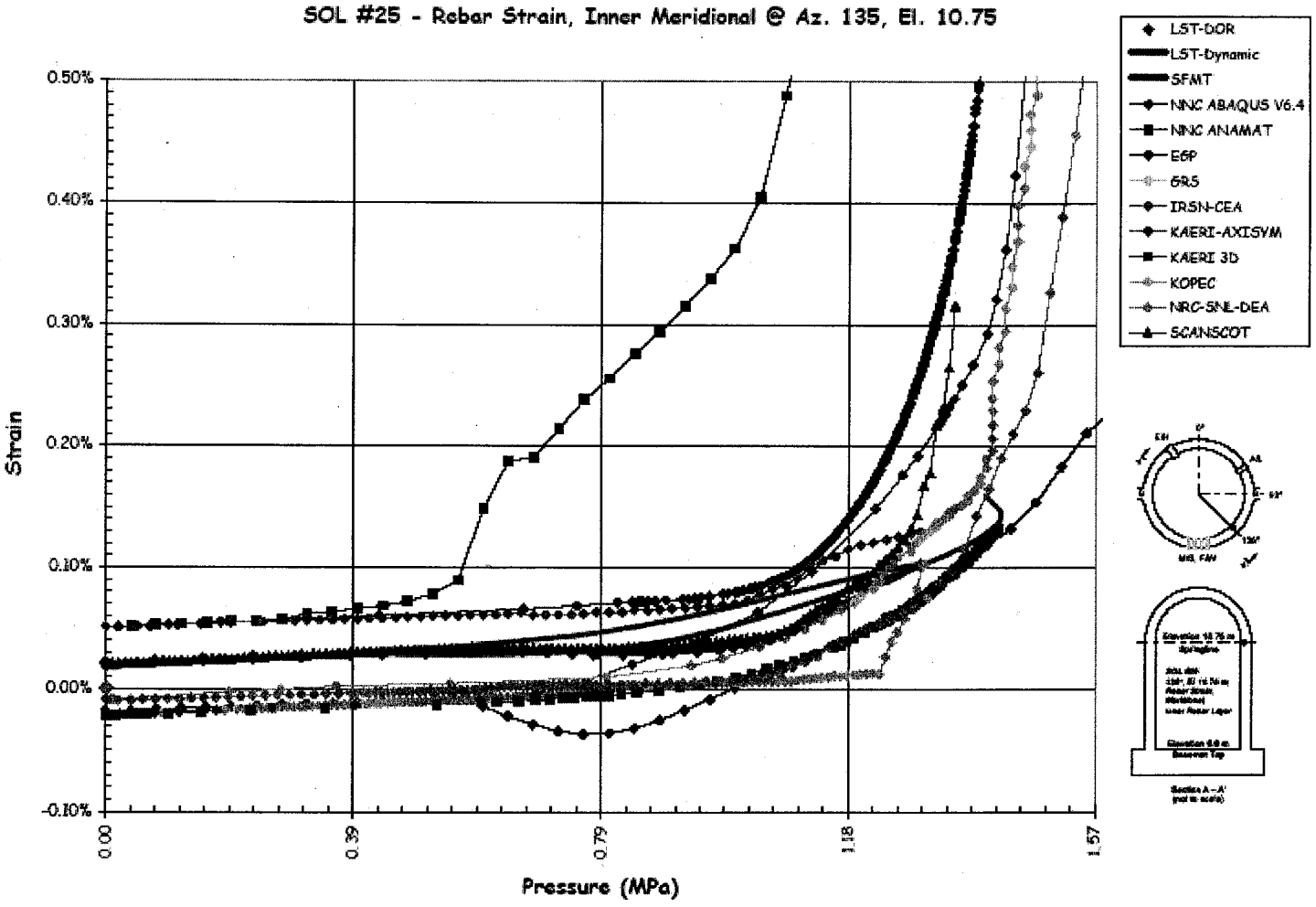
SOL #25 - Rebar Strain, Inner Meridional @ Az. 135, El. 10.75
LST-DOR
LST-Dynamic
SFMT
NNC ABAQUS V6.4
NNC ANAMAT
E6P
6R5
IRSN-CEA
KAERI-AXISYM
KAERI 3D
KOPEC
NRC-SNL-DEA
SCANSCOT
0.50%
0.40%
0.30%
0.20%
0.10%
0.00%
-0.10%
Strain
0.00
0.39
0.79
1.18
1.57
Pressure (MPa)

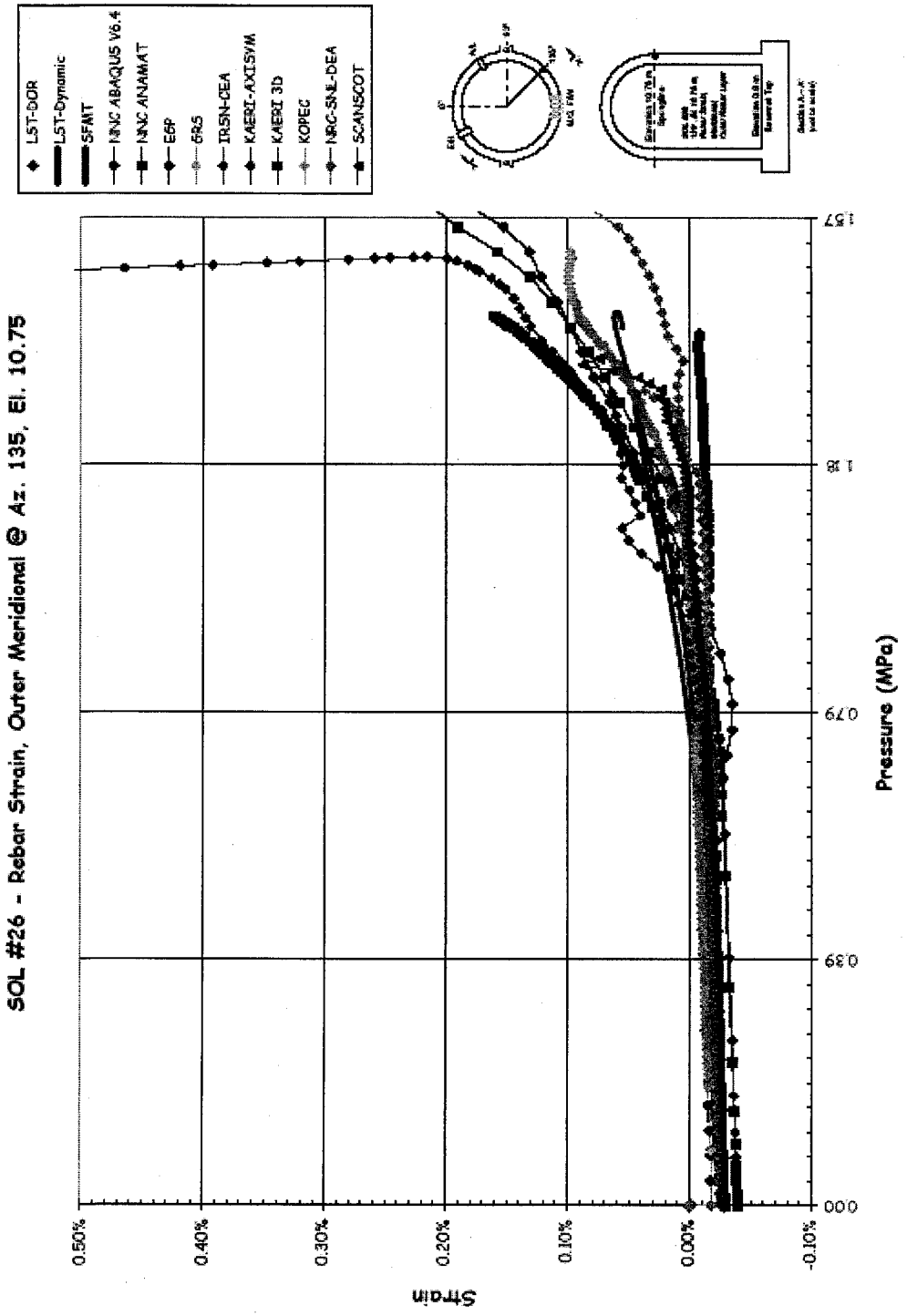
SOL #26 - Rebar Strain, Outer Meridional @ Az. 135, El. 10.75
LST-DOR
LST-Dynamic
SFMT
NNC ABAQUS V6.4
NNC ANAMAT
EGP
ERS
IRSN-CEA
KAERI-AXISVM
KAERI 3D
KOPEC
NRC-SNL-DEA
SCANSCOT
Strain
0.50%
0.40%
0.30%
0.20%
0.10%
0.00%
-0.10%
Pressure (MPa)
000
039
079
118
157

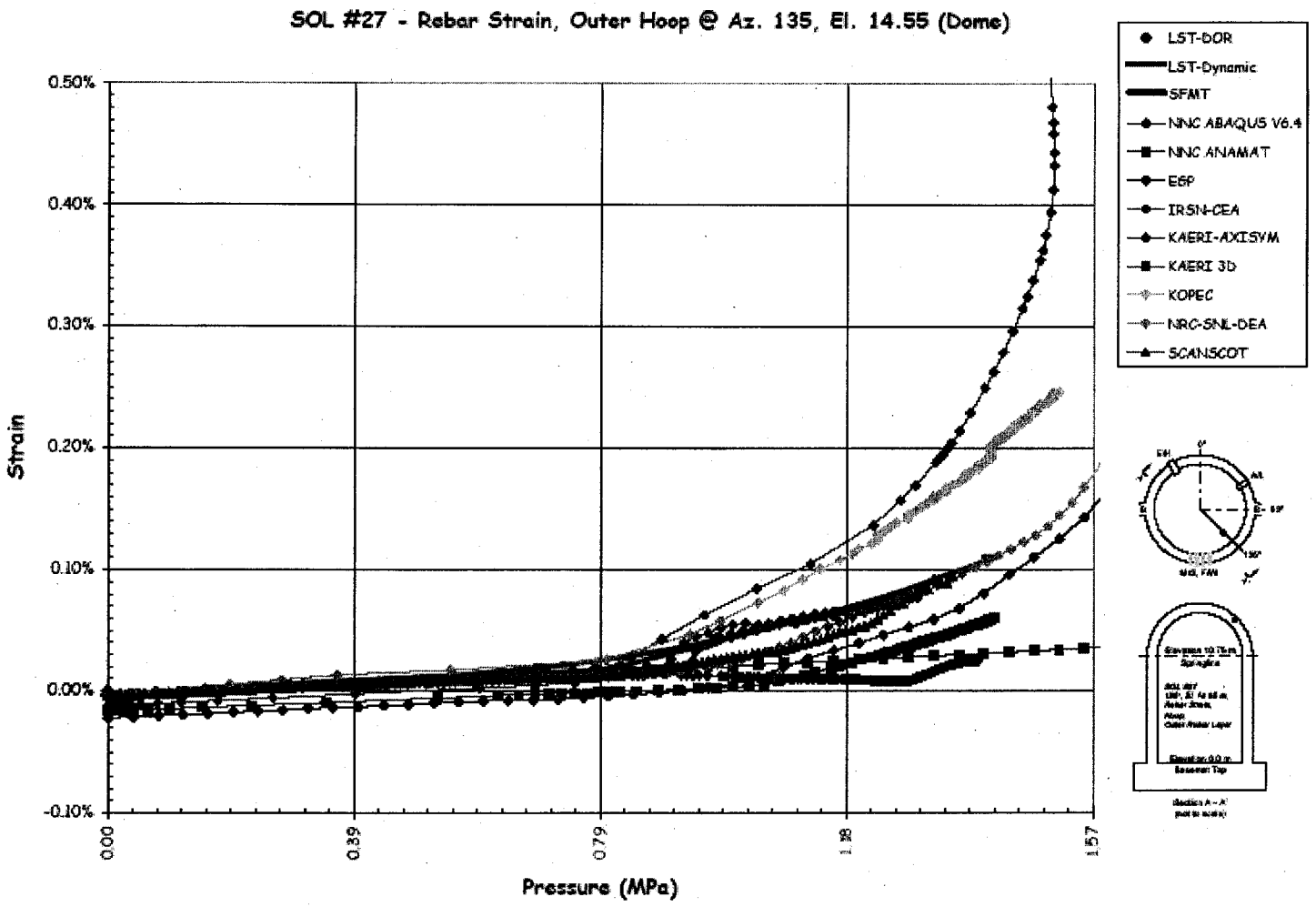
SOL #27 - Rebar Strain, Outer Hoop @ Az. 135, El. 14.55 (Dome)
Strain
0.50%
0.40%
0.30%
0.20%
0.10%
0.00%
-0.10%
0.00
0.39
0.79
1.18
1.57
Pressure (MPa)
LST-DOR
LST-Dynamic
SFMT
NNC ABAQUS V6.4
NNC ANAMAT
ESP
IRSN-CEA
KAERI-AXISYM
KAERI 3D
KOPEC
NRC-SNL-DEA
SCANSCOT

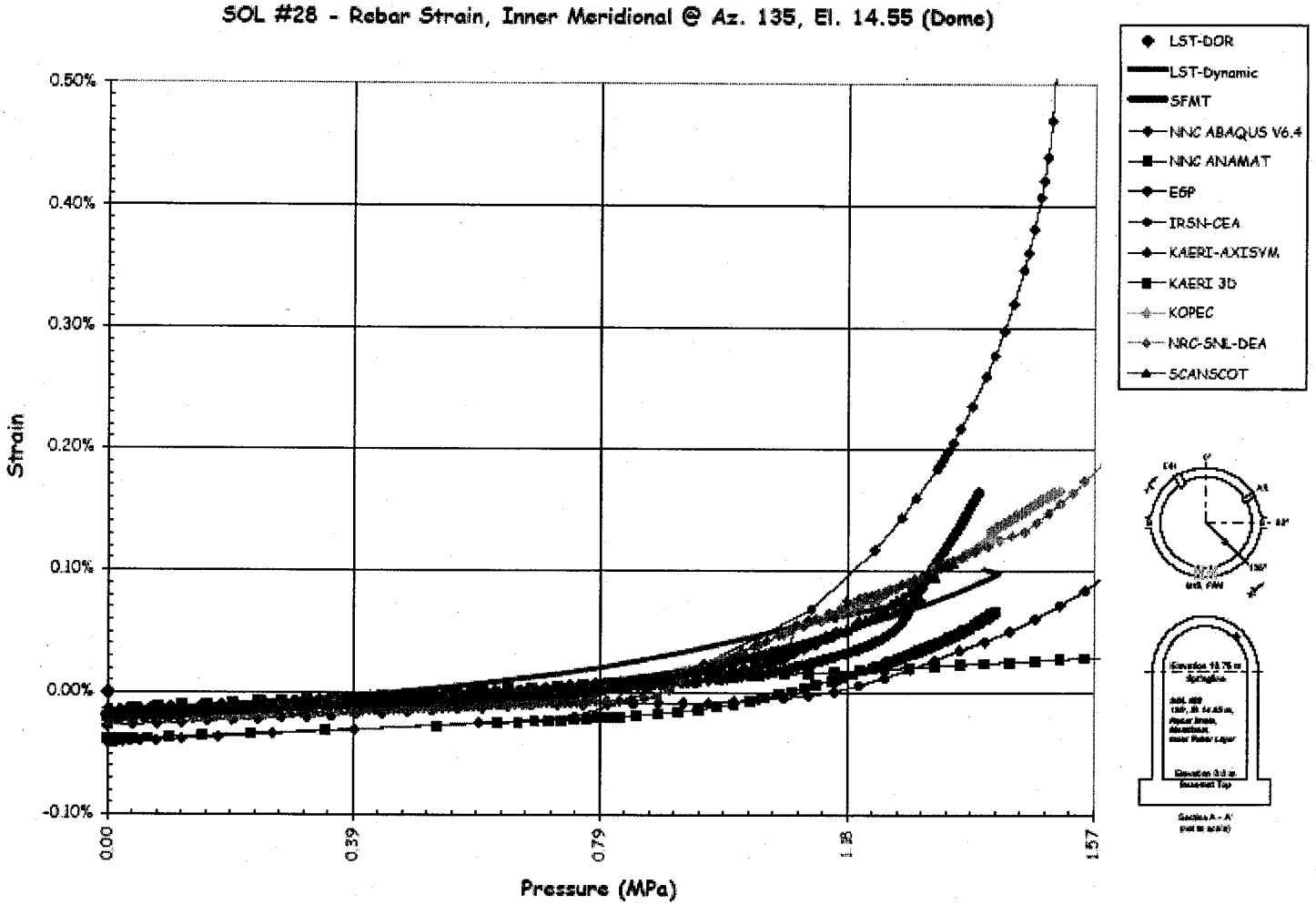
SOL #28 - Rebar Strain, Inner Meridional @ Az. 135, El. 14.55 (Dome)
Strain
0.50%
0.40%
0.30%
0.20%
0.10%
0.00%
-0.10%
0.00
0.39
0.79
1.18
1.57
Pressure (MPa)
LST-DOR
LST-Dynamic
SFMT
NNC ABAQUS V6.4
NNC ANAMAT
E6P
IRSN-CEA
KAERI-AXISYM
KAERI 3D
KOPEC
NRC-SNL-DEA
SCANSCOT

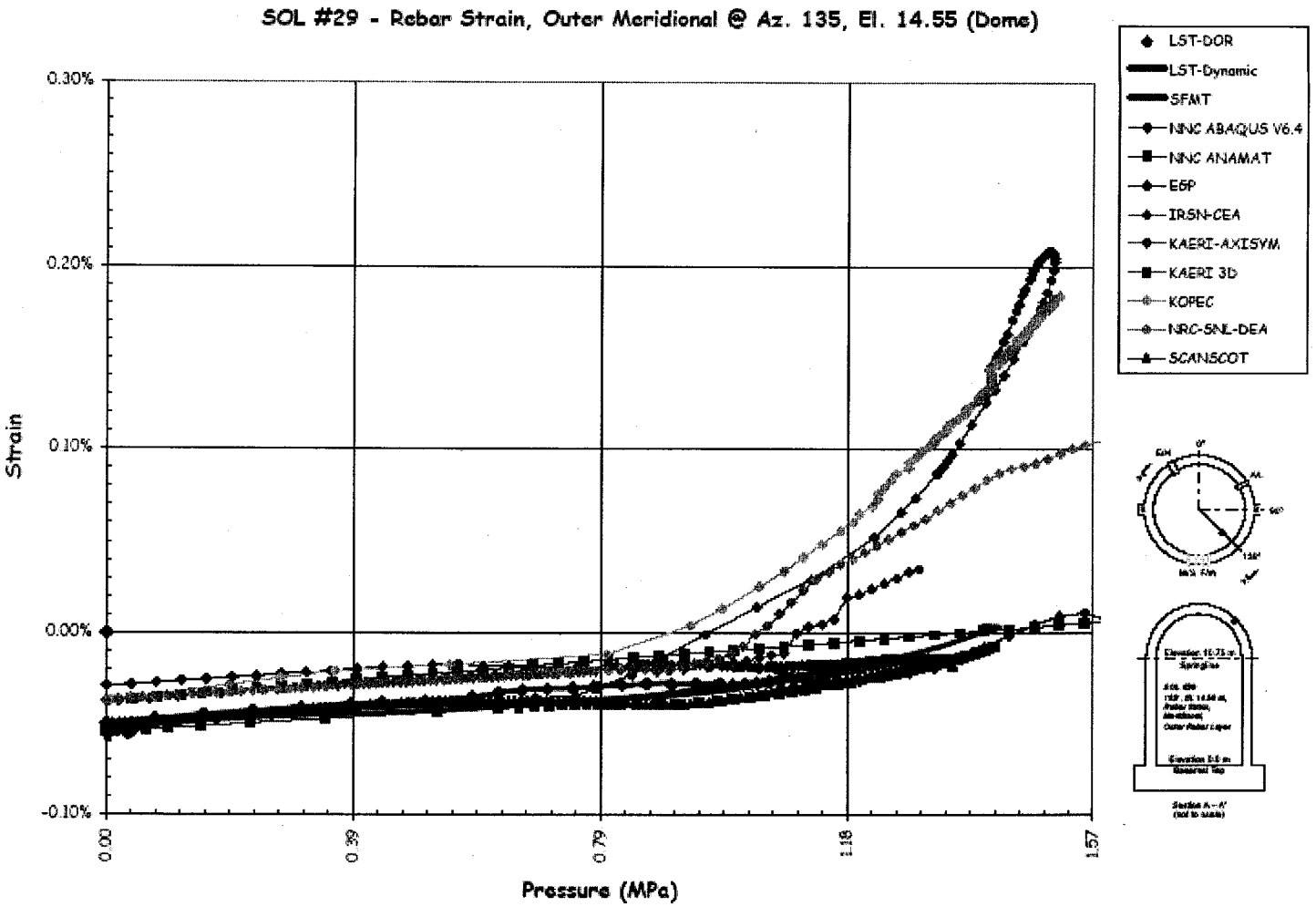
SOL #29 - Rebar Strain, Outer Meridional @ Az. 135, El. 14.55 (Dome)
0.30%
0.20%
0.10%
0.00%
-0.10%
Strain
0.00
0.39
0.79
1.18
1.57
Pressure (MPa)
LST-DOR
LST-Dynamic
SFMT
NNC ABAQUS V6.4
NNC ANAMAT
EGP
IRSN-CEA
KAERI-AXISYM
KAERI 3D
KOPEC
NRC-SNL-DEA
SCANSCOT

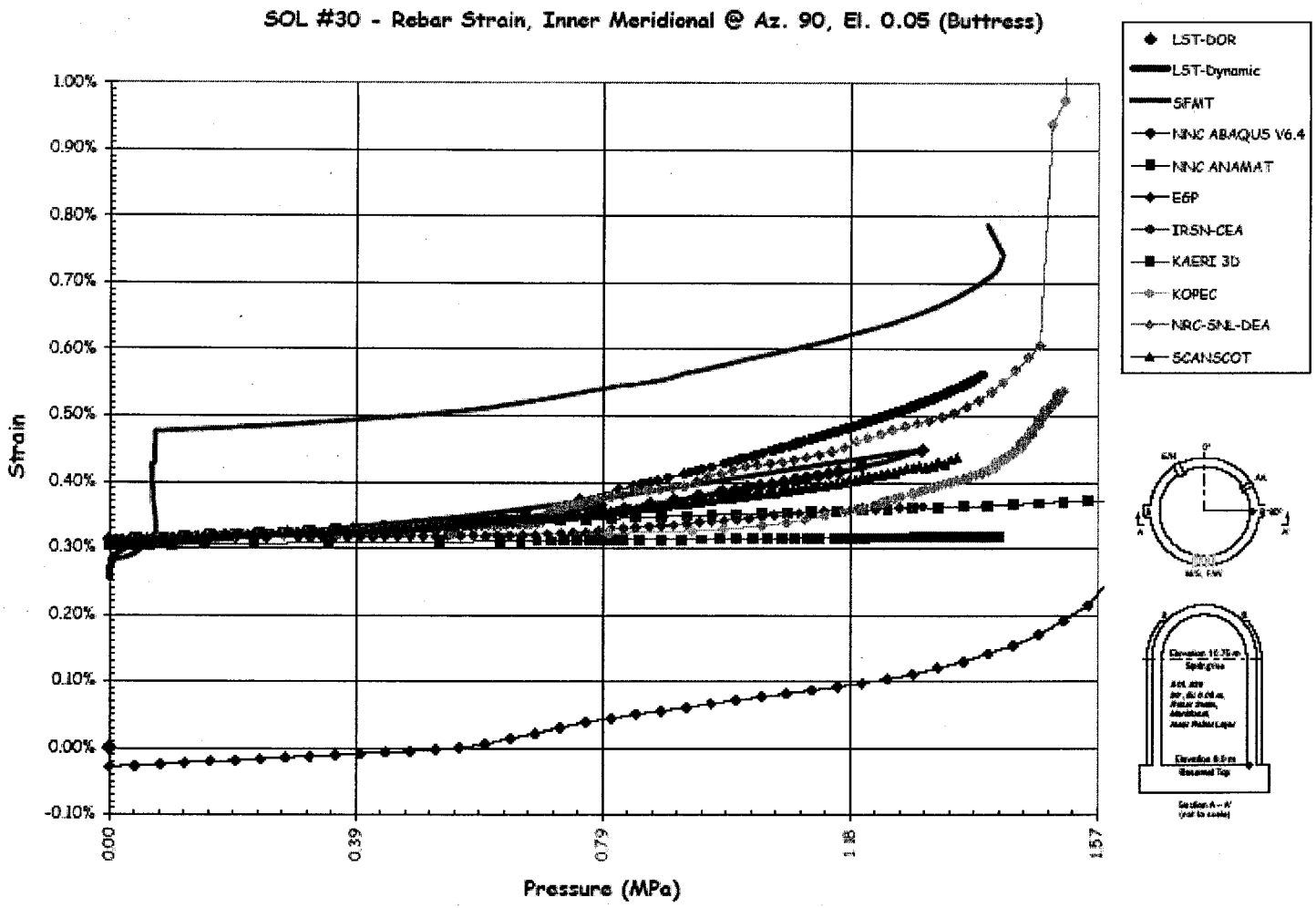
SOL #30 - Rebar Strain, Inner Meridional @ Az. 90, El. 0.05 (Buttress)
Strain
1.00%
0.90%
0.80%
0.70%
0.60%
0.50%
0.40%
0.30%
0.20%
0.10%
0.00%
-0.10%
0.00
0.39
0.79
1.18
1.57
Pressure (MPa)
LST-DOR
LST-Dynamic
SFMT
NNC ABAQUS V6.4
NNC ANAMAT
EGP
IRSN-CEA
KAERI 3D
KOPEC
NRC-SNL-DEA
SCANSCOT

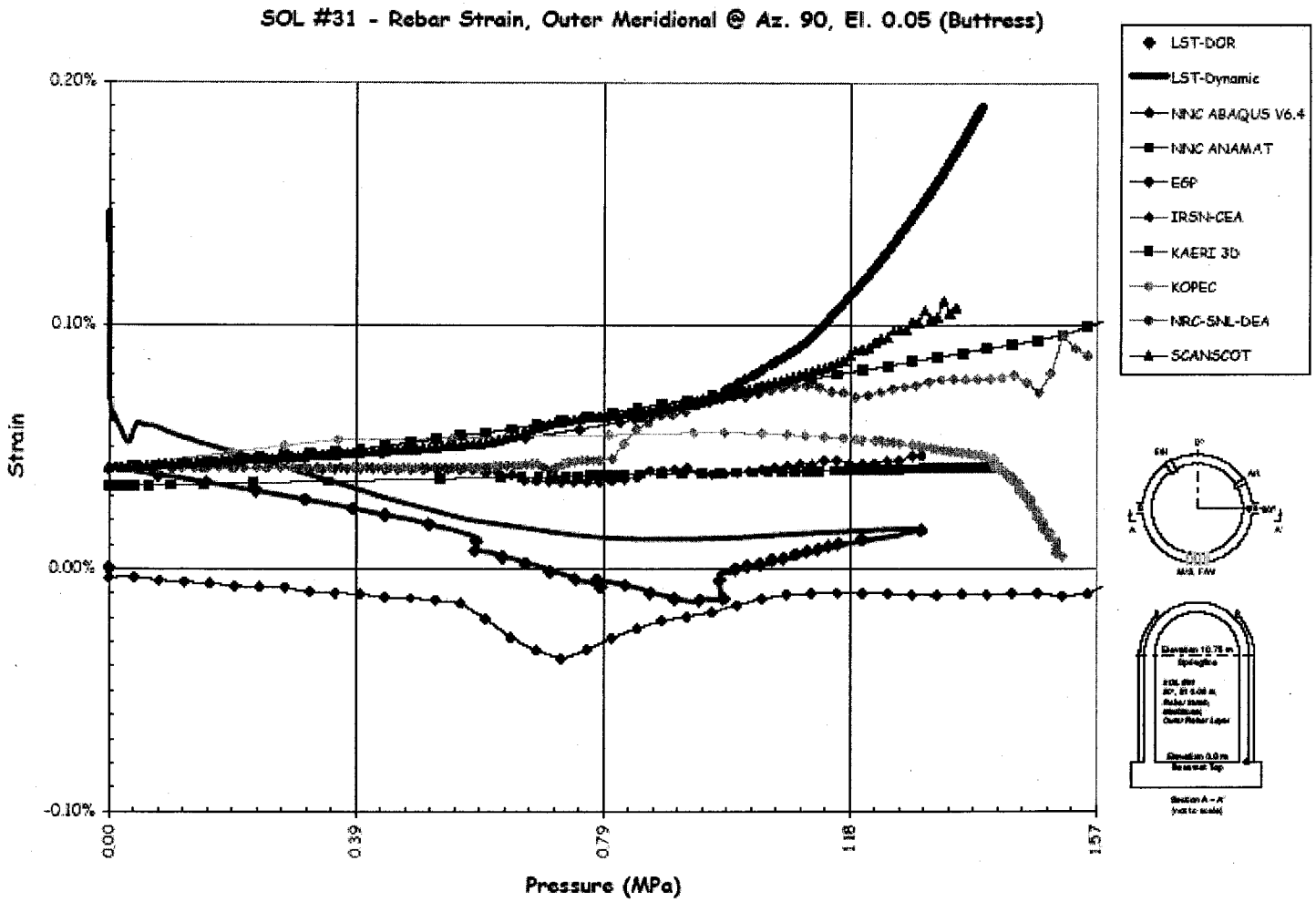
SOL #31 - Rebar Strain, Outer Meridional @ Az. 90, El. 0.05 (Buttress)
0.20%
0.10%
0.00%
-0.10%
Strain
0.00
0.39
0.79
1.18
1.57
Pressure (MPa)
LST-DOR
LST-Dynamic
NNC ABAQUS V6.4
NNC ANAMAT
E6P
IRSN-CEA
KAERI 3D
KOPEC
NRC-SNL-DEA
SCANSCOT

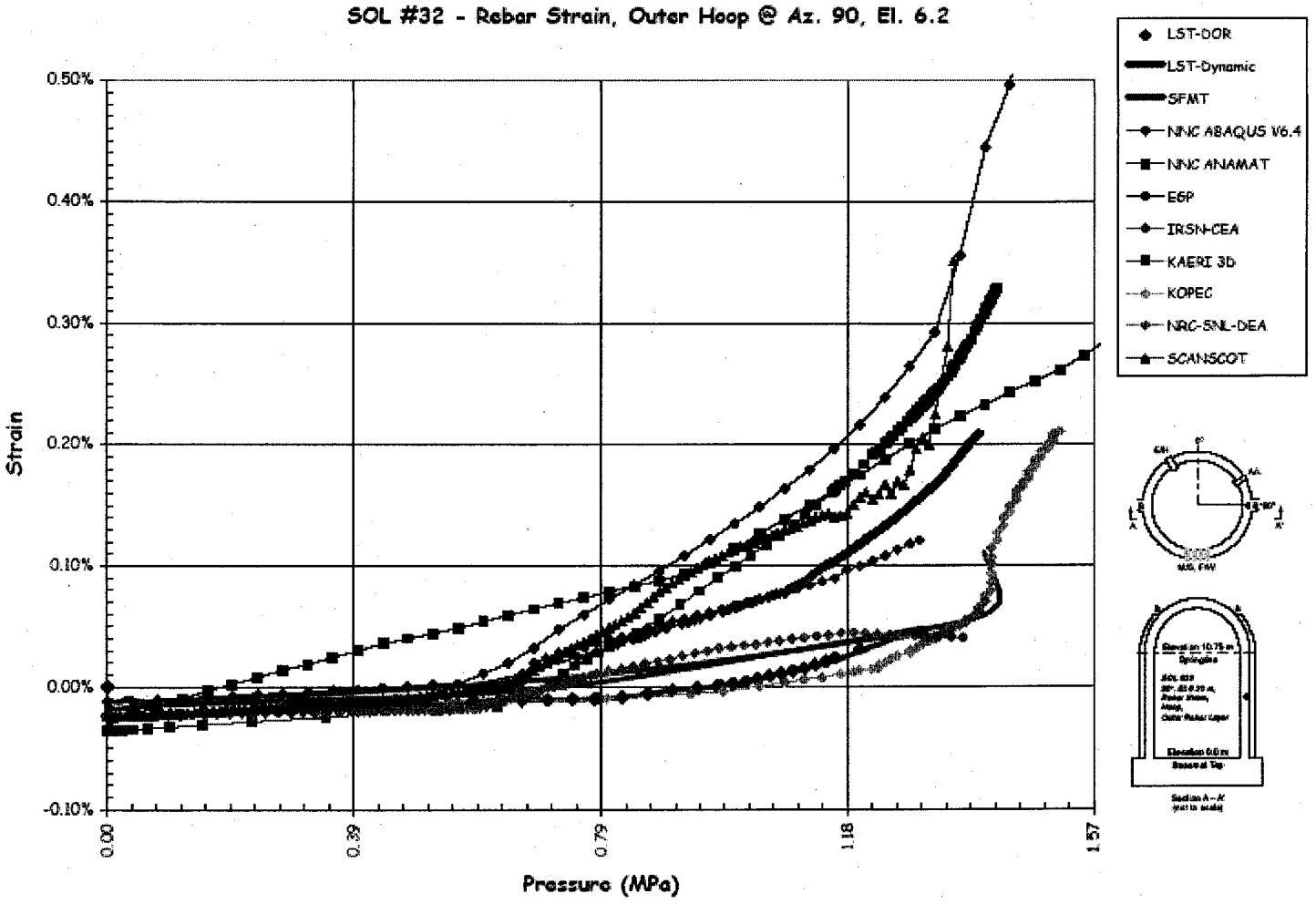
SOL #32 - Rebar Strain, Outer Hoop @ Az. 90, El. 6.2
0.50%
0.40%
0.30%
0.20%
0.10%
0.00%
-0.10%
Strain
0.00
0.39
0.79
1.18
1.57
Pressure (MPa)
LST-DOR
LST-Dynamic
SFMT
NNC ABAQUS V6.4
NNC ANAMAT
E6P
IRSN-CEA
KAERI 3D
KOPEC
NRC-SNL-DEA
SCANSCOT

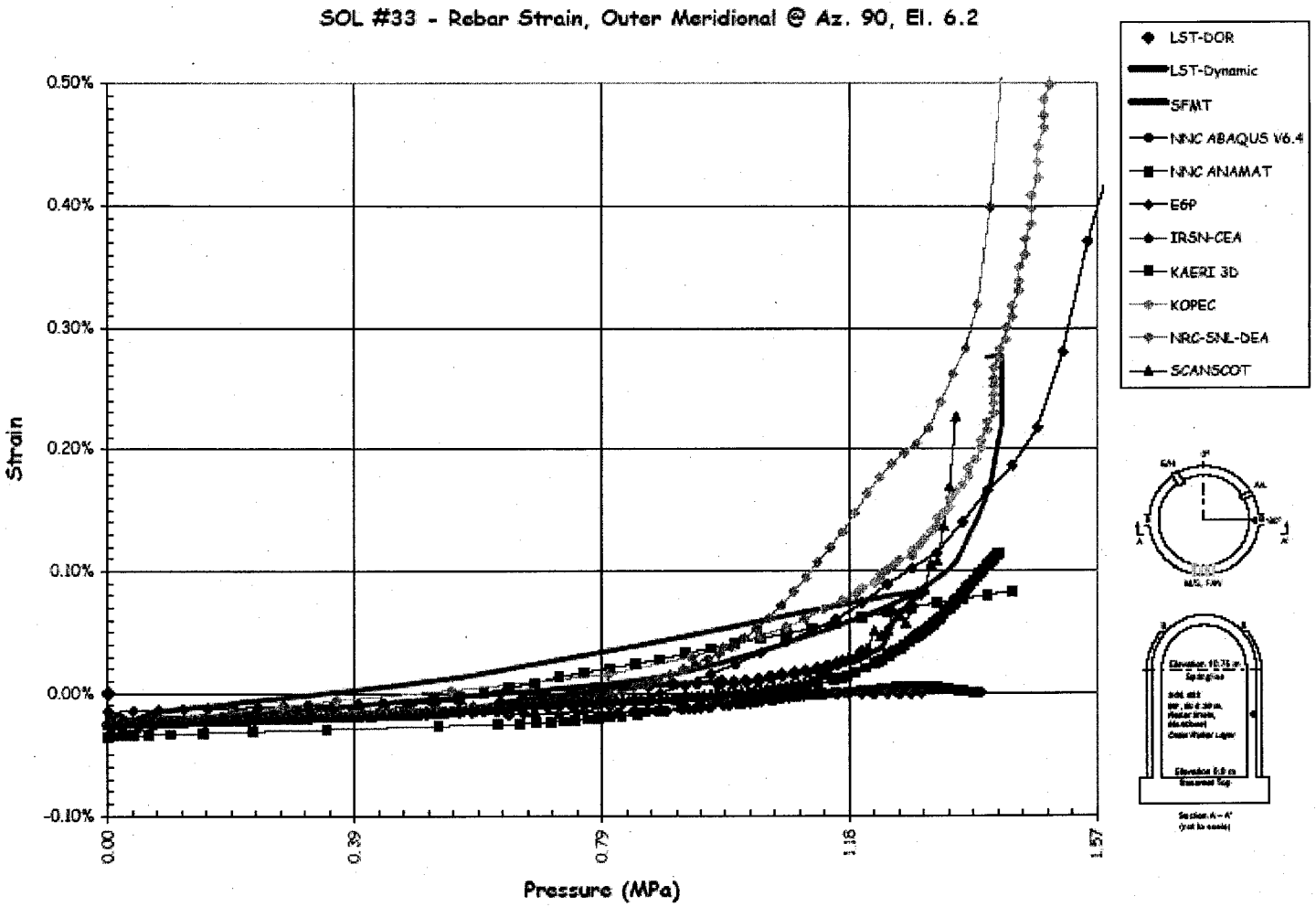
SOL #33 - Rebar Strain, Outer Meridional @ Az. 90, El. 6.2
Strain
0.50%
0.40%
0.30%
0.20%
0.10%
0.00%
-0.10%
0.00
0.39
0.79
1.18
1.57
Pressure (MPa)
LST-DOR
LST-Dynamic
SFMT
NNC ABAQUS V6.4
NNC ANAMAT
E6P
IRSN-CEA
KAERI 3D
KOPEC
NRC-SNL-DEA
SCANSCOT

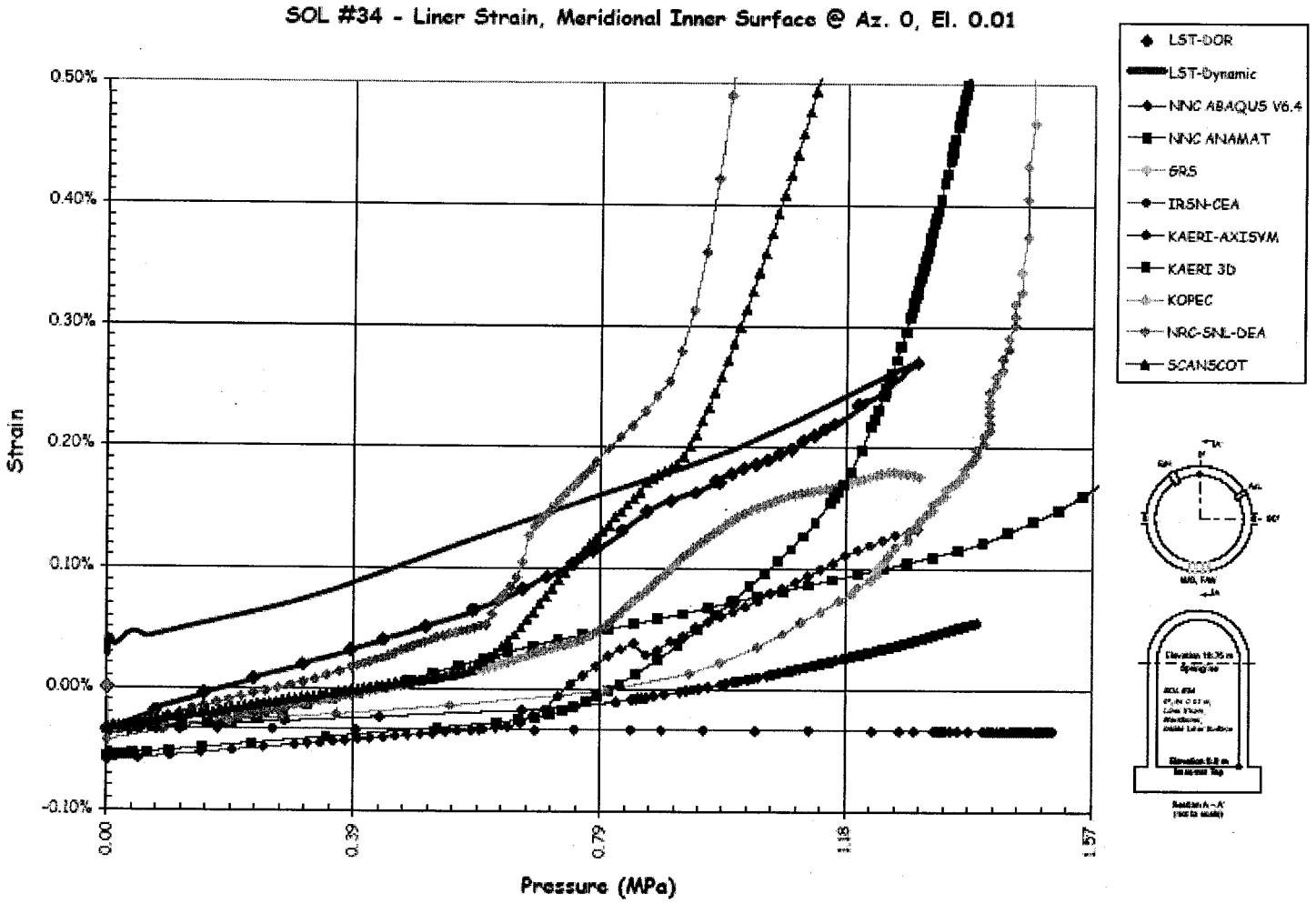
SOL #34 - Liner Strain, Meridional Inner Surface @ Az. 0, El. 0.01
Strain
0.50%
0.40%
0.30%
0.20%
0.10%
0.00%
-0.10%
0.00
0.39
0.79
1.18
1.57
Pressure (MPa)
LST-DOR
LST-Dynamic
NNC ABAQUS V6.4
NNC ANAMAT
SRS
IRSN-CEA
KAERI-AXISYM
KAERI 3D
KOPEC
NRC-SNL-DEA
SCANSCOT

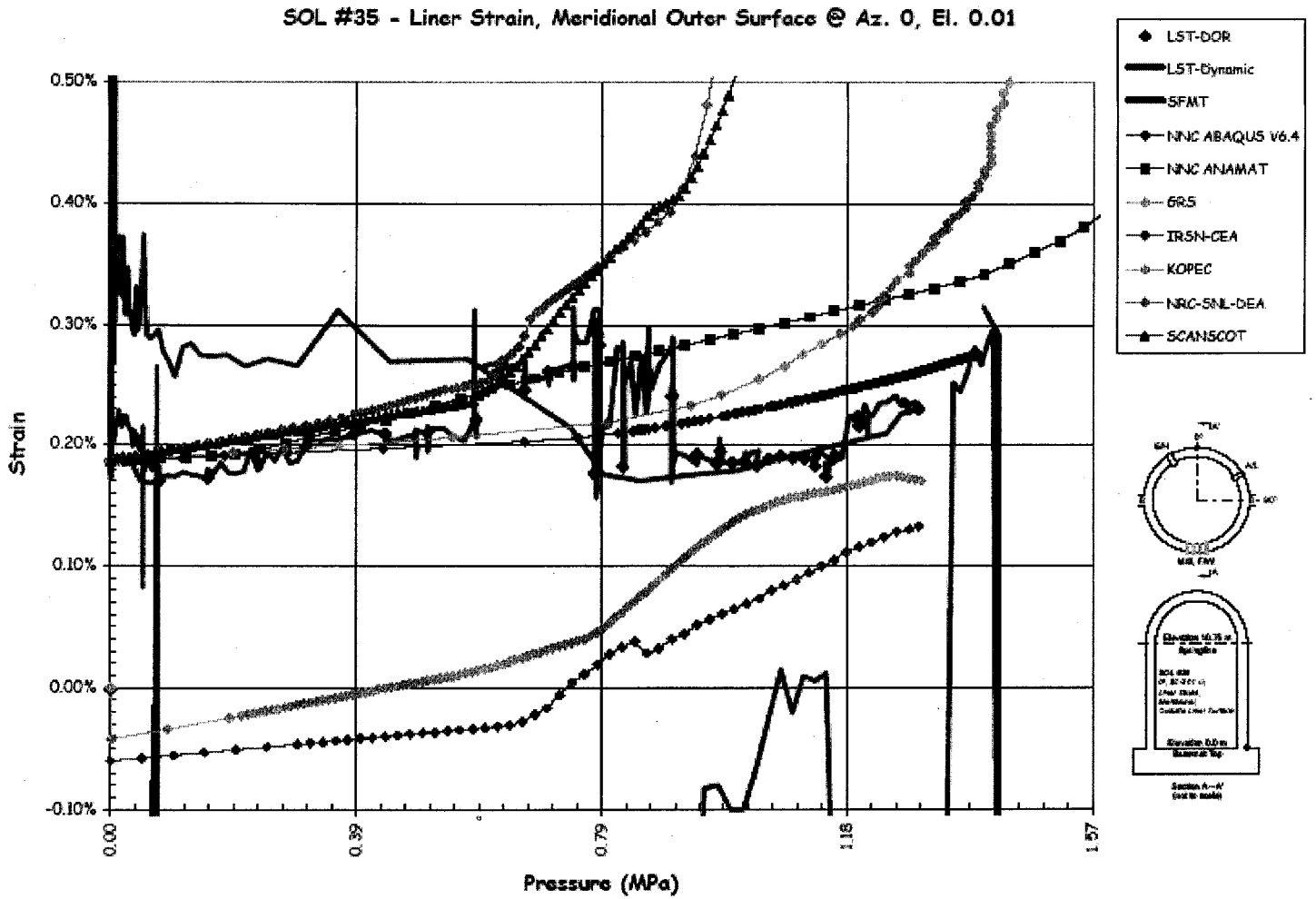
SOL #35 - Liner Strain, Meridional Outer Surface @ Az. 0, El. 0.01
Strain
0.50%
0.40%
0.30%
0.20%
0.10%
0.00%
-0.10%
0.00
0.39
0.79
1.18
1.57
Pressure (MPa)
LST-DOR
LST-Dynamic
SFMT
NNC ABAQUS V6.4
NNC ANAMAT
GRS
IRSN-CEA
KOPEC
NRC-SNL-DEA
SCANSCOT

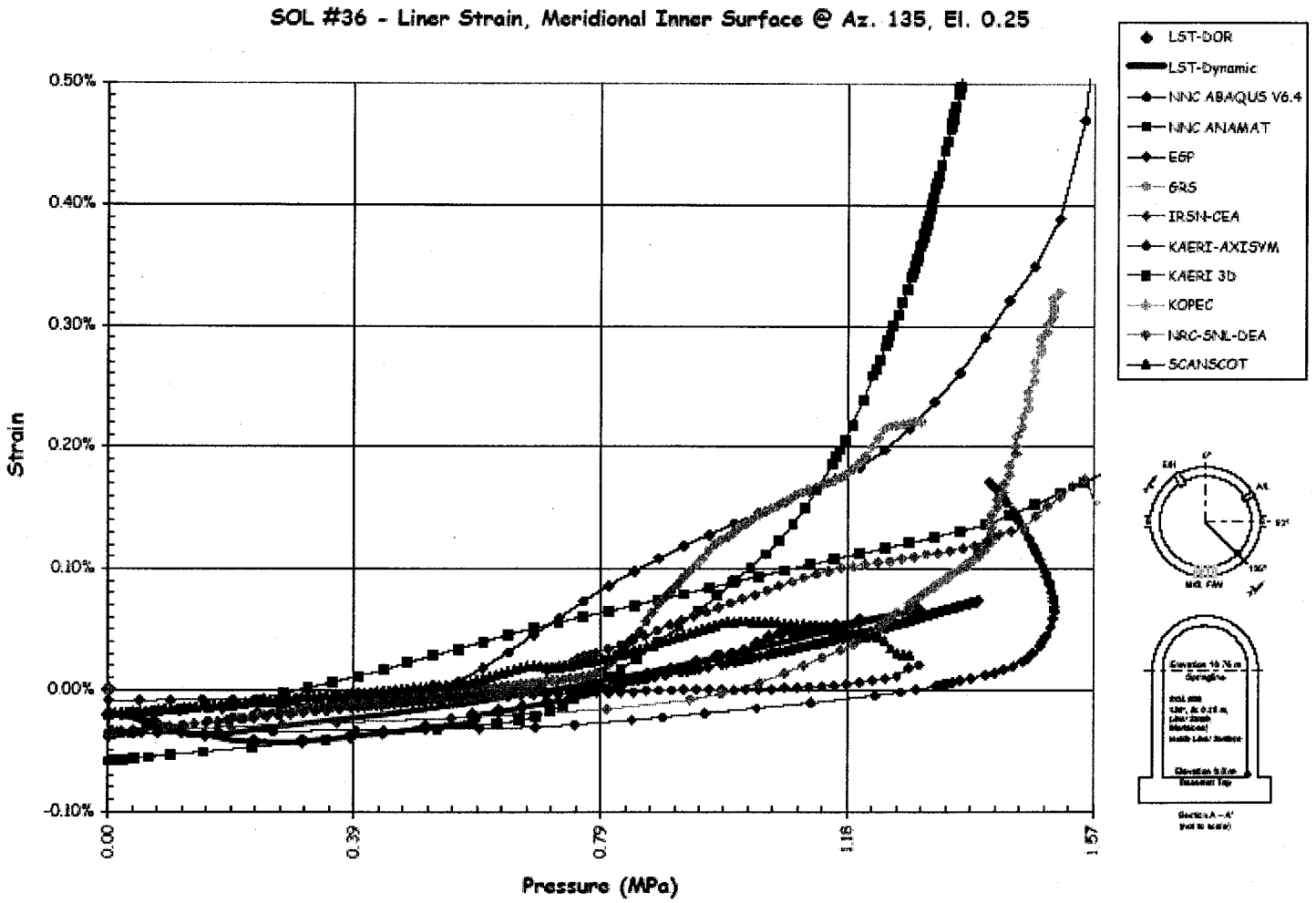
SOL #36 - Liner Strain, Meridional Inner Surface @ Az. 135, El. 0.25
Strain
0.50%
0.40%
0.30%
0.20%
0.10%
0.00%
-0.10%
0.00
0.39
0.79
1.18
1.57
Pressure (MPa)
LST-DOR
LST-Dynamic
NNC ABAQUS V6.4
NNC ANAMAT
EGP
GRS
IRSN-CEA
KAERI-AXISYM
KAERI 3D
KOPEC
NRC-SNL-DEA
SCANSCOT

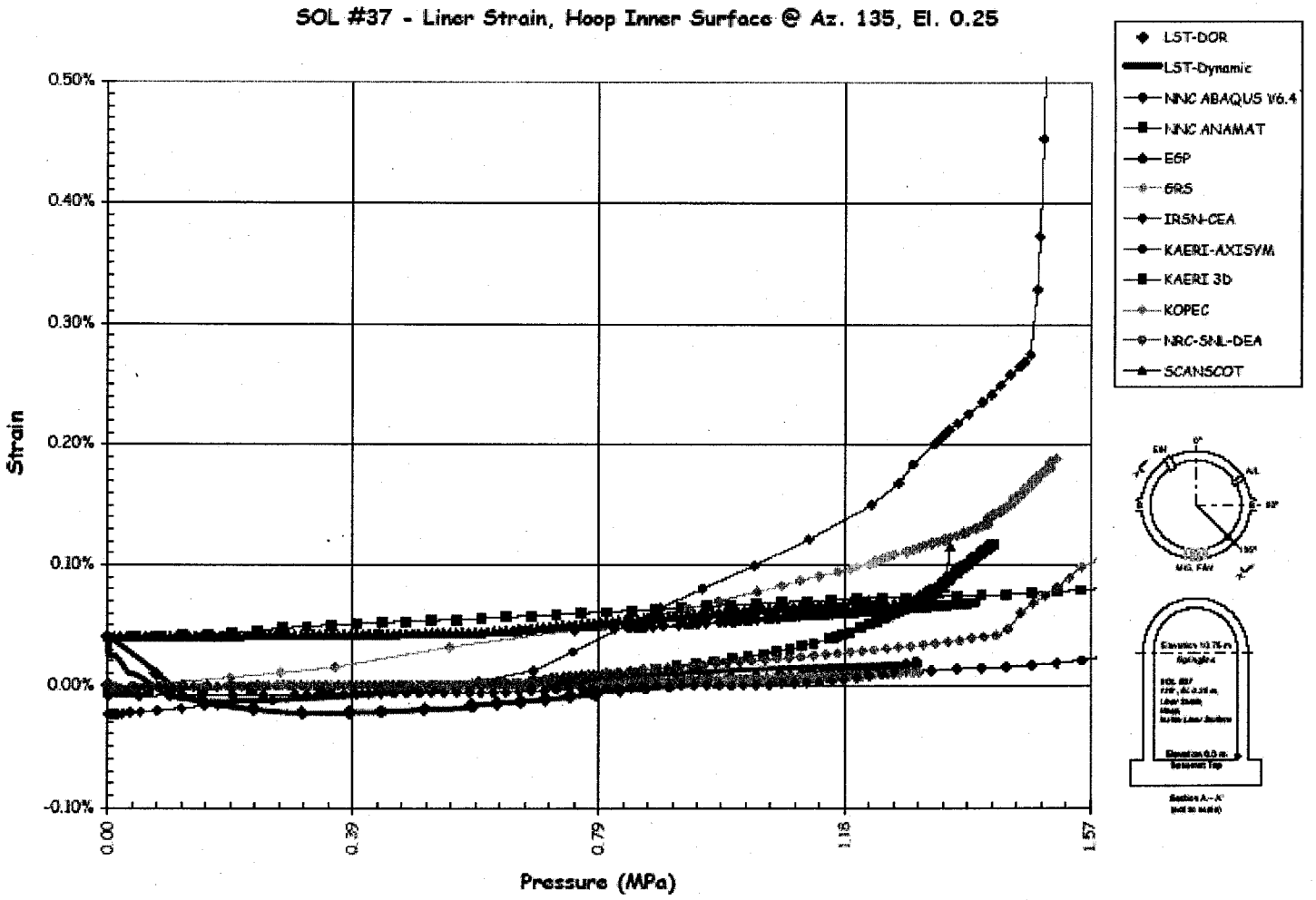
SOL #37 - Liner Strain, Hoop Inner Surface @ Az. 135, El. 0.25
Strain
0.50%
0.40%
0.30%
0.20%
0.10%
0.00%
-0.10%
0.00
0.39
0.79
1.18
1.57
Pressure (MPa)
L5T-DOR
L5T-Dynamic
NNC ABAQUS V6.4
NNC ANAMAT
E6P
6RS
IRSN-CEA
KAERI-AXISYM
KAERI 3D
KOPEC
NRC-SNL-DEA
SCANSCOT

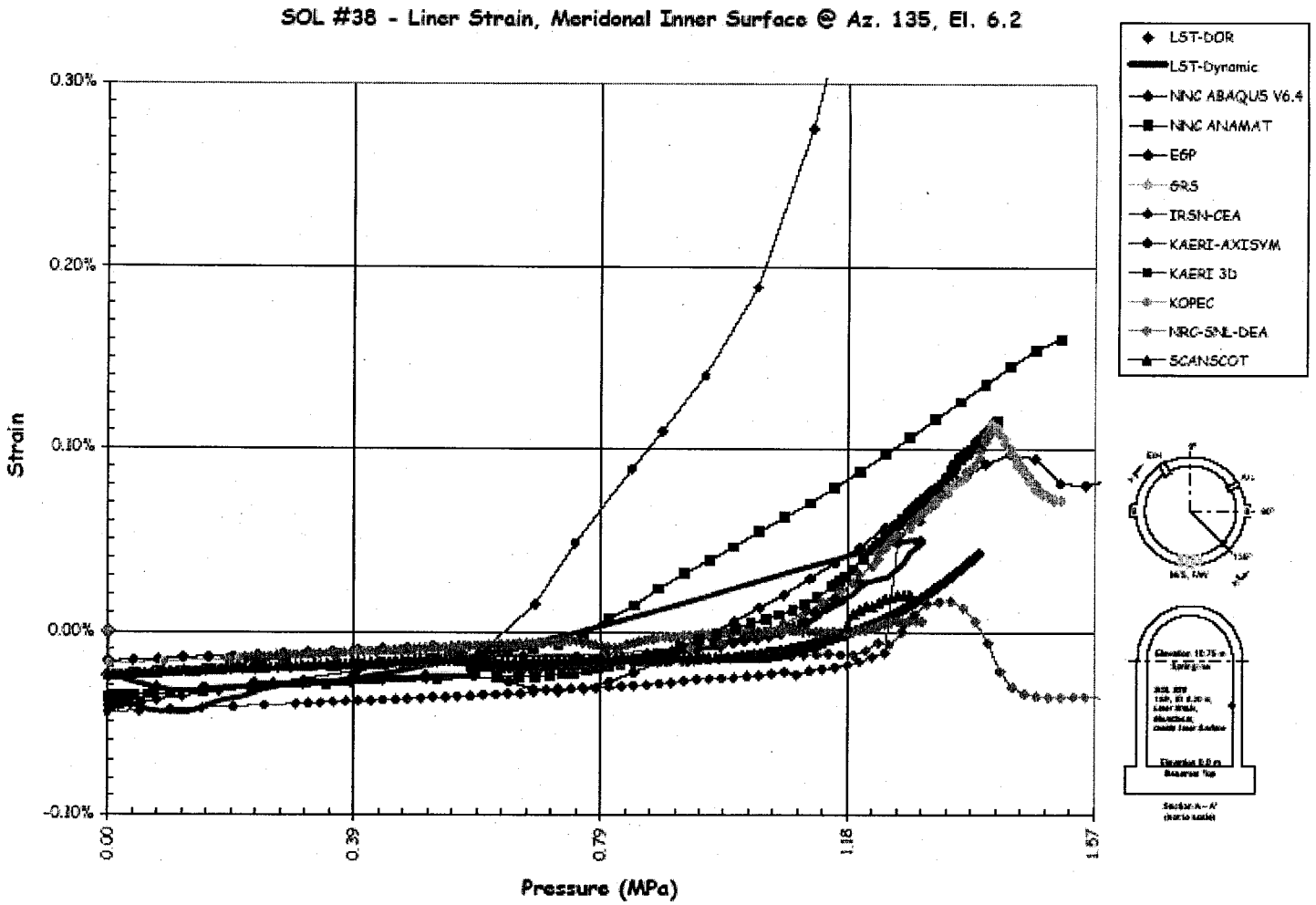
SOL #38 - Liner Strain, Meridonal Inner Surface @ Az. 135, El. 6.2
Strain
0.30%
0.20%
0.10%
0.00%
-0.10%
0.00
0.39
0.79
1.18
1.57
Pressure (MPa)
LST-DOR
LST-Dynamic
NNC ABAQUS V6.4
NNC ANAMAT
EGP
GRS
IRSN-CEA
KAERI-AXISYM
KAERI 3D
KOPEC
NRC-SNL-DEA
SCANSCOT

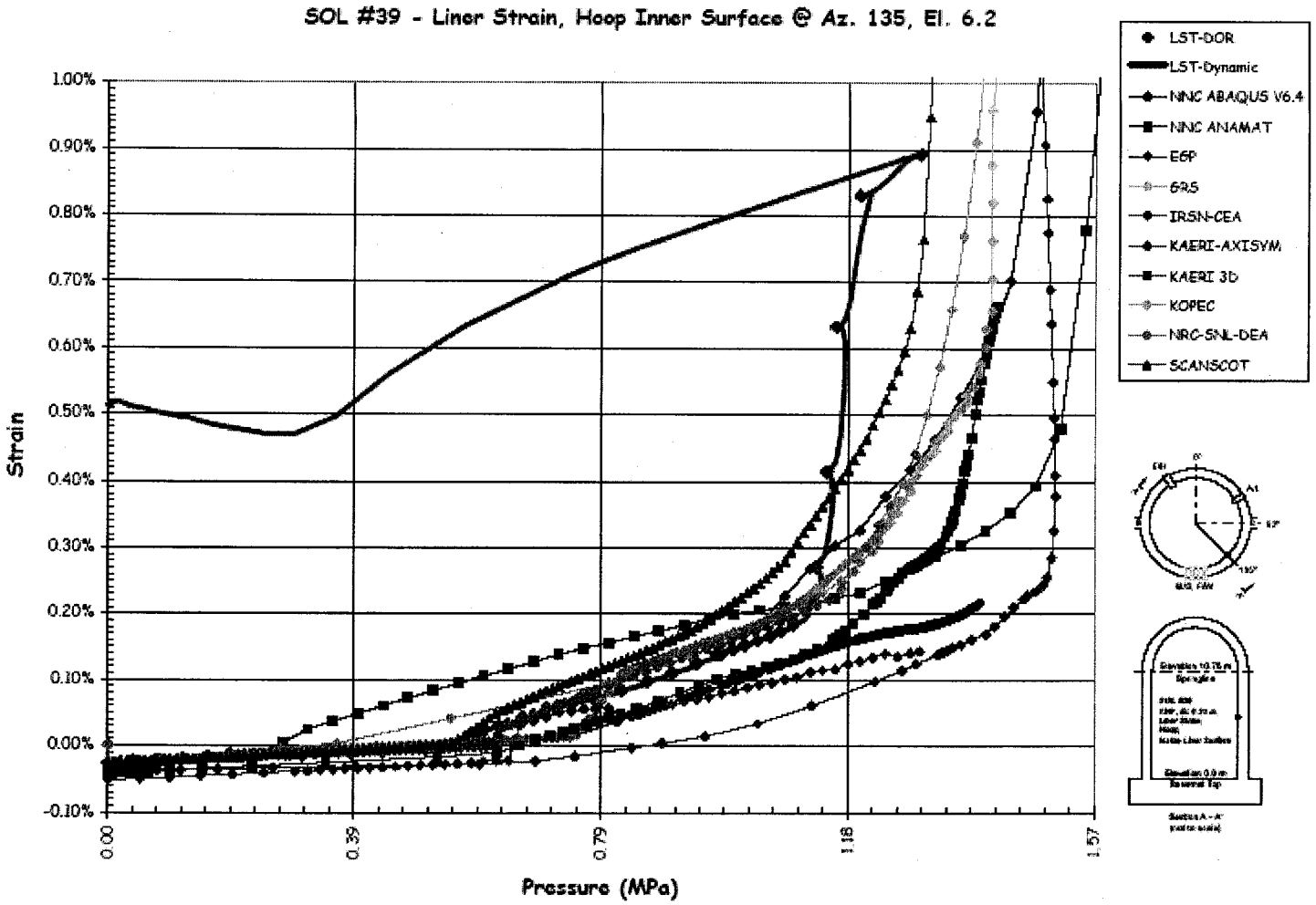
SOL #39 - Liner Strain, Hoop Inner Surface @ Az. 135, El. 6.2
Strain
1.00%
0.90%
0.80%
0.70%
0.60%
0.50%
0.40%
0.30%
0.20%
0.10%
0.00%
-0.10%
0.00
0.39
0.79
1.18
1.57
Pressure (MPa)
LST-DOR
LST-Dynamic
NNC ABAQUS V6.4
NNC ANAMAT
E6P
6R5
IRSN-CEA
KAERI-AXISYM
KAERI 3D
KOPEC
NRC-SNL-DEA
SCANSCOT

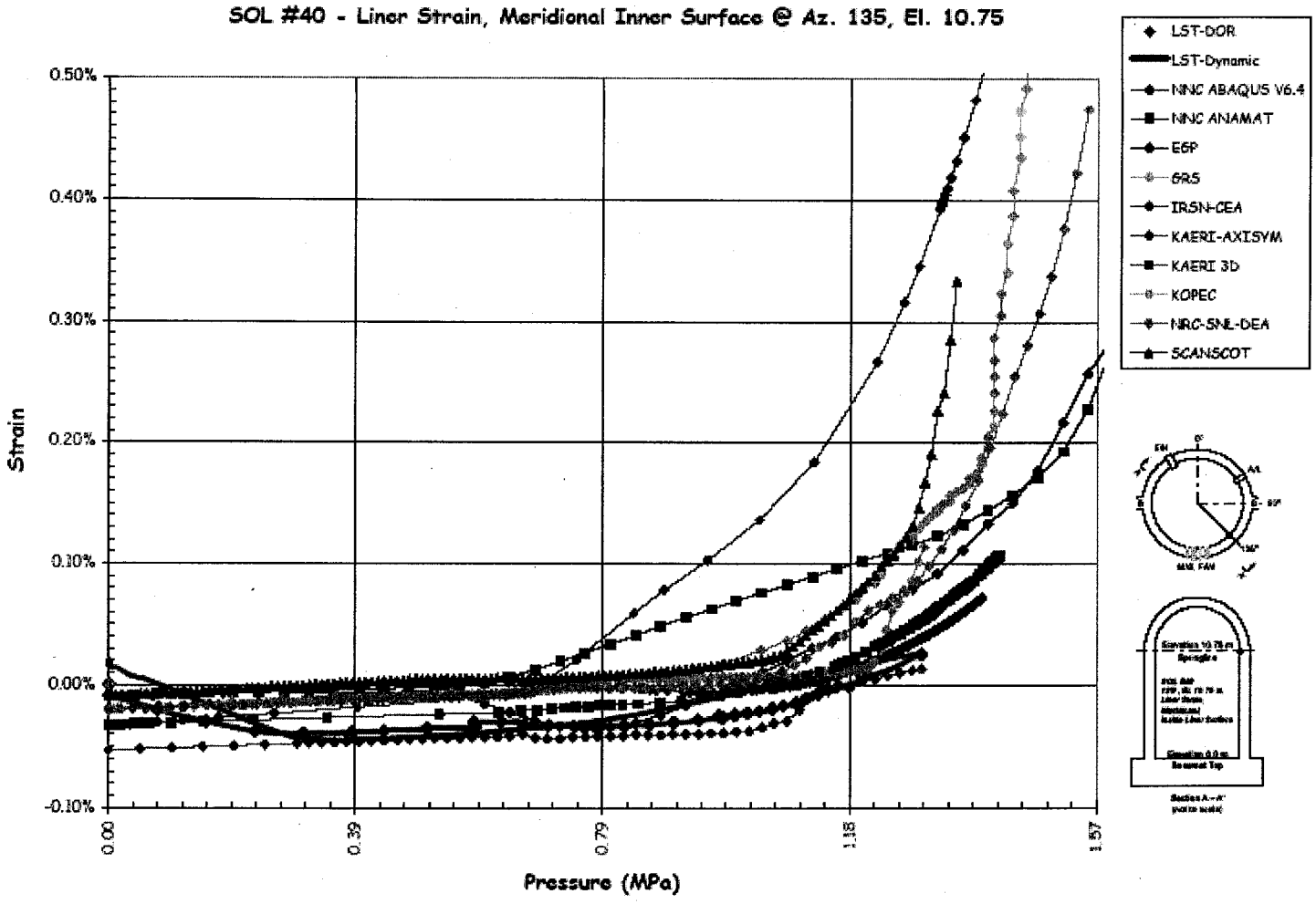
SOL #40 - Liner Strain, Meridional Inner Surface @ Az. 135, El. 10.75
Strain
0.50%
0.40%
0.30%
0.20%
0.10%
0.00%
-0.10%
0.00
0.39
0.79
1.18
1.57
Pressure (MPa)
LST-DOR
LST-Dynamic
NNC ABAQUS V6.4
NNC ANAMAT
E6P
6R5
IRSN-CEA
KAERI-AXISYM
KAERI 3D
KOPEC
NRC-SNL-DEA
SCANSCOT

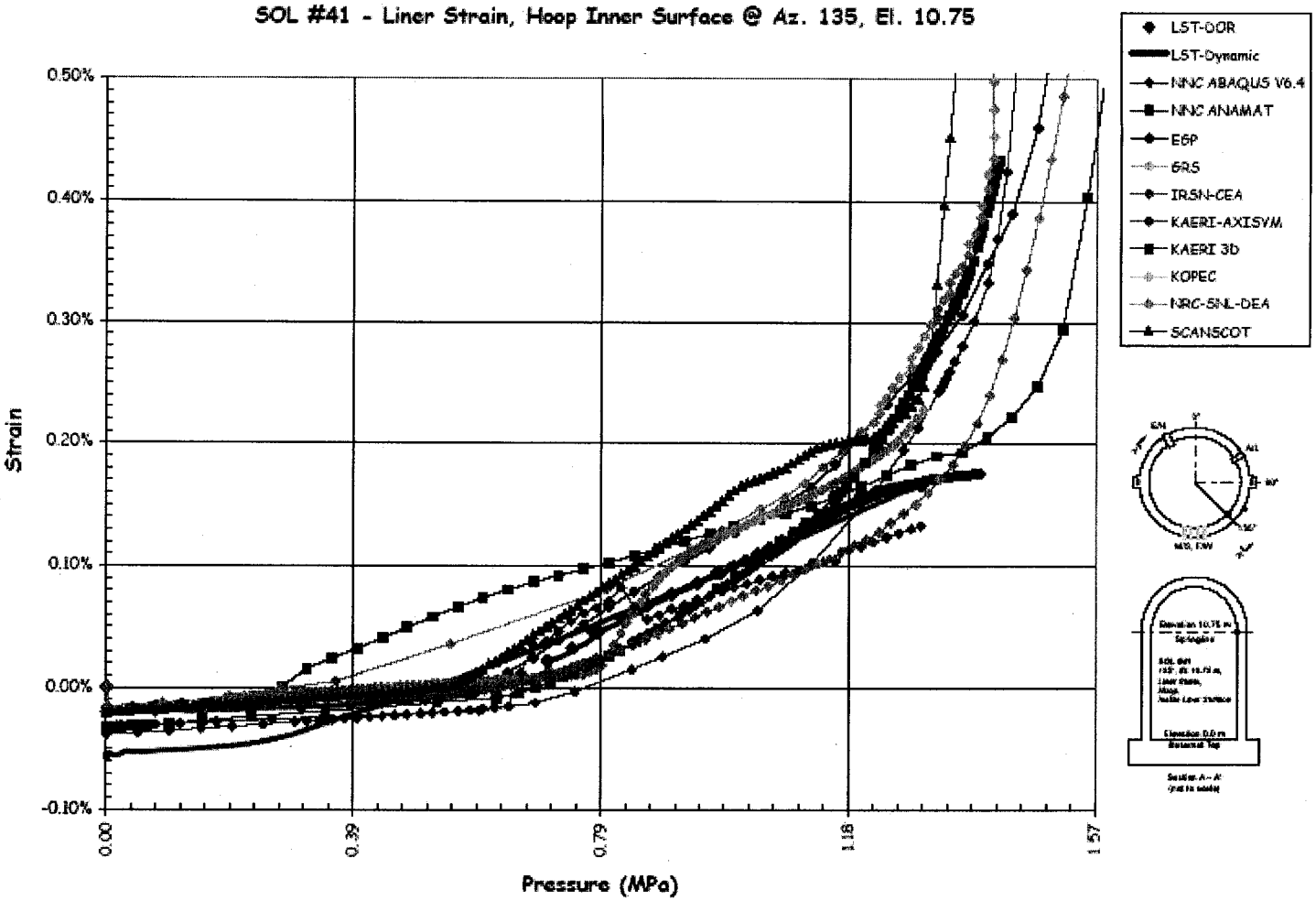
SOL #41 - Liner Strain, Hoop Inner Surface @ Az. 135, El. 10.75
Strain
0.50%
0.40%
0.30%
0.20%
0.10%
0.00%
-0.10%
0.00
0.39
0.79
1.18
1.57
Pressure (MPa)
LST-OOR
LST-Dynamic
NNC ABAQUS V6.4
NNC ANAMAT
E6P
6RS
IRSN-CEA
KAERI-AXISYM
KAERI 3D
KOPEC
NRC-SNL-DEA
SCANSCOT

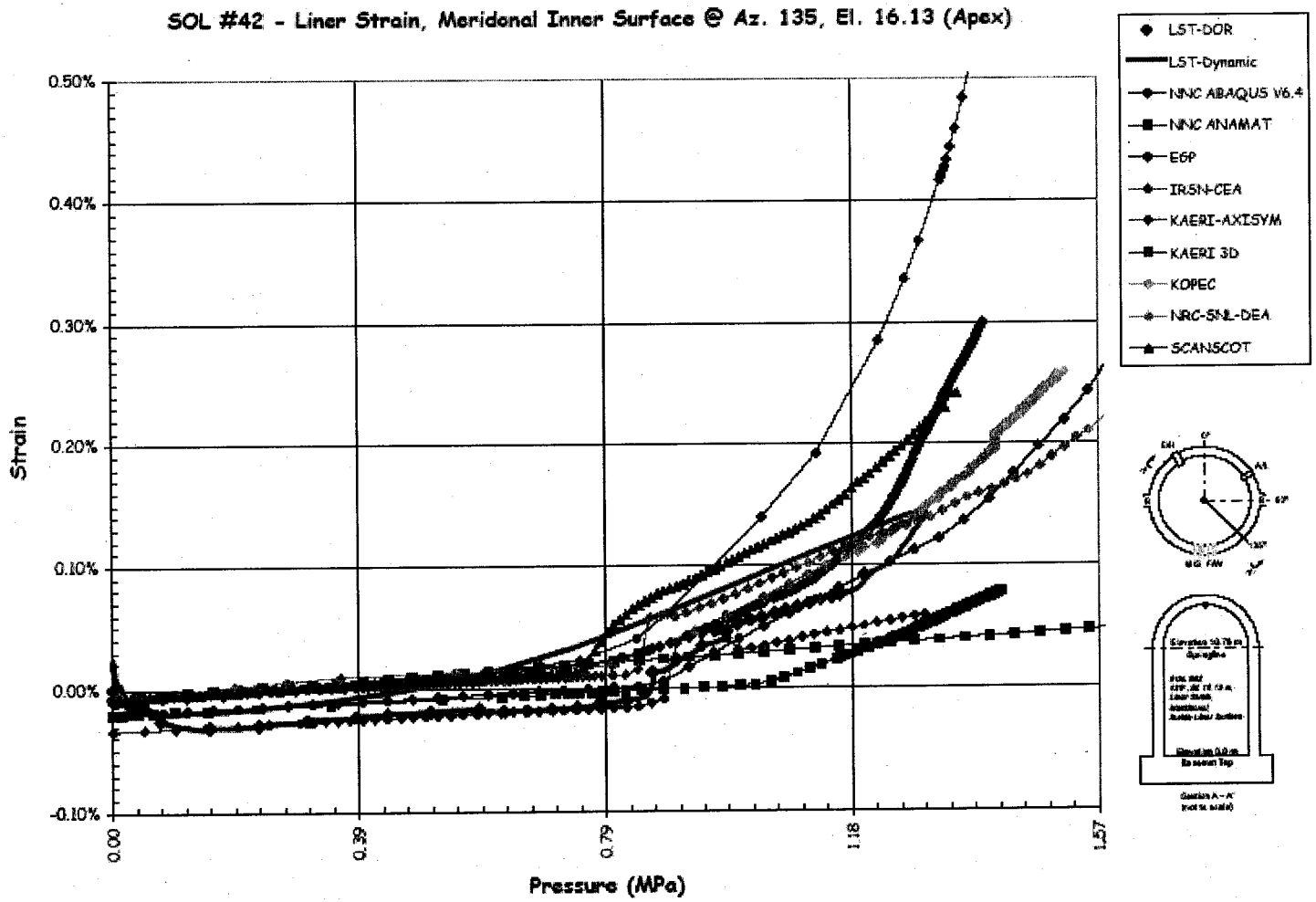
SOL #42 - Liner Strain, Meridonal Inner Surface @ Az. 135, El. 16.13 (Apex)
Strain
0.50%
0.40%
0.30%
0.20%
0.10%
0.00%
-0.10%
0.00
0.39
0.79
1.18
1.57
Pressure (MPa)
LST-DOR
LST-Dynamic
NNC ABAQUS V6.4
NNC ANAMAT
E6P
IRSN-CEA
KAERI-AXISYM
KAERI 3D
KOPEC
NRC-SNL-DEA
SCANSCOT

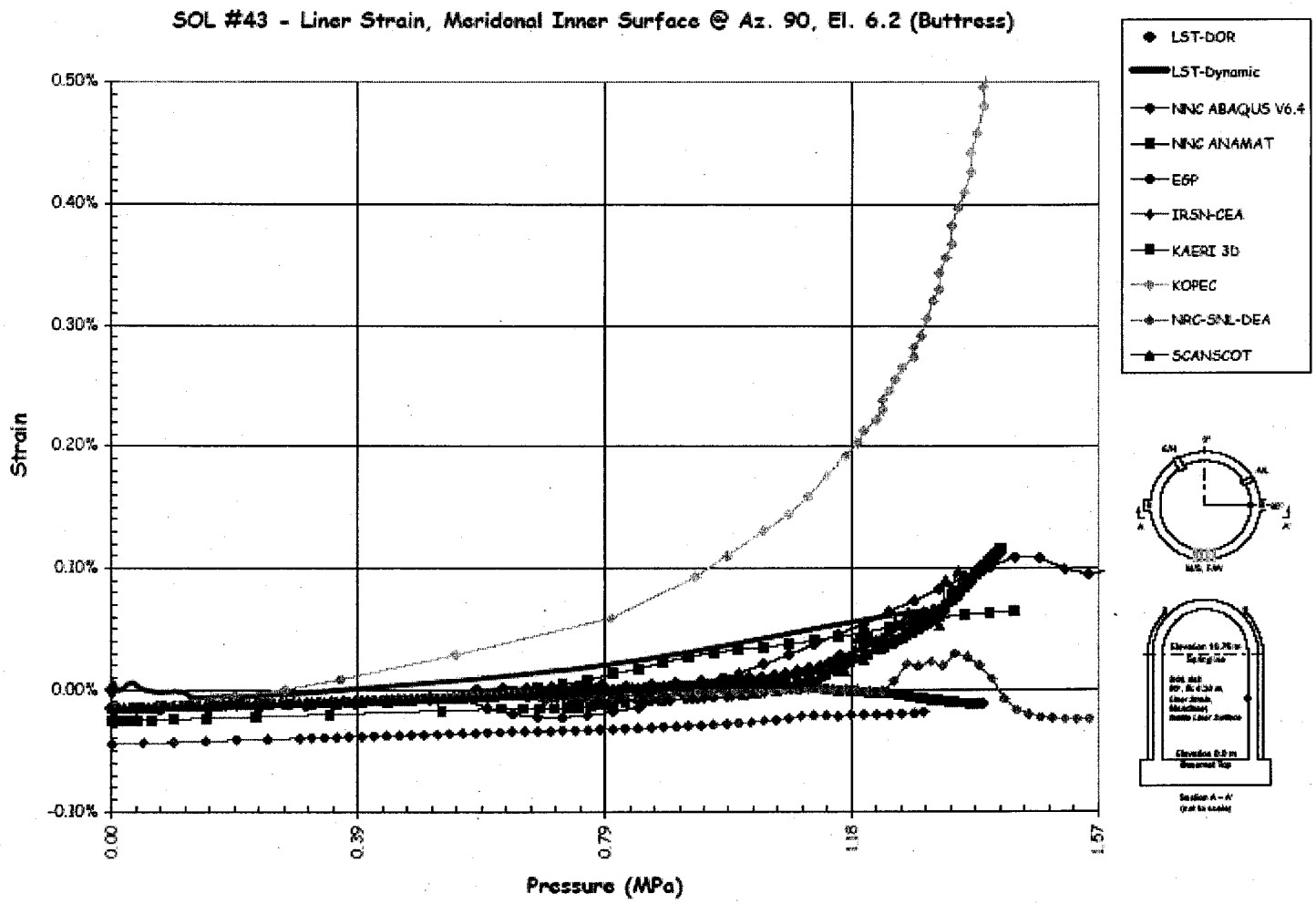
SOL #43 - Liner Strain, Meridonal Inner Surface @ Az. 90, El. 6.2 (Buttress)
Strain
0.50%
0.40%
0.30%
0.20%
0.10%
0.00%
-0.10%
0.00
0.39
0.79
1.18
1.57
Pressure (MPa)
LST-DOR
LST-Dynamic
NNC ABAQUS V6.4
NNC ANAMAT
E6P
IRSN-CEA
KAERI 3D
KOPEC
NRC-SNL-DEA
SCANSCOT

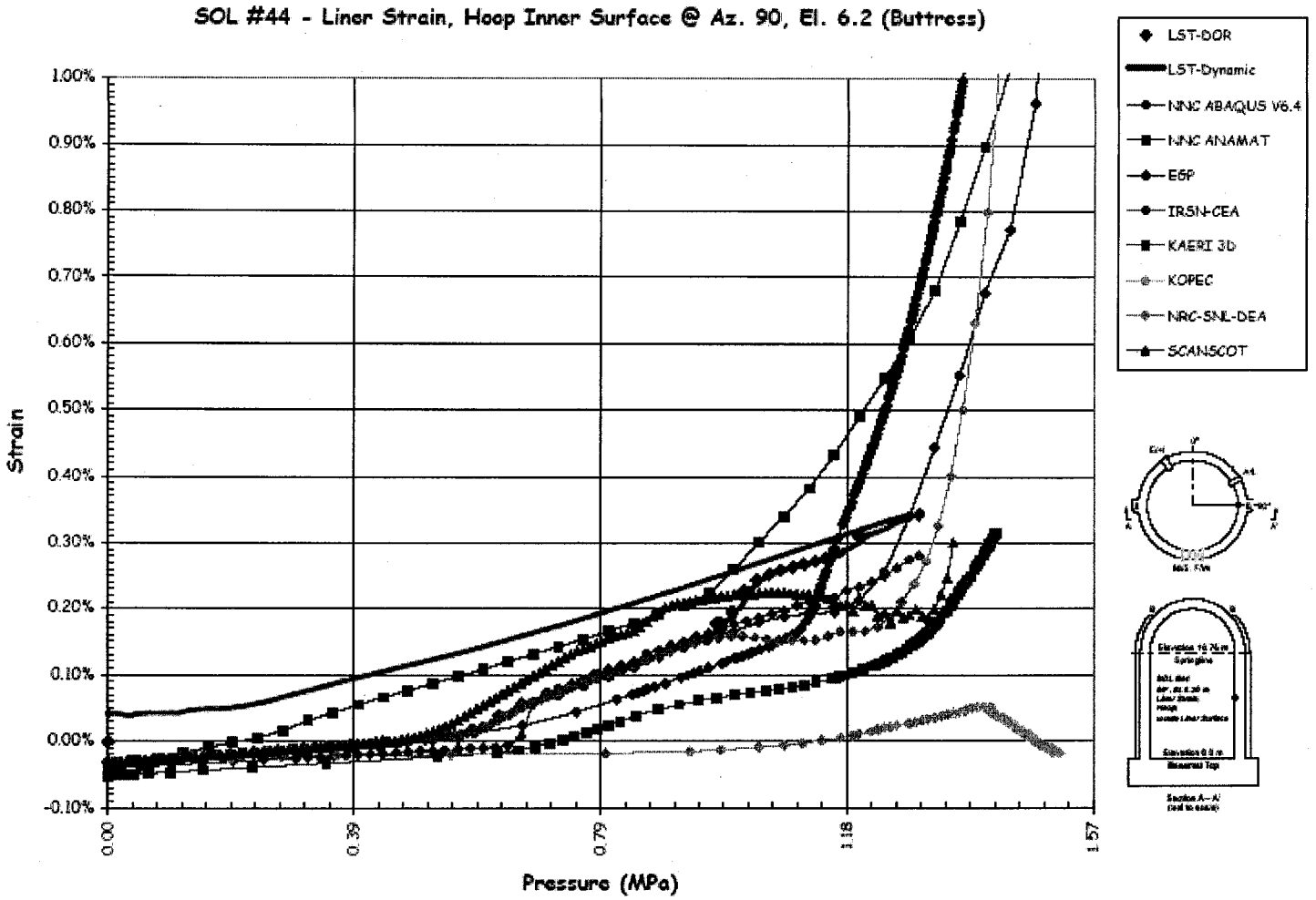
SOL #44 - Liner Strain, Hoop Inner Surface @ Az. 90, El. 6.2 (Buttress)
Strain
1.00%
0.90%
0.80%
0.70%
0.60%
0.50%
0.40%
0.30%
0.20%
0.10%
0.00%
-0.10%
0.00
0.39
0.79
1.18
1.57
Pressure (MPa)
LST-DOR
LST-Dynamic
NNC ABAQUS V6.4
NNC ANAMAT
E6P
IRSN-CEA
KAERI 3D
KOPEC
NRC-SNL-DEA
SCANSCOT

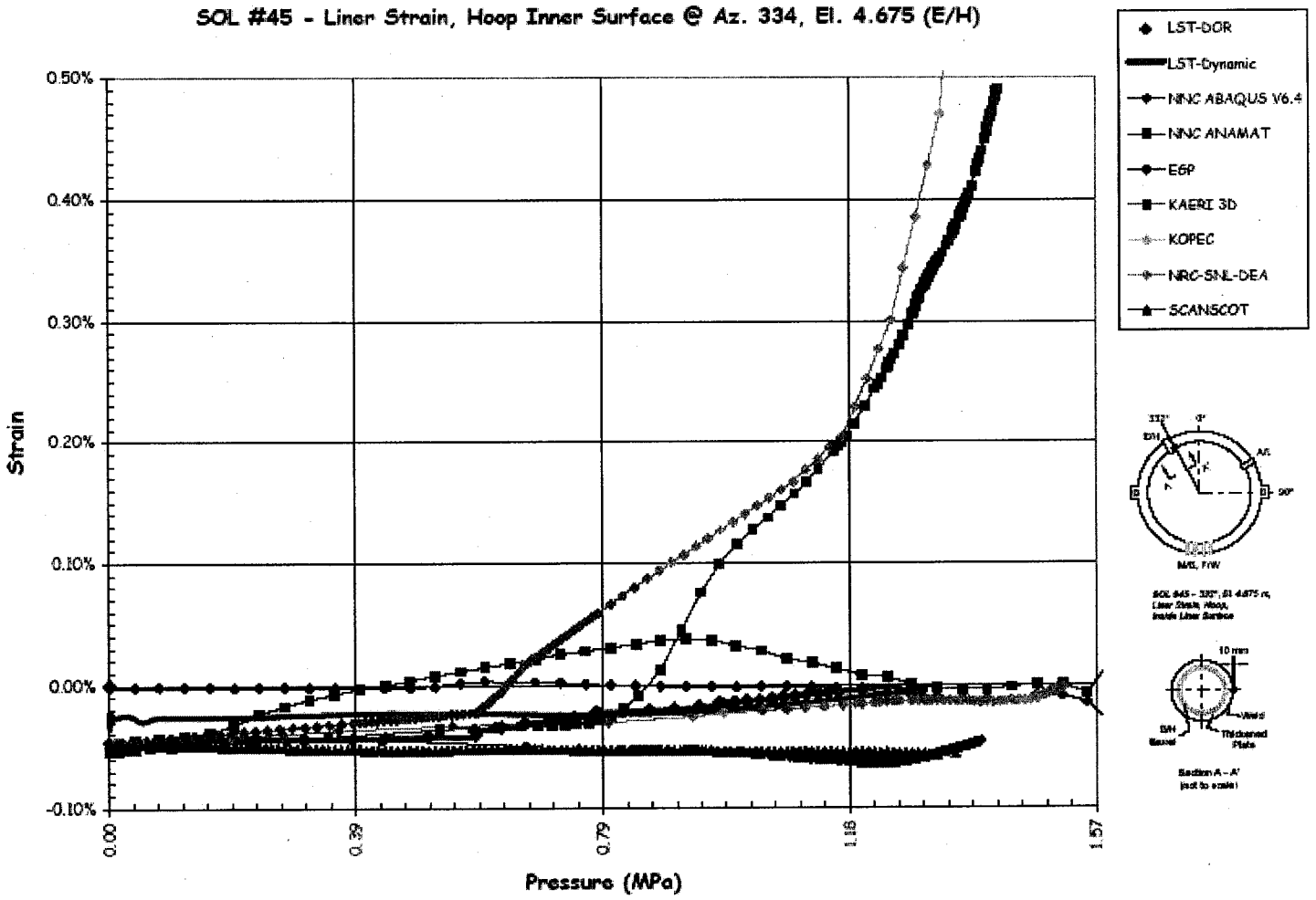
SOL #45 - Liner Strain, Hoop Inner Surface @ Az. 334, El. 4.675 (E/H)
0.50%
0.40%
0.30%
0.20%
0.10%
0.00%
-0.10%
Strain
0.00
0.39
0.79
1.18
1.57
Pressure (MPa)
LST-DOR
LST-Dynamic
NNC ABAQUS V6.4
NNC ANAMAT
E6P
KAERI 3D
KOPEC
NRC-SNL-DEA
SCANSCOT
10 mm
Weld
Thickened Plate
Section A - A'
(not to scale)

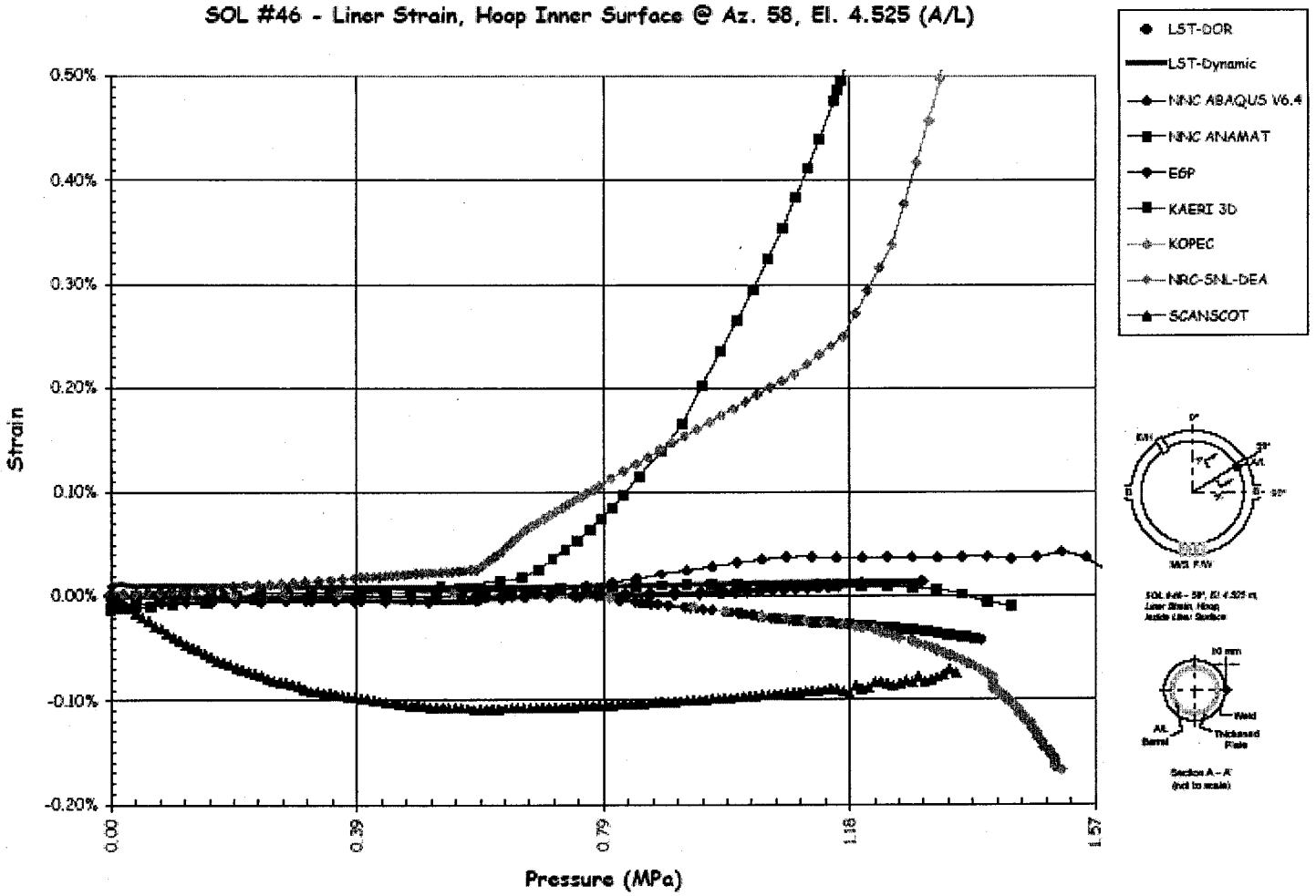
SOL #46 - Liner Strain, Hoop Inner Surface @ Az. 58, El. 4.525 (A/L)
0.50%
0.40%
0.30%
0.20%
0.10%
0.00%
-0.10%
-0.20%
Strain
0.00
0.39
0.79
1.18
1.57
Pressure (MPa)
LST-DOR
LST-Dynamic
NNC ABAQUS V6.4
NNC ANAMAT
EGP
KAERI 3D
KOPEC
NRC-SNL-DEA
SCANSCOT

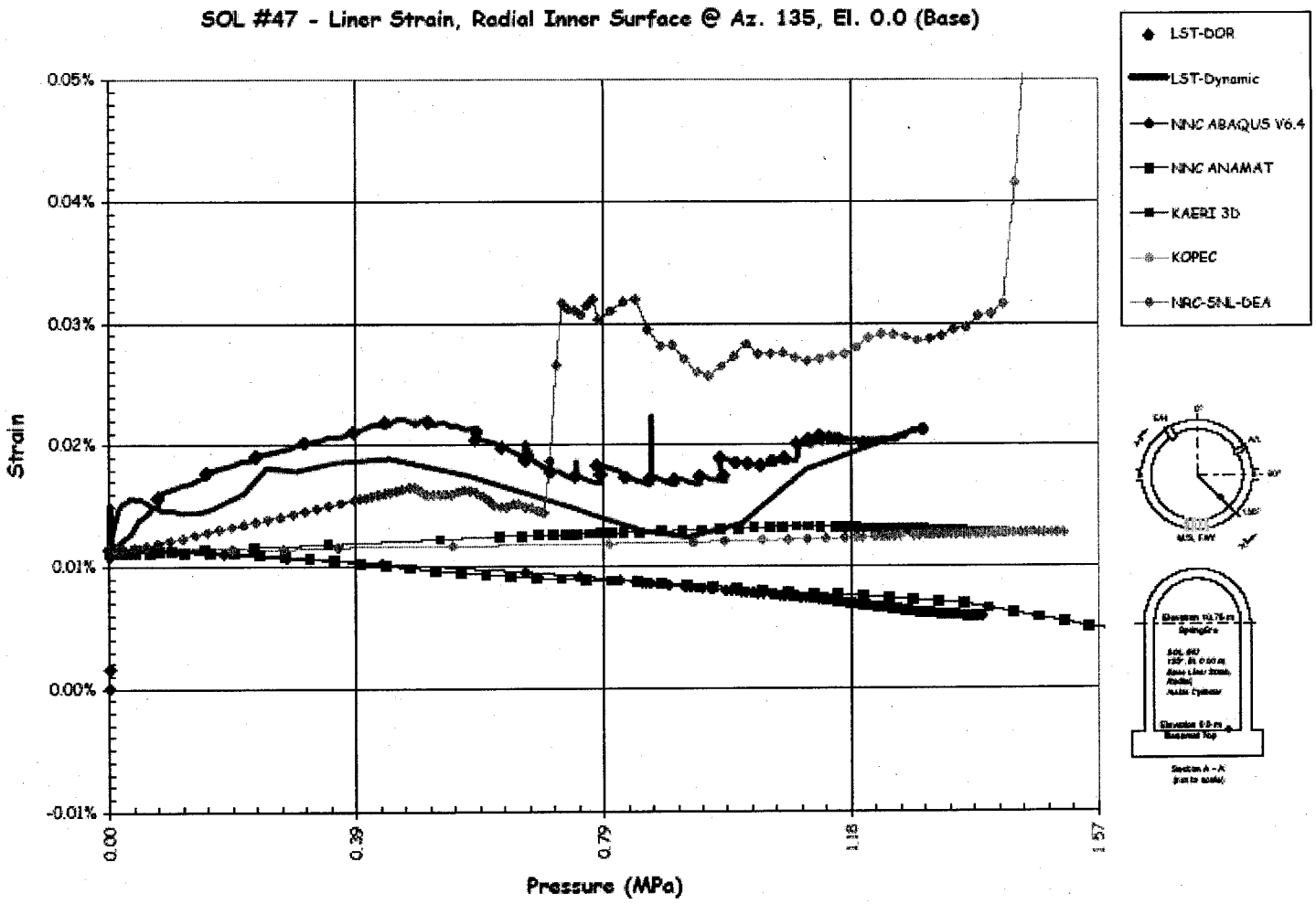
SOL #47 - Liner Strain, Radial Inner Surface @ Az. 135, El. 0.0 (Base)
LST-DOR
LST-Dynamic
NNC ABAQUS V6.4
NNC ANAMAT
KAERI 3D
KOPEC
NRC-SNL-DEA
0.05%
0.04%
0.03%
0.02%
0.01%
0.00%
-0.01%
Strain
0.00
0.39
0.79
1.18
1.57
Pressure (MPa)

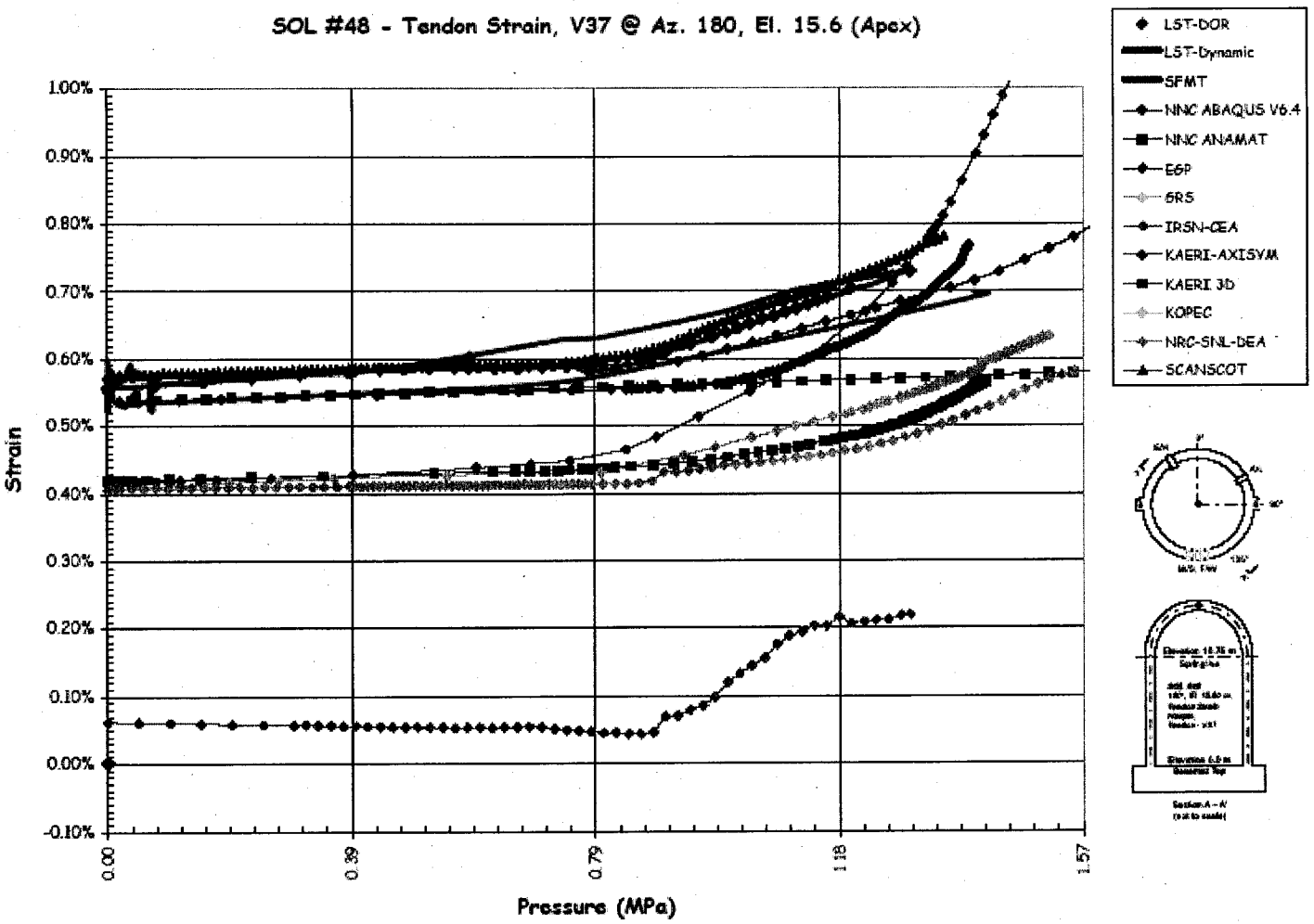
SOL #48 - Tendon Strain, V37 @ Az. 180, El. 15.6 (Apex)
Strain
1.00%
0.90%
0.80%
0.70%
0.60%
0.50%
0.40%
0.30%
0.20%
0.10%
0.00%
-0.10%
0.00
0.39
0.79
1.18
1.57
Pressure (MPa)
LST-DOR
LST-Dynamic
SFMT
NNC ABAQUS V6.4
NNC ANAMAT
E6P
6RS
IRSN-CEA
KAERI-AXISYM
KAERI 3D
KOPEC
NRC-SNL-DEA
SCANSCOT

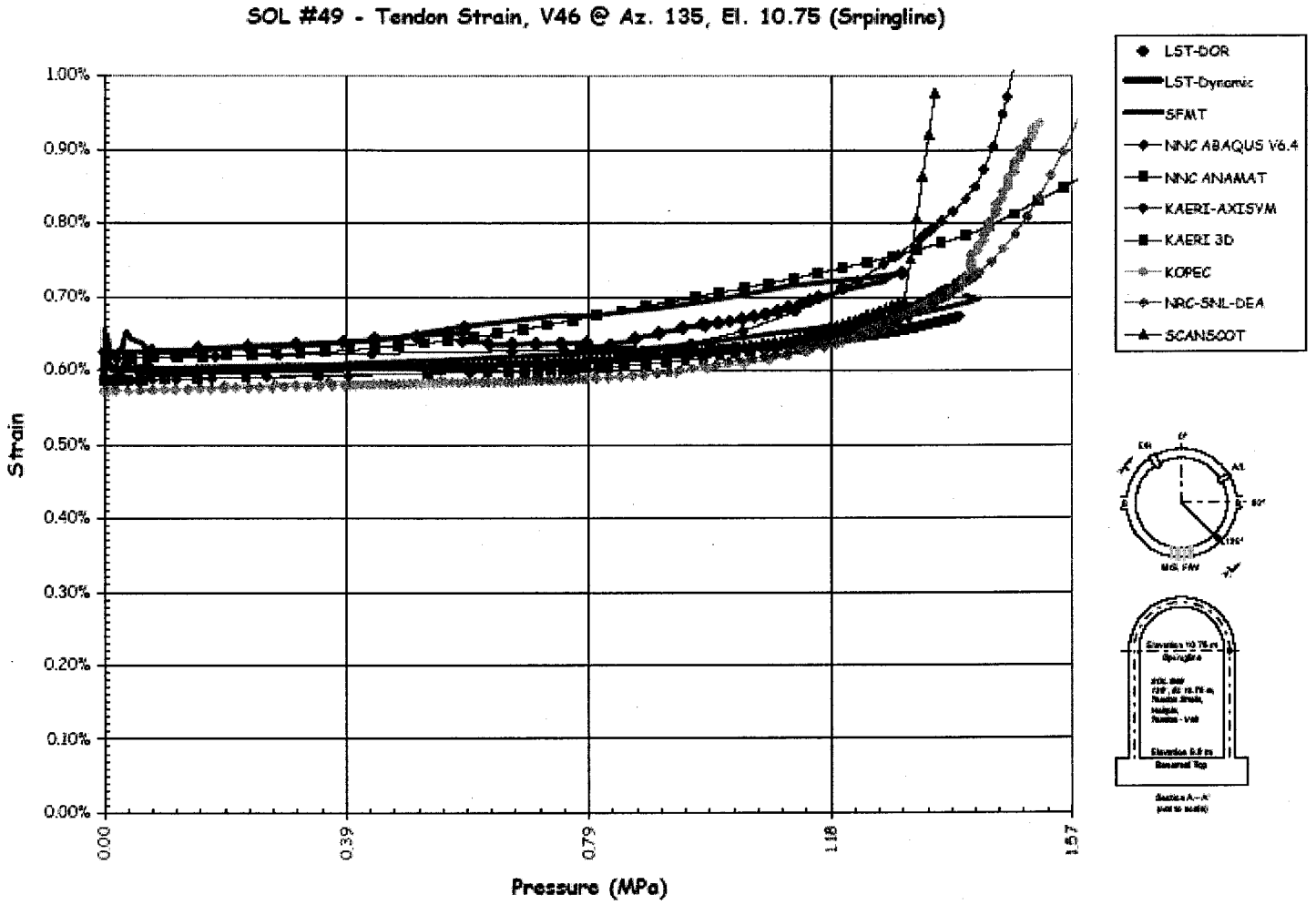
SOL #49 - Tendon Strain, V46 @ Az. 135, El. 10.75 (Srpingline)
Strain
1.00%
0.90%
0.80%
0.70%
0.60%
0.50%
0.40%
0.30%
0.20%
0.10%
0.00%
0.00
0.39
0.79
1.18
1.57
Pressure (MPa)
LST-DOR
LST-Dynamic
SFMT
NNC ABAQUS V6.4
NNC ANAMAT
KAERI-AXISYM
KAERI 3D
KOPEC
NRC-SNL-DEA
SCANSCDT

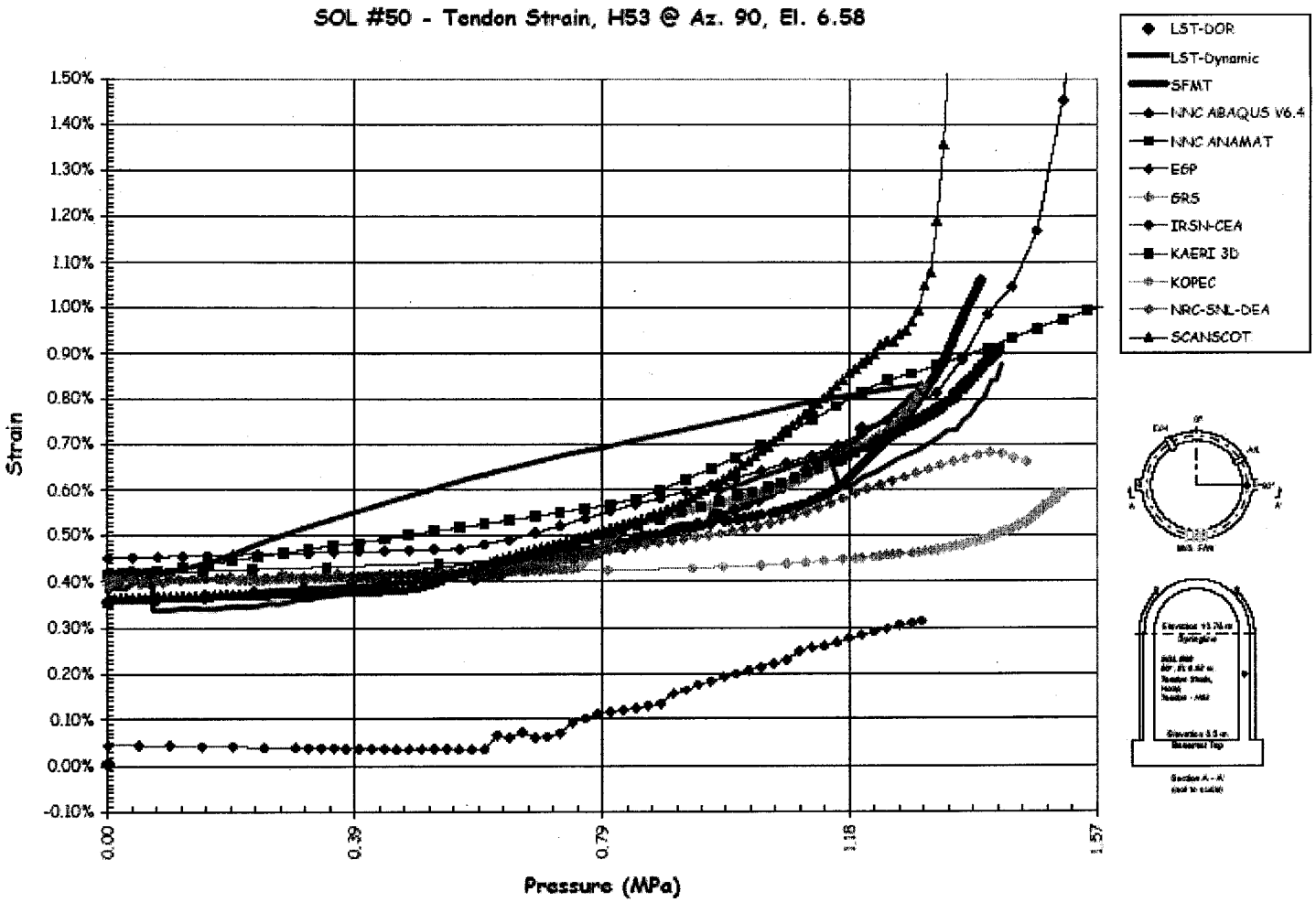
SOL #50 - Tendon Strain, H53 @ Az. 90, El. 6.58
Strain
1.50%
1.40%
1.30%
1.20%
1.10%
1.00%
0.90%
0.80%
0.70%
0.60%
0.50%
0.40%
0.30%
0.20%
0.10%
0.00%
-0.10%
0.00
0.39
0.79
1.18
1.57
Pressure (MPa)
LST-DOR
LST-Dynamic
SFMT
NNC ABAQUS V6.4
NNC ANAMAT
E6P
6R5
IRSN-CEA
KAERI 3D
KOPEC
NRC-SNL-DEA
SCANSCOT

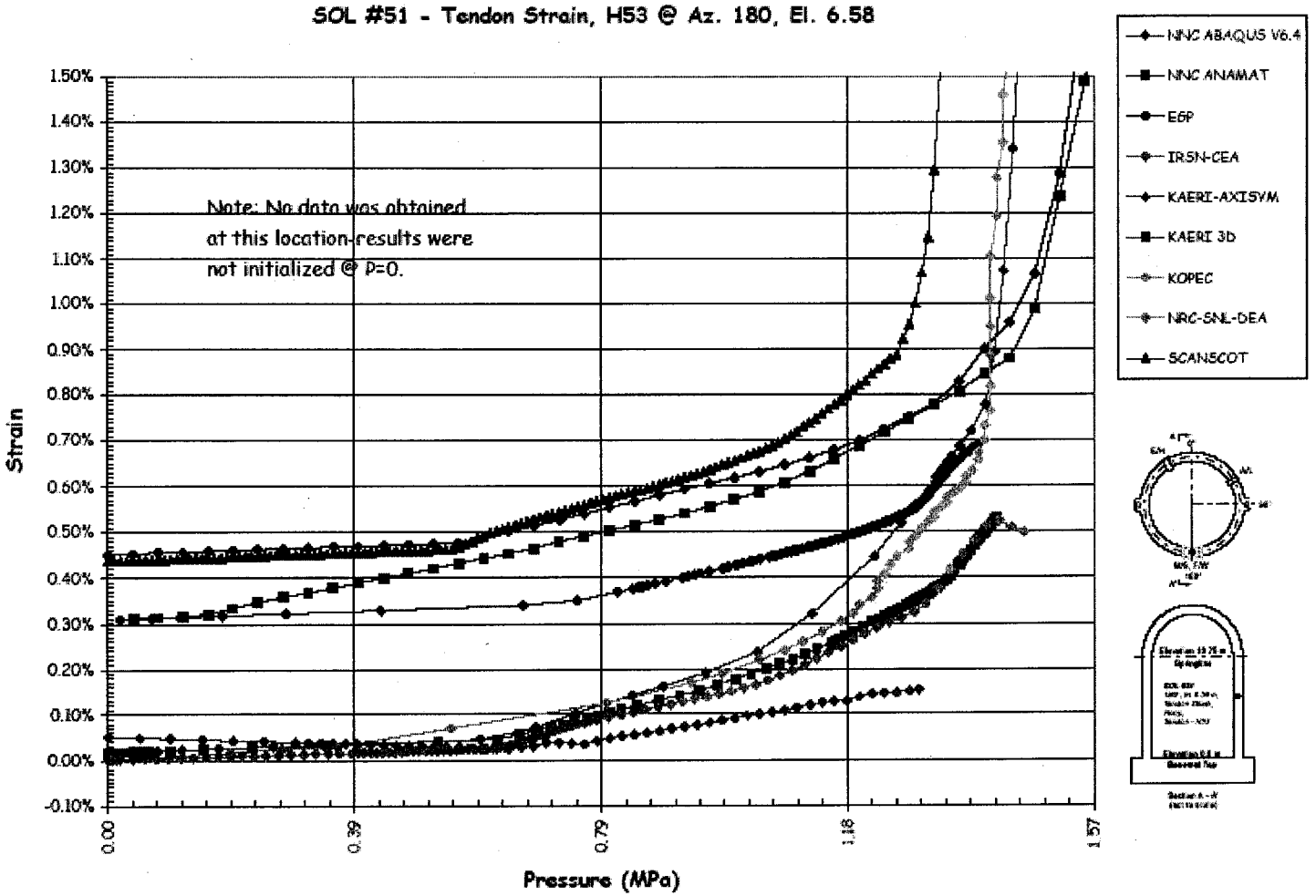
SOL #51 - Tendon Strain, H53 @ Az. 180, El. 6.58
Note: No data was obtained at this location-results were not initialized @ P=0.
Strain
1.50%
1.40%
1.30%
1.20%
1.10%
1.00%
0.90%
0.80%
0.70%
0.60%
0.50%
0.40%
0.30%
0.20%
0.10%
0.00%
-0.10%
0.00
0.39
0.79
1.18
1.57
Pressure (MPa)
NNC ABAQUS V6.4
NNC ANAMAT
EDF
IRSN-CEA
KAERI-AXISYM
KAERI 3D
KOPEC
NRC-SNL-DEA
SCANSCOT

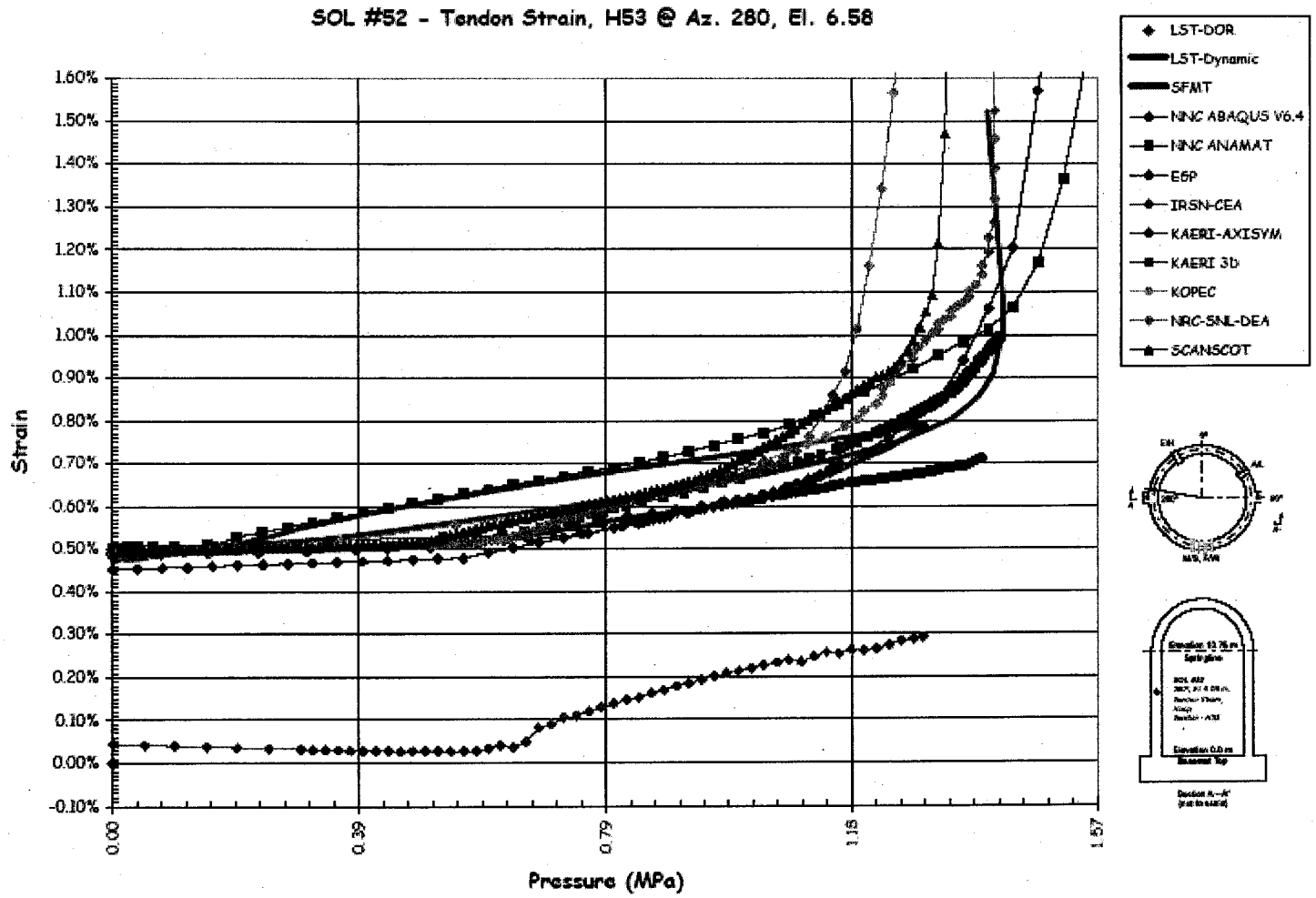
SOL #52 - Tendon Strain, H53 @ Az. 280, El. 6.58
Strain
1.60%
1.50%
1.40%
1.30%
1.20%
1.10%
1.00%
0.90%
0.80%
0.70%
0.60%
0.50%
0.40%
0.30%
0.20%
0.10%
0.00%
-0.10%
0.00
0.39
0.79
1.18
1.57
Pressure (MPa)
LST-DOR
LST-Dynamic
SFMT
NINC ABAQUS V6.4
NINC ANAMAT
E6P
IRSN-CEA
KAERI-AXISYM
KAERI 3D
KOPEC
NRC-SNL-DEA
SCANSCOT

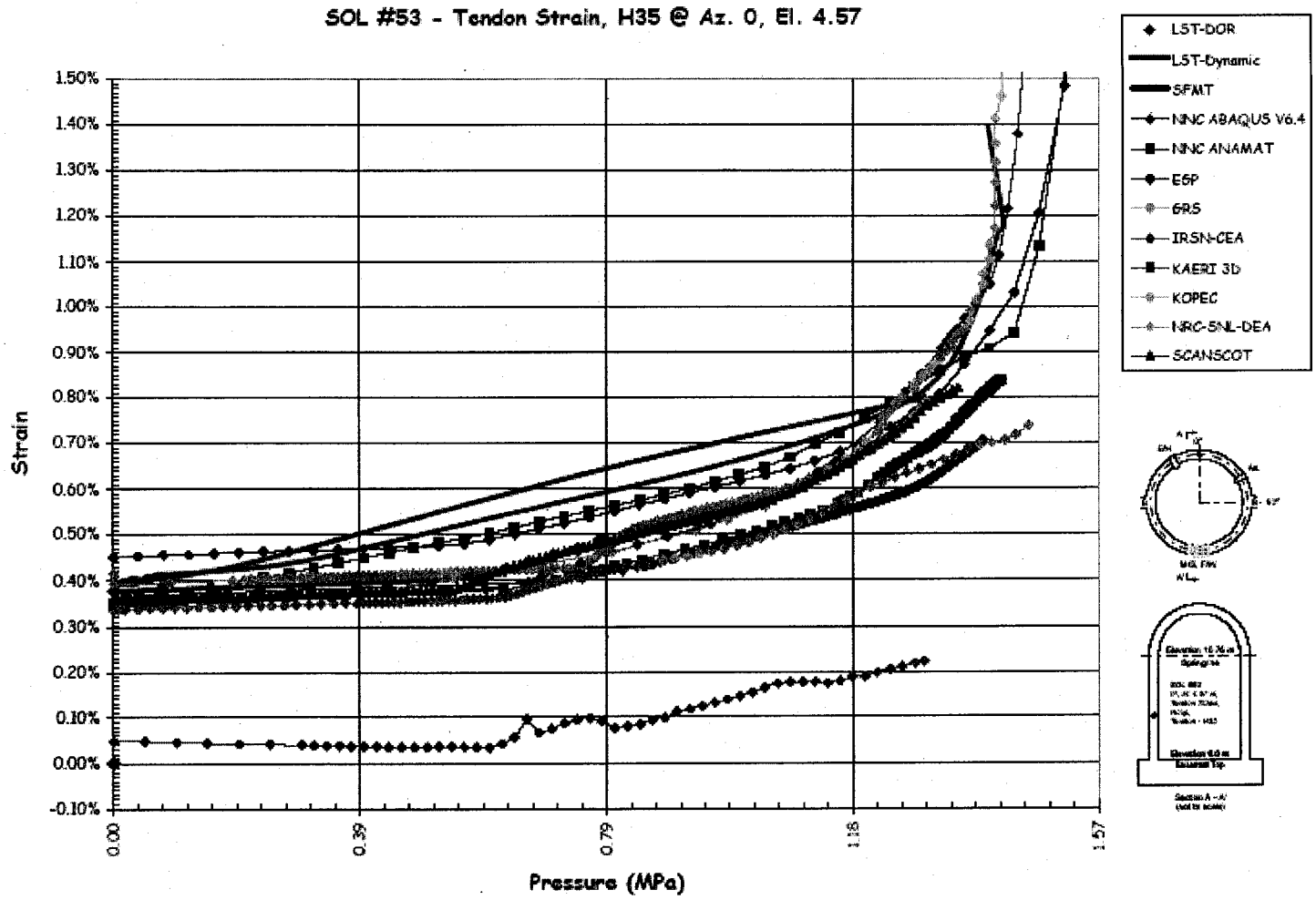
SOL #53 - Tendon Strain, H35 @ Az. 0, El. 4.57
Strain
1.50%
1.40%
1.30%
1.20%
1.10%
1.00%
0.90%
0.80%
0.70%
0.60%
0.50%
0.40%
0.30%
0.20%
0.10%
0.00%
-0.10%
0.00
0.39
0.79
1.18
1.57
Pressure (MPa)
L5T-DOR
L5T-Dynamic
SFMT
NNC ABAQUS V6.4
NNC ANAMAT
E6P
6RS
IRSN-CEA
KAERI 3D
KOPEC
NRC-SNL-DEA
SCANSCOT

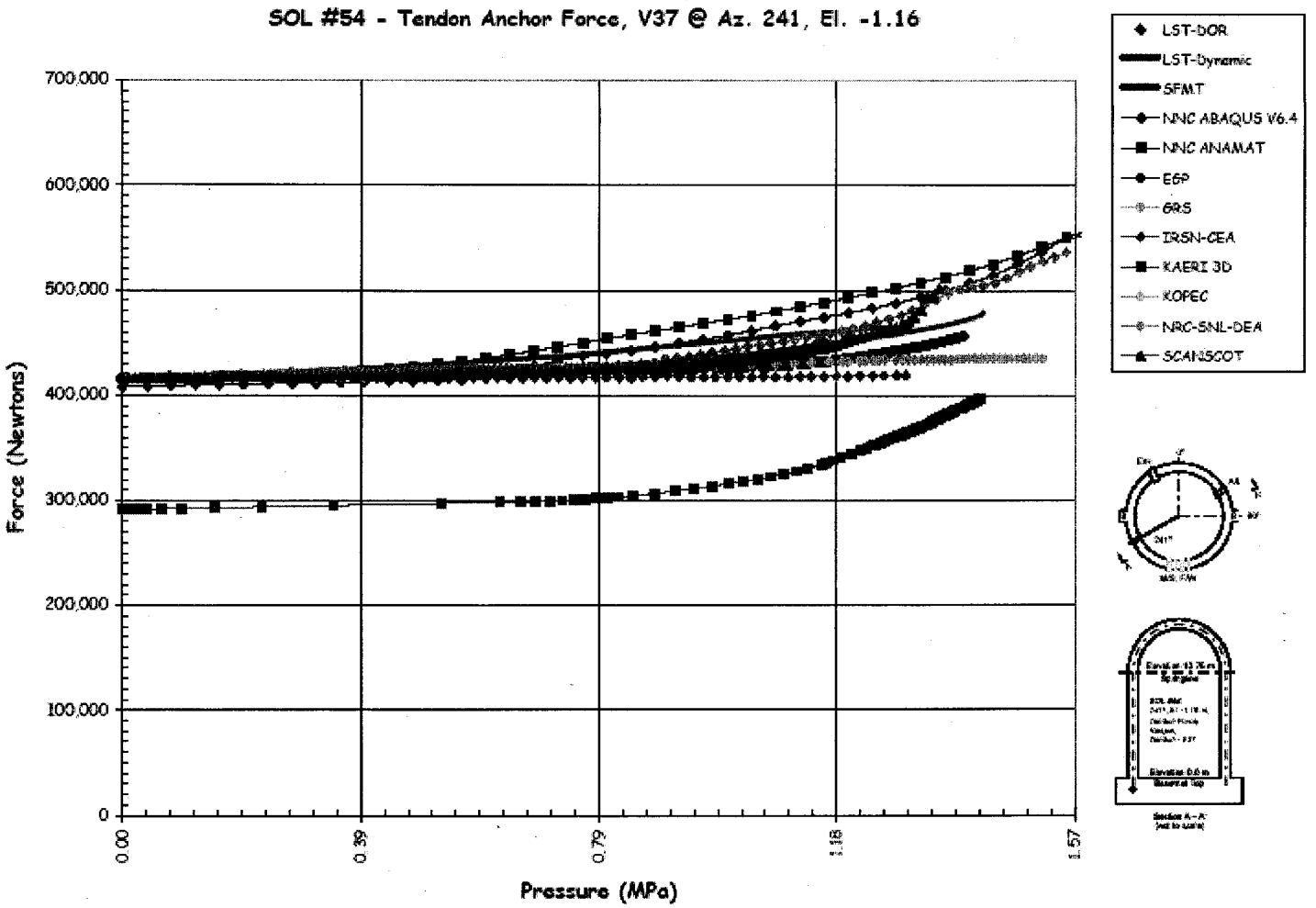
SOL #54 - Tendon Anchor Force, V37 @ Az. 241, El. -1.16
Force (Newtons)
700,000
600,000
500,000
400,000
300,000
200,000
100,000
0
0.00
0.39
0.79
1.18
1.57
Pressure (MPa)
LST-DOR
LST-Dynamic
SFMT
NNC ABAQUS V6.4
NNC ANAMAT
EGP
GRS
IRSN-CEA
KAERI 3D
KOPEC
NRC-SNL-DEA
SCANSCOT

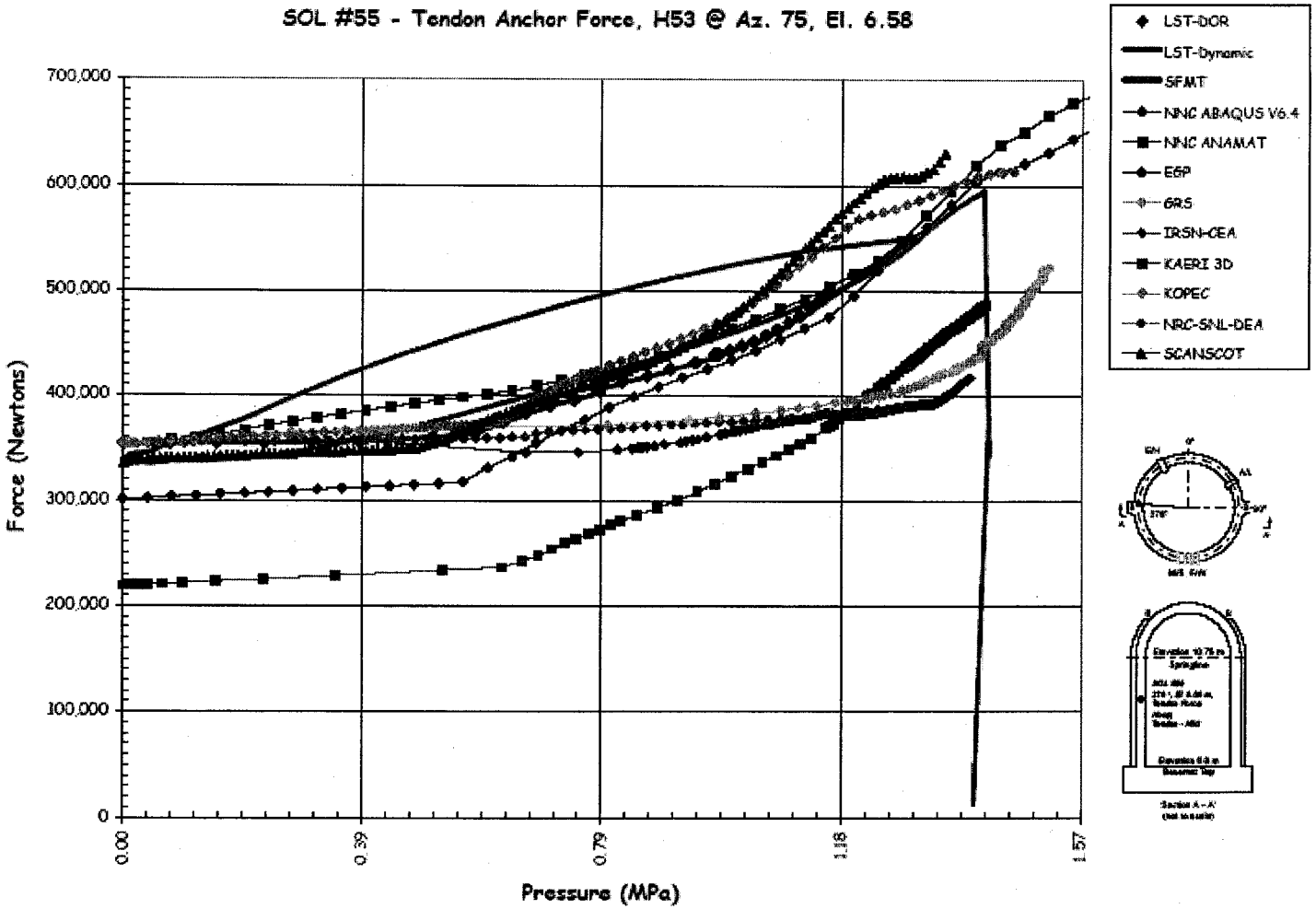
SOL #55 - Tendon Anchor Force, H53 @ Az. 75, El. 6.58
Force (Newtons)
700,000
600,000
500,000
400,000
300,000
200,000
100,000
0
0.00
0.39
0.79
1.18
1.57
Pressure (MPa)
LST-DOR
LST-Dynamic
SFMT
NNC ABAQUS V6.4
NNC ANAMAT
EGP
GRS
IRSN-CEA
KAERI 3D
KOPEC
NRC-SNL-DEA
SCANSCOT

Appendix B:

British Energy
Nuclear Installations Inspectorate/Health and Safety Executive
NNC Ltd

Contents

List of Tables

List of Figures

1 INTRODUCTION

At the June 2002 meeting of the Committee on the Safety of Nuclear Installations (CSNI), the proposal (Ref 1) for the International Standard Problem 48 (ISP48) on containment integrity was approved.

This report covers Phases 1 and 2 of the ISP 48 work done by NNC Limited under contract (C11248) from British Energy. NRC/NUPEC sponsored tests of the ¼ scale pre-stressed concrete containment vessel (PCCV) have been executed at Sandia National Laboratories (SNL) in USA. The Limit State Test (LST) executed during September 2000 was based on pneumatic pressurization of the vessel and achieved a maximum pressure of 1.3MPa (3.3 times the design pressure). The objectives of the ISP48 are to extend the understanding of capacities of actual containment structures based on the results of the PCCV LST and any other sources of available research.

Under contract to the United Kingdom Health and Safety Executive (HSE), NNC participated in the LST round robin exercise and completed the analysis (Ref 2) to predict the limit load of the vessel. Predictions from all the participants of the round robin were collated and published by SNL in August 2000 (Ref 3). The LST identified liner tearing as the mode of failure. Whilst there was no visible damage to the PCCV structure, the breach of the pressure boundary dictated the limit load due to the excessive leakage rate. It can be seen from Ref 3 that out of the total of 17 participants, the NNC/HSE model is one of only four that successfully predicted liner tearing as the failure mode. It was recognised at the international pre-test round robin meeting in October 1999 that the NNC/HSE model was one of the most sophisticated models. The NNC/HSE model was a full 3D global model, which took account of interaction between all the main structural features.

Following the pre-test round robin, NNC carried out the post-test analysis under HSE contract CE/GNSR/1 and the work was presented in Ref 4. This work consisted of a comparison between the FE analysis and the test results to give an assessment of the accuracy and reliability in predicting failure modes and limit loads of PCCV structures using finite element analysis. It also included analysis of the Structural Failure Mode Test (SFMT) executed in November 2001, in which hydraulic pressure was used to overpressurise the containment to total structural collapse. The results of the overpressurisation test have been published by SNL in Ref 5. The analysis carried out by NNC in Ref 4 predicted the failure location and the behaviour up to collapse with good accuracy.

All the test and the analysis work done to date has shown that leakage occurs before the burst pressure but in this study only the mechanical loading (gravity, prestress and internal pressure) was considered and thermal loading was ignored. In real containments, increase in internal pressure is associated with thermal loading. One of the aims of the ISP48 is to study the effects of accident temperatures and see if the onset of leakage is closer to the burst pressure in full size containments.

Technical background to the PCCV analysis work done under the international roundrobin is presented in section 2 and the scope of work for Phases 1 and 2 of the ISP48 project is give in section 3. A description of the finite element model is given in section 4. Review of the test data and subsequent changes to the FE model are presented in sections 5 and 6 respectively. The latest analysis results are given in section 7 followed by the assessment of results in section 8. The conclusions from this study are in section 9. Recommendations for the next Phase (3) work are made in section 10.

2 TECHNICAL BACKGROUND

The original LST test sponsored by the NRC/NUPEC attracted contributions from 17 participants from USA, Canada, France, Japan, Korea, UK, Spain, China, India and Russia who submitted their pre-test analysis results. 14 of these participants presented their results at the meeting held in October 1999 at Sandia Laboratories, USA. There was significant difference in the behaviour predicted by the participants. This was mainly due to the modelling approach, assumptions and interpretation of the design data. Many of the participants constructed global models of the PCCV reflecting their assumptions, to predict the limit load. Others made detailed models of local features like the penetrations and buttresses but did not have a full global model. The NNC/HSE model was the only full 3-D global model (see Ref 2) which had included sufficient details of all the important local features like the tendon layout, penetrations, buttresses, stressing gallery, soil foundation and the liner.

In Ref 2 the NNC/HSE model was analysed using version 5.8 of the ABAQUS general purpose FE code (Ref 6). It was found that the concrete material model in the 5.8 version of ABAQUS gave numerical problems and the global 3-D model could not be analysed beyond an internal pressure of 0.71 MPa. The analysis beyond 0.71MPa was completed by incorporating the ANACAP concrete material model routine supplied by ANATECH (Ref 7).

The main objective of the exercise was to predict the failure mode and the behaviour up to the limit load. The NNC/HSE model accurately predicted that the liner tearing would control the limit load. It also predicted accurately that the main structural components like the tendons and reinforcing bars would not fail before liner tearing. Whilst the failure mode was predicted accurately, there remained discrepancies between the history of the response recorded during the test and that predicted by the FE analysis. This could be because the model did not take account of the as-built conditions, which were investigated in the post-test analysis (Ref 4).

The test model had a design pressure, Pd, of 0.39Mpa and the Limit State Test (LST) achieved a pressure of 1.295MPa (3.3 Pd), which was well beyond the design basis. The test was limited because the vessel leak rates increased beyond the supply limit of the N_2 pressurization system. The overall PCCV structure remained substantially intact after the LST. The sponsors agreed to extend the test and SNL sealed the leaks and conducted the Structural Failure Mode Test (SFMT) by using a water pressurization system. The SFMT was conducted on 14 November 2001 and achieved its objective of causing global collapse of the PCCV structure, reaching a pressure of 1.423MPa (3.65 Pd).

The LST and SFMT data in conjunction with the pre-test and the post-test analyses show three stages of the structural response of the pressurized PCCV as it approaches its structural collapse load.

The first stage of predominantly elastic response can be predicted with very good accuracy using standard finite element technology. The second stage involving inelastic response with extensive concrete cracking required specialist concrete material models and detailed geometric representation of the main structural features. It is important to model the interaction between various structural elements to simulate load redistribution as some components yield or fail. Such local yielding or rupture may lead to loss of functionality or breach of pressure boundary. The third stage involving gross deformation leading to structural collapse required solution of a highly non-linear problem. Extensive concrete cracking, well beyond the tension stiffening range, occurs and requires robust constitutive models capable of simulating extensively cracked concrete. Provided such a specialist FE package is available, an experienced analyst can predict the collapse limit and failure mode with fair accuracy.

As part of the ISP48, additional information about the test has now been made available to the participants (Ref 5). For meaningful application of this research to real size containments, a number of issues like the effect of thermal loading and scaling remain to be resolved.

3 SCOPE

The full scope of the ISP48 is to perform a new stress analysis of the ¼ scale PCCV using the same models as for the post-test analysis (Ref 4), but incorporating thermal loading in addition to the mechanical loading. The existing FE results (from Refs 2 and 4) and the results from the new stress analysis will be compared with the test data to indicate the following:-

- Effect of accident temperatures on the containment capacity
- Would the onset of leakage be later and much closer to the burst pressure

The overall project comprises four phases of work as follows:

Phase 1: Data collection and identification

Phase 2: Calculation of the LST

Phase 3: Calculation of response to both thermal and mechanical loadings

Phase 4: Reporting workshop

This report addresses Phases 1 and 2 only, with recommendations for the way forward in phase 3. The scope of work for phases 1 and 2 covered by this report as follows:

3.1 PHASE 1: DATA COLLECTION AND IDENTIFICATION.

The purpose of this phase is to review construction and vessel load data collected by SNL during the LST/SFMT testing. Assessment includes reviewing the concrete, liner plate, tendon and rebar material properties and the tendon post-tensioning loads. This information has been issued to all ISP participants (Ref 5) who are to use the data for analysis. Necessary changes to the NNC model used in the previous analysis will be identified for the ISP.

It is also required that results are reported at the standard output locations used in the PCCV pretest round robin Figure 1. This will enable direct comparison between the analytical results of the participants. NNC has provided results at the 55 standard output locations in electronic format in an MS Excel spreadsheet.

3.2 PHASE 2: CALCULATION OF THE LIMIT STATE TEST (LST) PERFORMED AT SNL - MECHANICAL LOADING

This task requires updating of the FE model to take account of any new information from the Phase 1 review. The requirement is to analyse the LST (applying only the mechanical loads) to predict the extent of concrete cracking, liner tearing and tendon rupture. Comparison between the analytical and test results will be made. The peak sustainable load will also be calculated and compared with the test.

In the previous analysis work (Refs 2 and 4), the ANACAP routine supplied by ANATECH was used to remove some of the limitations of the ABAQUS version 5.8 concrete material model. Incorporation of this concrete model extended the range of pressure over which predictions could be made. A new concrete material model has been made available in the

latest release of ABAQUS version 6.4. It is proposed to use the latest concrete material model in ABAQUS v6.4 with the NNC's 3D global model to perform the LST analysis.

In this Phase, it is required of each participant to suggest a way forward for the following two topics: -

- Transposition to real size containments. This will include consideration of scaling issues.
- Definition of thermal loading for Phase 3.

4 ¼ SCALE PCCV FINITE ELEMENT MODEL

4.1 DESCRIPTION OF GLOBAL MODEL

Concrete components of the vessel are simulated with the ABAQUS eight-node solid element C3D8. The eight-node solid element is mathematically formulated such that it accommodates the inclusion of steel reinforcements. At a minority of locations, due to meshing requirements, six-node linear prism elements (C3D6) were used. Six-node prism elements do not support reinforcement capability. Within the cylinder, all solid elements are fully integrated, while the basemat and dome elements have reduced integration. Figure 2 shows the 3D global model of the PCCV model.

The origin of the FE model is at the centre of the top surface of the basemat. Directions 1, 2 and 3 are X, Y and Z respectively. X is along the 90° azimuth, Y is vertical and Z is along the 180° azimuth.

4.2 CYLINDER WALL AND DOME

The mesh density of the cylinder wall and dome in the circumferential direction was driven by the requirement to model the vertical post-tensioning tendons explicitly. Three elements were employed in the wall-thickness direction of the cylinder and dome. For the fully integrated elements, this gives a total of six integration points through the wall to provide adequate information in areas of high bending. To allow for the explicit representation of each vertical tendon, 184 solid elements were arranged around the circumference of the vessel. The resulting layout consists of a cylinder and dome wall mesh with elements at approximately 2 degree intervals in the circumferential direction.

The mesh density in the vertical direction was influenced by the specification of the hoop tendons in the concrete elements. The cylinder hoop tendons were arranged at vertical intervals of 112.7mm. The solid element nodes are meshed vertically to correspond with the spacing of the hoop tendons.

The height of the elements in the lower half of the dome is base on the vertical spacing of the dome hoop tendons. The dome elements are uniformly meshed up to a height of 14690mm, the location of the uppermost hoop tendon. The meshing of the dome in the hoop direction was dictated by the vertical plane of the tendons through the dome. In the dome apex region, a refined solid element mesh allows meshing of the vertical tendons where they intersect at the vessel crown. Figure 3 shows a detailed view of the model.

The buttresses at the 90° and the 270° azimuths are reinforced columns onto which the hoop tendons are anchored. The stiffness of the cylinder and the dome at the 90° and 270° azimuths is enhanced by the restraining effect of the buttresses. The reinforcement scheme of the buttresses comprises vertical, radial U bars and trim bars. Additional stiffening is provided by the steel plates at the tendon anchorage end-blocks. The buttresses and their reinforcement have been modelled explicitly.

4.3 BASEMAT

The basemat is a thick concrete reinforced slab supporting the vessel superstructure within which the vertical tendons are anchored. It is heavily reinforced at its top and bottom surfaces. The top surface reinforcement consists of a layer of hoop rebars sandwiched between two grids of radially spanning rebars. The bottom surface is reinforced with a rectangular grid of cross rebars. Additional reinforcement is provided in the vicinity of the tendon anchorage gallery. The flexural reinforcements were defined within each solid element. The basemat shear reinforcements were not modelled. Figure 4 shows a view of the basemat.

4.4 THE CYLINDER WALL PENETRATIONS

The cylinder wall penetrations and their immediate vicinity have been explicitly modelled. Structural features within the penetration area that are represented explicitly in the model are the enhanced reinforcement stiffening, thickened wall section (airlock and equipment hatch penetrations), steel plates lining the penetration cavity, the penetrations cover plates, the vertical and hoop tendons, internal vessel liner and the liner anchorage. The finite element meshes of the airlock, equipment hatch, main steam and feed water penetrations are shown in Figures 5, 6 and 7.

4.5 THE POST-TENSIONING TENDONS

The post-tensioning tendons have been modelled using two different approaches. The vertical tendons were modelled explicitly using the two-node, linear truss element T3D2. For each tendon, nodes have been generated coincident to the solid element concrete nodes along the tendon path. Typically, in the non-penetrated areas a vertical tendon consists of up to 220 elements, depending upon its location within the vessel. Each vertical tendon node lying within the cylinder of the vessel is constrained in the horizontal degrees of freedom (i.e. the X and Z directions) to the coincident concrete nodes. The vertical degree of freedom (Y) of tendon nodes within the cylinder were left unconstrained, allowing relative sliding of the tendons and concrete in the vertical direction. Within the cylinder, friction at the concrete/tendon interface is assumed to be negligible and has not been modelled. However, within the dome, the curved trajectory of the tendon causes appreciable friction at the concrete/tendon interface, resulting in a non-uniform variation of load in the tendon. Although interface behaviour has not been explicitly modelled, the non-uniform distribution of load in the vertical tendons over the dome is allowed for by constraining all coincident tendon and concrete nodal degrees of freedom. The vertical tendon mesh is shown in Figure 8

The hoop tendons are modelled as single rebars embedded within concrete elements. The concrete elements were defined such that an element edge lies along the path of the hoop tendon as this facilitated the placement of the hoop tendons with the elements. Each hoop tendon starts at one face of the buttress, completes a 360° loop around the vessel and is anchored at the opposite face on the same buttress. Alternative tendons are anchored at opposite buttresses. Interface behaviour between the concrete and the tendon has not been modelled. Frictional loss in the hoop tendons is discussed in section 5.3.

4.6 INTERNAL LINER AND LINER ANCHORAGE

The thicker insert plates surrounding the main steam and feed water penetrations are simulated with the shell element S4R. The S4R element is a general purpose shell element

suitable for both 'thick and thin shell' applications. It accounts for finite membrane strains and allows for change in thickness. Therefore it is suitable for large strain analysis. An S4R element has 4 nodes and 6 DOF at each node. In order to try to keep the size of the model within manageable limit, it was decided to model the general area of the liner with membrane type M3D4R elements. These elements are reduced integration 4 noded membrane elements with only two in-plane DOFs. Such elements are suitable for thin plates which offer strength in the plane of the element and have negligible bending stiffness. The liner elements are meshed around nodes defined independently but coincide with adjacent concrete nodes. The internal liner mesh is shown in Figure 2. The meshes of the plate lining the equipment hatch penetration cavity are presented in Figure 9

The liner-to-concrete anchorage was modelled by connecting the liner node to the corresponding coincident concrete node with three linear spring elements at each node, representing the radial, hoop and axial anchorage plate stiffness. Given that the pitch of the horizontal and vertical liner anchorage plates is not uniform, no attempt was made to simulate the anchorage plates at their exact locations. The spring stiffness values given in Table 5 are derived from test results for the pull-out of anchorage plates in tensile and shear modes, Ref 5, as follows.

The pull-out and shear test reported in Ref 5 are based on tests conducted on a number of pre-stressed and non-pre-stressed liner/concrete anchorage arrangements. In this work, test results from the pre-stressed liner/concrete anchorage arrangements have been used to derive the stiffness of the anchorage. The liner strip, 300mm wide, and embedded in a block of concrete was loaded first by tension load and then by shear load. In each case the stiffness of the arrangement was computed. For each case the average measured values were used as the basis for calculating the equivalent anchorage spring stiffness. The measured tensile and shear stiffness are respectively 127ton/mm and 59ton/mm.

In the finite element model, the radial tensile anchorage stiffness is represented by 36 springs in the hoop direction. The equivalent tensile spring stiffness is computed as follows:

$$\text{Tensile spring stiffness} = \frac{127 \times 1000 \times 9.81 \times 2\pi \times 5376}{36 \times 300}$$

$$= 3.89 \times 10^{6} \text{ N/mm}$$

There are 36 shear springs around the circumference of the vessel model. The shear spring stiffness is given as:

$$\text{Meridional/hoop spring stiffness} = \frac{59 \times 1000 \times 9.81 \times 2\pi \times 5376}{36 \times 300}$$

$$= 1.82 \times 10^{6} \text{ N/mm}$$

4.7 CONCRETE REINFORCEMENTS

The grid of reinforcing bars in the vessel has been represented as rebar smeared within the parent solid elements. The orientation, cross-sectional area, spacing and material properties are taken from the construction drawings, Ref 9.

The duct-supporting steel frame construction is modelled as single rebars within the parent solid elements. The properties of the steel frame are given in Ref 9.

4.8 PCCV SUPPORT CONDITIONS

The basemat is constructed on a 150mm thick un-reinforced slab which itself is supported on an engineered sand and gravel subgrade. The soil stiffness was characterised as exhibiting a settlement of less than 25mm due to a bearing pressure of 35Ton/m^2, Ref 10.

The soil was represented using grounded spring elements (SPRING1). Each node on the bottom surface of the basemat was supported on a spring element, Figure 10. The spring stiffness was computed based on the influence area of each spring node.

The vessel was constrained to eliminate rigid body translations and rotations at four nodal positions on the top surface of the basemat in the horizontal degrees of freedom Figure 4

5 REVIEW OF TEST DATA

5.1 CONCRETE MATERIALS

A full review of the concrete material test data versus the original LST analysis was carried out. During this phase of the review, in the process of upgrading the input files from Version 5.8 to 6.4, it was decided that the model would now incorporate three different material models for each of the three main components of the PCCV global model. Therefore separate materials would be used for the cylinder, dome and basemat regions.

The concrete material properties that were assessed for review in the global model are: -

- Young's modulus
- Density
- Poisson's Ratio
- Compressive Strength
- Tensile Strength

Each property was assessed and an average selected for each region of the model.

5.1.1 Young's Modulus

Previously the model only used a single Young's modulus for all of the components. The new analysis has three Young's moduli specified as shown in Table 1.

From Table 1 it can be seen that the Young's modulus has increased for the dome component. However, it has decreased for the basemat and the cylinder components. The largest change is the decrease of approximately 8% for the cylinder.

5.1.2 Density

Once again three densities have been specified for the new analysis and are given in Table 2. The table of densities shows that there was a little difference between the values used in the original LST analysis and the actual test data, giving rise to a small decrease in mass.

5.1.3 Poisson's Ratio

The Poisson's ratio has increased quite considerably for all of the components of the global model. The increase in Poisson's ratio would give a marginal rise in displacements for the same vessel with the same internal pressure. The values used for Poisson's ratio are given in Table 3

5.1.4 Compressive & Tensile Strength

The compressive and tensile strengths of the concrete define the starting point for the non-linear portion of concrete material model. The non-linear portion of the concrete material model incorporates effects of tension stiffening, damaged plasticity and compression hardening. In the global model of the PCCV a non-linear material used is for the main cylinder wall and the dome. From the concrete test data the values in Table 4 were calculated.

These properties have been incorporated into the latest ABAQUS concrete material model, which is described in section 6.

5.2 TENDON / REBAR MATERIALS

The tendon and rebar materials in the global model were once again assessed during the SFMT analysis. A review of the data supplied in Ref 5 showed that the material properties were identical to those used for the SFMT therefore no modification to the material properties was required.

5.3 VESSEL PRE-TENSIONING

The load distribution within the tendons was non-uniform because of friction between the tendons and ducts. This was taken into account during the pre-test analysis by using the design values of the anchorage loads of 350kN and 471kN for the hoop and vertical tendons respectively. Variation in the tendon loads due to frictional loss was obtained by applying the following Equation 1.

$$P = P_{1,2}\, e^{(-\mu\beta - 0.001L)} \qquad \textit{Equation 1}$$

Where

$P_{1,2}$ = Load at the tensioning end 1 or 2.

β = Change of angle from tensioning end.

P = Load at β from tensioning end.

μ = Friction Coefficient.

L = Length of Tendon.

Hydraulic jacks were used to tension the tendons to the desired load. They were then anchored at the buttresses and the base mat for the hoop and vertical tendons respectively. Each hoop tendon was modelled by 183 elements, and from the element nodal coordinate, the average change of angle from the anchorage was calculated. The same procedure was used for the vertical tendons, but only over the dome area. Friction losses for the vertical tendons in the wall region were assumed to be negligible.

A sample of the pre-loads for a selection of hoop and vertical tendons were measured at the time of the test. It was seen that the values observed before the test were not consistent with the design loads. The pre-loads specified in the pre-test analysis were up to 10% higher than the pre-load values in the test. The comparison is shown in Figure 12 and Figure 13 for vertical and horizontal tendons respectively. The tendon pre-load values within the input decks were then altered to simulate the test results taking into account the distribution of the load due to friction. Not all tendon values were measured, so the tendons for which there were known measured values were altered individually, and the intervening tendon loads were assigned an average value.

The equipment hatch, airlock and mainstream penetrations were modelled separately from the cylinder, so the areas where tendons passed through the penetrations were assigned an average value around that section of the tendon.

At the "Post-Test Meeting" it was confirmed that seating-loss of the tendons had a larger effect on the vessel than that initially calculated. The seating loss occurs when the tendons are initially tensioned and then released by the hydraulic jacks. The tendons contract slightly as they "settle in". The pre-test analysis did not take into account this seating loss acting on the tendons and had assumed that the loss was negligible. Allowance for this was made in the post-test analysis and was assumed to act over a 90° segment (45° sections on each side of the buttress). The average seating loss of 24757N was taken from the PCCV test results, and was included in the calculations for the pre-loads. The modelling assumed that the seating loss was linear throughout the 90° segment. Figure 14 shows the variation in tendon load due to friction and the seating loss. The friction coefficient of 0.21 for the steel tendons was kept unchanged.

6 MODEL UPDATE TO ABAQUS V6.4

The PCCV global model was updated from ABAQUS Version 5.8 to the most recent version of 6.4. The main difference between the two versions of ABAQUS is the format in which the input files are created. . Using a utility included in version 6.4, the version 5.8 input files were reformatted for use with version 6.4. Once the conversion was completed the input files were checked against the original to check all the changes made had been implemented correctly.

6.1 CONCRETE MATERIAL MODEL

ABAQUS version 6.4 includes an improved concrete damaged plasticity model. It uses concepts of isotropic damaged elasticity in combination with isotropic tensile and compressive plasticity to represent the inelastic behaviour of concrete.

The parameters, which are required for definition of the concrete model, are as follows: -

- Tension stiffening
- Tension damage
- Compression damage (optional)
- Compression hardening

All of the above parameters are required, with the exception of the compression damage as little damage occurs during the pre-stressing of the vessel.

The concrete model is a continuum, plasticity based, damage model for concrete. It assumes that the two failure mechanisms are tensile cracking and compressive crushing.

The model assumes that the tensile cracking of the concrete is characterised by damaged plasticity. Under uniaxial tension the stress-strain response is linear until the failure stress is reached. It is at this point micro cracking of the concrete is initiated. Once beyond the failure stress the cracking of the concrete is represented by a strain softening approach.

6.1.1 Tension Stiffening

The tension stiffening option is used to model the interaction and load transfer between the concrete and the steel reinforcement. The tension stiffening can be simulated in ABAQUS either by a post failure stress-strain approach or by applying a fracture energy criterion.

The post failure stress-strain is defined as a yield stress versus a cracking strain or displacement. ABAQUS converts the cracking strain or displacement into plastic strain automatically. A reasonable estimate of tension stiffening for heavily reinforced concrete is to assume that the strain softening after failure reduces the stress linearly to zero at a total strain of about 10 times the initial cracking strain. This approach can be seen in Figure 15

The fracture energy approach uses an initial yield stress and a value for the fracture energy, which was available from the test data.

6.1.2 Tension & Compression Damage

The degree of tension and/or compression damage determines the amount of post cracking damage (or stiffness degradation). This also determines the amount of recovery that can take place in the concrete after unloading. This is defined by using a damage variable and a direct cracking strain or displacement.

6.1.3 Compression Hardening

This parameter is used to define the changes in compressive strength of the concrete as shown in Figure 16. The compression hardening is defined in terms of a stress versus a crushing strain. During uniaxial compression, the response is linear until the value of initial yield (σ_c). In the plastic regime the response is characterised by a stress hardening and then a strain softening approach that occurs after the ultimate stress (σ_{cu}) is reached.

6.2 CHANGES TO MODEL PARAMETERS

The properties for the linear portion of the concrete modelling, which includes the basemat and buttresses was updated in line with the material data provided in section 5.1.1 to 3.

The properties for the Non-Linear portion of the modelling (for the cylinder and dome), however, provided some problems. In order to be able to use the updated concrete model within ABAQUS Version 6.4, the material test data had to be reviewed in line with the new concrete material model.

Initial runs using the test data from Ref 5 produced convergence problems due to the initial onset of micro cracking and premature failure of the global model under tension. Therefore some sensitivity models were run in order to deduce a correct tensile material property that could be used in the global model.

The model built for testing the concrete properties was a solid cylindrical specimen of 150mm in diameter by 300mm long. A pressure was applied to one end of the cylinder with the other end being fixed in the axial degree of freedom. This put the concrete specimen under uniaxial tension.

The material properties, which give rise to the failure of the concrete within the global model, are the tension stiffening and the tension damage parameters. The tension stiffening can be controlled by various different means as stated previously. It can be controlled either by the fracture energy or by specifying the stress-strain or stress-displacement curves.

All three approaches for modelling the tension stiffening were considered and data implemented from the uniaxial tensile tests on the concrete specimens. Firstly the strain approach was adopted and this proved that failure of the concrete occurred too early due to the initial yield stress being too low and complete cracking of the concrete had occurred before 0.6MPa. With increased tensile strength at a value of 4.4 N/mm^2 the model ran much further before running into convergence problems.

Secondly the fracture energy approach was adopted and an average value from the material test data of 0.121 N/mm was used. This was checked against values from the CEB-FIP Model Code 1990 and was found to be a reasonable value if not a little too high for the

aggregate size (10mm) being used. The code gave a value of approximately 0.11 N/mm. The fracture energy approach once again produced convergence problems at a low pressure and complete failure occurred at approximately 0.5 MPa.

Finally the stress versus displacement approach was tested, again using data from the material tests. This approach gave complete failure of the concrete to be at around 0.52Mpa even with an increased yield of 4.4MPa.

The reason for the increased yield stress for the concrete was to take into account the effect of the steel rebar within the concrete, which would delay the initial onset of micro cracking.

The tension damage option as explained previously must be used in order to simulate the complete failure of the concrete. If this option is not used then as the concrete passes its ultimate stress and proceeds into the plastic region, it will continue behaving as a plastic material and not fail completely.

In conclusion to the sensitivity studies the tension stiffening was defined by the stress-strain approach. The compression hardening was also defined by the stress-strain approach.

Using the stress-strain approach gave the best results for comparison with the LST and the previous analysis using the ANAMAT concrete material model.

The final material properties used in the analysis are given in Table 6.

7 LST ANALYSIS RESULTS

The finite element model data as presented in Figures 17 to 71 have the initial values reset as to line up with the Limit State Test Results.

7.1 COMPARISON WITH TEST DATA – GLOBAL DISPLACEMENTS / STRAINS

Figures 17 to 71 are the comparison of the new ABAQUS 6.4 global model against the LST test data. As the concrete material model is relatively new, it was decided that the previous analysis using the ANAMAT concrete material model would also be included in this comparison.

The other reason for this is that after reviewing the data from both of these analyses, the final deformed shape is different. The model using the ABAQUS concrete material shows its maximum displacement at the equipment hatch location, whereas the ANAMAT material model shows it to be on the 0° azimuth at an elevation of 7.73m. The location of maximum displacement as exhibited by the ANAMAT model agrees with the failure location of the SFMT test. The difference in location can be seen in Figures 72 and 73 for the ANAMAT and ABAQUS respectively. Even with the above differences, the ABAQUS V6.4 analysis gives a better agreement for the initial state of the model. This could be due to the updated elastic material properties that are the latest test data supplied. This is discussed further in section 8.1.

7.2 CALCULATION OF LIMIT LOAD

The limit load is determined by the inability of the vessel to retain pressure and this is dependent on the integrity of the steel liner. The steel liner has low ductility at the welded locations, where an average rupture strain of 22% was observed in the original tests performed on the liner material. More recent test data shows that the actual rupture strain was more likely to be in the region of 6%.

From the global model high localised strains were found to be present at the locations where junctions between thick insert plates and the thinner Liner plate. These are at the airlock and equipment hatch and main steam feed penetrations. The junction of the two plates at the equipment hatch was examined using a local 2D plate model as described in Ref 8 and the model mesh can be seen in Figure 74 and the plastic strains can be seen in Figure 75. The equivalent plastic strains can be seen in Figures 76 and 77 for the ANAMAT and the ABAQUS analyses respectively. Previously the model showed that a free field strain of 3% gave rise to an 11% strain at the thick/thin plate junction. Now with the test data showing the rupture strain to be 6% the strain in the free field only needs to reach 1.5%. Figure 78 shows the response of the liner at location 44 for the meridional strain. This gives a limit load range of approximately 1.2 to 1.4Mpa, which compared with the pressure of 2.5Pd (1.0Mpa) when substantial leakage was observed during the LST.

8 ASSESSMENT OF RESULTS

The primary objective of this phase of the ISP is to present the results from the LST analysis of the PCCV utilising the information presented in SNL's test report (Ref. 3). This ensures all participants in the ISP are using the same data. This section presents NNC's results. Comparisons are also made with the test data and results reported for the post-test analysis of the PCCV reported in reference C6635/TR/001.

8.1 ELASTIC RESPONSE OF VESSEL

Figures 17 to 31 present the displacement histories for locations 1 to 15 during the LST pressurisation. Comparing the test and analytical results highlights two facets of the vessel response.

At internal pressures up to 0.6MPa, the vessels response remains essentially elastic. At 0.6MPa concrete cracking is initiated (see. section 8.2) and an increasing non-linear response can be seen. The non-linear response increases up to the LST limit of 1.3MPa. This is caused by crack progression in the concrete and yielding in some regions of the steel liner as the pressure increases. The response of the vessel over the LST pressure range is predicted by both analysis models and is confirmed by the test. Complete failure of the vessel is not achieved.

As Figures 32 to 71 have been reset at the beginning of the test we cannot see the original offset between the two finite element models and the Limit State Test results. However, the ABAQUS v6.4 results demonstrate that at the beginning of vessel pressurisation the initial conditions obtained from the analysis correspond well with the test data. This is a significant improvement on the results predicted by the ANAMAT analysis. Previously, the difference in initial conditions between the test and ANAMAT results was attributed to shrinkage and creep effects in the concrete (Ref 4). These effects had not been fully captured in the analysis. However, the primary difference between the ANAMAT and the ABAQUS v6.4 analyses are the values of the concrete material elastic constants Young's modulus (E) and Poisson's ratio (v), as discussed in section 5.1. This would indicate that the elastic properties have a significant influence on the initial conditions predicted by analysis, whilst also retaining the global elastic response of the vessel.

8.2 ASSESSMENT OF CONCRETE CRACKING

The ABAQUS 6.4 analysis confirms crack initiation in the concrete occurs at 0.6MPa. This is predominantly in the vertical direction and local to the intersection of the cylinder wall and buttresses. Figure 79 highlights the areas of damaged concrete from the analysis. As the vessel is pressurised, the inner surface of the wall experiences tension caused by local bending about the buttresses. The deformed shape of the cylinder, presented in Figure 80, highlights this. These analytical results are in close agreement with the test results. Figure 81 presents output from the acoustic monitoring system used for the LST test. This confirms a number of cracks are initiated local to the wall buttress at the 270^0 azimuth at a pressure of approximately 1.5 Pd (0.59MPa).

8.3 ASSESSMENT OF LINER TEARING

Section 7.2 highlights that liner tearing is initiated at the junction of the thick insert plates and steel liner local to the wall penetrations. Figure 77 shows the areas of high liner strain in these regions. The analysis estimates tearing in the pressure range 1.2 to 1.4MPa. The inspection results of the liner after the LST test presented in Figure 82, confirm the largest liner tear local to the equipment hatch penetration. However, tearing occurs at a pressure of 1.0MPa (2.5 Pd). The difference in the predicted and test pressures are attributed to variations inherent in the vessel construction. The analytical pressure calculated is based on a rupture strain of 6% for the welded liner. This is obtained from tensile tests of liner specimens conducted after the model testing (Ref 5). The number of specimens tested was limited and variations in the results obtained can be expected throughout the actual structure.

8.4 ASSESSMENT OF TENDON RESPONSE

Figure 83 presents a plot of the displaced shape of the PCCV vertical tendons at a pressure of 1.4MPa. This figure also presents the axial stress distribution in each tendon. As expected, it is observed that the tendon displacements follow the wall radial displacements. Also as would be expected, the highest loaded tendons occur in the free-field region adjacent to the 0° azimuth. This is the location of the wall experiencing the largest radial displacements. An axial stress of approximately 1419N/mm^2 is calculated for these tendons. This is less than the yield stress of 1741N/mm^2. Stress concentrations are seen in the tendons surrounding the wall penetrations. This is due to the reduced length of these tendons in the analysis, which are restrained axially local to the openings.
Inspection of Figures 64 to 71 indicates that none of the vertical or horizontal tendons break during the LST.

9 CONCLUSION

Conclusions from the analysis of the LST, utilising the data supplied for the ISP are summarised as follows: -

(i) Catastrophic structural failure of the PCCV does not occur in the LST pressure range.

(ii) Excessive leakage rate due to liner tearing is predicted as the limiting fault for the test. Initiation of liner tearing is predicted in the range 1.2 to 1.4MPa.

(iii) The location of liner tear at the insert plate junction predicted by analysis is confirmed by LST.

(iv) Concrete cracking is first observed at a pressure of 0.6MPa on the inner surface of the cylinder walls, local to the buttresses.

(v) The values of elastic material constants used for analysis are influential in predicting initial conditions for the containment. This is demonstrated in the ABAQUS v6.4 analysis for which closer correlation with the test results is seen. Good correlation is also obtained for the linear/elastic range of the response.

(vi) Tendons do not yield during the LST.

(vii) The concrete material modelling facility in ABAQUS v6.4 now offers a viable package for analysis of failure modes in concrete structures.

10 PROPOSALS FOR PHASE 3

Two objectives are proposed for phase 3 of the ISP.

- To assess issues relating to the translation of the LST test results to a full size structure.
- Evaluate the effects of elevated temperatures on the failure mode and limit load of the containment.

The way forward is to be discussed at a meeting of the participants, scheduled for March 2004. Issues pertinent to those discussions are summarised in sections 10.1 and 10.2. Section 10.3 is specific to discussing creep issues at elevated temperatures.

10.1 ASSESSMENT OF FULL SIZE CONTAINMENTS

The LST results are all specific to the ¼ scale model. A fundamental issue associated with testing models is with what confidence can the failure mode obtained be expected to occur in full size containments.

It is important to recognise that some physical parameters, such as gravity and friction, cannot be scaled and may have a disproportionate effect on the results from the test. For example, preload losses in the tendons caused by friction interaction with the vessel wall are known to be significant. Friction is a physical constant so will losses in the test model be proportionally higher than for full size containments? Gravity is another physical constant. Are its effects more influential on the smaller test model or full size containments? How significant are the preload losses due to tendon anchorage at the seatings and how is this affected by scaling?

Fabrication issues relevant to construction may also affect the failure mode predicted. This is particularly applicable to the liner. The liner for the LST model is 3mm thick and welding such a thin plate is fraught with problems. For example, are the residual stresses and heat-affected zone disproportionately high compared to a full size vessel? Also, can construction tolerances be scaled and are those for the test model achievable in reality? In full size containments these issues may not be as significant and liner tearing may occur at higher pressures to that predicted by the test. This may result in a different initiating fault for the full size containment to that predicted by the model.

These parameters should be debated and conclusions drawn as to how the response of full size containments may be different.

10.2 DEFINITION OF THERMAL LOADING.

Common approaches for calculating thermal distributions using numerical analysis include nodal mapping of temperatures and heat transfer analysis. Both options provide a temperature profile throughout the structure for transient heating/cooling cycles and steady state conditions.

Nodal mapping requires the specification of a temperature at each node in the FE model. Temperatures are specified for the initial condition of the structure and the elevated condition at steady state or each increment of a transient. Thermal strains are calculated from the temperature differentials. The mapping is mesh sensitive and may not be directly

applicable to a pre-existing model. To alleviate this discrepancy, a post-processing routine would be required for interpolation of the temperatures to a model with a different mesh.

Heat transfer analysis offers a more generic approach. All aspects of thermal behaviour can be replicated, whether it is conduction, convection or radiation. A key aspect of this approach is that the analysis is not mesh dependant. The thermal behaviour is defined in terms of heat transfer coefficients, boundary temperatures and concentrated heat fluxes. For these reasons, heat transfer would be the preferred analysis method to adopt in Phase 3. However, it will require detailed definition of the thermal properties and thermal boundary conditions.

For any thermal cycle the inertias associated with the components of a PCCV will result in different responses at different times. The liner is a thin shell and will expand quickly in response to increasing temperature. It is therefore more susceptible to localised high compressive strains during the heat up phase. Thermal expansion of the liner may also delay liner rupture when internal pressure is applied. Peak temperatures are achieved at steady state. During the cool down phase the concrete is susceptible to cracking induced by tensile strains. The ISP meeting must therefore assess which aspect of the PCCV's response is considered important when defining the thermal analysis for Phase 3.

10.3 CREEP BEHAVIOUR AT ELEVATED TEMPERATURES

The results from the LST analysis indicate that the material elastic constants used for the analysis are a major influence on the initial conditions and linear response of the vessel. However, containments are required to withstand high temperature fault conditions. Under such conditions redistribution of stress due to creep behaviour in the concrete and steel components can be expected. This could influence the containments integrity at elevated temperatures.

11 REFERENCES

Ref	Title
1	International Standard Problem on Containment Capacity (ISP48), Working Group on Ageing of Concrete Structures (IAGE/CONCRETE), CSNI Proposal, IAGEWG(2002)15, Rev 0, June 2002
2	HSE/NNC Pretest Analysis Report for ¼ Scale PCCV Model, NNC Report C5769/TR/002.
3	Pretest Round Robin Analysis of a Prestressed Concrete Containment Vessel, Sandia National Lab., NUREG/CR-6678, SANDE 00-1535, August 2000
4	HSE/NNC PCCV Round Robin Post Test Analysis, NNC Report C6635/TR/001, Issue 01, Dec 2002
5	Overpressurisation Test of a 1:4 Scale Prestress Concrete Containment Vessel Model, Sandia National Lab., NUREG/CR-6810, SAND2003-0840P, Project Report No. R-SN-P-010, March 2003
6	ABAQUS/Standard, ABAQUS/CAE, ABAQUS/Viewer, ABAQUS Inc., USA
7	ANACAP-ANATECH Concrete Analysis Program Users Guide, ANATECH Research Corp., USA
8	HSE/NNC Pretest Analysis Report for ¼ Scale PCCV Model, NNC Report C5769/TR/004.
9	Obayashi Corporation package of construction drawings of PCCV model
10	Sandia National Laboratory PCCV Design Package, Material Properties Report

12 NOTATION

α	Coefficient of thermal expansion
β	Azimuth angle
ε_0	Initial strain (creep + shrinkage)
ε	Strain
σ	Stress
σ_c	Compressive Yield Stress
σ_{cu}	Ultimate Compressive Yield Stress
σ_t	Tensile Yield Stress
μ	Coefficient of friction
E	Young's modulus
E_0	Initial Young's modulus
L	Length of tendon
P1, P2	Tension loads at the tensioning ends
Pd	Design pressure = 0.39MPa
T	Temperature

12.1 ABBREVIATIONS

FE	Finite Element
LST	Limit State Test
PCCV	Pre-stressed Concrete Containment Vessel
SFMT	Structural Failure Mode Test
SNL	Sandia National Laboratories

Table 1 **Original and updated Young's Modulus**

Component [Abaqus Version]	Young's modulus (N/mm^2)
All [V5.8] (original)	27950
Basemat [V6.4]	26973
Dome [V6.4]	28270
Cylinder [V6.4]	25831

Table 2 **Original and updated Density**

Component [Abaqus Version]	Density (tonne/mm^3)
All [V5.8] (original)	$2.21 * 10^{-9}$
Basemat [V6.4]	$2.19 * 10^{-9}$
Dome [V6.4]	$2.20 * 10^{-9}$
Cylinder [V6.4]	$2.14 * 10^{-9}$

Table 3 **Original and updated Poisson's Ratio**

Component [Abaqus Version]	Poisson's Ratio
All [V5.8] (original)	0.180
Basemat [V6.4]	0.214
Dome [V6.4]	0.217
Cylinder [V6.4]	0.218

Table 4 **Original and updated Compressive & Tensile Strength for cylinder wall**

Material Property [Abaqus Version]	Value (N/mm^2)
Compressive Strength [V5.8] (original)	24
Tensile Strength [V5.8] (original)	4.4
Compressive Strength [V6.4]	55.86
Tensile Strength [V6.4]	2.06

Table 5 Anchorage properties

Description of Spring	Stiffness (N/mm)
Liner tensile pull-out stiffness	3890000
Liner shear stiffness	1820000
Penetration lining anchor	581000

Table 6 Material properties for the ABAQUS Version 6.4 analysis

Material Property	Dome	Cylinder	Basemat
Young's Modulus (N/mm^2)	$2.8358 * 10^4$	$2.58 * 10^4$	$2.758 * 10^4$
Poisson's Ratio	0.217	0.218	0.214
Density ($tonne/mm^3$)	$2.258 * 10^{-9}$	$2.1458 * 10^{-9}$	$2.1958 * 10^{-9}$
Concrete Damaged Plasticity (dilation angle,,,,viscosity)	35.0,,,,0.001	35.0,,,,0.001	Not Used*
Concrete Compression hardening (yield stress, inelastic crushing strain)	42.4,0.00 59.64,0.00099	42.4,0.00 59.64,0.00099	Not Used*
Concrete Tension Stiffening (direct stress post cracking, direct strain)	4.4,0 0.04458,0.006058	4.4,0 0.04458,0.006058	Not Used*
Concrete Tension Damage (tensile damage variable, direct strain)	0,0 $0.99,6.058 * 10^{-3}$	0,0 $0.99,6.058 * 10^{-3}$	Not Used*

NB: Stress in MPa

* Items marked as Not Used are due to the material properties for these components being linear.

Figure 1 Standard Output Locations

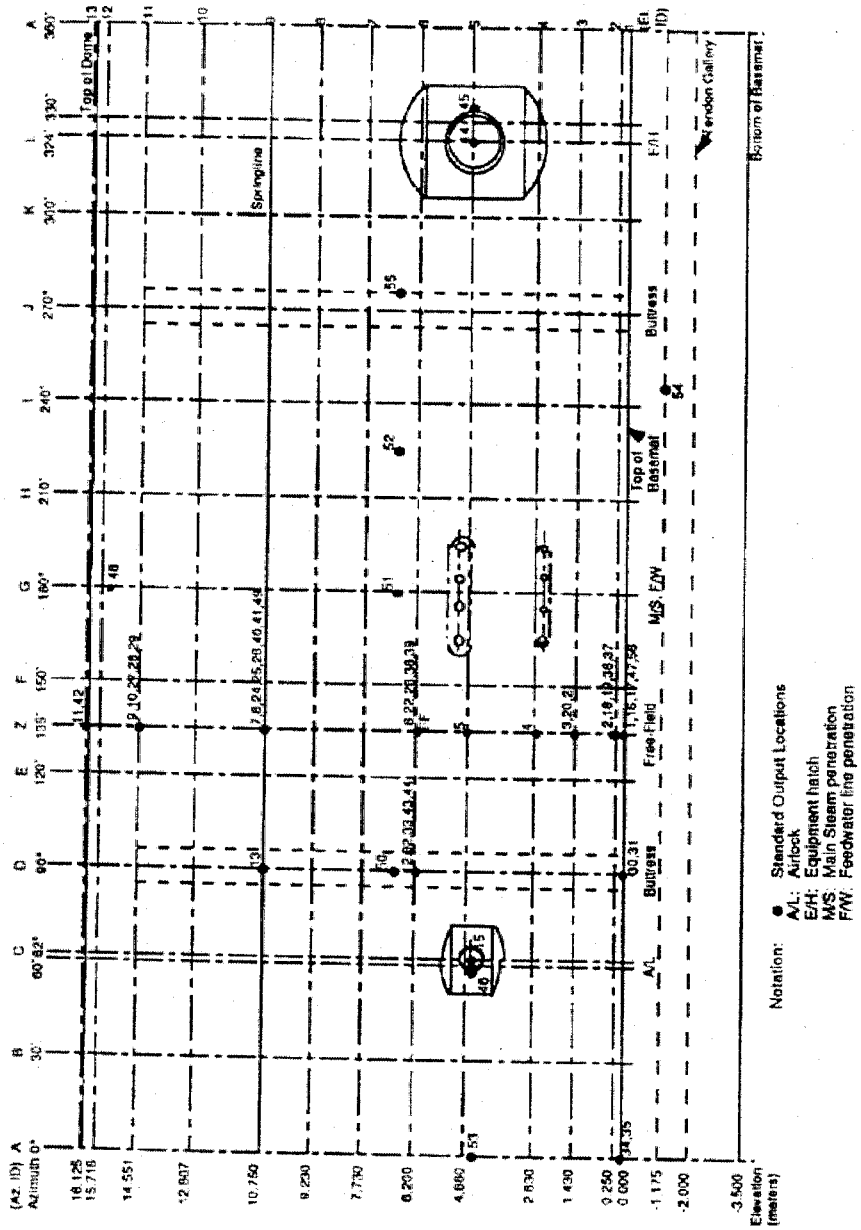

Figure 2 Finite Element Representation of the PCCV

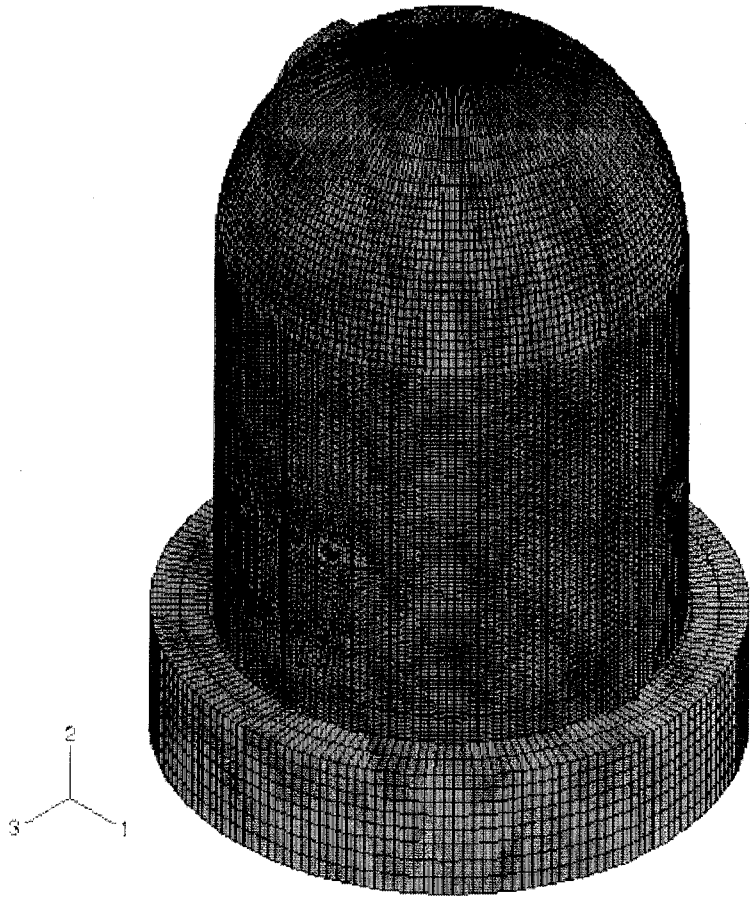

Figure 3 Detail view of the PCCV dome model

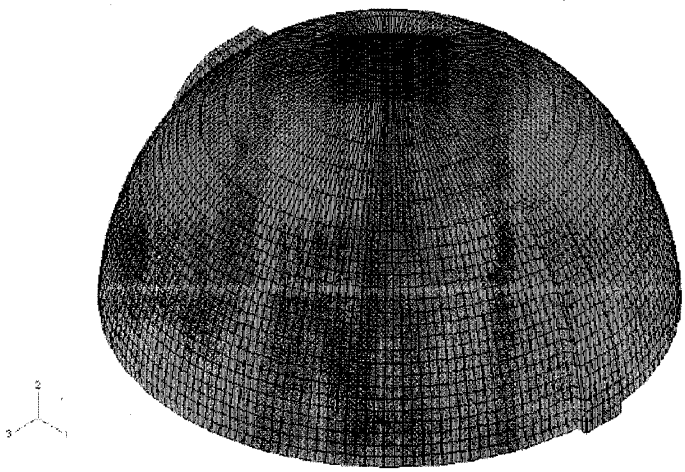

Figure 4 The basemat model showing locations of global restraints

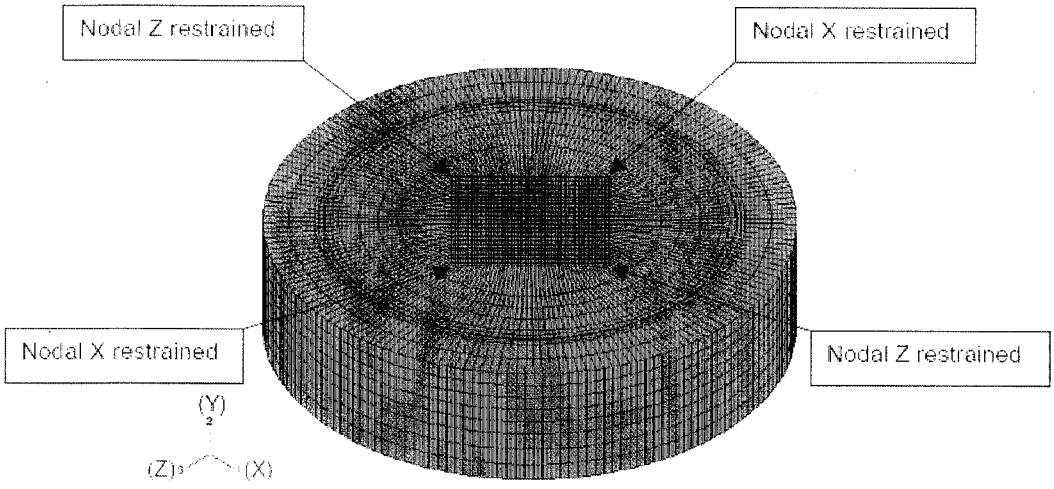

Figure 5 Detailed view of the equipment hatch penetration model

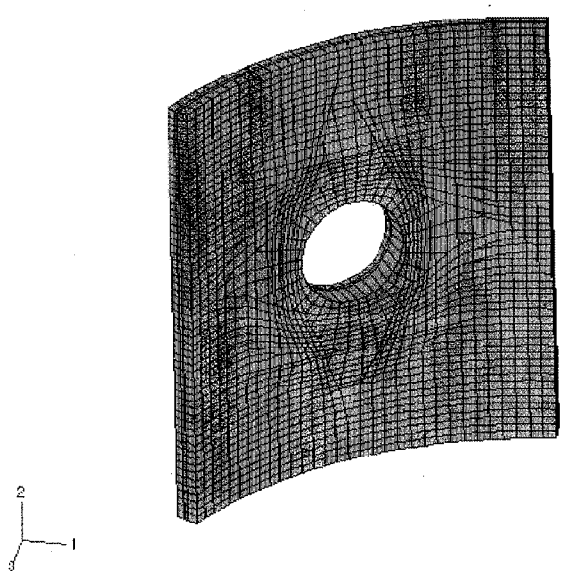

Figure 6 Detailed view of the airlock penetration model

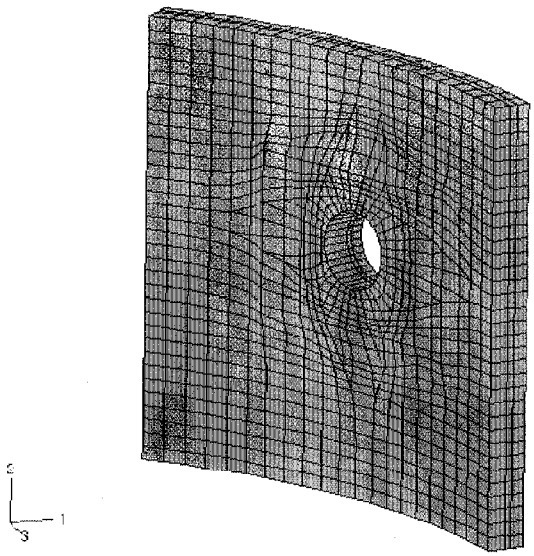

Figure 7 Detailed view of the main steam and feed water penetration model

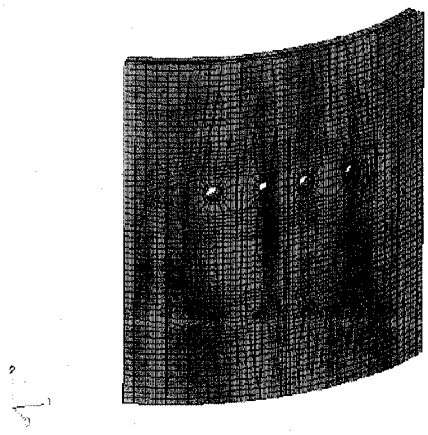

Figure 8 PCCV vertical tendons model

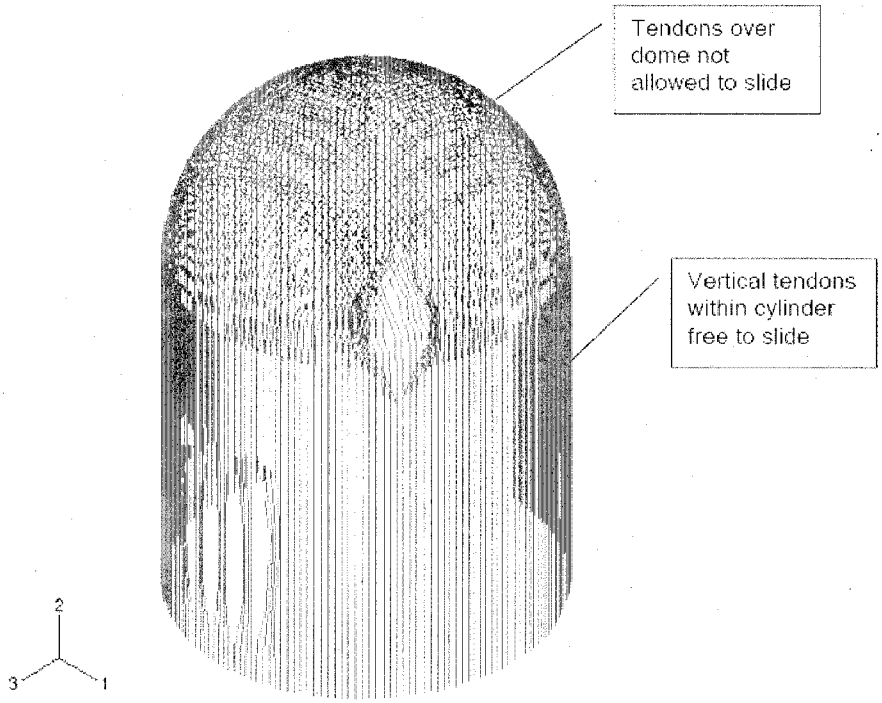

Figure 9 Equipment hatch penetration lining and cover plate

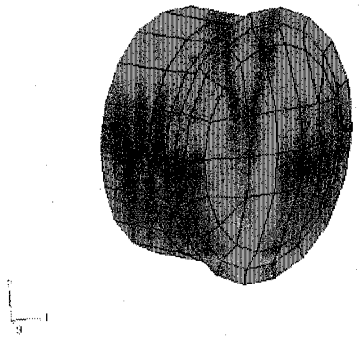

Figure 10 PCCV model supported on soil springs

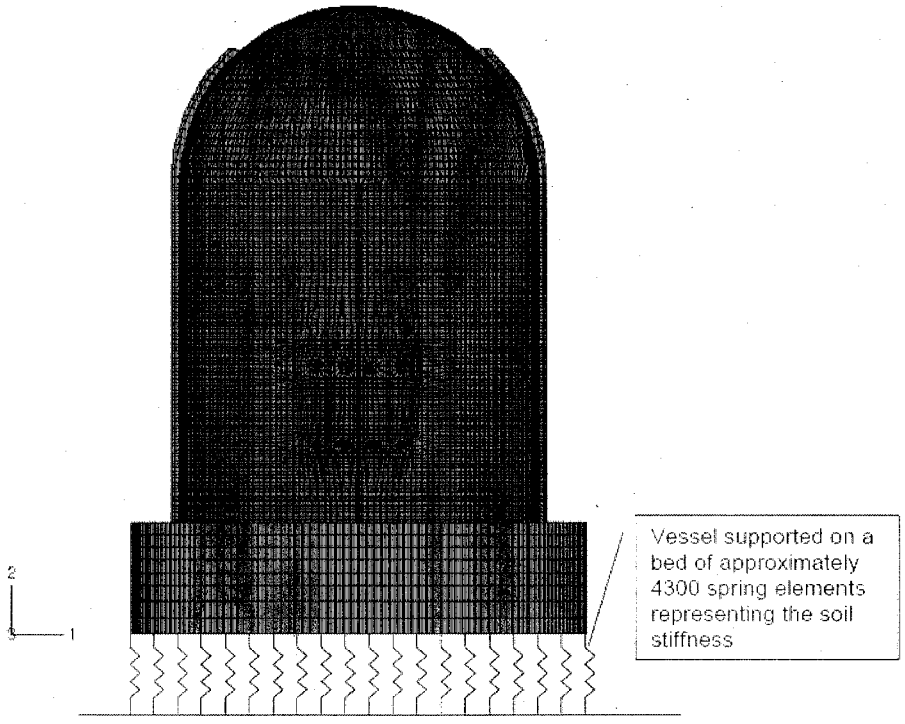

Figure 11 **Internal liner model, showing detail around the main steam and feedwater penetrations**

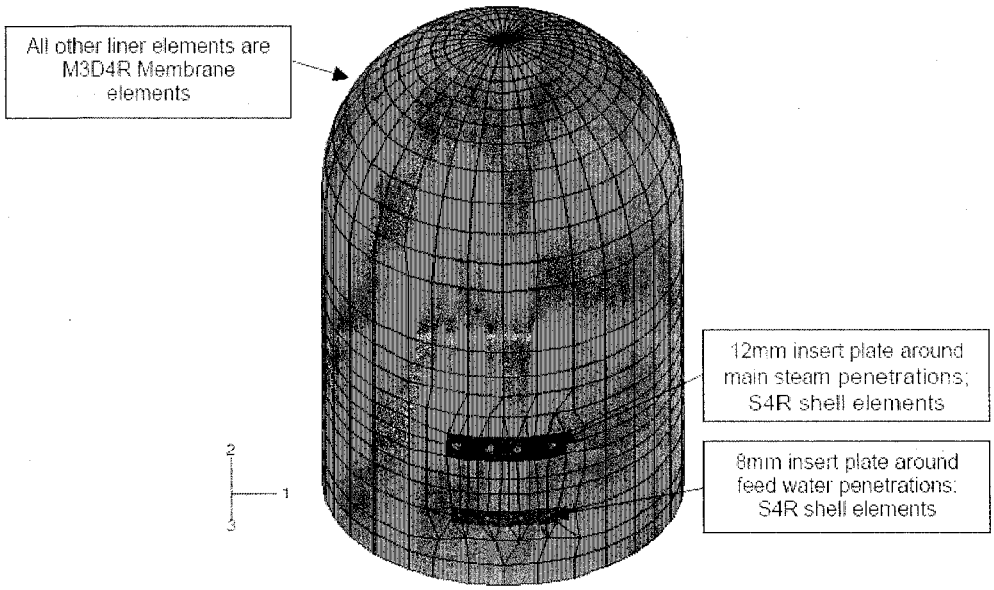

Figure 12 **Comparison of Test & Pre-test Vertical Tendon Loads**

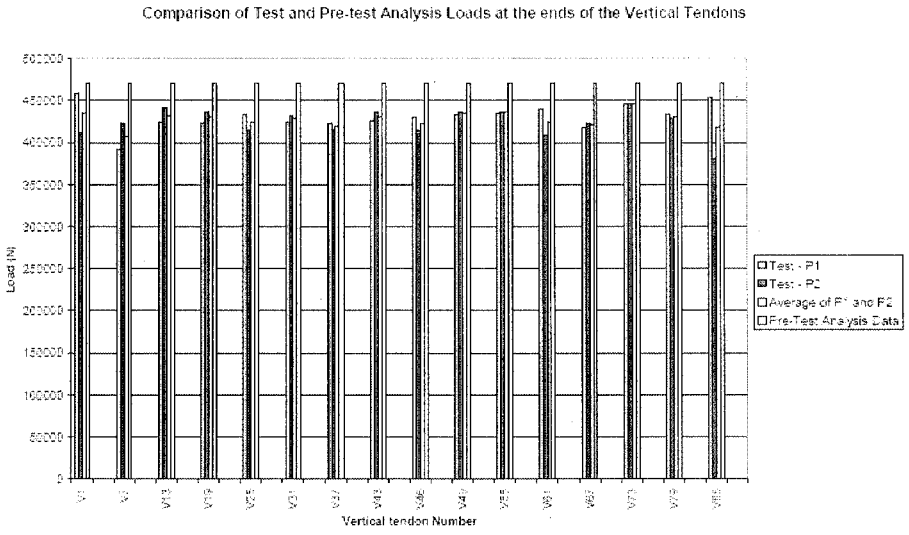

Figure 13 Comparison of Test & Pre-test Hoop Tendon Loads

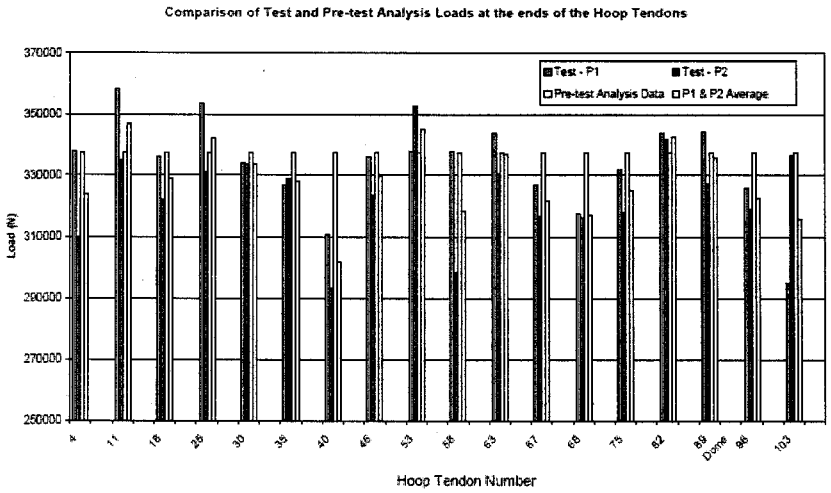

Figure 14 Variation in tendon load due to friction and seating loss

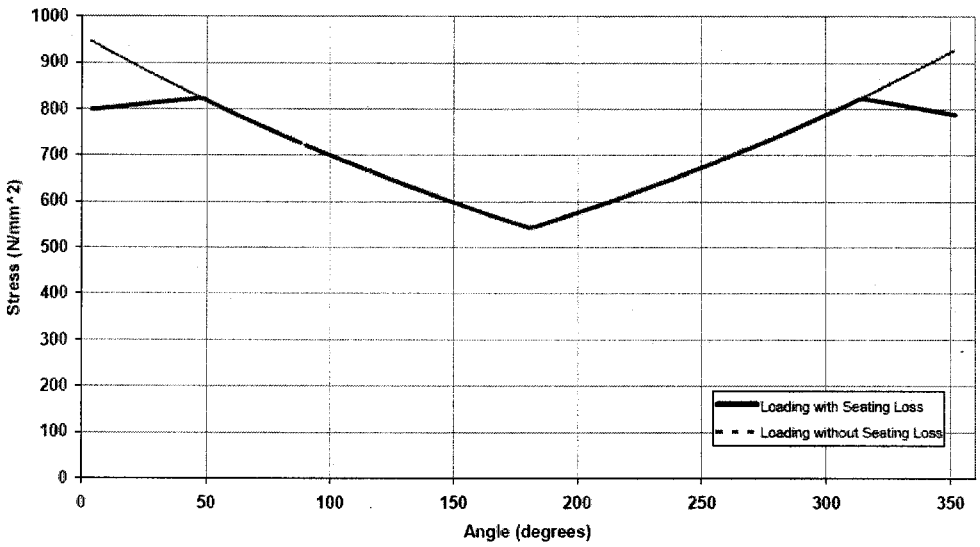

Figure 15 Stress-Strain Tension Stiffening Relationship

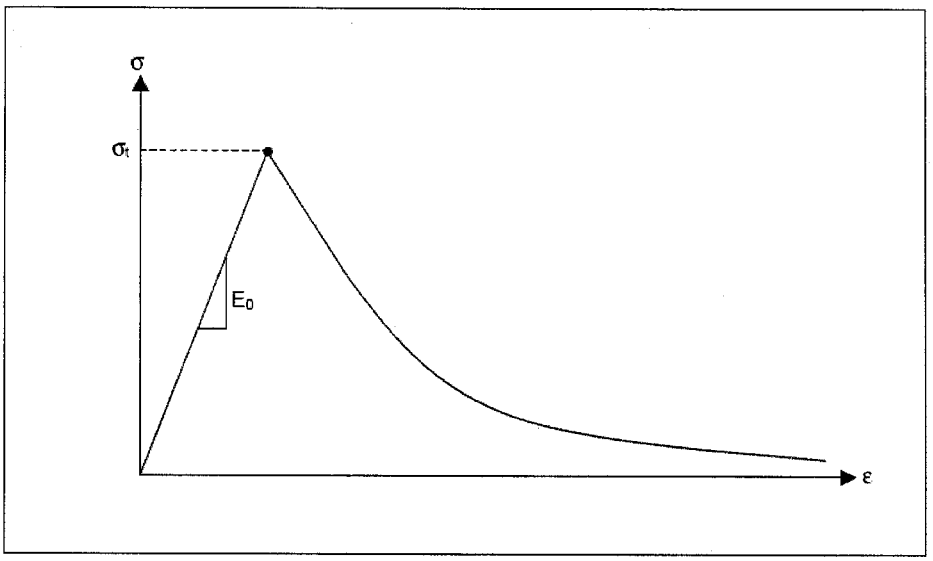

Figure 16 Stress-Strain Compression Hardening Relationship

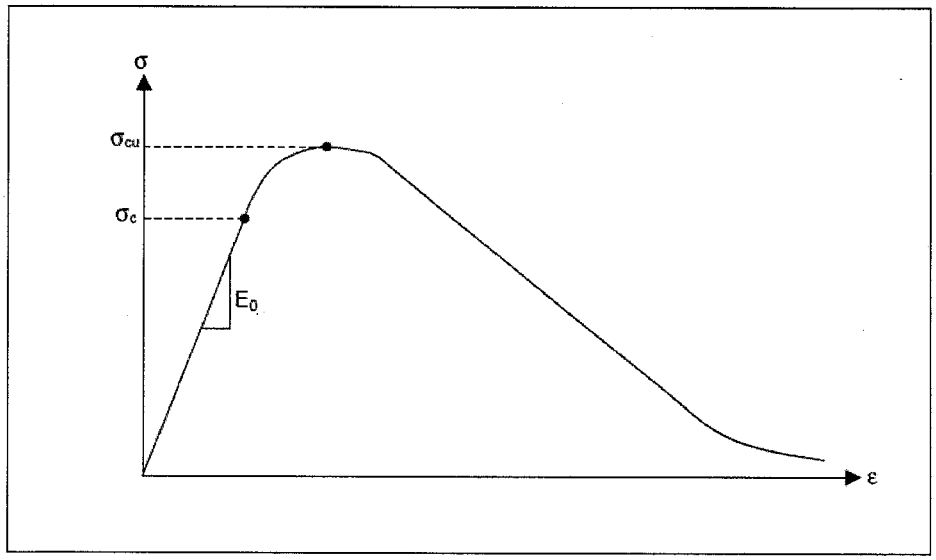

Figure 17 Location 1 Vertical Displacement

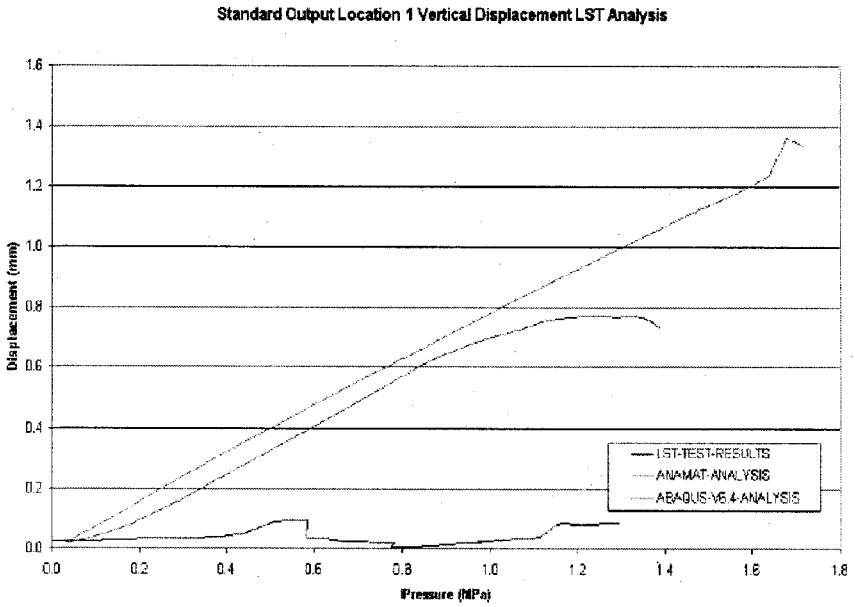

Figure 18 Location 2 Radial Displacement

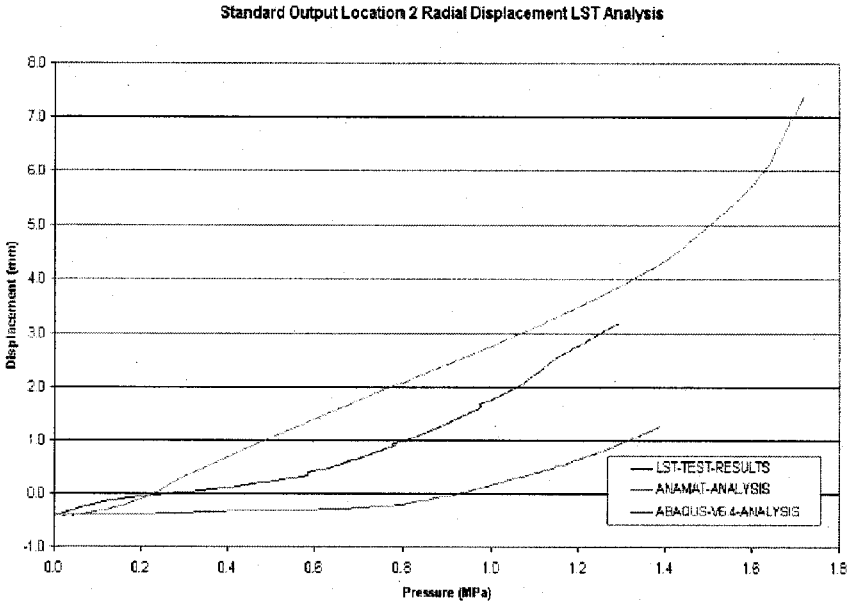

Figure 19 Location 3 Radial Displacement

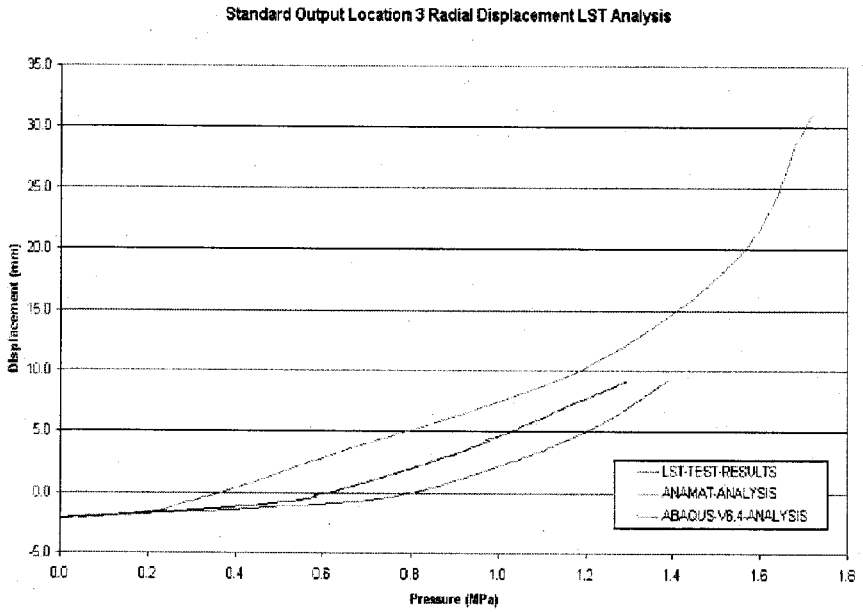

Figure 20 Location 4 Radial Displacement

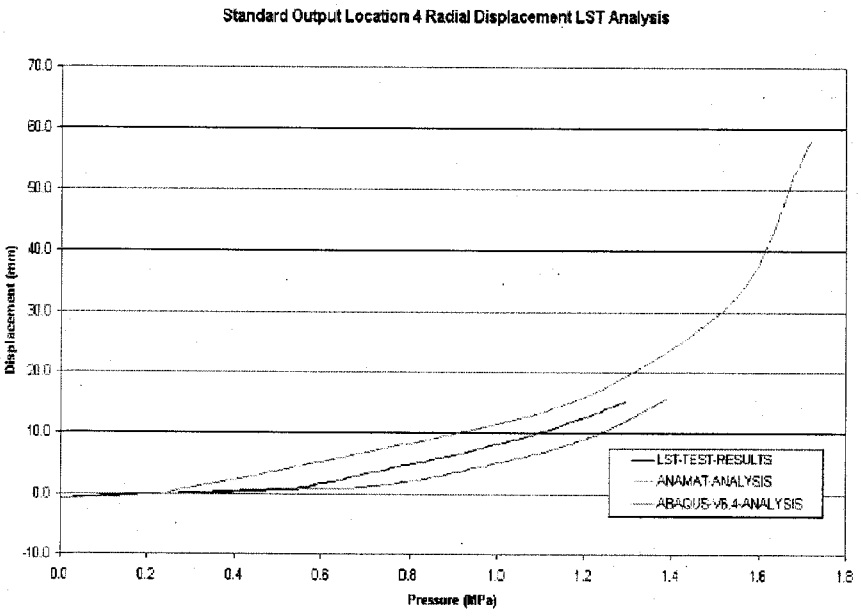

Figure 21 Location 5 Radial Displacement

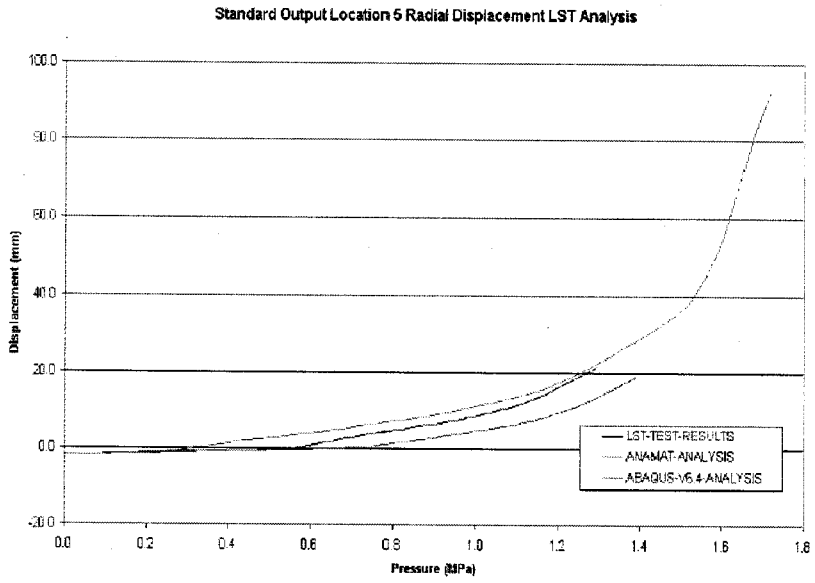

Figure 22 Location 6 Radial Displacement

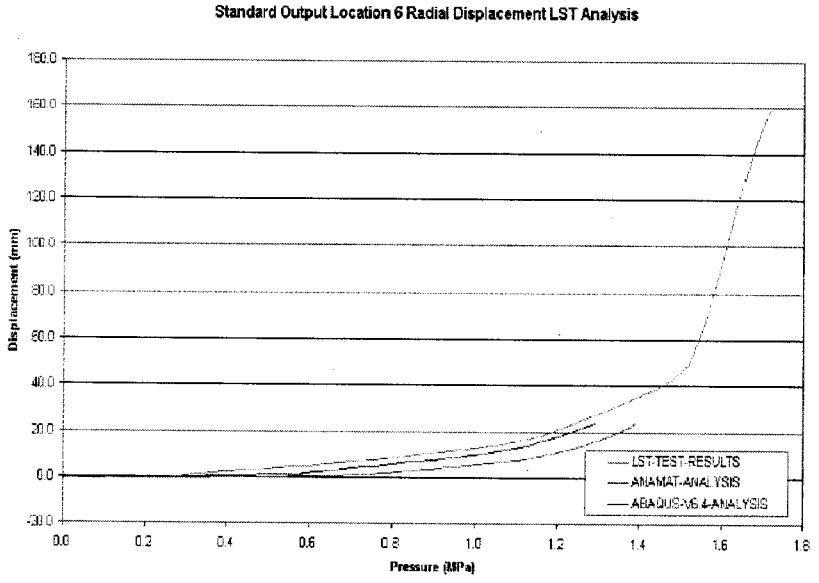

Figure 23 Location 7 Radial Displacement

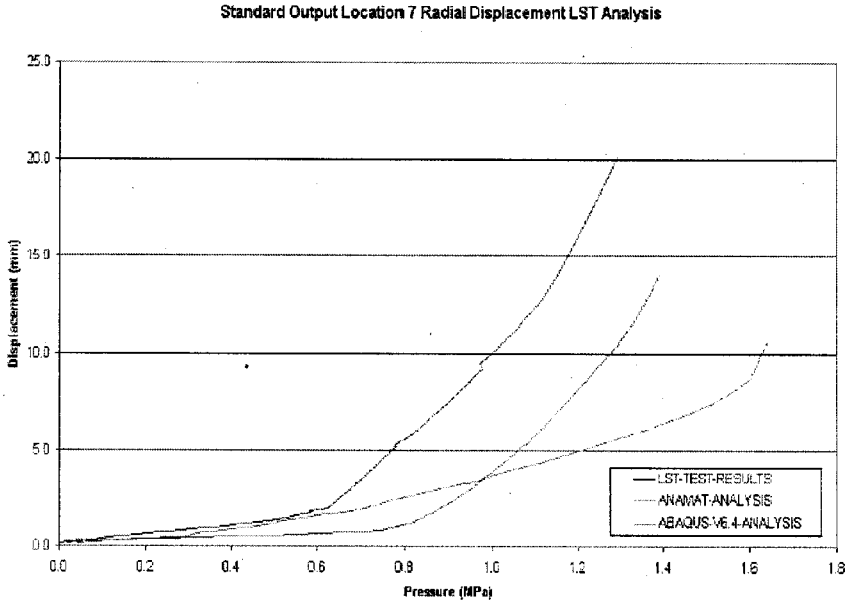

Figure 24 Location 8 Vertical Displacement

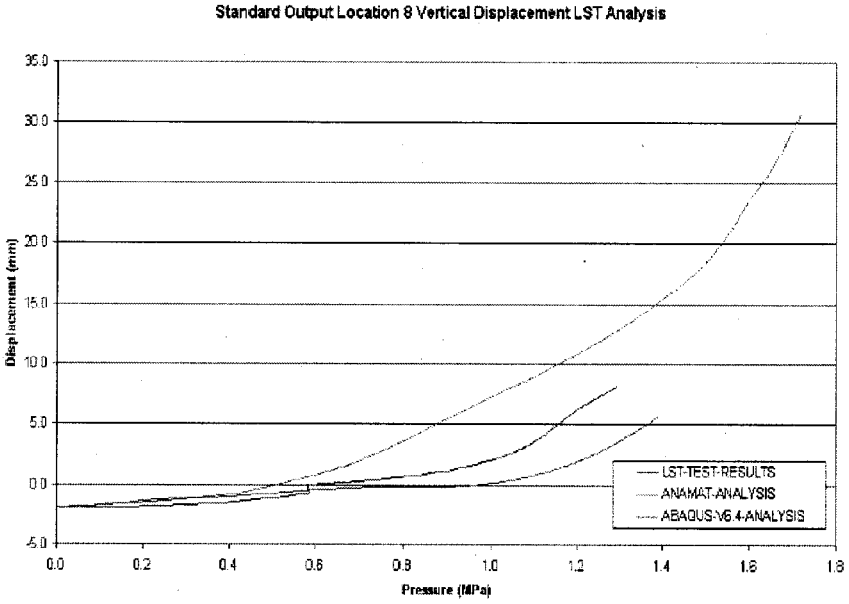

Figure 25 Location 9 Radial Displacement

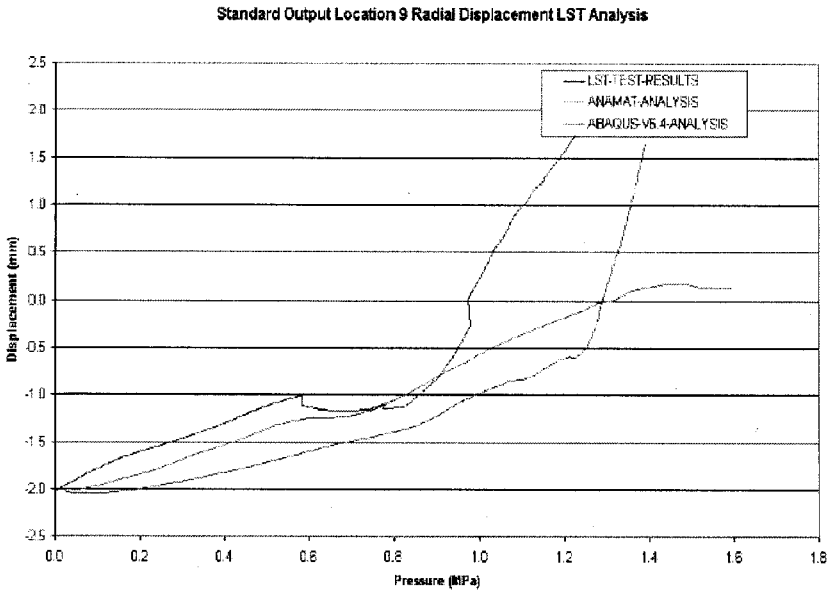

Figure 26 Location 10 Vertical Displacement

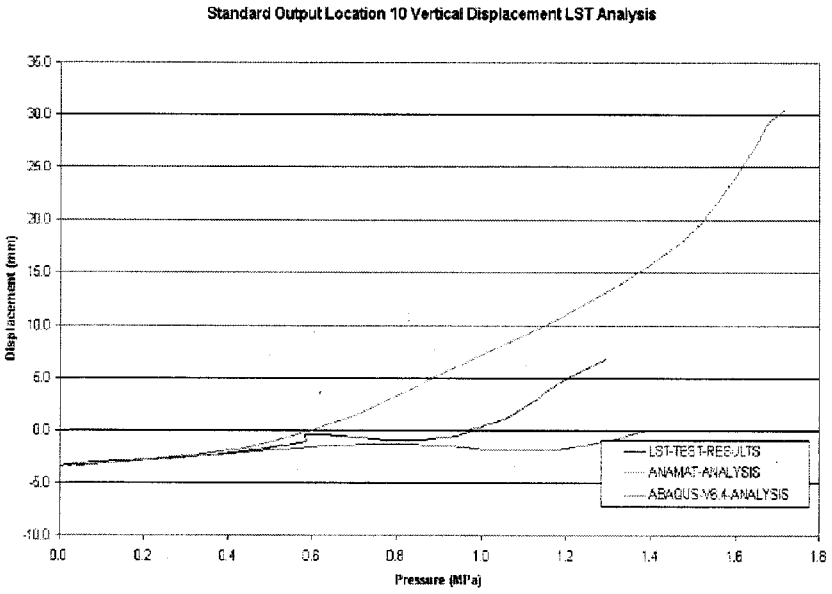

Figure 27 Location 11 Vertical Displacement

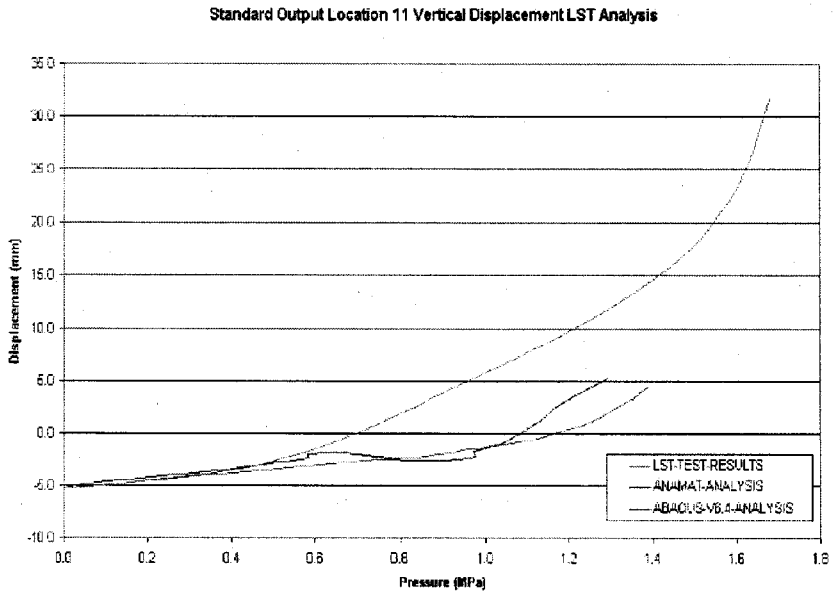

Figure 28 Location 12 Radial Displacement

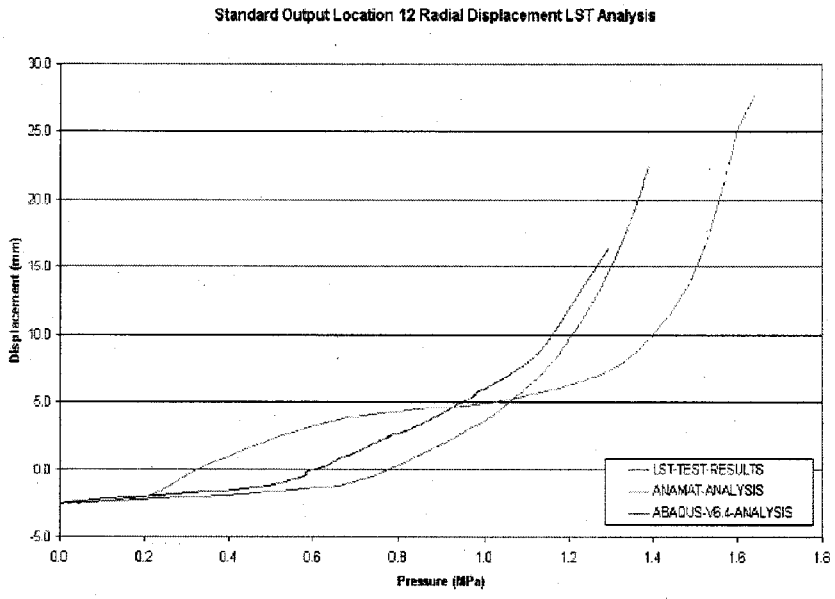

Figure 29 Location 13 Radial Displacement

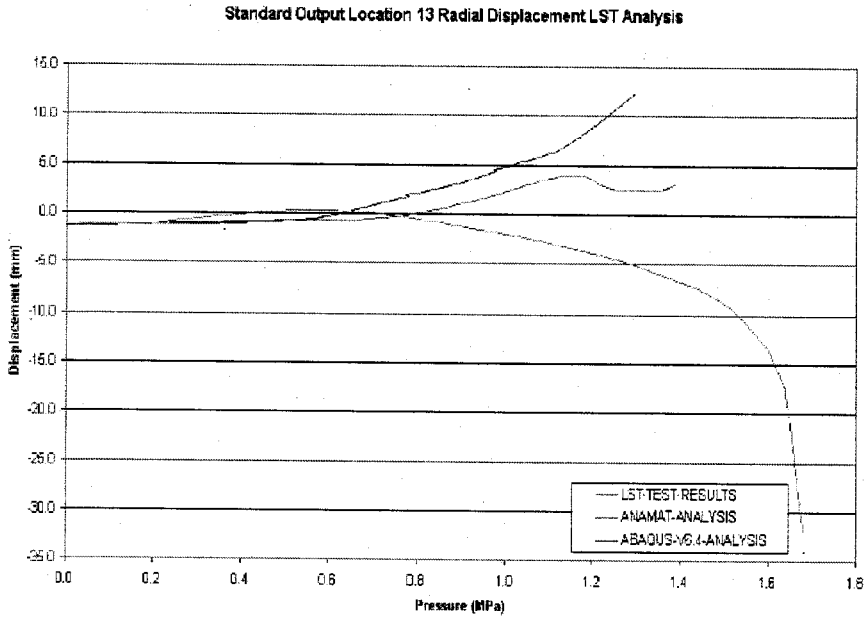

Figure 30 Location 14 Radial Displacement

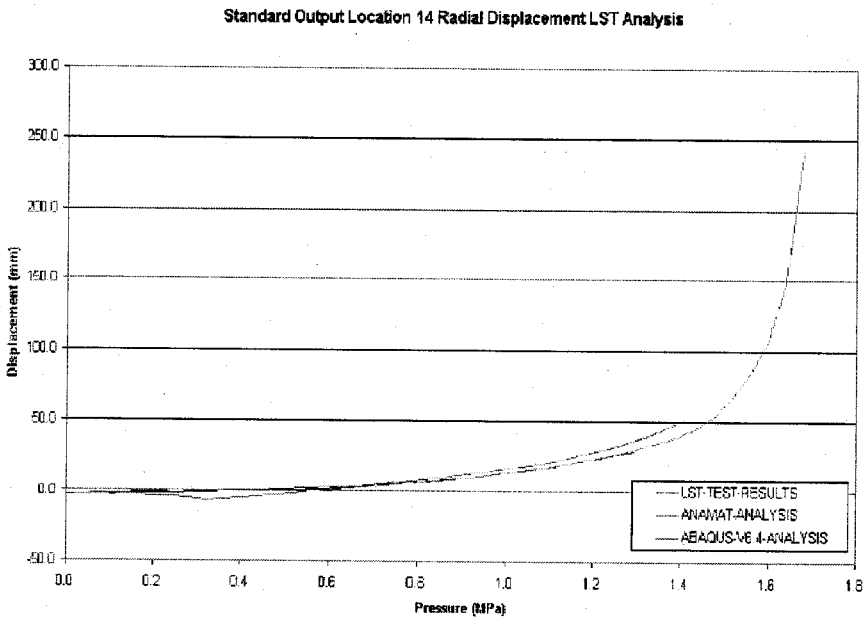

Figure 31 Location 15 Radial Displacement

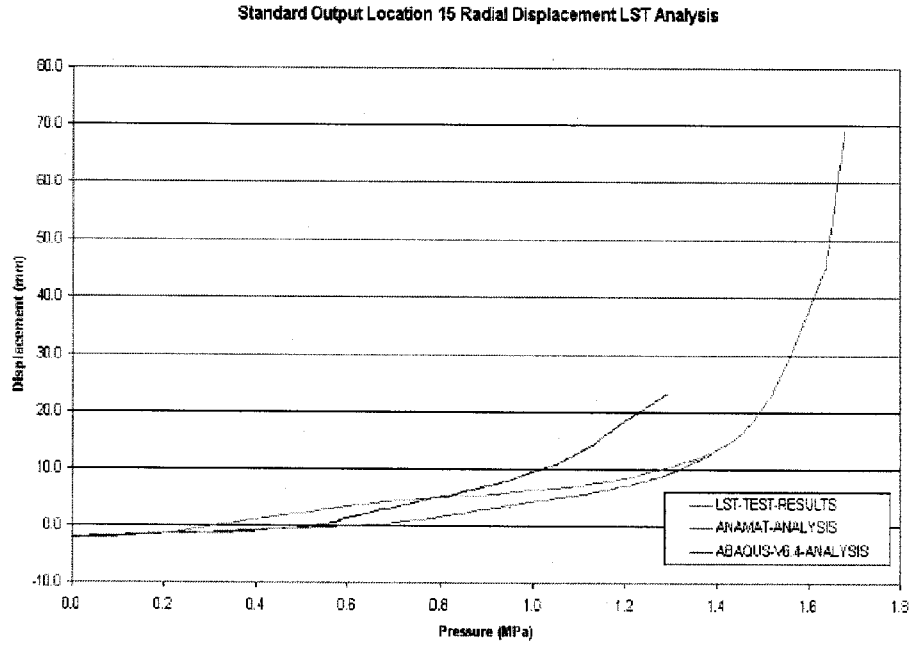

Figure 32 Location 16 Meridional Rebar Strain

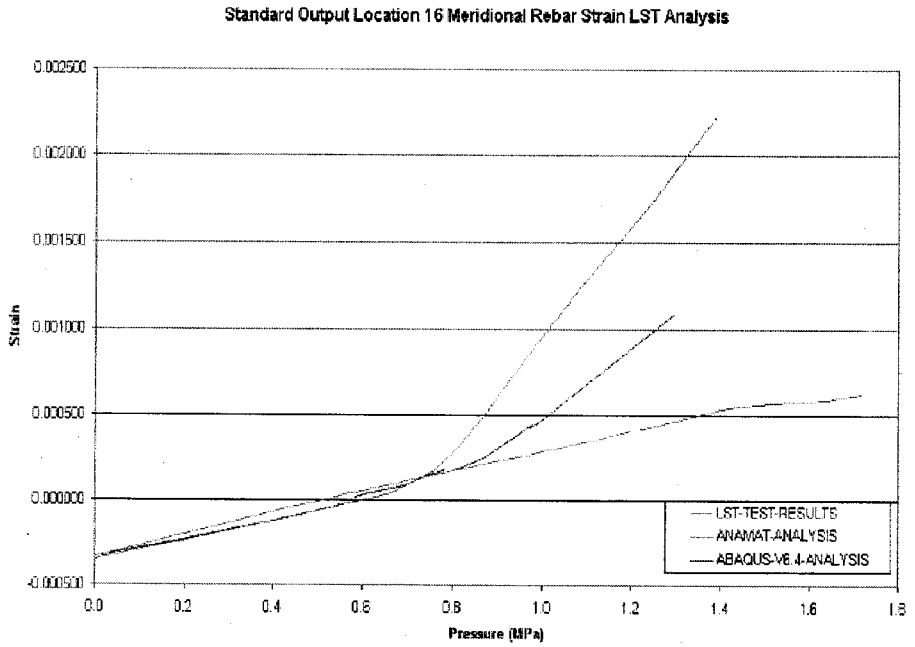

Figure 33 Location 17 Meridional Rebar Strain

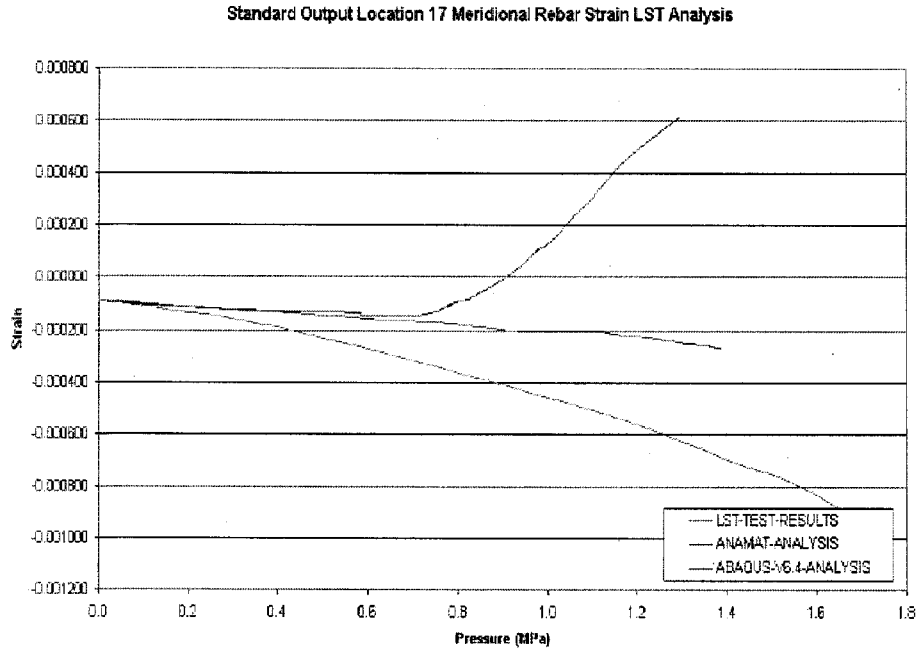

Figure 34 Location 18 Meridional Rebar Strain

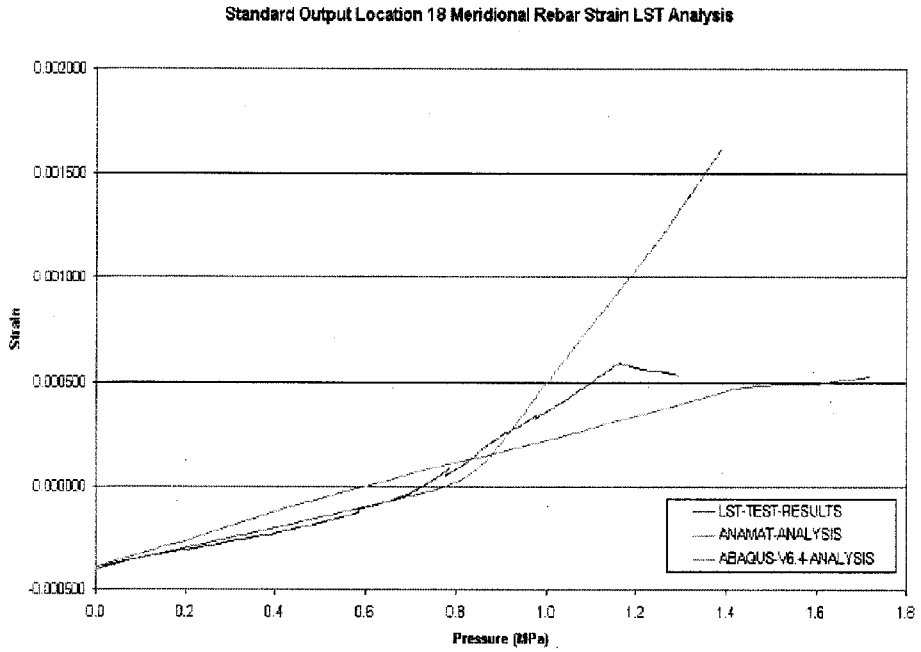

Figure 35 Location 19 Meridional Rebar Strain

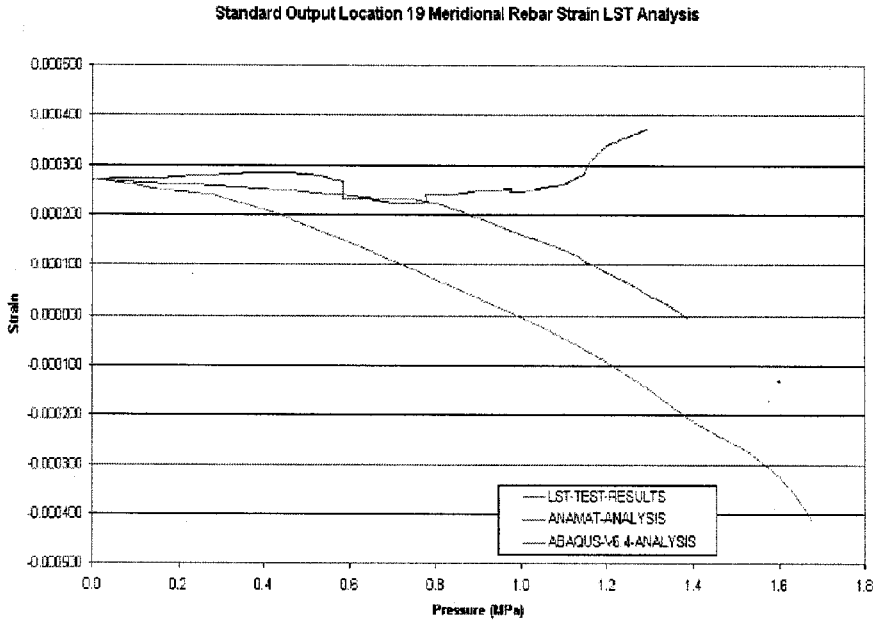

Figure 36 Location 20 Meridional Rebar Strain

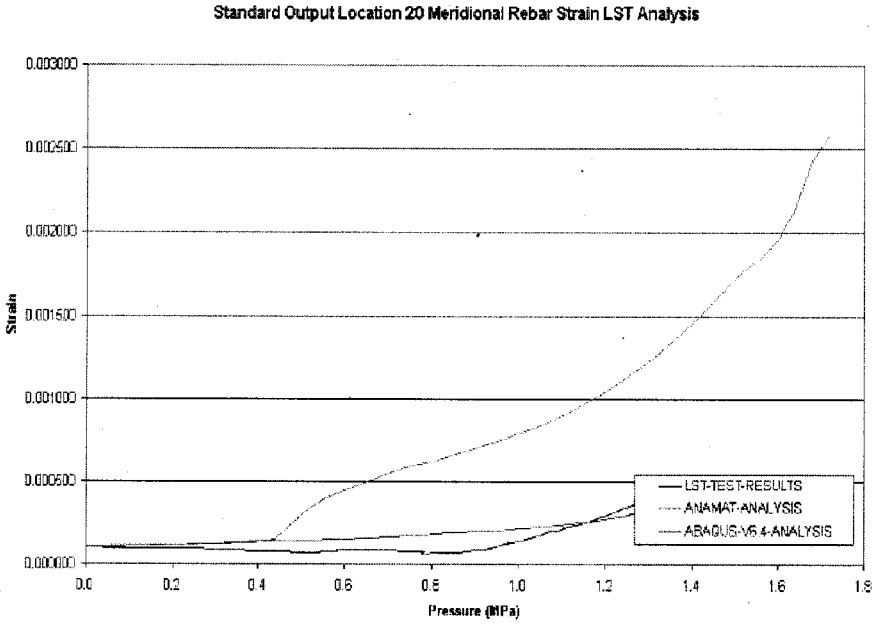

Figure 37 Location 21 Meridional Rebar Strain

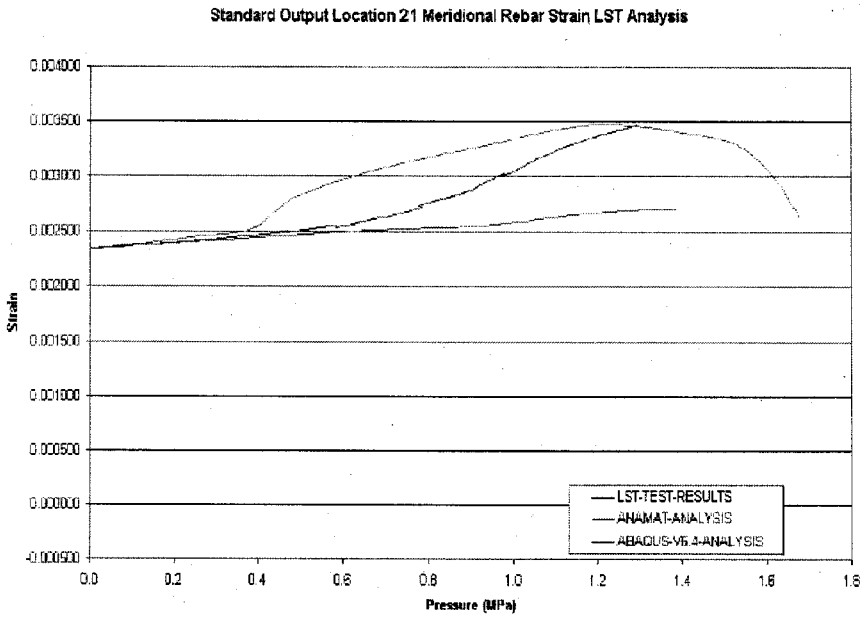

Figure 38 Location 22 Hoop Rebar Strain

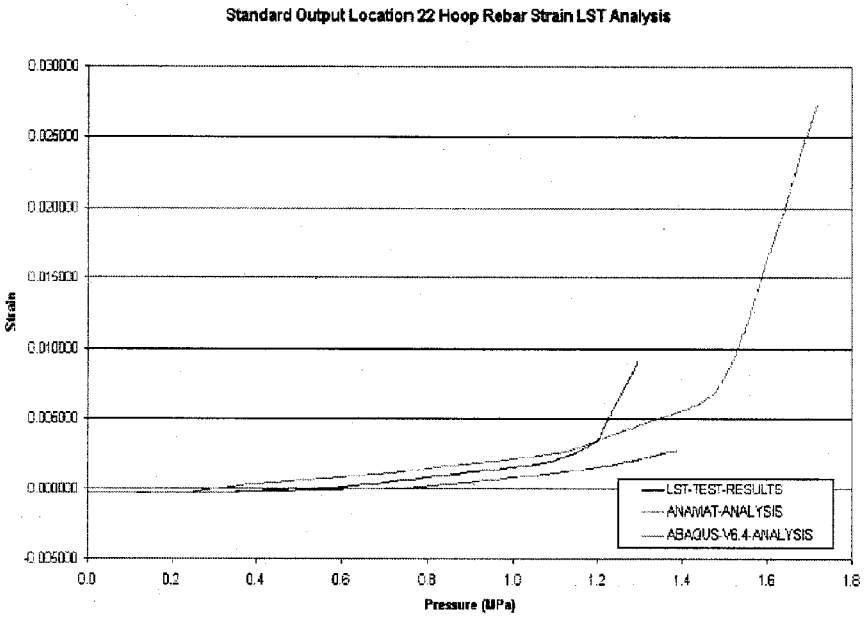

Figure 39 Location 23 Meridional Rebar Strain

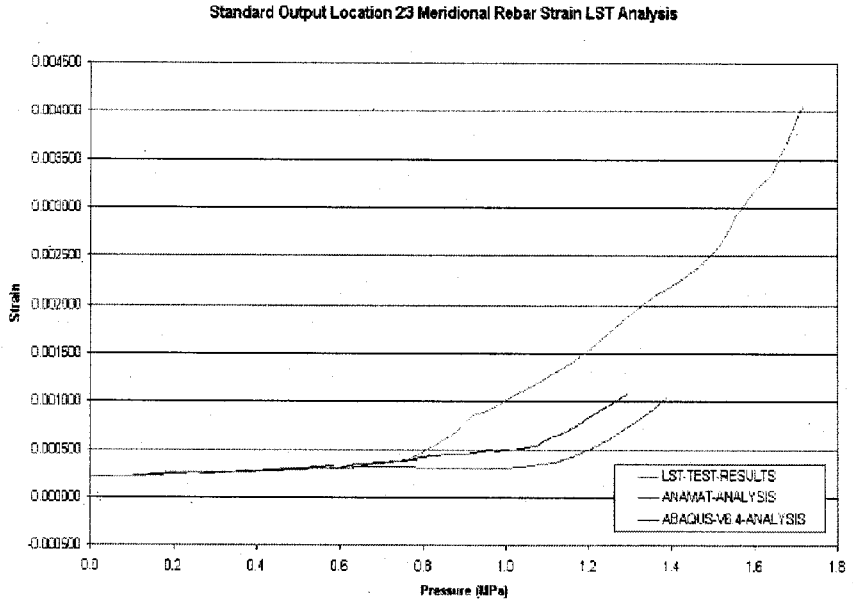

Figure 40 Location 24 Hoop Rebar Strain

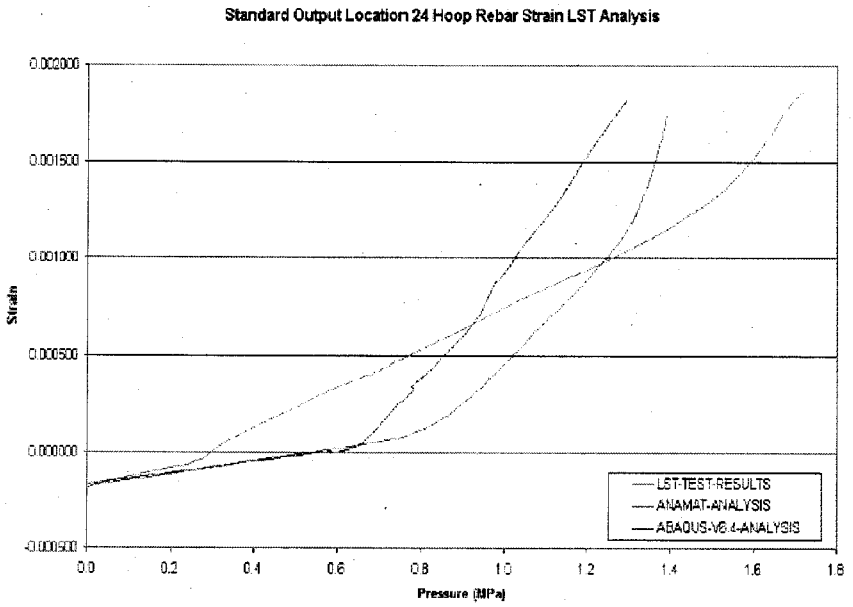

Figure 41 Location 25 Meridional Rebar Strain

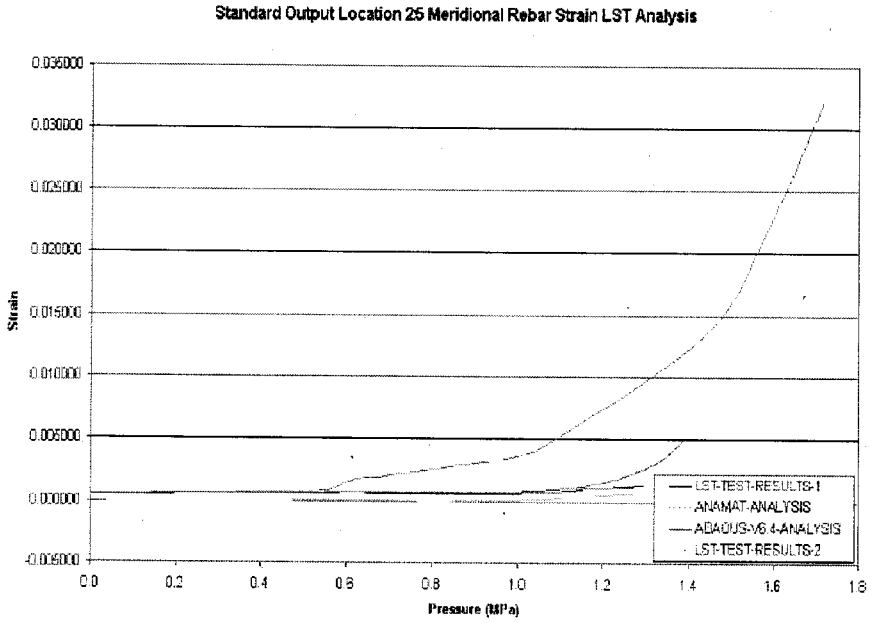

Figure 42 Location 26 Meridional Rebar Strain

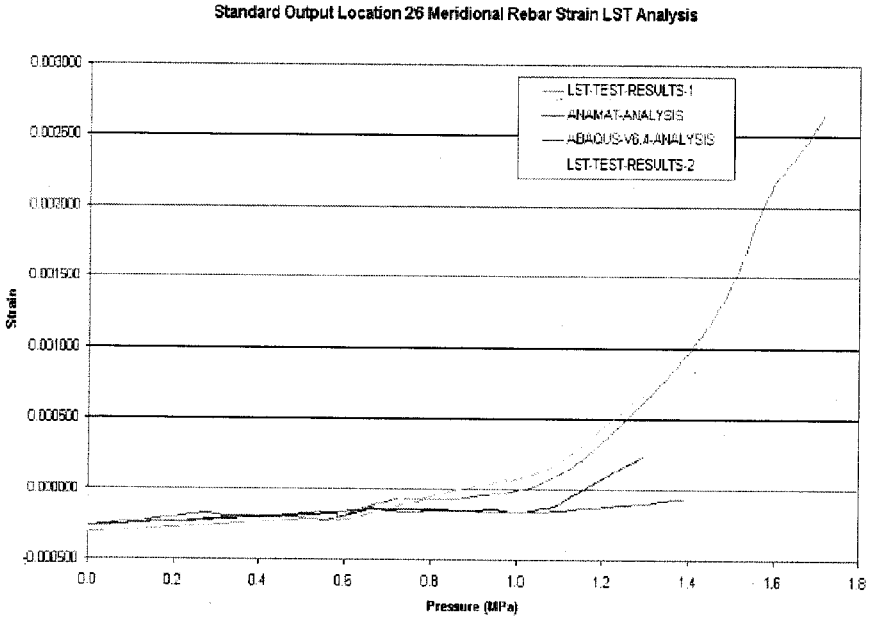

Figure 43 Location 27 Hoop Rebar Strain

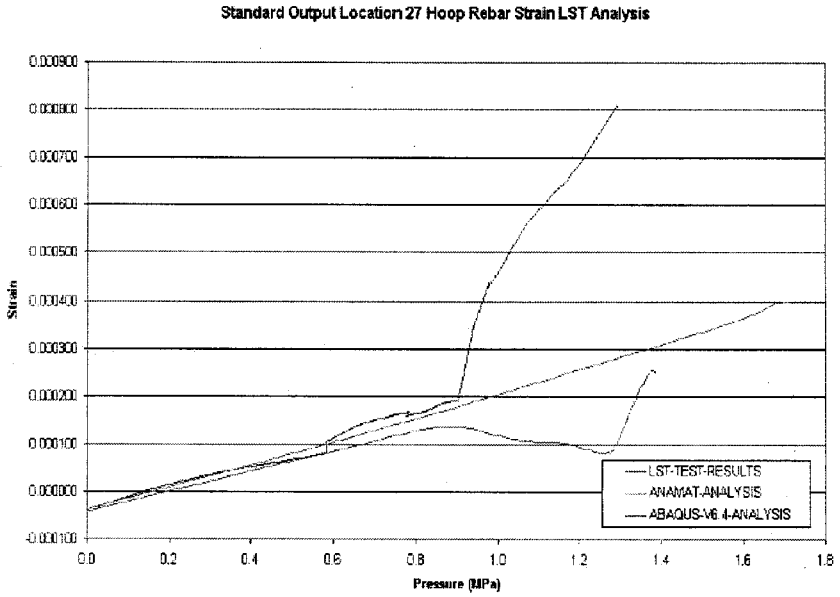

Figure 44 Location 28 Meridional Rebar Strain

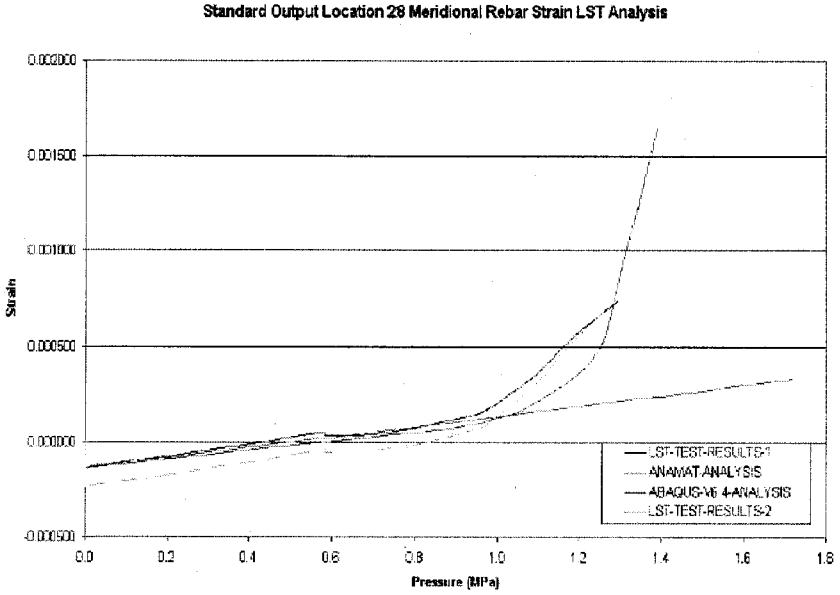

Figure 45 Location 29 Meridional Rebar Strain

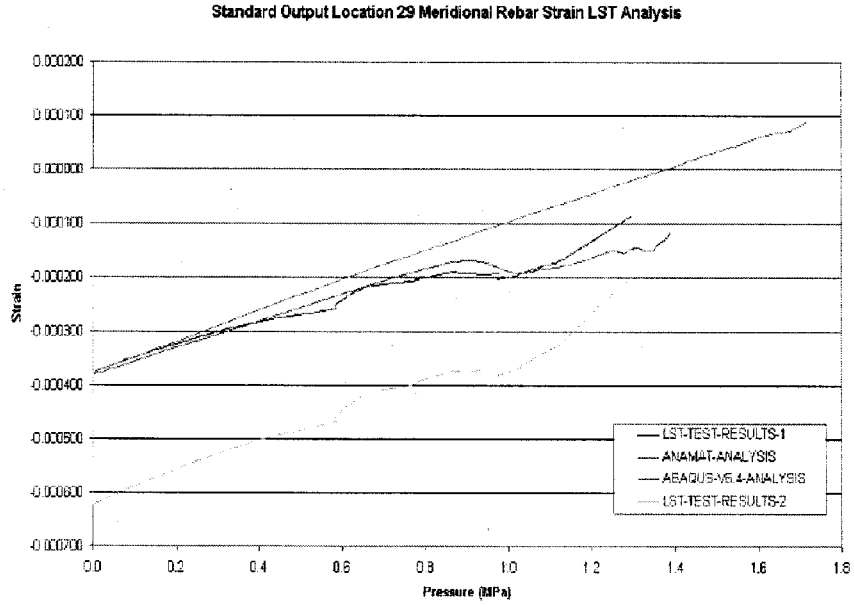

Figure 46 Location 30 Meridional Rebar Strain

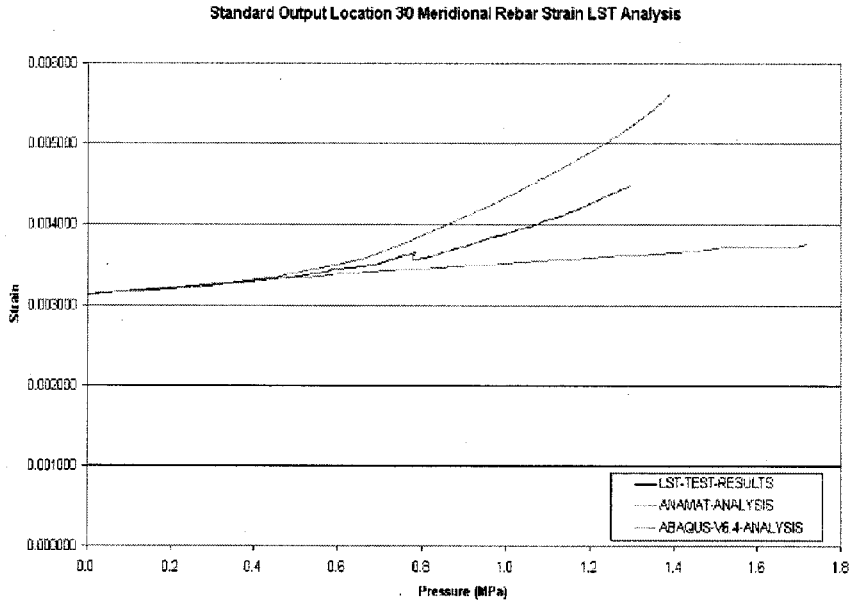

Figure 47 Location 31 Meridional Rebar Strain

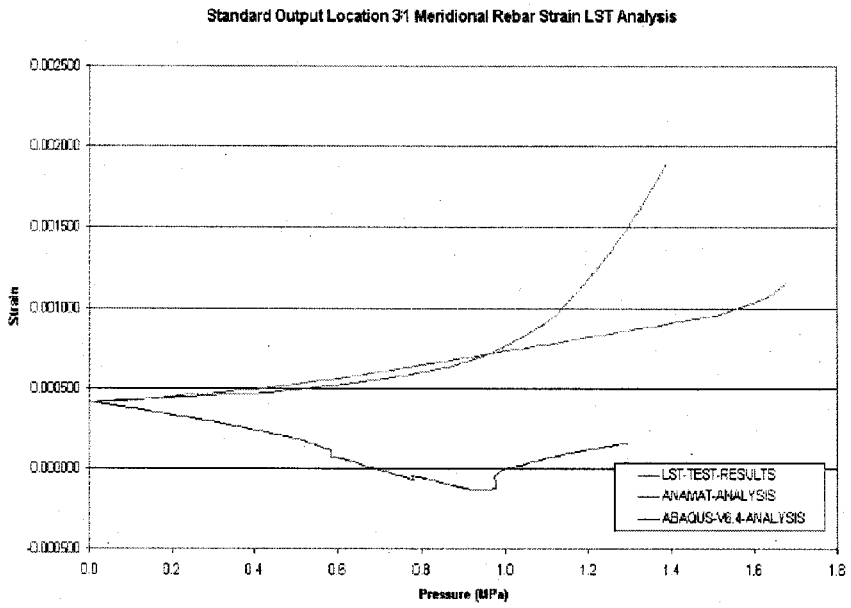

Figure 48 Location 32 Hoop Rebar Strain

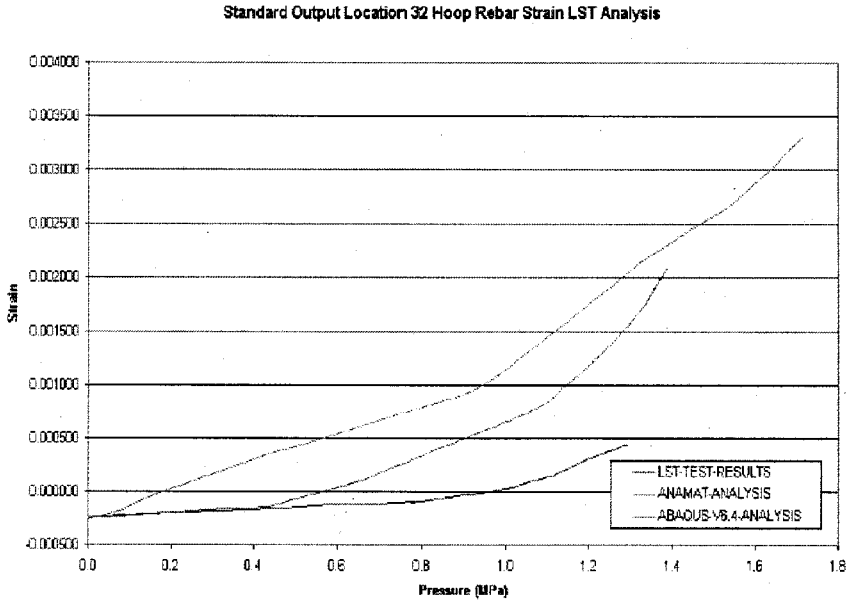

Figure 49 Location 33 Meridional Rebar Strain

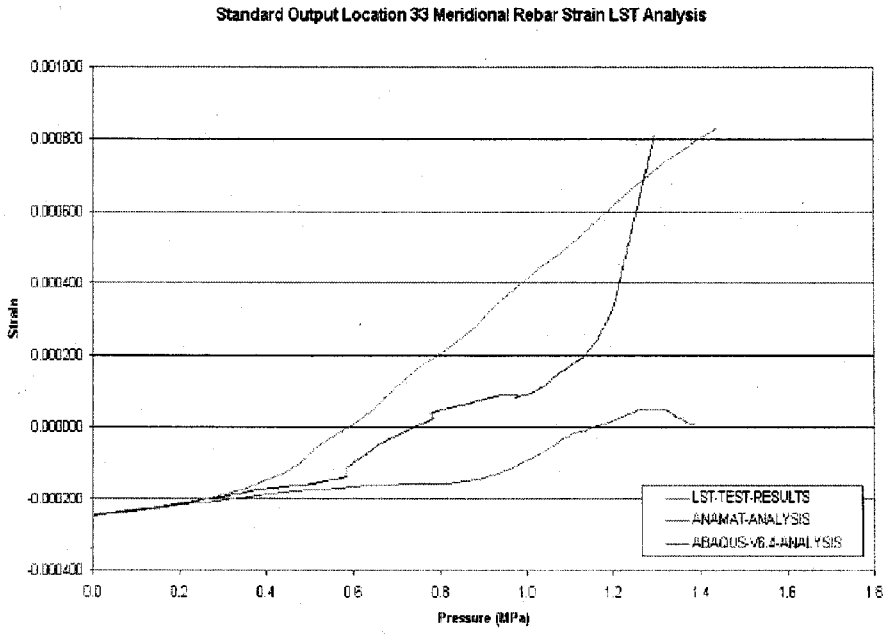

Figure 50 Location 34 Meridional Liner Strain

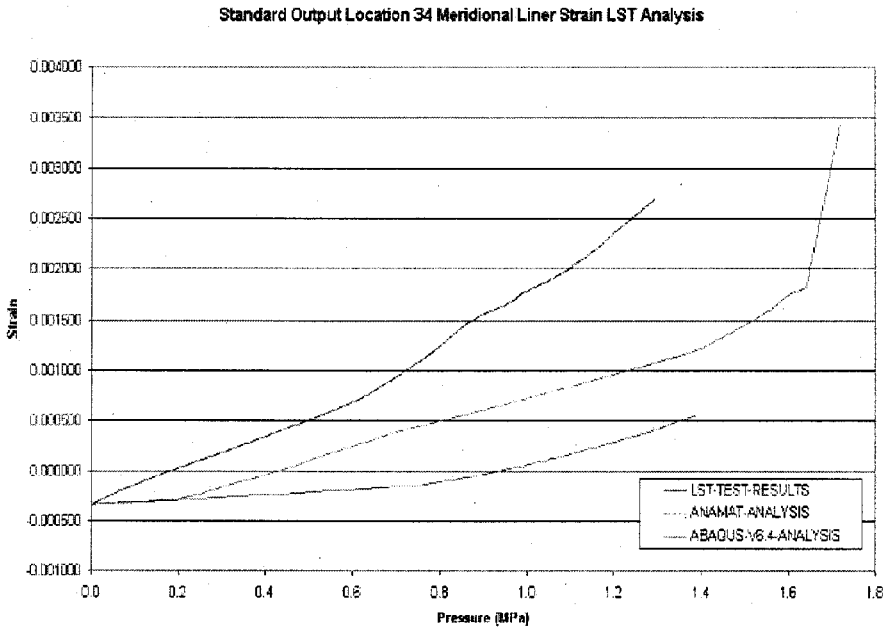

Figure 51 Location 35 Meridional Liner Strain

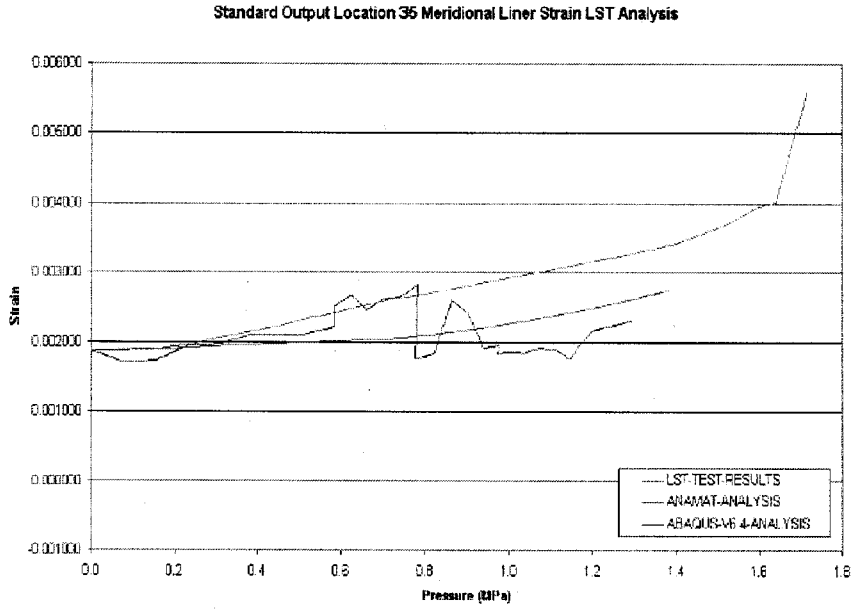

Figure 52 Location 36 Meridional Liner Strain

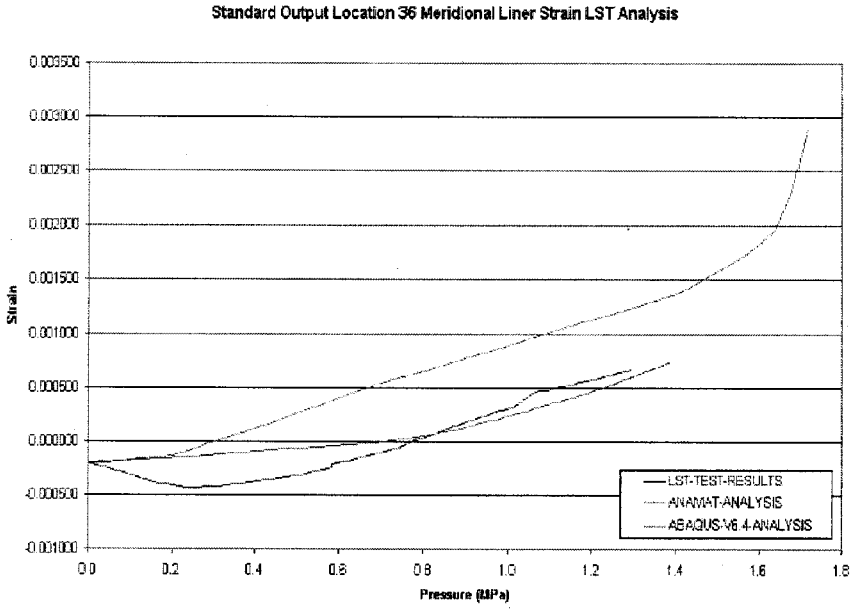

Figure 53 Location 37 Hoop Liner Strain

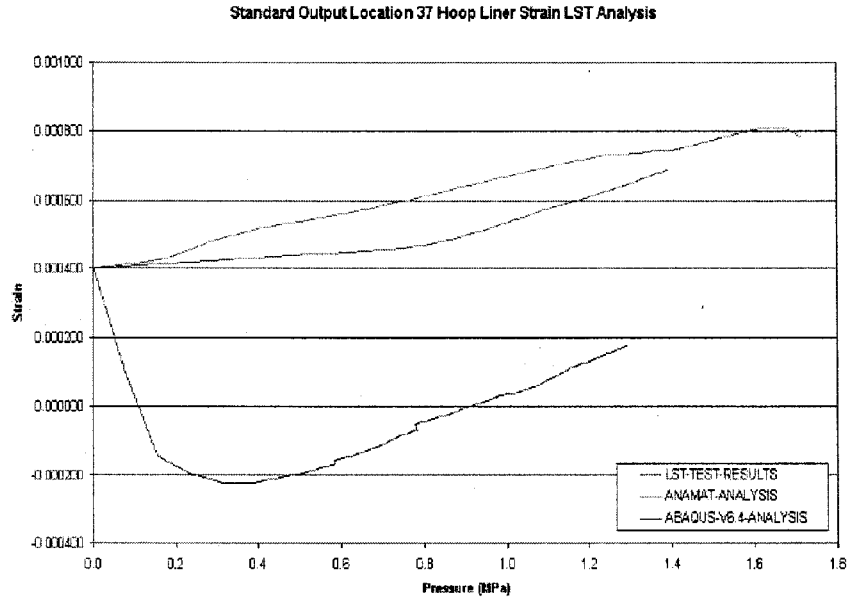

Figure 54 Location 38 Meridional Liner Strain

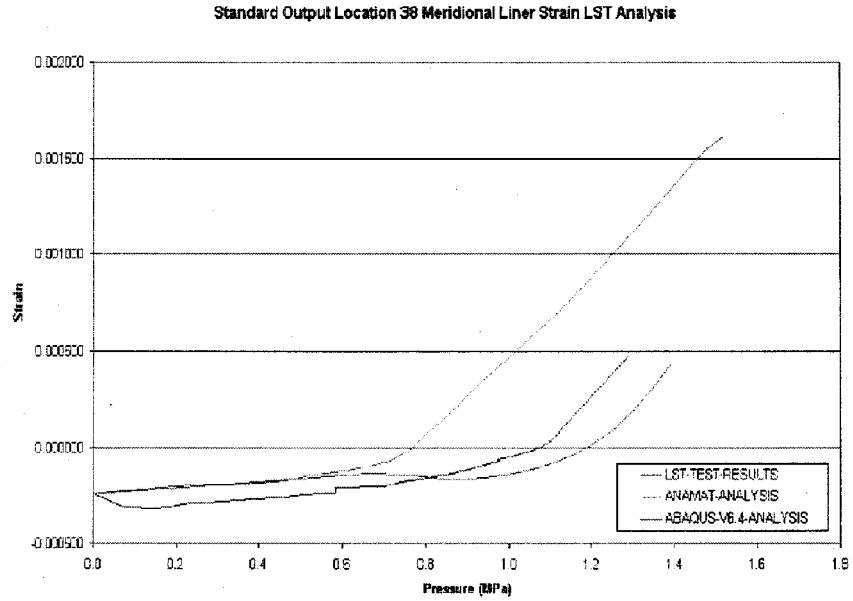

Figure 55 Location 39 Hoop Liner Strain

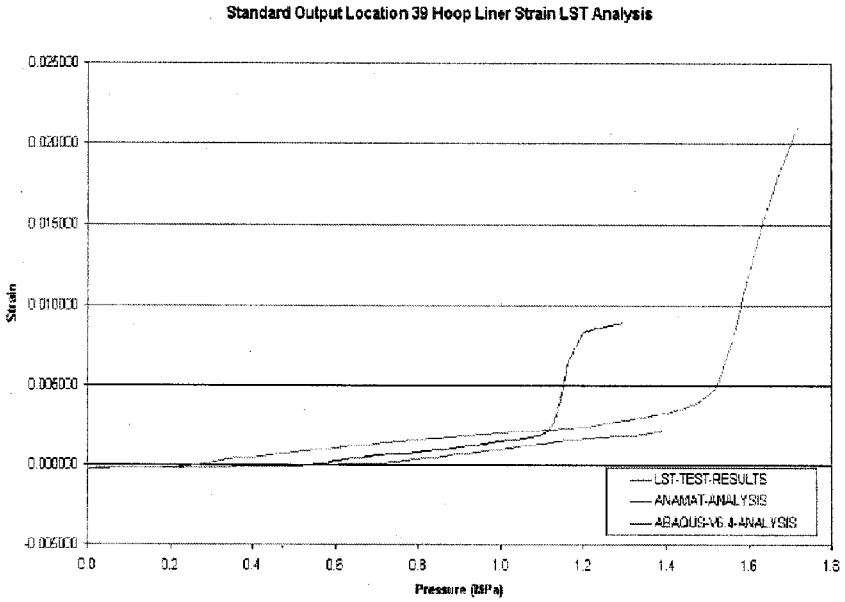

Figure 56 Location 40 Meridional Liner Strain

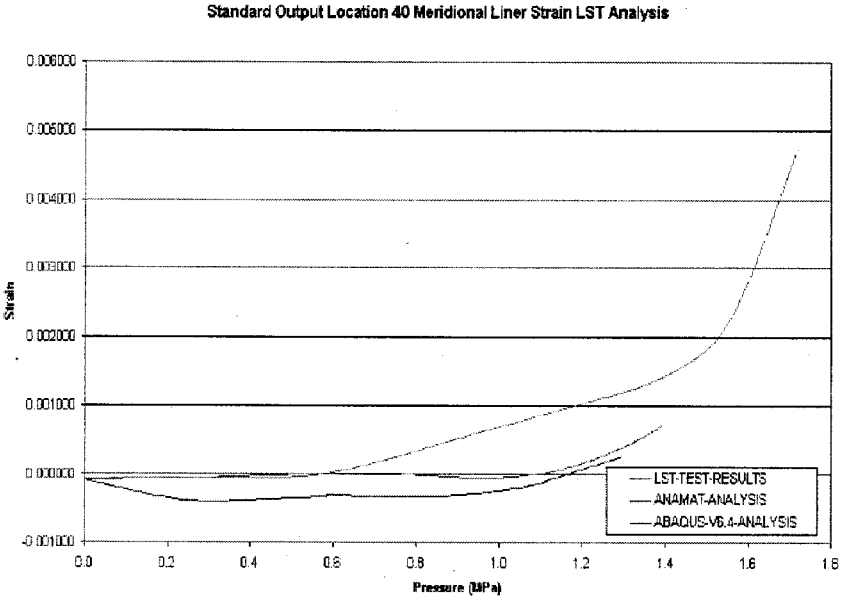

Figure 57 Location 41 Hoop Liner Strain

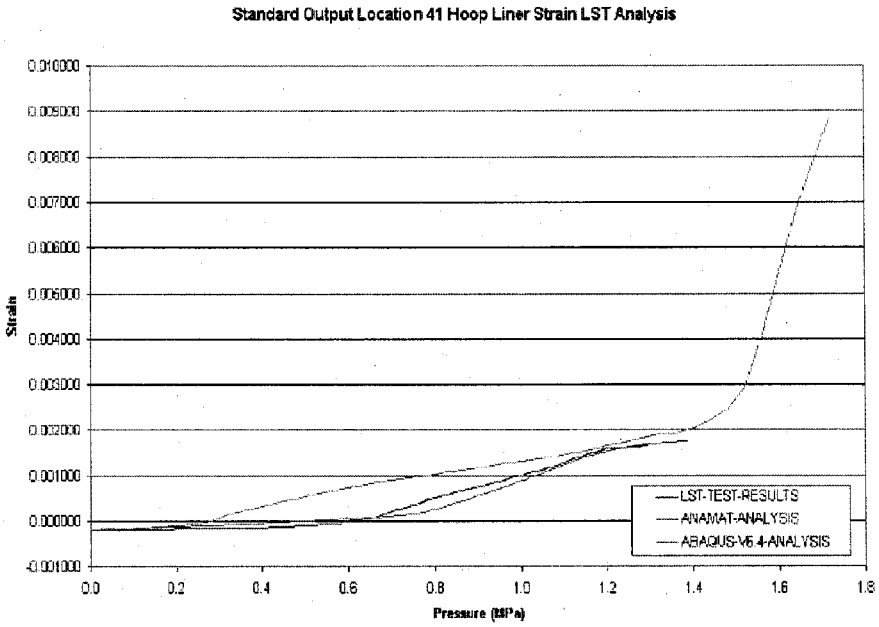

Figure 58 Location 42 Meridional Liner Strain

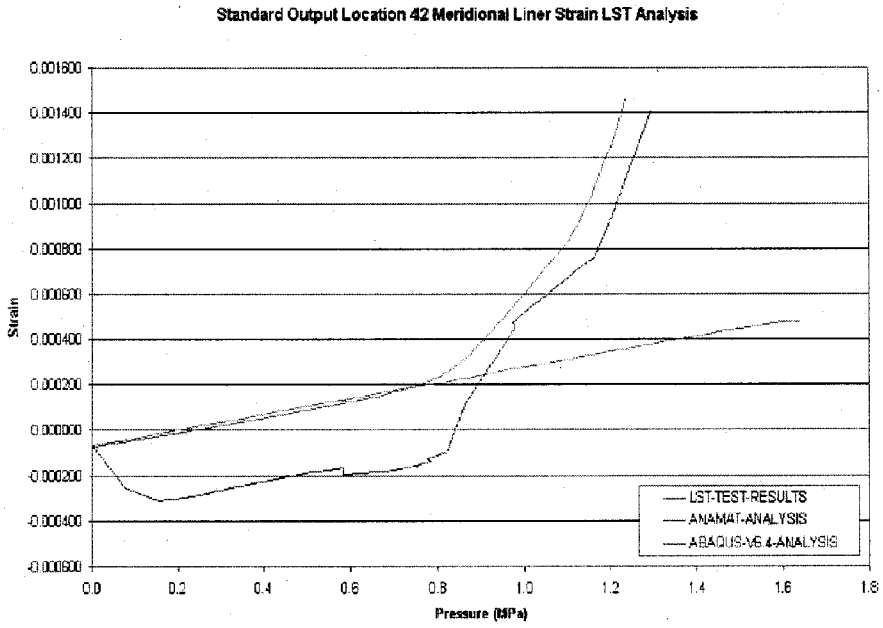

Figure 59 Location 43 Meridional Liner Strain

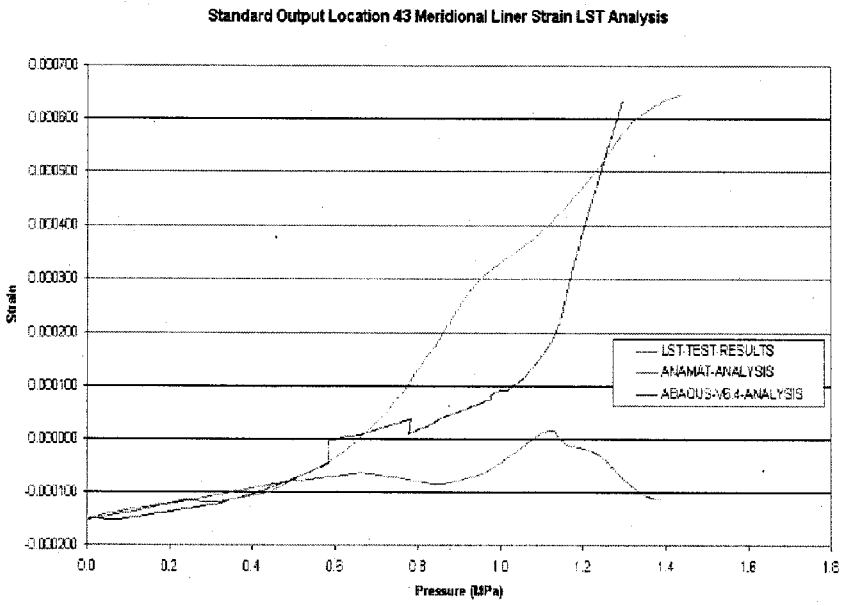

Figure 60 Location 44 Hoop Liner Strain

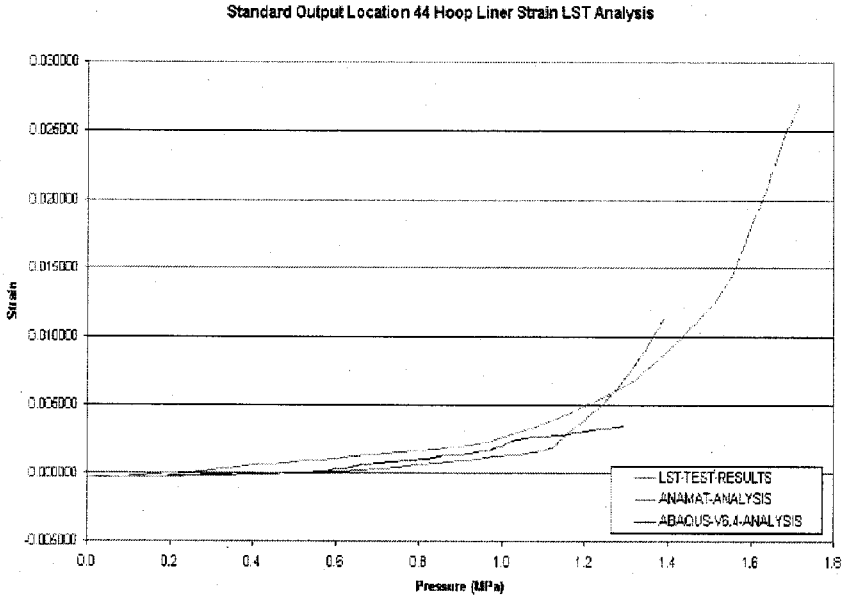

Figure 61 Location 45 Hoop Liner Strain

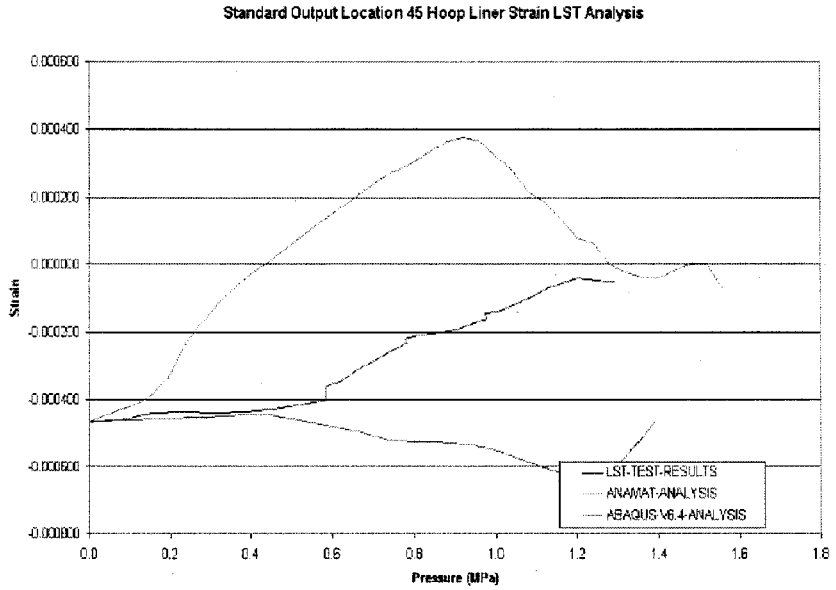

Figure 62 Location 46 Hoop Liner Strain

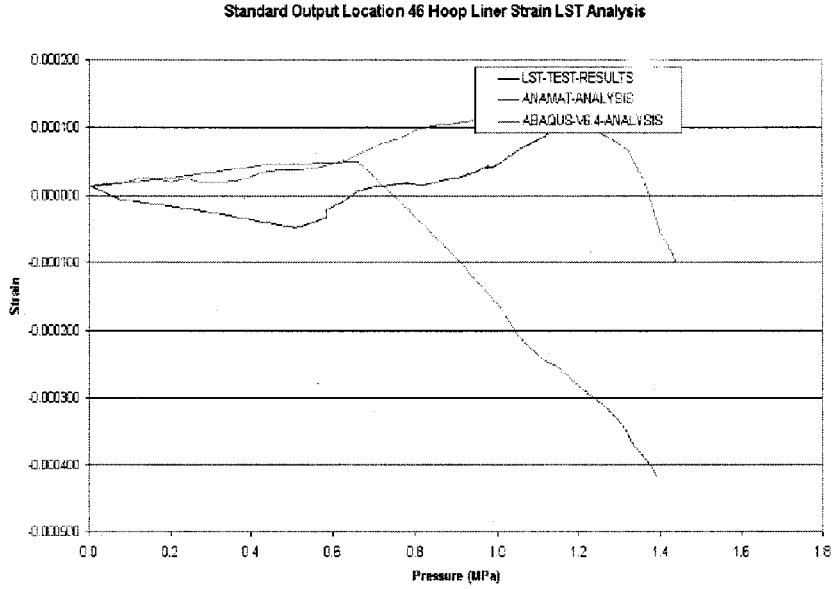

Figure 63 Location 47 Radial Base Liner Strain

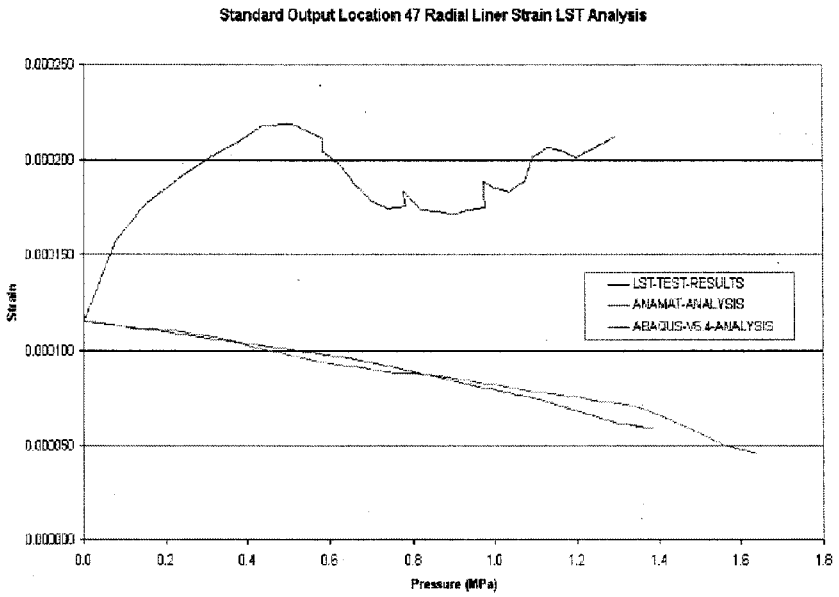

Figure 64 Location 48 Hairpin Tendon Strain

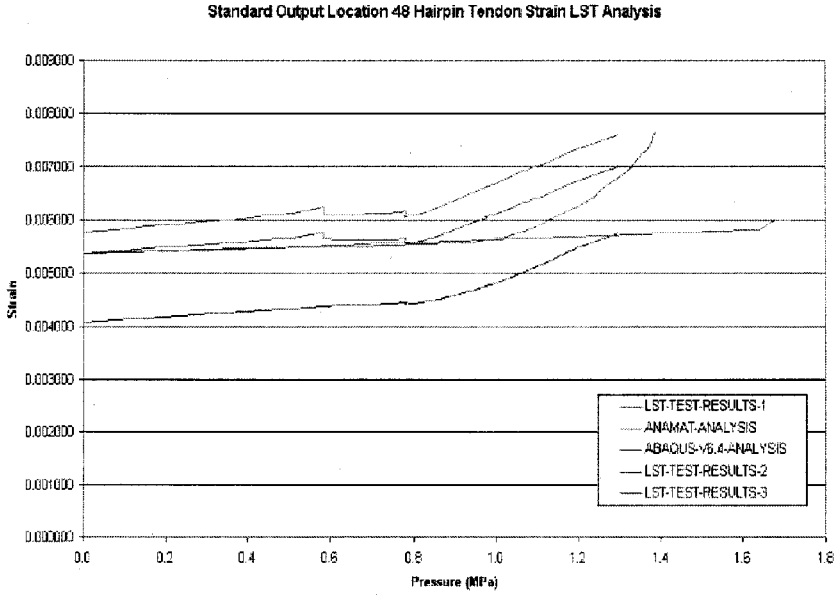

Figure 65 Location 49 Hairpin Tendon Strain

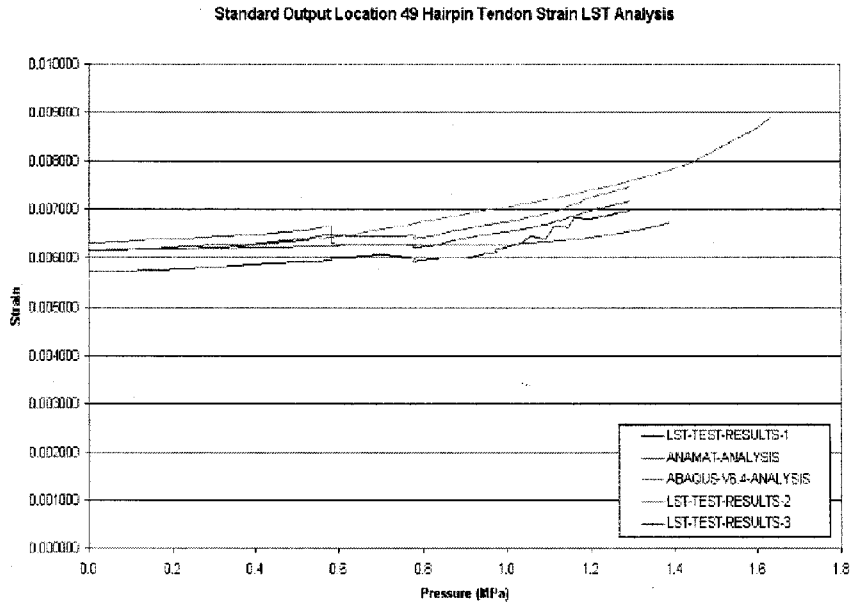

Figure 66 Location 50 Hoop Tendon Strain

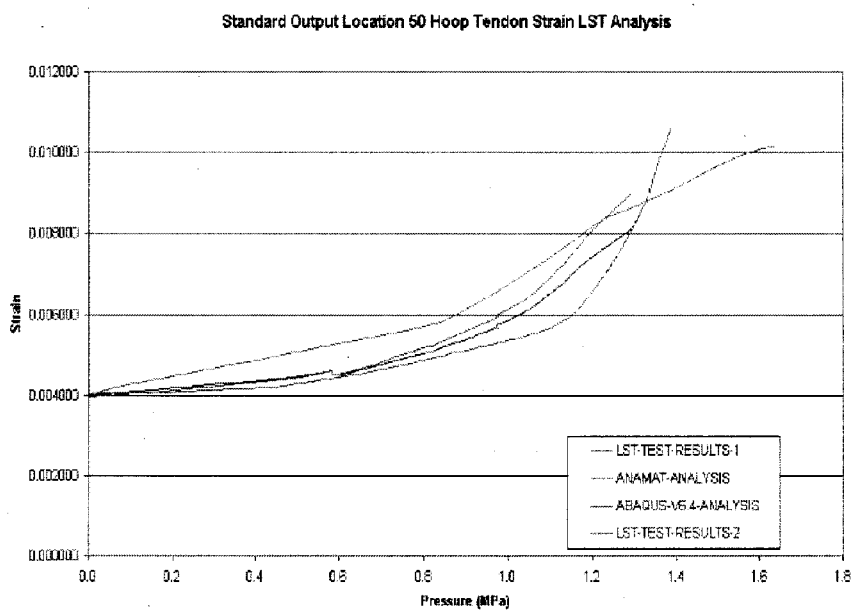

Figure 67 Location 51 Hoop Tendon Strain

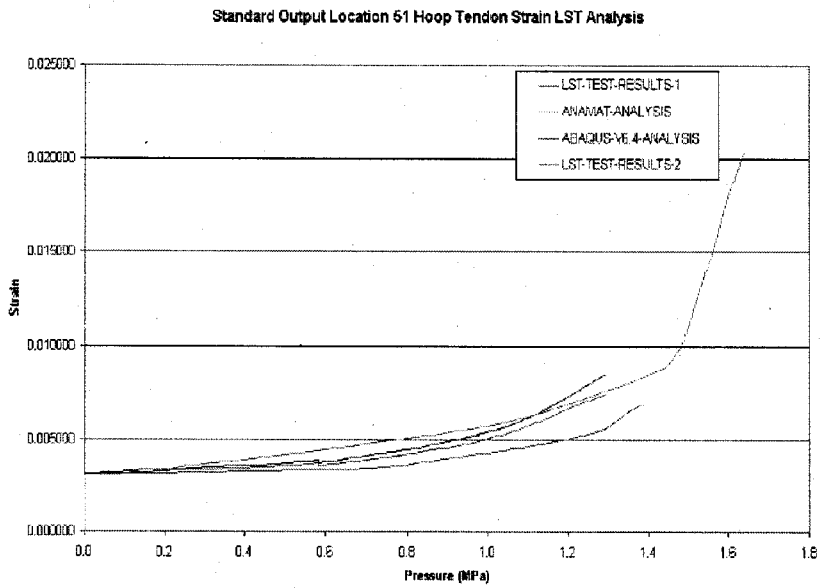

Figure 68 Location 52 Hoop Tendon Strain

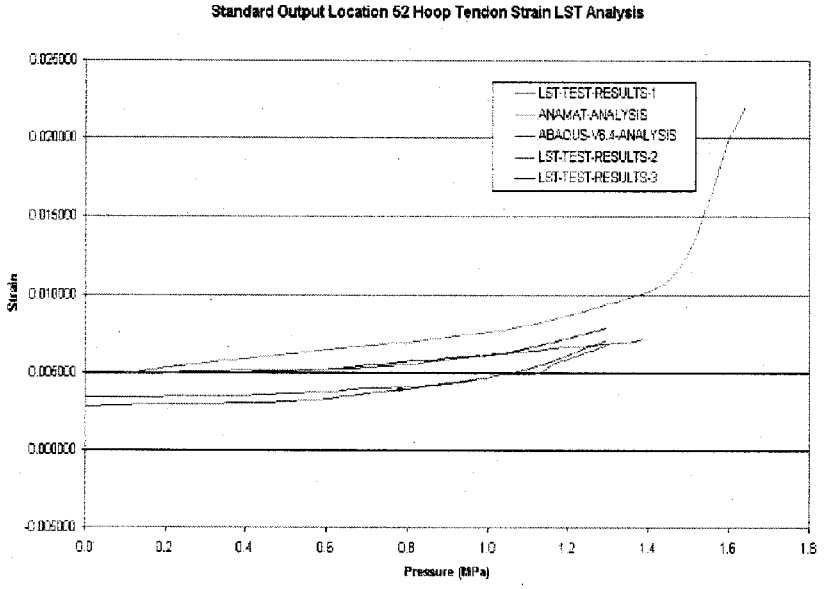

Figure 69 Location 53 Hoop Tendon Strain

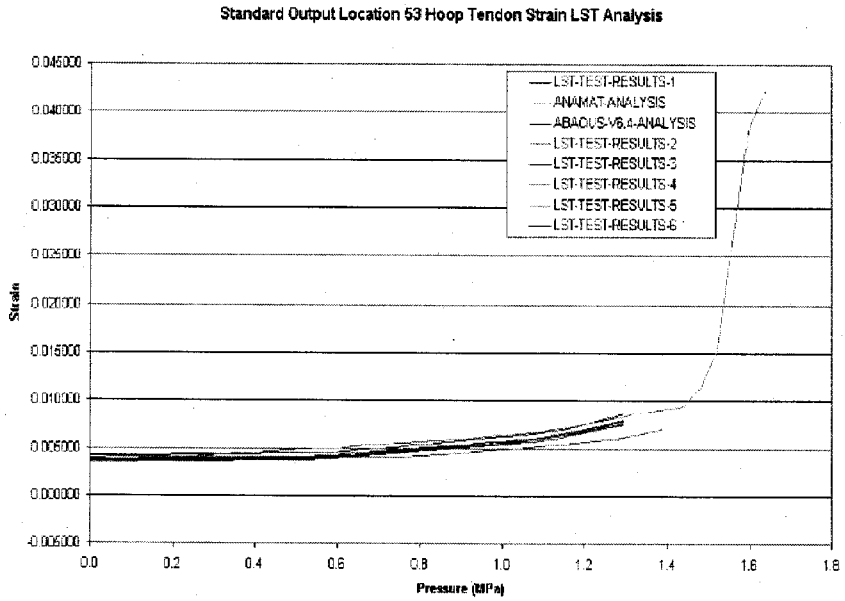

Figure 70 Location 54 Hairpin Tendon Force

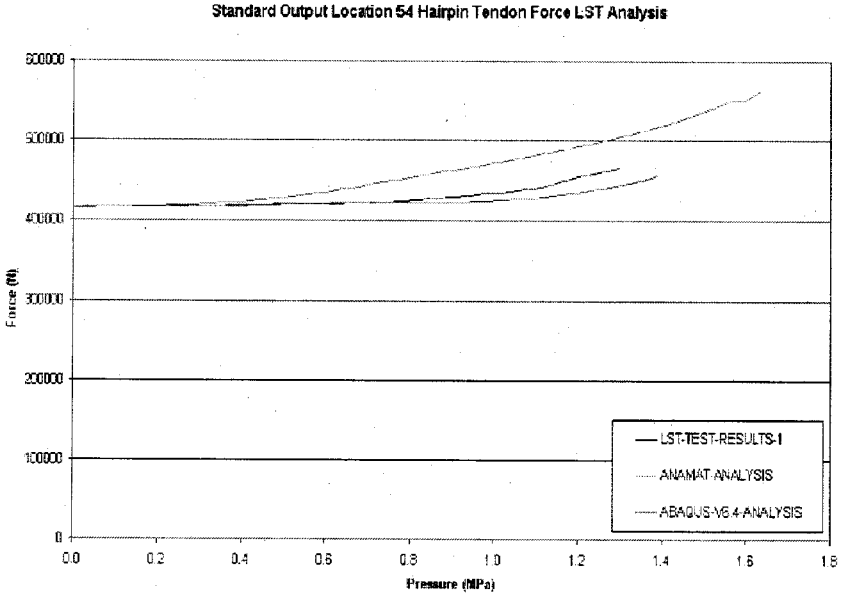

Figure 71 Location 55 Hoop Tendon Force

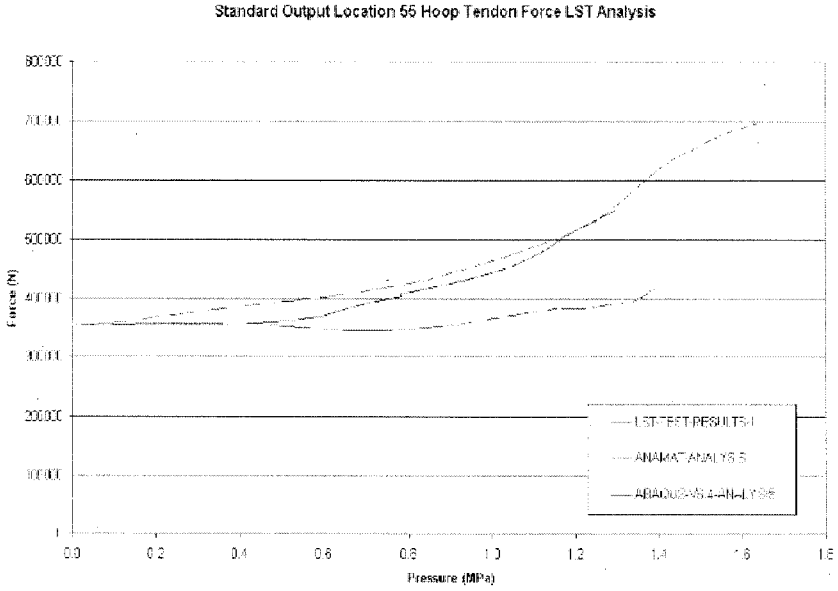

Figure 72 Displaced shape using ANAMAT concrete material model @ 1.72MPa

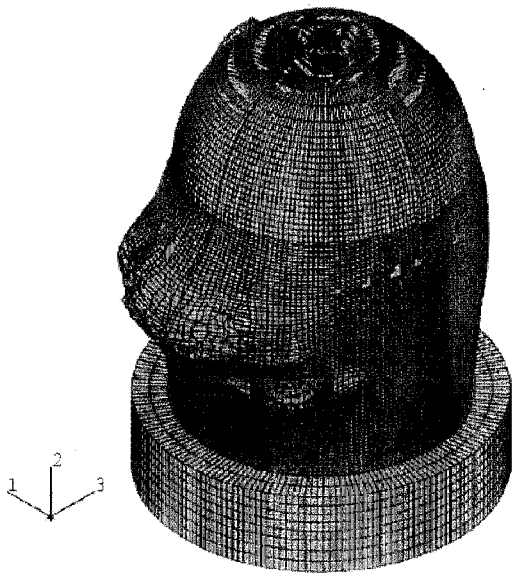

Figure 73 Displaced shape using ABAQUS concrete material model @ 1.40MPa

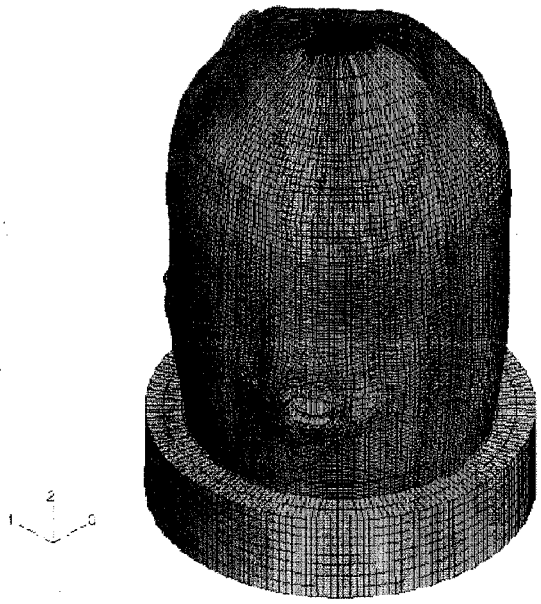

Figure 74 Finite element model at junction of thin/thick liner plate

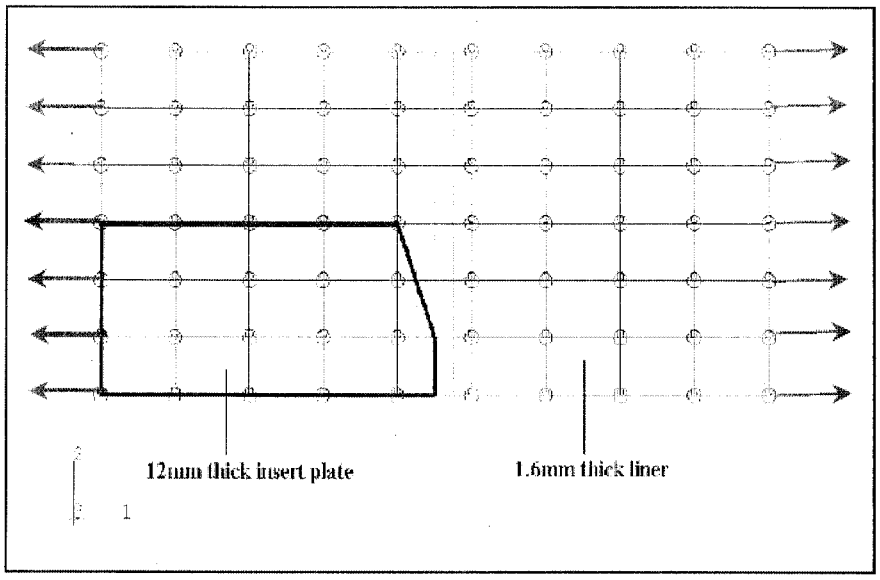

Figure 75 Equivalent plastic strain contour at junction of thin/thick liner plate

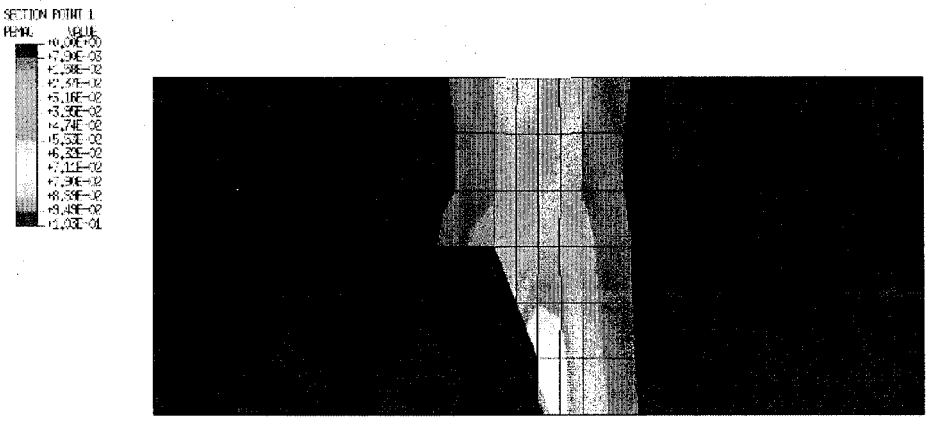

Figure 76 Equivalent plastic liner strains for ANAMAT analysis

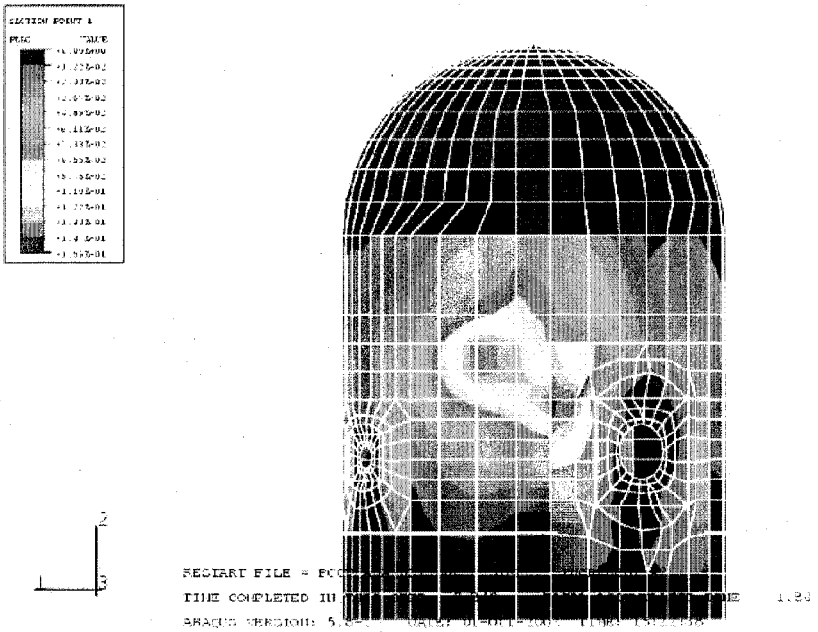

Figure 77 Equivalent plastic liner strains for ABAQUS analysis

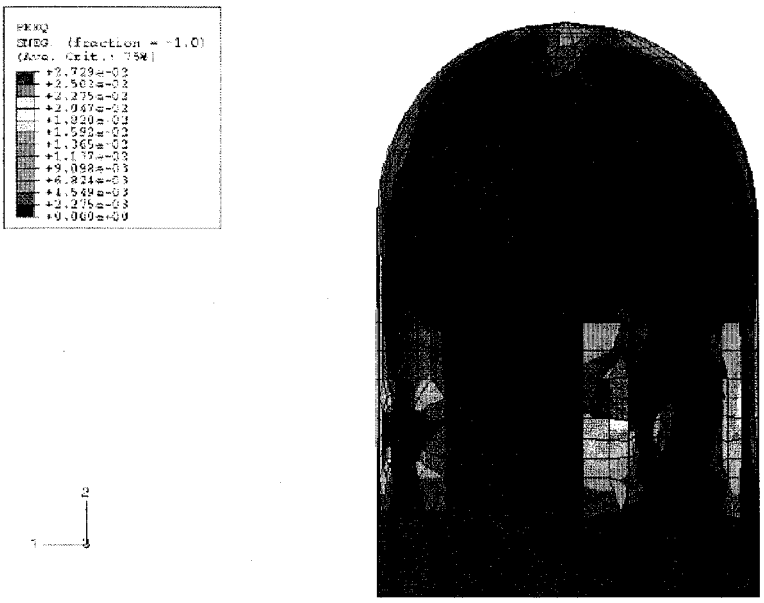

Figure 78 Limit Load Range

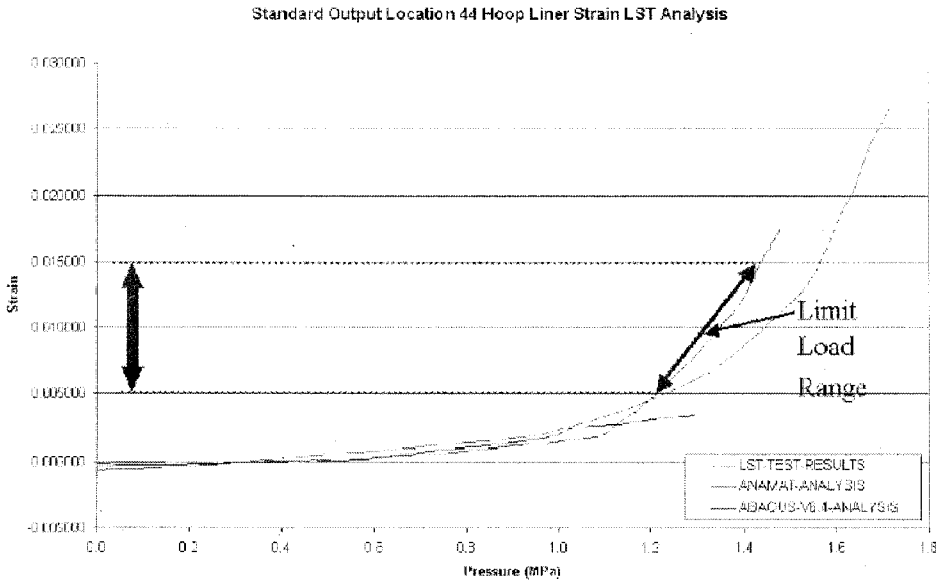

Figure 79 Contour plot showing concrete damage @ 0.66MPa

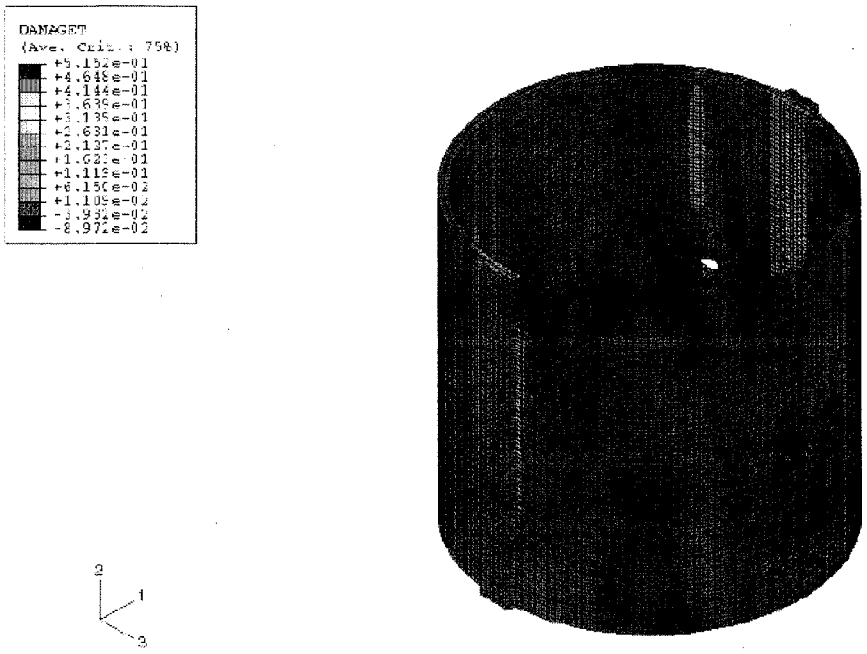

Figure 80 Displaced shape of cylinder showing butterfly mode @ 1.4MPa

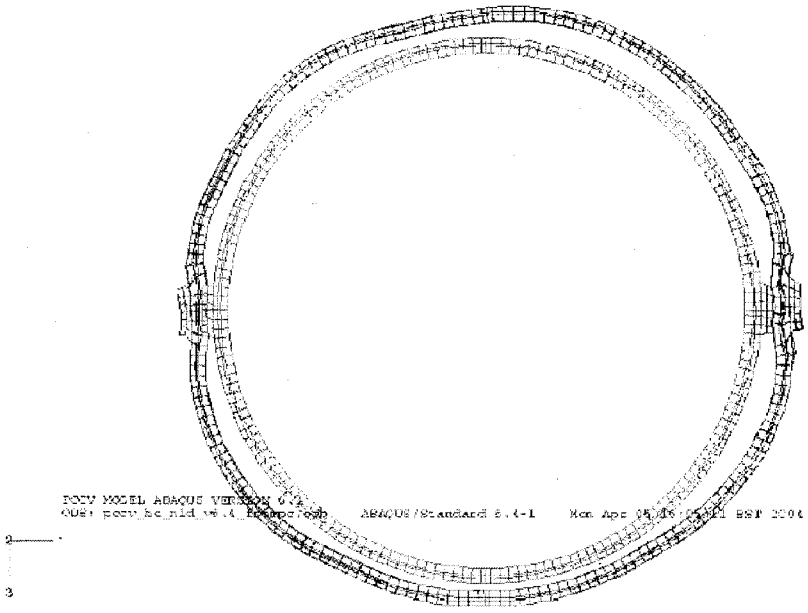

Figure 81 Concrete acoustic monitoring system

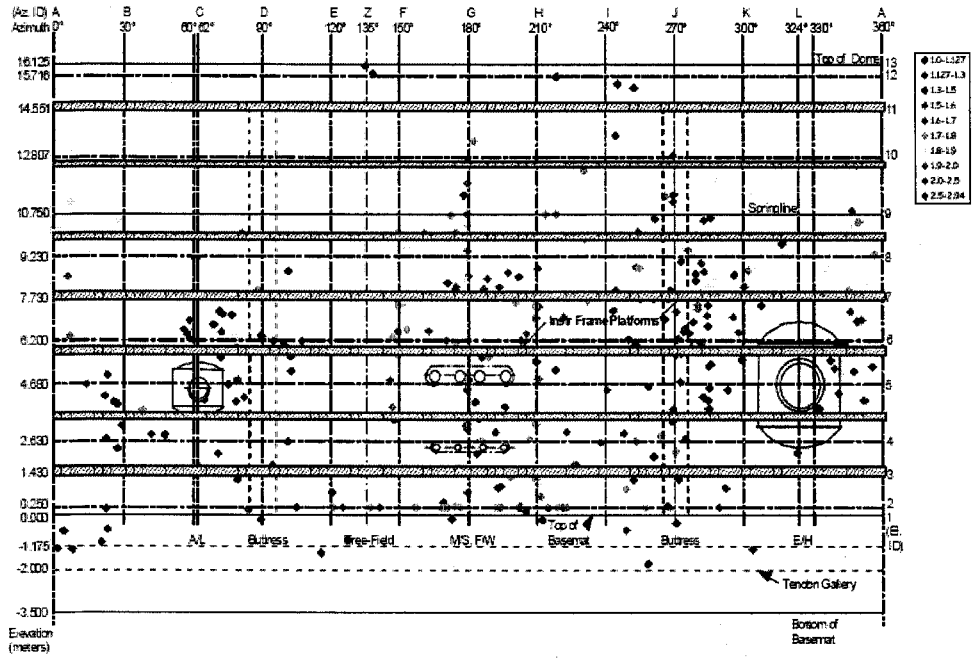

Figure 82 Liner tears after LST

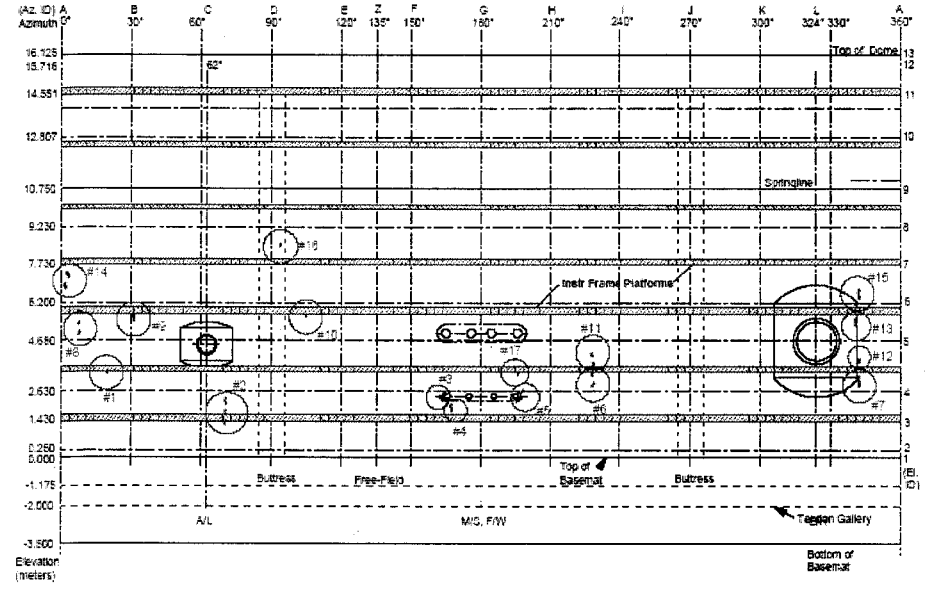

Figure 83 Vertical tendon axial load @1.4MPa

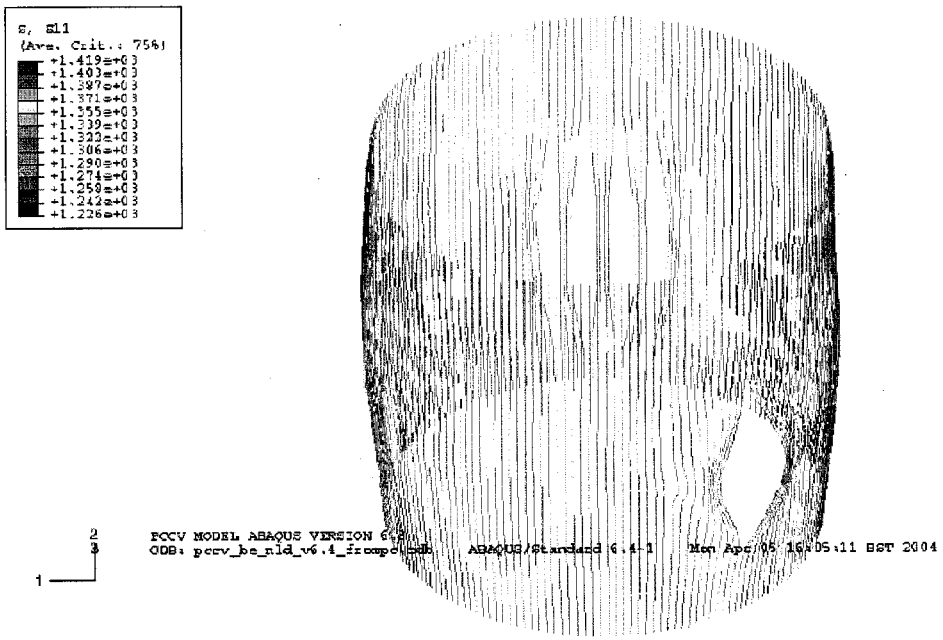

Appendix C:

Energoprojekt Praha, UJV Rez. Div.

ISP48 Phase II Analysis Results

Jan Stepan, Jan Maly
UJV Rez div. Energoprojekt Praha

Analysis model

The analysis model is created in Abaqus general-purpose finite element program. The principal objective of the model was model behaviour of the whole structure including openings. The concrete is basic part of the model and is modeled by brick elements. Rod elements model rebars and prestressing tendons and they are embedded into concrete elements. Liner is modeled by plate elements connected on inner surface with concrete elements. Model includes EH and AL openings including change of wall thickness and changes in rebar and prestressing tendons. M/S openings weren't modeled because they have small impact on global response of structure and only added rebar rods were considered in model. The first version of model includes basement as well but due to limitations of model size (Abaqus error no. 3495 – regardless of size of installed memory is maximum available memory for Abaqus pre-processor about 1300MB under Windows systems) the size of model had to be decreased. Then the final version of model includes only cylindrical and dome part of the structure.

Basics characteristics and simplifications are abstracted into next points:

- The model includes concrete wall of cylindrical and dome part of structure. Basement wasn't modeled, its stiffness was neglected and connection between cylindrical wall and basement is modeled by external fix support, which eliminates displacements and rotations (effect of this simplification is small because the stiffness of basement is much more higher in comparison with the stiffness of remain parts of structure).
- Rebar and prestressing tendons were modeled by rod elements considering actual geometry around openings. Two simplifications were applied – the radial rebar wasn't modeled due to size limit of model and anchors of hoop cables were replaced by continual connections of elements due to elimination of cracks and instabilities in anchor area at buttress.
- Prestressing tendons were modeled as bonded tendons. Prestressing force along tendons was considered as uniform by mean value of measured force.
- Connection of liner and concrete doesn't respect actual design and is performed by common nodes of liner and concrete elements. So, results in liner corresponding of global behavior but there could be differences in places with local peak of stress (connection of liner to frame of openings, connection with basement).
- Starting state of analysis was unbroken structure. Cracking due to shrinkage was modeled by decreasing of modulus of elasticity along with lower tensile strength of concrete in tension.

Material characteristics were sets pursuant to results of tests. Abaqus Concrete damage plasticity model was used for modeling of non-linear behavior of concrete. The behavior of concrete in compression was assigned by Euro code 2, the behavior in tension was assigned by tensile strength and fracture energy. The non-linear behavior of rebar, presstresing tendons and liner was modeled by Abaqus Iron plasticity model. The basic values of material characteristics are in the following table:

Material	Modulus of elasticity	Strenght
Concrete	28 000 MPa	53 MPa in compression, 3.8 MPa in tension (decreased at 0.5 MPa)
Liner	210 000 MPa	yield stress 380 MPa, ultimate stress 450 MPa
Tendons	200 000 MPa	yield stress 1600 MPa, ultimate stress 1950 MPa
Rebar SD345	210 000 MPa	yield stress 360 MPa, ultimate stress 500 MPa
Rebar SD390	210 000 MPa	yield stress 470 MPa, ultimate stress 600 MPa

As indicated above, the prestressing tendons were modeled as bonded cables and their prestressing force was set by mean value of measured force. The prestressing force of hoop tendons is 30kN, the prestressing force of vertical tendons is 41kN.

Analysis was performed in two steps. The firs step was application of prestressing and dead load. The second step was application of internal overpressure. The presstresing was applied by initial conditions type stress. The internal overpressure was applied at liner elements. Forces in nodes at border of openings replaced the effect of internal ovepressure at locks. Response of structure at increasing overpressure was evaluated as sequence of static analysis at first. Due to decreasing of step time after beginning of cracks development and conjoin increasing of total analysis time, the Abaqus/Explicit quasi-static analysis was used. Change of overpressure in time was defined by linear function with the end at 1.6 MPa.

Analysis results

Results of the first analysis demonstrated higher stiffness of model, especially after cracks development, in comparison with response of real structure. Reevaluation was performed and tendon prestressing forces (due to higher prestressing forces the response of the model was below the response of structure) and tendon stress-strain curve (due to higher yield stress and ultimate stress the model had higher stiffness at high overpressure) were changed. Now the model shows quite good agreement with global structure response.

The global failure of structure and maximum internal overpressure is determined by bearing capacity of prestressing tendons. Theoretical, due to plastic capacity of liner, the tightness could be preserved till global failure. The results of real structure test shows that the tears of liner appear before the failure of structure (detailed inspections after LST revealed 26 discrete tears in the liner, all located at vertical field welds, and fabrication defects contributed to nearly all of the liner tears). Analogous, the breaking of tendons started at hoop strain approximately 1% although the tests of cables assign the breaking at strain 3.5%. So, question is how to set the limits of plastic strain of liner and tendons. For purpose of this analysis the strain at breaking of tendon was set at 1% and the onset of liner tearing was set at reaching of liner yield stress.

Figures 6-9 show total deformation at selected internal overpressures. Figure 10 shows comparison of test results and analysis results for radial displacements at 135°. History of deformation shows rapid increasing after 1.3MPa. It corresponds with reaching of yield stress in tendons at 1.25MPa. Figure 11 shows comparison of radial displacements at 90° (buttress) and at openings. Figure 12 shows comparison of vertical displacements. History of deformation shows higher model dome response to decreasing of stiffness of cylinder due to cracking in comparison with results of test.

Figures 13-14 shows liner strain in circumferential direction at 1.0MPa (stress in liner reaches the yield stress) and 1.25MPa (stress in tendons reaches the yield stress). In both cases the peak of strain is between openings next to E/H (approximately at 0°) due to change of curvature of the concrete wall. Additional concentrations of strain are at buttresses and at ending of additional rebar around openings.

Figures 15-16 shows tendon strain 1.25MPa (stress in tendons reaches the yield stress) and 1.52MPa (strain in tendons reaches 2%). Especially at overpressure 1.52MPa there is the expressive difference in distribution of strain along tendons due to rigid connection between tendons nodes and nodes of concrete wall. This type of connection doesn't make possible to correctly simulate tendon failure in case of structures prestressed by unbonded tendons. Despite it, the final failure mode during SFMT corresponds with state of stress detected by analysis. The comparison of tendons strain history in Figure 17 shows, that the collapse of structure happened when started the rapid increasing of tendons strain after reaching of the yield point.

The basic milestones of structure behaviour during overpressuration are summarized in the following table:

Pressure	Event
0.44 MPa	Beginning of cracking around E/H
0.60 MPa	Beginning of cracking of cylinder in circumferential direction
0.90 MPa	Continual horizontal cracks in cylinder
0.98 MPa	Yielding stress in liner
1.25 MPa	Yielding stress in tendons
1.30-1.50 MPa	Collapse of structure after breaking some tendons

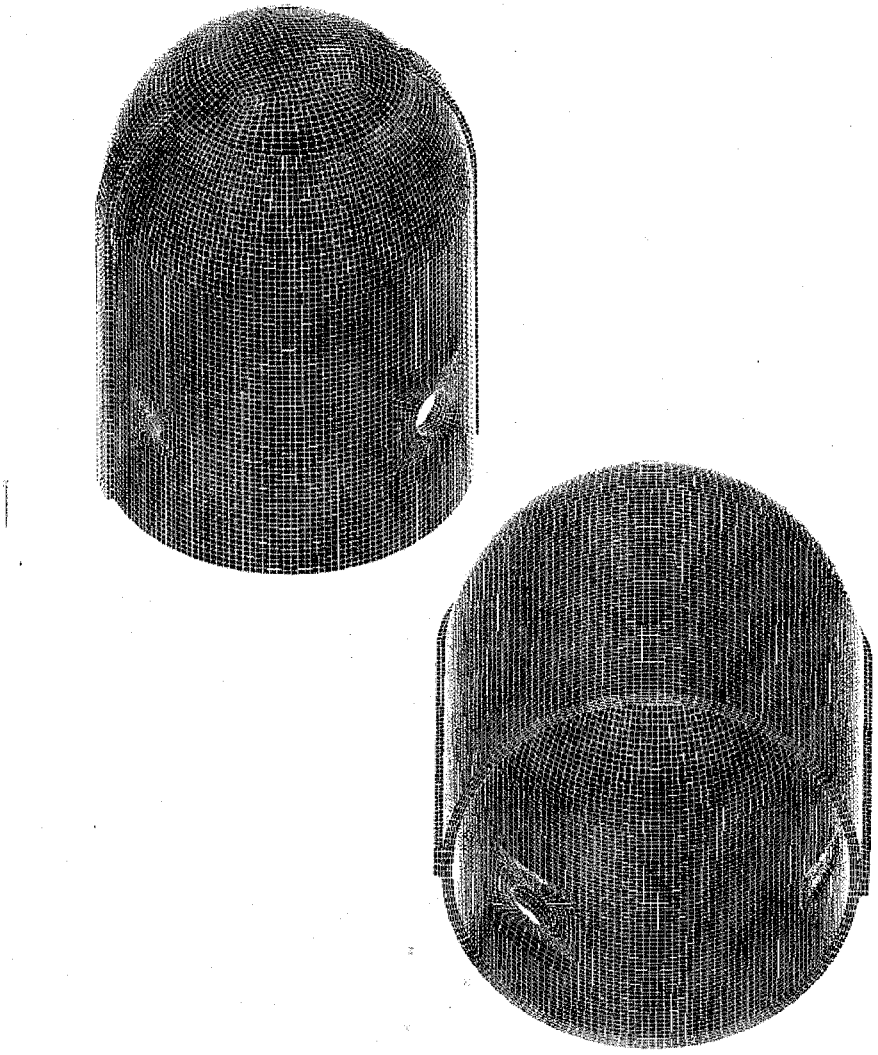

Figure 1 FEM model

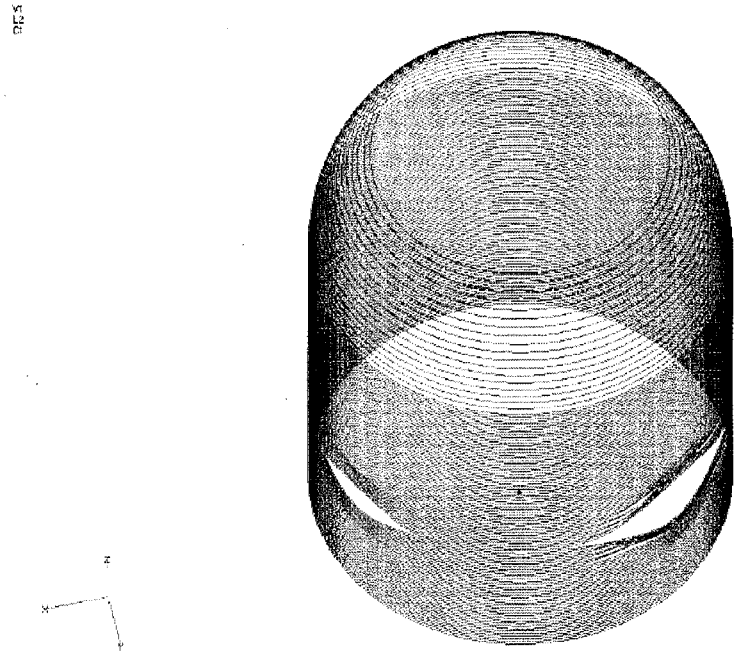

Figure 2 Prestressed tendons elements – hoop tendons

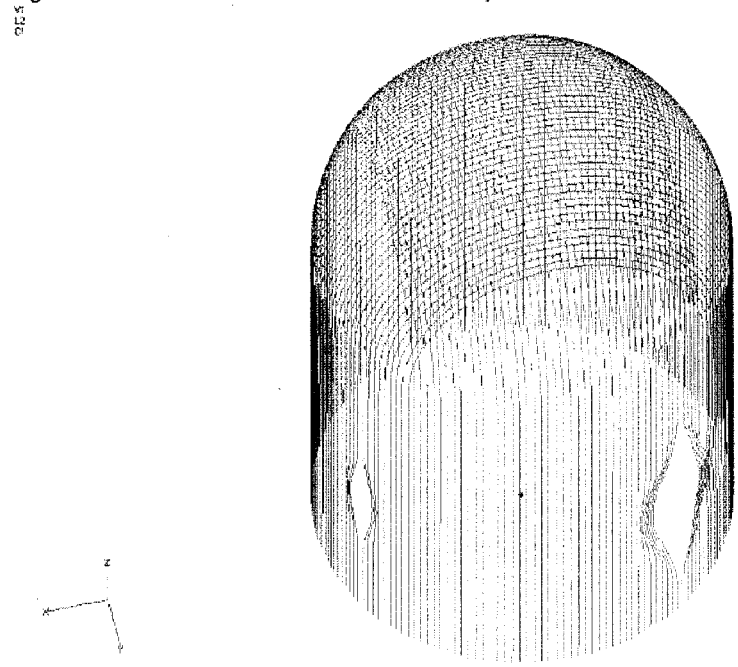

Figure 3 Prestressed tendons elements – vertical tendons

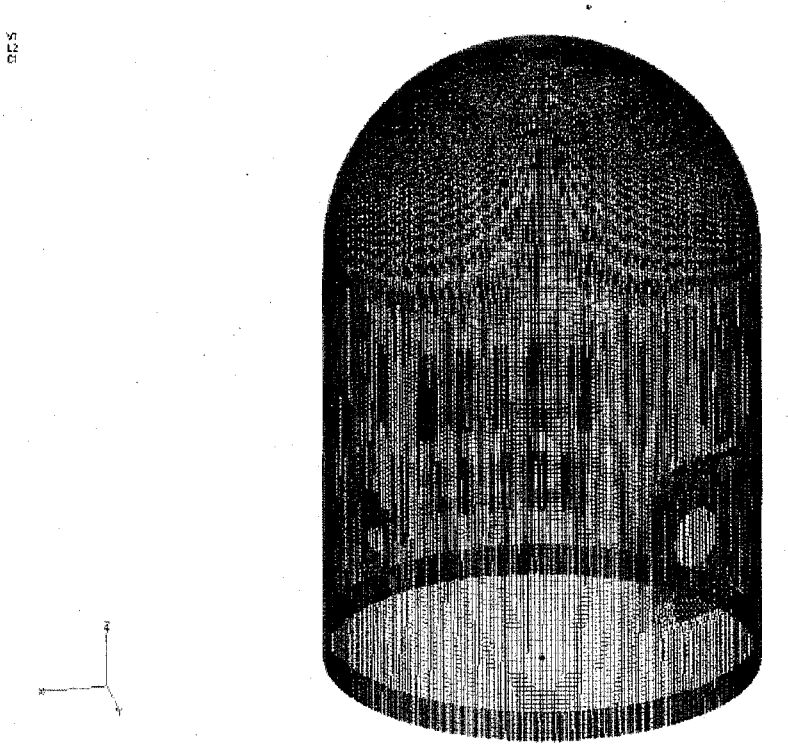

Figure 4 Rebar elements – inner row

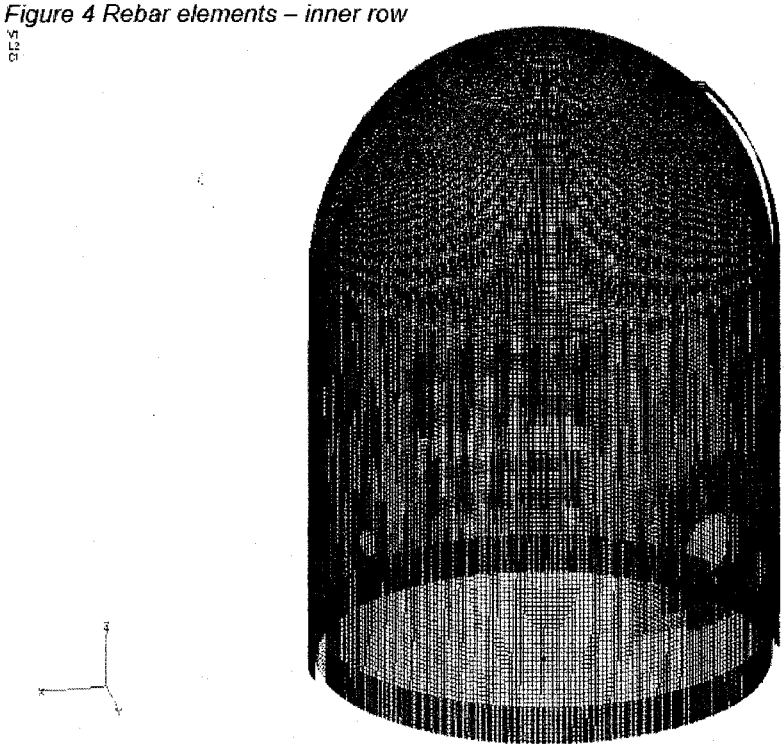

Figure 5 Rebar elements – outer row

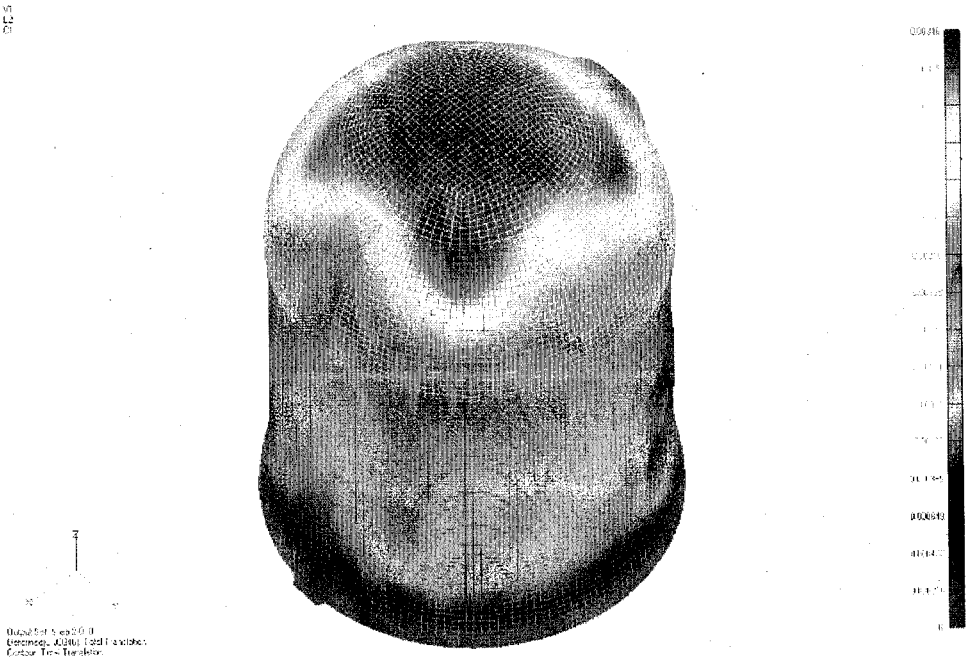

Figure 6 Total deformation (m) after loading by prestressing and dead load

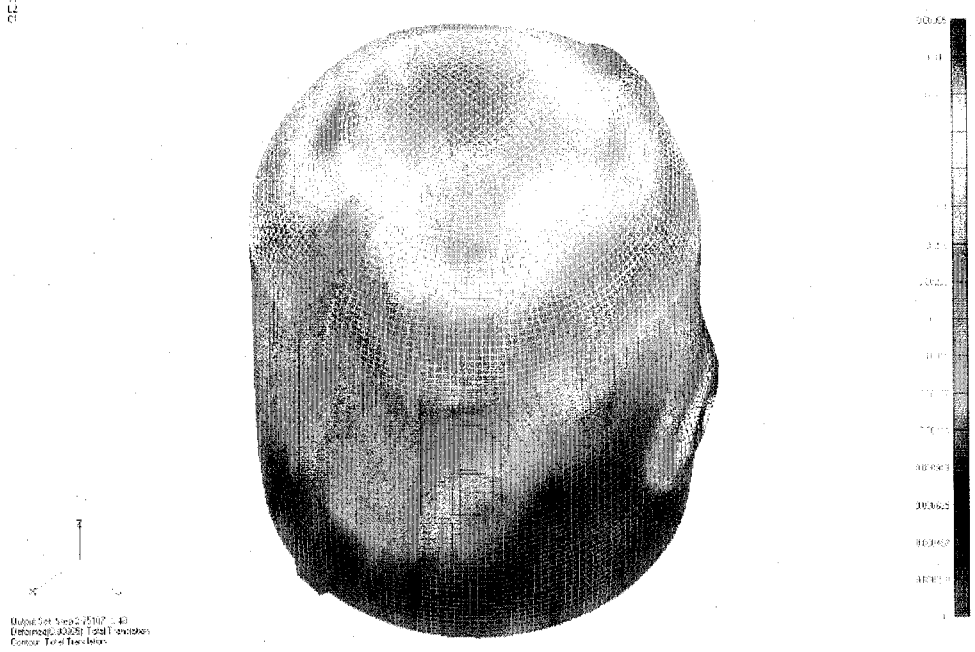

Figure 7 Total deformation (m) at 0.6MPa – concrete starts to crack in circumferential direction

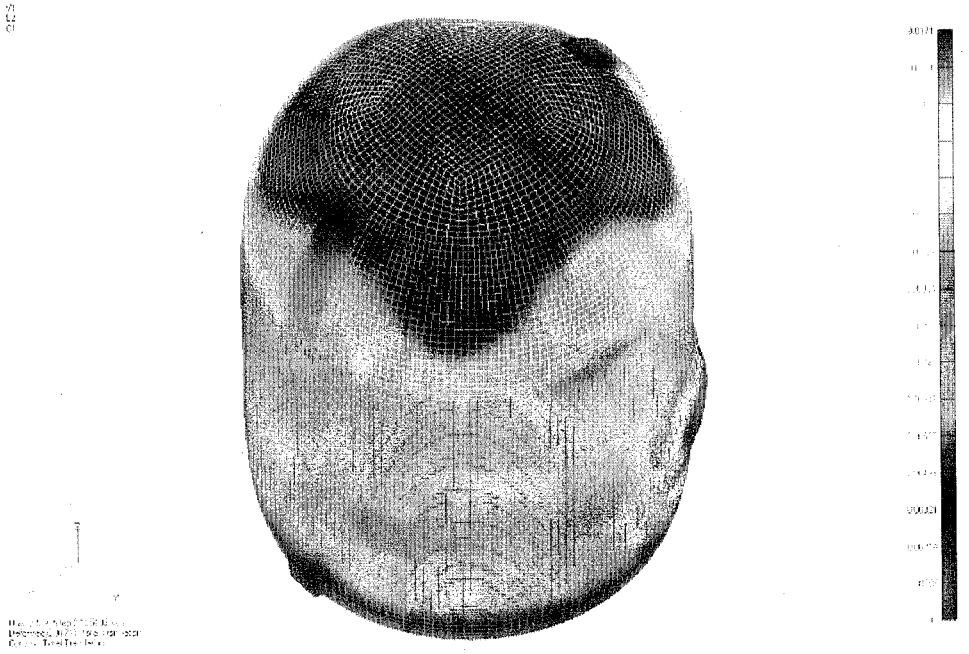

Figure 8 Total deformation (m) at 1.0MPa – continuous cracks in concrete in meridian direction

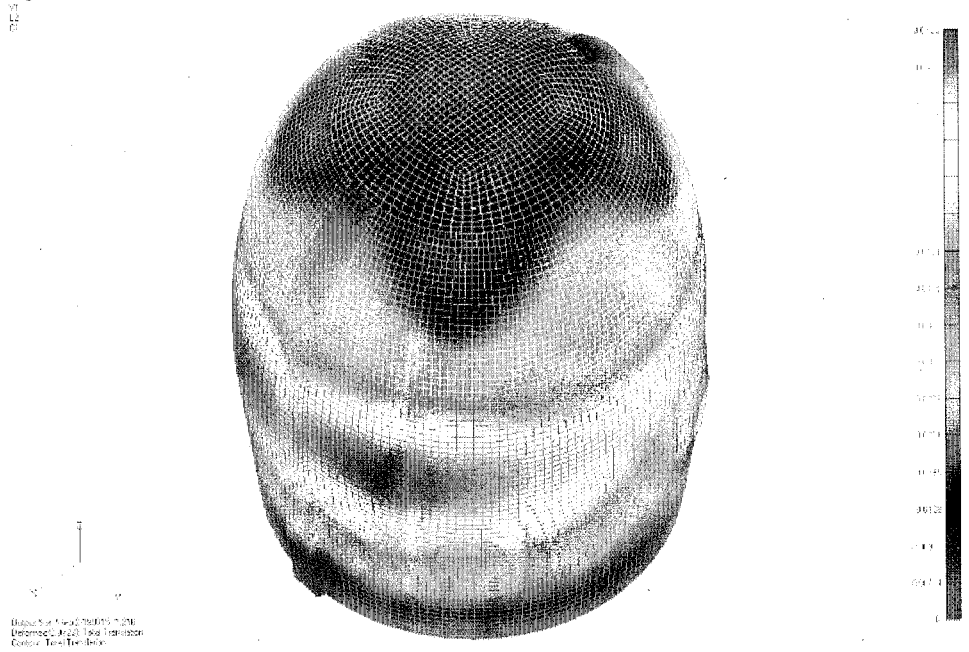

Figure 9 Total deformation (m) at 1.52MPa – strain of tendons reaches 2%

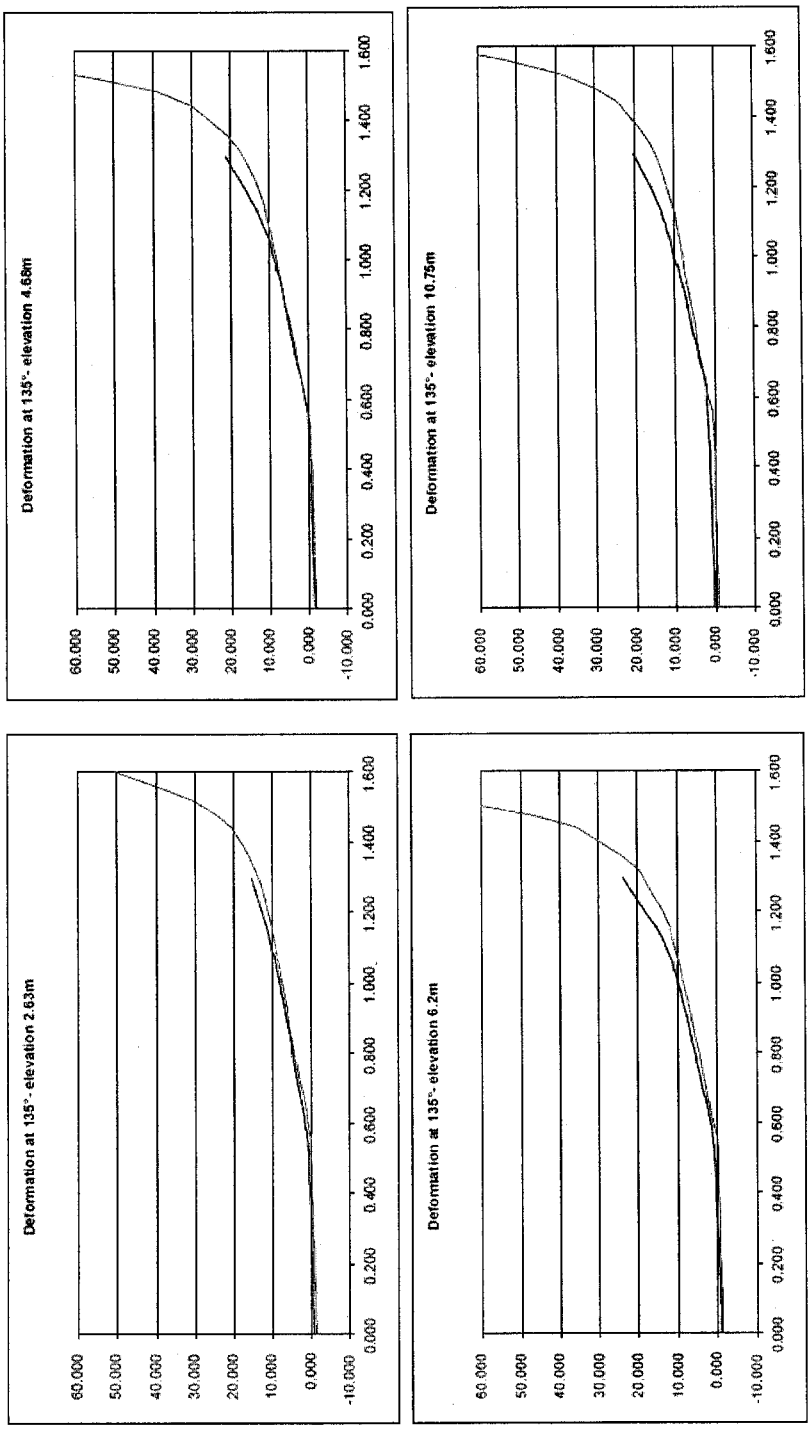

Figure 10 Comparison of radial displacements at 135 degrees (mm, MPa)

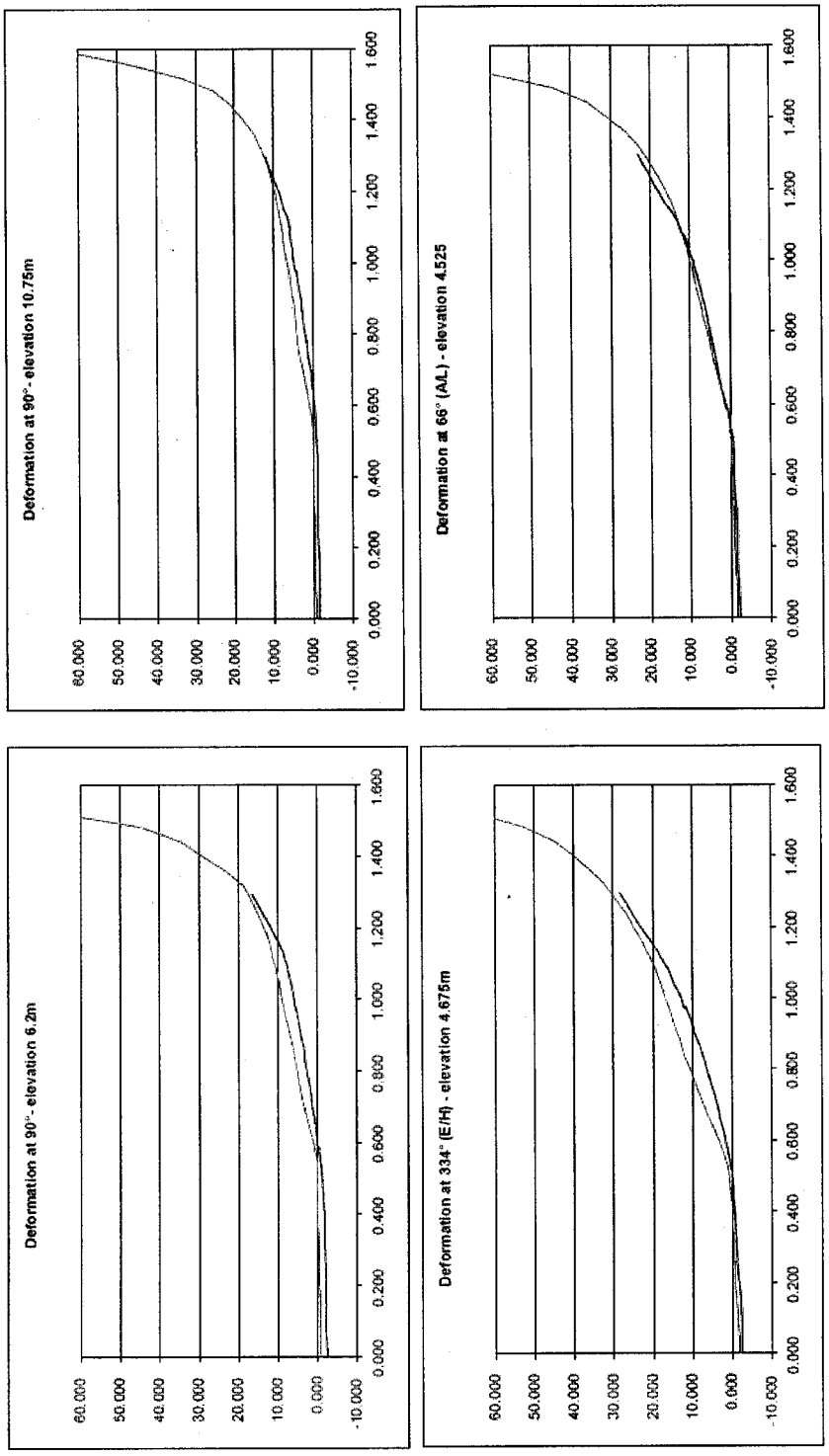

Figure 11 Comparison of radial displacements at 90 degrees and openings (mm, MPa)

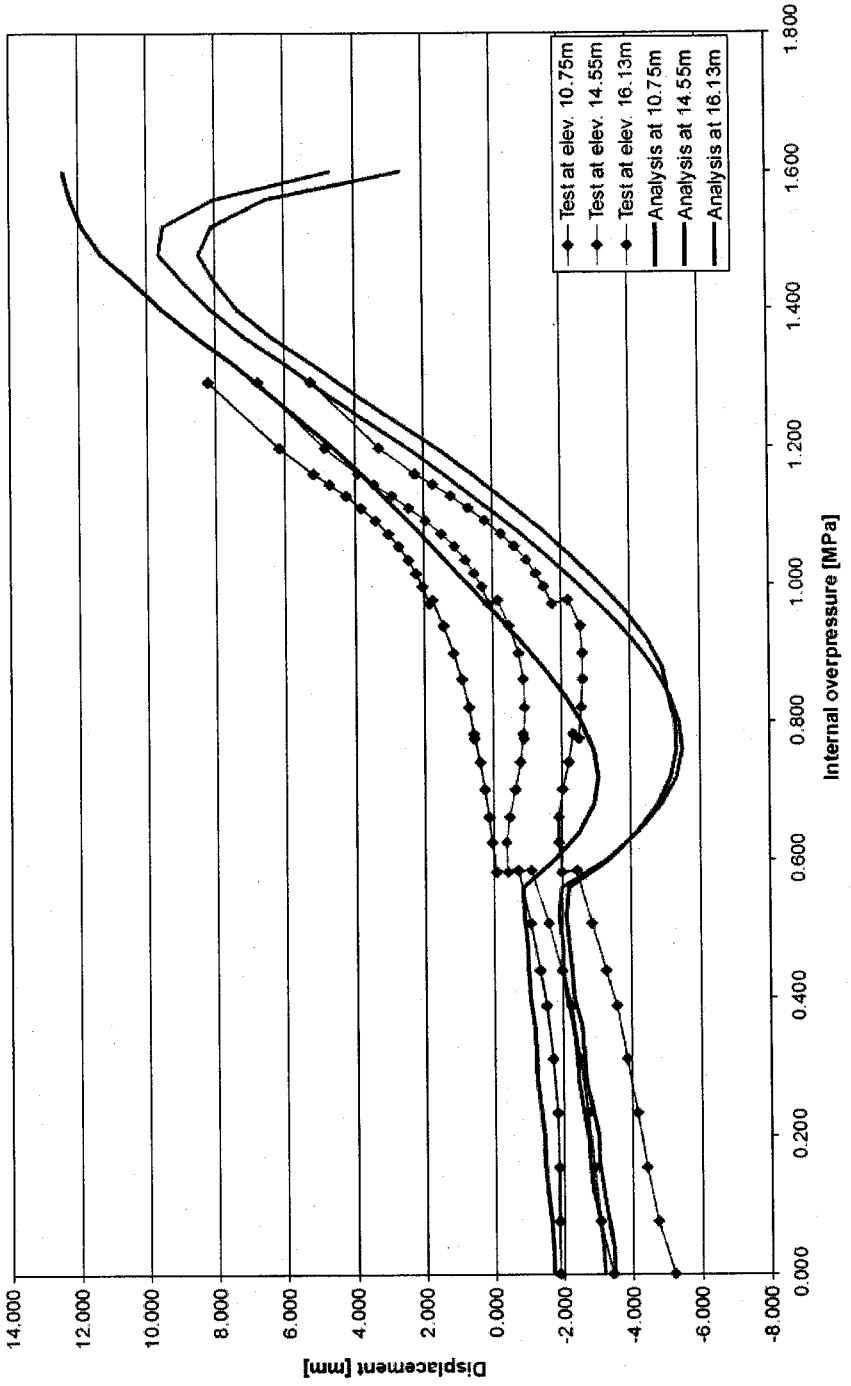

Figure 12 Comparison of vertical displacements

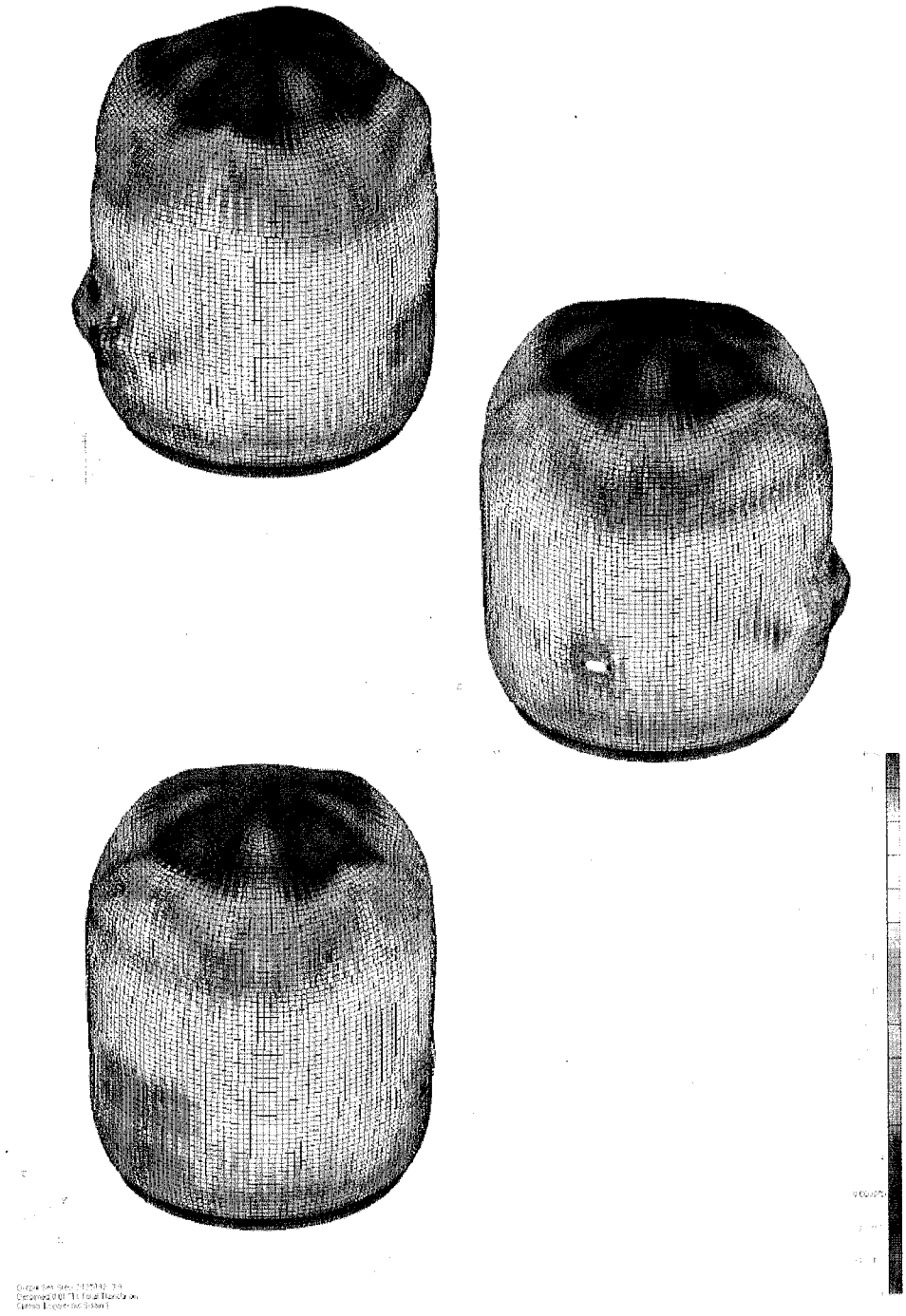

Figure 13 Liner strain in circumferential direction at 1.0MPa – stress in liner reaches yield stress

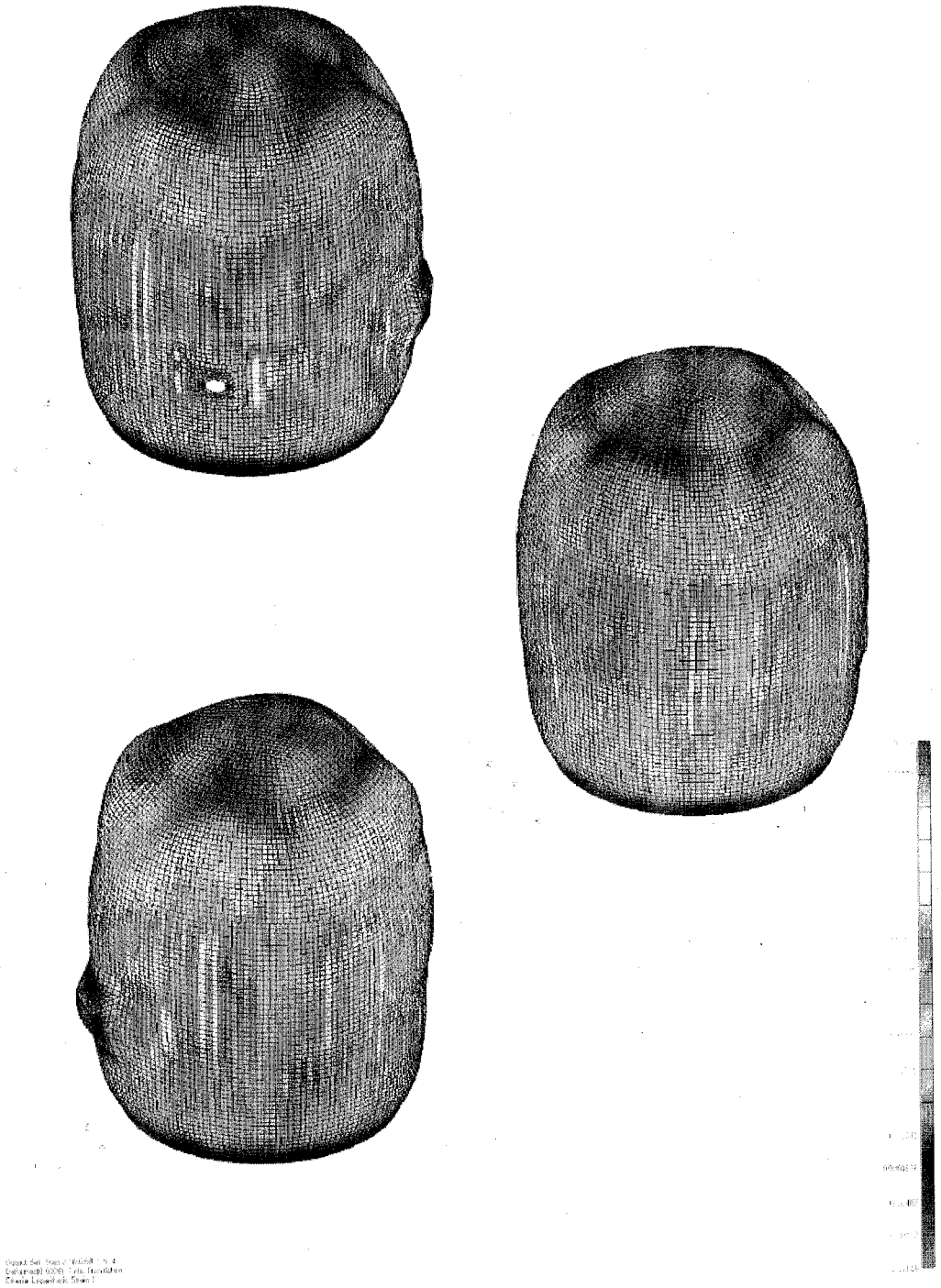

Figure 14 Liner strain in circumferential direction at 1.25MPa – stress in tendons reaches yield stress

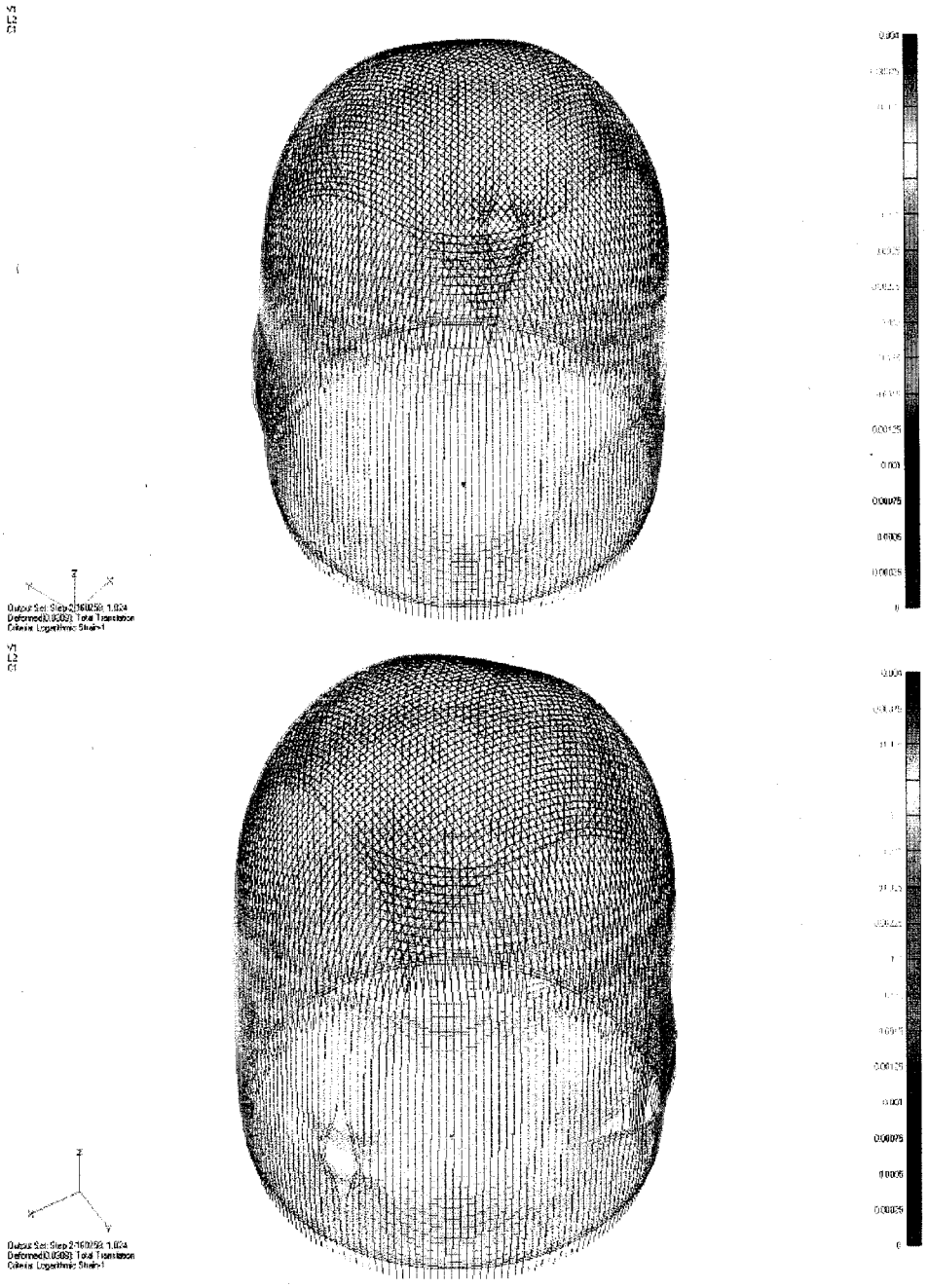

Figure 15 Tendon strain at 1.25MPa – stress in tendons reaches yield stress

Figure 16 Tendon strain at 1.52MPa – strain in tendons reaches 2%

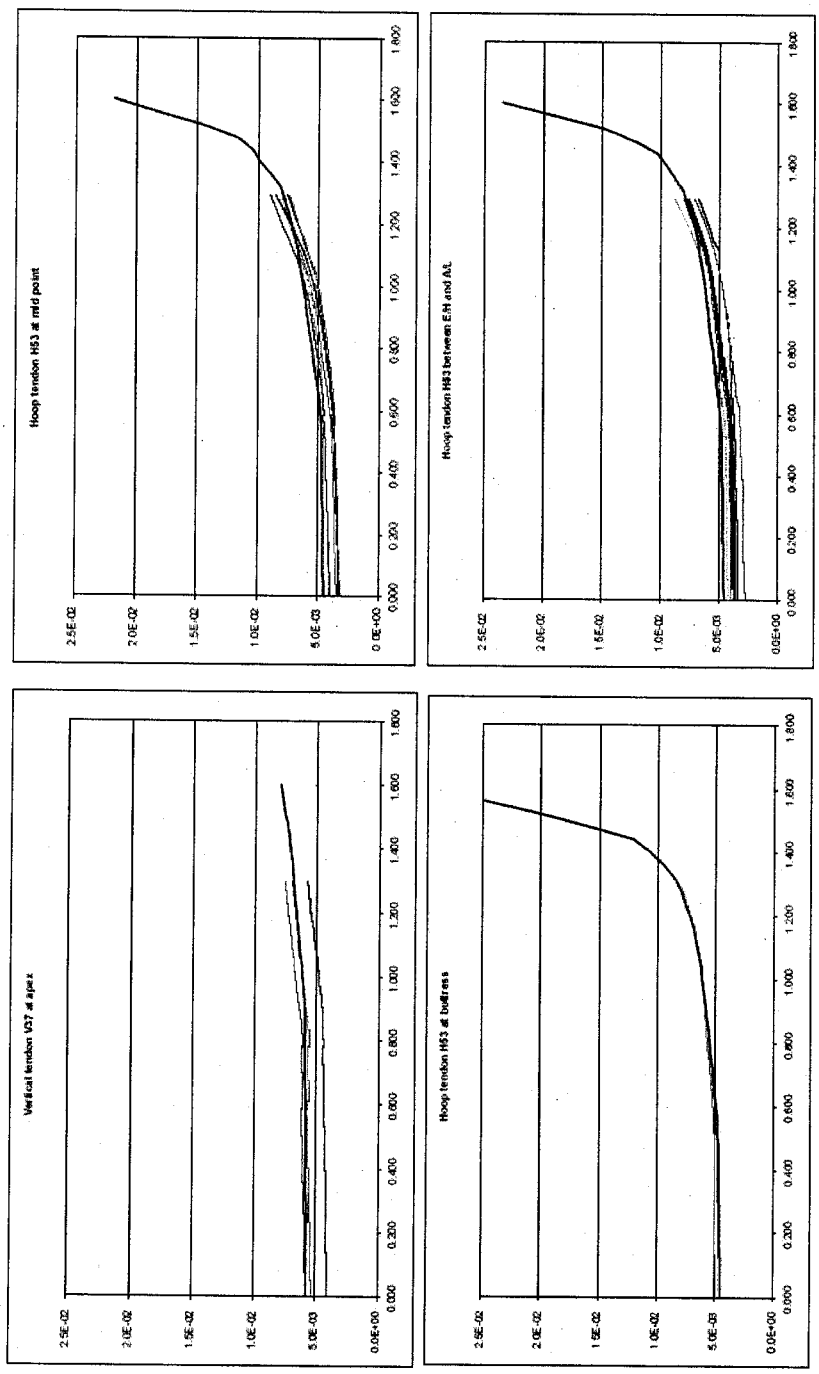

Figure 17 Comparison of tendons strain (m/m, MPa, analysis is black curve)

Appendix D:

Structure Mechanics Analysis of the Prestressed Concrete Model Containment Tested at Sandia National Laboratories

Structure mechanics analysis of the prestressed concrete model containment tested at Sandia National Laboratories - Contribution to International Standard Problem (ISP) 48

H. Grebner, J. Sievers
Gesellschaft für Anlagen- und Reaktorsicherheit (GRS) mbH, Köln, Germany

Introduction

Tests of the failure behaviour of a 1:4 scaled prestressed concrete containment vessel were performed at Sandia National Laboratories (Albuquerque, New Mexico) in the years 2000 and 2001. **Fig. 1** gives a schematic view of the containment model.

In combination with the tests calculations were carried out by several institutions. After completion of the tests the International Standard Problem ISP 48, supported by CSNI-IAGE working group, was defined to perform an international comparative study on the present state of analysis methods used for the assessment of prestressed concrete containments concerning load-carrying capacity and leaktightness. Especially the failure behaviour as well as the estimation of leak rates through cracks in the steel liner and the concrete are of interest. GRS participates in ISP 48. In the following preliminary analysis results are summarized.

Basis of the standard problem is the so-called limit state test [1] which was finished with an internal pressure of 1.3 MPa (about 3.3 times design pressure). At this pressure the leak rate through leaks in the steel liner and the concrete was higher than the amount which could be compensated by the nitrogen supply system.

GRS – Finite-Element-Model

Up to now an axisymmetric model is used without consideration of geometric inhomogenities due to penetrations in the wall. **Fig. 2** shows the model and its main components.The steel liner at the inner surface and the concrete parts are made of 8-node isoparametric elements with 4 integration points, while the rebar and tendon parts

are modelled as truss elements (with 3 nodes for the meridional and radial ones and one node for those in hoop direction). A stiff coupling between steel and concrete is simulated. Dimensions and material data are taken from [1].

For the liner and the rebar elements elastic-plastic material models with multi-linear stress-strain curves are used (see **Fig. 3**). The behaviour of the tendons is simulated by a nonlinear-elastic material model (also shown in **Fig. 3**). The end points of the curves correspond with the uniaxial rupture strains of the materials. As the rebar and tendon elements behave primarily uniaxial the end values of the curves in Fig. 3 may be used directly for the assessment of rebar and tendon elements. In the case of the liner a reduction by the stress multiaxiality has to be taken into account. The concrete material model includes the formation of micro-cracks for tensile stresses exceeding a critical value as well as crushing for high compressive stresses. **Fig. 4** shows schematically the uniaxial stress-strain curve used in the model. **Tables 1** to **4** show the material data used as input for the Finite-Element-Calculations. For the calculations the Finite-Element-Program ADINA [2] was used.

The prestressing of the tendons is simulated by initial strains in the respective truss-elements. The containment model is loaded by increasing internal pressure.

Analysis results

In the calculations small increments are used for the increase of the internal pressure (totally about 1200 time steps). Despite of this, convergence problems arise and above about 1.0 MPa internal pressure the calculation is performed without equilibrium iterations. As discussed in [3] the error caused by such a proceeding may be neglected.

Some typical results are presented in the **Figs. 5** to **28**.

Figs. 5 to **8** show the deformation of the complete model for different values of internal pressure.

The development of circumferential micro-cracks in the cylindrical part of the model is presented in **Fig. 9**. Only a small pressure increment (about 0.01 MPa) is necessary to get from only a few micro-cracks to a situation with micro-cracks at all integration points

through the wall at the section shown in Fig. 9. The formation of radial micro-cracks in the cylinder starts at a higher pressure level (about 0.9 MPa as shown in **Fig. 10**). Above 1.1 MPa also meridional micro-cracks are found.

Figs. 11 to **28** give a compilation of the results at the standard output locations contributed by GRS to ISP 48, especially displacements and strains of the liner, the rebars, the tendons and the concrete.

A few examples of comparisons between calculation and measurement are shown in **Figs. 14** to **16**, **19**, **20**, **24** and **26** to **28** for locations in the cylindrical part of the model. While **Figs. 14** and **15** present the radial displacement at the inner surface of the liner, **Fig. 16** shows the vertical displacement at the transition of cylindrical part to dome. The other figures show comparisons of the strain from measurement and calculation for the liner (**Figs. 19** and **20**), a hoop rebar (**Fig. 24**), 2 hoop tendons (**Figs. 26** and **27**) and the concrete (**Fig. 28**).

For pressure loading up to 0.6 MPa (about 1.5 times design pressure) the calculated results of displacements and strain in the liner, the rebars, the tendons and the concrete agree very well with measured data. Major differences between experiment and analysis are found in the pressure region of about 0.6 to 0.74 MPa. In this pressure region the deviations may be due to a too stiff coupling of concrete and steel in our Finite-Element-Model, which will be investigated by further studies.

In the pressure region 0.74 to 0.75 MPa the formation of micro-cracks predominantly in circumferential direction is calculated.

For the pressure region 0.75 to 1.0 MPa mostly a good coincidence of calculation and measurement is found. Above 1.0 MPa plastification starts in the hoop rebars and again larger differences between experiment and calculation are found. At maximum load (1.3 MPa) hoop tendon strains of nearly 1% are found, which is about 1/3 of the uniaxial rupture strain. The maximum strain values in the rebars and the liner lie below 1%. Thus a larger difference to the uniaxial rupture strain is found in this case.

The deformation behaviour of the dome part of the containment is not simulated very well by our Finite-Element-Model. This is partly due to the fact that an axisymmetric model is used which can not provide an adequate modelling of the hairpin tendons in the upper dome part. Furthermore the formation of micro-cracks and the post-cracking

stiffening behaviour have influence on the vertical deformation of the dome. Further investigations are in progress.

Summary

GRS participates in the International Standard Problem (ISP) 48 with Finite-Element-Calculations. An axisymmetric Finite-Element-Model was developed, in which the liner at the inner surface and the concrete parts are simulated by 8-node elements. Rebar and tendon parts are modelled by truss-elements. The necessary input-data for the nonlinear material models used are gained from Sandia-measurements. The model is loaded by the prestressing of the tendons and by increasing internal pressure (up to 1.3 MPa).

The analyses results in terms of displacements and strains in the liner, the rebars, the tendons and the concrete of the cylindrical part agree well with measured data up to about 0.6 MPa internal pressure (i.e. 1.5 times design pressure). First circumferential micro-cracks in the concrete are found at about 0.75 MPa. With increasing pressure micro-cracks are present through the whole wall. Above about 0.9 MPa the formation of micro-cracks in radial and meridional direction is calculated. At the maximum load (1.3 MPa) almost all concrete parts of the model have micro-cracks which may cause leaks.

Nevertheless the failure of the containment model is not expected for loads up to 1.3 MPa without consideration of geometric inhomogenities due to penetrations in the wall. Although the calculated strains in liner, rebars and tendons show some plastification, the maximum values are below the critical ones. The safety margin against failure is smallest in some hoop tendons.

At present parametric studies are performed to investigate the differences between calculations and measured data. Furthermore three-dimensional models are developed to simulate the wall penetrations in the Sandia containment model.

The work described in this Technical Report is sponsored by the German Ministry of Economics and Labor.

References

[1] Hessheimer, M. F., et al.: Overpressurization test of a 1:4 scale pre-stressed concrete containment model. NUREG/CR-6810 (2003).

[2] ADINA – A Finite-Element-Program for Automatic Dynamic Incremental Nonlinear Analysis, Version 8.1 – Theory and Modeling Guide, Volume I: ADINA. ADINA R&D, Inc. (2003).

[3] Bachmann, P., et al.: Analyse zur Bestimmung des Versagensdruckes und des Versagensverhaltens eines Stahlbetoncontainments im Maßstab 1:6 (Vorausberechnungen). GRS-A-1415 (1988).

Table 1: Material data of the liner steel (see Fig. 3)

General data		"True" stress-strain values for multilinear curve	
		Strain [-]	Stress [MPa]
		0.002	380
Young' modulus	219000 MPa	0.01	403
Poisson ratio	0.3	0.02	430
Density	7800 kg/m^3	0.03	452
		0.04	470
		0.05	480
		0.28	670

Table 2: Material data of the rebar steel

General data		"True" stress-strain values for multilinear curve	
		Strain [-]	Stress [MPa]
		0.002	420
Young' modulus	200000 MPa	0.01	455
Poisson ratio	0.3	0.03	520
Density	7800 kg/m^3	0.05	580
		0.075	620

Table 3: Material data of the tendon strands

General data		"True" stress-strain values for nonlinear-elastic curve	
		Strain [-]	Stress [MPa]
		0.0	0
Young's modulus	216200 MPa	0.0074	1600
Poisson ratio	0.3	0.0080	1650

Density	7800 kg/m^3	0.0092	1734
		0.0100	1760
		0.0200	1880
		0.0325	2000

Table 4: Material data of the concrete (see Fig. 3)

Density	2176 kg/m^3
Initial Youngs' modulus	27000 MPa
Poisson ratio	0.18
Maximum tensile stress	3.45 MPa
Strain at maximum tensile stress	0.000128
Parameter to describe post-cracking stiffening ξ	8
Maximum stress in compression	-47.3
Strain at maximum compressive stress	-0.00186
Strain at beginning of crushing	-0.0032
Stress at beginning of crushing	-30

Figures

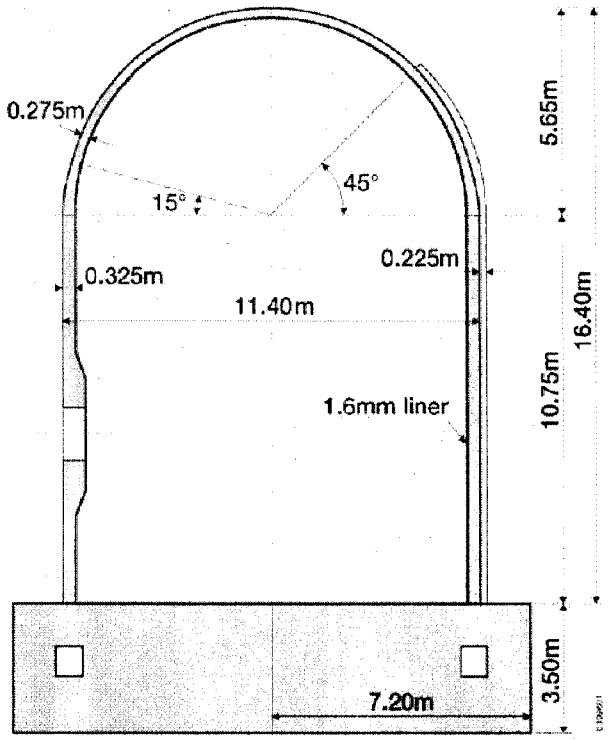

Fig. 1: Major dimensions of the containment model

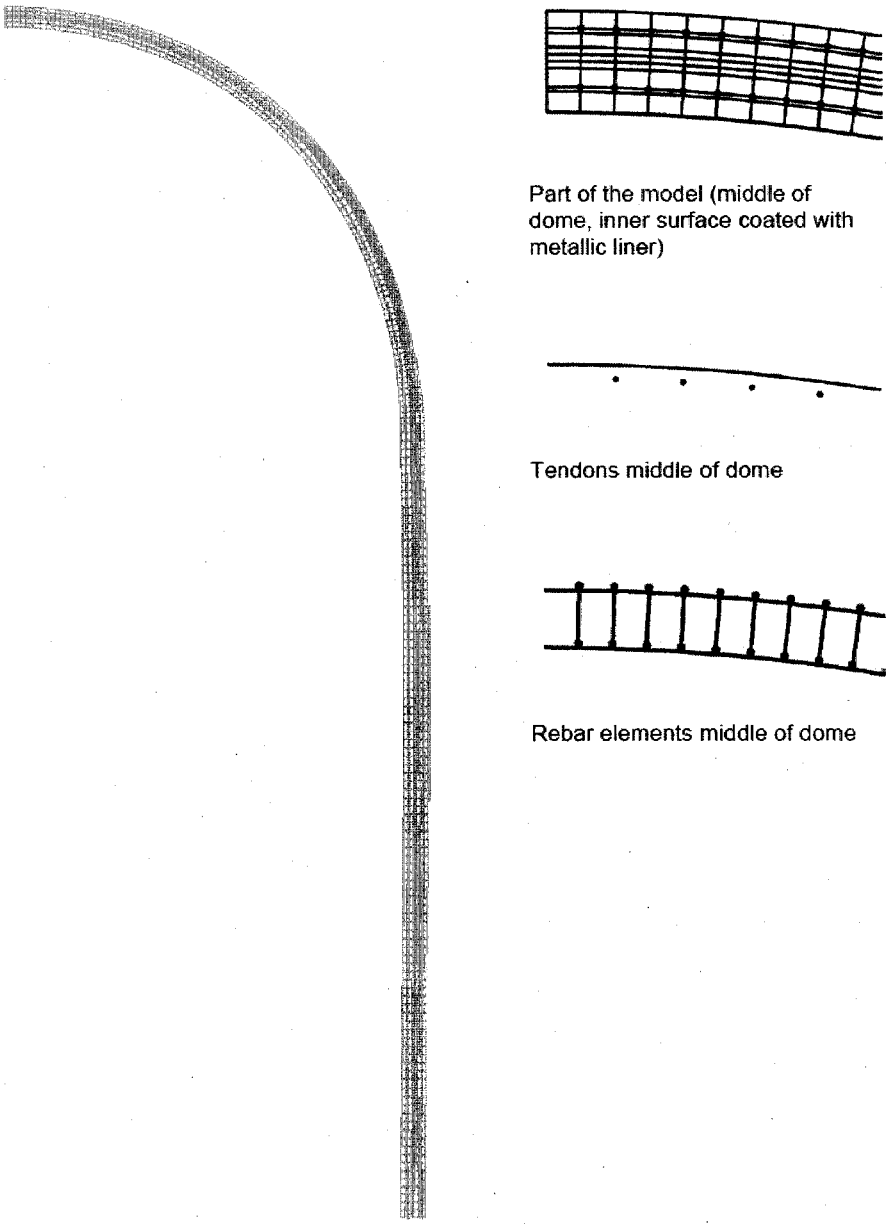

Fig. 2: Finite element model of prestressed concrete model containment

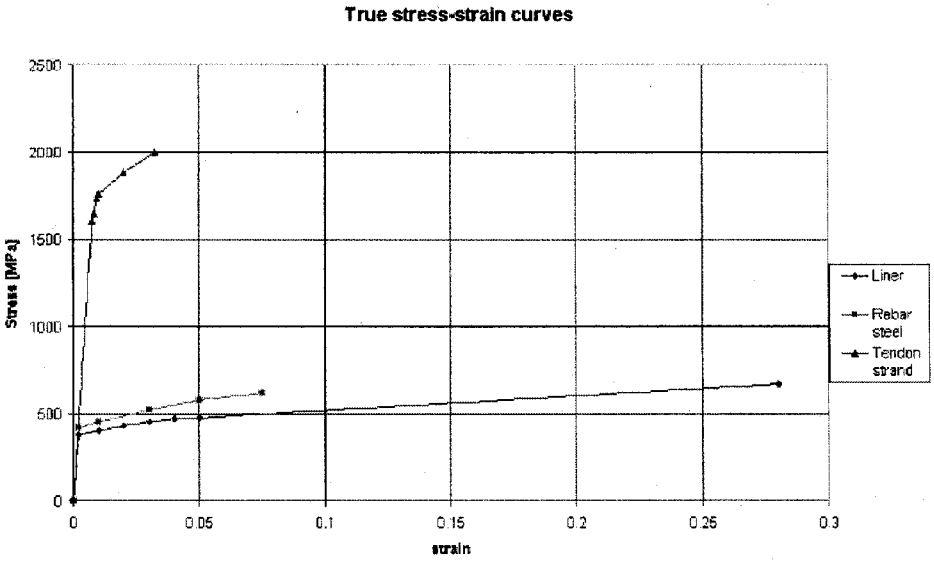

Fig. 3: True stress-strain curves of liner and rebar steel as well as tendon strand as used as input for the finite-element-calculations

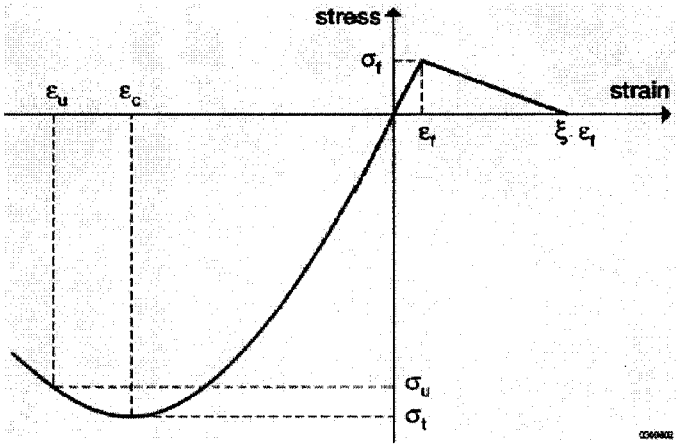

Fig. 4: Uniaxial stress-strain curve used in the concrete model

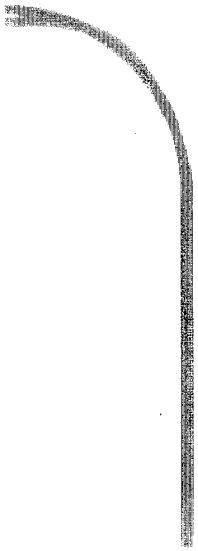

Fig. 5: Deformed model at 0.7 MPa (magnifcation of displacements = 50)

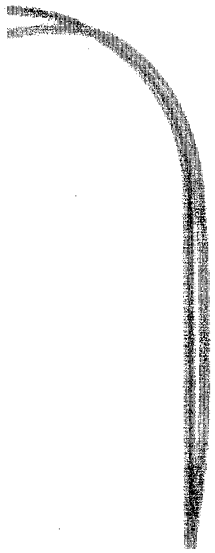

Fig. 6: Deformed model at 1.0 MPa (magnifcation of displacements = 50)

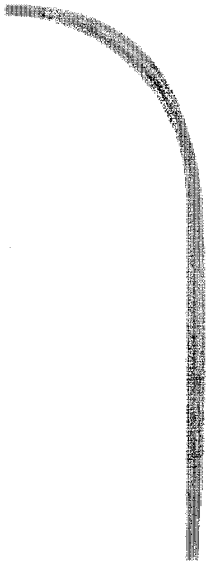

Fig. 7: Deformed model at 1.3 MPa (magnifcation of displacements = 10)

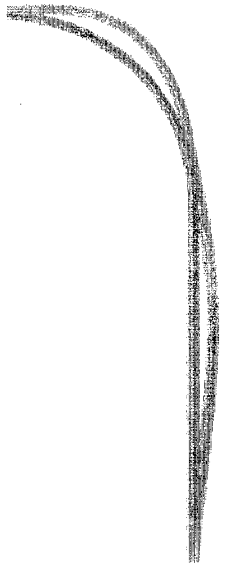

Fig. 8: Deformed model at 1.4 MPa (only in calculation, magnifcation of displacements = 10)

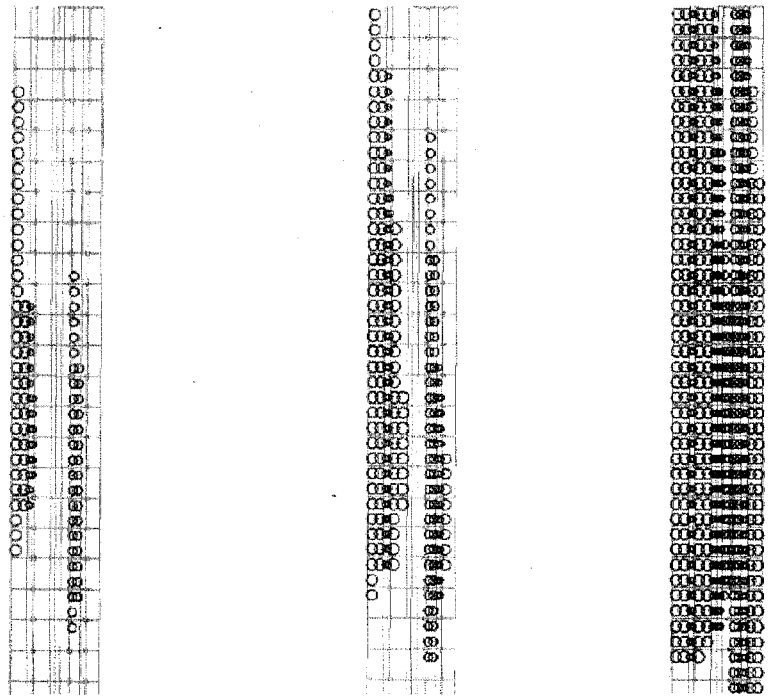

p = 0.740 MPa p = 0.742 MPa p = 0.745 MPa

Fig. 9: Development of circumferential micro-cracks (shown by red circles) in the cylindrical part of the model (height about 3 m)

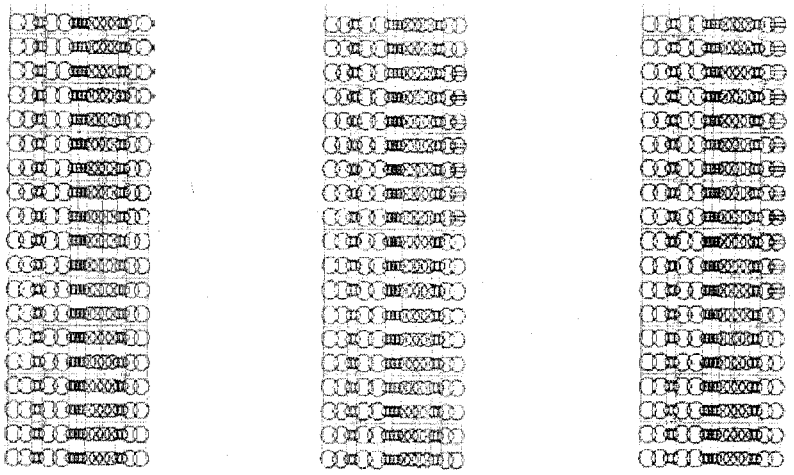

p = 0.910 MPa p = 0.915 MPa p = 0.920 MPa

Fig. 10: Development of circumferential and radial micro-cracks (parallel straight red lines) in the cylindrical part of the model (height about 3 m)

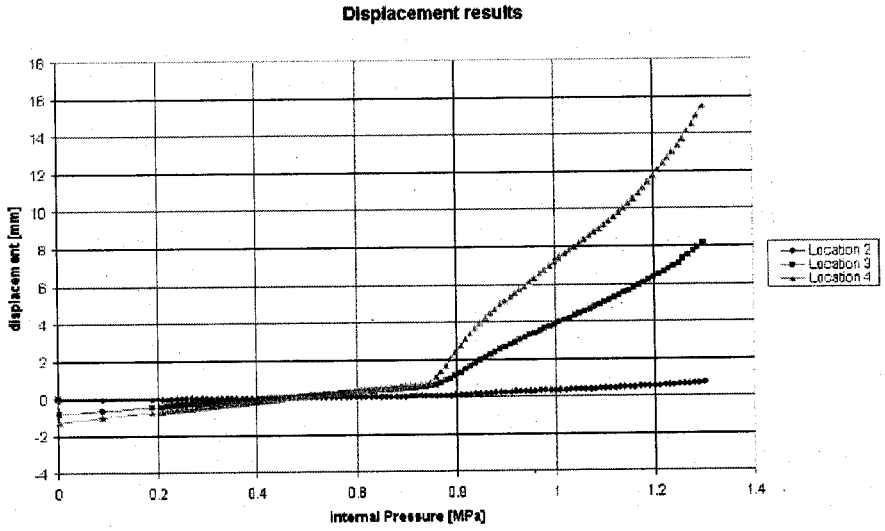

Fig. 11: Radial displacement results at inner surface of the liner (location 2: height 0.25 m, location 3: height 1.43 m, location 4: height 2.63 m)

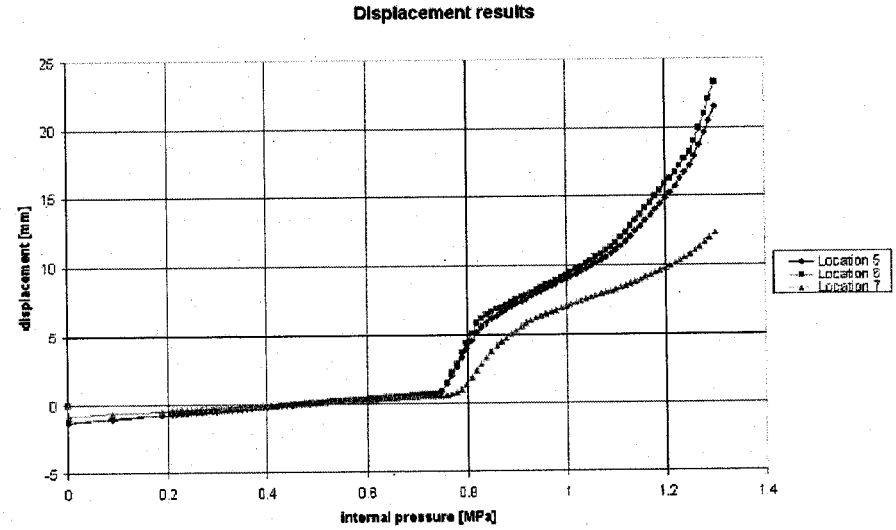

Fig. 12: Radial displacement results at inner surface of the liner (location 5: height 4.68 m, location 6: height 6.2 m, location 7: height 10.75 m)

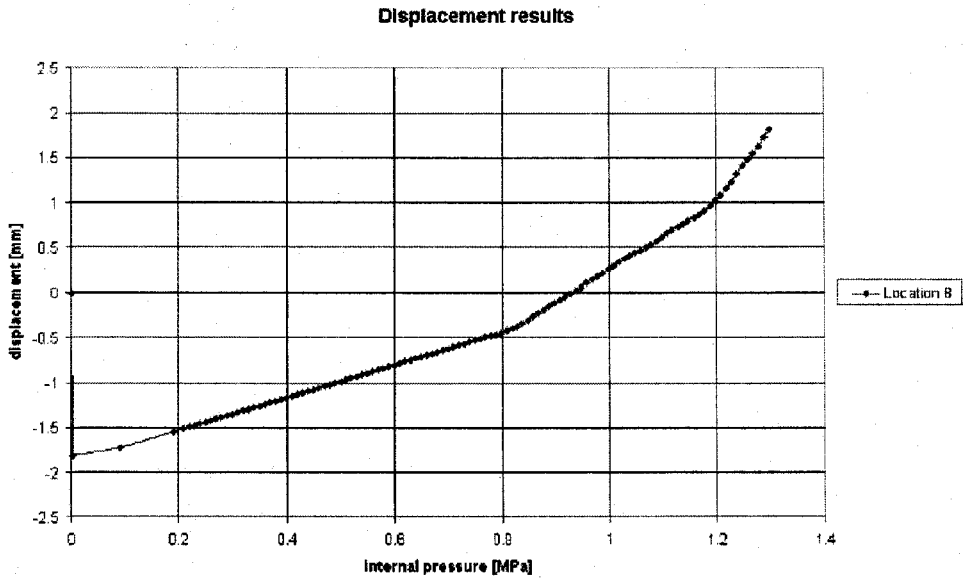

Fig. 13: Vertical displacement results at inner surface of the liner (location 8: height 10.75 m)

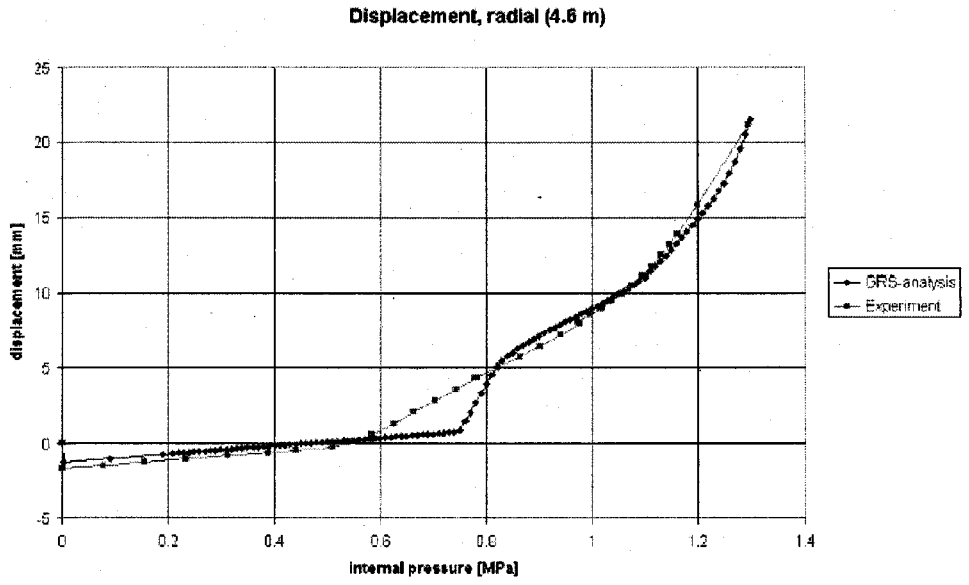

Fig. 14: Radial displacement at the inner surface of the liner (vertical position 4.6 m above top of basemat) from measurement and calculation

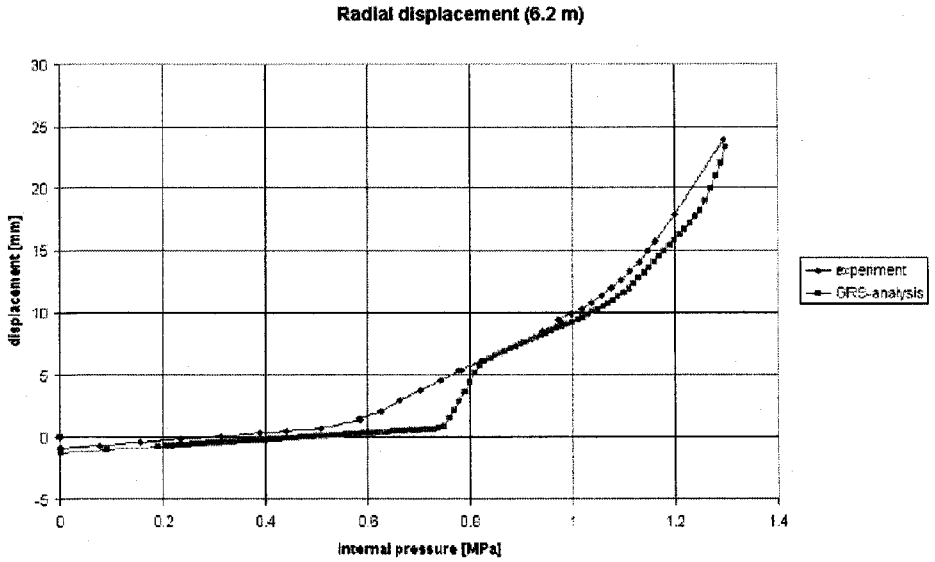

Fig. 15: Radial displacement at the inner surface of the liner (vertical position 6.2 m above top of basemat) from measurement and calculation

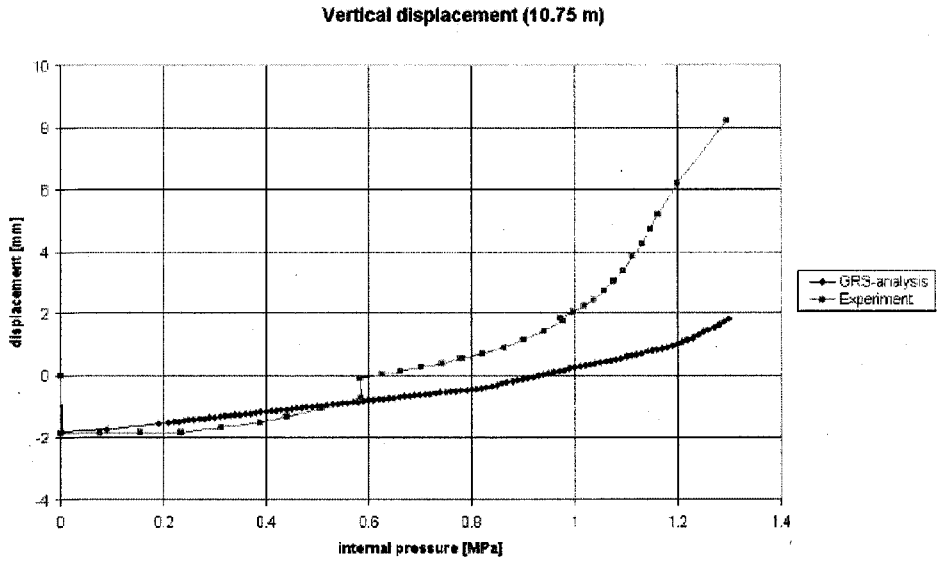

Fig. 16: Vertical displacement at the inner surface of the liner (vertical position 10.75 m above top of basemat) from measurement and calculation

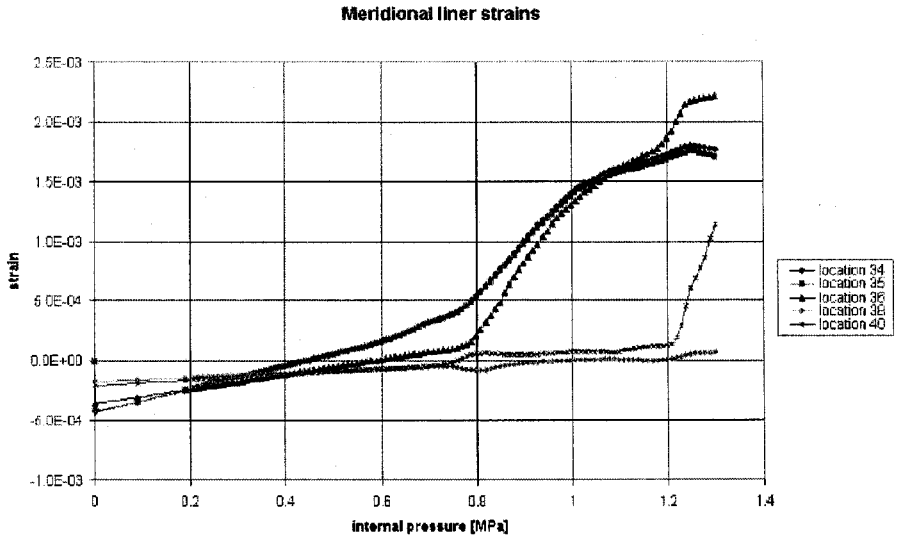

Fig. 17: Meridional liner strains at different standard output locations (location 34: height 0.01 m, location 35: height 0.01 m, location 36: height 0.25 m, location 38: height 6.2 m, location 40: height 10.75 m; all at inner liner surface except location 35, which is at outside liner surface)

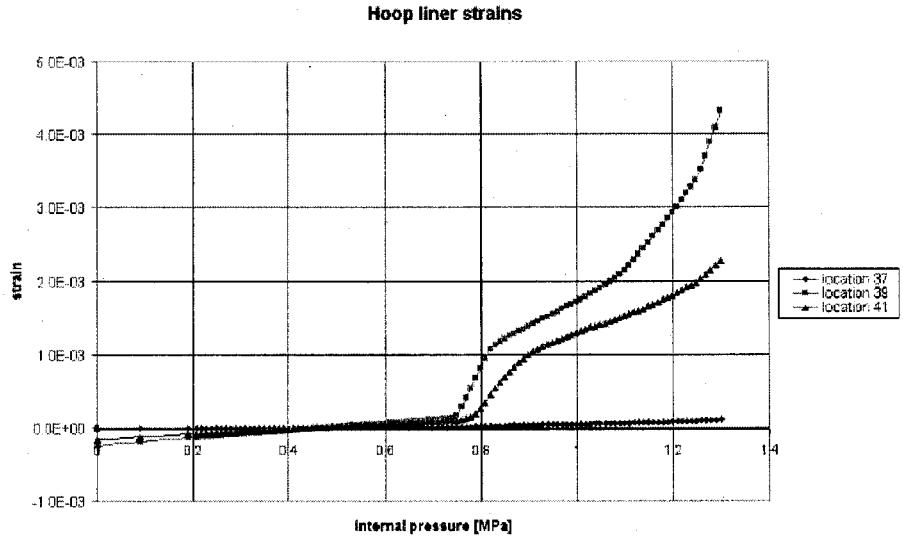

Fig. 18: Hoop liner strains at inner liner surface for different standard output locations (location 37: height 0.25 m, location 39: height 6.2 m, location 41: height 10.75 m)

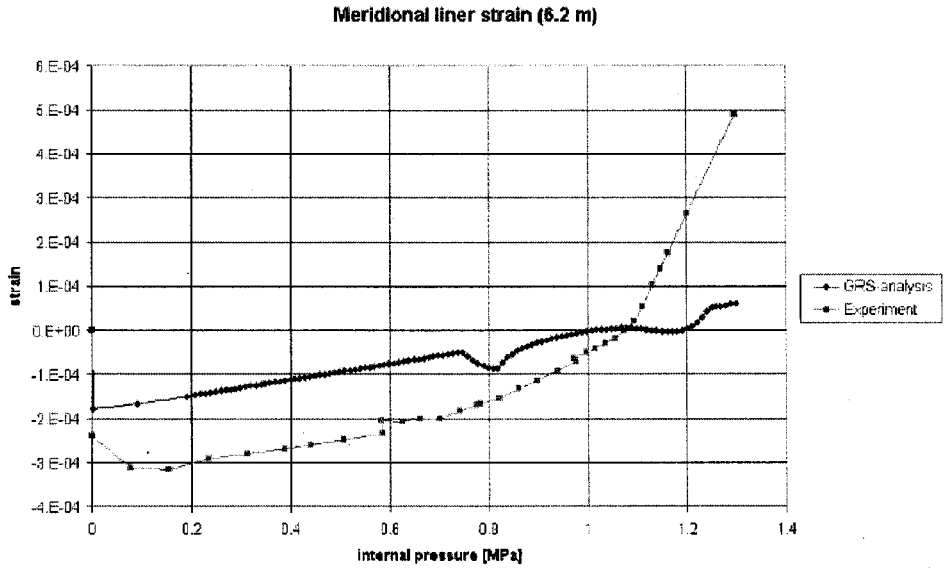

Fig. 19: Meridional strain in liner (vertical position 6.2 m above top of basemat) from measurement and calculation

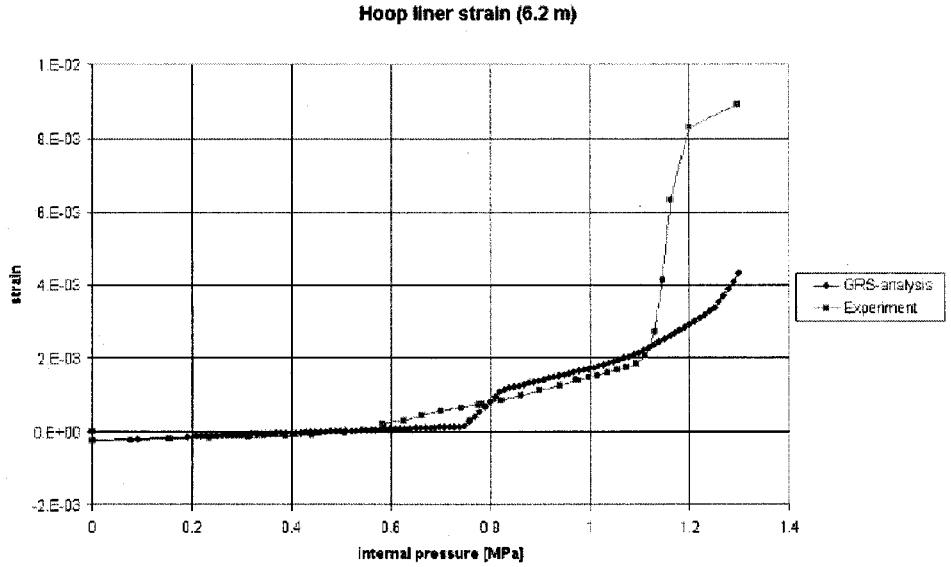

Fig. 20: Hoop strain in liner (vertical position 6.2 m above top of basemat) from measurement and calculation

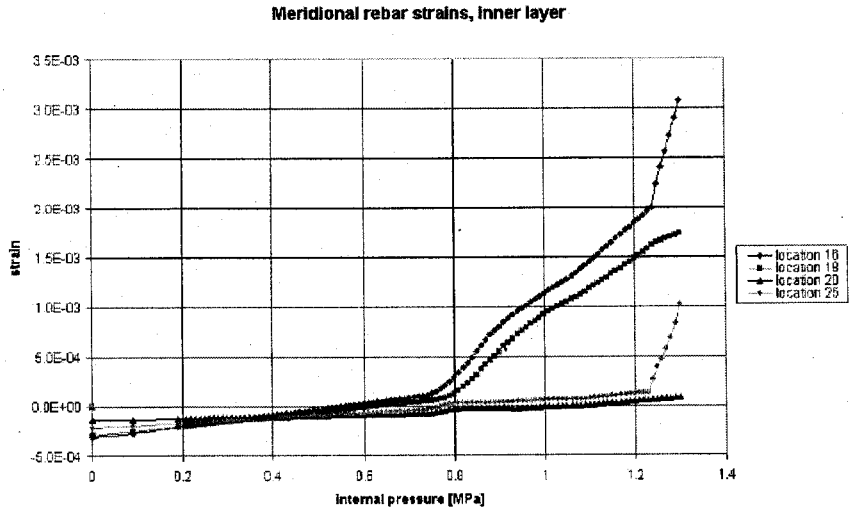

Fig. 21: Inner layer meridional rebar strains at different standard output locations (location 16: height 0.05 m, location 18: height 0.25 m, location 20: height 1.43 m, location 25: height 10.75 m)

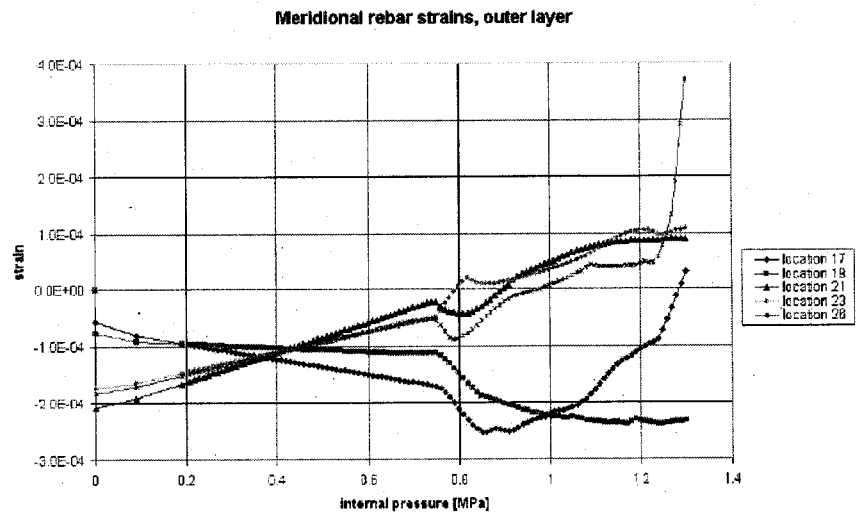

Fig. 22: Outer layer meridional rebar strains at different standard output locations (location 17: height 0.05 m, location 19: height 0.25 m, location 21: height 1.43 m, location 23: height 6.2 m, location 26: height 10.75 m)

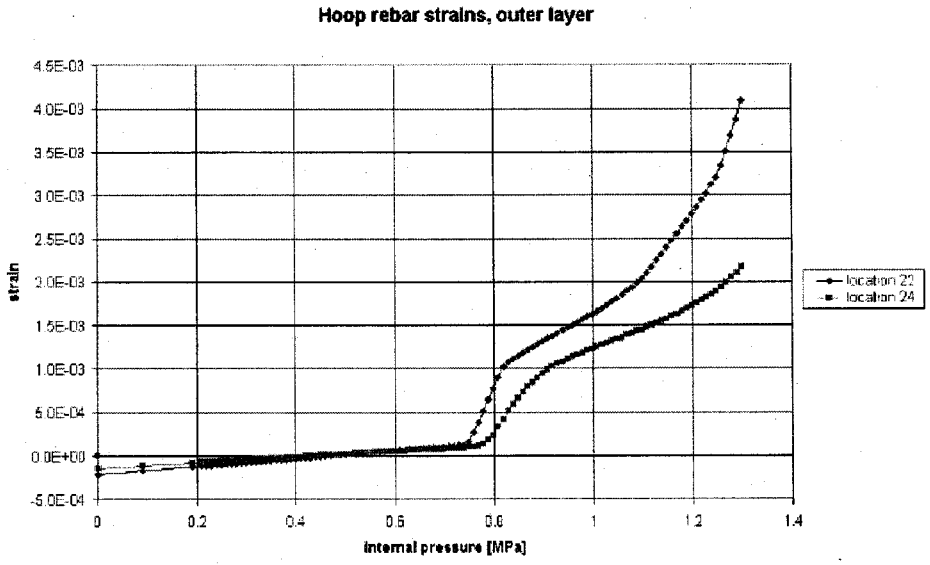

Fig. 23: Outer layer hoop rebar strains at different standard output locations (location 22: height 6.2 m, location 24: height 10.75 m)

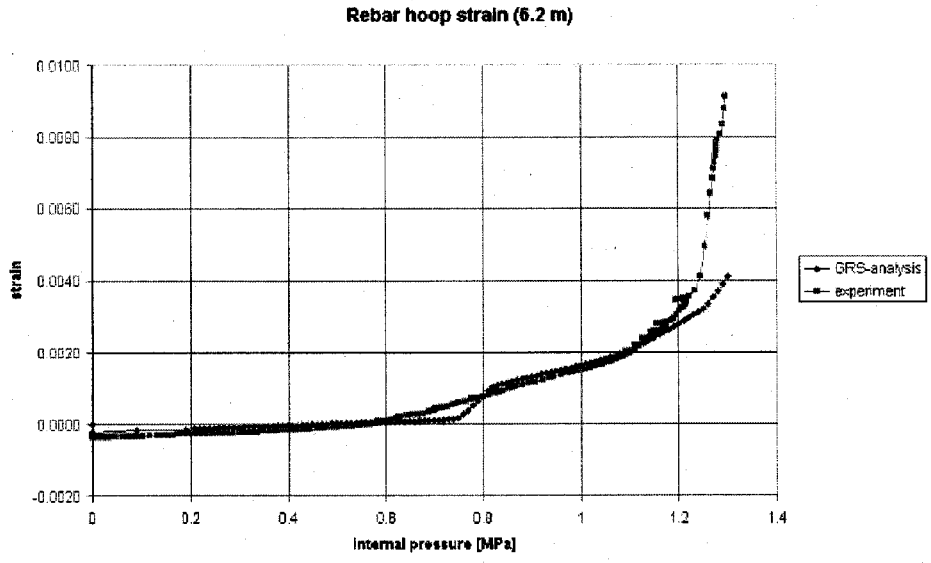

Fig. 24: Rebar hoop strain at outer hoop rebar (vertical position 6.2 m above top of basemat) from measurement and calculation

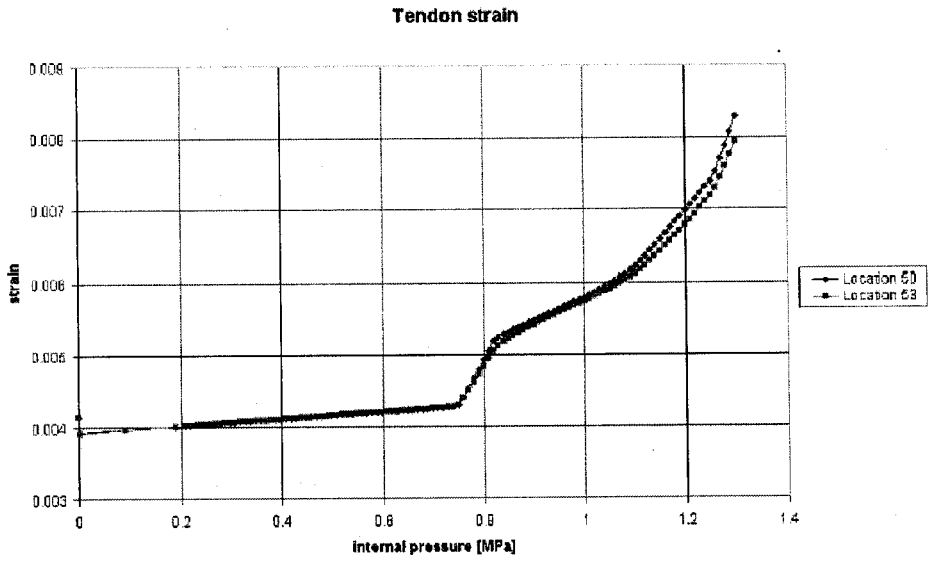

Fig. 25: Hoop tendon strains at different standard output locations (location 50: height 6.58 m, location 53: height 4.57 m)

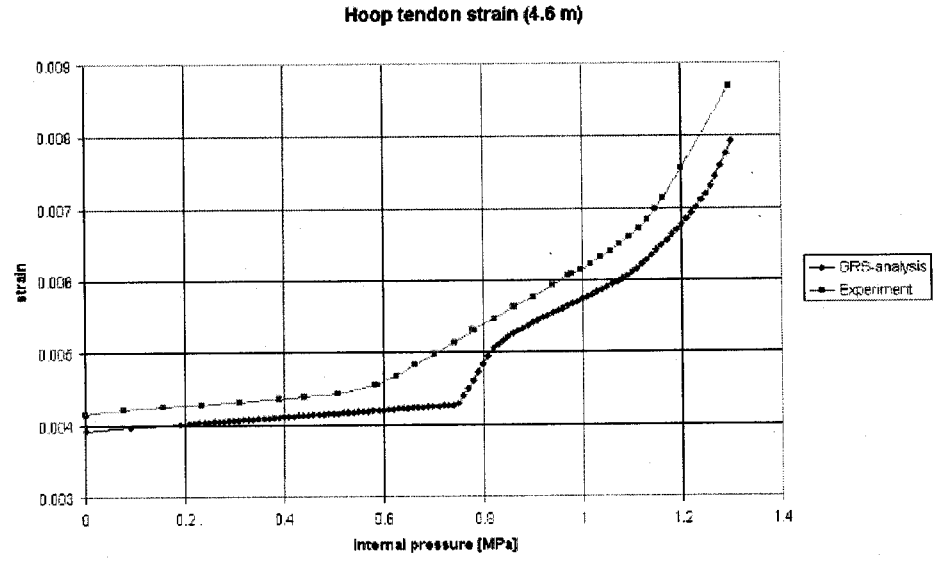

Fig. 26: Strain in hoop tendon (vertical position 4.6 m above top of basemat) from measurement and calculation

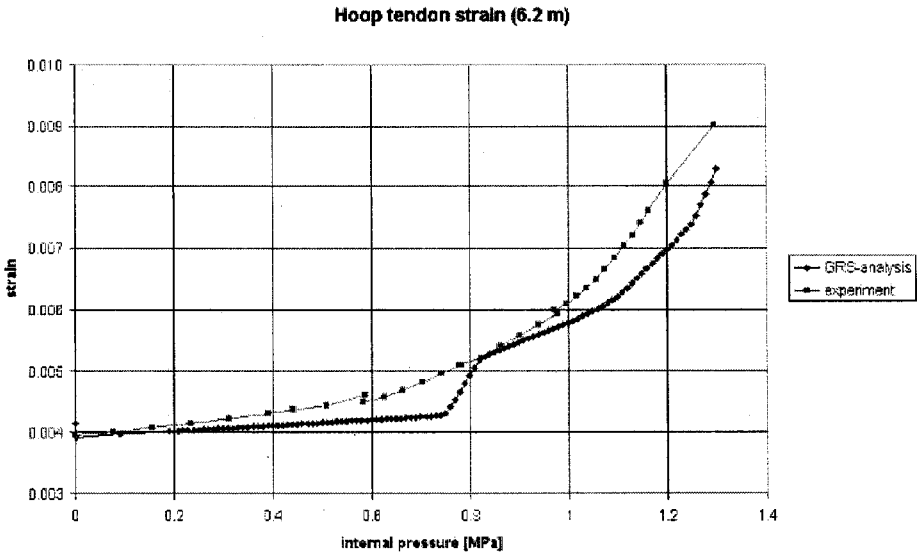

Fig. 27: Strain in hoop tendon (vertical position 6.2 m above top of basemat) from measurement and calculation

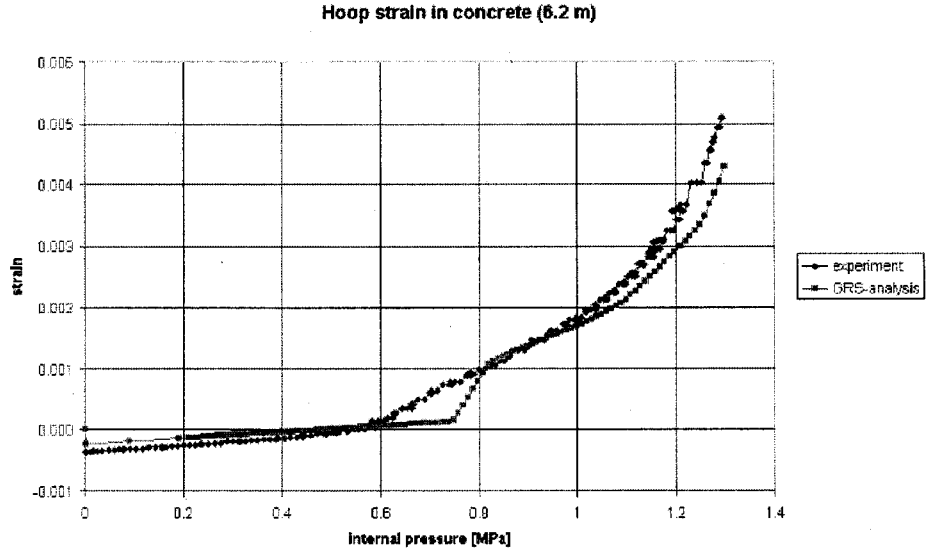

Fig. 28: Hoop strain in the concrete nearby the liner (vertical position 6.2 m above top of base-mat) from measurement and calculation

Appendix E:

Institut de Radioprotection et de Sûreté Nucléaire

ABSTRACT

Objective of this paper is to describe the modelling and the computation of the NRC/NUPEC Sandia test of a Prestressed Concrete Containment Vessel (PCCV) model. The model was a 1:4 scale of a Japanese nuclear power plant (ohi-3) The work is part of the ISP48 international benchmark. In this paper is described the finite element model, the prestressed stage and the computation of the Limit State Test (LST) which consists in increasing the internal pressure as much as possible.

1 Introduction

This work has been performed by IRSN (French Institut de Radioprotection et de Surete Nucleaire) and CEA (French Commissariat à l'Energie Atomique) in the frame of the ISP 48 (International Standard Problem).
The computation of the containment has been performed with the Cast3M finite element code of CEA. All input data has been collected in the ISP 48 PCCV Data Package edited by Mr Hessheimer.

2 Finite element model

2.1 Geometry

The finite element model is a 3-D model with the modelling of the Equipment hatch and of the Personal Air Lock penetrations. The two opposite buttress are also taken into account as well as the basemat and the tendon gallery.

The concrete part is represented by solid linear elements (hexahedron 8 nodes). Four elements in the thickness of the wall and the mean size of elements is 0,5 metre in the vertical direction and 0,4 metre in the hoop direction. 16834 elements and 19736 nodes compose the complete model, including basemat. (Fig 1)

The reinforcing steel is represented by linear 2 nodes elements. The mean size of elements is 0,5 metre as well as for the wall as for the basemat. There are 130556 elements and 112532 nodes representing reinforcing steels. Meshes of concrete and of reinforcing steel are independent. Nodes of reinforcing steels will be attached to concrete by means of relations between displacements unknowns. Reinforcing steel are well meshed in the basemat and in the cylindrical wall but simplifications are made around penetrations and dome (fig 2)

The 198 tendons are also meshed with their deviations around penetrations. Size of elements is around 0,5 metre and there are 15174 elements with 15372 nodes. Figures 3 to 14 represent tendons by group.

Liner is meshed by 3 or 4 nodes shell elements. There are 2694 elements with 2672 nodes (Fig 15).

The whole mesh including attach relations between unknowns represented a total of 700.000 degrees of freedom.

2.2 Material characteristics

2.2.1 Concrete

The Concrete is modelled by the OTTOSEN model, which is a smeared cracks model. There are two different concrete. The first is for the basemat and characteristics are:

- Young modulus E = 29030 MPa

- Poisson ratio $\nu = 0.2$
- Voluminal mass $\rho=2250\ kg/m^3$
- U T S $\sigma_{traction} = 3.93\ MPa$
- GFTR GFTR=135 J/ m^2

The second concrete is for the wall of the containment, characteristics are:

- Young modulus $E = 31970\ MPa$
- Poisson ratio $\nu = 0,2$
- Voluminal mass $\rho=2500\ kg/m^3$
- U T S $\sigma_{traction} = 4.21\ MPa$
- GFTR GFTR=135 J/ m^2

For the prestressing part of the computation concrete is supposed to remain elastic.

2.2.2 Reinforcing steel

The general behaviour of steel is elastoplastic. Characteristics depend on the size of diameter of irons. Elastic modulus of steel is extract from tensile curves.

Figure 16 to 21 give tensile curves for irons depending on irons diameter.

- Young modulus $E = 183600\ MPa$
- Poisson ratio $\nu = 0.3$
- Voluminal mass $\rho = 7850\ kg/m^3$

2.2.3 Tendons

The general behaviour of tendon is elastoplastic. Characteristics are:

- Young modulus $E = 200\ 000\ MPa$
- Poisson ratio $\nu = 0.3$
- Voluminal mass $\rho=7800\ kg/m^3$
- Yield limit $\sigma_e = 1400\ MPa$
- Ultimate strength $\sigma_u = 1900\ MPa$

The tensile curve is given Fig 22

2.2.4 Liner

The general behaviour of the liner is elastoplastic. Characteristics are

- Young modulus $E = 156\ 500\ MPa$
- Poisson ratio $\nu = 0,3$

- Voluminal mass ρ=7800 kg/m^3
- Yield limit σ_e = 375 MPa
- Ultimate strength σ_u = 450 MPa

The tensile curve is given Fig 23

2.3 Prestressing

The prestressing of the containment represents the real sequence of physical prestressing of the mock-up. There are 12 steps in the prestressing loading. The following table gives details on each step.

Prestressing steps	
Step	Tendons
1	H91 H92 H95 H96 H99 H100 H103 H104 H107 H108
2	V1 V3 V5 V7 V39 V41 V43 V45 V46 V48 V50 V52 V84 V86 V88 V90
3	V21 V32 V25 V66 V68 V70
4	V9 V11 V13 V15 V17 V19 V27 V29 V31 V33 V35 V37 V54 V56 V58 V60 V62 V64 V72 V74 V76 V78 V80 V82
5	H3 H4 H7 H8 H11 H12 H15 H16 H19 H20 H23 H24 H27 H28 H31 H32 H35 H36 H39 H40 H43 H44 H47 H48 H51 H52 H59 H60 H63 H64 H67 H68
6	H93 H94 H97 H98 H101 H102 H105 H106
7	H71 H72 H75 H76 H79 H80 H83 H84 H87 H88
8	V2 V4 V6 V8 V38 V40 V42 V44 V47 V49 V51 V53 V83 V85 V87 V89
9	V20 V22 V24 V26 V65 V67 V69 V71
10	V10 V12 V14 V16 V18 V28 V30 V32 V34 V36 V55 V57 V59 V61 V63 V73 V75 V79 V81
11	H1 H2 H5 H6 H9 H10 H13 H14 H17 H18 H21 H22 H25 H26 H29 H30 H33 H34 H37 H38 H41 H42 H45 H46 H49 H50 H53 H54 H57 H58 H61 H62 H65 H66 H69 H70
12	H77 H78 H73 H74 H81 H82 H85 H86 H89 H90

The effective loads are different for hoop tendons and vertical tendons. For the hoop tendons the tension applied to the end of the tendon is F_h = 453300 N. For the vertical tendon the applied tension at the end of the tendon is F_v = 503100 N.

All formulas to describe shrink of concrete, creep of concrete and lost of tension along a tendon are coming from the French standard BPEL99. Coefficients used for these formulas are the following:

Ff = 0,18	coefficient of angular friction
Phif = 0,002	coefficient of linear friction
Ganc = 0,008 m	seating loss
Rmu0 = 0,43	relaxation coefficient of irons
Fprg = 1978 MPa	ultimate strenght of tendon
Rh10 = 1,5	relaxation at 1000 hours in %

The prestressing of the containment starts 180 days after the end of the building of the containment. Tensioning of group of tendons takes place every 5 days and the containment can creep for another period of 125 days before the Limit state Test. We will use " this last date as the "end of the prestressing period".

3 Results of prestressing state

Displacements, loads in tendons and stresses in concrete and in the liner are shown hereafter.

3.1 Displacements after prestressing

The following figure presents the measured values of radial displacements during the building of the mock-up at elevation 4.860 meter from the top of the basemat.

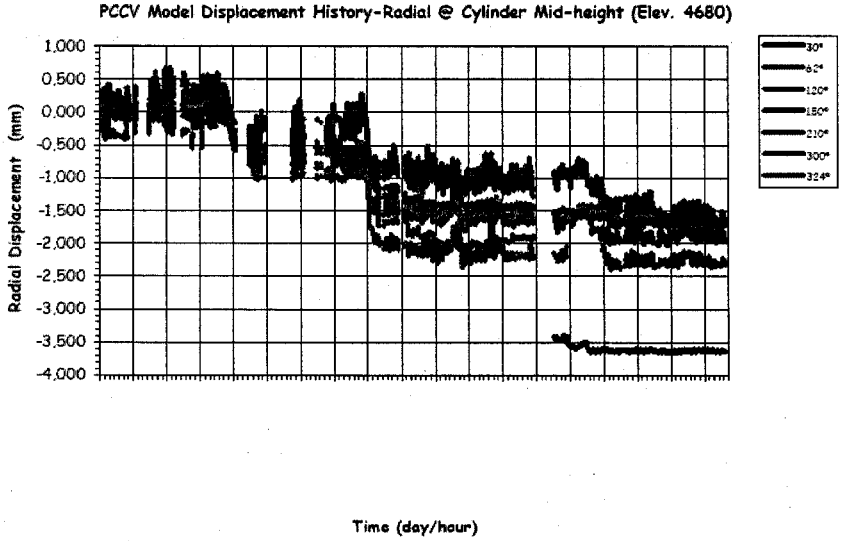

If we consider the maximum values for displacements measured on the mock-up, we obtain:

30°	62°	120°	150°	210°	300°	324°
4680	4680	4680	4680	4680	4680	4680
-2,030E+00	-1,770E+00	-1,730E+00	-1,710E+00	-3,660E+00	-1,760E+00	-2,400E+00

As it can be seen from figure 25 the computation leads to the same profile of distribution along azimuth and values are of the same order. Computation leads to a maximum value of 4mm for radial displacement at this elevation in front of 3.66mm. The Fig 24 presents the initial mesh and the deformed one after prestressing. The figure 25 is an isovalue of computed radial displacements for the containment after prestressing.

3.2 Tensions along tendons

The following tables give maximum, mean and minimum computed load for each tendon. The three first tables are for vertical tendons and next ones are for hoop tendons.

Group	tendon	Minimum tension(N)	Mean tension (N)	Maximum tension(N)	Group	tendon	Minimum tension(N)	Mean tension (N)	Maximum tension (N)
2	1	300019	376556	434065	3	1	334755	403216	430225
	2	320414	391775	433236		2	334798	403290	429818
	3	328655	396079	434309		3	333882	403205	430203
	4	323287	387681	424530		4	310250	383593	431428
	5	332137	400990	430912		5	333034	398572	431503
	6	341750	401109	433760		6	323485	391522	431452
	7	343291	402597	432672		**move**	**328367**	**397233**	**430772**
	8	334169	403391	433717		**mini**	**310250**	**383593**	**429818**
	9	338722	404181	431166		**maxi**	**334798**	**403290**	**431503**

10	344444	402557	431118
11	343969	401524	431041
12	333732	400700	430956
13	284743	370825	430825
14	280585	371020	430849
15	282583	372585	430857
16	289537	375929	430918
moye	**312289**	**387415**	**430966**
mini	**280585**	**370825**	**424530**
maxi	**344444**	**404181**	**434309**

Prestressing of groups 2 and 3 for vertical tendons

Group	tendon	Minimum tension(N)	Mean tension (N)	Maximum tension (N)	**Group**	tendon	Minimum tension(N)	Mean tension (N)	Maximum tension (N)
4	1	306891	383075	437933	8	1	320244	396468	451811
	2	315723	389293	432213		2	333767	407313	452011
	3	338587	404562	436420		3	339977	408768	444691
	4	344453	407189	432556		4	314643	390796	443919
	5	344130	406977	432526		5	345184	415314	434529
	6	343614	407104	432099		6	346147	415899	434589
	7	343369	407069	432034		7	357836	416344	451980
	8	344182	406900	432370		8	358924	417654	451662
	9	344088	407019	432466		9	349733	417766	440686
	10	343595	406715	432520		10	357442	416531	440340
	11	343749	406499	432505		11	356295	415790	439761
	12	335243	406206	432457		12	345490	414976	439854
	13	336046	406071	432367		13	303706	384992	439970
	14	335735	406175	432430		14	298685	384746	439771
	15	334307	402328	432411		15	301218	386389	439958
	16	325098	394111	432458		16	299019	386669	440500
	17	306344	382433	432468		**moye**	**326449**	**400982**	**440105**
	18	333120	401129	432432		**mini**	**298685**	**384746**	**434529**
	19	324445	392948	427724		**maxi**	**358924**	**417766**	**452011**
	20	335680	400843	428112					
	21	310392	381780	421832					
	22	314682	386563	425942					
	23	293700	379181	432430					
	24	289187	374851	432307					
	moye	**313444**	**387466**	**429156**					
	mini	**289187**	**374851**	**421832**					
	maxi	**344453**	**407189**	**437933**					

Prestressing of groups 4 and 8 for vertical tendons

Group	tendon	Minimum tension(N)	Mean tension (N)	Maximum tension (N)	Group	tendon	Minimum tension(N)	Mean tension (N)	Maximum tension (N)
9	1	353411	417069	439631	10	1	326593	400438	443527
	2	346753	417454	440971		2	339235	412382	444767
	3	346531	417447	440864		3	358758	422470	445221
	4	353387	417062	439485		4	358687	422432	445376
	5	336337	404555	440013		5	358567	422001	445392
	6	336138	406133	440383		6	358457	421996	445465
	7	345651	413288	440585		7	358612	422403	445243
	8	322049	397460	440560		8	358569	422386	444914
	moye	**342532**	**411309**	**440312**		9	358909	422460	444581
	mini	**322049**	**397460**	**439485**		10	349988	422419	443113
	maxi	**353411**	**417454**	**440971**		11	350107	422478	450005
						12	349844	422325	450264
						13	340857	414374	446551
						14	327198	403651	446646
						15	353438	419766	446650
						16	346289	413700	449120
						17	312727	391875	440900
						18	328412	402921	437344
						19	321368	396070	441376
						20	311444	393223	449975
						moye	**330217**	**404448**	**444820**
						mini	**311444**	**391875**	**437344**
						maxi	**358909**	**422478**	**450264**

Prestressing of groups 9 and 10 for vertical tendons

Group	tendon	Minimum tension(N)	Mean tension (N)	Maximum tension (N)	Group	tendon	Minimum tension(N)	Mean tension(N)	Maximum tension (N)
1	1	243656	306874	367344	5	1	249771	316371	377433
	2	244379	308034	368960		2	248599	315397	376776
	3	246895	308544	358041		3	244796	310879	371480
	4	247270	308166	358135		4	244109	309963	370921
	5	245568	303982	356254		5	239005	306254	367209
	6	242061	302523	355487		6	240162	305549	366613
	7	245020	299969	357464		7	231870	301011	364606
	8	245496	297731	355804		8	231791	299799	365157
	9	238609	290025	342464		9	234067	301847	363253
	10	239121	288198	334459		10	235704	300671	354342
	moye	**243755**	**299892**	**352264**		11	228603	300604	363031
	mini	**238609**	**288198**	**334459**		12	231554	297463	360902
	maxi	**247270**	**308544**	**368960**		13	218865	295365	360374
						14	222375	287934	360601
						15	211400	288456	359740
						16	222186	289635	349982
						17	188711	277083	356206
						18	213737	287716	357490

19	211017	285120	356242
20	210154	284596	357694
21	217381	293386	356662
22	226640	294444	358029
23	230298	299703	362388
24	236154	298283	360488
25	236430	301270	361565
26	236482	301142	363198
27	236121	300739	360883
28	236174	300634	363621
29	235844	300197	360222
30	235849	300082	362545
31	235437	299613	359534
32	235356	299486	361769
33	234972	299037	358890
34	234723	298952	360994
moye	**235560**	**299843**	**361057**
mini	**188711**	**277083**	**349982**
maxi	**249771**	**316371**	**377433**

Prestressing of groups 1 and 5 for hoop tendons

Group	tendon	Minimum tension(N)	Mean tension (N)	Maximum tension (N)	**Group**	tendon	Minimum tension(N)	Mean tension (N)	Maximum tension (N)
6	1	250278	313425	374316	7	1	240012	304566	364797
	2	250639	314255	375858		2	239894	304699	366640
	3	252470	314714	365149		3	240569	305257	365549
	4	252261	314155	365518		4	240568	305370	367320
	5	252271	310174	367845		5	241401	306335	366720
	6	250255	309638	363504		6	241519	306546	368489
	7	251280	305185	364801		7	242669	307870	368354
	8	249328	302996	359101		8	243032	308240	370164
	moye	**251098**	**310568**	**367012**		9	245088	310265	370811
	mini	**249328**	**302996**	**359101**		10	245687	310769	372556
	maxi	**252470**	**314714**	**375858**		**moye**	**242567**	**307582**	**368745**
						mini	**239894**	**304566**	**364797**
						maxi	**245687**	**310769**	**372556**

Prestressing of groups 6 and 7 for hoop tendons

Group	tendon	Minimum tension(N)	Mean tension (N)	Maximum tension (N)	**Group**	tendon	Minimum tension(N)	Mean tension (N)	Maximum tension (N)
11	1	258229	324538	386023	12	1	254456	320246	381470
	2	257681	324135	385835		2	254388	320267	382217
	3	255856	322209	383578		3	254547	320388	381634

	4	255541	321863	383474
	5	254218	320342	381557
	6	254036	320102	381626
	7	247418	317515	380222
	8	252526	317061	380465
	9	245406	315593	379474
	10	251840	316936	380463
	11	251811	317009	379331
	12	251637	314761	378619
	13	242292	314520	378426
	14	244663	311923	378461
	15	225902	307735	378234
	16	234774	305609	378403
	17	220341	301836	367722
	18	229677	305639	375646
	19	222362	299325	375146
	20	224152	300939	375698
	21	228052	304931	375238
	22	229075	301931	375792
	23	243096	314492	368489
	24	245010	313502	375968
	25	245410	315864	379027
	26	251505	315922	378331
	27	251615	317476	378613
	28	251630	317406	379925
	29	251304	317007	378078
	30	251262	316909	379375
	31	250883	316383	377387
	32	250744	316241	378536
	33	250228	315551	376465
	34	250061	315397	377503
	35	249362	314554	375385
	36	249014	314396	376372
	moye	**250357**	**315805**	**377388**
	mini	**220341**	**299325**	**367722**
	maxi	**258229**	**324538**	**386023**

4	254542	320443	382371
5	254780	320707	381991
6	254813	320771	382679
7	255299	321292	382618
8	255420	321398	383278
9	256336	322203	383584
10	256502	322365	384165
moye	**255280**	**321196**	**382790**
mini	**254388**	**320246**	**381470**
maxi	**256502**	**322365**	**384165**

Prestressing of groups 11 and 12 for hoop tendons

From all these values we can see that there is a good homogeneity in the tension of all tendons. Figures 27 to 34 present tensions along tendons H11, H35, H53, H67, H68, V37, V46 and V85.

3.3 Stresses in concrete

Results show a good uniform state of stresses in the concrete as expected.

The following table present a summary of maximum and minimum computed values of stresses at the end of prestressing period.

	Minimum value (MPa)	Maximum value (MPa)
Radial stresses	-7,4	2,0
Hoop stresses	-14	0,1
Meridional stresses	-8,85	2,5
Principal stress 1	-2,9	4,2
Principal stress 2	-6,25	1,0
Principal stress 3	-13,2	2,5

Summary table for stresses in the concrete

Values obtained in normal zones are in agreement with the value of the tension of tendons. Figures 35 to 36 present a visualisation of the stresses state in the concrete.

3.4 Stresses in the liner

The following table presents a summary of the computed stresses in the liner.

	Minimum value (MPa)	Maximum value (MPa)
Principal stress 1	-147	-12,5
Principal stress 2	-250	-28

It appears that the liner is everywhere in a compressive state.

3.5 Conclusion for prestressing computation

The computed prestressed state has displacements a bit higher than in experiment and tensions of tendons a bit smaller than in experiment. Stresses are also a little too small. All this may be explained by the use of the French BPEL99 rules for creep and shrink. The quality of concrete in front of creep and shrink has been taken from French rules and this seems to over estimate the creep and the shrink of the concrete.

Another difference in the computation in front of experiment is that the computation considers that as soon as a tendon is in tension it is sealed in the concrete.

Nevertheless the computed prestressed state of the containment seams to be in a good agreement with the experiment. This state will be used, as an initial state, to perform the Limit State Test.

4 Limit State Test computation

The already computed prestressed state of the containment is used as initial state at the beginning of the increasing of pressure.

4.1 Loads

Starting from the initial state computed after the prestressing of the concrete, an inside pressure, given by air pressure, increase up to 1,295 MPa as in the experimental test. Looking at results, and especially at curve 14 giving radial displacement just nearby the Equipment Hatch, we have noticed that we have applied the pressure on the surface of the hatch in the wrong way. This affects the local results but is not important for global results.

4.2 Analysis of results

The beginning of the cracking of concrete is around 0.67 MPa, which is in a good agreement with experiment. First cracks appear at the junction of the cylindrical wall and the basemat.

After this level of pressure it seems that the response of the structure is more or less the response of tendons and irons.

At a level of 1,2 MPa a new type of behaviour takes place. In the experiment this appears at a level of 1,05 MPa.

We can notice that the change of behaviour in the experiment is slow while it seems to be sharper in the computation. This may come from the perfect connection between irons and concrete in the computation while in the reality this connection breaks here and there for high level of pressure.

In the computation, the extremity of a tendon is not well represented because the end node is attached in the concrete and it creates local stresses that do not exist. Then results, in the concrete along buttress are not workable.

Results are plotted for two different pressure levels, after the beginning of cracking and at the end of the computation for a pressure of 1,295 MPa (Figures 43 to 59).

A series of curves (displacements, deformations, loads) comparing computation and experiment are also given.

4.2.1 Displacements

Looking at curves 1 to 15 we can notice that displacements for node, which are near the basemat, are not very good. This is because the computation considers that all nodes at the bottom of the basemat have a zero displacement in the axial direction. For that reason all results for nodes too close to basemat are not very good. In another hand, values of displacements are not very large and this may not influence the global behaviour of the structure. Starting with curve 3 at an elevation of 1,43 metre results have the same shape than experimental ones.
For most of the curves displacements at the starting of loading are higher than experimental ones. This can be explaining by the fact that the creep given by French rules BPEL99 with French coefficients taken for south of France are not valid for Sandia experiment.

Looking at curve 10 we can see that computation follows pretty well the general behaviour of the dome.
Curve 14 which gives radial displacements at nodes just by Equipment hatch, shows clearly that in the computation, pressure was not applied in the rigth direction.

4.2.2 Deformations

Again all results concerning rebars too close to the basemat are not easy to compare. For others rebars, by example curve 24 for a rebar at an elevation of 10,75 metre results are in a good agreement with experimental results. In this curve it can be seen that creep during prestressing is too important.

It must be pointed here that, in the computation, rebars are perfectly clamped in the concrete. This fact in conjunction with the fact that the cracking concrete behaviour is a smeared one induced that results along a rebar can be very different for one point to another one.

For the curves giving deformations in the hoop direction we find the type of curve giving radial displacements which is obvious and which is not so clear for experimental results.

4.2.3 Tensions in tendons

In the computation tendons are perfectly clamped in the concrete and therefore no redistribution of tensions occurs in the computation. This explains the oscillations observed in curves (Fig 55 - 56 - 57).
At the beginning of the LST the general level of tensions of tendons are a little too small. This is also due to the excessive creep during prestressing of the concrete.

4.2.4 Cracks

The first change of response of the structure can be observed around 0,67 MPa, this is due to the first cracks in the concrete. As we have taken the OTTOSEN model for concrete, which is a smeared one, we can observe that cracks concern often one row of elements out of two.

At a level of 0,71 MPa we can clearly observed vertical cracks due to excessive hoop stresses, especially in the region between the two penetrations (Fig 50)

If we do not consider results around buttress, the main crack, even at a level of pressure of 0,71MPa, is between the two penetrations which is the failure point during experimental test. The computation is able to predict where the failure will occur.

5 Conclusion

The computation of a prestressed concrete containment vessel has been conducted through a pressure of 1,295 MPa. The mesh is 3D with very little simplifications of concrete part or irons part. There are 700 000 degrees of freedoms in the structure and the computation with

Cast3m has been possible because of all improvments made these three last years under the direction of IRSN .
First, the prestressing is computed using French regulatory rules for creep and shrinkage. For this part, the prestressing has been applied in twelve steps and results are in a good agreement with experimental data's.
Then the limit state test, consisting in increasing internal pressure, is computed up to the end of the experiment. After a long computation (1 000 000 seconds CPU) results are in a good range in front of experimental results. The prediction of the failure mode seems to be possible from the computation.

LIST OF FIGURES

LIST OF COMPARISONS EXPERIMENT / COMPUTATION

Curve 1	Displacement vertical	AZ 135	el	0.0	m	outside cylinder
Curve 2	Displacement radial	Az 135	el	0.25	m	inside liner surface
Curve 3	Displacement radial	Az 135	el	1.43	m	inside liner surface
Curve 4	Displacement radial	Az 135	el	2.63	m	inside liner surface
Curve 5	Displacement radial	Az 135	el	4.68	m	inside liner surface
Curve 6	Displacement radial	Az 135	el	6.2	m	inside liner surface
Curve 7	Displacement radial	Az 135	el	10.75	m	inside liner surface
Curve 8	Displacement vertical	Az 135	el	10.75	m	inside liner surface
Curve 9	Displacement radial	Az 135	el	14.55	m	inside liner surface
Curve 10	Displacement vertical	Az 135	el	14.55	m	inside liner surface
Curve 11	Displacement vertical,	Az 135	el	16.13	m	inside liner surface
Curve 12	Displacement radial	Az 90	el	6.2	m	inside liner surface
Curve 13	Displacement radial	Az 90	el	10.75	m	inside liner surface
Curve 14	Displacement radial	Az 334	el	4.675	m	inside liner surface
Curve 15	Displacement radial	Az 66	el	4.525	m	inside liner surface
Curve 16	Rebar strain meridional	Az 135	el	0.05	m	inner rebar layer
Curve 17	Rebar strain meridional	Az 135	el	0.05	m	outer rebar layer
Curve 18	Rebar strain meridional	Az 135	el	0.25	m	inner rebar layer
Curve 19	Rebar strain meridional	Az 135	el	0.25	m	outer rebar layer
Curve 20	Rebar strain meridional	Az 135	el	1.43	m	inner rebar layer
Curve 21	Rebar strain meridional	Az 135	el	1.43	m	outer rebar layer
Curve 22	Rebar strain hoop	Az 135	el	6.2	m	outer rebar layer
Curve 23	Rebar strain meridional	Az 135	el	6.2	m	outer rebar layer
Curve 24	Rebar strain hoop	Az 135	el	10.75	m	outer rebar layer
Curve 25	Rebar strain meridional	Az 135	el	10.75	m	inner rebar layer
Curve 26	Rebar strain meridional	Az 135	el	10.75	m	outer rebar layer
Curve 27	Rebar strain hoop	Az 135	el	14.55	m	outer rebar layer
Curve 28	Rebar strain meridional	Az 135	el	14.55	m	inner rebar layer
Curve 29	Rebar strain meridional	Az 135	el	14.55	m	outer rebar layer
Curve 30	Rebar strain hoop	Az 90	el	0.05	m	inner rebar layer
Curve 31	Rebar strain meridional	Az 90	el	0.05	m	outer rebar layer
Curve 32	Rebar strain hoop	Az 90	el	6.2	m	outer rebar layer
Curve 33	Rebar strain meridional	Az 90	el	6.2	m	outer rebar layer
Curve 34	Liner strain meridional	Az 0	el	0.01	m	inside liner surface
Curve 35	Liner strain meridional	Az 0	el	0.01	m	outside liner surface
Curve 36	Liner strain meridional	Az 135	el	0.25	m	inside liner surface
Curve 37	Liner strain hoop	Az 135	el	0.25	m	inside liner surface
Curve 38	Liner strain meridional	Az 135	el	6.2	m	inside liner surface
Curve 39	Liner strain hoop	Az 135	el	6.2	m	inside liner surface
Curve 40	Liner strain meridional	Az 135	el	10.75	m	inside liner surface
Curve 41	Liner strain hoop	Az 135	el	10.75	m	inside liner surface
Curve 42	Liner strain meridional	Az 135	el	16.13	m	inside liner surface
Curve 43	Liner strain meridional	Az 90	el	6.2	m	inside liner surface
Curve 44	Liner strain hoop	Az 90	el	6.2	m	inside liner surface

Curve 45	Liner strain hoop	Az 334	el	4.675	m	inside liner surface
Curve 46	Liner strain hoop	Az 58	el	4.525	m	inside liner surface
Curve 47	base liner radial	Az 135	el	0.		100 mm inside cylinder
Curve 48	Tendon strain hairpin	Az 180	el	15.6	m	tendon V37
Curve 49	Tendon strain hairpin	Az 135	el	10.75	m	tendon V46
Curve 50	Tendon strain hoop	Az 90	el	6.58	m	tendon H53
Curve 51	Tendon strain hoop	Az 180	el	6.58	m	tendon H53
Curve 52	Tendon strain hoop	Az 280	el	6.58	m	tendon H53
Curve 53	Tendon strain hoop	Az 0	el	4.57	m	tendon H35
Curve 54	Tendon force hairpin	Az 241	el	-1.16	m	tendon V37
Curve 55	Tendon force hoop	Az 275	el	6.58	m	tendon H53

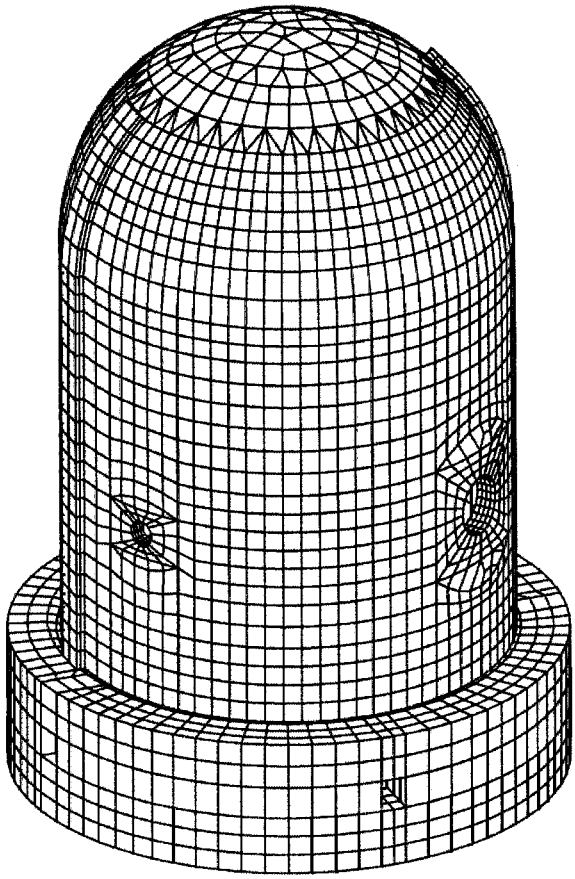

maillage beton 16384 elements 19736 noeuds

Fig 1: mesh of the concrete of the containment with basemat

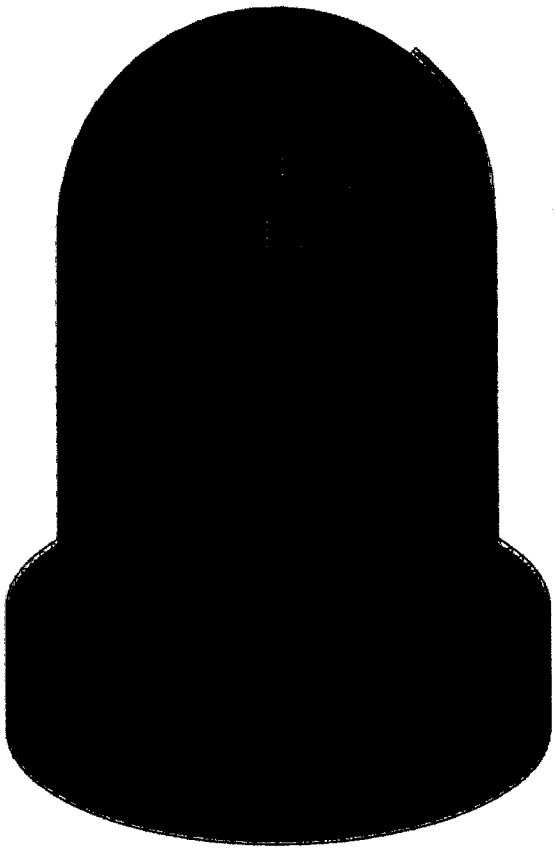

maillage des fers passifs 118556 elements 130525 noeuds

Fig 2: mesh of the irons!

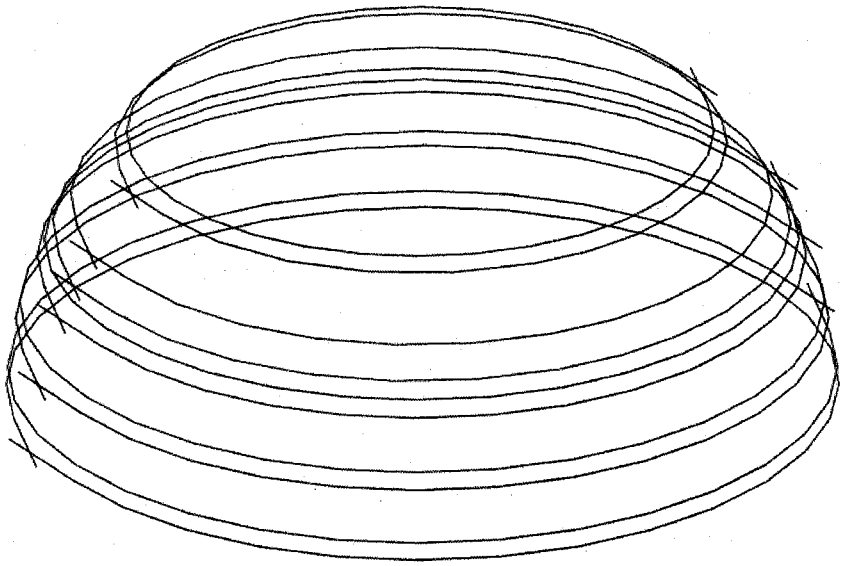

cables groupe 1, 666 elements 676 noeuds

Fig 3: mesh of first group of tendons

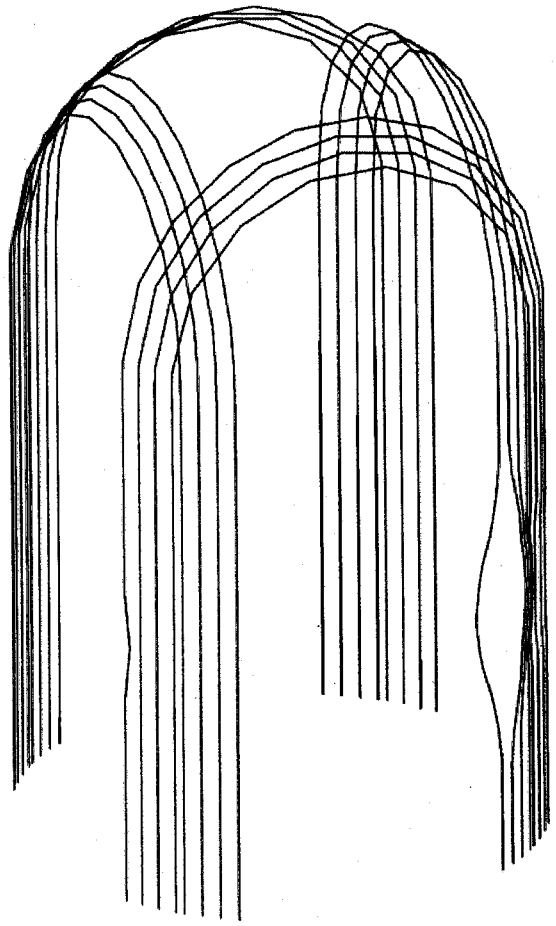

cables groupe 2, 1340 elements 1356 noeuds

Fig 4: second group of tendons

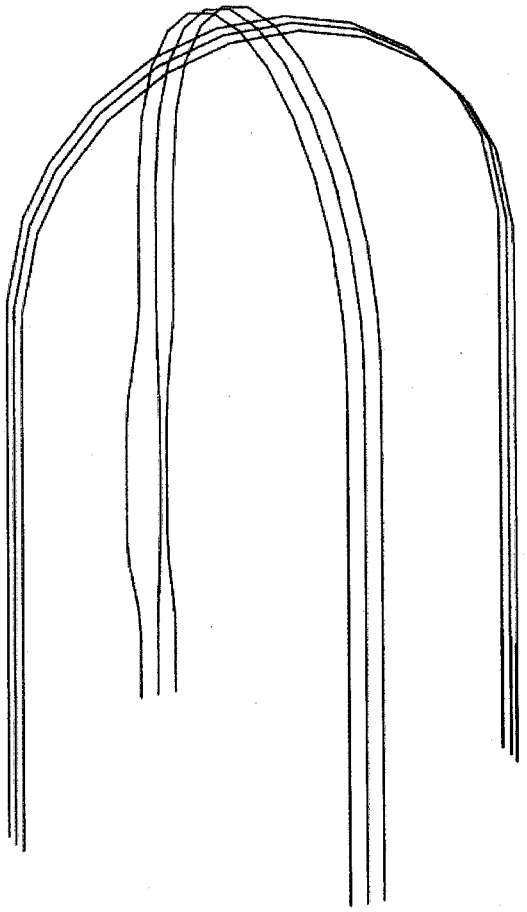

cables groupe 3, 513 elements 519 noeuds

Fig 5: Third group of tendons

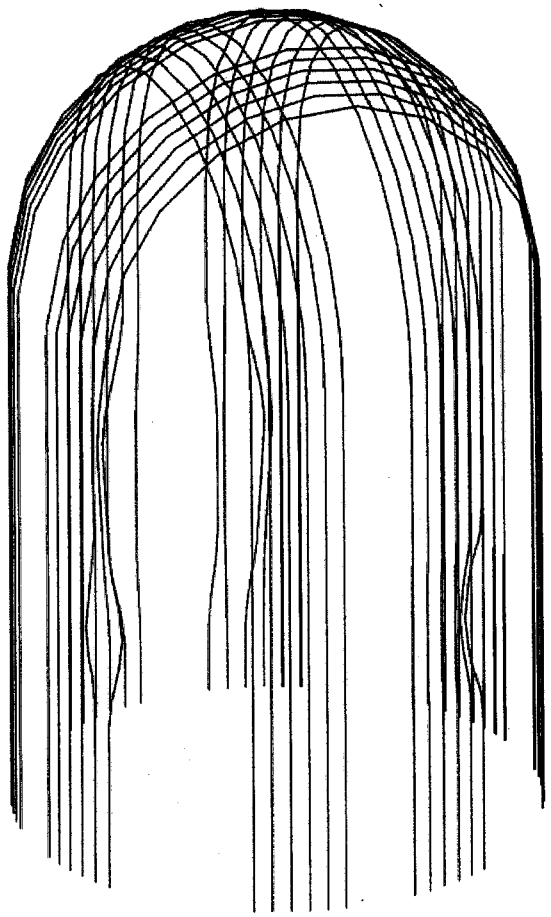

cables groupe 4, 2124 elements 2148 noeuds

Fig 6: Fourth group of tendons

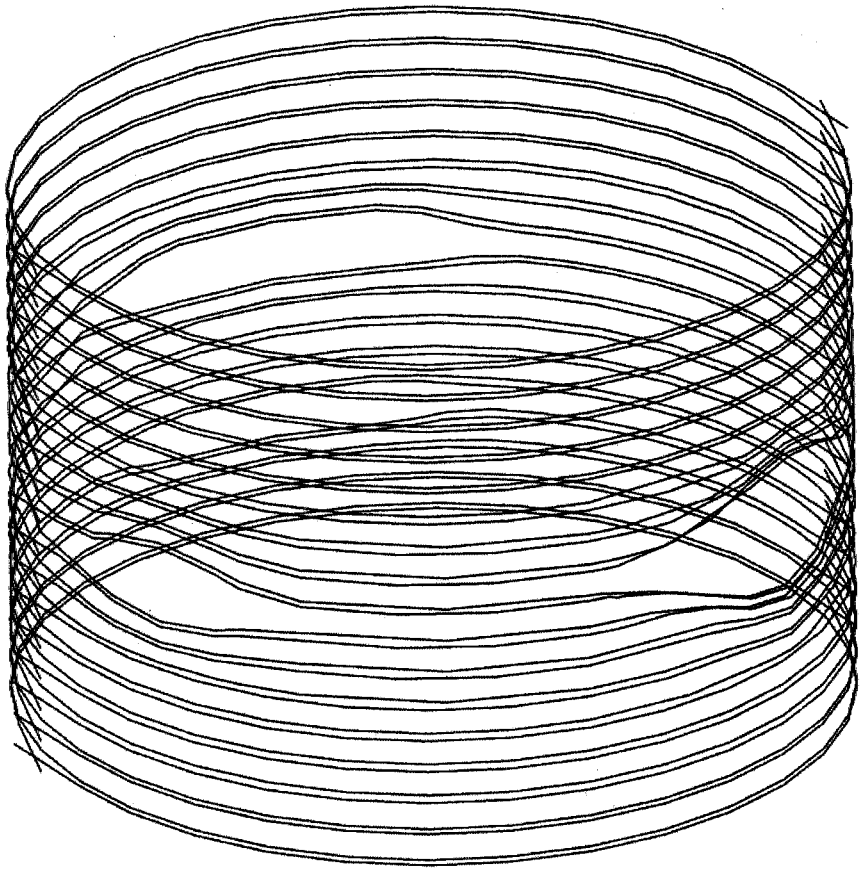

cables groupe 5, 2399 elements 2433 noeuds

Fig 7: Fifth group of tendons

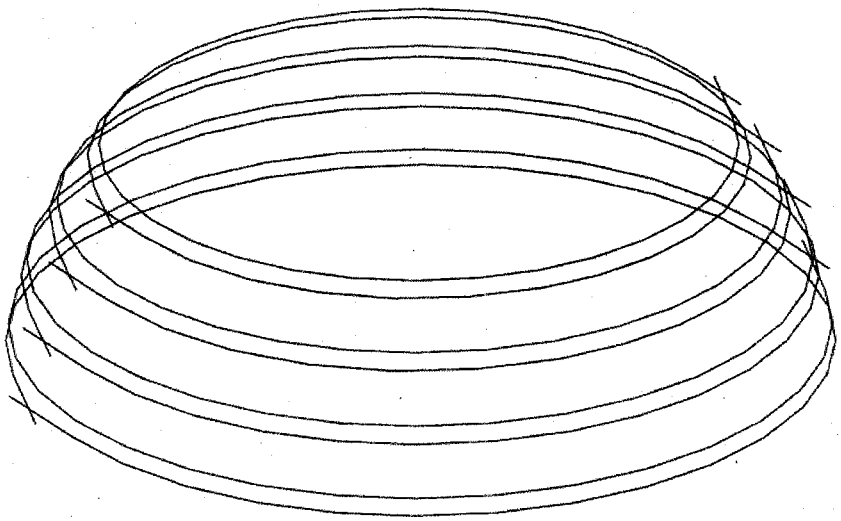

Fig 8: Sixth group of tendons

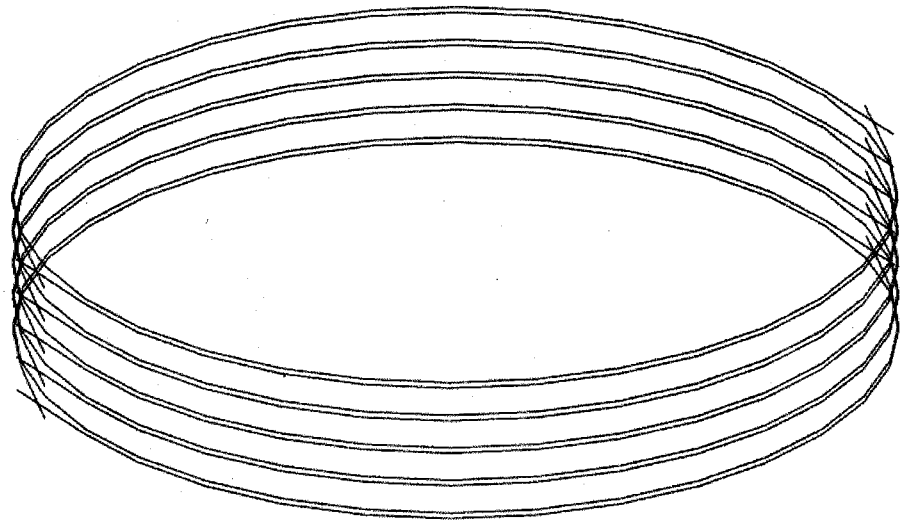

cables groupe 7, 660 elements 670 noeuds

Fig 9: Seventh group of tendons

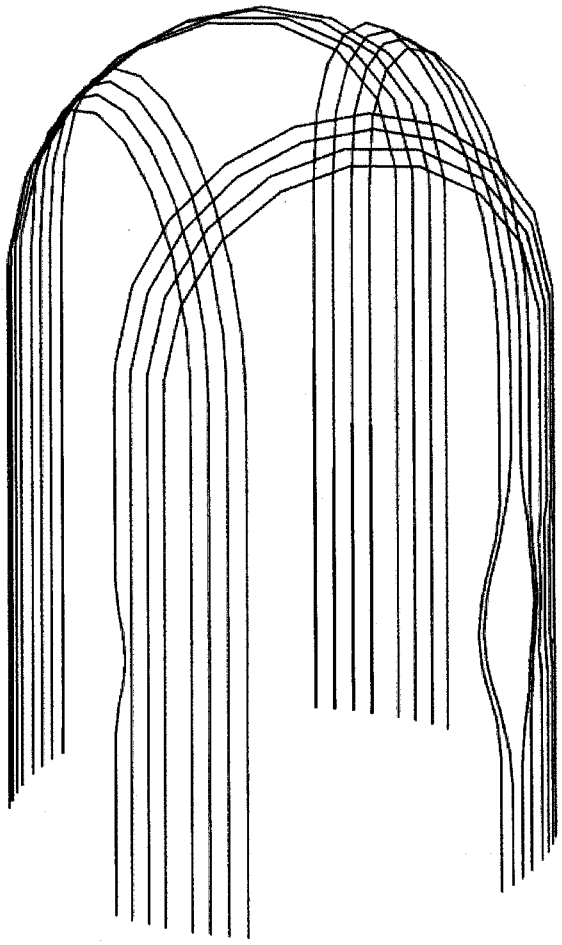

cables groupe 8, 1332 elements 1348 noeuds

Fig 10: Eighth group of tendons

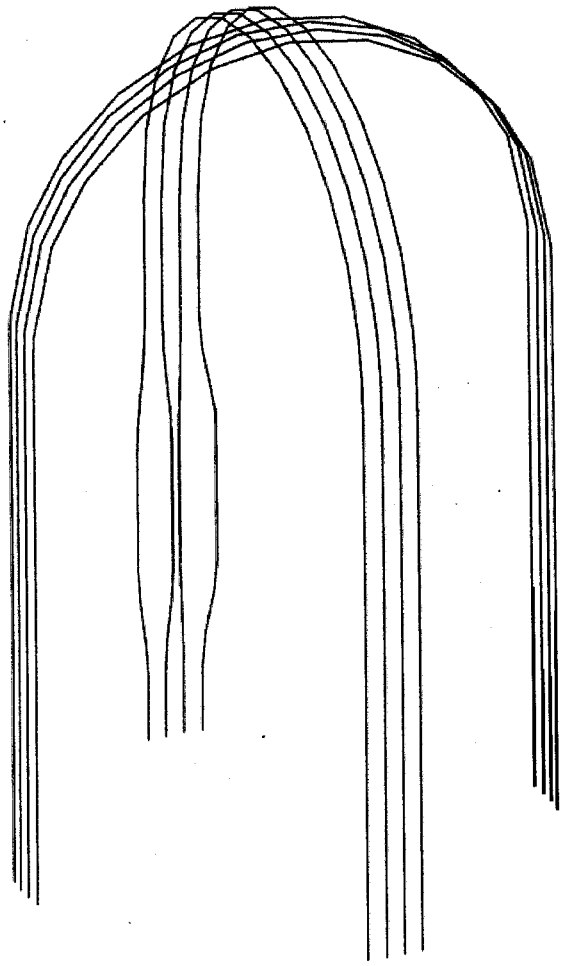

cables groupe 9, 690 elements 698 noeuds

Fig 11: Ninth group of tendons

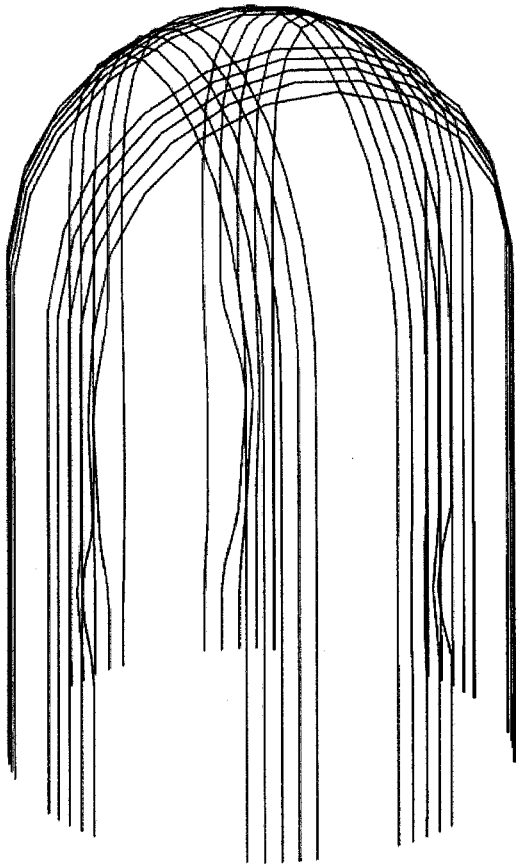

cables groupe 10, 1753 elements 1773 noeuds

Fig 12: Tenth group of tendons

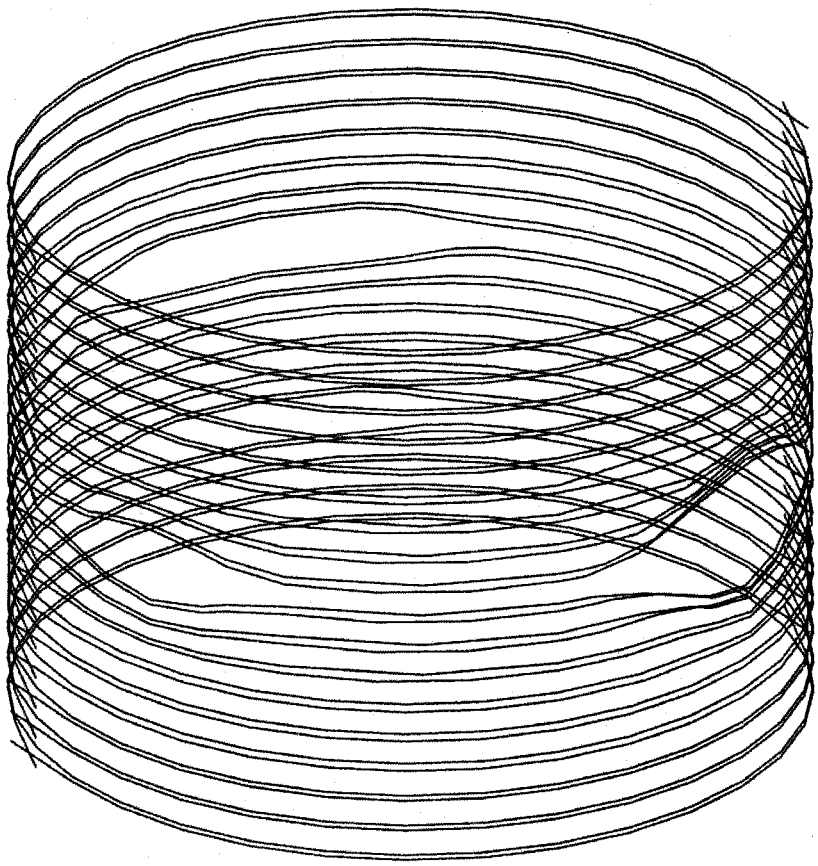

cables groupe 11, 2505 elements 2541 noeuds

Fig 13: Eleventh group of tendons

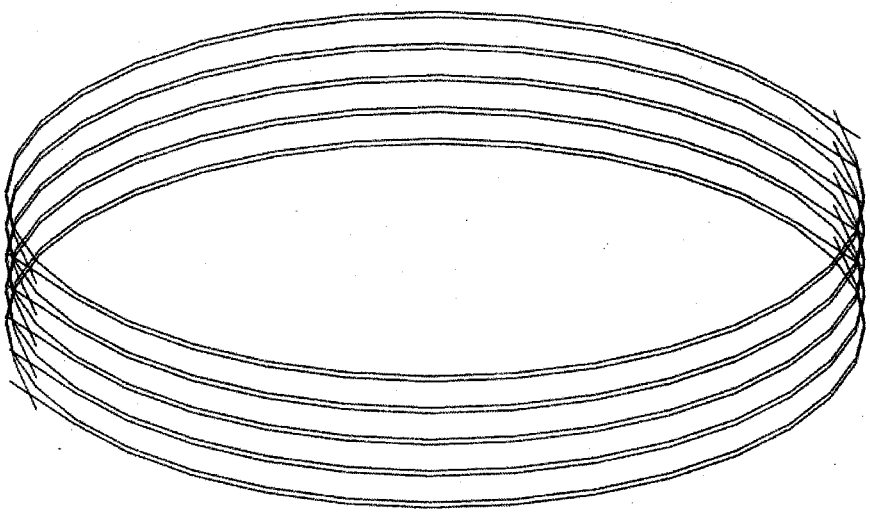

cables groupe 12, 660 elements 670 noeuds

Fig 14: Twelfth group of tendons

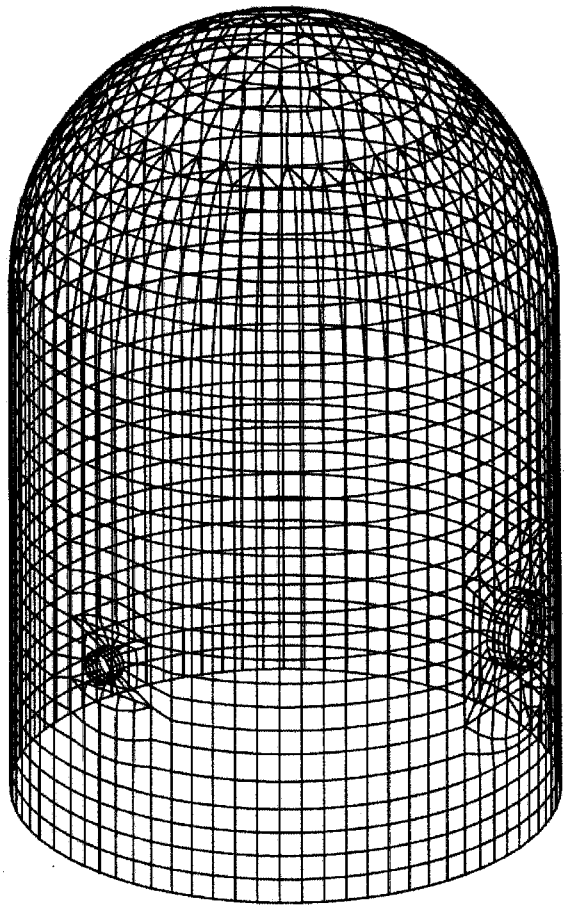

maillage de la peau 2694 elements 2672 noeuds

Fig 15: Mesh of the liner

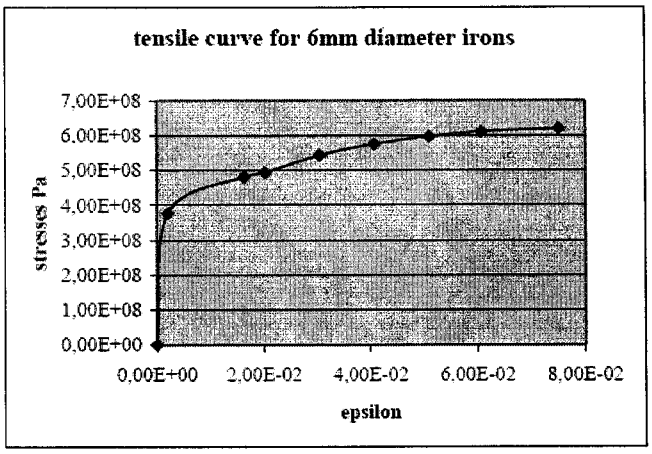

Fig 16: tensile curve for 6mm diameter irons

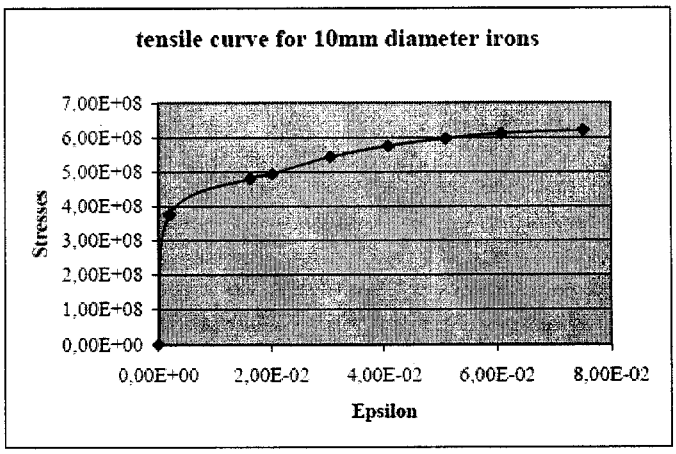

Fig 17: tensile curve for 10mm diameter irons

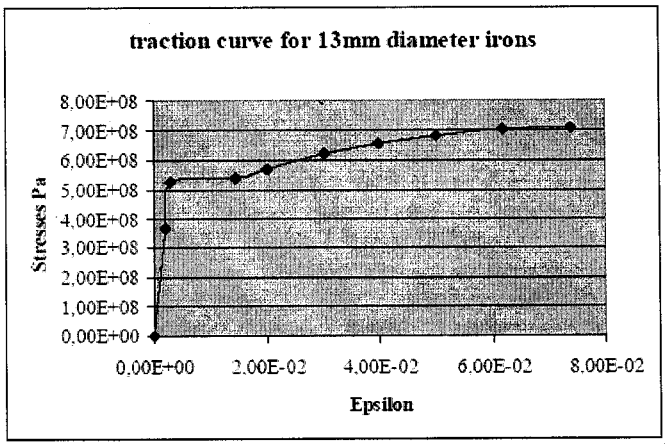

Fig 18: tensile curve for 13mm diameter irons

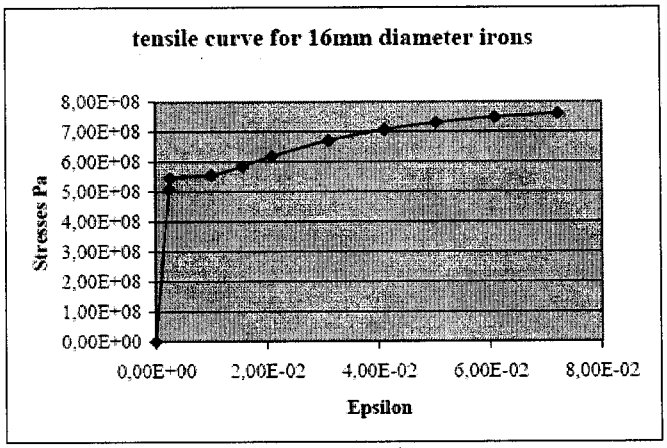

Fig 19: tensile curve for 16mm diameter irons

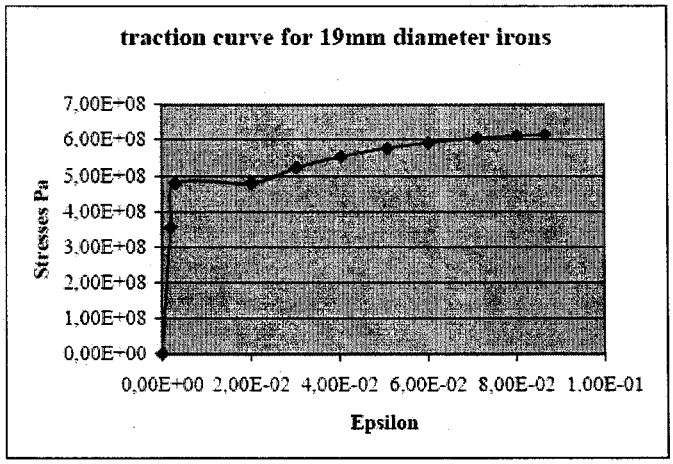

Fig 20: tensile curve for 19mm diameter irons

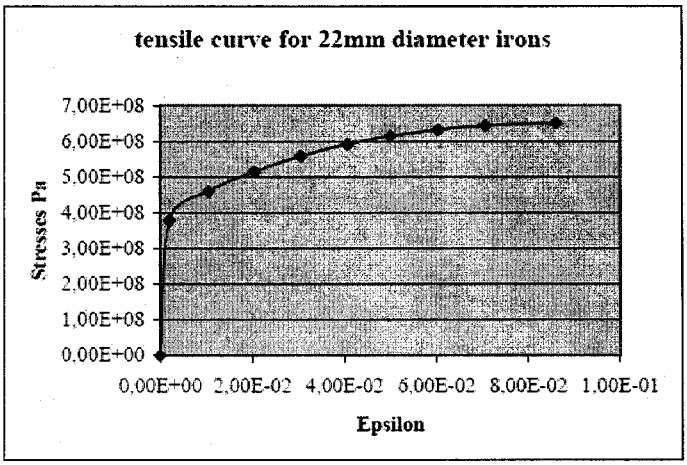

Fig 21: tensile curve for 22mm diameter irons

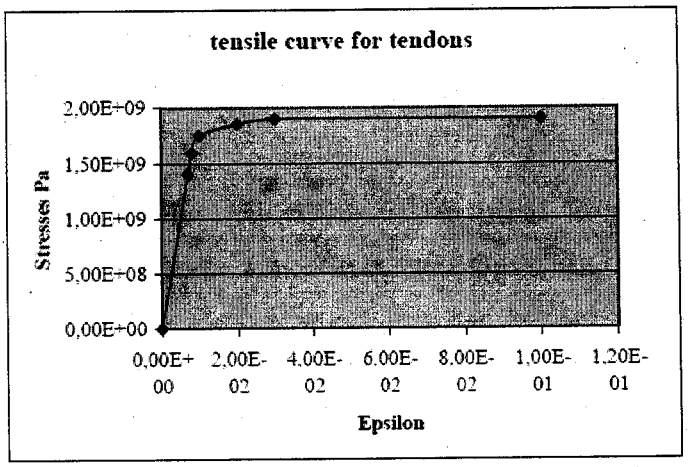

Fig 22: tensile curve for tendons

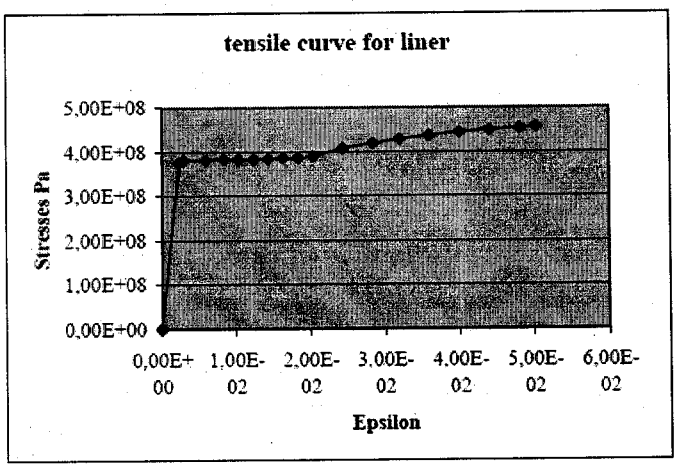

Fig 23: tensile curve for liner

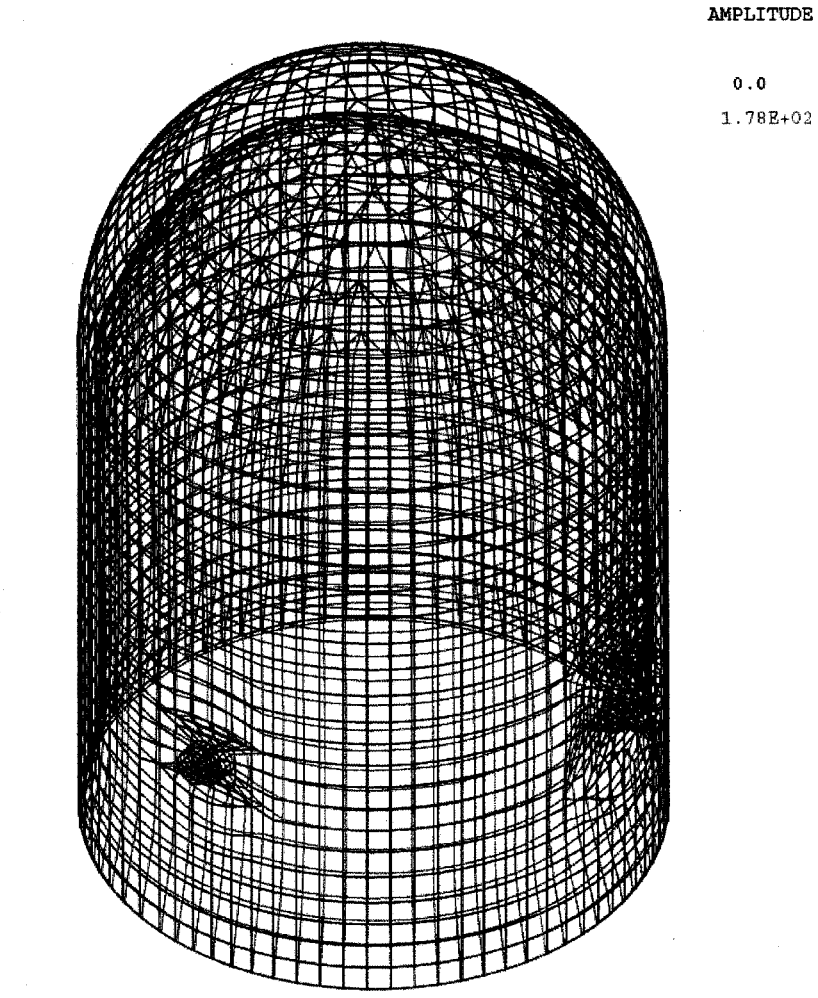

Fig 24: End of prestressing – initial mesh and final mesh

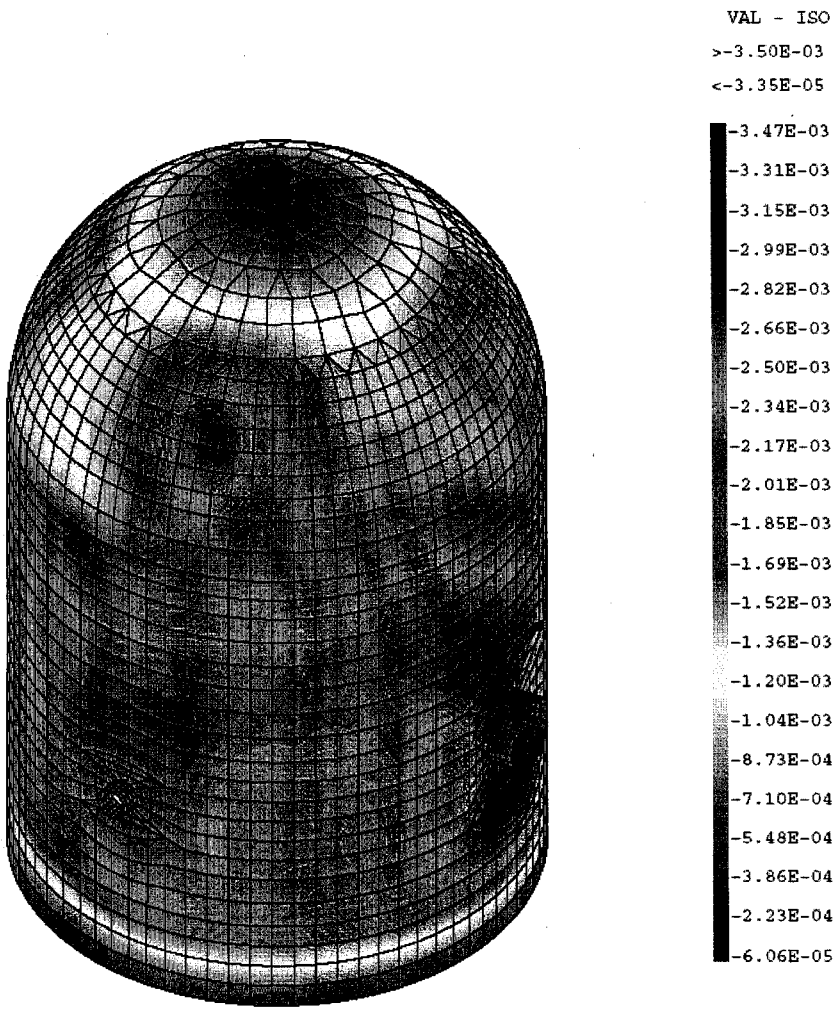

FIN PRECONTRAINTE - ISOVALEURS DE DEPLACEMENTS RADIAUX POUR LA PEAU

Fig 25: End of prestressing – radial displacements (mm)

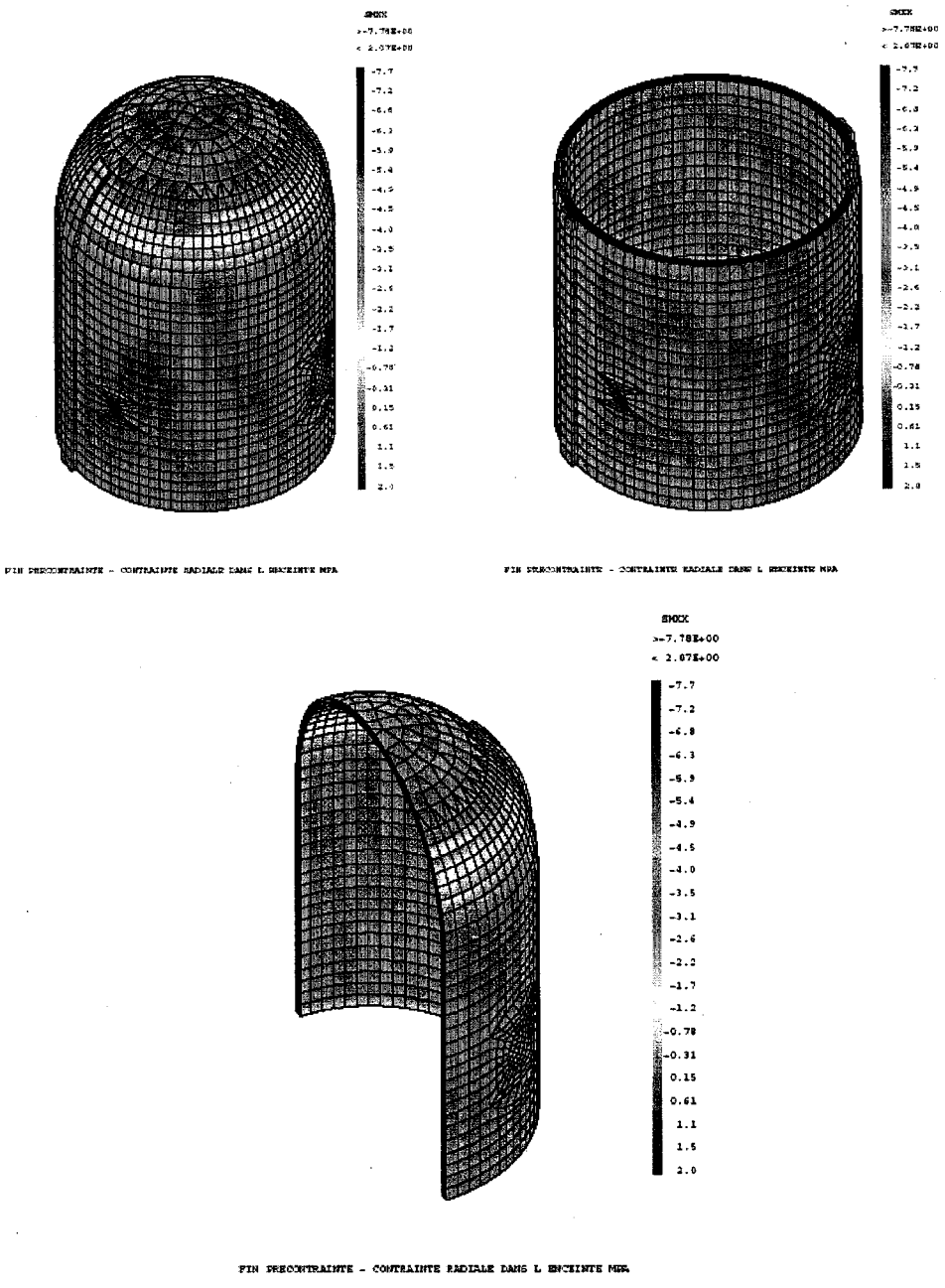

Fig 26: End of prestressing – Radial stresses in the concrete vessel

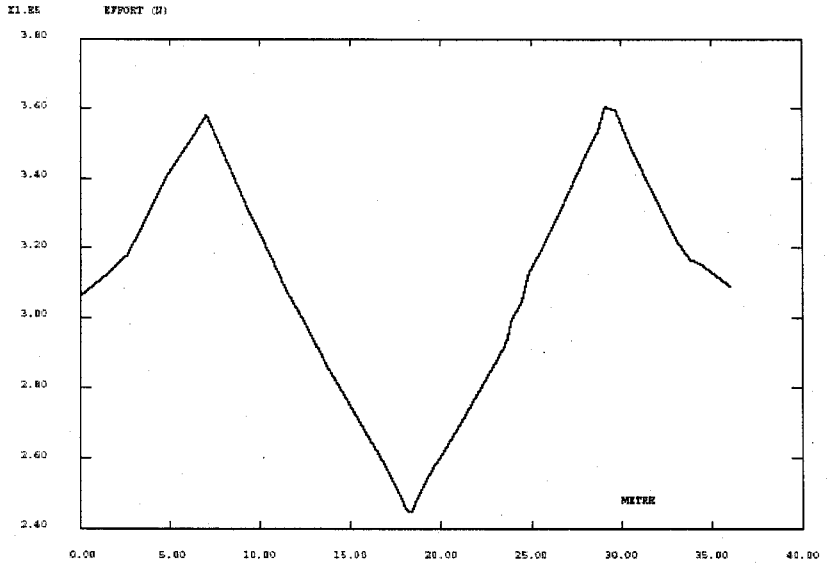

Fig 27: End of prestressing – tension of tendon H11 (N)

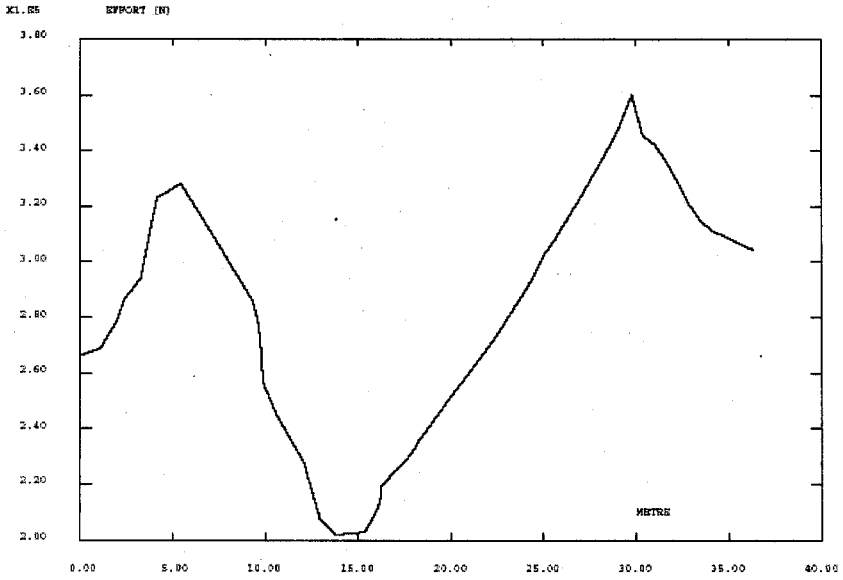

Fig 28: End of prestressing – Tension of tendon H35 (N)

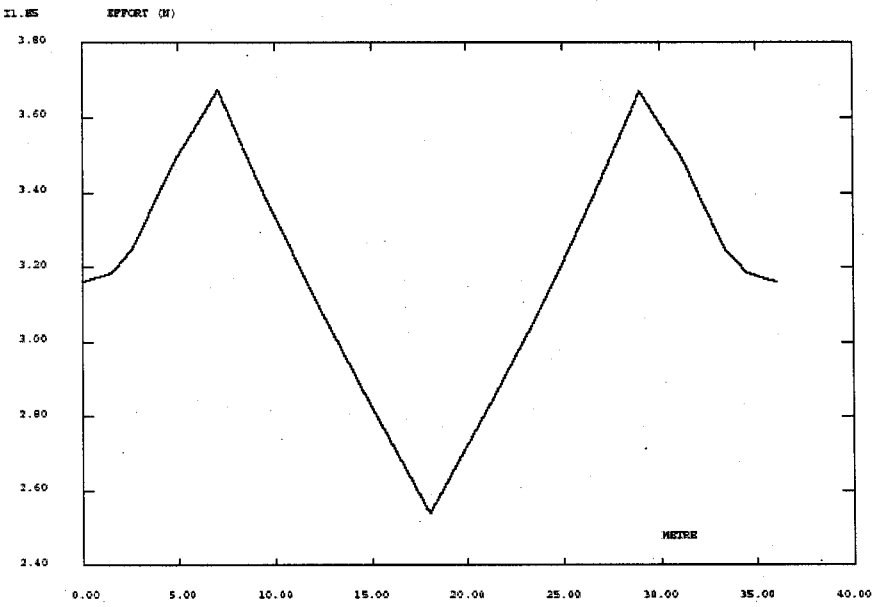

Fig 29: End of prestressing – Tension of tendon H53 (N)

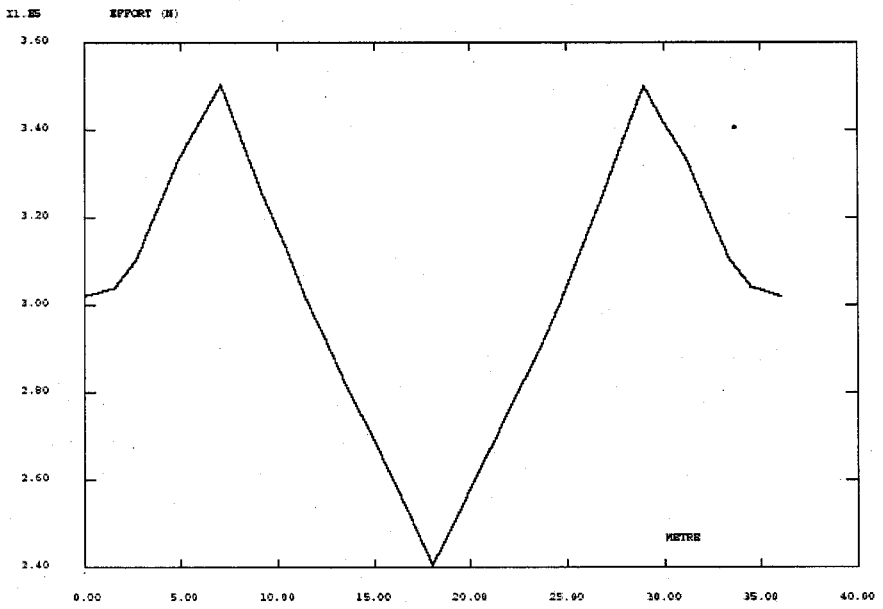

Fig 30: End of prestressing – Tension of tendon H67 (N)

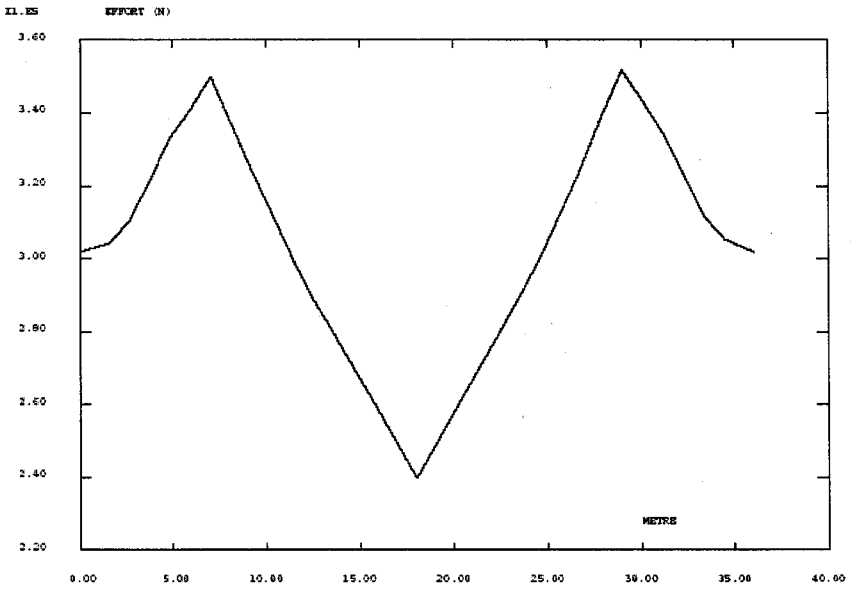

Fig 31: End of prestressing - Tension of tendon H68 (N)

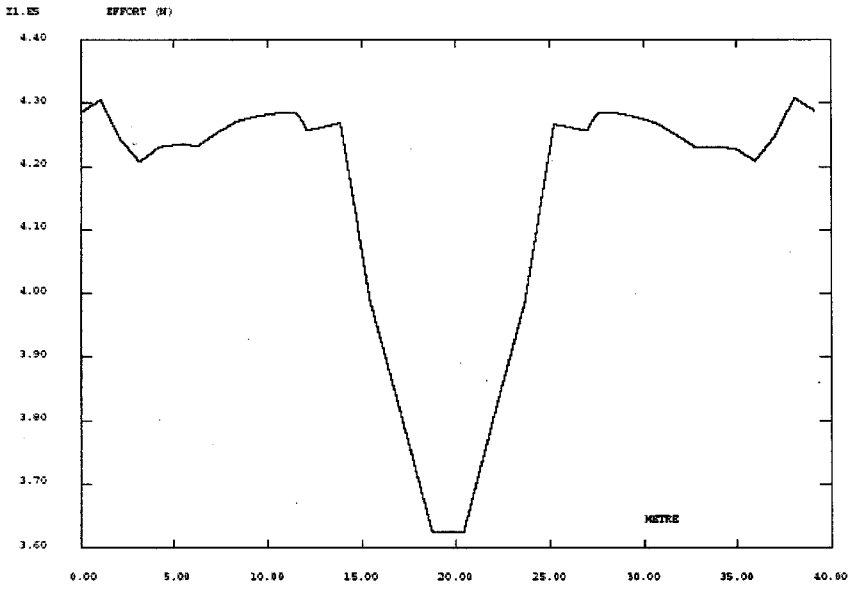

Fig 32: End of prestressing – tension of tendon V37 (N)

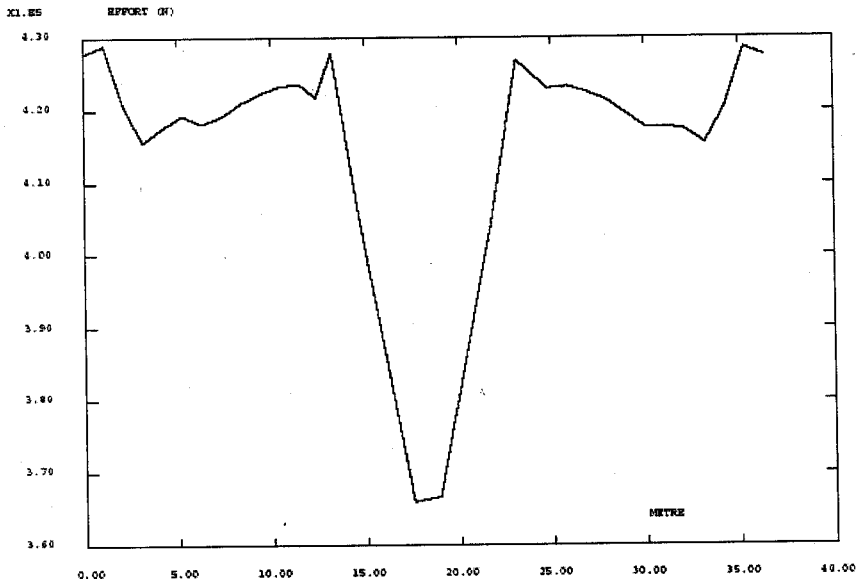

Fig 33: End of prestressing – Tension of tendon V46 (N)

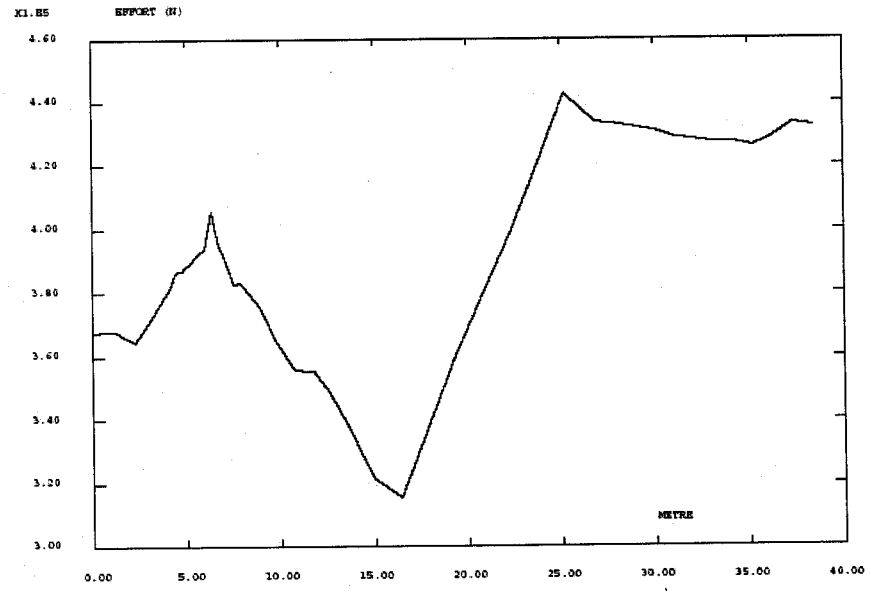

Fig 34: End of prestressing - Tension of tendon V85 (N)

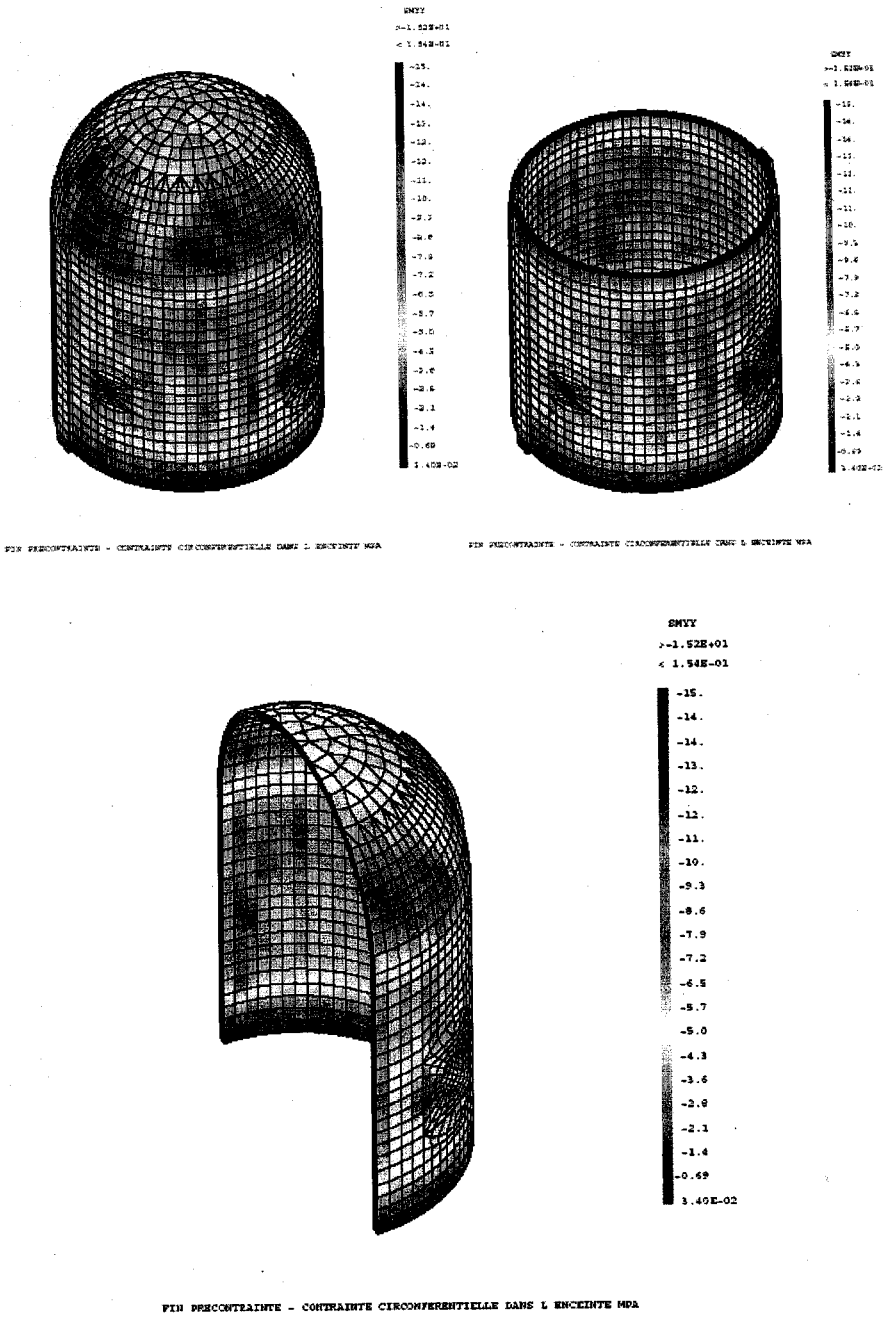

Fig 35: End of prestressing – Hoop stresses in the concrete vessel (MPa)

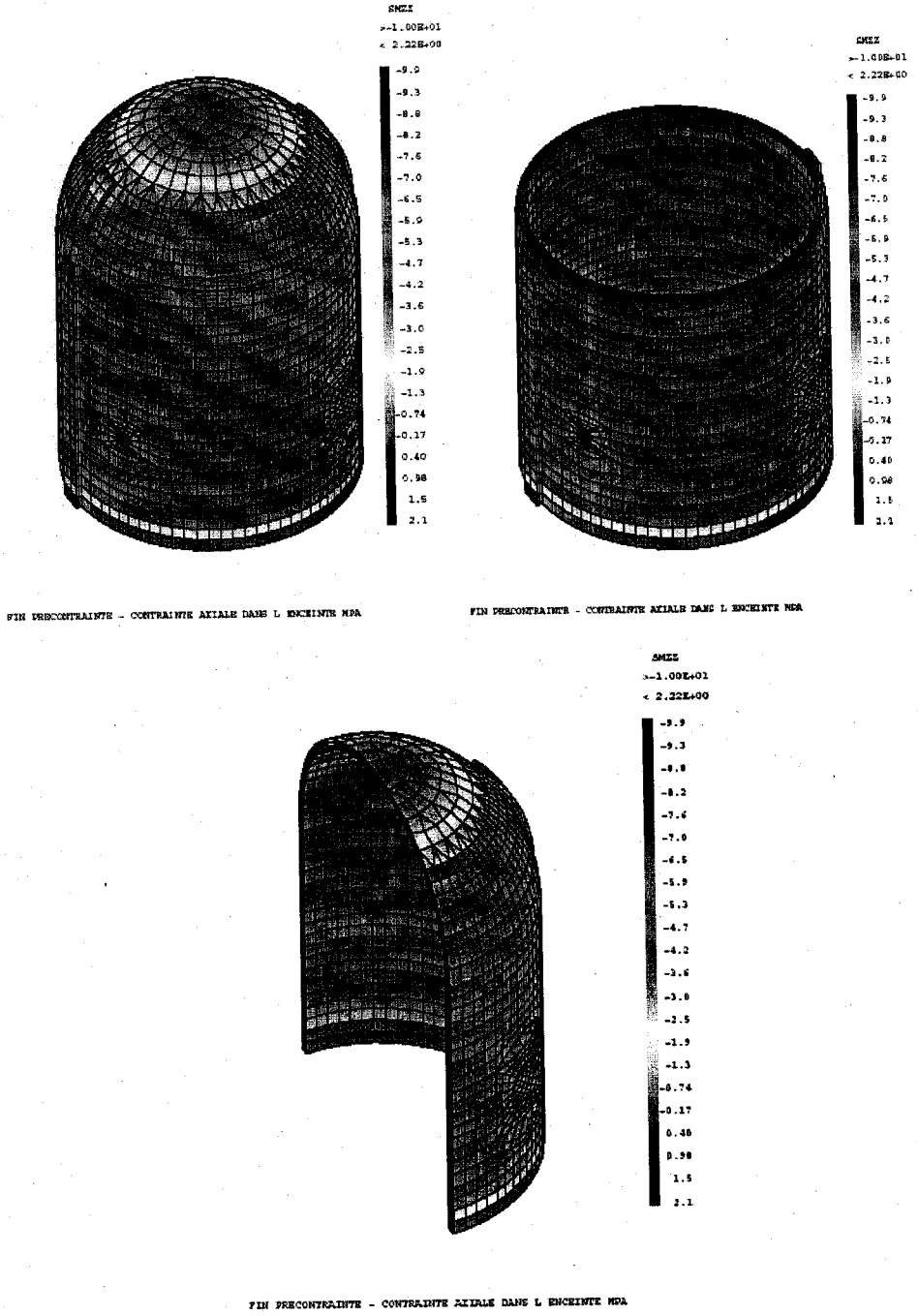

Fig 36: End of prestressing – vertical stresses in the concrete vessel (MPa)

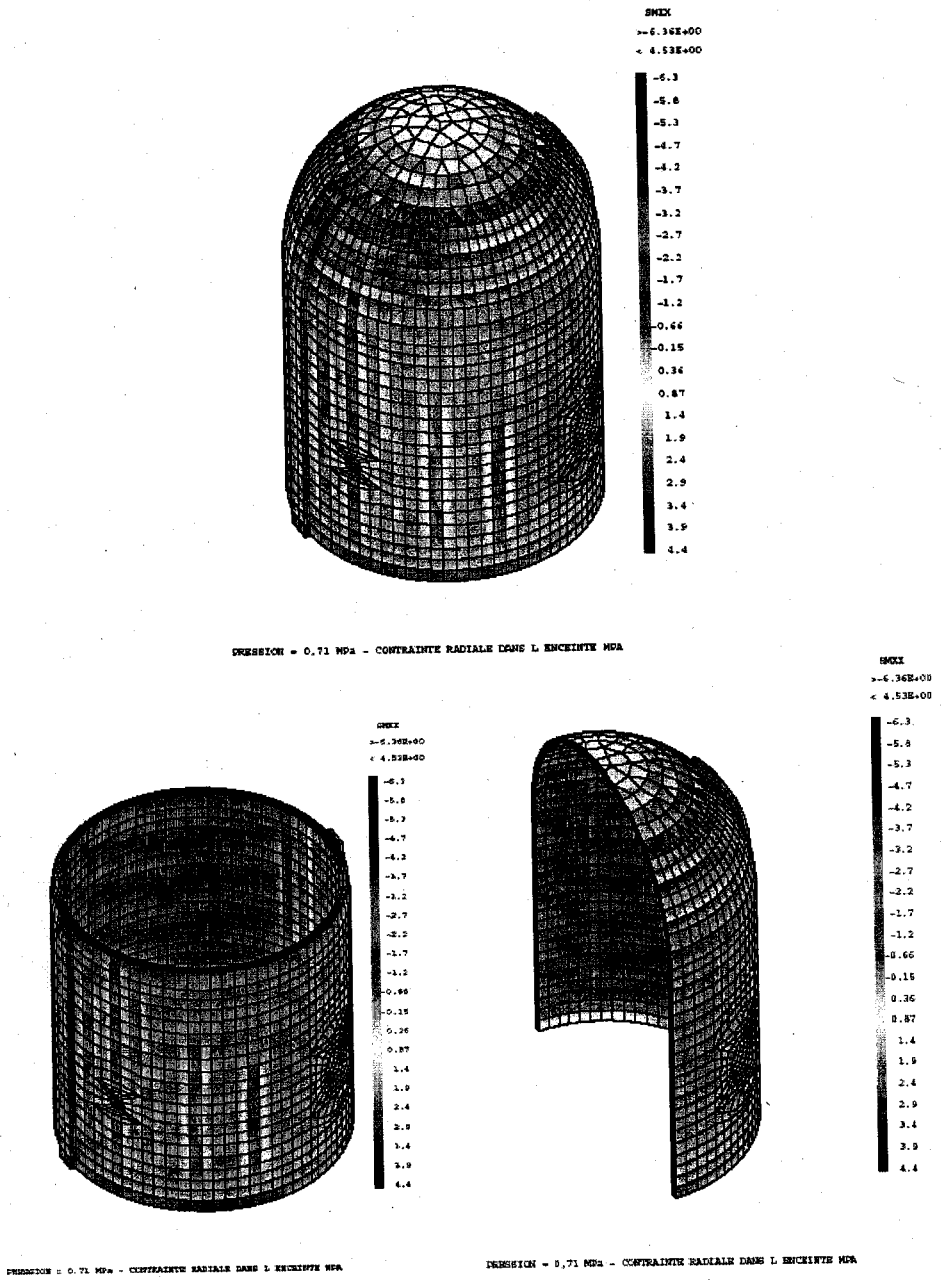

Fig 37: Pressure 0,71 MPa – Radial stresses in the wall (MPa)

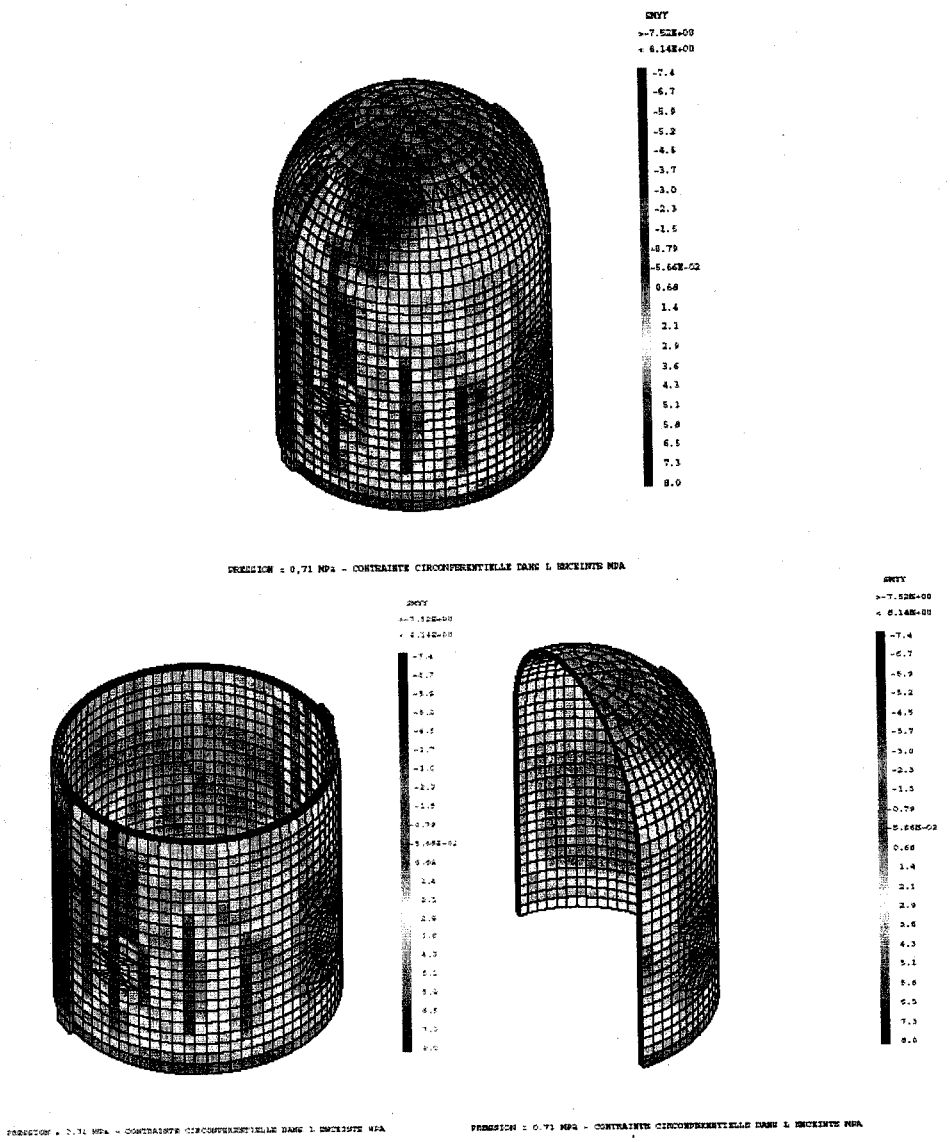

Fig 38: Pressure 0.71 MPa – Hoop stresses in the wall (MPa)

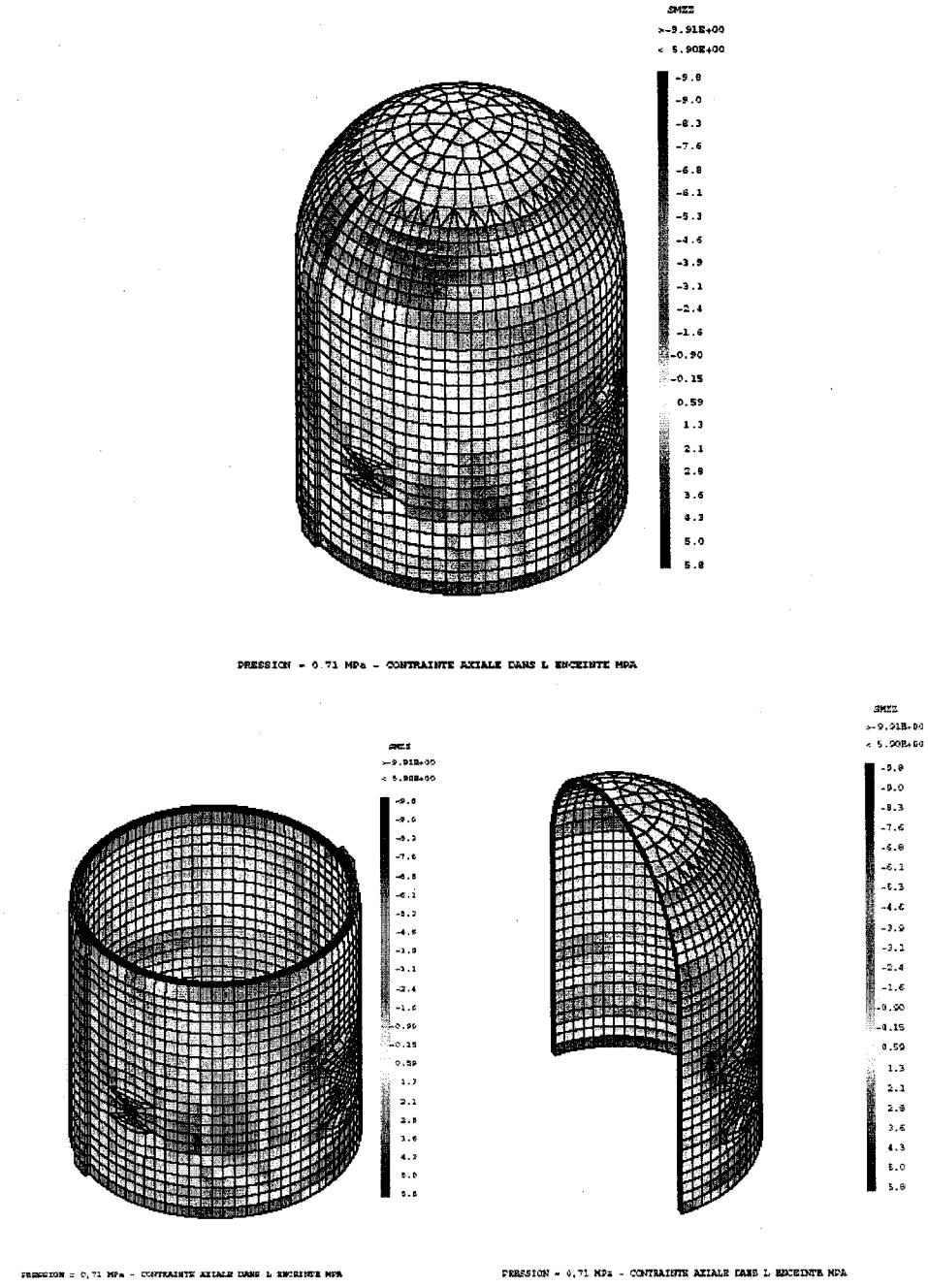

Fig 39: Pressure 0,71 MPa – vertical stresses in the wall (MPa)

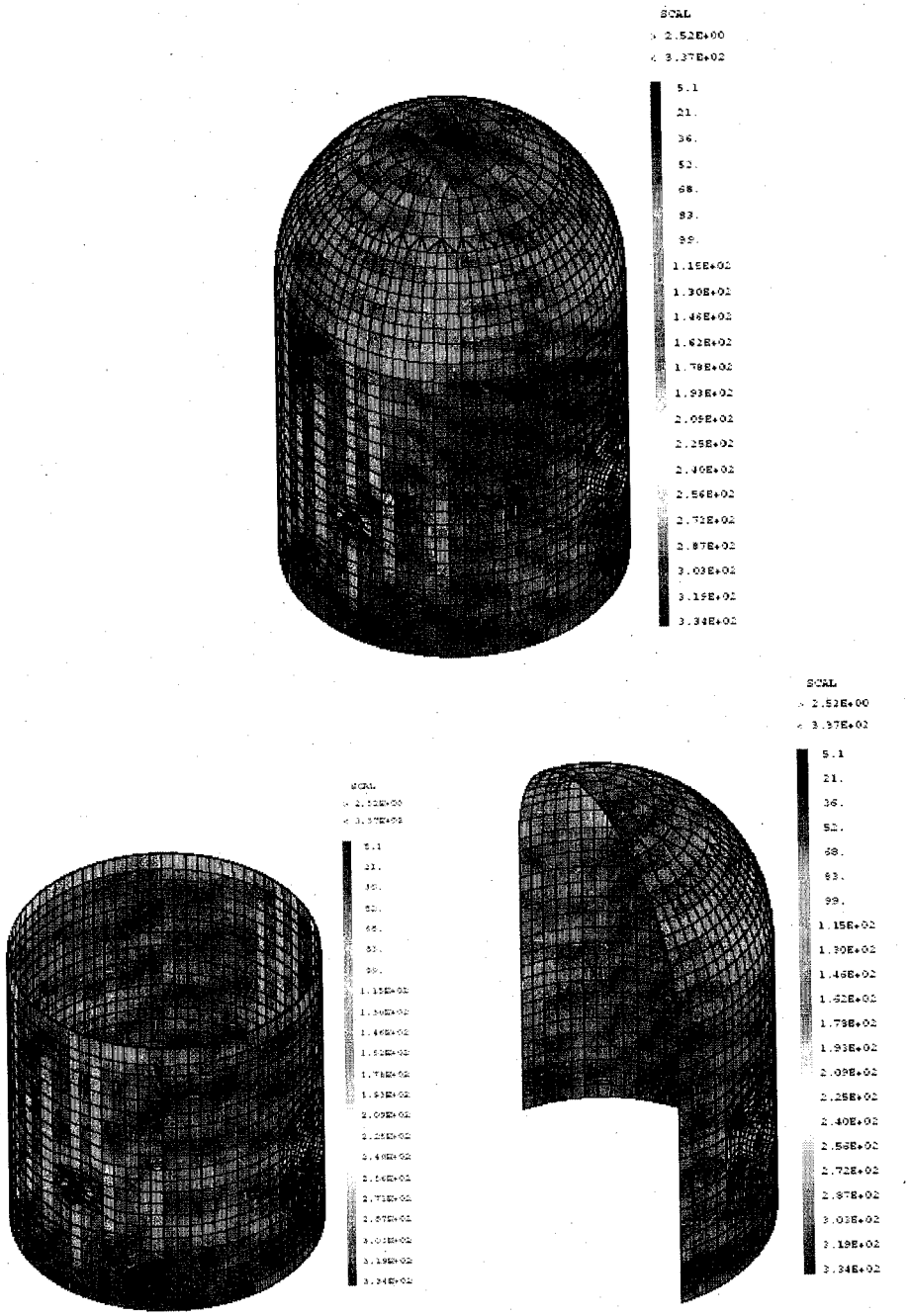

Fig 40: Pressure 0.71 MPa – Von Mises stresses in the liner (MPa)

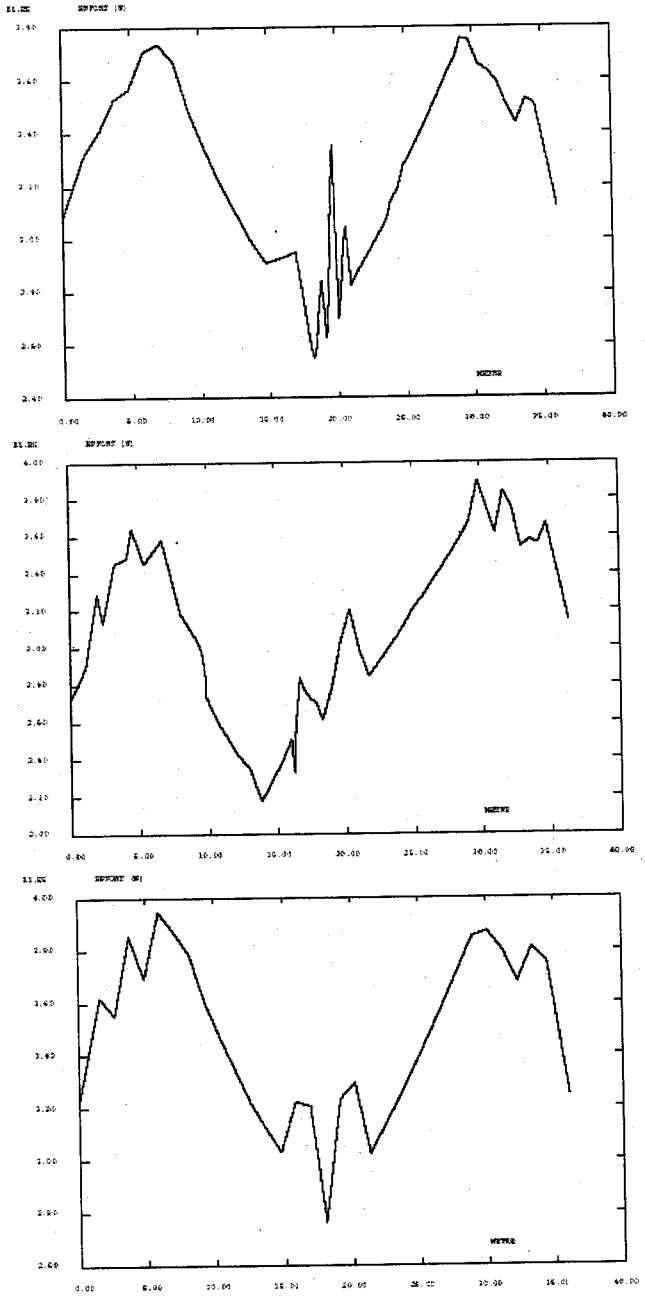

Fig 41: Pressure 0,71 MPa – Tensions in tendons H11, H35, H53 (N)

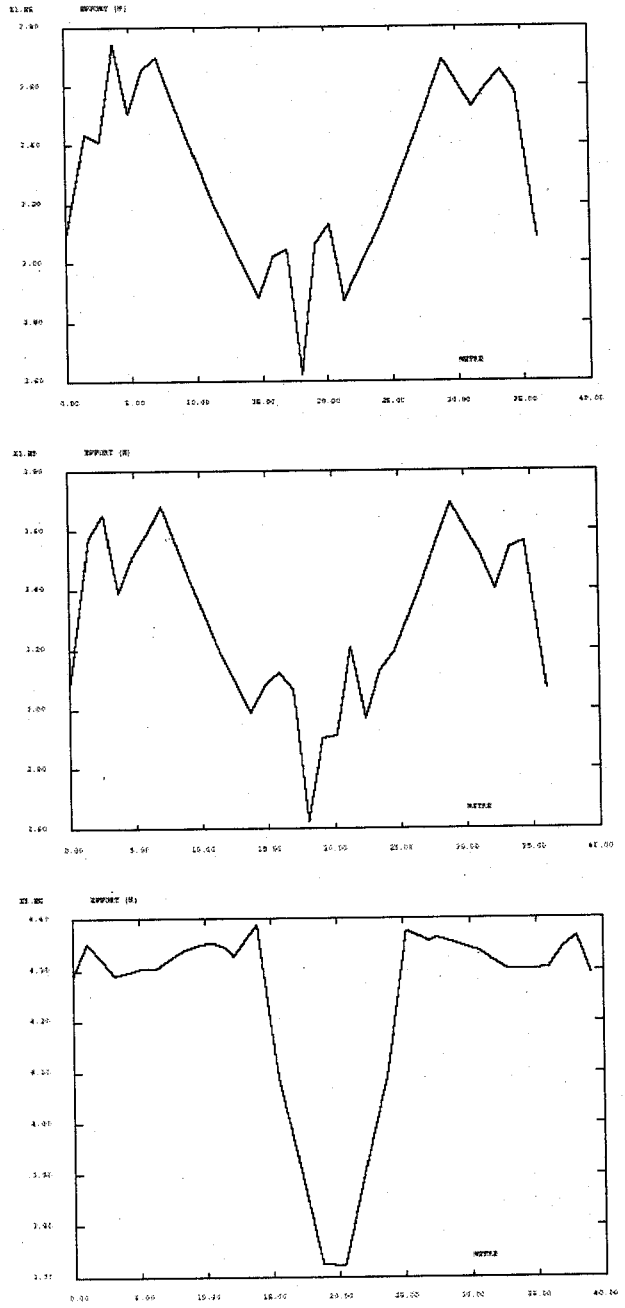

Fig 42: Pressure 0,71 MPa – tensions of tendons H67. H68. V37 (N)

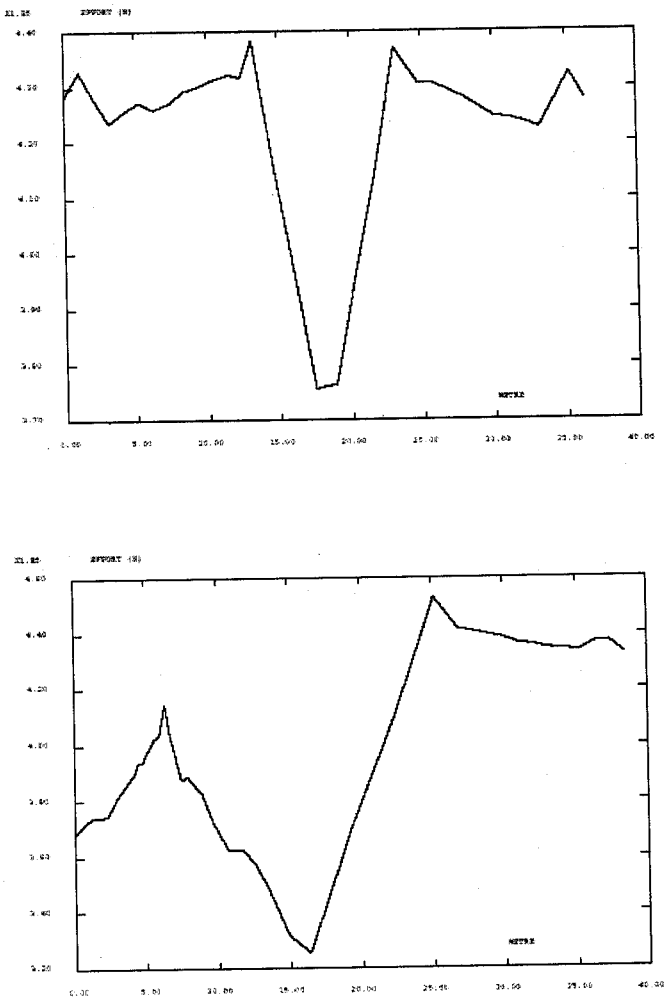

Fig 43: Pressure 0,71 MPa – tensions of tendons V46, V85

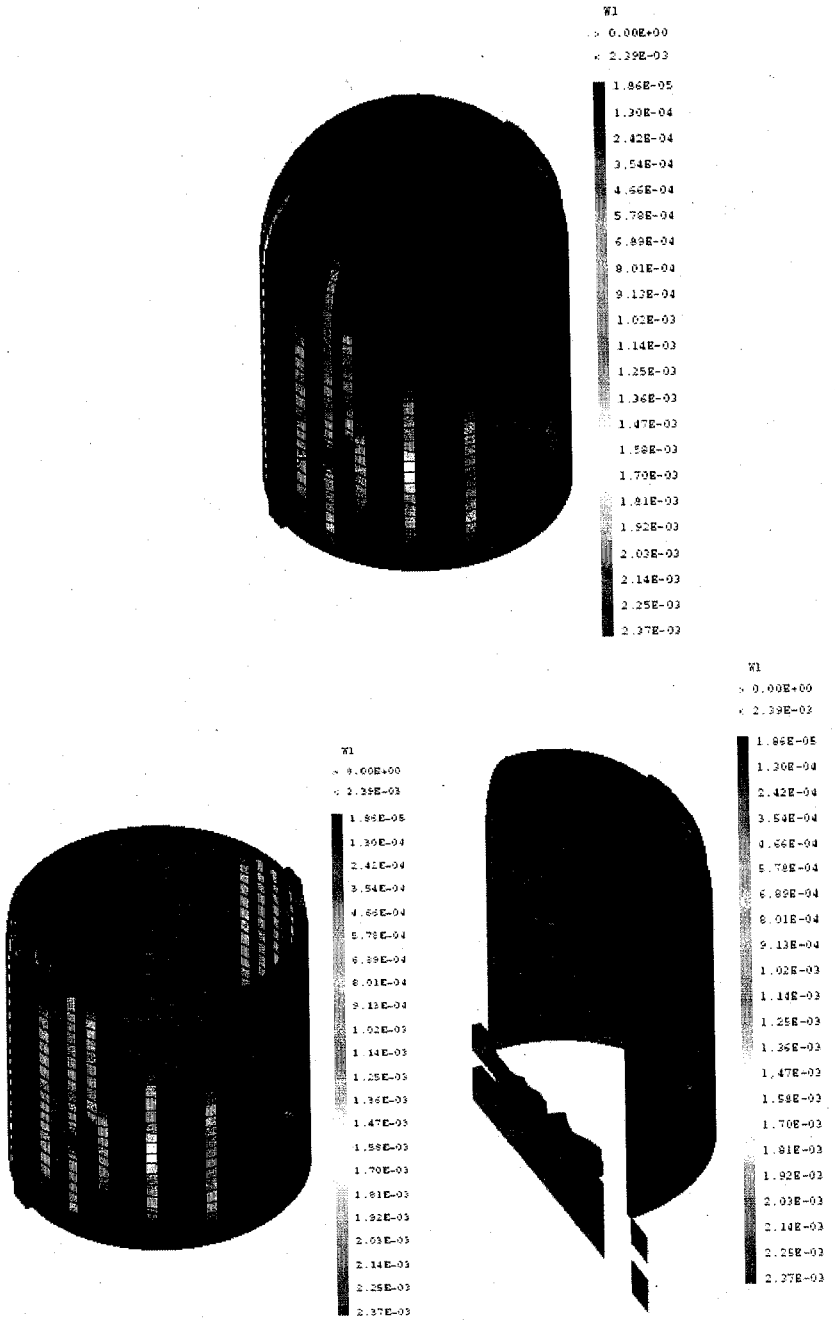

Fig 44 : Pressure 0.71 MPa – First opening cracks in the wall (Metre)

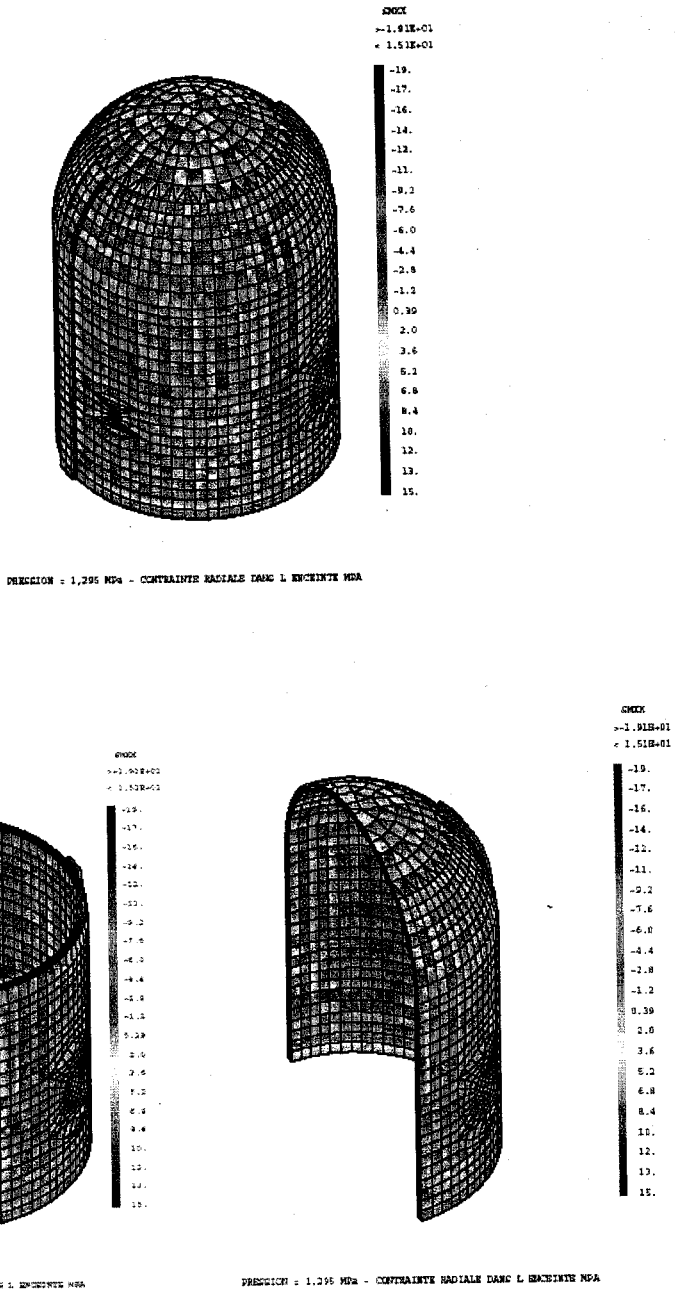

Fig 46 : Pressure 1.295 MPa – radial stresses in the wall (MPa)

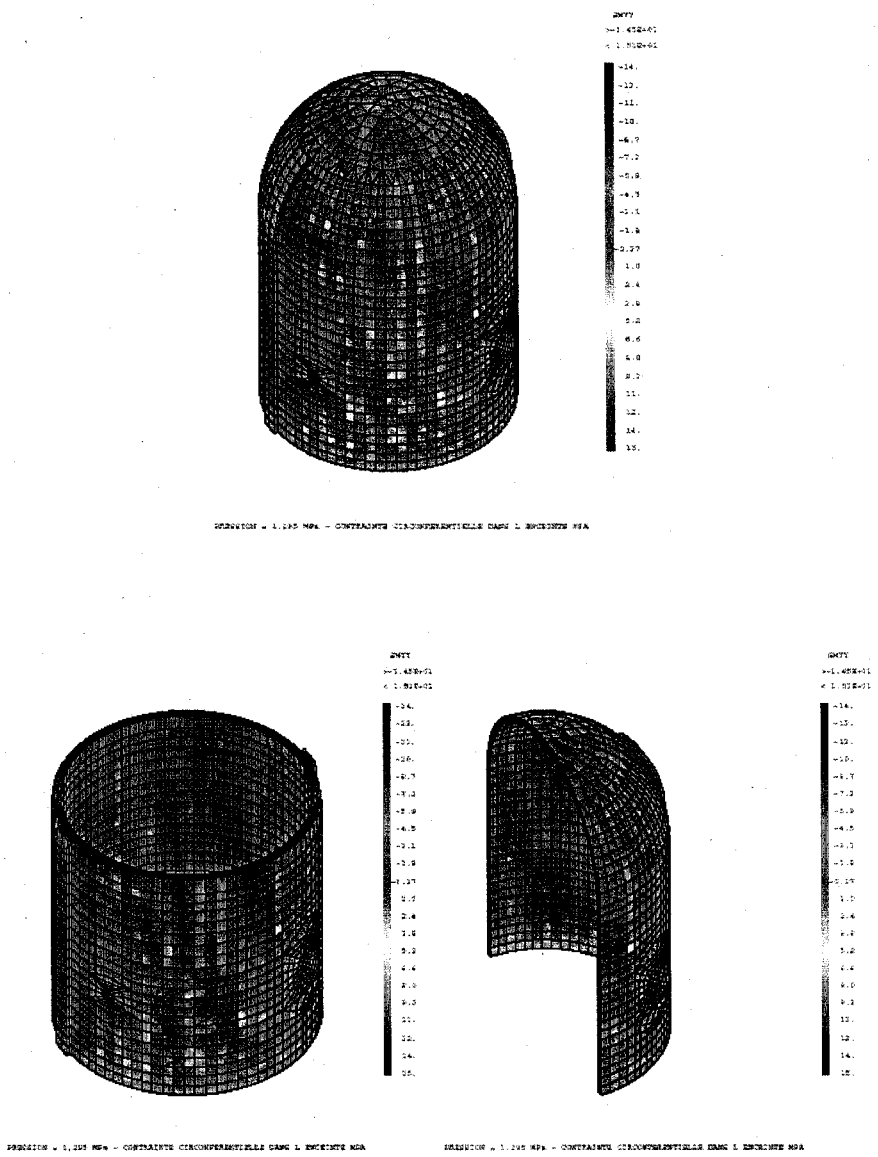

Fig 46: Pressure 1.295 MPa – Hoop stresses in the wall (MPa)

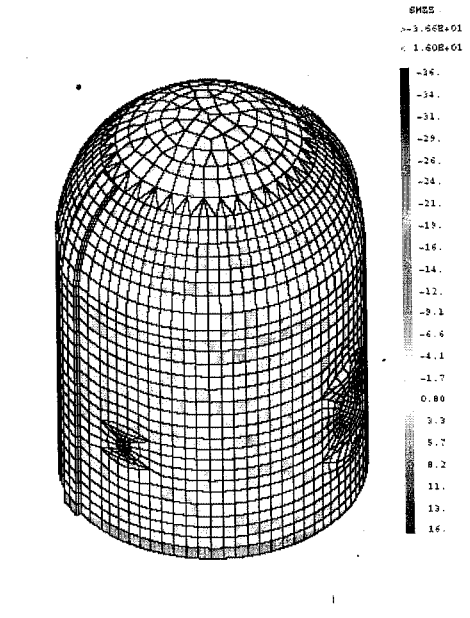

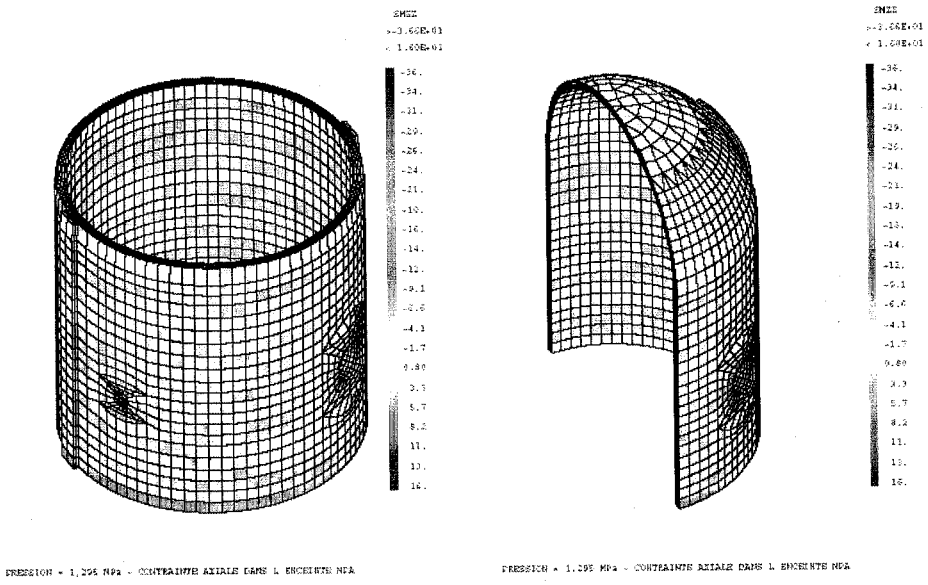

Fig 47 : Pressure 1.295 MPa – Vertical stresses in the wall (MPa)

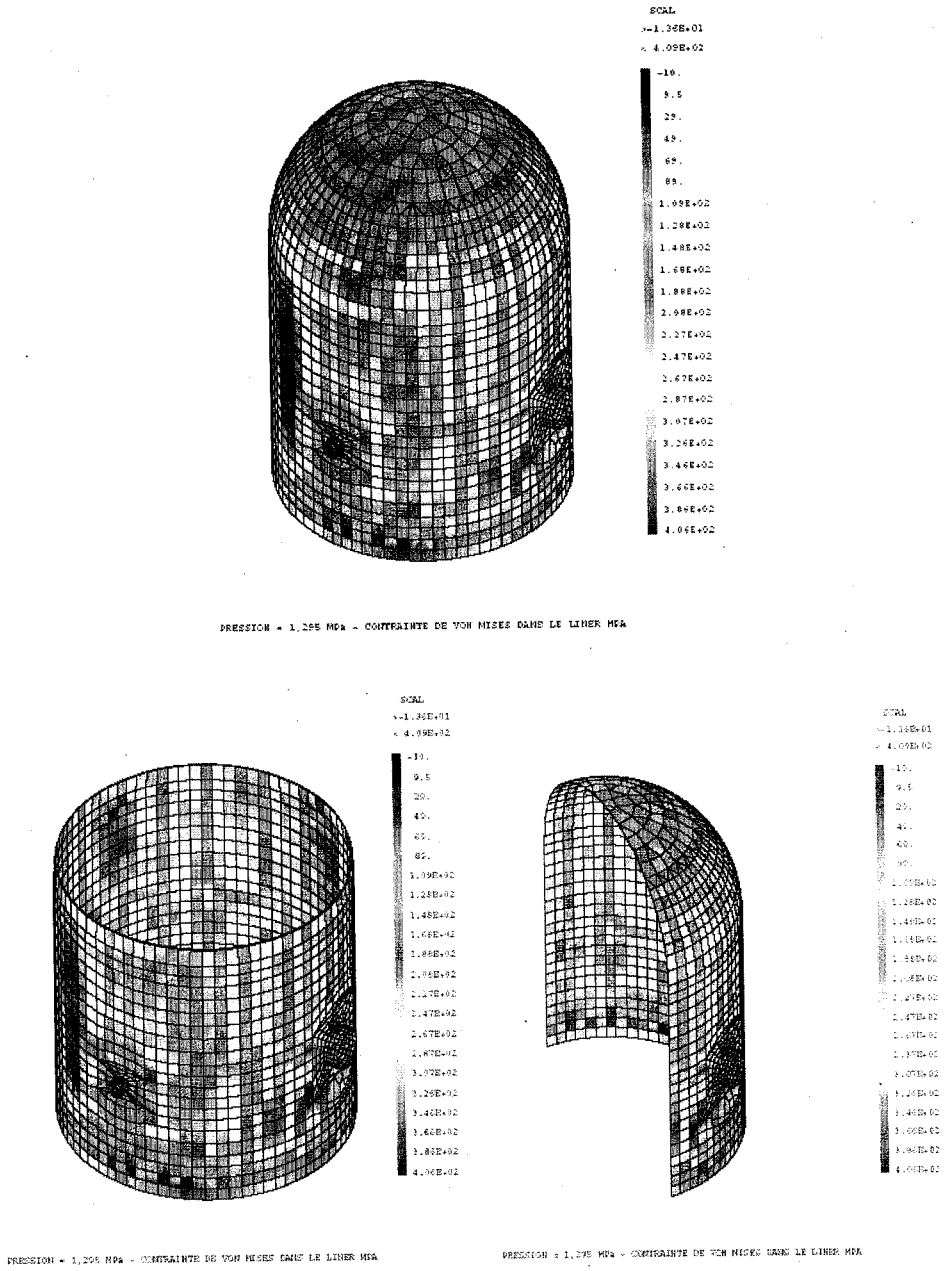

Fig 48 : Pressure 1.295 MPa – Von Mises stresses in the liner (MPa)

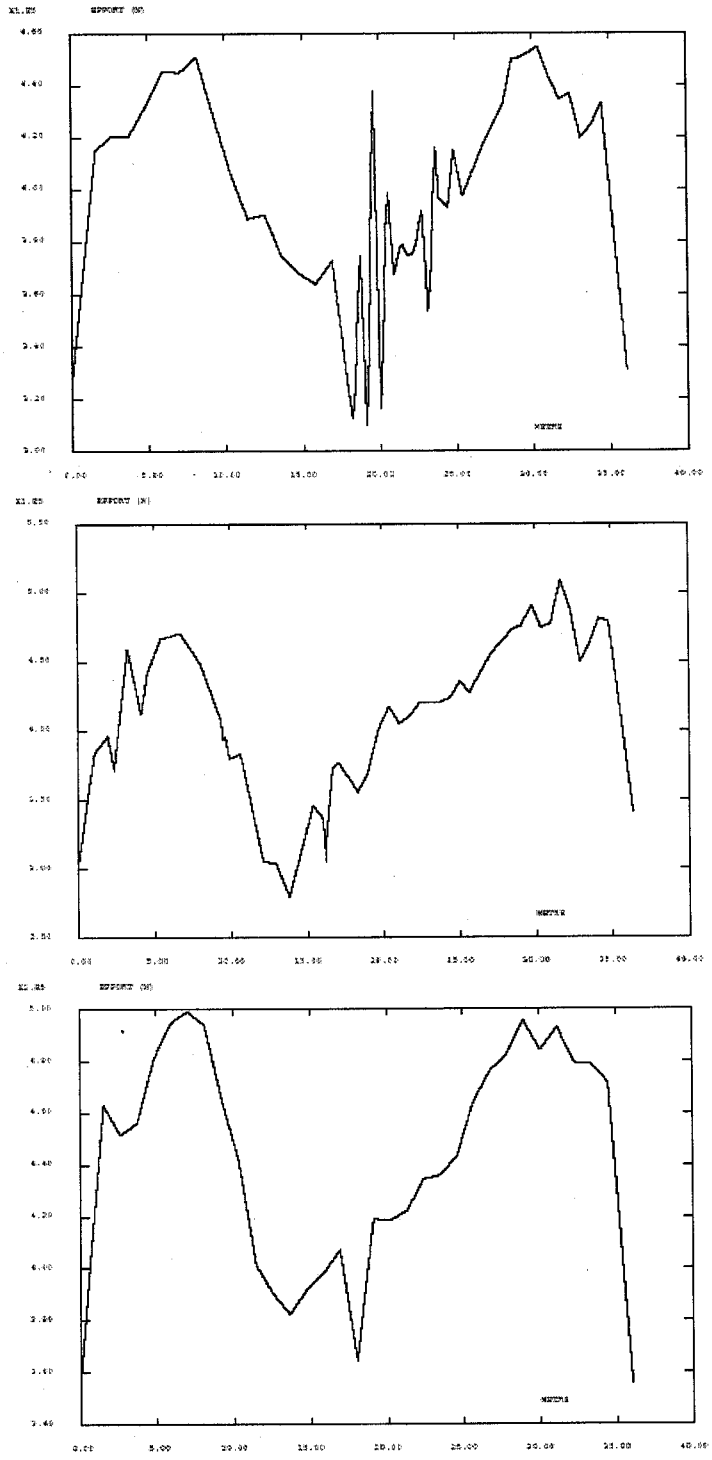

Fig 49 : Pressure 1,295 MPa – Tensions of tendons H11, H35, H53 (N)

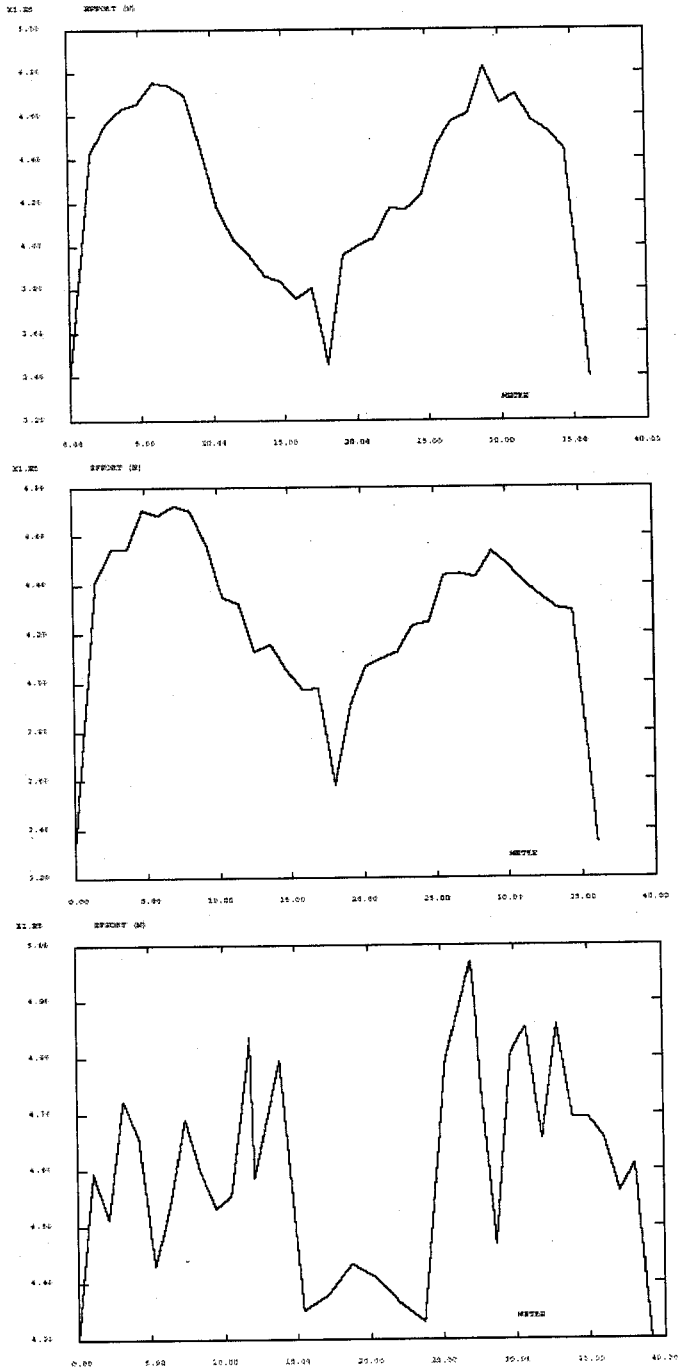

Fig 50 : Pressure 1.295 MPa – Tensions of tendons H67, H68, V37 (N)

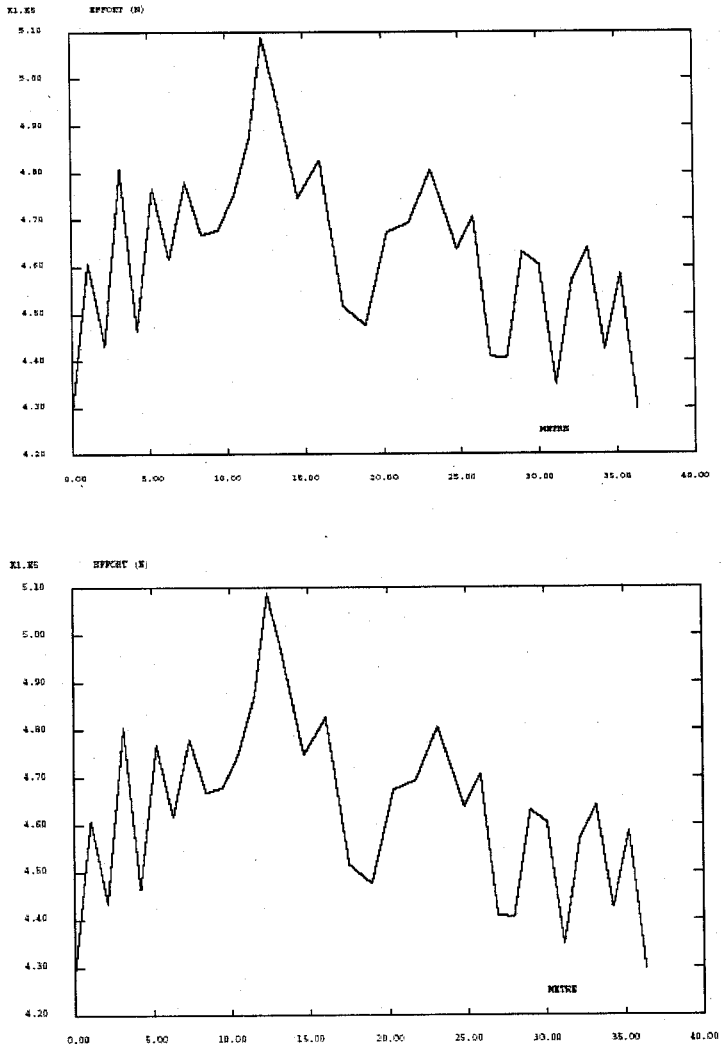

Fig 51 : Pressure 1,295 MPa – tensions of tendons V46, V85 (N)

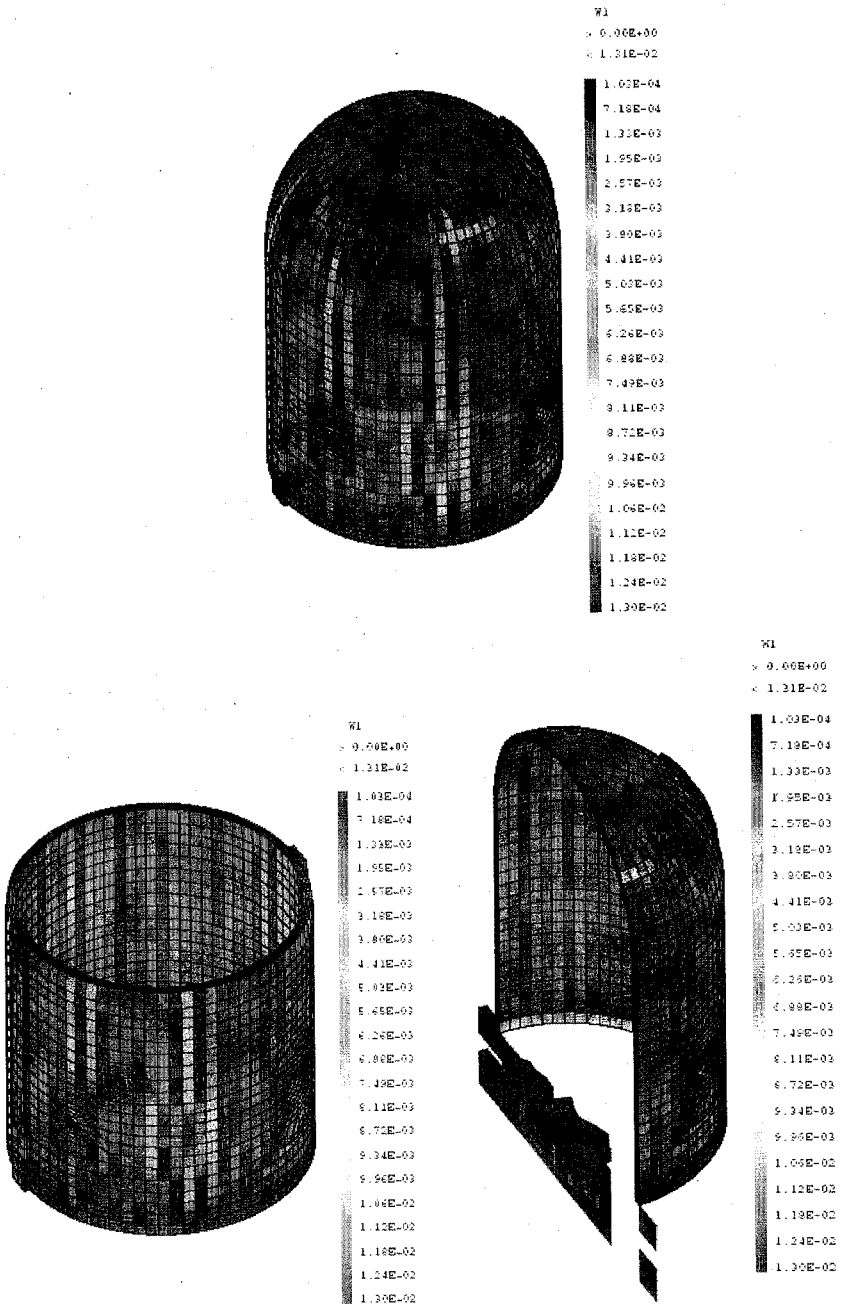

Fig 52 : Pressure 1.295 MPa – Hoop crack opening (metre)

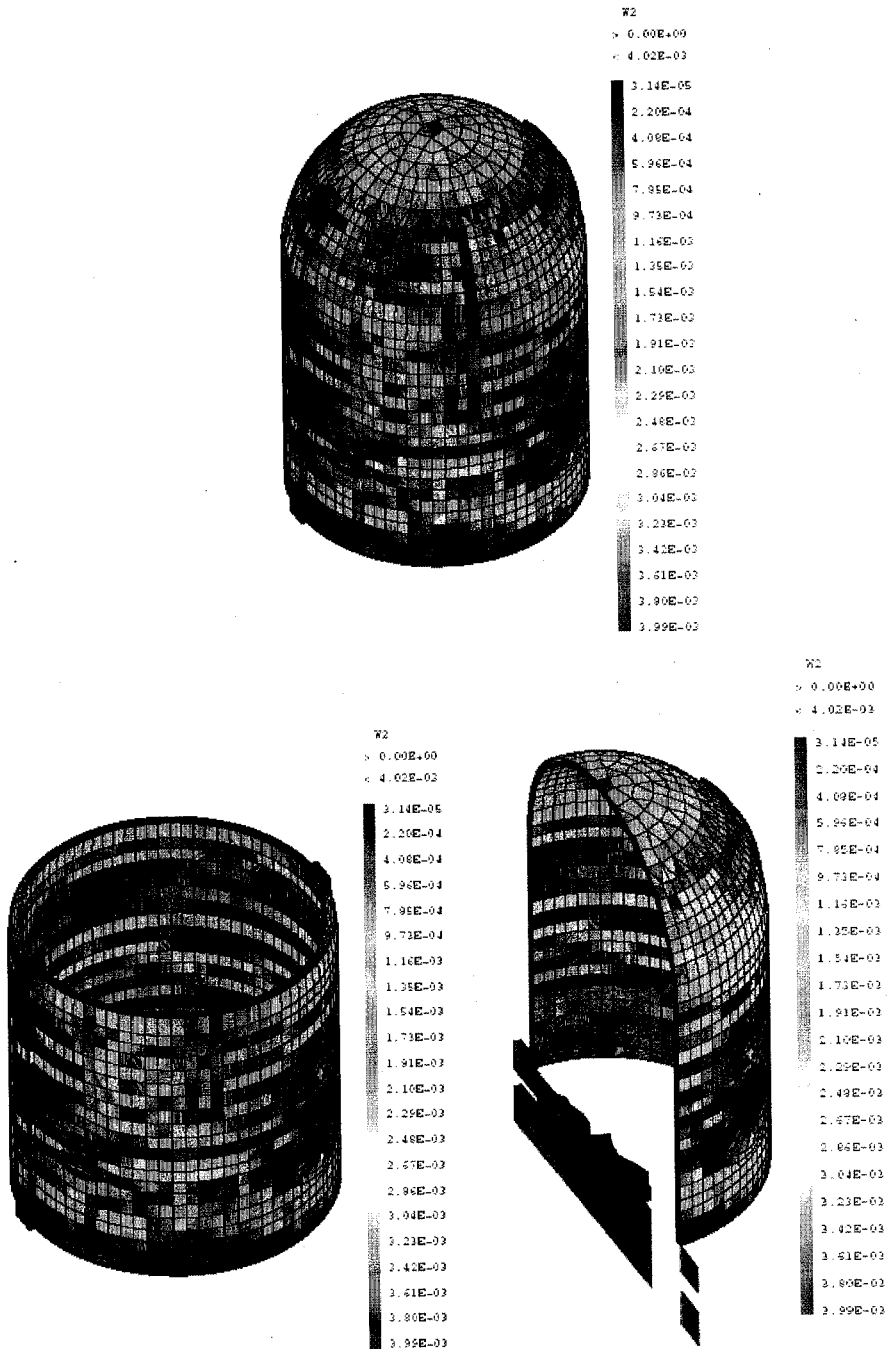

Fig 53 : Pressure 1.295 MPa – Vertical crack opening (metre)

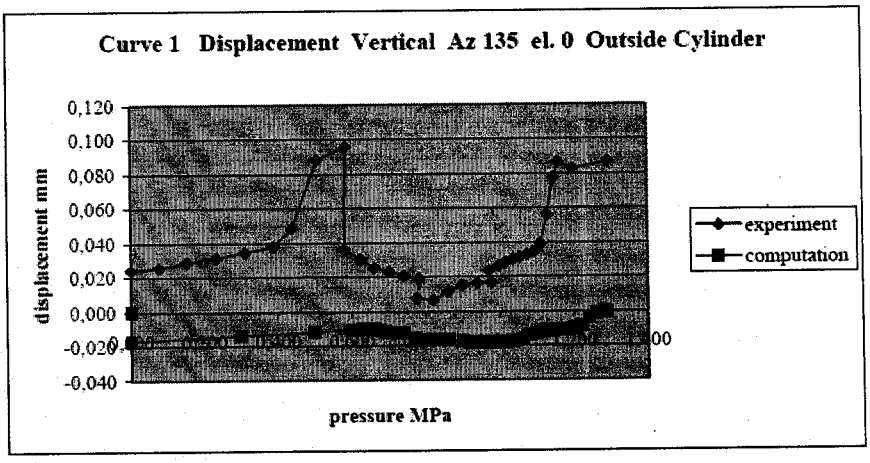
Curve 1 Displacement Vertical Az 135 el. 0 Outside Cylinder
0,120
0,100
0,080
0,060
0,040
0,020
0,000
-0,020
-0,040
displacement mm
pressure MPa
experiment
computation

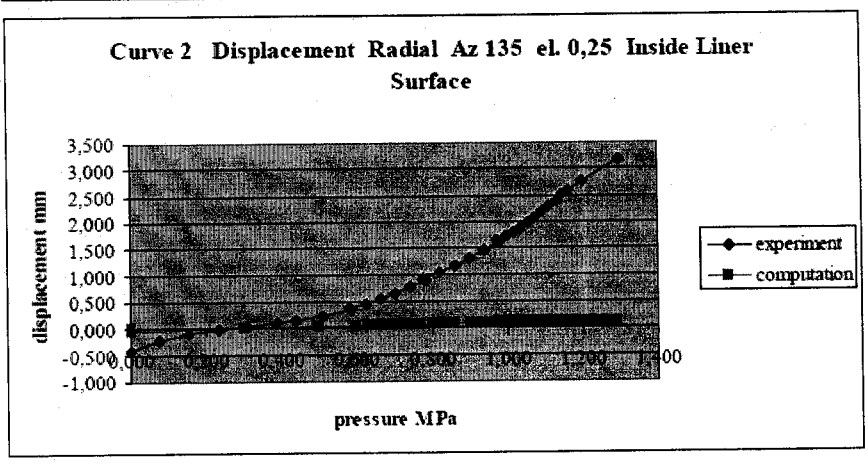
Curve 2 Displacement Radial Az 135 el. 0,25 Inside Liner Surface
3,500
3,000
2,500
2,000
1,500
1,000
0,500
0,000
-0,500
-1,000
displacement mm
pressure MPa
experiment
computation

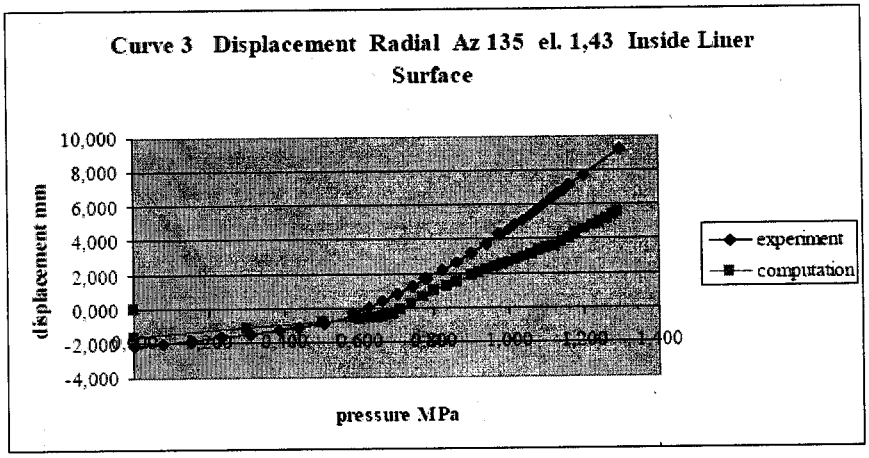
Curve 3 Displacement Radial Az 135 el. 1,43 Inside Liner Surface
10,000
8,000
6,000
4,000
2,000
0,000
-2,000
-4,000
displacement mm
pressure MPa
experiment
computation

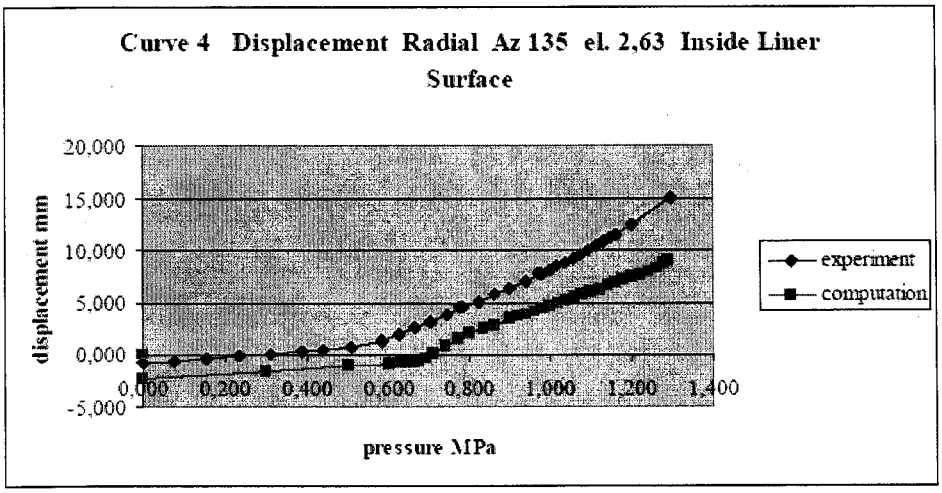
Curve 4 Displacement Radial Az 135 el. 2,63 Inside Liner Surface
displacement mm
20,000
15,000
10,000
5,000
0,000
-5,000
0,000
0,200
0,400
0,600
0,800
1,000
1,200
1,400
pressure MPa
experiment
computation

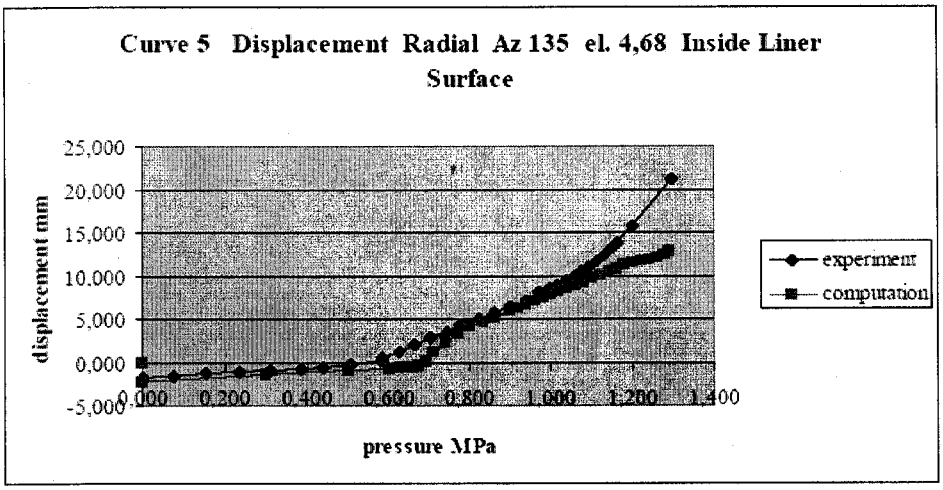
Curve 5 Displacement Radial Az 135 el. 4,68 Inside Liner Surface
displacement mm
25,000
20,000
15,000
10,000
5,000
0,000
-5,000
0,000
0,200
0,400
0,600
0,800
1,000
1,200
1,400
pressure MPa
experiment
computation

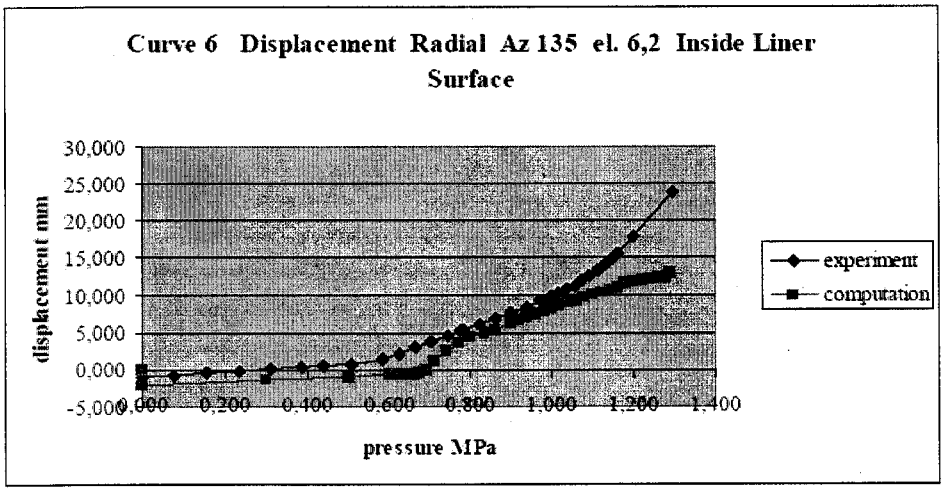
Curve 6 Displacement Radial Az 135 el. 6,2 Inside Liner Surface
displacement mm
30,000
25,000
20,000
15,000
10,000
5,000
0,000
-5,000
0,000
0,200
0,400
0,600
0,800
1,000
1,200
1,400
pressure MPa
experiment
computation

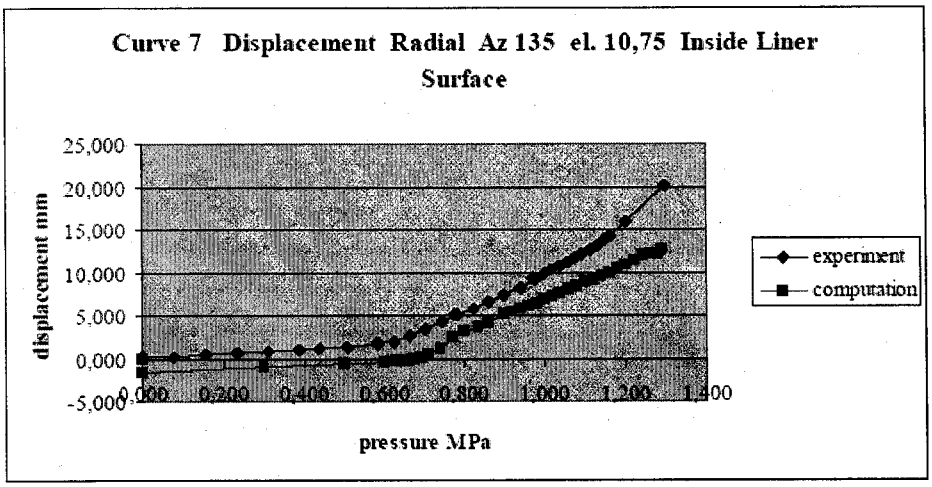
Curve 7 Displacement Radial Az 135 el. 10,75 Inside Liner Surface
25,000
20,000
15,000
10,000
5,000
0,000
-5,000
displacement mm
0,000
0,200
0,400
0,600
0,800
1,000
1,200
1,400
pressure MPa
experiment
computation

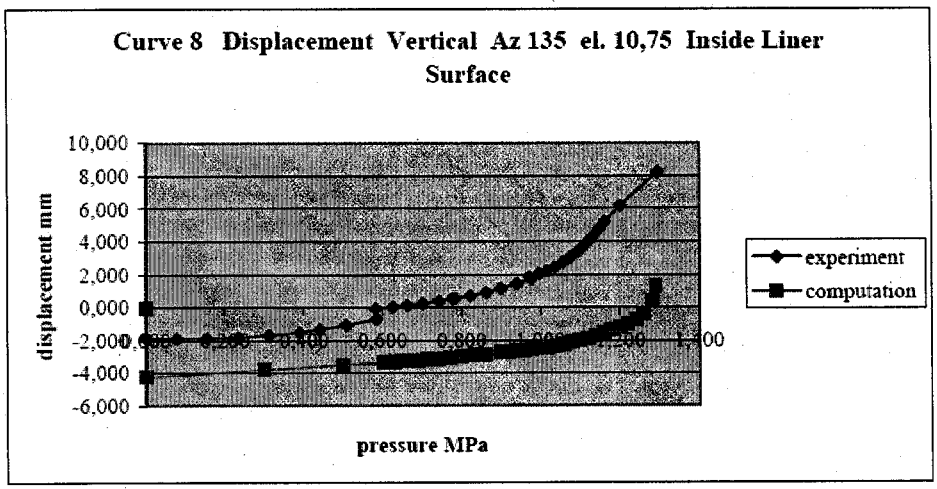
Curve 8 Displacement Vertical Az 135 el. 10,75 Inside Liner Surface
10,000
8,000
6,000
4,000
2,000
0,000
-2,000
-4,000
-6,000
displacement mm
pressure MPa
experiment
computation

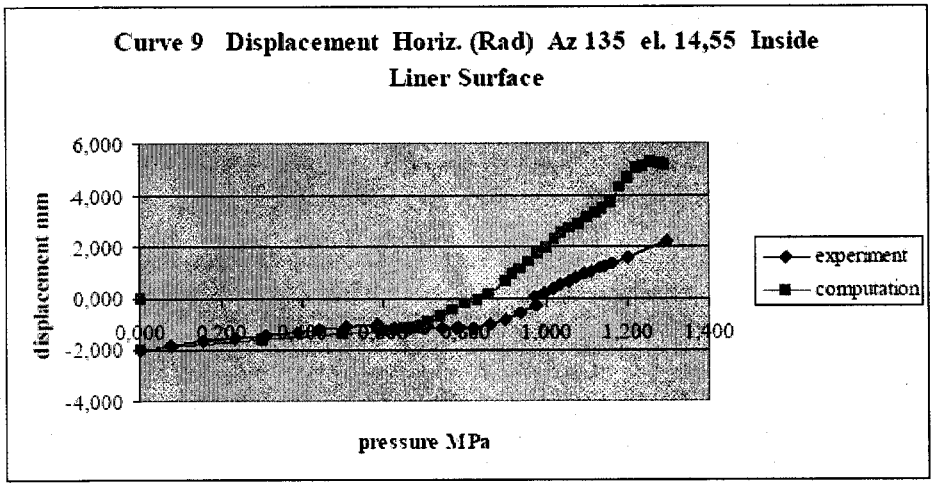
Curve 9 Displacement Horiz. (Rad) Az 135 el. 14,55 Inside Liner Surface
6,000
4,000
2,000
0,000
-2,000
-4,000
displacement mm
0,000
0,200
0,400
0,600
0,800
1,000
1,200
1,400
pressure MPa
experiment
computation

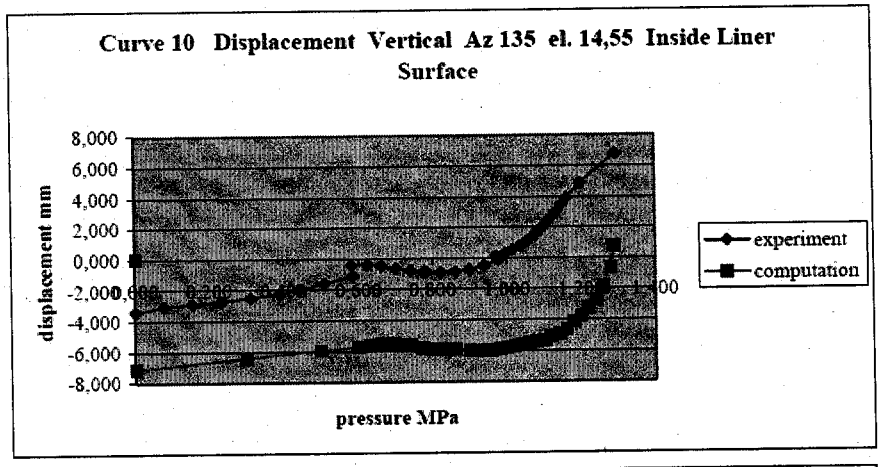
Curve 10 Displacement Vertical Az 135 el. 14,55 Inside Liner Surface
displacement mm
8,000
6,000
4,000
2,000
0,000
-2,000
-4,000
-6,000
-8,000
pressure MPa
experiment
computation

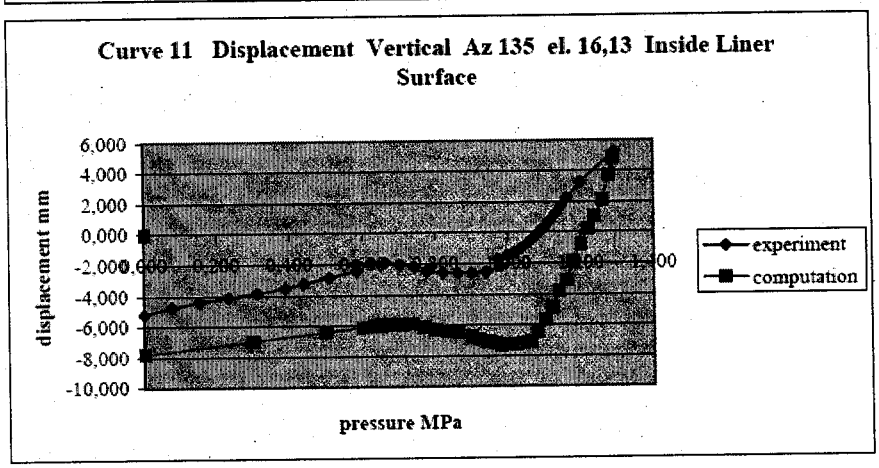
Curve 11 Displacement Vertical Az 135 el. 16,13 Inside Liner Surface
displacement mm
6,000
4,000
2,000
0,000
-2,000
-4,000
-6,000
-8,000
-10,000
pressure MPa
experiment
computation

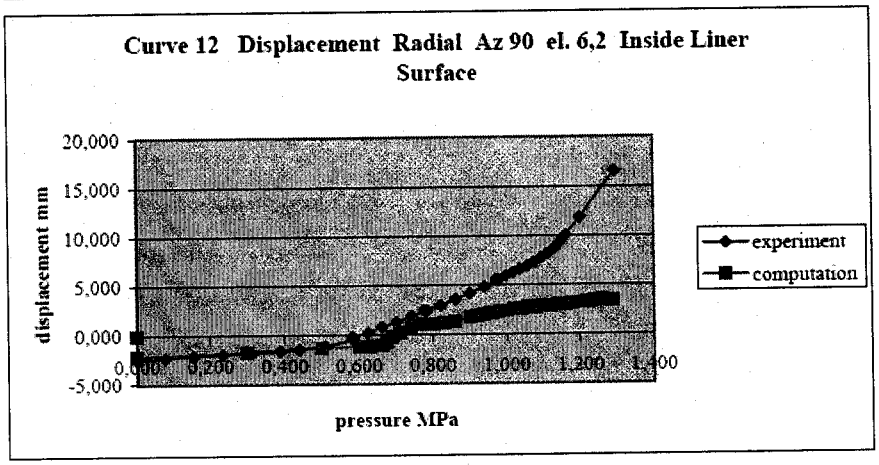
Curve 12 Displacement Radial Az 90 el. 6,2 Inside Liner Surface
displacement mm
20,000
15,000
10,000
5,000
0,000
-5,000
0,200
0,400
0,600
0,800
1,000
1,200
1,400
pressure MPa
experiment
computation

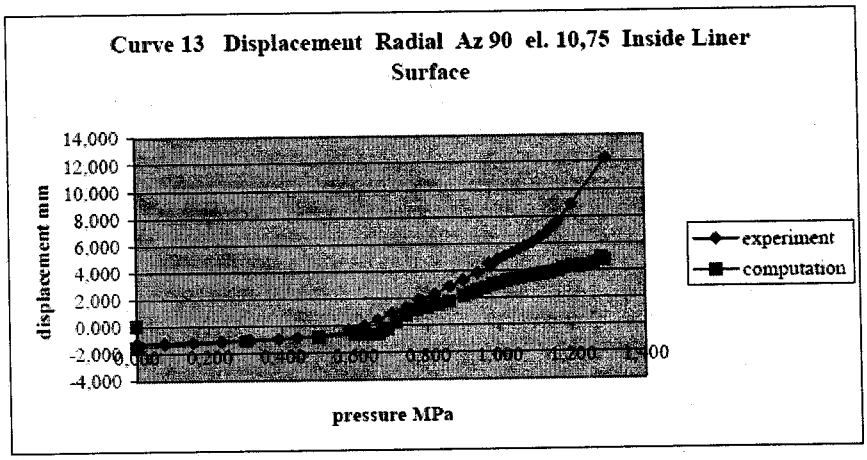
Curve 13 Displacement Radial Az 90 el. 10,75 Inside Liner Surface
displacement mm
14,000
12,000
10,000
8,000
6,000
4,000
2,000
0,000
-2,000
-4,000
0,000
0,200
0,400
0,600
0,800
1,000
1,200
1,400
pressure MPa
experiment
computation

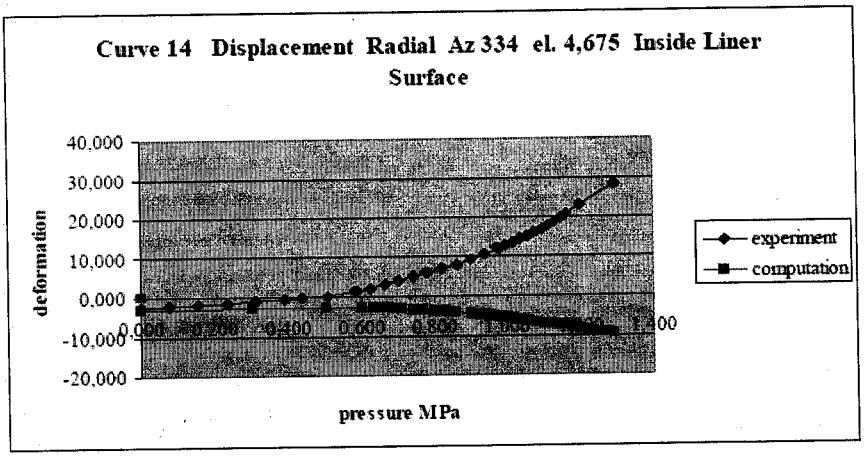
Curve 14 Displacement Radial Az 334 el. 4,675 Inside Liner Surface
deformation
40,000
30,000
20,000
10,000
0,000
-10,000
-20,000
0,000
0,200
0,400
0,600
0,800
1,000
1,200
1,400
pressure MPa
experiment
computation

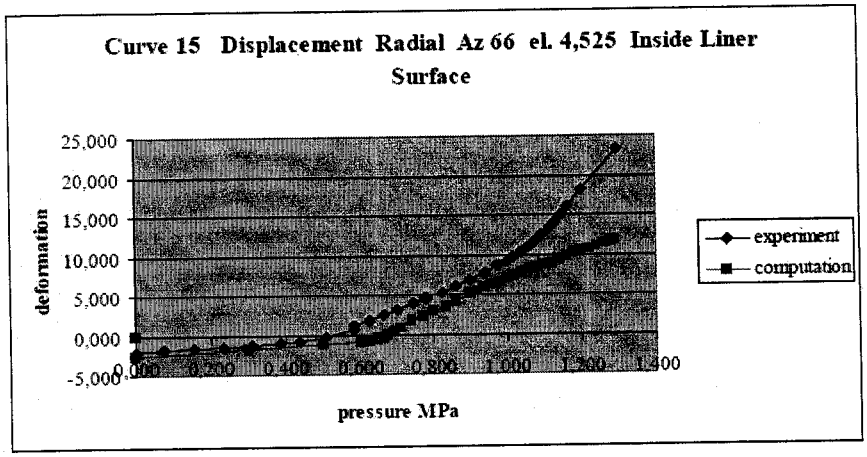
Curve 15 Displacement Radial Az 66 el. 4,525 Inside Liner Surface
deformation
25,000
20,000
15,000
10,000
5,000
0,000
-5,000
0,000
0,200
0,400
0,600
0,800
1,000
1,200
1,400
pressure MPa
experiment
computation

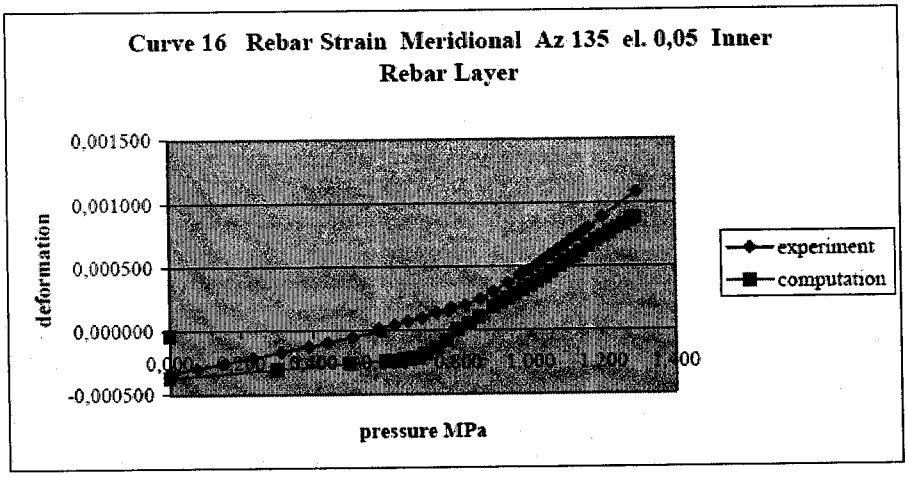
Curve 16 Rebar Strain Meridional Az 135 el. 0,05 Inner Rebar Layer
0,001500
0,001000
0,000500
0,000000
-0,000500
deformation
pressure MPa
experiment
computation

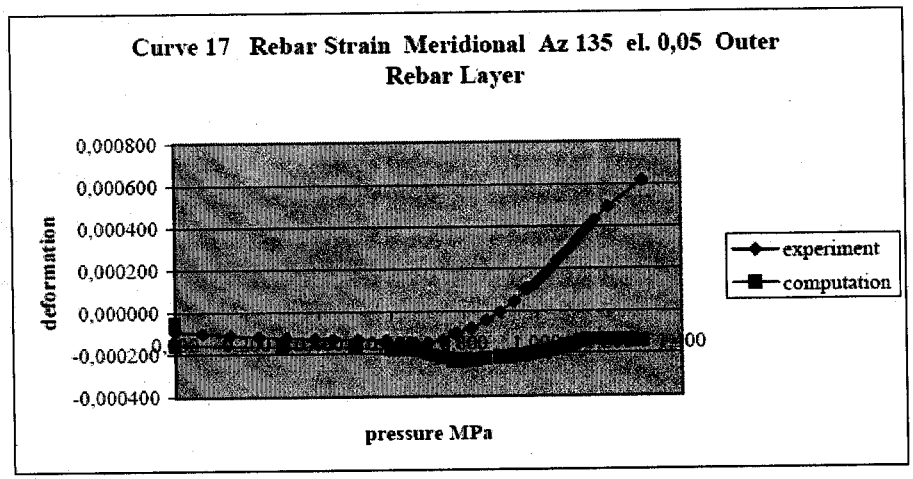
Curve 17 Rebar Strain Meridional Az 135 el. 0,05 Outer Rebar Layer
0,000800
0,000600
0,000400
0,000200
0,000000
-0,000200
-0,000400
deformation
pressure MPa
experiment
computation

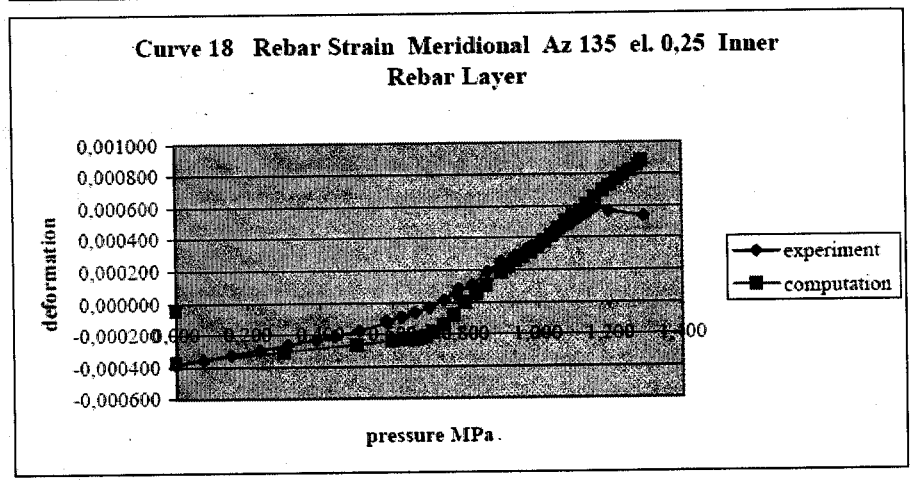
Curve 18 Rebar Strain Meridional Az 135 el. 0,25 Inner Rebar Layer
0,001000
0,000800
0,000600
0,000400
0,000200
0,000000
-0,000200
-0,000400
-0,000600
deformation
pressure MPa
experiment
computation

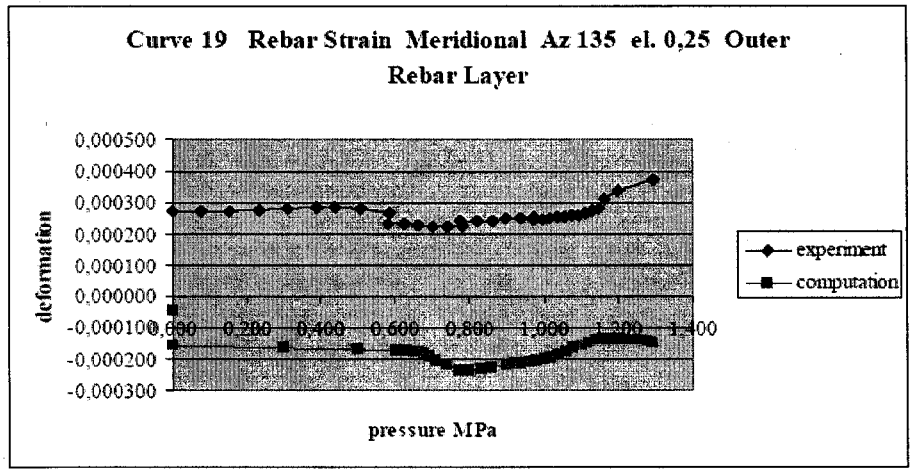
Curve 19 Rebar Strain Meridional Az 135 el. 0,25 Outer Rebar Layer
deformation
0,000500
0,000400
0,000300
0,000200
0,000100
0,000000
-0,000100
-0,000200
-0,000300
0,000 0,200 0,400 0,600 0,800 1,000 1,200 1,400
pressure MPa
experiment
computation

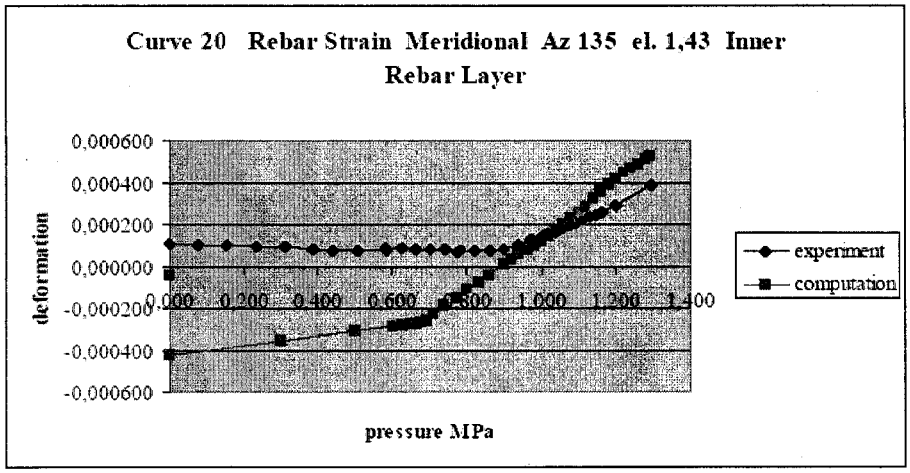
Curve 20 Rebar Strain Meridional Az 135 el. 1,43 Inner Rebar Layer
deformation
0,000600
0,000400
0,000200
0,000000
-0,000200
-0,000400
-0,000600
0,000 0,200 0,400 0,600 0,800 1,000 1,200 1,400
pressure MPa
experiment
computation

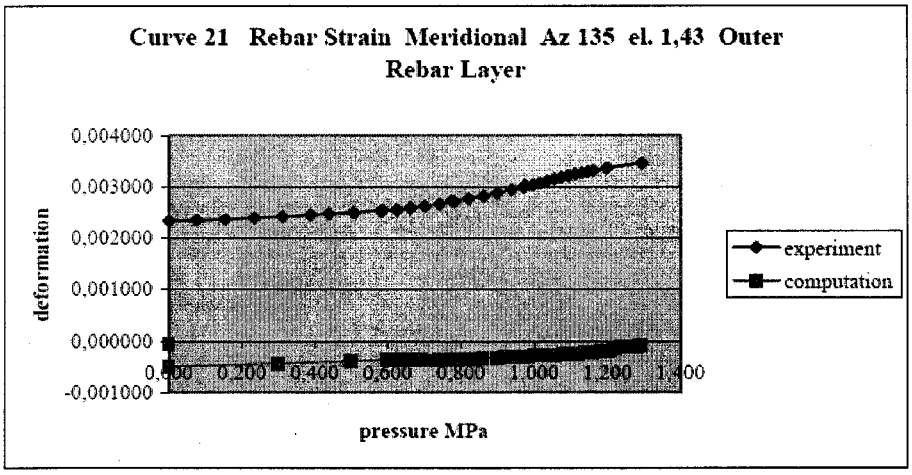
Curve 21 Rebar Strain Meridional Az 135 el. 1,43 Outer Rebar Layer
deformation
0,004000
0,003000
0,002000
0,001000
0,000000
-0,001000
0,000 0,200 0,400 0,600 0,800 1,000 1,200 1,400
pressure MPa
experiment
computation

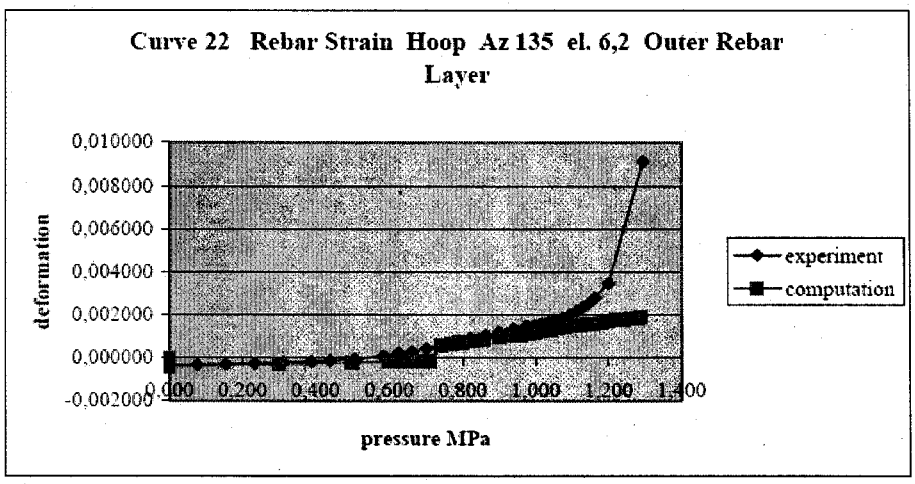
Curve 22 Rebar Strain Hoop Az 135 el. 6,2 Outer Rebar Layer
0,010000
0,008000
0,006000
0,004000
0,002000
0,000000
-0,002000
deformation
0,000
0,200
0,400
0,600
0,800
1,000
1,200
1,400
pressure MPa
experiment
computation

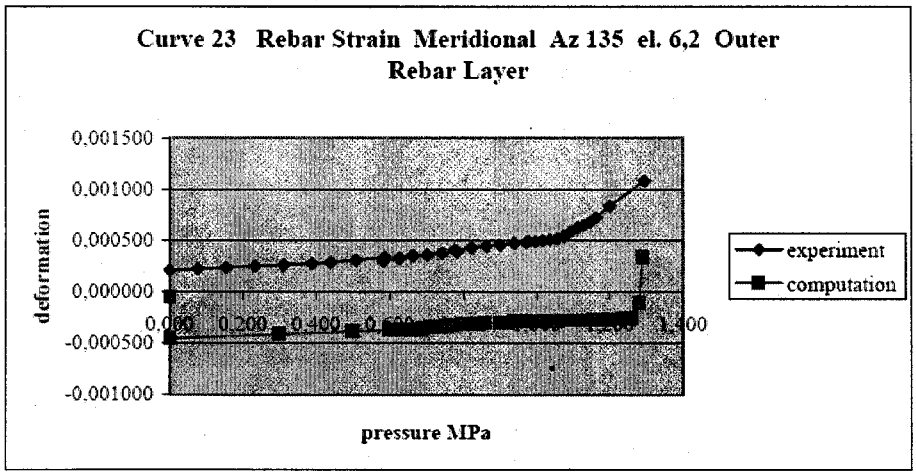
Curve 23 Rebar Strain Meridional Az 135 el. 6,2 Outer Rebar Layer
0,001500
0,001000
0,000500
0,000000
-0,000500
-0,001000
deformation
0,000
0,200
0,400
1,400
pressure MPa
experiment
computation

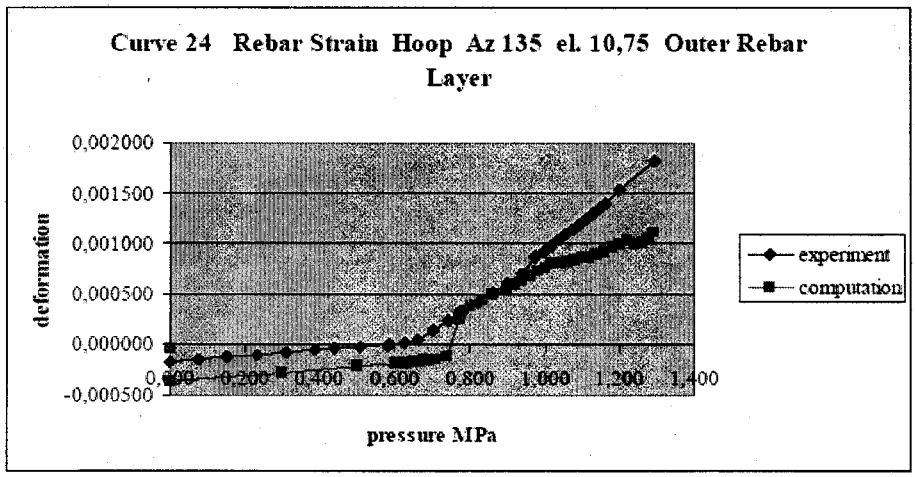
Curve 24 Rebar Strain Hoop Az 135 el. 10,75 Outer Rebar Layer
0,002000
0,001500
0,001000
0,000500
0,000000
-0,000500
deformation
0,000
0,200
0,400
0,600
0,800
1,000
1,200
1,400
pressure MPa
experiment
computation

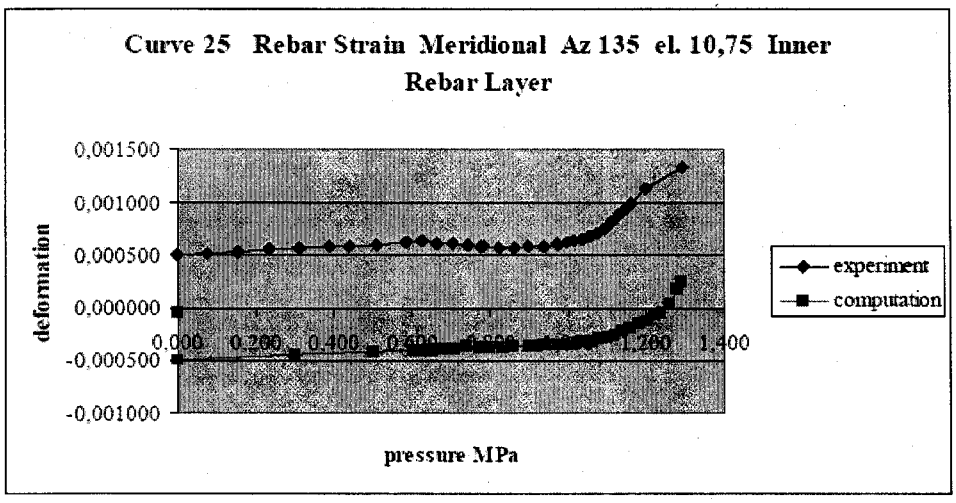
Curve 25 Rebar Strain Meridional Az 135 el. 10,75 Inner Rebar Layer
0,001500
0,001000
0,000500
0,000000
-0,000500
-0,001000
deformation
0,000
0,200
0,400
1,200
1,400
pressure MPa
experiment
computation

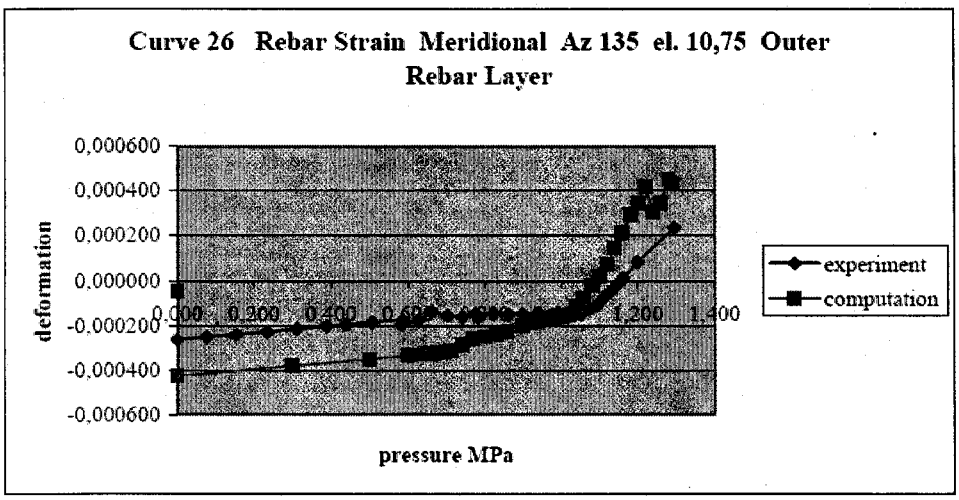
Curve 26 Rebar Strain Meridional Az 135 el. 10,75 Outer Rebar Layer
0,000600
0,000400
0,000200
0,000000
-0,000200
-0,000400
-0,000600
deformation
0,000
0,200
0,400
1,200
1,400
pressure MPa
experiment
computation

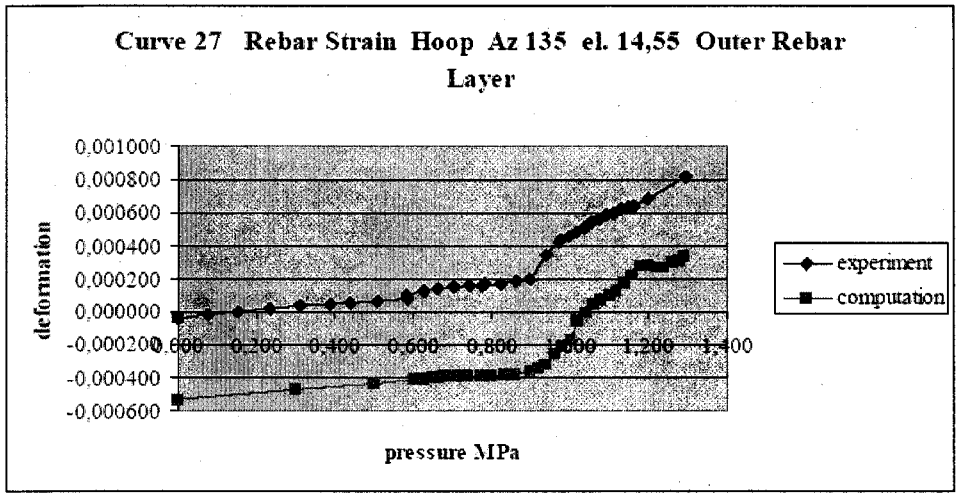
Curve 27 Rebar Strain Hoop Az 135 el. 14,55 Outer Rebar Layer
0,001000
0,000800
0,000600
0,000400
0,000200
0,000000
-0,000200
-0,000400
-0,000600
deformation
0,200
0,400
0,600
0,800
1,200
1,400
pressure MPa
experiment
computation

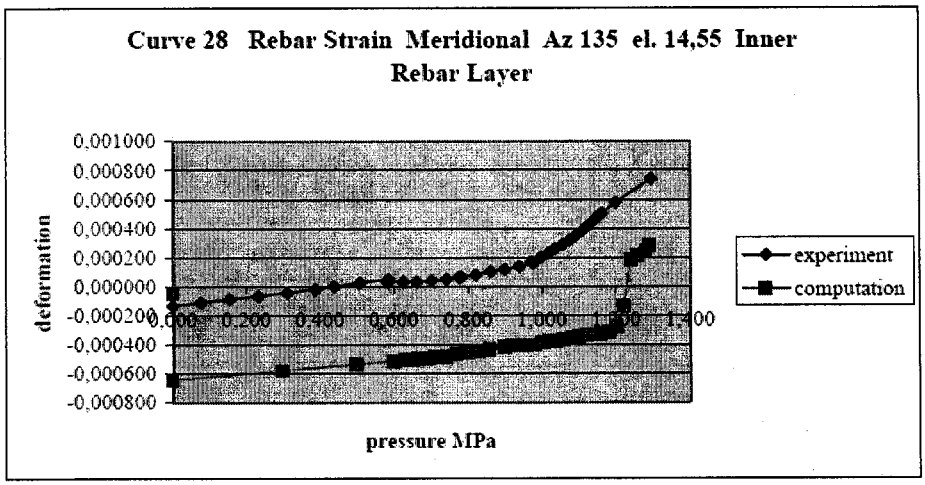
Curve 28 Rebar Strain Meridional Az 135 el. 14,55 Inner Rebar Layer
0,001000
0,000800
0,000600
0,000400
0,000200
0,000000
-0,000200
-0,000400
-0,000600
-0,000800
deformation
0,000 0,200 0,400 0,600 0,800 1,000 1,200 1,400
pressure MPa
experiment
computation

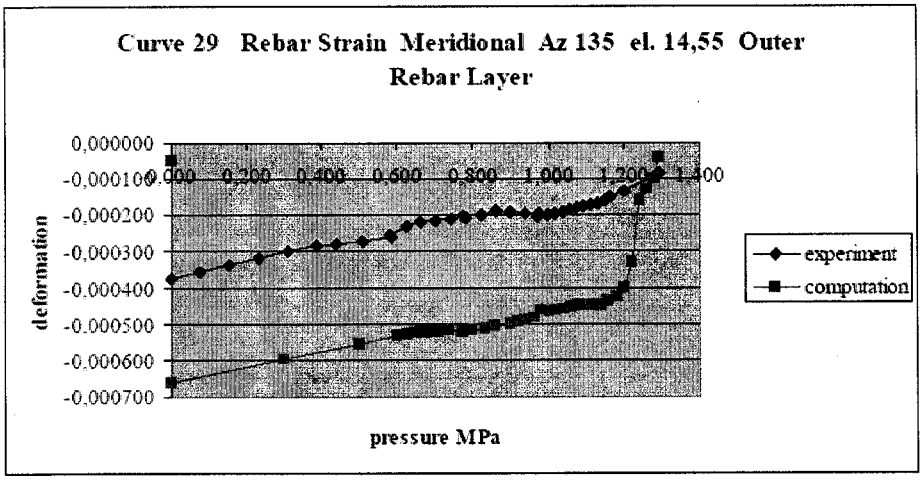
Curve 29 Rebar Strain Meridional Az 135 el. 14,55 Outer Rebar Layer
0,000000
-0,000100
-0,000200
-0,000300
-0,000400
-0,000500
-0,000600
-0,000700
deformation
0,000 0,200 0,400 0,600 0,800 1,000 1,200 1,400
pressure MPa
experiment
computation

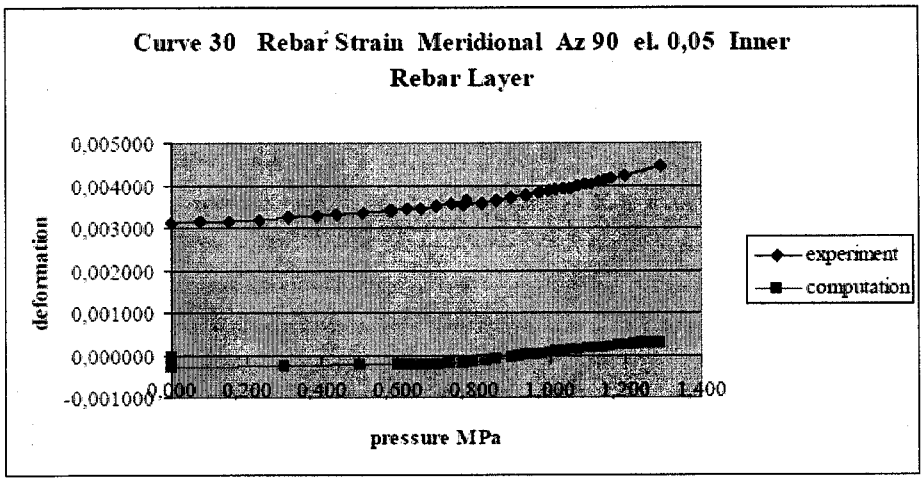
Curve 30 Rebar Strain Meridional Az 90 el. 0,05 Inner Rebar Layer
0,005000
0,004000
0,003000
0,002000
0,001000
0,000000
-0,001000
deformation
0,000 0,200 0,400 0,600 0,800 1,000 1,200 1,400
pressure MPa
experiment
computation

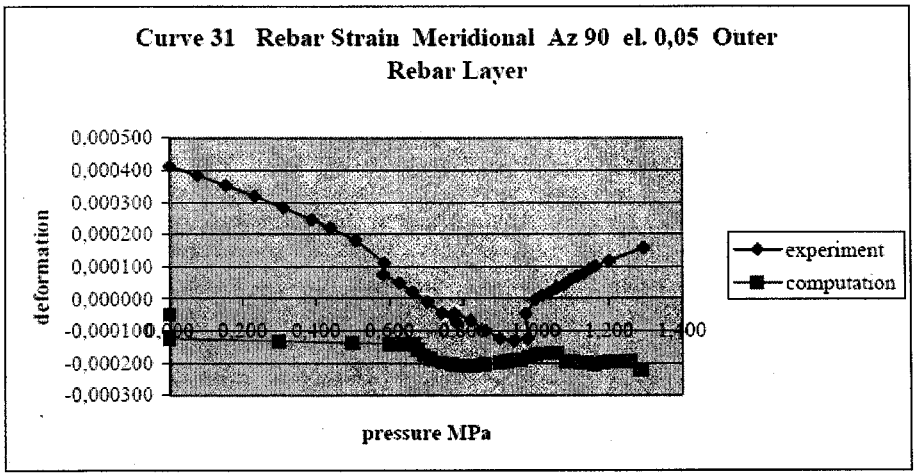
Curve 31 Rebar Strain Meridional Az 90 el. 0,05 Outer Rebar Layer
0,000500
0,000400
0,000300
0,000200
0,000100
0,000000
-0,000100
-0,000200
-0,000300
deformation
0,000
0,200
0,400
0,600
0,800
1,000
1,200
1,400
pressure MPa
experiment
computation

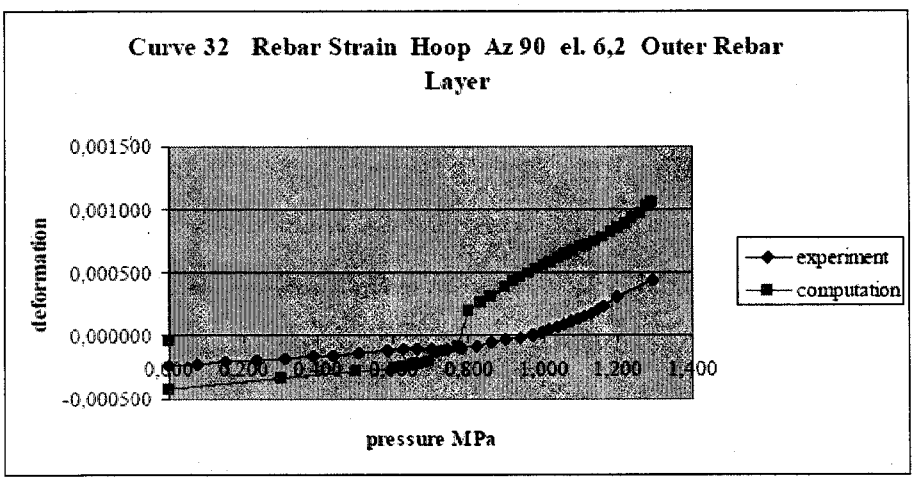
Curve 32 Rebar Strain Hoop Az 90 el. 6,2 Outer Rebar Layer
0,001500
0,001000
0,000500
0,000000
-0,000500
deformation
0,000
0,200
0,400
0,600
0,800
1,000
1,200
1,400
pressure MPa
experiment
computation

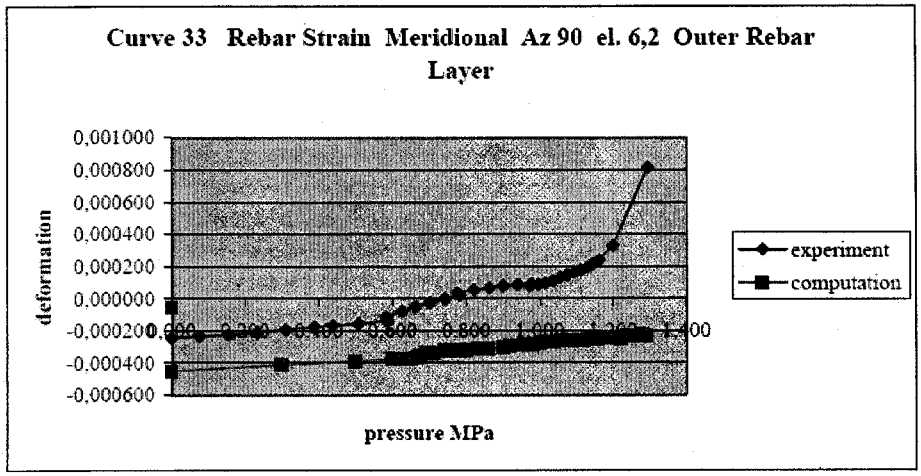
Curve 33 Rebar Strain Meridional Az 90 el. 6,2 Outer Rebar Layer
0,001000
0,000800
0,000600
0,000400
0,000200
0,000000
-0,000200
-0,000400
-0,000600
deformation
0,000
0,200
0,400
0,600
0,800
1,000
1,200
1,400
pressure MPa
experiment
computation

Curve 34 Liner Strain Meridional Az 0 el. 0,01 Inside Liner Surface

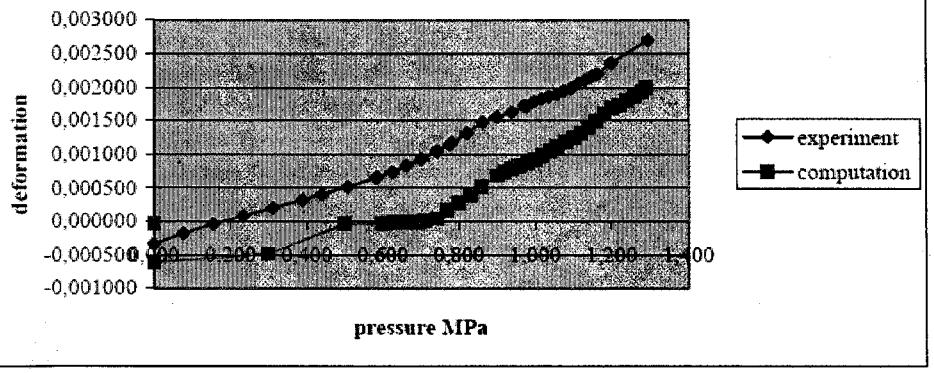

Curve 35 Liner Strain Meridional Az 0 el. 0,01 Outside Liner Surface

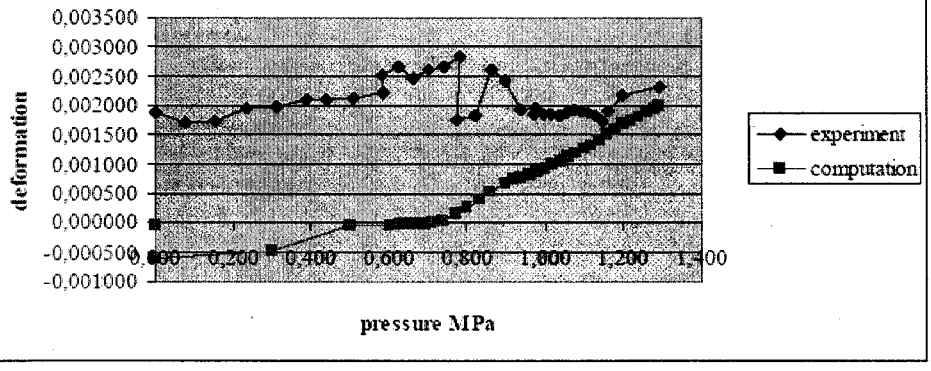

Curve 36 Liner Strain Meridional Az 135 el. 0,25 Inside Liner Surface

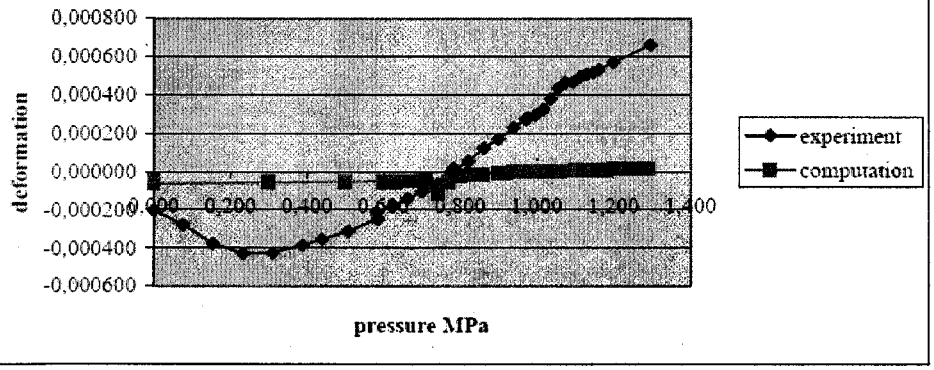

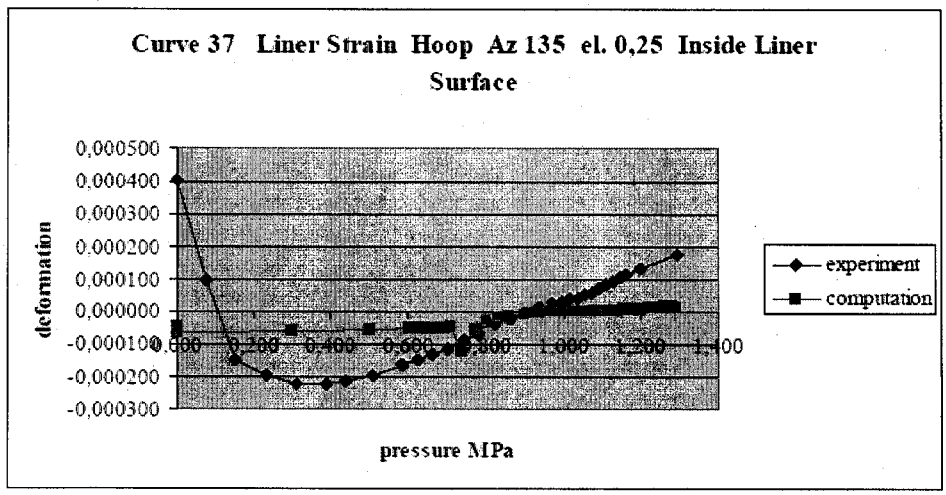
Curve 37 Liner Strain Hoop Az 135 el. 0,25 Inside Liner Surface
0,000500
0,000400
0,000300
0,000200
0,000100
0,000000
-0,000100
-0,000200
-0,000300
deformation
0,000
0,200
0,400
0,600
0,800
1,000
1,200
1,400
pressure MPa
experiment
computation

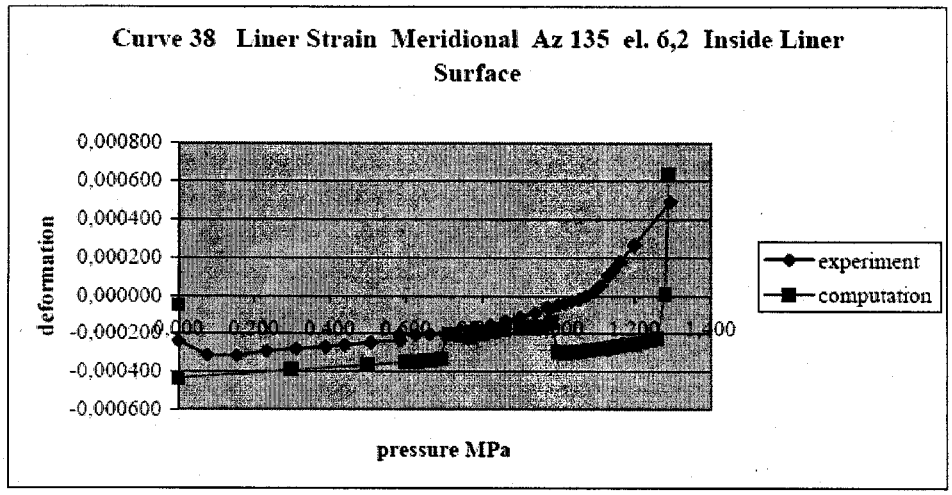
Curve 38 Liner Strain Meridional Az 135 el. 6,2 Inside Liner Surface
0,000800
0,000600
0,000400
0,000200
0,000000
-0,000200
-0,000400
-0,000600
deformation
0,000
0,200
0,400
0,600
0,800
1,000
1,200
1,400
pressure MPa
experiment
computation

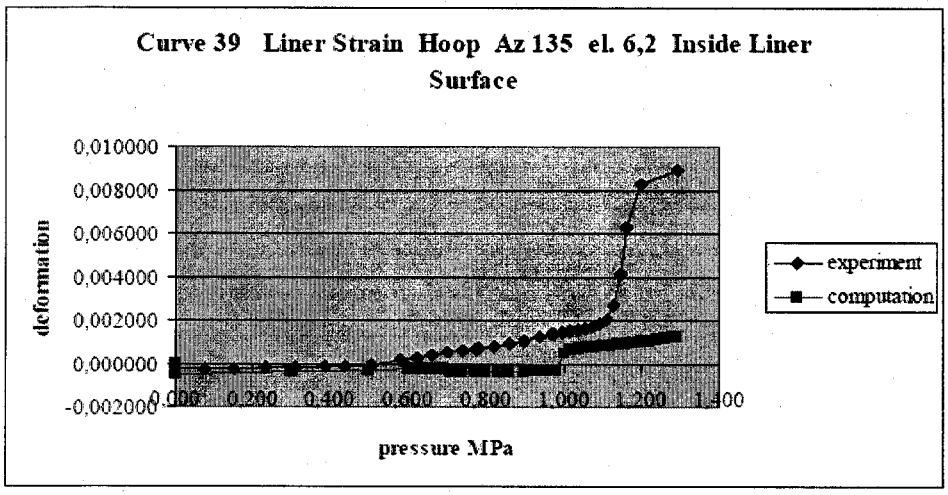
Curve 39 Liner Strain Hoop Az 135 el. 6,2 Inside Liner Surface
0,010000
0,008000
0,006000
0,004000
0,002000
0,000000
-0,002000
deformation
0,000
0,200
0,400
0,600
0,800
1,000
1,200
1,400
pressure MPa
experiment
computation

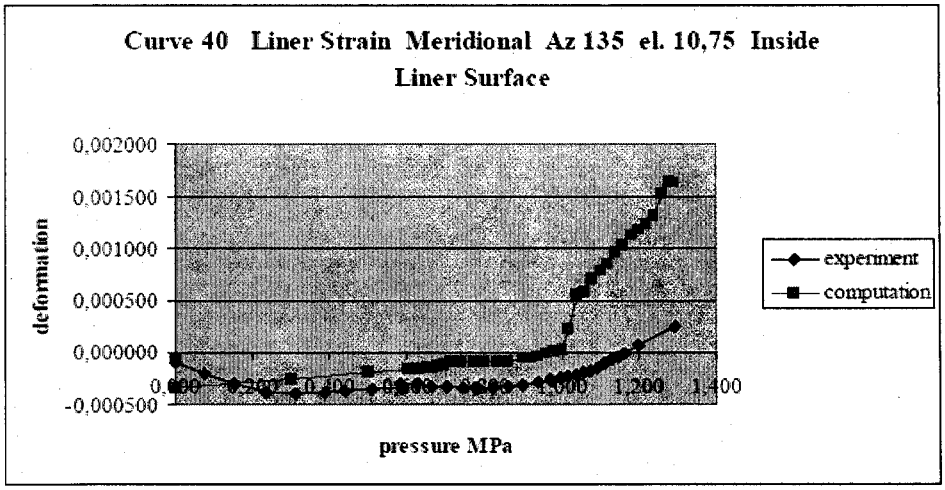
Curve 40 Liner Strain Meridional Az 135 el. 10,75 Inside Liner Surface
deformation
0,002000
0,001500
0,001000
0,000500
0,000000
-0,000500
0,000
0,200
0,400
1,000
1,200
1,400
pressure MPa
experiment
computation

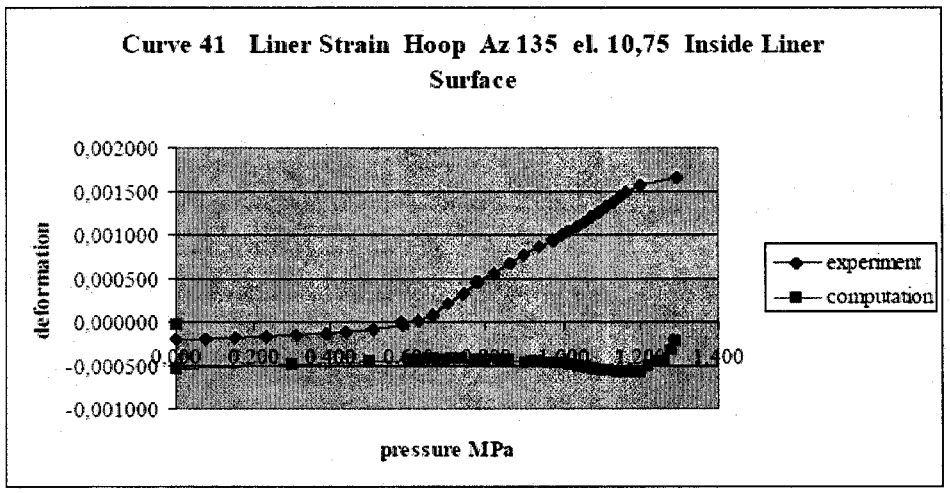
Curve 41 Liner Strain Hoop Az 135 el. 10,75 Inside Liner Surface
deformation
0,002000
0,001500
0,001000
0,000500
0,000000
-0,000500
-0,001000
0,000
0,200
0,400
1,200
1,400
pressure MPa
experiment
computation

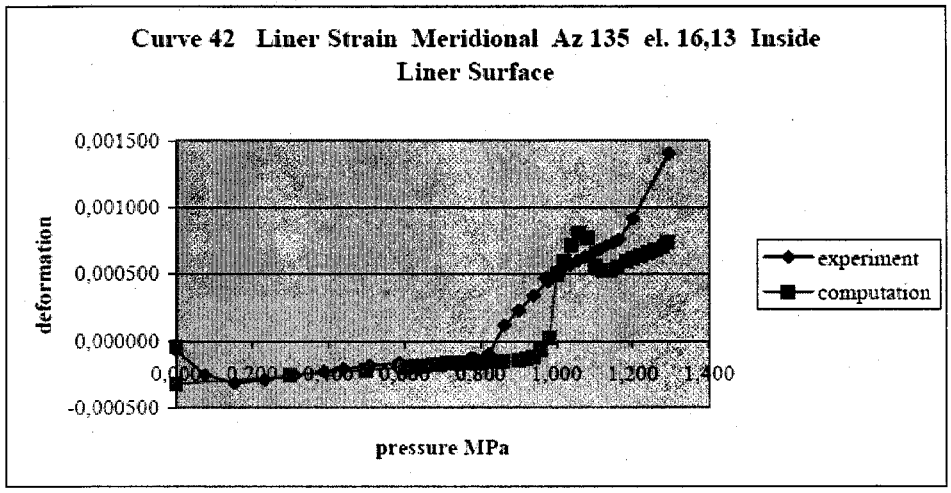
Curve 42 Liner Strain Meridional Az 135 el. 16,13 Inside Liner Surface
deformation
0,001500
0,001000
0,000500
0,000000
-0,000500
0,000
0,200
0,400
0,800
1,000
1,200
1,400
pressure MPa
experiment
computation

Curve 43 Liner Strain Meridional Az 90 el. 6,2 Inside Liner Surface

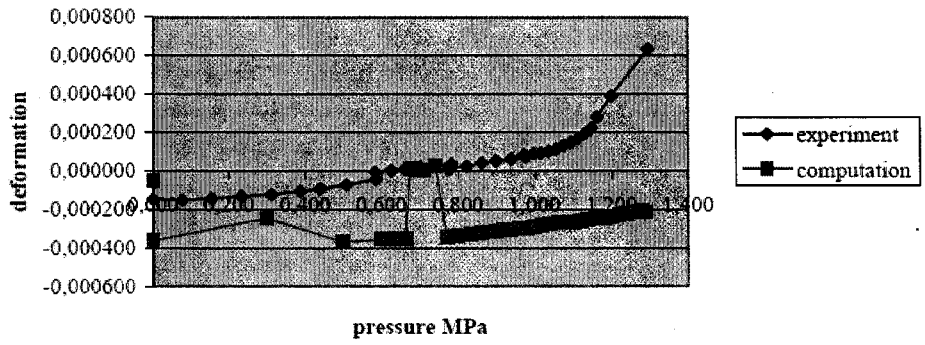

Curve 44 Liner Strain Hoop Az 90 el. 6,2 Inside Liner Surface

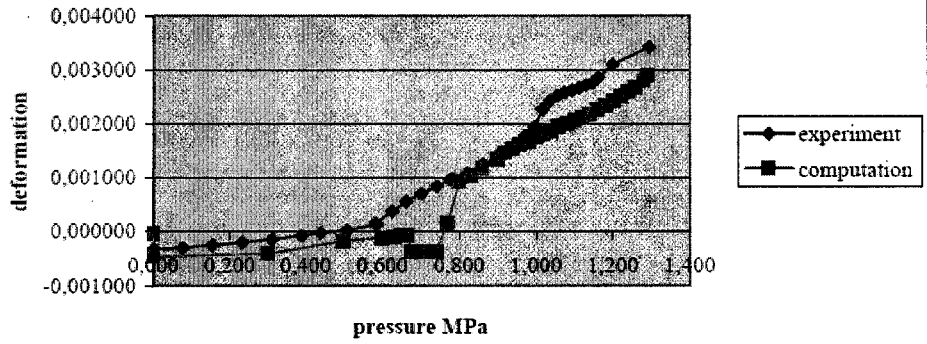

Curve 45 Liner Strain Hoop Az 334 el. 4,675 Inside Liner Surface

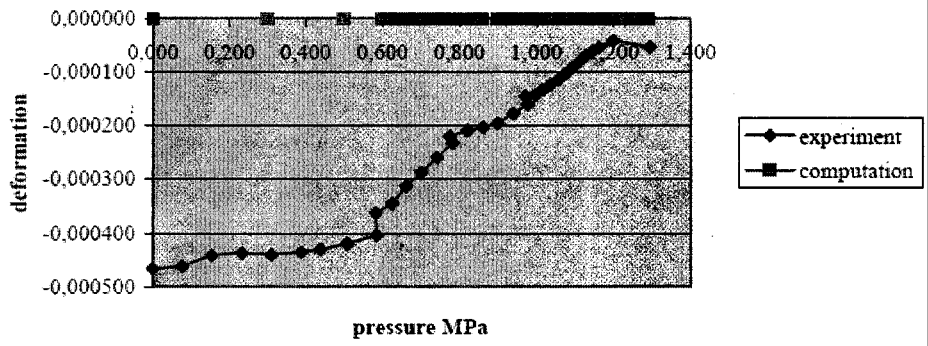

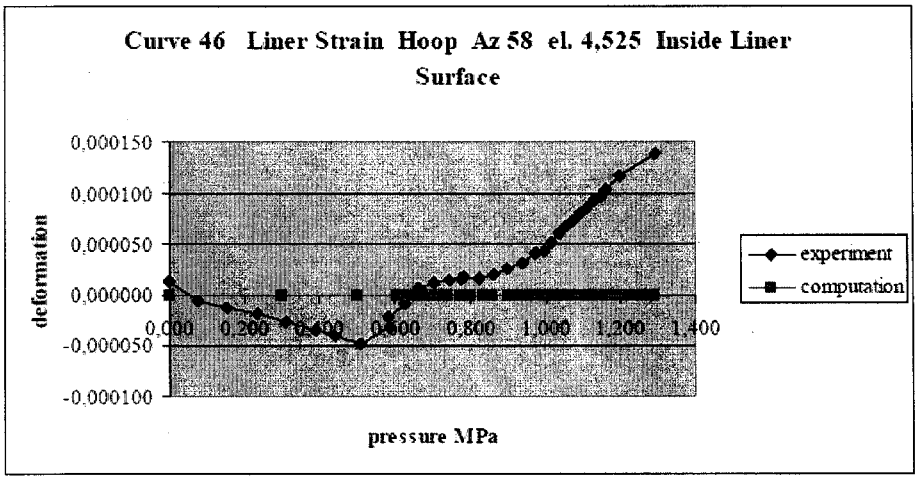
Curve 46 Liner Strain Hoop Az 58 el. 4,525 Inside Liner Surface
0,000150
0,000100
0,000050
0,000000
-0,000050
-0,000100
deformation
0,000 0,200 0,400 0,600 0,800 1,000 1,200 1,400
pressure MPa
experiment
computation

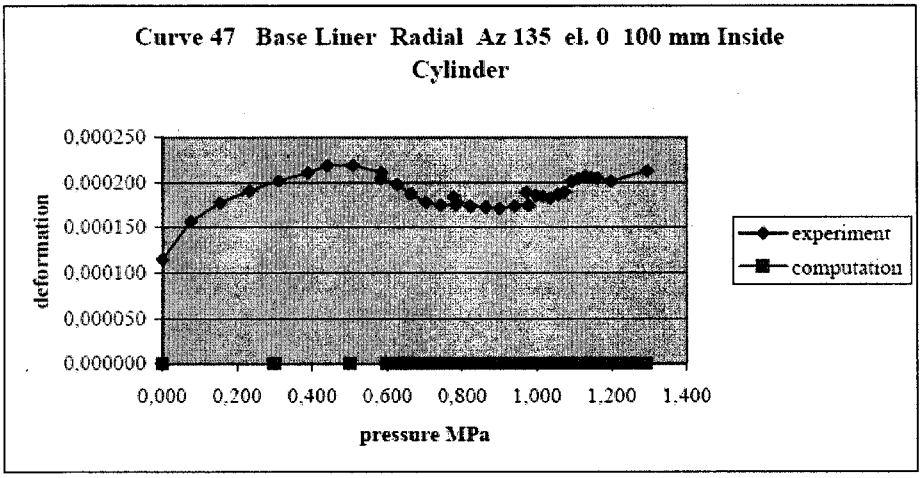
Curve 47 Base Liner Radial Az 135 el. 0 100 mm Inside Cylinder
0,000250
0,000200
0,000150
0,000100
0,000050
0,000000
deformation
0,000 0,200 0,400 0,600 0,800 1,000 1,200 1,400
pressure MPa
experiment
computation

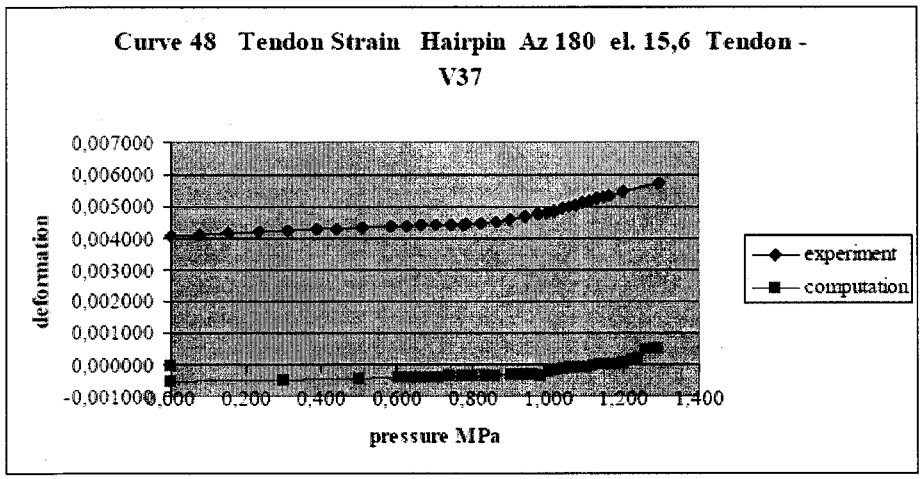
Curve 48 Tendon Strain Hairpin Az 180 el. 15,6 Tendon - V37
0,007000
0,006000
0,005000
0,004000
0,003000
0,002000
0,001000
0,000000
-0,001000
deformation
0,000 0,200 0,400 0,600 0,800 1,000 1,200 1,400
pressure MPa
experiment
computation

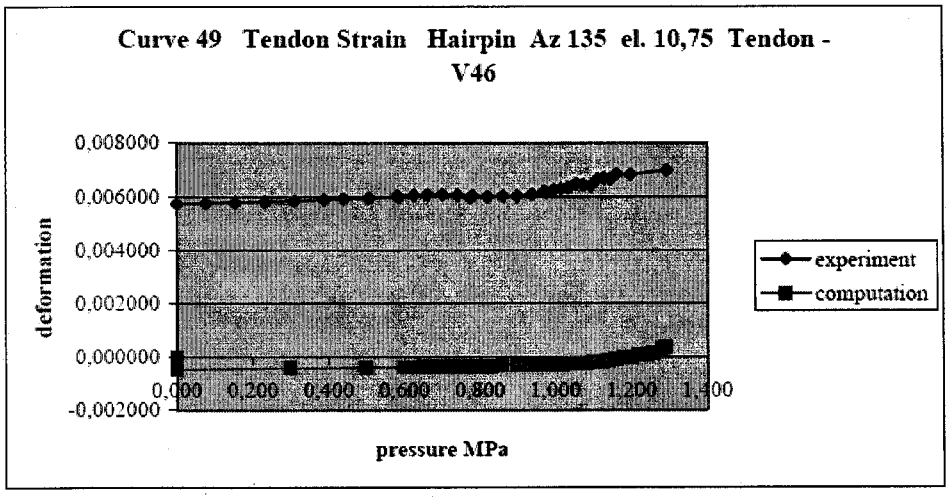
Curve 49 Tendon Strain Hairpin Az 135 el. 10,75 Tendon - V46
0,008000
0,006000
0,004000
0,002000
0,000000
-0,002000
deformation
0,000
0,200
0,400
0,600
0,800
1,000
1,200
1,400
pressure MPa
experiment
computation

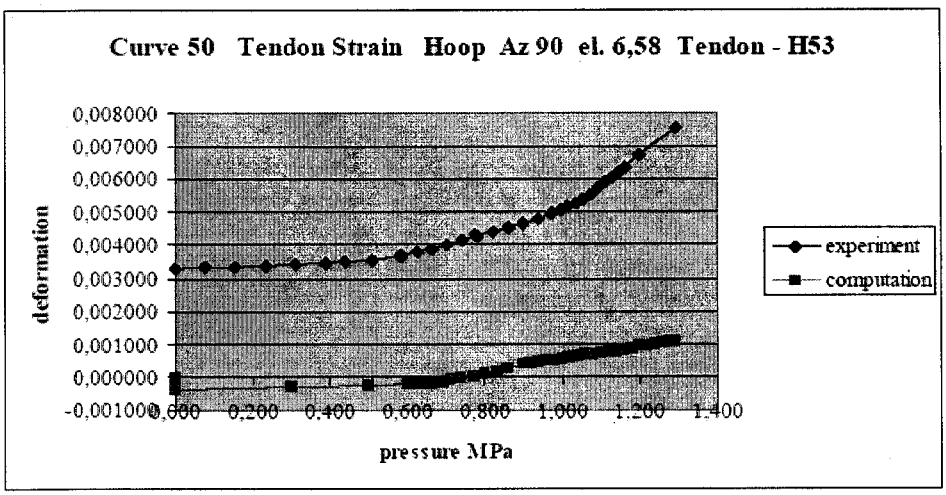
Curve 50 Tendon Strain Hoop Az 90 el. 6,58 Tendon - H53
0,008000
0,007000
0,006000
0,005000
0,004000
0,003000
0,002000
0,001000
0,000000
-0,001000
deformation
0,000
0,200
0,400
0,600
0,800
1,000
1,200
1,400
pressure MPa
experiment
computation

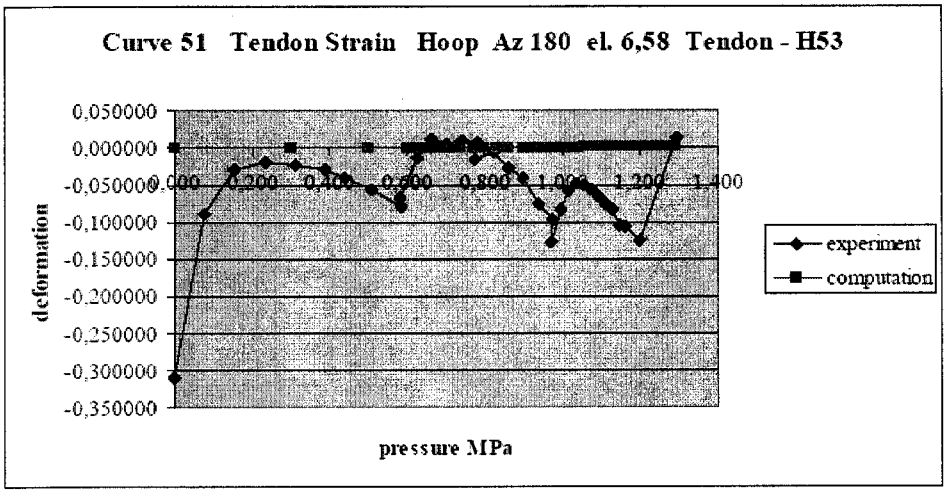
Curve 51 Tendon Strain Hoop Az 180 el. 6,58 Tendon - H53
0,050000
0,000000
-0,050000
-0,100000
-0,150000
-0,200000
-0,250000
-0,300000
-0,350000
deformation
0,000
0,200
0,400
0,600
0,800
1,000
1,200
1,400
pressure MPa
experiment
computation

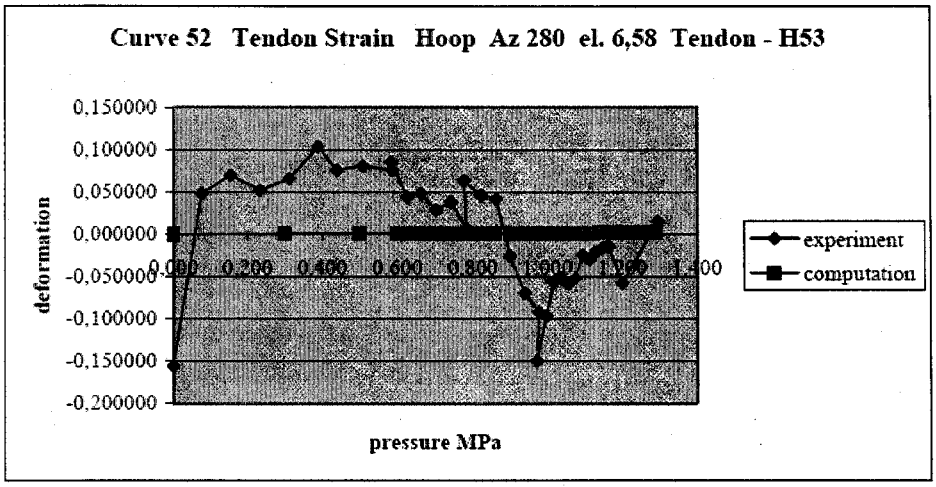
Curve 52 Tendon Strain Hoop Az 280 el. 6,58 Tendon - H53
0,150000
0,100000
0,050000
0,000000
-0,050000
-0,100000
-0,150000
-0,200000
deformation
0,000
0,200
0,400
0,600
0,800
1,000
1,200
1,400
pressure MPa
experiment
computation

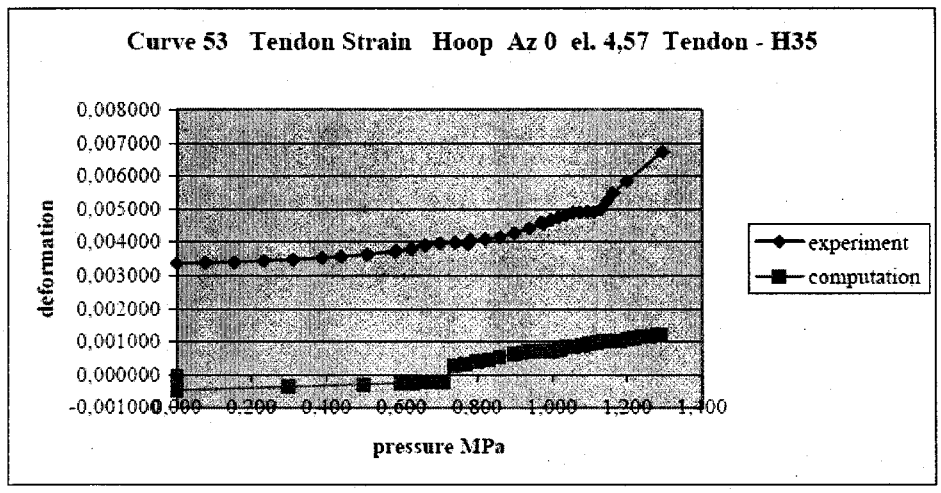
Curve 53 Tendon Strain Hoop Az 0 el. 4,57 Tendon - H35
0,008000
0,007000
0,006000
0,005000
0,004000
0,003000
0,002000
0,001000
0,000000
-0,001000
deformation
0,000
0,200
0,400
0,600
0,800
1,000
1,200
1,400
pressure MPa
experiment
computation

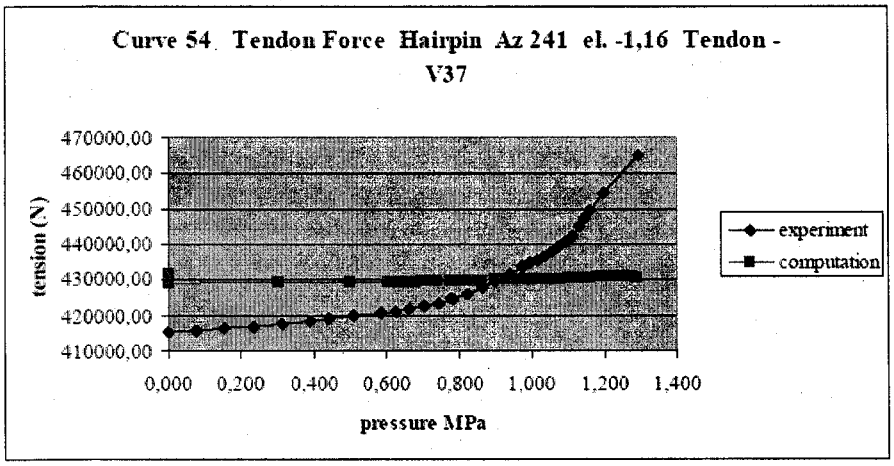
Curve 54 Tendon Force Hairpin Az 241 el. -1,16 Tendon - V37
470000,00
460000,00
450000,00
440000,00
430000,00
420000,00
410000,00
tension (N)
0,000
0,200
0,400
0,600
0,800
1,000
1,200
1,400
pressure MPa
experiment
computation

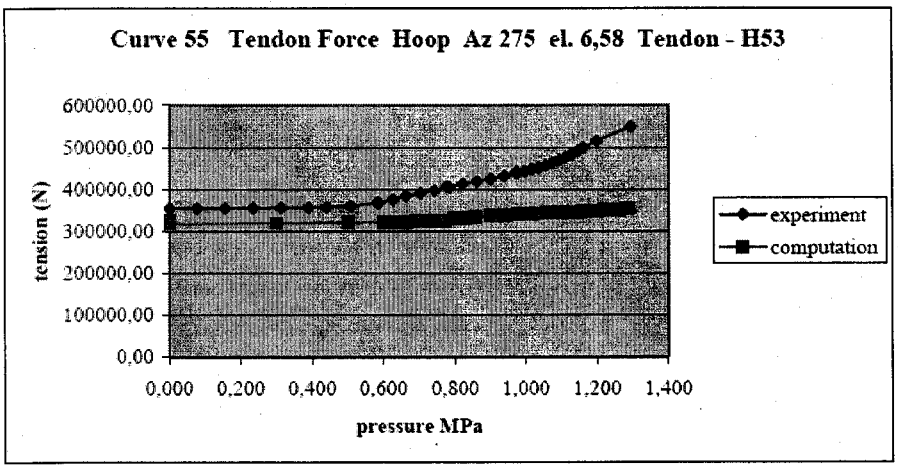
Curve 55 Tendon Force Hoop Az 275 el. 6,58 Tendon - H53
600000,00
500000,00
400000,00
300000,00
200000,00
100000,00
0,00
tension (N)
0,000
0,200
0,400
0,600
0,800
1,000
1,200
1,400
pressure MPa
experiment
computation

Appendix F:

Korea Atomic Energy Research Institute

FINITE ELEMENT ANALYSIS OF A 1:4 SCALE PCCV MODEL

Hong-pyo Lee, Young-sun Choun
Korea Atomic Energy Research Institute, Korea

Abstract

This report describes the finite element (FE) analysis results of a 1:4 scale model of a pre-stressed concrete containment vessel (PCCV) model. The objective of the present FE analysis is to evaluate the ultimate internal pressure capacity of the PCCV as well as its failure mechanism when the PCCV model is subjected to a monotonous internal pressure beyond its design pressure. The FE analysis used two concrete failure criteria with the commercial code ABAQUS. One is axi-symmetric model with modified Drucker-Prager failure criteria and the other is 3-dimensional model with damaged plasticity model. Finally, the FE analysis results on the ultimate pressure and failure modes have a good agreement with experimental data.

Introduction

This report describes the finite element (FE) analysis results of a 1:4 scale model of a pre-stressed concrete containment vessel (PCCV) tested by the Nuclear Power Engineering Corporation (NUPEC) of Japan and the U.S. Nuclear Regulatory Commission (NRC) [1]. The main objective of the present FE analysis is to evaluate the failure load of the PCCV as well as its failure mechanism when the PCCV model is subjected to a monotonous internal pressure beyond its design pressure 0.4MPa. In addition we try to evaluate the performance of the existing numerical simulation tool and intend to use its results as future numerical reference solutions.

Two FE models such as 2-dimensional axi-symmetric model and 3-dimensional model with opening and two buttresses are considered in the present nonlinear FE analysis. In the axi-symmetric model, all the portions of PCCV such as the cylinder wall, dome and basemat are considered in the FE analysis. Concrete part was modeled with 4-node axi-symmetric solid element and the steel liner was modeled with 2-node axi-symmetric membrane element. In addition, reinforcement and tendon were modeled with rebar element. Modified Drucker-Prager model [2] is used for concrete failure criterion. In the 3-dimensional model, concrete part was modeled with 8-node solid element and the steel liner was modeled with 4-node membrane element. Reinforcement and tendon are modeled with the embedded element. A damaged plasticity model [3] is adopted to be used as concrete failure criterion.

This report summarizes the FE analysis results produced by Korea Atomic Energy Research Institute (KAERI) with the above two FE models using the commercial code ABAQUS [4]. The material properties and detailed structural geometry used in the present FE analysis are provided in the following sections with numerical results.

Material Properties used in FE analysis

The material properties for concrete, steel rebars, post-tensioned tendons and steel liner are prepared by using the experiment data provided by Sandia National Laboratories (SNL)[1]. In this section, the material properties used in FE analysis are briefly described.

Concrete

Two types of concrete such as a normal strength concrete and a high strength concrete were used to construct the SNL PCCV test model [1]. In the present FE analysis, the material property data for the trial mix concrete based on a field curing are used. The material properties adopted in the FE analysis are described in Table 1.

Reinforcing Steel

The material properties for each type of rebar are selected from the test data. The material properties are summarized in Table 2 and the test data for reinforcing bar is illustrated in Figure 1 [1]. In FE analysis, we adopt the mean value for the material properties of rebar: (a) SD490 is used for the

basemat part; (b) SD390 is used for the cylinder wall and dome parts.

- Elastic modulus : 1.86E5 MPa (basemat), 1.848E5 MPa (wall and dome)
- Yield stress : 512.2 MPa (basemat), 479.9 MPa (wall and dome)
- Ultimate stress : 709.7 MPa (basemat), 628.7 MPa (wall and dome)
- Poisson's ratio : 0.3
- Elongation(%) : 17.8 MPa (basemat), 21.32 MPa (wall and dome)

Prestressing Tendon

TAISEI performed the calibration tests of six samples of a three-strand tendon assembly. The stress-stain data are calculated by the division of the measured forces by the initial cross section area ($339mm^2$) as shown in Figure 2 [5]. The ultimate stress and strain test data are summarized in Table 3[2].

Steel Liner Plate

Two sets of material samples for the steel liner plate, LPY in vertical direction and LPX in circumferential direction, were tested to evaluate their material properties. Each test set consists of three samples. The stress-strain data is illustrated in Figure 3 and the test results are summarized in Table 4.

Table 1. Material data for trial mix concrete (unit: MPa)

Material / Item	f_c'=29.42 (basemat)		f_c'=44.13 (dome & wall)	
	Standard curing	Field curing	Standard curing	Field curing
Compressive strength	51.39	41.68	60.21	48.84
Tensile strength	3.93	3.37	4.21	3.45
Flexural strength	5.37	4.00	5.58	5.51
Young's modulus	29,030	27,950	31,970	26,970
Poisson's ratio	0.20	0.18	0.20	0.18
Density (ton/m^3)	2.25	2.21	2.26	2.19

Figure 1. Stress-strain relationship for steel

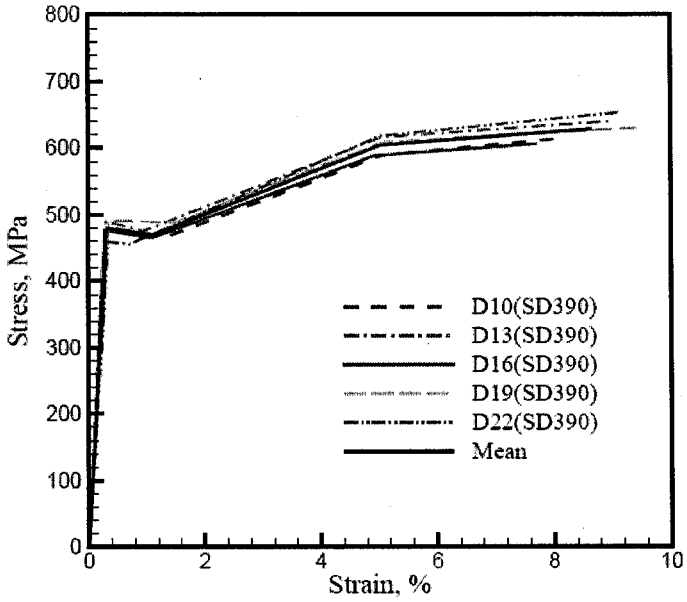

Table 2. rebar material properties (unit:MPa)

Material / Item	D10 (SD390)	D13 (SD390)	D16 (SD390)	D19 (SD390)	D22 (SD390)	D19 (SD490)
Elastic modulus	1.83E5	1.83E5	1.83E5	1.84E5	1.91E5	1.86E5
Poisson's ratio	0.3	0.3	0.3	0.3	0.3	0.3
Yield stress	482.0	490.1	476.6	491.9	459.0	512.2
Ultimate stress	613.6	640.4	606.2	630.4	653.2	709.7
Elongation (%)	20.5	24.2	22.1	21.1	18.7	17.8

Figure 2. Stress-Strain relationship for tendons

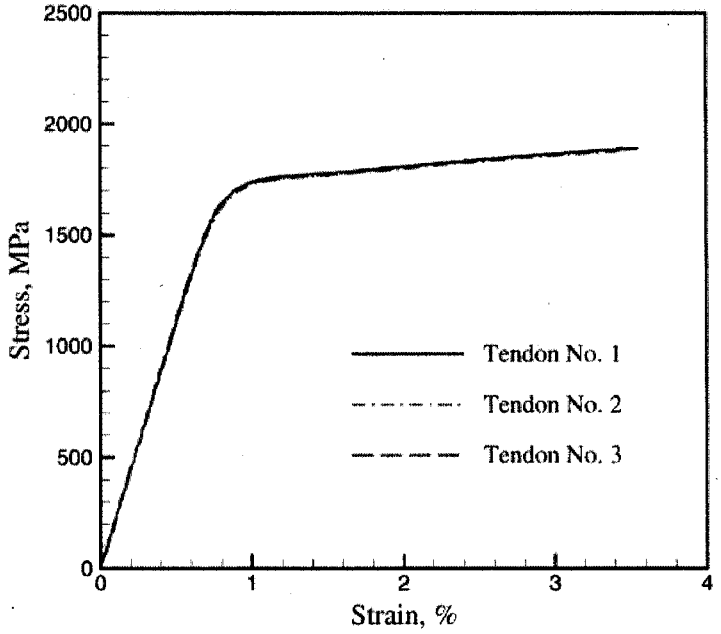

Table 3. Tendon material data

Test specimen	Ultimate stress (MPa)	Failure strain (%)
Specimen 1	1,924	3.32
Specimen 2	1,912	3.51
Specimen 3	1,932	3.36
Specimen 4	1,921	No strain gages
Specimen 5	1,934	No strain gages
Specimen 6	1,924	3.3
Mean	1,924.5	3.3

* Estimate based on surviving strain gages

Figure 3. Stress-strain relationship for steel liner

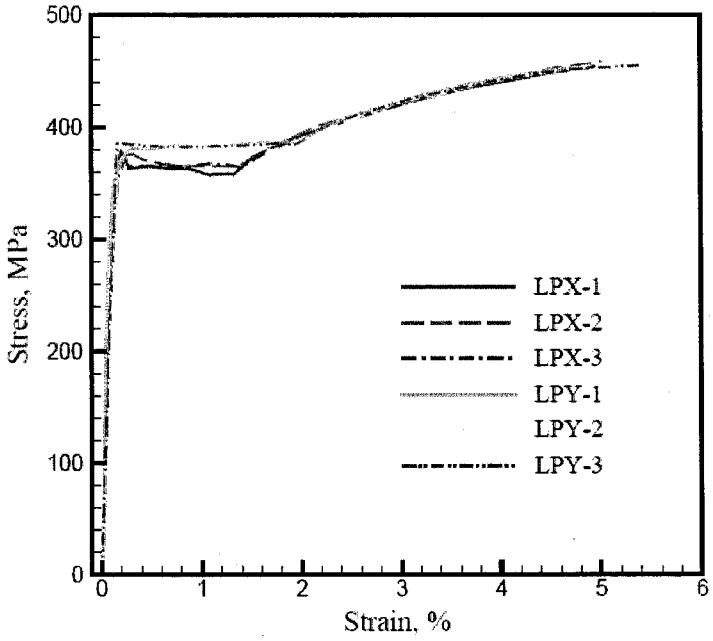

Table 4. Material data for steel liner

Material	Temperature	Test sample	Yield stress (MPa)	Ultimate stress (MPa)	Elongation (%)
SGV410	R.T.(23 °C)	LPY-1	381.5	495.2	33.8
"	"	LPY-2	403.1	498.2	33.0
"	"	LPY-3	385.4	497.2	33.6
"	"	LPX-1	377.6	499.2	33.0
"	"	LPX-2	377.6	500.1	33.0
"	"	LPX-3	370.7	497.2	33.0
Average			382.7	497.85	33.2

Constitutive Models

As briefly mentioned before, two FE models are prepared for the nonlinear analysis of 1:4-scale PCCV model. One is axi-symmetric FE model and the other is three-dimensional FE model considering the penetrations such as equipment hatch and personal airlock. This section describes the constitutive models used for two FE models.

Concrete model

2-dimensional axi-symmetric model

The modified Drucker-Prager's model [2] is used for 2-dimensional axi-symmetric FE analysis. In this model, three different yield criteria based on the shape of the yield surface in the meridional plane are provided in ABAQUS. These yield surfaces are a linear form, a hyperbolic form and a general exponent form. In the present analysis, the yield surface with linear form is adopted. The linear model used in FE analysis is written in terms of all three stress invariants.

$$F = t - p\tan\beta - d = 0 \tag{1}$$

where $t = \frac{1}{2}q\left[1 + \frac{1}{K} - \left(1 - \frac{1}{K}\right)\left(\frac{r}{q}\right)^3\right]$

p , q , r are stress invariants defined in stress and strain measurements.

β is the slope of the linear yield and is commonly referred to as the friction angle of the material,

d is the cohesion of the material and

K is the ratio of the yield stress in triaxial tension to the yield stress in triaxial compression and, thus controls the dependency of the yield surface on the value of the intermediate principal stress.

The values of K=1, t=q imply that the yield surface is the von Mises circle in the deviatoric principal stress plane (the π-plane), in which case the yield stresses in triaxial tension and compression are the same. It requires $0.778 \le K \le 1.0$ to ensure that the yield surface remains convex. In the present FE analysis, the friction angle and the dilation angle such as 71.56 degrees and

56.97 degrees are adopted respectively.

Figure 4. Typical yield and flow surfaces of the linear model in the deviatoric plane.

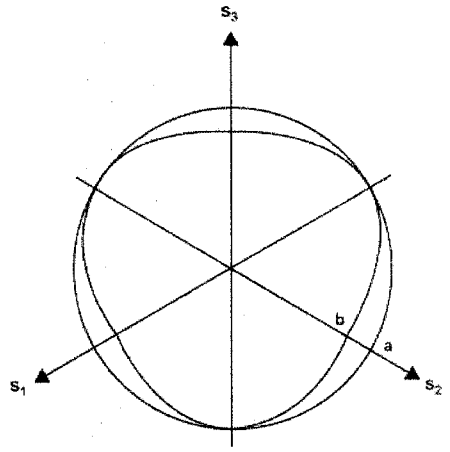

$$t = \frac{1}{2}q\left[1 + \frac{1}{k} - \left(1 - \frac{1}{k}\right)\left(\frac{r}{q}\right)^3\right]$$

Curve	K
a	1.0
b	0.8

3-dimensional model

The damaged plasticity model [3] is used for concrete material in the 3-dimentional FE analysis. Specifically, two main failure mechanisms such as tensile cracking and compressive crushing of the concrete material are considered in this model. The evolution of the yield (or failure) surface is controlled by two hardening variables, $\overline{\varepsilon}_t^{pl}$ and $\overline{\varepsilon}_c^{pl}$ which are related to failure mechanisms under tension and compression loading respectively. We refer to $\overline{\varepsilon}_t^{pl}$ and $\overline{\varepsilon}_c^{pl}$ as tensile and compressive equivalent plastic strains respectively.

In this model, the uniaxial tensile and compressive response of concrete is characterized by the damaged plasticity model as shown in Figure 5. Under uniaxial tension, the stress-strain relationship follows a linear elastic relationship until the value of the failure stress (σ_{t0}). The failure stress corresponds to the onset of micro-cracking in the concrete material. Beyond the failure stress, the formation of micro-cracks is represented macroscopically with a softening stress-strain response, which induces strain localization in the concrete structure. Under uniaxial compression the response is linear until the value of initial yield (σ_{c0}). In the plastic regime the response is typically characterized by a stress hardening followed by strain softening beyond the ultimate stress σ_{cu}.

It is assumed that the uniaxial stress-strain curves can be converted into stress versus plastic-strain curves. Thus,

$$\begin{aligned}\sigma_t &= \sigma_t\left(\bar{\varepsilon}_t^{pl}, \dot{\bar{\varepsilon}}_t^{pl}, \theta, f_i\right)\\ \sigma_c &= \sigma_c\left(\bar{\varepsilon}_c^{pl}, \dot{\bar{\varepsilon}}_c^{pl}, \theta, f_i\right)\end{aligned} \tag{2}$$

where the subscripts t and c refer to tension and compression respectively. $\bar{\varepsilon}_t^{pl}$ and $\bar{\varepsilon}_c^{pl}$ are the equivalent plastic strains and $\dot{\bar{\varepsilon}}_t^{pl}$ and $\dot{\bar{\varepsilon}}_c^{pl}$ are the corresponding plastic strain rates. θ is the temperature and $f_i\left(i = 1, 2, \ldots\right)$ are other predefined field variables.

As shown in Figure 5, when the concrete specimen is unloaded from any point on to the strain softening branch of the stress-strain curves, the unloading response is weakened and the elastic stiffness of the material appears to be damaged (or degraded). The degradation of the elastic stiffness is characterized by two damage variables, d_t and d_c, which are assumed to be functions of the plastic strains, temperature, and field variables:

$$\begin{aligned}d_t &= d_t\left(\bar{\varepsilon}_t^{pl}, \theta, f_i\right); \quad 0 \le d_t \le 1\\ d_c &= d_c\left(\bar{\varepsilon}_c^{pl}, \theta, f_i\right); \quad 0 \le d_c \le 1\end{aligned} \tag{3}$$

Figure 5. Response of concrete to uniaxial loading in tension (left) and compression (right)

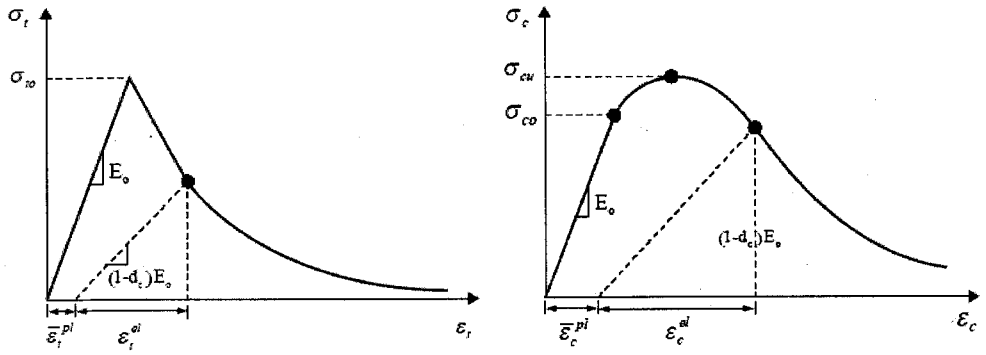

The damage variables can take values from zero, representing the undamaged material, to one, which represents total loss of strength. If E_0 is the initial (undamaged) elastic stiffness of the material, the stress-strain relations under uniaxial tension and compression loading are

$$\begin{aligned} \sigma_t &= (1-d_t)E_0\left(\varepsilon_t - \overline{\varepsilon}_t^{pl}\right) \\ \sigma_c &= (1-d_c)E_0\left(\varepsilon_c - \overline{\varepsilon}_c^{pl}\right) \end{aligned} \tag{4}$$

Tension stiffening model

Owing to the bond effect between concrete and reinforcing bars, the concrete can take a part of the tensile force even after crack formation. It makes that the stiffness of reinforced concrete remains higher than that of the reinforcing bars alone. This phenomenon is so called '*tension stiffening effect*'. In numerical simulation, this effect can be represented in two ways: one is to modify the stiffness of reinforcing bars and the other is to modify the stiffness of the concrete so that the concrete can carry the tensile force after cracks. In the present FE analysis, the latter tension-stiffening model proposed by Okamura [6] is adopted (see Figure 6).

From Okamura's study [6],

Ascending branch ($\varepsilon_t \le \varepsilon_{cr}$):

$$\sigma_t = E_c \cdot \varepsilon_t \tag{5}$$

Descending branch ($\varepsilon_t > \varepsilon_{cr}$):

$$\sigma_t = f_t\left(\frac{\varepsilon_{cr}}{\varepsilon_t}\right)^{0.2} \tag{6}$$

where ε_t is total strain in concrete, ε_{cr} is the cracking strain and f_t is the stress corresponding to the cracking strain.

Figure 6. Tension stiffening model for concrete

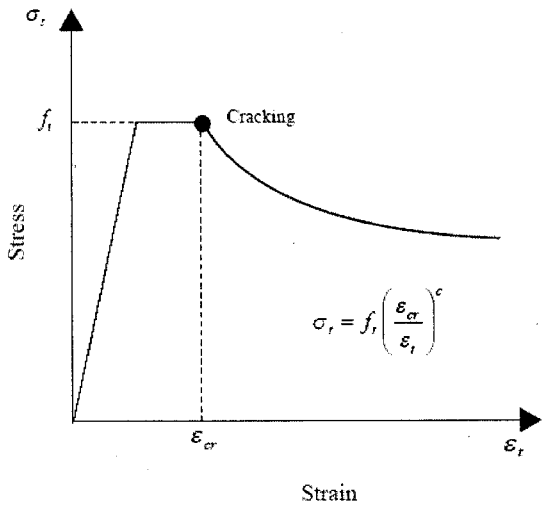

Steel model

The stress-strain relationship of the mild steel is usually assumed to be elasto-perfectly plastic with a distinct yield stress of f_y. However, when the reinforcing bars are surrounded by concrete, the average stress-strain relationship exhibits a quite different behaviour to the bare bar as shown in Figure 7. To consider this behaviour, we generally underestimate the yield stress f_y. In the present FE analysis, the stress-strain relationship for the steel bar is represented by Hsu's model [7] as follows:

$$\frac{\overline{f}_y}{f_y} = 1 - \frac{4}{\rho}\left(\frac{f_{cr}}{f_y}\right)^{1.5} \tag{7}$$

where f_y and $\overline{f}_y$ are the yield stresses of bare bar and embedded bar in concrete respectively. ρ is the reinforcement ratio and f_{cr} is the cracking stress value.

Figure 7. Average yield stress-strain curve

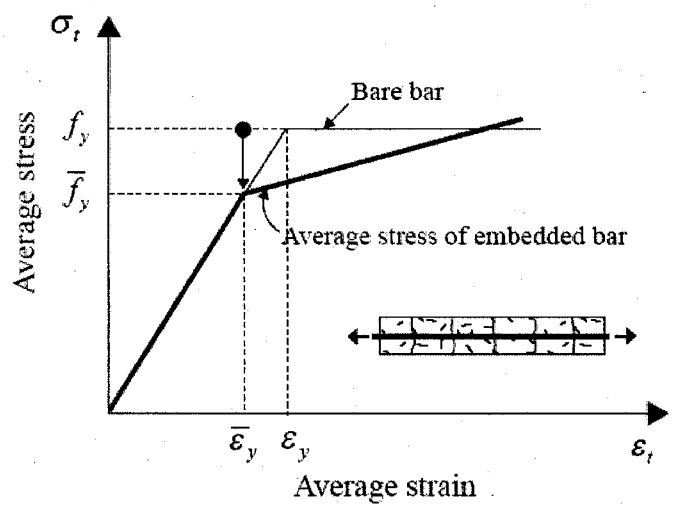

Tendon model

The stress-strain relationship for the tendons is evaluated from the tensile test results of the PCCV tendon system and the static tensile test of PCCV tendon strand. The tendon is theoretically modeled as an elasto-plastic material model with *PLASTIC option in ABAQUS. In the FE analysis, the stress-strain curve having three main data points is used as shown in Figure 8. The first point A represents the elastic limit value which is straight line up to $0.7 f_{pu}$ from zero point, where f_{pu} is the ultimate strength of the tendon. The third point C is the representative ultimate strength of the tendon. The prestressing data such as the average measured values of forces, friction and seating losses are summarized in Table 5.

The following material properties of tendon are used to prepare the input data for the FE analysis:

- Elastic modulus : 2.197E5 MPa
- Poission's ratio : 0.3
- Yield stress : 1,621 MPa
- Ultimate stress : 1,875.8 MPa
- Elongation : 3.42%

Figure 8. Stress-strain curve for tendon

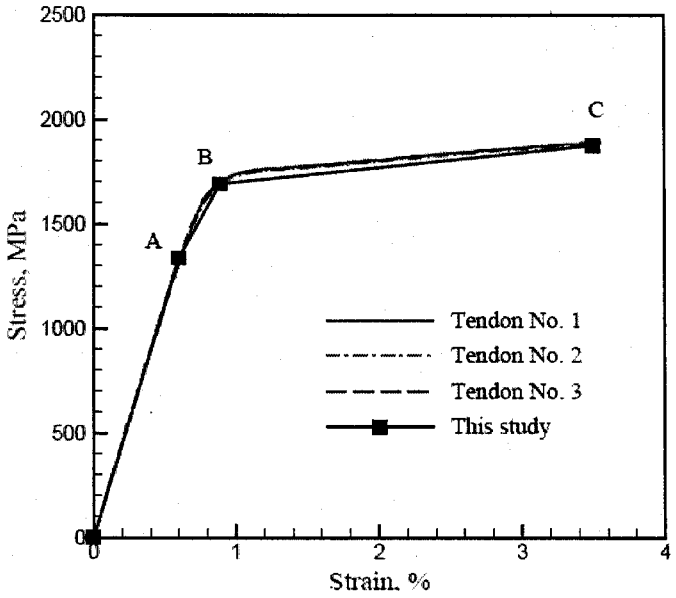

Table 5. Prestressing data summary

Item	Hoop tendons		Vertical tendons	
Average Tensile Force:				
Design:	44.41 T	97.9 kips	49.57 T	109.00 kips
Jack:	43.53 T	95.97 kips	49.02 T	108.07 kips
Jack(w/ Load Cells only):	43.61 T	96.14 kips	49.09 T	108.23 kips
Load Cell:	43.21 T	95.27 kips	48.20 T	106.27 kips
Average Lift-off Force:				
Design:	34.11 T	75.2 kips	46.31 T	102.10 kips
Jack:	34.02 T	75.01 kips	44.22 T	97.49 kips
Average Friction Coefficient:	0.18		0.22	
Average Seating Loss:	3.95mm	0.16 inch	4.95mm	0.19 inch
Jack:	9.51 T	20.96 kips	4.80 T	10.58 kips
Load Cell:	9.86 T	21.75 kips	4.64 T	10.23 kips
Average Final Load Cell Force:	33.34 T	73.52 kips	43.56 T	96.04 kips
Average Elastic Loss:	0.27 T	0.59 kips	0.58 T	1.29 kips

Liner plate model

The steel liner plate is modeled by using an elasto-plastic material model with *PLASTIC option in ABAQUS. In Figure 9, the stress-strain curve for the FE analysis is compared with experimental data provided by SNL.

The following material properties of liner plate are used to prepare the input data for the present FE analysis:

- Elastic moduls : 2.187E5 MPa
- Poission's ratio : 0.3
- Yield stress(MPa) : 382.7 MPa
- Ultimate tensile stress : 497.85 MPa
- Elongation(%) : 33.2

Figure 9. Stress-strain curve for liner plate

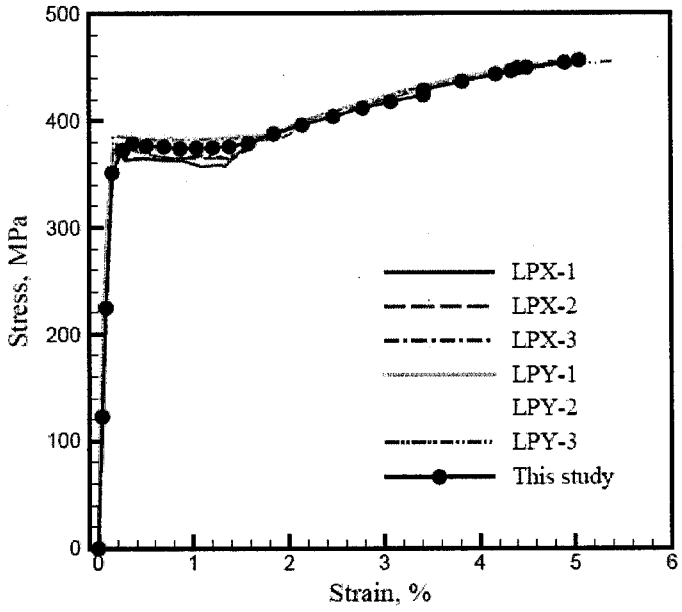

FE Analysis Procedure for ABAQUS Code

The numerical analysis steps used in the present FE analysis are:

(1) Gravity + Pre-stress force
(2) Gravity + Pre-stress force + Internal pressure

An initial load step in which the PCCV is brought into static equilibrium with the initial post-tensioning tendon loads and the self-weight is established. The weight of the embedded steel reinforcements and tendons has not been included as part of the total vessel weight.

After initial load step, a uniform pressure is applied to the faces of the liner plate elements that comprise of the internal surface of the vessel. The internal pressure is also applied to the penetrations cover plates such as personal airlock and equipment hatch.

Finite Element Model

2-dimensional axi-symmetric model

The axi-symmetric FE model used in the prediction of the overall response of the PCCV is illustrated in Figure 10. The FE model consists of 768 axi-symmetric 4-node solid elements (CAX4) to represent concrete layer and 2-node 203 axi-symmetric membrane elements (MAX1) to represent liner layer as shown in Figure 10. All rebars and tendons are modeled by using the rebar sub-element provided in the code ABAQUS. Therefore, they are assumed to be rigidly bonded to the concrete. The pre-stressing force for tendon is represented by the *INITIAL CONDITION option in ABAQUS. The boundary condition for the bottom of the base slab is assumed to be fixed so that the present FE model can not simulate the possible vertical uplift during internal pressurization.

3-dimensional model

The 3-dimensional FE model with large penetrations such as equipment hatch and air lock is also adopted as shown in Figure 11 and 12. The 3-dimensional model consists of 6,992 8-node solid elements (C3D8), 3,100 4-node liner elements (M3D4) and 9.522 truss elements (T3D3). The rebar

and tendon are modeled with embedded element. The layout of tendon used in the present FE analysis is illustrated in Figure 13. The pre-stressing force for tendon is represented by the *INITIAL CONDITION option in ABAQUS. The tendons are assumed to remain rigidly bonded to the concrete. Therefore, the slippage of a tendon within the tendon sheath can not be considered in the present FE analysis model. The boundary condition for the bottom of the base slab is assumed to be fixed similar to that used in the axi-symmetric model and this model also can not simulate the possible vertical uplift during internal pressurization.

Figure 10. Axi-symmetric finite element model

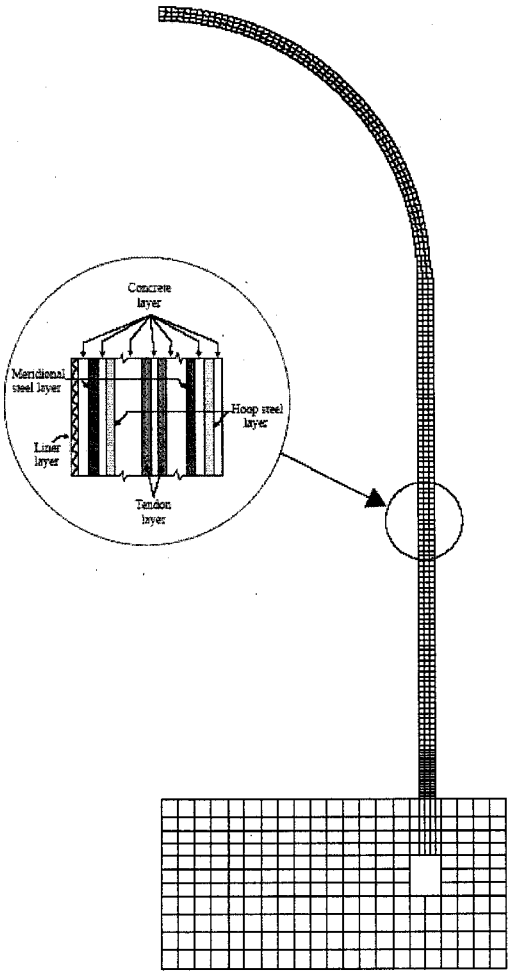

Figure 11. 3D FE mesh

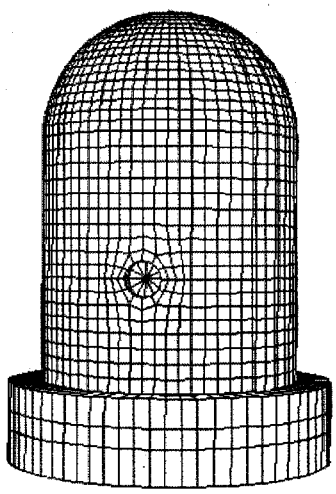

Figure 12. Buttress and Basemat FE mesh

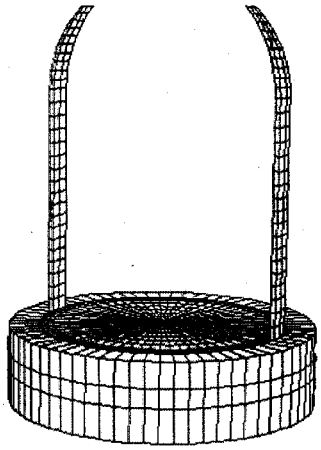

Figure 13. Hoop tendon (left) and meridional tendon (right)

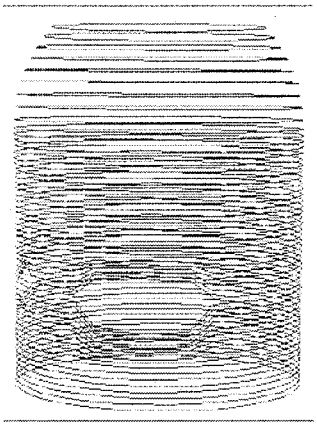

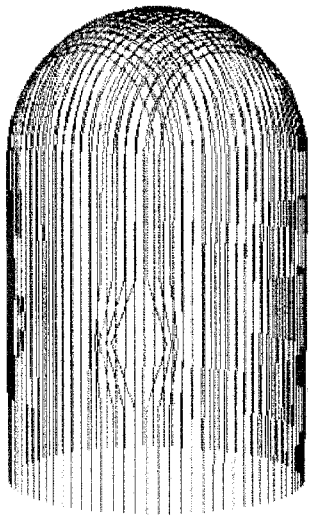

FE Analysis Results

The present FE analysis produces results at 37 standard output locations (SOLs) which are obtained from the axi-symmetric model and 52 standard output locations except SOL #35, #54, #55 from 3-dimensional model.

Axi-symmetric analysis results

The first cracking of concrete in cylinder wall due to hoop stress occurred at the value of 0.59MPa in the cylinder. The cracking of the cylinder due to meridional stress is initiated at the same pressure level at mid-height of the cylinder wall. Then, cracks spread all over the cylinder of the PCCV from the value of 0.67MPa.

The first crack occurs in the lower part of the dome and the cracks are observed at the values of 0.67MPa and 0.77MPa in the upper part of the dome.

The first yielding of hoop rebar is initiated at 1.036MPa at mid-height of the cylinder wall and the yielding of meridional rebar in wall-basemat juncture begun at 1.29MPa. The maximum strain of the rebar in the hoop direction is observed as 14.37% in the mid-height of the cylinder wall at the final stage.

The strain values of hoop tendons in cylinder wall reach 1%, 2% and 3% associated with the stress values of 1.43MPa, 1.47MPa and 1.50MPa respectively. The maximum strain of hoop tendon in cylinder wall is observed as a value of 15.26% at the final stage.

The deformed shape of axi-symmetric model at ultimate pressure state is shown in Figure 14.

Three-dimensional analysis results

The first hoop and meridional cracking of the cylinder wall are occurred at 0.62MPa as shown in Figure 15. This is a larger pressure value than the corresponding cracking pressure obtained from the axi-symmeric model. The first crack occurs at the lower part of dome and the cracks are also observed at the upper part of the dome at the values of 0.675MPa and 1.06MPa.

The first yielding of hoop rebar is initiated at 0.94MPa at mid-height of the cylinder wall as shown in Figure 16 and the yielding of meridional rebar in wall-basemat juncture begun at 1.19MPa. The maximum strain of hoop rebar is observed at midheight of the cylinder wall with the value of 0.55% at the final stage. The maximum value of the strain in the hoop tendon is observed as 0.51% at the final stage. Because numerical instability has occurred, there is no indication of tendon or rebar failure at the final load step. The deformed shape of 3-dimensional model at ultimate pressure state is illustrated in Figure 17.

Displacement verses internal pressure relationship comparisons at several Standard Output Locations (SOLs) such as mid-height of the cylinder, springline and dome apex are made in Figure 18 through Figure 21. There is a very good agreement for vertical displacement in the springline (Figure 20) as well as radial displacement in the mid-height of the cylinder (Figure 18) and springline (Figure 19) between analysis and test. As mentioned above, the first crack is occurred at 0.62MPa. The analysis and the test consistently exhibit a sharp jump in displacement at cracking pressure. There is poor correlation between analysis and test data for vertical displacement in dome apex. Unfortunately, test data between LST DOR and SFMT DYN has a quite different aspect.

Finally, The pressure levels due to the event milestones requested by SNL are summarized in Table 6.

Table 6. Pressure level due to the event milestones (unit: MPa)

Event milestones	Axi-symmetric model	3D model
First cracking of concrete in cylinder due to hoop stress	0.59	0.62
First cracking of concrete in cylinder due to meridional stress	0.59	0.62
First yield of hoop rebar in cylinder	1.036	0.94
First yield of meridional rebar in wall-basemat juncture	1.29	1.19
First cracking of dome concrete above 45° dome angel	0.77	1.06
First cracking of dome concrete below 45° dome angle	0.67	0.675
Hoop tendons in cylinder reaching 1% strain	1.43	-
Hoop tendons in cylinder reaching 2% strain	1.47	-
Hoop tendons in cylinder reaching 3% strain	1.50	-

Figure 14. Deformed shape of axi-symmetric model at ultimate pressure (x100)

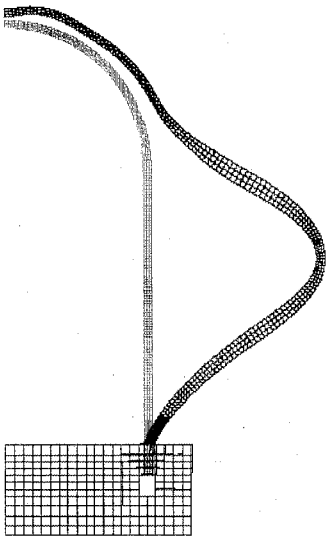

Figure 15. The first crack location of the concrete

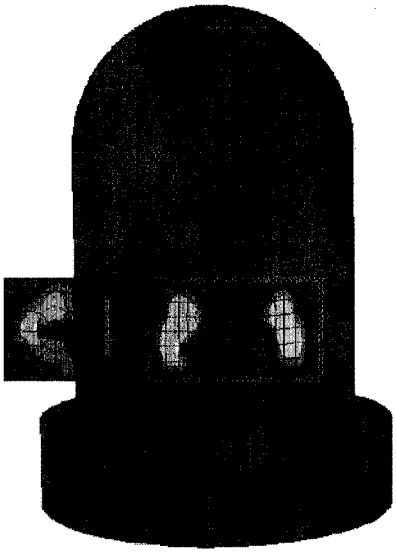

Figure 16. The first yielding location of the rebar

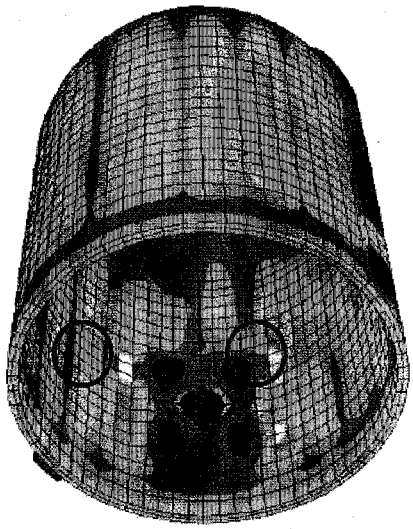

Figure 17. Deformed shape of 3D model at ultimate pressure (x100)

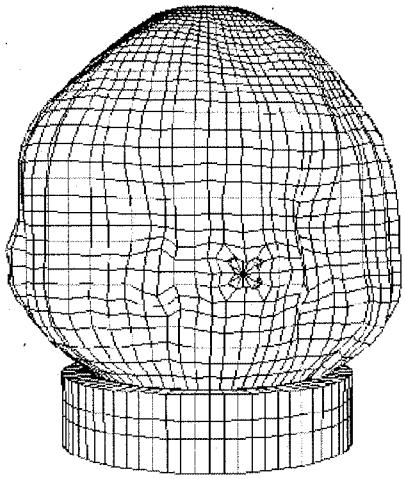

Figure 18. Radial displacement at the mid-height of cylinder (SOL #6)

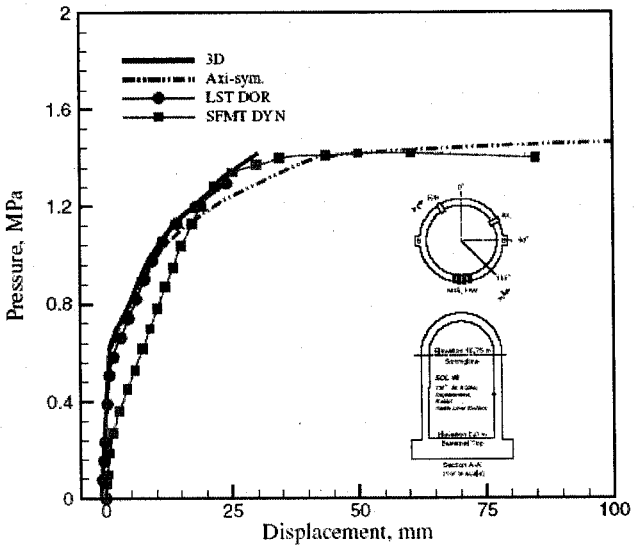

Figure 19. Radial displacement at springline (SOL #7)

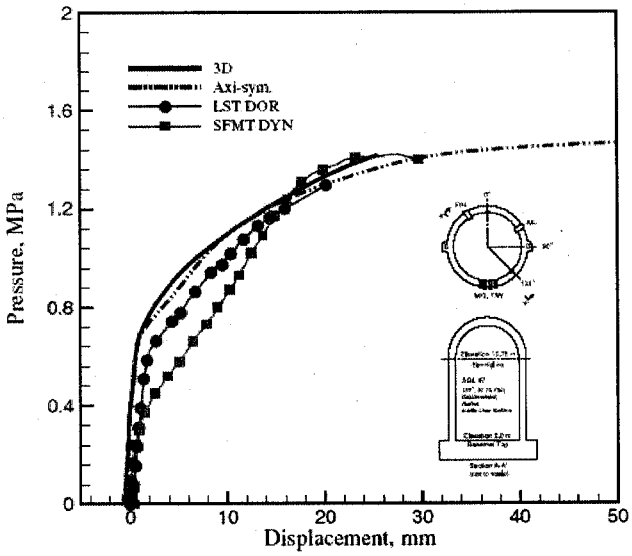

Figure 20. Vertical displacement at springline (SOL #8)

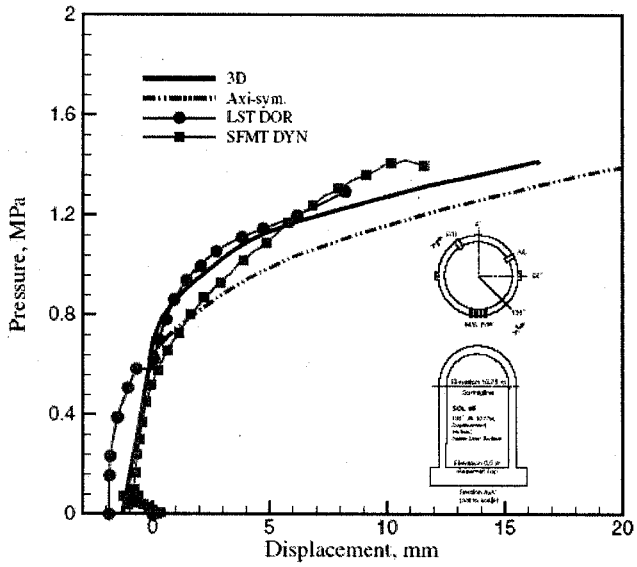

Figure 21. Vertical displacement at dome apex (SOL #11)

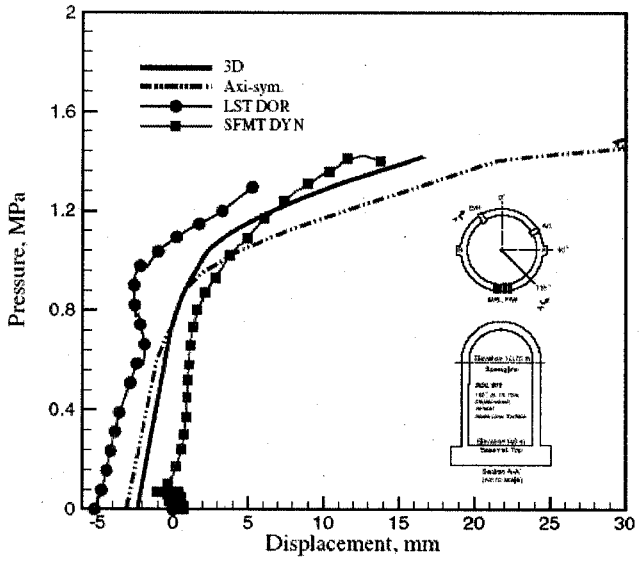

References

[1] Letter from V.K. Luk to M.N. Gray (1998), "PCCV Round Robin Analysis".

[2] Drucker, D.C. and W. Prager (1951), "A more fundamental approach to plastic stress-strain relation," *Proc. Natl, Inst. Appl. Mech.*, pp. 487-491.

[3] Lee, J. and G.L. Fenves (1998), "Plastic-damaged model for cyclic loading of concrete structures," *Journal of engineering mechanics*, Vol. 124, No. 8, pp. 892-900.

[4] Hibbit, H.D. (2002), ABAQUS User's Manual, Version 6.3, HKS Inc.

[5] Tendon Diskette (1999), Sandia National laboratories.

[6] Okamura, H., K. Maekawa and S. Sivasubramaniyam (1985), "Verification of modeling for reinforced concrete finite element, finite element analysis of reinforced concrete structures, " *ASCE*, pp. 528-543.

[7] Hsu, T.T.C. and A. Belarbi (1994), "Constitutive laws of concrete in tension and reinforcing bars stiffened by concrete," *ACI Structural Journal*, Vol. 91, No. 4, pp. 465-474.

Appendix G:

Korea Power Engineering Company

Posttest Analysis of a Prestressed Concrete Containment Vessel Model

(Ultimate Pressure Capacity of 1:4 scale PCCV)

KOREA POWER ENGINEERING COMPANY

Contents

1. Introduction

The purpose of the work contained herein is to summarize the posttest analysis results performed by Korea Power Engineering Company to simulate the structural responses accurately comparing the measured responses from SFMT (Structural Failure Mode Test) tested at Sandia National Laboratories [1].

To simulate the failure loading as well as the failure mode of the PCCV model, a three-dimensional full model involves at least two critical features for the structural idealization: one is by geometry model considering the effects due to presence of the openings and the buttresses in the PCCV. The other is by material property models for concrete, reinforcement, tendon and liner plate.

The computer program ABAQUS [2] was used to analyze a three dimensional model of containment with nonlinear material properties of concrete, liner plate, reinforcing steel, and prestressing tendon by increasing the internal pressure to failure. Thereby, the final results including the failure mode and the corresponding internal pressure level are determined.

The modeling approaches of geometry and materials and the analysis results with comparing the test results are summarized in the following sections.

2. Material Property and Modeling

2.1 General

To simulate the SFMT test results of the 1:4-scale prestressed concrete containment structure, the actual properties are used for the concrete, reinforcing steel, post-tensioning tendon, liner plate and soil. The actual material properties for these materials are established from test data provided by Sandia National Laboratories used in the construction of the 1:4-scale PCCV [3].

2.2 Concrete

Material Model

The concrete is characterized by a materially nonlinear deformation behavior. The material non-linearity is assumed to occur due to cracking of concrete in tension and plasticity of concrete in compression. However, the material non-linearity due to the latter is relatively less influence than that due to the former on the failure mode of the containment structure under internal pressure. Therefore, the Modified Drucker-Prager's failure model that is known to be suitable to represent the tensile concrete cracking of the three-dimensional finite element model is introduced in the numerical analysis.

The yield surface and flow potential parameters for elastic-plastic material yield surface in the modified Drucker-Prager's failure model with a non-associated flow potential and the strain hardening are defined by the model parameters K-factor, the friction angle β, and the dilation angle ψ. The material parameter $K(\theta, f_\alpha)$ controls the shape of the yield surface in the deviatoric plane and angle β is the angle between the yield surface and the pressure stress axis in the meridian plane [4].

The concrete structure was appeared to be damaged during the Limit State Test. Thus, to evaluate the effect of tensile and compression damage on the analysis results, the damage index $d_t = 0.1$ considering the micro damage level corresponding to the surface crack status showing some tensile cracking is introduced in the analysis [5]:

Material Property

The following concrete properties from the uniaxial strength test data for trial mix concrete are used in the analysis of the 1:4 scale PCCV model.

Table 1 Concrete Material Property

Property	Value for Basemat	Value for Shell & Dome
Elastic Modulus	27950 Mpa	26970 MPa
Uniaxial Compressive Strength	39.16 Mpa	47.30 MPa
Uniaxial Tensile Strength	3.37Mpa	3.45 MPa
Poisson's Ratio	0.18	0.18

2.3 Reinforcement Steels (Rebars)

Material Model

Rebar materials are generally incompressible when they deform plastically and yielding is independent of the pressure stress. The Von Mises failure criterion is therefore used for this steel material.

Hsu's study result [6] noted that the stress-strain curves for bare steel bar and for steel bar embedded in concrete are quite different as shown in Figure 1. Therefore, the stress-strain relationship of rebar embedded in concrete has been recommended in reinforced concrete structure to simulate the realistic behavior of the rebar in concrete.

The stress-strain curve of the rebar for the numerical analysis is idealized by bilinear curve having a slope of E_s before yielding and a slope of E_p after yielding as illustrated in Figure 1. The equations of two lines are expressed with the stress level designated as f_y' at which the two straight lines intersect

as equation (1) and (2). The plastic modulus E_p' after yielding can be taken a small fraction of the elastic modulus E_s.

$$f_s = E_s \varepsilon_s \qquad \text{for } f_s \le f_y' \tag{1}$$

$$f_s = f_o' + E_p' \varepsilon_s \qquad \text{for } f_s \succ f_y' \tag{2}$$

where f_o' is the vertical intercept of the post-yield straight line. The intersection stress level f_y' and the plastic modulus E_p' depend mainly on the level of the apparent yield stress f_y* illustrated in Figure 1. The values of f_y' and E_p' in the stress-strain relatinship introduced to the numerical analysis are calculated as equations (3) and (4) using the apparent yield stress f_y* and the strain-hardening modulus of the bare bar E_p from the actual material properties.

$$\frac{f_y'}{f_y} = 0.43 + 0.5\frac{f_y^*}{f_y} \tag{3}$$

$$\frac{E_p'}{E_p} = 3.3 - 2.5\frac{f_y^*}{f_y} \tag{4}$$

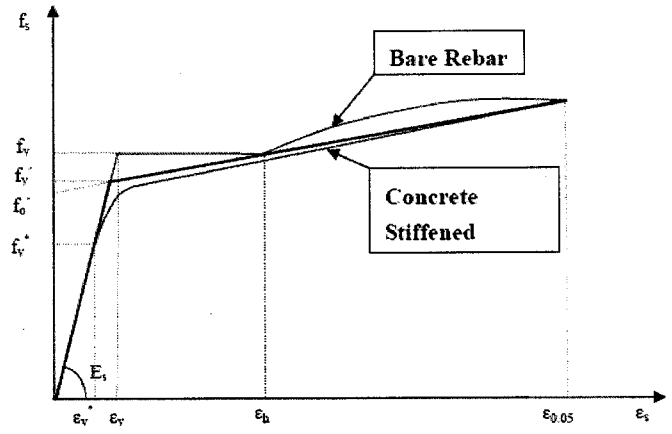

Figure 1 Stress-strain relationship of rebar using bilinear model

Material Property

The test results provided in the appendix of References [3] are used the rebar material properties. Table 2 presents the modulus of elasticity for each type and each size of the reinforcement steel.

Table 2 Reinforcing Material Properties

	D6 (SD345)	D10 (SD390)	D13 (SD390)	D16 (SD390)	D19 (SD390)	D22 (SD390)	D19 (SD490)
Elastic Modulus(Mpa)	1.69E5	1.83E5	1.83E5	1.83E5	1.84E5	1.91E5	1.86E5
Poisson's ratio	0.3	0.3	0.3	0.3	0.3	0.3	0.3
Yield Stress(Mpa)	369.4	472.9	432.3	457.5	473.1	459.0	512.2
Tensile Stress (Mpa)	489.4	665.9	610.6	616.5	658.3	680.8	709.7
Extension(%)	30.4	20.5	24.2	22.1	21.1	18.7	17.8

2.4 Prestressing Tendon

Material Model

The stress-strain curve of a bare prestressing tendon consisted of two straight lines jointed by curve knee shown in Figure 2 is used for the numerical analysis. The first part of the curve is a straight-line up to $0.7f_{pu}$ and the second part is expressed by Ramberg-Osgood equation(5) that meets the first part at the stress level of $0.7f_{pu}$.

$$f_p = \frac{E_{ps}{}'\varepsilon_p}{\left[1+\left(\frac{E_{ps}{}'\varepsilon_p}{f_{pu}}\right)^4\right]^{1/4}} \tag{5}$$

where f_{pu}, f_p, E_p' and ε_p is the ultimate strength of the tendon, the strength in the tendon, the tangential modulus Ramberg-Osgood curve at zero load and the sum of strain in the tendon, respectively [5].

The finite element code ABAQUS has no function to express the unbonded tendon and thus the prestressing tendons are modeled by the embedded approach available in ABAQUS using the rebar subelement in concrete. That is, the numerical modeling of tendons as rebar sub-elements implies that the tendons are assumed bonded to the concrete and the slippage of the tendon in the tendon sheath is not considered in the numerical analysis.

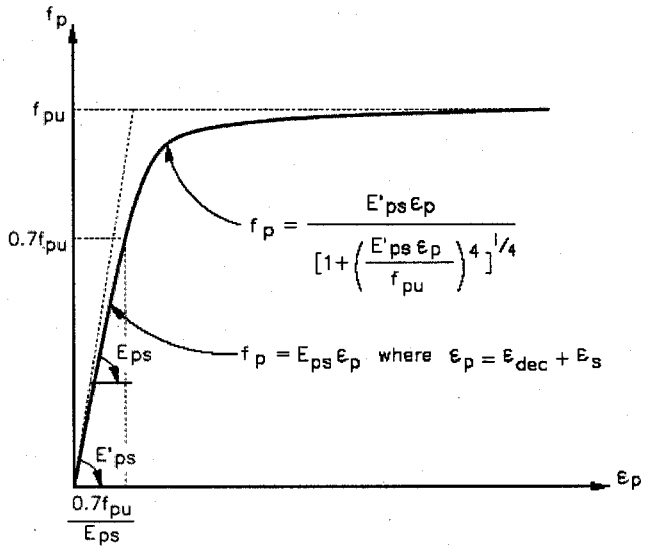

Figure 2 Stress-strain relationship of prestressing tendon

Material Property

The following material properties from Sandia Laboratories are used for the tendon modeling.

Table 3 Tendon Material Properties

Property	Values
Elastic Modulus	191000 MPa
Elatic Limit Stress	1339 Mpa
Yield Strength	1691 Mpa
Poisson's Ratio	0.3
Ultimate Strength	1912 MPa
Extension	4.5%

2.5 Steel Liner Plate

Material Model

The liner plate was partially teared during Limit State Test, but it is considered to contribute to the

structural strength during SFMT. Thus, the stress-strain behavior of the liner plate steel is modeled by using elasto-plastic model that is available in ABAQUS. The von Mises failure surface with kinematic hardening is used to represent the nonlinear behavior of the material.

Material Property

The material properties for liner plate introduced to the numerical analysis are as shown in Table 4.

Table 4 Steel Liner Material Properties

Property	Values
Elastic Modulus	218700 MPa
Elatic Limit Stress	1339 Mpa
Yield Strength	375.595 Mpa
Poisson's Ratio	0.3
Ultimate Tensile Strength	499.158 MPa

3. Finite Element Model

3.1 General

The three-dimensional finite element model includes two buttresses and large penetrations such as equipment hatch and airlock. These non-axisymmetric factors may cause deviation from an axisymmetric response and decrease the ultimate pressure capability of the PCCV. An interconnection between shell element in the base slab(or basemat) and shell elements in the wall is modeled by the composite shell element with orientation to properly simulate the shell/slab junction. All rebars embeded in the prestressed containment structure were modeled by using the rebar subelement provided by ABAQUS and the liner was modeled as a thin inner layer of the shell elements.

The model consists of 1822 four-node shell elements, 278 nonlinear soil spring elements and 1509 nodal points and the overall finite meshes are shown as Figure 4.

3.2 Shell and Dome Model

The dome and cylindrical wall are modeled with multi-layer shell elements consisting of a thin inner layer of steel representing the liner and a much thicker outer concrete layer including rebar and tendon. In order to simulate accurate displacements versus internal pressure extracted from the test data near these regions, a more refined mesh was considered around openings and the opening sleeve and hatch cover are also modeled using shell element as shown in Figure 5. All reinforcing bars in the

dome and cylindrical wall are modeled by using the rebar sub-element provided by ABAQUS computer program.

Due to limitation of the computer program ABAQUS, the tendons are assumed to remain rigidly bonded to the concrete and thus modeled by using the rebar sub-element with introducing prestressing stress provided by ABAQUS. Therefore, the actual condition including the slippage of tendon in the tendon sheath can not be considered in the analysis model. Prestressing stresses being induced in the tendons are expressed by using the *INITIAL STRESS command with the *PRESTRESS HOLD option in ABAQUS computer code to remain the tendon stresses at predetermined levels.

3.3 Base Slab Model

The reinforced concrete base slab is also modeled by four-node multi-layer shell elements consisting of an inner thin layer of steel representing the liner and a much thicker outer concrete layer. Since the base slab is modeled by shell elements, the tendon gallery is not included in the three-dimensional model.

The bottom of the base slab rests on soil foundation that is modeled by the nonlinear soil spring with tension cut-off. The soil properties were also not provided and thus an appropriate elastic modulus was introduced only to simulate the uplift by using the nonlinear spring with tension cut-off. That is, the compression stiffness was considered as the empirically large value not to develop the compressive behavior while the tension stiffness was neglected. All rebars in the basemat are modeled one-for-one by using the rebar sub-element of ABAQUS similarly to the wall and dome parts.

3.4 Prestressing Forces in Tendon

The meridional stress and hoop stress along the length of the tendon in the concrete are estimated as shown in Figure 6 with the prestressing losses at the time of testing and the prestressing force was introduced prior to applying the internal pressure to the numerical model. The four types of losses given specific modeling consideration are (1) the friction between the tendon and the concrete, (2) the elastic shortening of the concrete, (3) the creep and shrinkage of the concrete, and (4) the stress relaxation in the prestressed tendons.

The vertical prestressing forces of 106.27kips before anchoring and 96.04kips after anchoring are introduced from the PCCV Model-General Arrangement. Based on the prestressing forces at anchorage, the magnitudes of the vertical tendon stress are calculated along the length of the vertical tendon and considered in the finite element analysis model with considering the losses shown in Table 5. Similarly, the hoop tendon forces of 95.27kips before anchoring and 73.52kips after anchoring are used in the calculation of hoop tendon stress.

Table 5. Prestressing Losses

	Vertical Tendon Loss MPa (ksi)	Hoop Tendon Loss MPa (ksi)
Elastic shortening of concrete	31.855 (4.620)	31.855 (4.620)
Creep of concrete	66.999 (9.717)	83.829 (12.158)
Shrinkage of concrete	129.309 (18.754)	129.309 (18.754)
Steel relaxation	19.747 (2.864)	14.473 (2.099)
Total losses	247.910 (35.955)	259.473 (37.632)

3.5 Self-weight, Water Pressure and Internal Pressure

Because of the elastic support below the bottom slab, the effect of the weight of the structure had to be initially considered prior to internal pressurization. This is accomplished by specifying as mass proportional load for each material included in the 1:4 scale PCCV model prior to initiating the internal pressure. The weights of each material are considered in the numerical model by using the GRAVITY parameter of *DEAD LOAD option of ABAQUS.

The hydrostatic pressures from the water filled to 1.5m from the dome apex are calculated with Pascal's principle and loaded on the surface of the wall and base slab prior to internal pressurization. Internal pressure loads are specified to act as a uniformly-distributed force, remaining normal to the interior element surface of the containment shell, dome and base slab as it deformed.

4. Analysis Results and Discussion

All analysis results at 55 standard locations are selected and prepared as excel file to compare with SFMT test results. The three-dimensional finite element model (3DFEM) provided a good simulation of the SFMT test results. Most of the behavior comparisons show generally good correlation excepting some results of the 3DFEM showing differences between the 3DFEM and the SFMT (see Figures 7 through 10).

4.1 Displacements

The displacement transducer were 'zeroed' prior to the start of the SFMT before filling the vessel with water and thus the measured displacements reflect only the response to pressure (including the hydrostatic pressure) and not the effects of prestressing, nor any other previous loading [3]. Therefore, the numerical analysis displacements excluding the responses due to prestressing and dead load were

plotted and compared with the corresponding measured displacements. Most of the displacements comparisons show generally good correlation excepting some results of the 3DFEM showing differences between the 3DFEM and the SFMT (see Figure 7).

The displacements at EL. 1.43m and 2.63m show good agreement between the analysis and the test as shown in Figure 7(a) and (b). At the base of the wall (below EL. 0.25m), however, the numerical model deforms radially outward while the test measurement shows very small inward deformation (as shown in Figure 7(c)). This reverse trends near wall-mat junction is judged to come from the characteristics of the numerical model introducing shell element to basemat and putting soil spring under basemat to simulate uplift. That is, in the numerical analysis some flexural behaviors seem to be occurred in the basemat due to the overestimated uplift and plate bending larger than the test measurements reflected the actual behavior of the massive rigid basemat.

4.2 Rebar Strains

The residual rebar strain remained at each gage after LST was the initial strain at the start of the SFMT. Thus, both the analysis initial stains prior to pressure and the measured initial residual strains should be compared. Also, the strains due to only pressure need to compare for both the analysis and the test as the pressure increased.

The hoop outer rebar at the mid-height of cylinder (135°, EL. 6.20m) is the reinforcing steel D16 having a yield strain 0.25% calculated from a yield stress 457.5Mpa and elastic modulus 1.83E+05 in Table 2 [3]. The 3DFEM shows that the hoop outer rebar at the mid-height of cylinder is judged to yield at the pressure level of 1.10Mpa and the maximum strain in the hoop rebar indicates 3.8% at pressure level of 1.52Mpa(see Figure 8).

The strains in the meridional outer rebar at the elevation 0.05m and 0.25m show different trends. That is, the numerical model show the outer rebar strain changing from tension to compression while the test measurement indicates the outer rebar strain is very small but changing from compression to tension (as shown in Figure 9). These reverse trends near wall-mat junction are judged to come from the same reason as for the reverse trends for radial displacements at the same locations aforementioned in section 4.1. Also, to investigate the effects of the basemat uplift on the behaviors near the wall-mat junction, the outer rebar strains are compared depending on the boundary condition at the base of the cylidrical wall.

4.3 Tendon Strains

Tendon strains gages were 're-zeroed' before the SFMT [3] and thus the analysis tendon strains prior to the start of pressurization were deducted from the tendon strains during pressure to directly

compare with the measured tendon strain.

Most of the tendon strains simulated by the 3DFEM model exhibit a good agreement with the test measured tendon strains as shown Figures 10(a) through (c). However, the strains measured at the hoop tendon passing near buttress (Az.90°, EL. 6.58m) show much larger values than those of 3DFEM as shown in Figure 10(d). The hoop tendon at the mid-height of the wall is started to yield at pressure level of 1.43Mpa and the maximum strain corresponding to the pressure of 1.54Mpa is appeared to reach 3.74%.

4.4 Liner Strains

The response of liner was not a critical objective during the SFMT and thus the measurements are not provided for comparison. The analysis results show that the liner at the mid-height of cylindrical wall, especially the regions near equipment hatch, is started to yield at the pressure level of 0.84 Mpa and the yield in liner is appeared extend to the bottom of wall at 1.45Mpa as shown in Figure 11.

4.5 Concrete Cracking

The finite element analysis results show that the first concrete cracking in the numerical model occurs at a pressure level of 0.58Mpa and is located at the surface of cylindrical wall at the wall and basemat joint. At the pressure level of 0.60Mpa, the elements near large openings of wall cylinder are cracked in both the hoop and meridional directions as shown in Figure 12.

Figure 13 illustrates the strain at the pressure level of 1.52 MPa judged to be the structural failure mode in the analysis and the distribution of concrete cracking at the failure can be indirectly compared with the test results. According to the strain distributions in the model, the final failure appeared to occur between the edge of equipment hatch and the buttress for the x-direction and there were large strains from the spring line upto 45 degrees of dome.

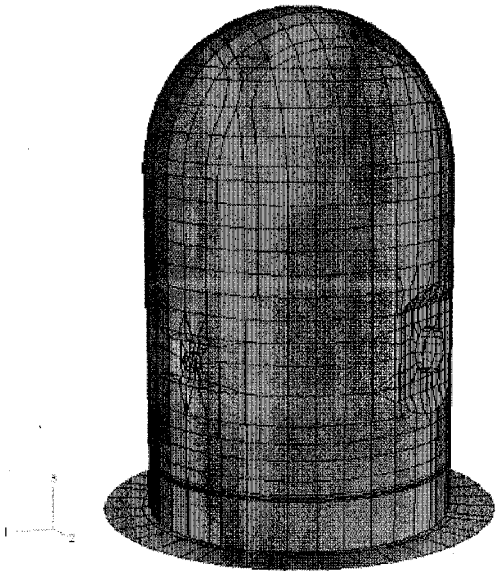

Figure 4 Overall View of Three-dimensional Finite Element Model

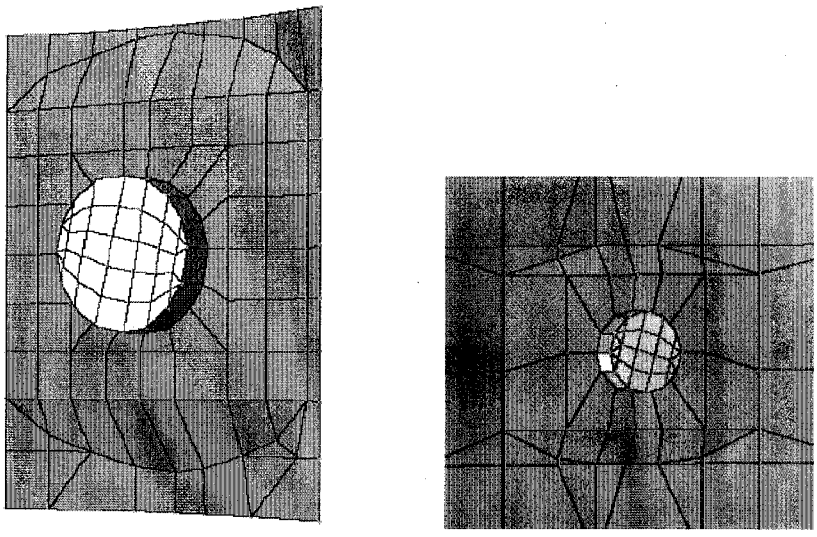

(a) Equipment Hatch (b) Personal Airlock

Figure 5 Refined Mesh around Large Penetrations in Model (Inside Surface)

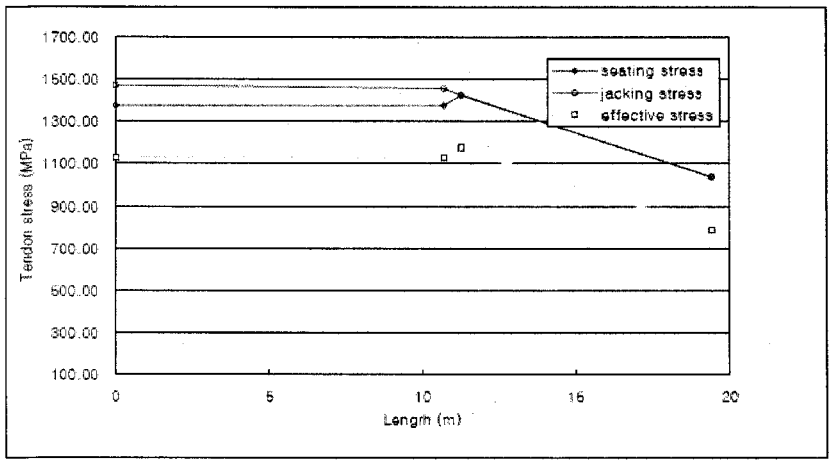

(a) Vertical Tendon Stress

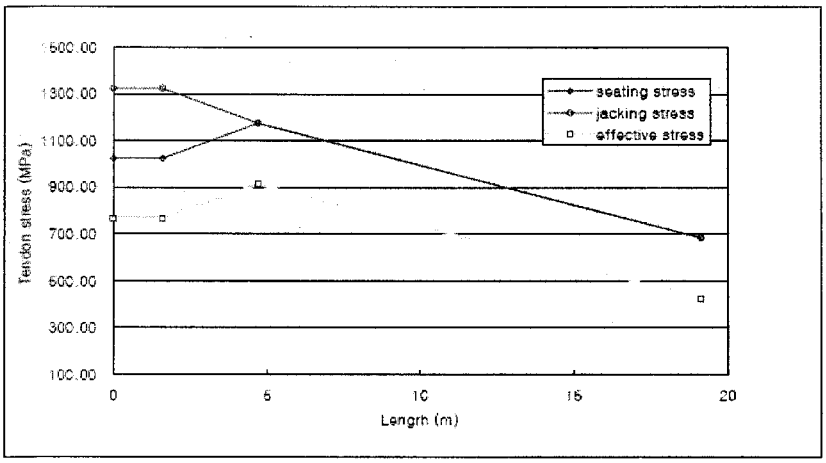

(b) Hoop Tendon Stress

Figure 6 Prestressing Stress Profile

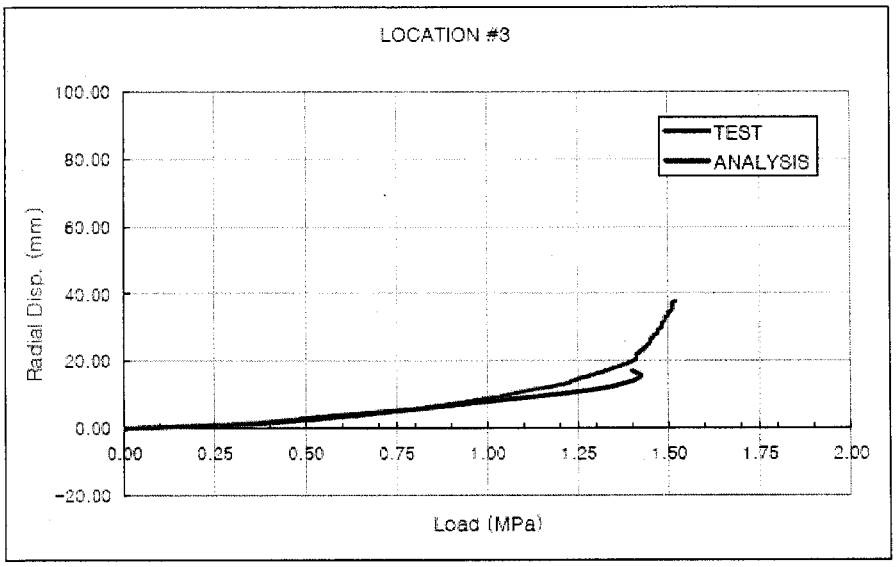

(a) Radial Displacement at AZ. 135°, EL. 1.43m

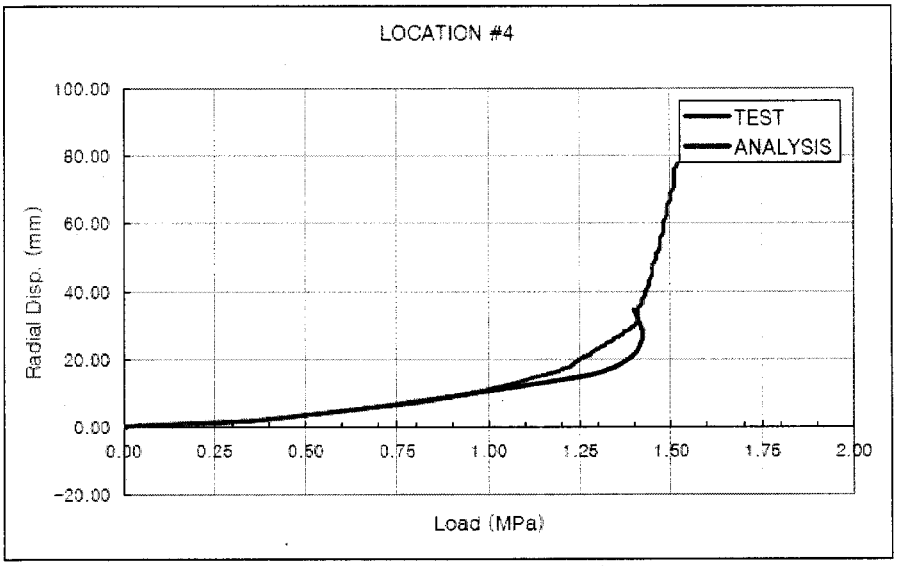

(b) Radial Displacement at AZ. 135°, EL. 2.63m

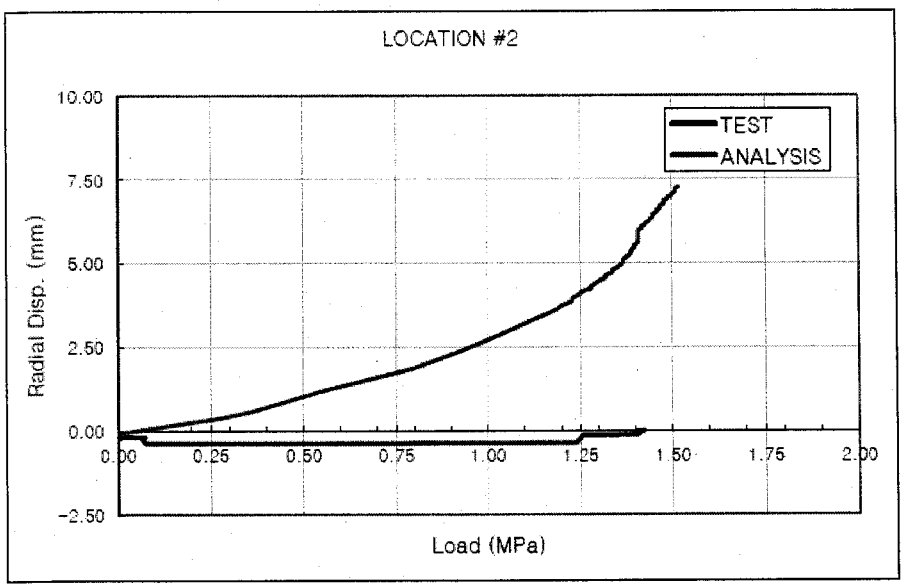

(c) Radial Displacements at AZ. 135°, EL. 0.25m

Figure 7 Radial Displacements at EL. 1.43m, EL. 2.63m, EL.0.25m

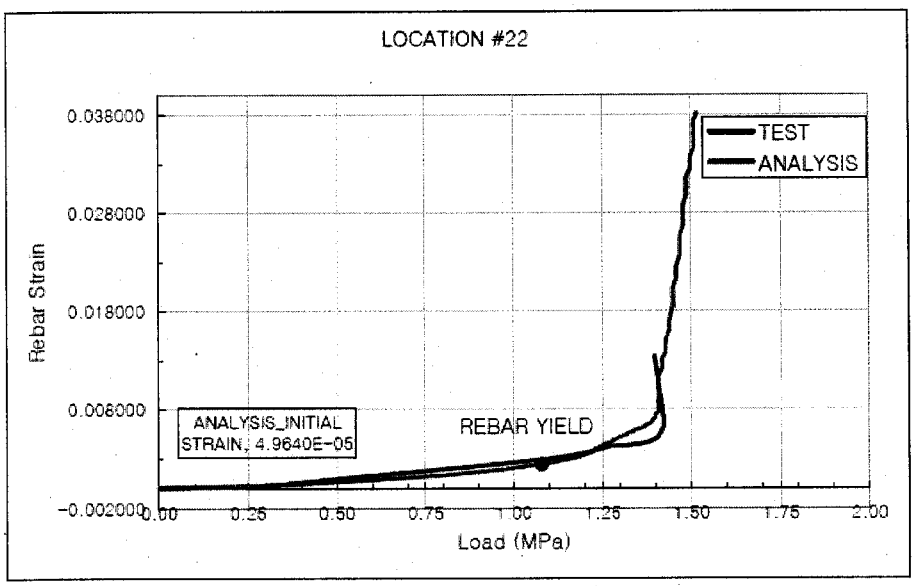

Figure 8 Hoop Rebar Strain at Mid-height

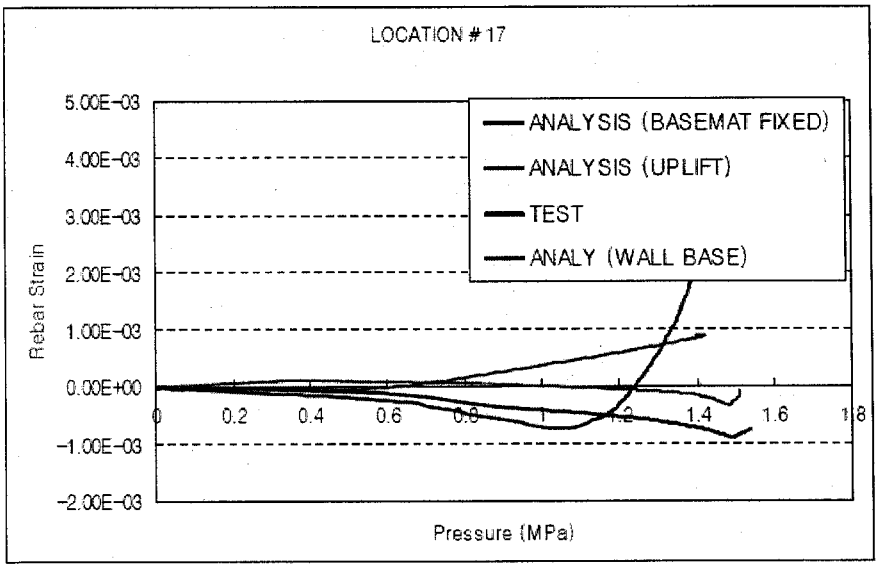

(a) At EL. 0.05m

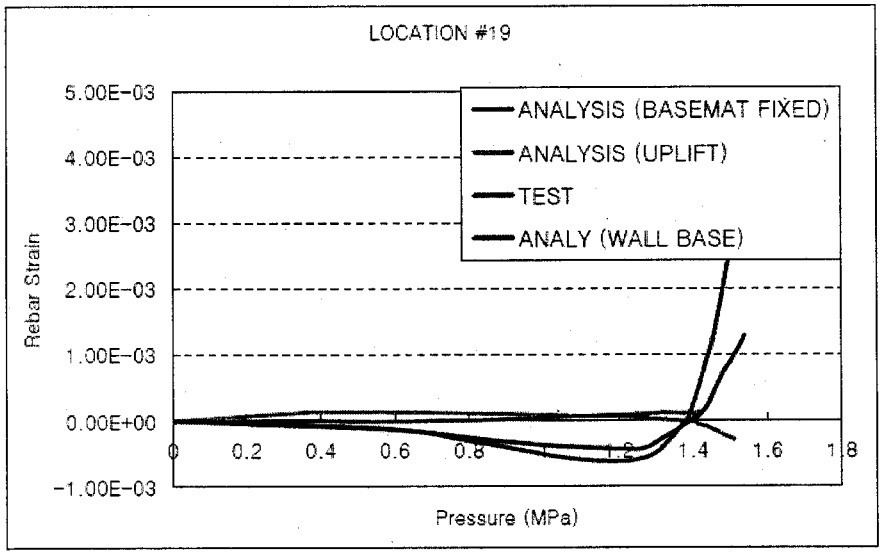

(b) At EL.0.25m

Figure 9 Comparisons of the outer Meridional Rebar Behavior at Wall Base

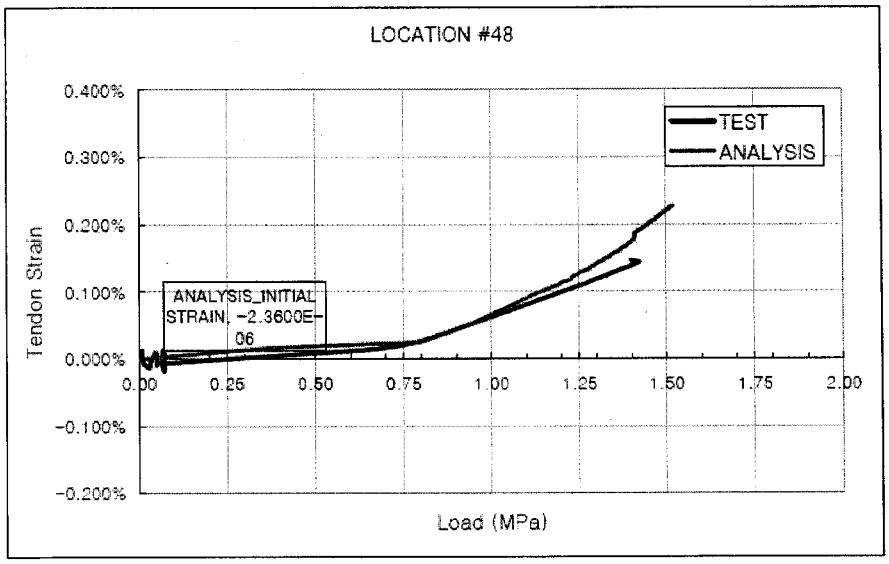

(a) Tendon Strain Hairpin around Dome Apex (180°, EL. 15.60m)

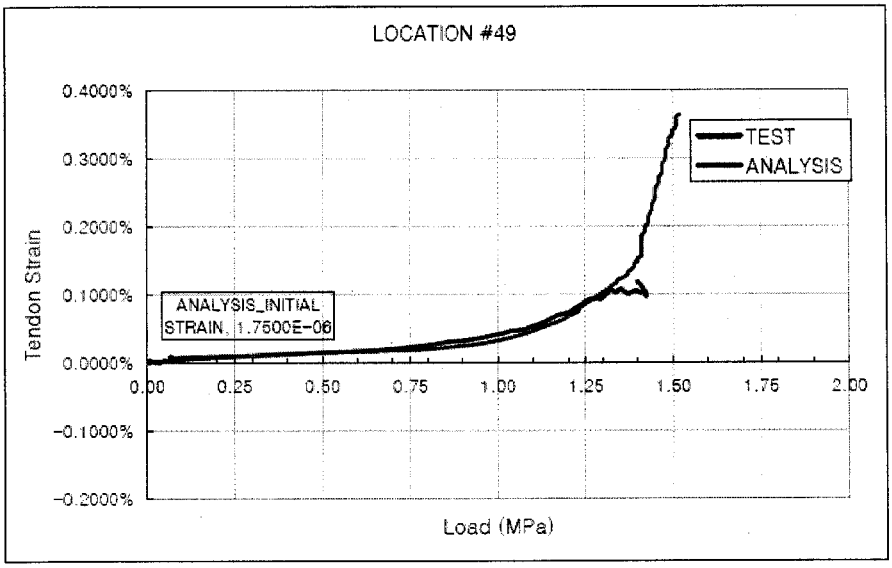

(b) Tendon Strain Hairpin at Spring Line (135°, EL. 10.75m)

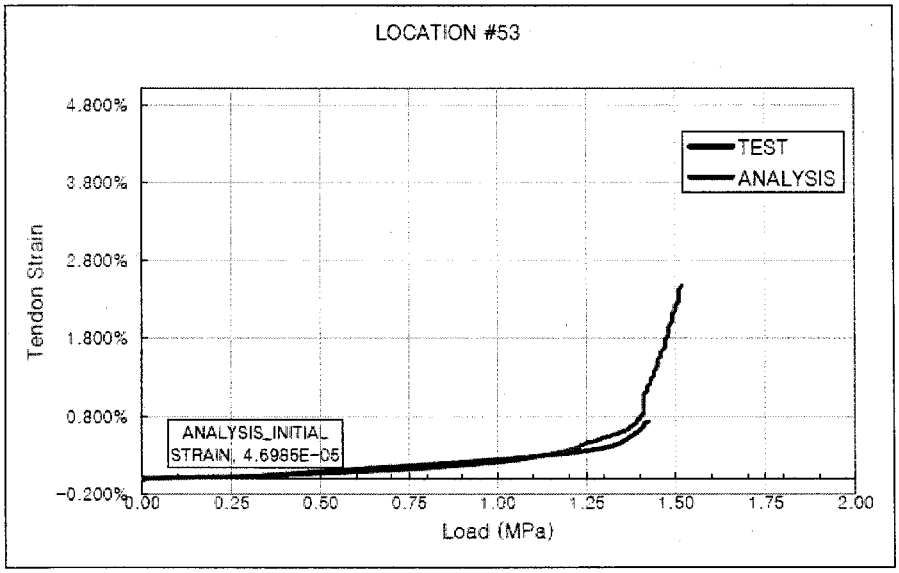

(c) Tendon Strain Hoop Tendon below Mid-height (0°, EL. 4.57m)

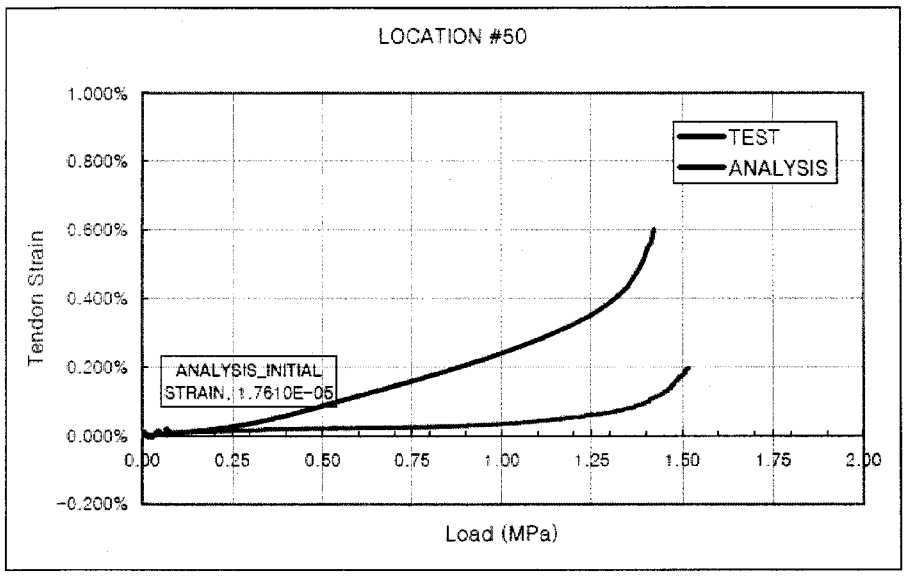

(d) Tendon Strain Hoop Tendon above Mid-height (at buttress, Az. 90°, EL. 6.58)

Figure 10 Comparisons of Tendon Strains

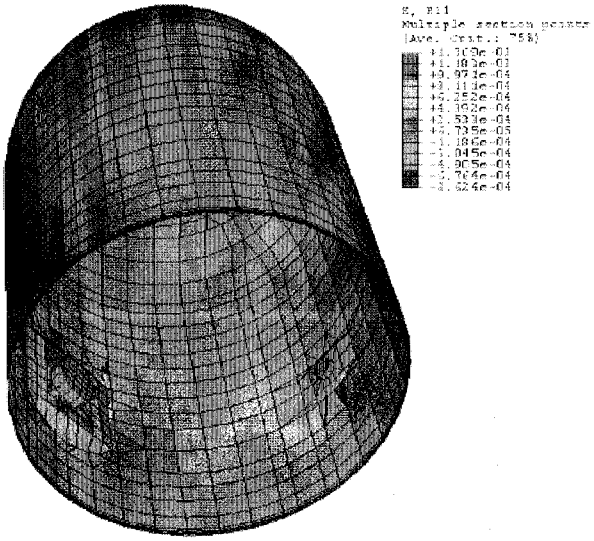

(a) The Regions of Liner Yield (at the pressure level of 0.84MPa)

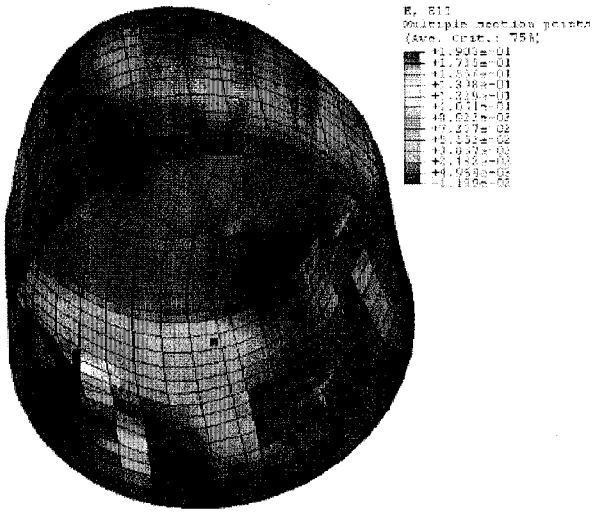

(b) Liner Tearing (1.45MPa, Liner Fracture Strain 19% considering Triaxial Factor)

Figure 11 Stress Contours for Liner Yield and Tearing

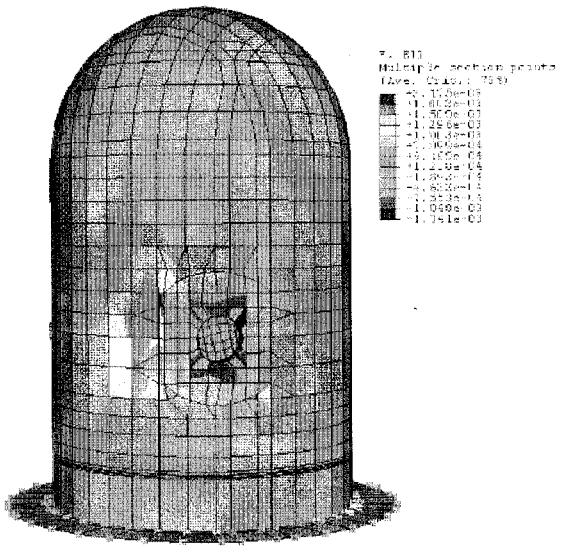

Figure 12 View of Initial Concrete Cracking Zone (at the pressure level of 0.60Mpa)

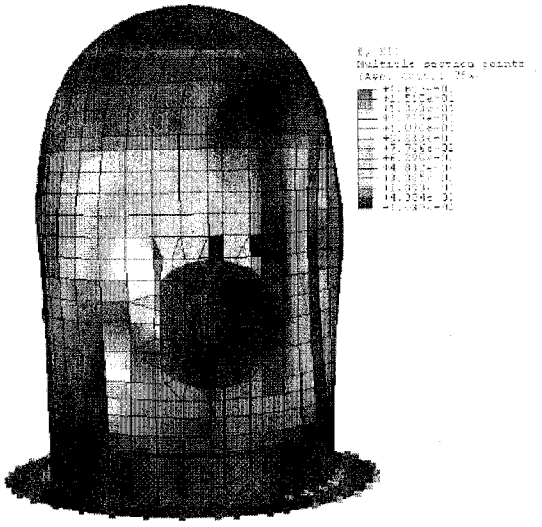

(a) X-Direction Strain (E11)

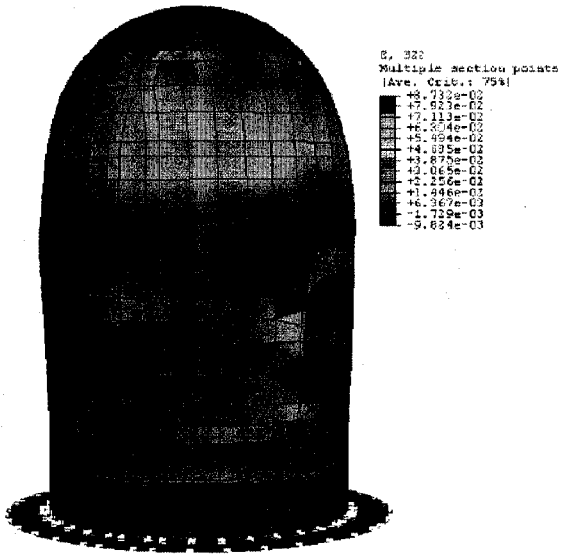

(b) Y-Direction Strain (E22)

Figure 11 Concrete Strains at Structural Failure (Pressure Level :1.52MPa)

5. References

1. R.A. Dameron, B.E. Hansen, D.R. Parker and Y.R. Rashid, *Posttest Analysis of NUPEC/NRC 1:4 Scale Prestresssed Concrete Containment Vessel Model*, NUREG/CR-6809 SAND2003-0839P ANA-01-0330, Sandia National Laboratories, Albuquerque, NM, March 2003.
2. ABAQUS User's Manual, Version 6.4, 2003. ABAQUS Inc.
3. M.F. Hessheimer, E.W. Klamerus, L.D. Lambert and G.S. Rightley, *Overpressurization Test of a 1:4-Scale Prestressed Concrete Containment Vessel Model*, NUREG/CR-6810, SAND2003-0840P, Sandia National Laboratories, Albuquerque, March 2003.
4. ABAQUS Theory Manual, Version 6.4, 2003. ABAQUS Inc.
5. Mazars J., Dube J.F., Flejou J.L. and Ghavamian Sh., *A Damage Multi-layered F.E. Model for the Seismic Response of R.C. Structures – A Tool for Understanding the Real Behaviour*, Proceeding 10th EAEE, 1994.
6. Thomas T.C. Hsu, *Unified Theory of Reinforced Concrete*, CRC Press 1993, 205-218 pp.

Appendix H:

US Nuclear Regulatory Commission

Analysis of a 1:4-Scale Prestressed Concrete Containment Vessel Model and Post-test Analytical Studies of Tendon Friction

Sandia / DEA report to NEA/CSNI's Int'l Standard Problem 48 (Phase 2 – Mechanical Loading)

R. A. Dameron[1)], B. E. Hansen[1)], E. R. Kelley[2)], and M. F. Hessheimer[2)]

1) David Evans and Associates, Inc., San Diego, CA, USA
3) Sandia National Laboratories, Albuquerque, NM, USA[1]

BACKGROUND and INTRODUCTION

The Nuclear Power Engineering Corporation (NUPEC) of Japan and the U.S. Nuclear Regulatory Commission (NRC), Office of Nuclear Regulatory Research, co-sponsored a Cooperative Containment Research Program at Sandia National Laboratories (SNL) in Albuquerque, New Mexico. As part of the program, a prestressed concrete containment vessel (PCCV) model (shown in Figure 1) was subjected to a series of overpressurization tests at SNL beginning in July 2000 and culminating in a functional failure mode or Limit State Test (LST) in September 2000 and a Structural Failure Mode Test (SFMT) in November 2001. The PCCV model, uniformly scaled at 1:4, is representative of the containment structure of an actual Pressurized Water Reactor (PWR) plant (OHI-3) in Japan. The objectives of the pressurization tests were to obtain measurement of the structural response to pressure loading beyond design basis accident in order to validate analytical modeling, to find pressure capacity of the model, and to observe its failure mechanisms. The model's limit state reached during the LST was liner tearing and leakage at various locations in the cylinder, as shown in Figure 2. The structural failure mode during the SFMT was gross rupture of the cylinder wall as shown in the post-SFMT photograph of Figure 3.

Sandia National Labs is also participating in the International Standard Problem (ISP 48) on containment integrity and providing assistance to NEA/CNSI in distributing data and interpretations from the PCCV model test to participants in the analysis exercise. David Evans & Associates, under a contract with SNL which began in 2003 is supporting SNL's involvement in the ISP 48 and conducting additional post-test analytical studies. This work is especially focusing on aspects of the PCCV behavior where analytical predictions were significantly different than the test measurements, and on possible scaling issues and "test model artifacts" that may influence interpretations and judgment which can be obtained from the test.

This report represents SNL's submittal to the ISP 48 Analysis Exercise, Phase 2 – Mechanical Loading. It compares results of pretest analytical studies of the PCCV model to the PCCV high pressure test measurements and describes results of post-test analytical studies. All of the pretest analyses and most of the post-test analyses have been performed by ANATECH Corp. under contract with SNL. These analyses conducted through 2002 are documented in detail in References [1], [2], and [3]. This ISP-48 submittal summarizes the modeling approach and analysis tools, comparisons between measured behavior and predicted behavior of the liner, concrete, rebar, and tendons, and the various failure modes and locations that were investigated. Comparison of pretest and post-LST analysis results to the SFMT data and additional analyses, to provide insight into the mechanisms leading to the structural failure, are also included in this report. Observations on the accuracy and adequacy of the prediction analyses, lessons learned from the 1:4 Scale PCCV, such as the modeling and behavior of prestressing and some unique liner seam details, are also discussed.

---

[1] *Sandia is a multi program laboratory operated by Sandia Corporation, a Lockheed Martin Company, for the U.S. Department of Energy under Contract Number DE-AC04-94AL85000..*

SUMMARY OF PRETEST ANALYSIS

The models that constituted the final pretest predictions were the global axisymmetric, the semi-global three-dimensional cylinder midheight (3DCM) model, and local models of the E/H, Personnel Airlock (A/L), and Mainsteam (M/S) penetrations. These models are shown in Figures 4-7. (Figure 7 also shows strain contour result information plotted onto the finite element model.)

The ABAQUS general purpose finite element program [4] and the ANACAP-U concrete and steel constitutive modeling modules [5] were used for the analysis. Tendons and their prestressing were modeled to replicate expected tendon stress-strain behavior and friction effects. Concrete cracking was simulated with the "smeared crack" approach, where cracking is introduced at the finite element integration points. Cracks can form at orthogonal directions, up to three cracks per integration point, and once a crack forms, it can never heal. Rebar was always modeled with ABAQUS rebar subelements, which reside within the "parent" concrete element, and therefore, are required to have strain compatibility with the concrete. However, the rebar stress-strain law is completely different than the concrete and is represented by a J-2 plasticity model available within ANACAP-U. The tendons were modeled in various ways for the different models, depending on the level of detail. In some cases, the tendons were modeled with rebar subelements, and in other cases, modeled individually with beam elements in which the tendon elements were allowed to slide relative to the concrete. In these cases, friction was represented in various ways. Tendon friction modeling was studied in detail in this work, and this is described later in this report.

The local failure predictions were all driven by response versus pressure histories calculated by the 3DCM model. The only changes made between the 1999 pretest predictions reported in [2] and the final (2000) pretest predictions were to material properties and prestressing levels. Because visual inspection of the model revealed the existence of micro-cracking (probably due to curing and shrinkage) throughout the cylinder, the concrete tensile strength was reduced to a cracking strain of $e_{cr} = 40 \times 10\text{-}6$, based on prior experience with similar test structures. A new suite of concrete compressive tests became available in February, 2000, so these were also incorporated into the final pretest analyses.

The failure predictions consisted of liner tearing locations, all occurring near the midheight of the cylinder near penetrations and weld seams with "rat-hole" details. The most likely location for the liner tearing failure was predicted to be near the Equipment Hatch (E/H) at the ending point of a vertical T-anchor, near where the liner is attached to the thickened liner insert plate (also a weld seam). The failure pressure was predicted to be 3.2 times the design pressure (P_d) of 0.39 MPa or 1.27 MPa.

COMPARISON OF PRETEST ANALYSIS TO THE TEST MEASUREMENTS

During the LST, liner tearing and leakage failure was first detected at a pressure of 2.5 P_d, and a subsequent increase in pressure to 3.3 P_d resulted in very extensive tearing at many strain concentration locations. Ultimately, the leak rate through the tears exceeded the flow capacity of the pressurization system so the test was concluded. In reviewing the PCCV test data, the 55 Standard Output Locations (SOLs) used for the Round Robin prediction exercise held in 1999 [6] were very useful comparison points. Pretest analysis test data comparisons (e.g., Figures 8-18) show comparisons of typical displacements, liner strains, and rebar strains. (Post-test analysis curves, described in the next section are also included on these plots.) Analysis data curves were "rezeroed" to the first point of the test data, i.e. the data reading occurring at the start of the test. This slightly shifted the analysis data, but it simplified the comparison of the response to internal pressure and eliminated differences in response to dead load, prestressing and creep or other time-dependent effects. This is justified because most of the PCCV instrumentation was initialized in March, 2000; after dead loads were applied, the model was prestressed, and underwent six months of outdoor temperature fluctuations and low- pressure testing prior to the start of the LST (September, 2000).

The conclusions from the comparisons of the pretest analysis with the LST were as follows:

- Radial displacements in the cylinder wall (Figure 8 and Figure 9) were well predicted by global axisymmetric analysis, but dome and overall vertical displacements (Figure 9 and Figure 10) were overpredicted.
- Wall-base juncture behavior, including many rebar and liner strain measurements, (e.g., Figure 1) were well predicted by the detailed wall-base juncture (axisymmetric) modeling.
- Functional failure (i.e. leakage in excess of 1% mass/day) at a pressure of 2.5 P_d occurred at a liner tear in an area of high strain that was not examined in detail by analysis, but was probably amplified due to defects associated with weld seam repair.
- Maximum pressure, 187.9 psig (3.30 P_d), was closely predicted by analysis, but the predicted failure location did not manifest. (Maximum pressure was also limited by the capacity of the pressurization system.) Ultimately, liner tears at many locations occurred, and many of these were identified by analysis.
- The average radial displacement at the midheight of the cylinder of 20mm at maximum pressure, equivalent to an average hoop strain of 0.37%, is within 10% of that predicted by global analysis (21.9 mm or 0.41%).
- Maximum radial displacement at E/H = 29mm, equivalent hoop strain of 0.0054, was reasonably predicted by 3DCM model, but prediction of displacements at other azimuths–like the buttresses–were poorly predicted by 3DCM model.
- Hoop tendon stress distribution simulated by analysis at start of LST showed fair agreement with measurements, implying that the angular friction and anchor set modeling assumptions at the start of the test were reasonable. Vertical tendon stress distribution at the start of the LST were less consistent with the initial modeling assumptions.
- For the hoop tendon stress distribution, gages interior from the ends were underpredicted by analysis *and* the anchor forces (gages near the ends) were overpredicted. The cylinder hoop tendon data, in total, shows evidence of the tendons slipping during pressurization, and measurements indicate that the shape of the tendon stress profile changes from its initial friction dominated "V-shape" to a nearly uniform stress profile during pressurization.

POST TEST ANALYSES

Global Axisymmetric posttest analyses were performed after the LST. Vertical and dome displacement comparisons were significantly improved by redistributing soil basemat springs according to tributary area, and by improving the dome meridional tendon representation to account for the added stiffness of the overlapping tendons due to the rectilinear "hairpin" layout. Comparisons were also improved by using no vertical tendon friction in the cylinder.

Extensive additional studies were also performed for the posttest 3DCM analysis. In the pretest analyses, the 3DCM model was developed to investigate the non-axisymmetric behavior of the cylinder wall and provide more realistic boundary conditions for the penetration's submodels. Buttresses above and below the 3DCM model boundaries have vertical beam stiffnesses that are not accounted for in a cylinder slice model. Equivalent spring properties were derived and then applied as radial spring elements. The other modeling assumption found to be at significant variance with observed test behavior was the tendon modeling, especially the representation of friction. As shown in Figure 19, the pretest models used tendon friction truss ties oriented at an angle of arctan(0.21) to simulate angular friction. Two important observations were made from the test about the hoop tendon behavior:

1. When pressure overcomes prestress, P = 0.59 MPa, tendon stress distributions change from the classical angular friction design assumption to an approximately uniform distribution; then they

stay fairly uniform at most higher pressures. Toward the end of the test, some tendon interior forces even slightly exceed the force at the anchor.

2. The apparent strain increases in tendons corresponding to force/strain gage readings are significantly larger (e.g. 0.48% versus 0.35%, for H53 as shown in Figure 20) than the strain that corresponds purely to radial expansion. This can only be explained by force redistribution associated with sliding. Thus the position of the tendon relative to the concrete must be allowed to change after initial prestress in order to adequately simulate tendon behavior during overpressurization. (The analytically predicted tendon force distributions are also shown in Figure 20.)

These observations led to changes in tendon friction modeling of the 3DCM model. Because observed tendon friction behavior turned out to be quite complex, new analysis strategies were chosen to bracket tendon behavior:

Model 6. Apply prestress. Then, by using the ABAQUS *MODEL CHANGE capability, fix the tendon nodes at their initially deformed position relative to the concrete. In other words, start from classical design prestress with friction and then effectively bond the tendons.

Model 7. Perform original analysis up to P = 1.5 P_d (0.59 MPa), then "MODEL CHANGE" friction elements to non-friction elements (truss ties aligned perpendicular to the tendons). In other words, perfectly unbond tendons.

Model 9. After prestress, keep the initial friction elements, but add friction elements in the reverse orientation so that if points on the tendon move relative to concrete in the reverse direction from that of initial prestress, they will experience reverse direction friction.

In general, the tendon friction simulation runs 6, 7, and 9 showed progressively better agreement with test measurements, with run 9 (tendon force profile shown in Figure 21) showing the best agreement at the anchors and at most points interior to the tendon ends. Based on these and the other observations, the results of run 9 were used to drive the submodels for E/H and M/S (and estimated feedwater (F/W)) penetrations posttest analysis. On tendon friction behavior, the test measurements and analytical evidence support the conclusion that tendon friction is important to the tendon behavior, but traditional friction design formulas that predict tendon stress distribution begin to break down once pressurization exceeds the pressure that overcomes prestress (in this case, roughly 1.5 P_d). The coefficient of angular friction appears to lessen, allowing sliding and force redistribution as the vessel expands, but more importantly, some parts of the tendon are forced to reverse direction of travel relative to the duct, reverse it from the direction of travel experienced during prestressing. Under this action, angular friction properties probably still hold, but the direction of friction must change sign from that assumed in a design calculation.

Posttest analyses were also performed for the penetration submodels. Liner strains measured in the vicinity of the E/H penetration collar were much lower than predicted by pretest analysis (Figure 22). Since the predicted high strain locations were fundamental to the failure predictions, significant effort was spent reanalyzing the E/H model after the test. As a result of this work, two hypotheses were developed.

Hypothesis 1: The liner in the E/H area had a high degree of bond-friction with concrete, preventing slippage of the liner relative to the concrete; relative slippage is required for elevated strains to develop near local discontinuities like T-anchors and stiffeners. This highly localized effect was not captured in the pretest analysis.

Hypothesis 2: A major crack near edge of E/H embossment further concentrated liner strains at edge of embossment.

Posttest analysis showed that by preventing relative slip between liner and concrete, the overall behavior of the system (concrete strains, tendon strains, liner strains away from the hatch) remained the same, but the elevated strains close to the collar were eliminated. In the final case, directed cracks were introduced to one row of elements, and a discrete crack was formed by adding double rows of nodes along an assumed crack line. This was found to create elevated liner strain. The additional strain concentration coincides with rat-hole weld seam details, and in the LST, elevated strains were measured and numerous tears occurred at these details. Based on results of detailed liner rat-hole analysis, the additional strains associated with such details is enough to exceed the liner tearing strain criteria. This shows that with discrete crack modeling and local rat-hole modeling, a liner tear could have been predicted to occur as early as 2.8 P_d. Based on the evidence provided by liner strain gages and by acoustic monitoring, one of the tears along this embossment edge may have even occurred as early as 2.5 P_d. (Note that this posttest analysis did not attempt to include as-built liner defects, such as local thinning or residual stresses resulting from initial fabrication or subsequent repairs.) The posttest E/H study thus presents a modeling strategy with results that correlate well with the LST measurements and observations. A somewhat higher strain prediction might be possible if a discrete crack (separate rows of nodes) were propagated all the way through the concrete wall, but this would require a change in rebar modeling strategy–one that is probably not practical even for very detailed analysis of containments.

The M/S and F/W penetration hot spots (both analysis and LST observations) occurred near the vertical T-anchor terminations and near the 'equator' of the thickened insert plate surrounding the penetration group, i.e. at the 3:00 and 9:00 positions as was previously shown in the strain contour of Figure 7. For the posttest analysis effort, no changes to the M/S model were necessary, other than updating the applied displacement versus pressure histories that were obtained from 3DCM posttest Model 9. After studying the F/W geometry in the posttest phase of the project, it was determined that the F/W penetration model was similar enough to the M/S penetration model that it would be assumed the posttest M/S model was reasonably representative of the F/W penetration. Several observations could be made from the well-instrumented M/S and F/W locations that are relevant to response predictions around containment penetrations.

- Many of the highest strains recorded during the LST are near the M/S and the F/W.
- There is wide variation in peak strain measurements, even at locations that are theoretically identical in geometry; factors contributing to these differences are: slight variations in liner thickness (due to manufacturing and weld repair grinding), gage position relative to the collar/weld, material properties (including welding heat effects), etc.
- The highest strain measurements can, but do not always, correspond to tear locations. Sometimes a gage can show evidence of rising prior to tear occurrence, then declining due to the stress relief caused by the tear; a gage located near a tear crack tip, on the other hand can show quite low strain up to 3.1 P_d and then suddenly jump.

Comparisons of analysis to the M/S and F/W liner strain gages showed that the posttest analysis of the M/S penetrations captured the strains measured in the LST quite well for both the M/S and F/W penetrations.

POST-TEST ANALYSIS OF LINER TEARS WHICH OCCURRED AWAY FROM PENETRATIONS

Detailed analytical investigation was conducted of liner tears that occurred away from penetrations but where welding details may have caused local liner strain concentrations. The PCCV model exhibited 16 distinct locations at which liner tears occurred. All 16 locations were near vertical weld seams, but with some variation in the configuration of a horizontal stiffener or rat-hole. By comparing "before and after" photos taken by SNL (such as shown in Figure 23) and with reference

to a posttest metallurgical study [6], it was observed that liner welding irregularities were present at almost all of the tear locations. These irregularities included points of extensive repair, such as grinding, points of discontinuous or missing back-up bars, or points with weld and liner seam fit-up irregular geometry. Some locations, where a seam and rat-hole existed and high strains were measured, but a tear did not occur provide additional evidence of the importance of the welding details to liner tearing. Ultrasonic measurements showed substantial reductions in thickness near many tears. Measurements showed ~23% thickness reduction in many locations, and more (up to 40% in a few locations).

A posttest liner seam analysis study (using the model shown in Figure 24) was aimed at quantifying effects of welding irregularities and distinguishing these from strain concentrations solely related to geometry. A mesh-size sensitivity study was conducted. Analyses were then conducted to assess material and geometry variations. The first variation implemented varying material properties near the weld areas. This included assignment of different material properties to the base metal, heat affected zone (HAZ), and weld fusion zone (WFZ) regions of the model. The second variation only modified the material in the WFZ. The final phase incorporated geometry modifications to the model near the weld lines. This included thinning of elements and varying the extent of thinning in the vicinity of the welds due to grinding. The geometry modifications were coupled with modified material properties ranging from uniform to including variations of base metal, HAZ, and WFZ regions. A typical strain contour result for one of the detailed liner analyses is shown in Figure 25.

The conclusions of the liner seam/rat-hole modeling study are summarized below:

- By comparison with strain gages and posttest liner tear observations, some of the finite element weld seam analyses are able to generate strain fields in and around the rat-holes and liner welds which agree reasonably well with strain gage measurements and which exceed the liner tearing strain criteria at locations where tears were observed.
- Competing mechanisms between the weld zone and ends of stiffeners make yield and ultimate strength adjustments to the HAZ material properties necessary to correctly predict strain concentration location and intensity.
- The models with back-up bars, nominal geometric properties, and best-estimate material properties yielded the best simulations of defect-free construction of rat-hole/weld-seam details. However, even models without back-up bars also provided reasonable correlation with gages at these locations.
- A case with severe (~40%) amounts of thinning appears to provide the best simulation of the behavior of tear occurrences in which severe liner thinning (due to weld repair grinding) was reported.
- If a rat-hole/liner-seam detail is subjected to additionally elevated strain (i.e. strain across the liner model that is larger than free-field global strain) a tear even earlier than 3.0 P_d can be justified. In practice, such a prediction could approximately be made using a strain concentration factor approach. The strain concentration factors (K = peak ε_{eff} divided by global ε_{hoop}) implied by this liner seam study are as follows: K = 48 (tear at stiffener end, no back-up bar); K = 45 (tear at stiffener end, with back-up bar); K = 59 (tear at HAZ, no back-up bar, and 40% thickness reduction due to grinding); K = 91 if a short segment of horizontal weld seam back-up bar is missing.
- Using a model of the rat-hole/seam locations without defects showed that liner tears still would have developed by pressure of 3.4 P_d, so liner tearing and leakage would still have been the failure mode (for quasi-static pressurization) even in the absence of liner welding irregularities.

ANALYSIS OF THE STRUCTURAL FAILURE MODE TEST

The LST resulted in liner tearing and leakage, but not a structural failure. Structural damage was limited to concrete cracking, and the overall structural response (displacements, rebar and tendon strains, etc.) was only slightly beyond yield. (Global hoop strains at the midheight of the cylinder only reached 0.4%, approximately twice the yield strain in steel.) In order to provide additional structural response data to compare with in-elastic response conditions, the PCCV model was resealed, filled nearly full with water, as shown in Figure 26, and repressurized during the SFMT to a maximum pressure of 3.6 P_d. The test ended when a catastrophic rupture occurred as was shown in Figure 3. The SFMT posttest analysis showed that good simulation of the PCCV global behavior through and including tendon rupture is possible with a 3D shell model as shown in Figure 27. The main limitations of the shell model were a lack of local liner strain concentration prediction and a lack of accuracy in the predictions of local wall-base-juncture behavior. However, accuracy in global behavior prediction did not seem to be lost when a bonded tendon assumption was used.

The SFMT model provided additional insight as to how the structural failure likely developed. Near the 0 - 6 degree azimuth of the cylinder, there is a reduction in inner and outer hoop rebar area of 38% (from alternating D19, D16 bars to a pattern of 1D16/3D13 bars). At 3.49 P_d, the wall and tendon strain at the 0 - 6 degree location is higher than all other azimuths as shown in Figure 28, and a tendon rupture occurs. The analysis then shows neighboring tendons rupturing and deformations spreading quickly along this azimuth. The secondary tendon ruptures spread upward. From review of test video, this appears to agree with observations. By 3.65 P_d, the analysis shows rupture to have spread over a vertical line spanning about 6 m. This also agrees with observations. A comparison of cylinder midheight radial displacement, test versus SFMT post-test analysis is shown in Figure 29. Deformed shape "slice" views of the cylinder midheight radial displacements can be seen in Figure 30, showing the development of the failure near the 0 degree azimuth.

After wall rupture, a secondary event occurred in the SFMT: through-wall failure around the circumference of the wall at about 1.5 m elevation. While it is difficult to say at what azimuth this failure initiated, it seems clear that this was a shear or combined shear/flexural failure of the wall. The plotting of analysis shear results in the SFMT analysis model showed that such failure may have initiated at the buttresses (evidenced by the high shear stresses predicted there) and then "unzipped." With the triggering event of a massive wall rupture, one of two mechanisms may have caused shear demand to exceed capacity: 1) a large deformation of the wall opening, creating large rotations near the base of the wall, would crush the outer concrete of the flexural section and thereby reduce the capacity, or 2) the water jet-induced momentum imbalance would cause added shear demand; this would create tangential shear at some azimuths and would be the maximum at the buttresses; such shear acting in combination with the already high radial shear stresses could have increased shear stress demand enough to induce the shear failure.

SPECIAL STUDIES ON TENDON FRICTION MODELING

In 2003, a new approach to modeling the tendon friction was investigated. To begin the study the final post-test 3DCM model ("Run 9") was reduced to a ring model representing an infinitely long cylinder as shown in Figure 31. Similar to the semi-global 3DCM model the concrete was modeled with brick elements, the liner with shell elements and the rebar was included as rebar sub-elements. Tendons were modeled with a truss element and, initially, friction truss-ties to adjacent concrete nodes. The initial run with the truss-ties was used to compare with the original 3DCM model and establish a baseline ring model to evaluate the effects of varying tendon modeling parameters.

Once the baseline ring model had been developed and tested, the friction truss-ties were removed and replaced with a sliding contact surface, coefficient of friction equal to 0.21. In the original 3DCM analysis the stress in the tendon was applied through an initial stress in elastic elements, external to the concrete mesh, at the end of each tendon. Anchor set losses in the tendons were simulated by adjusting the orientation of the friction truss-ties near the end of each tendon. The

friction truss-ties required the use of "small displacement" theory so that the tendon friction would be oriented correctly regardless of the movement of tendon nodes relative to concrete nodes. However, because the orientation of the truss-ties does not change, the shape of the tendon stress profile is "locked in," and this was found to have potentially significant effects on the analysis at intermediate pressures (pressures in the range of 1.5 Pd to 3 Pd). Because the truss-ties were eliminated in the contact surface model, the tendons could be stressed in two steps, similar to the way stressing operations occur in the field. The tendons were stressed first to the full design stress and then the stressing is reduced to simulate the anchor set losses. This second step, reducing the stress, allows the ends of the tendon to slip relative to the concrete. Because there is fairly large displacement of the tendon relative to the concrete nodes, now large displacement theory (geometric nonlinearity) was needed (in ABAQUS, done by including the "NLGEOM" parameter). Without activating large displacement theory the loss in the tendon as a result of reducing the stress was effective over the entire length of the tendon rather than just the anchor loss zone. By switching to large displacement theory the tendon stress profile matched the design stress profile quite closely. The initial tendon stress profiles of the two methods are shown to be nearly identical in Figure 32. But Figure 33 and Figure 36 show how the two models begin differing substantially once significant pressure is applied. Figures 32-34 show tendon stress comparisons and Figures 35-37 show radial deformation. At pressures of about 2.0 P_d and larger, the results using the two methods differ significantly. Comparison to the measured radial displacements shown in Figure 38 show that the contact surface model provides the best prediction of 3D behavior of the cylinder, even at intermediate pressures.

Two models were run with the contact surface. In Model 1 the initial stress profile attempted to match the stress profile from the latest post-test analysis, namely a relatively small anchor set, corresponding to ~2 mm. In the post-test analysis this was accomplished by orienting the truss-ties perpendicular to the tendon over the anchor set zone of ~15 degrees of azimuth. For the ring model with the contact surface, the stress profile was obtained by reducing the initial stress from 100% to 97%. Model 2 included an anchor loss zone of approximately 45 degrees, which corresponds to the design anchor set of ~6 mm. For this analysis the anchor stress was reduced to 89%. Once the initial stress profile was determined for each of the analyses, pressure loads were applied the same as to the 3DCM model. Comparisons are presented for tendon force and displaced shapes for each of the models in Figures 39-42.

When comparing the displaced shapes, significant differences exist between the contact model with different anchor sets at P=2.0 P_d. In the large anchor set model the largest radial displacements are occurring near the buttress location similar to the 3DCM model. This creates an elliptical displaced shape. However, in the small anchor set model the displacement is more uniform over the entire circumference of the model with the smallest displacements occurring at the buttress. This has been judged to be closer to what was observed in the test.

The comparisons of tendon force show that, overall, the tendon behavior is quite similar between all three models. Because the tendon forces are similar and the displaced shapes are quite different, it indicates that there is significant sliding of the tendon relative to the concrete that the truss-tie approach may not be capturing correctly. Further evidenceof this is provided in Figure 43 which shows tangential motion of Tendon H68 relative to the concrete at the anchorage (azimuth 90 degrees) and at 180 degrees from the anchorage (Azimuth 270 degrees). All deviations from the "flat" line are sliding movements of the tendon after anchorage lock-off; these appear to be somewhat important to include in analytical simulations.

The overall conclusions of the study are that the contact surface approach provides improved simulation of cylinder response and tendon behavior at intermediate pressures of say 1.5 P_d to 3P_d, but that near the tendon limit state of ~3.5 P_d, all methods provide a reasonable prediction. Further, it is concluded that the PCCV test model probably experienced anchor set lower than the design value of 6 mm, and probably in the range of 3-4 mm.

DISCUSSION OF MODEL SCALING ISSUES

One of the goals of the final phase of SNL's containment research is to apply lessons learned from scale model testing and analysis to full scale containments. This is also a parallel goal of the ISP48 exercise. Before making direct comparisons of the 1:4 scale PCCV to full scale prototypes, however, examination and analyses of several model scaling issues was performed, and this is summarized below.

Three basic analytical models were developed at full scale: global axisymmetric, the "ring model" for examining tendon friction, and the local liner model of liner welded connections. Each finite element model was changed to full scale based on comparison of geometry of the existing 1:4 scale models to the OHI-3 containment geometry. In the global axisymmetric model, the density was reduced in the full scale model so that with the application of gravity, the vertical stress in the cylinder at the base of the wall was the same at full and quarter scale.

Some results of the full scale axisymmetric model compared to the quarter scale results are shown in Figures 44-46. Figure 44 shows comparisons of radial displacement at cylinder midheight, vertical displacement at springline, and strain in meridional rebar near the inner surface of the wall-base juncture. Here the displacements of the scale model were multiplied by 4 in order to make direct comparison. These plots show that while hoop response of the cylinders are "identical," vertical displacement and flexural strains at the wall-base juncture are somewhat reduced. The wall-base flexure response illustrates the difficulties encountered in concrete model scaling, because shear and flexure behavior tend to scale differently. These differences are also illustrated in the strain comparison plots of Figure 45 and Figure 46. The vertical and shear strains are somewhat lower in the full scale prototype model. The vertical strains show that the neutral axis has shifted somewhat. The shear strains are an indicator of damage to the concrete in the wall base juncture. The result implies increased separation of cylinder midheight versus wall-base juncture shear failure modes for a full scale versus 1:4 scale model. This is actually a favorable result because it means that the scaling of the 1:4 scale PCCV did not "mask" a failure mode that could be more likely to occur at full scale. Instead, the analysis results indicate that quarter-scaling could make a wall-base shear failure somewhat more likely than in the prototype.

Full scale axisymmetric analysis was also used to examine the effects of including the reactor pit in the center of the basemat (as shown for OHI-3 in Figure 47). These studies showed virtually no influence on the basemat or the cylinder response, except for some very localized strain differences in the immediate vicinity of the pit at the center of the basemat.

Full scale liner weld seam (rat-hole) model analysis showed similar strain concentrations as the 1:4 scale model. However, the 1:4 scale liner rat-hole models which were found to best simulate the observed behavior of the LST were those with 20% and 40% liner thickness reductions due to "over-grinding" near welds that were found present in the 1:4 scale model. Since grinding and other thickness irregularities are likely to scale closer to 1:1 than 1:4, such conditions, if they exist at all, would only scale to, at most, 5%-10% of total liner thicknes. When these thickness reductions were introduced, the intensity of strain concentrations near the weld seams was significantly reduced. Conclusion: premature tears of the type that occurred as early as 2.5 P_d in the 1:4 scale PCCV are much less likely to occur in full scale containment. On the other hand, the 1:4 scale liner rat-hole studies of models without thickness reductions predicted liner tear at ~3.4 P_d and these results are judged to be fully applicable at full scale. It should also be noted that most full scale containment liners use back-up bars at all liner seam weld locations, and this was found through earlier analytical studies to further reduce the possibility of premature liner tear near weld seams.

Finally, with regard to tendon scaling, the axisymmetric model offers some insights about vertical tendons and the ring model provided insights into hoop tendon scaling issues. Comparison of vertical tendon behavior at 1:4 scale to full scale showed the 1:4 scale structure had a larger level overall prestress in the cylinder than would be found in a full scale containment. This stems from the fact that angular friction losses in the dome at 1:4 scale were much larger than at full scale (again,

0.21 friction versus the normal 0.11 friction), so prestress had to be increased to compensate for this. The result of this scaling difference, however, was not found to have any significant influence on behavior.

The hoop tendon stress and displacement comparisons between 1:4 scale and "equivalent full scale" shown in Figures 48-51. The changes at "full scale" are two-fold: 1) Friction coefficient is reduced from 0.21 to 0.11 (0.11 is the traditional assumption in design, while for the smaller radius 1:4 scale model, tests conducted by NUPEC resulted in 0.21); 2) Extent of affected azimuth of anchor set is reduced, because anchor set is a length, on the order of 3 to 6 mm, regardless of scaling. For purposes of this study, 6 mm of anchor set was assumed, which produces an anchor set zone of influence of ~15 degrees for a full scale containment. The results show that with the results of earlier sensitivity studies, these scaling differences in hoop tendon friction affect cylinder radial deformed shape at intermediate pressures of ~2.0 P_d to 3.0 P_d (with the full scale shape being more "pinched" at the buttresses), but at pressures higher than 3.0 P_d when the tendons begin reaching yield, behaviors of all friction and anchor set assumptions approach the same deformed shape and tendon stress distribution.

CONCLUSIONS AND LESSONS LEARNED

The 1:4 scale PCCV test showed that the response quantity driving the limit state of the vessel is cylinder radial expansion. This aspect of response must be predicted correctly in order to reasonably predict vessel capacity and predict, at least approximately, the many other local aspects of response (local liner strains, etc.) that are driven by the cylinder expansion. With this test, as with other steel-lined concrete vessel tests, many competing strain concentrations occur around the mid-height of the cylinder. Although it is difficult to predict which local liner detail will tear first, and although some particular response quantities, like basemat uplift, were not predicted exactly by the ANATECH/SNL pretest analysis of the PCCV model, the radial expansion of the cylinder was predicted very accurately. A response mechanism that also appears to have been well predicted was cylinder wall-base flexure and shear, another mechanism that, if predicted incorrectly, could lead to erroneous pressure capacity/failure mode conclusions. The minimum requirement for a containment overpressure evaluation should certainly be a robust axisymmetric analysis.

Other steps, guidelines, and lessons learned are provided in [3]. The lessons learned which may be most novel that result from this work are those related to tendon friction behavior. It was found that the best calculation methods recommended for tendon friction modeling are, in descending order of preference, 1) an advanced contact friction surface between the tendons and the concrete, 2) pre-set friction ties applied in one direction during prestressing and then added in the other direction during pressurization (3DCM run 9) and 3) if neither of these methods are practical within the scope of the calculation, it is best to start with an "average" stress level (using a friction loss design formula), but assume uniform stress distribution in the tendons throughout pressurization, i.e., an unbonded tendon assumption, and finally 4) same as 3, but using a bonded tendon assumption.

By recently examining some possible scaling issues, it has also been concluded that this work, and the analysis methods demonstrated, are also highly relevant to full size prestressed concrete containments. Cylindrical hoop expansion behaviors were found to be the same, regardless of scaling, except for minor variations that occur at intermediate pressures (~2.0 P_d to ~3.0 P_d) due to tendon friction differences. Wall-base flexure/shear behavior and vertical response of the containment are slightly influenced by scaling, but the likelihood of a wall-base shear failure appears to be even lower at full scale than at 1:4 scale. And finally, liner tearing near liner stiffness discontinuities remains the most likely "first" failure mode from static pressurization, but very early tears due to flaws near liner weld seams appears to be much less likely at full scale than what was observed in the 1:4 scale PCCV.

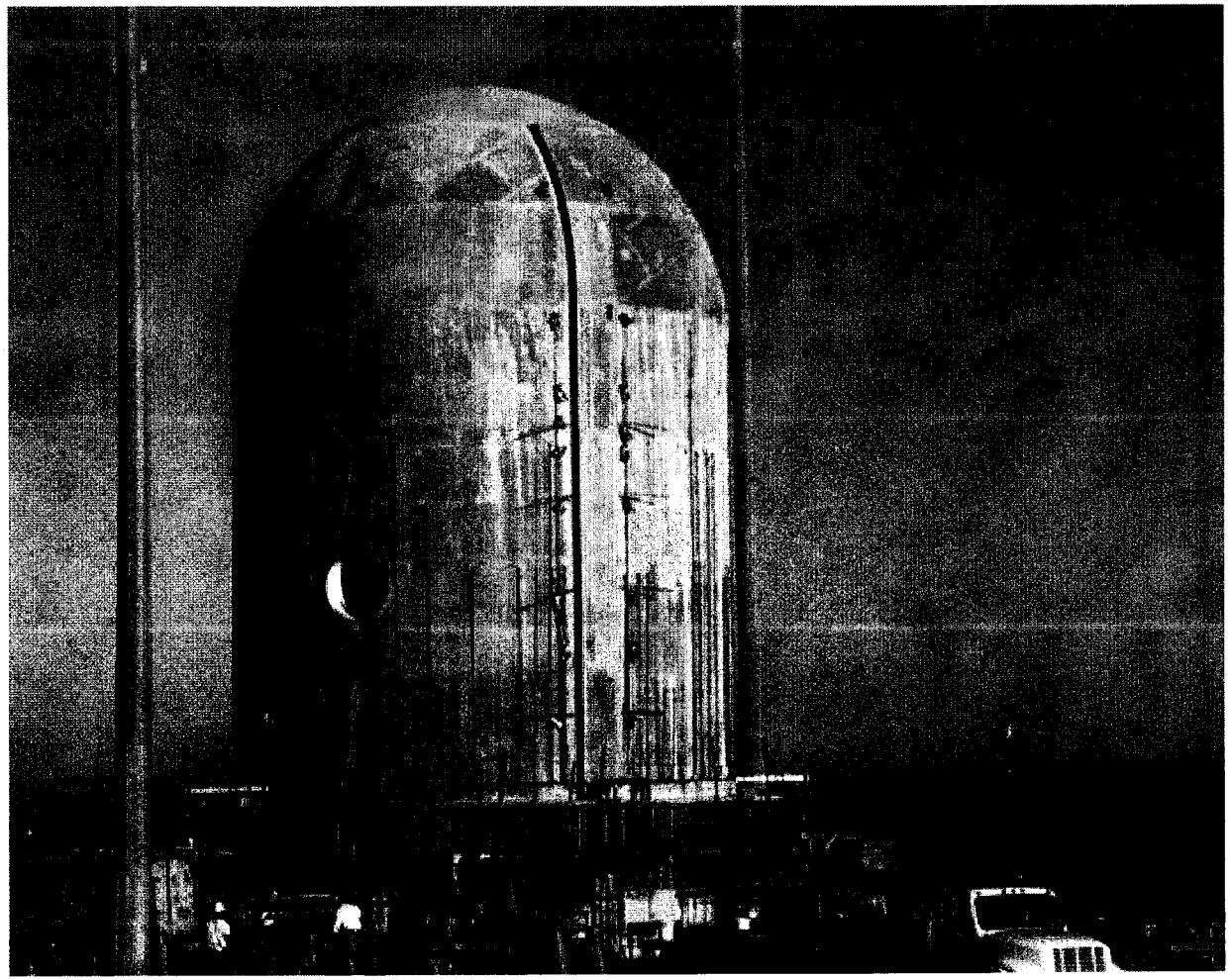

Figure 1. NUPEC/NRC 1:4 Scale PCCV Model Built at Sandia National Laboratories

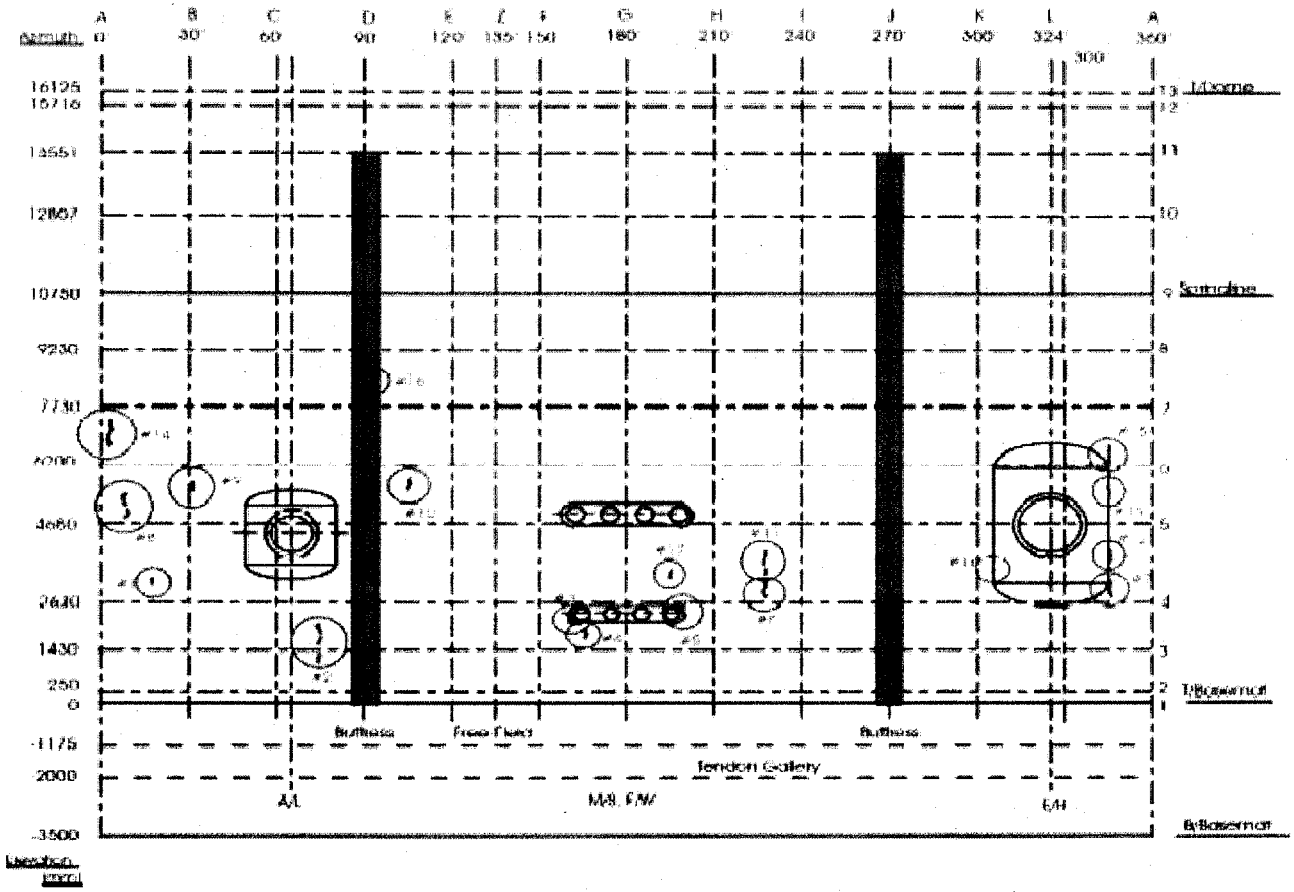

Figure 2. Liner Tears Observed After LST

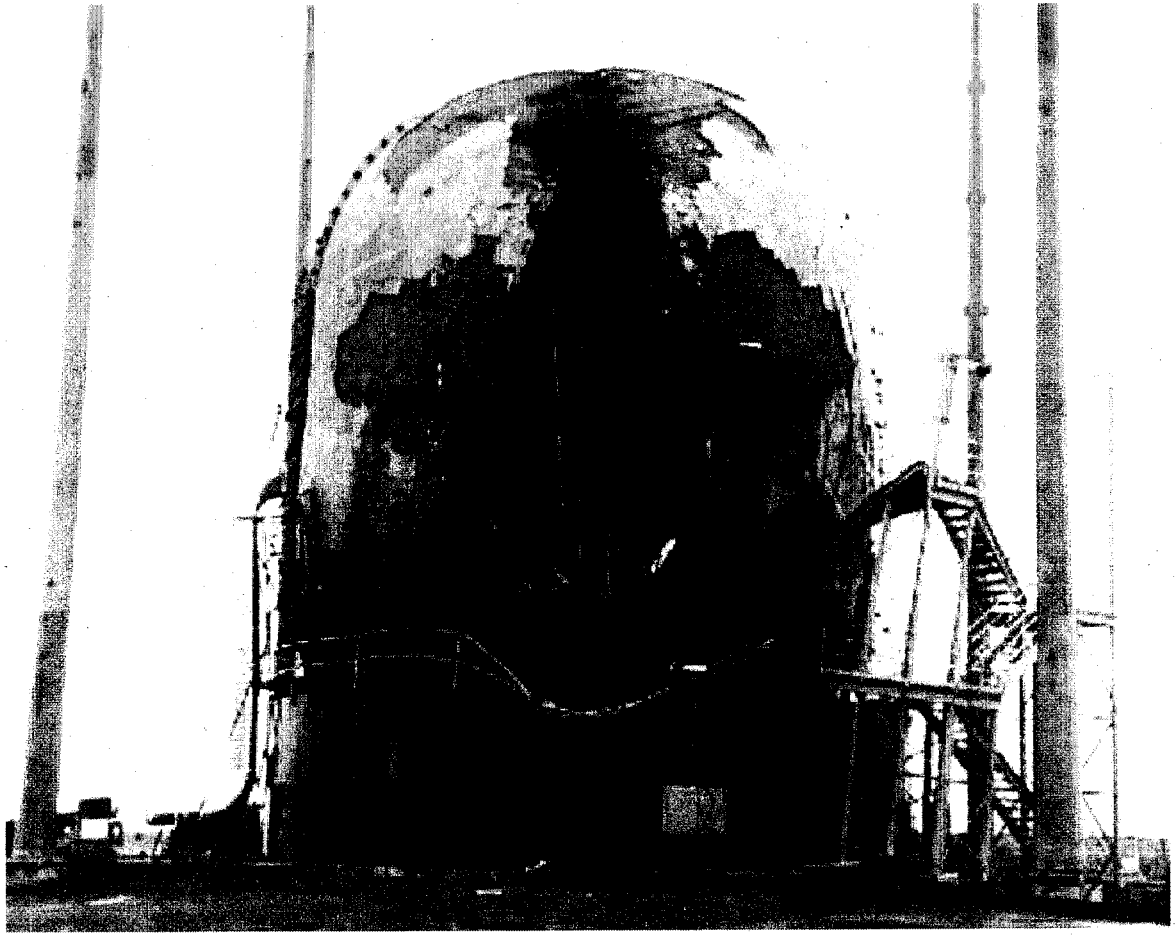

Figure 3. PCCV Model after Structural Failure Mode Test

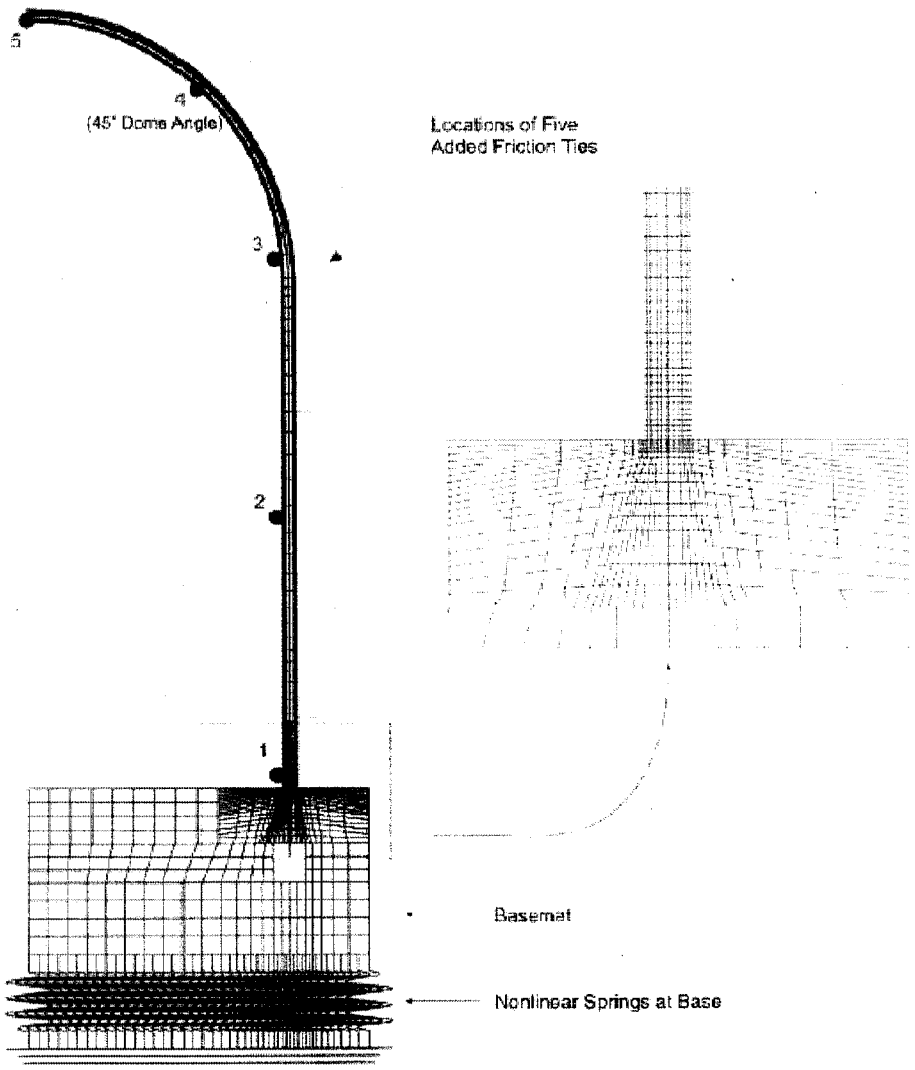

Figure 4. Axisymmetric Model of PCCV and Locations for Plotted Output

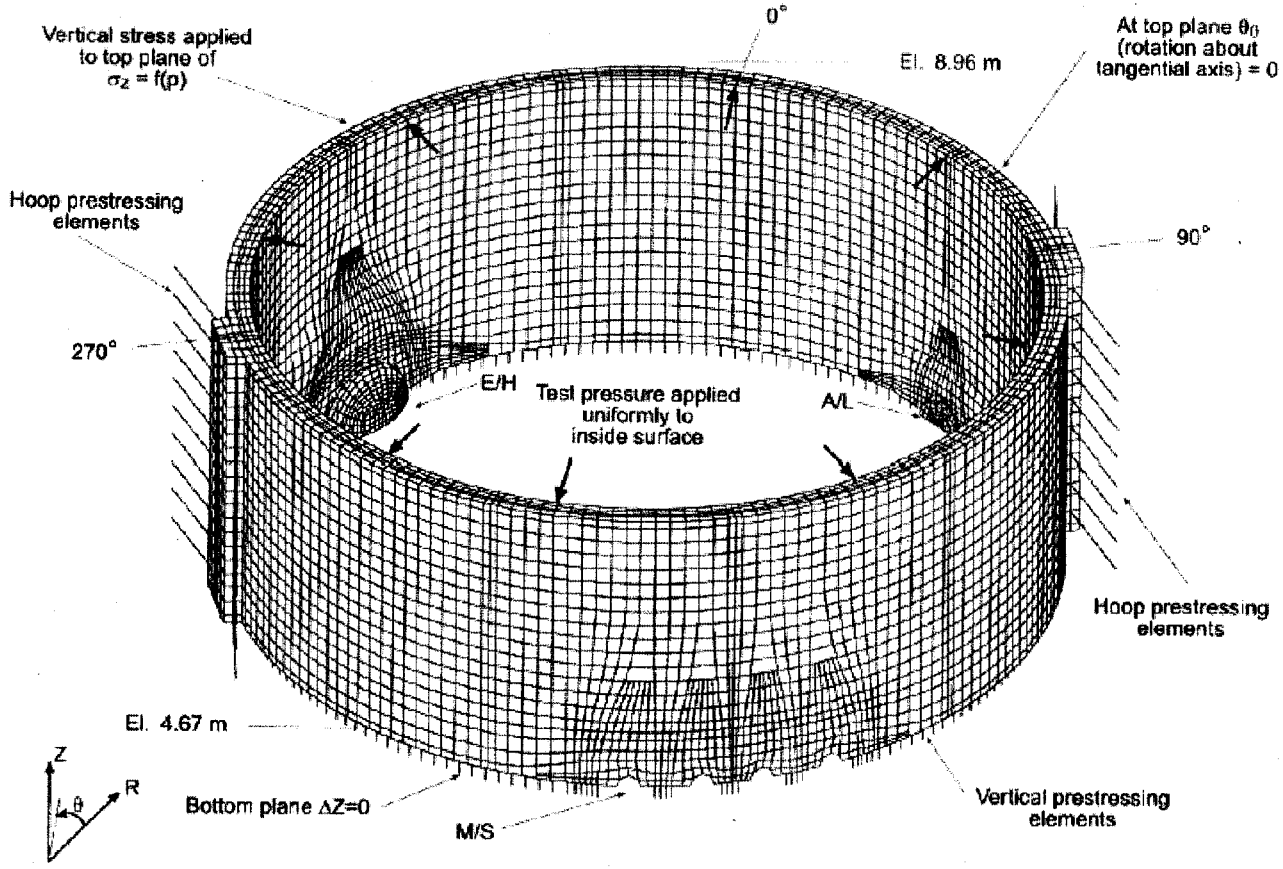

Figure 5. 3DCM Model and Vertical Boundary Conditions

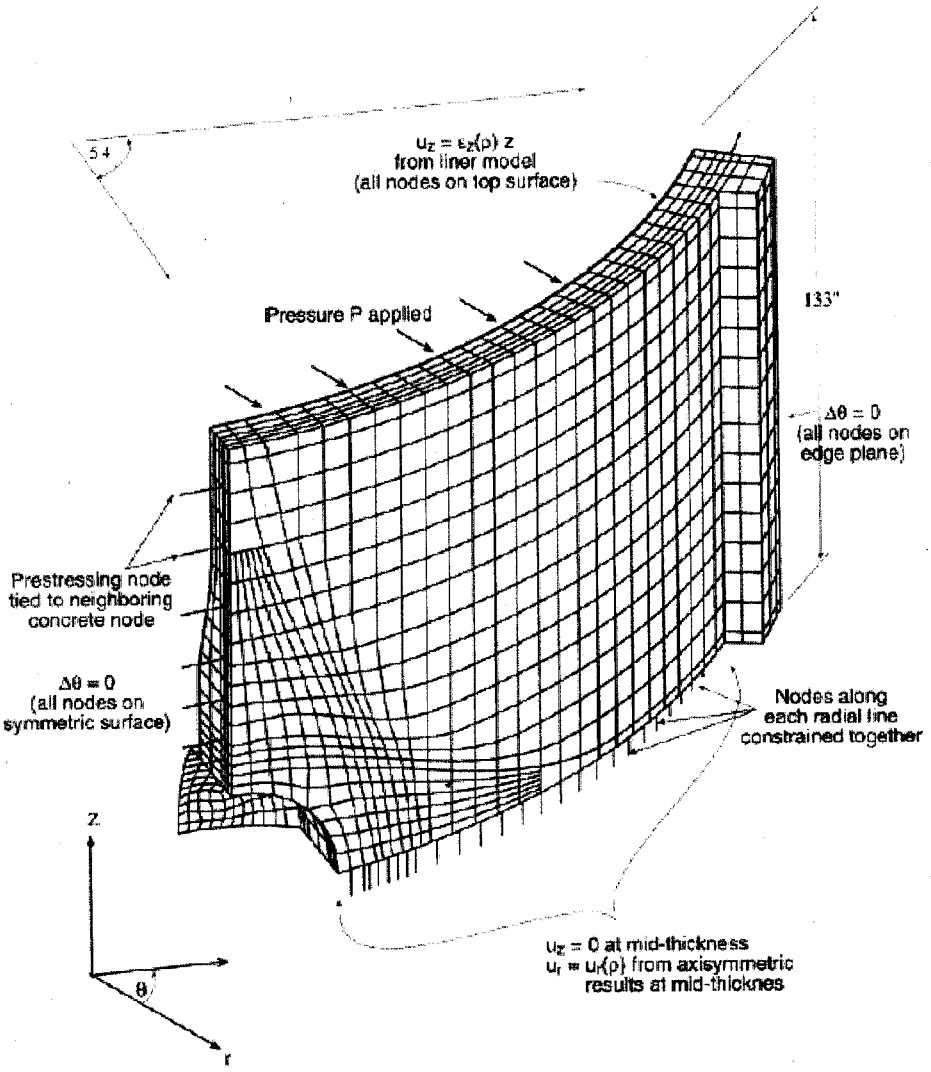

Figure 6. Boundary Conditions and Geometry for the 3D E/H Model Used in Pretest Analysis

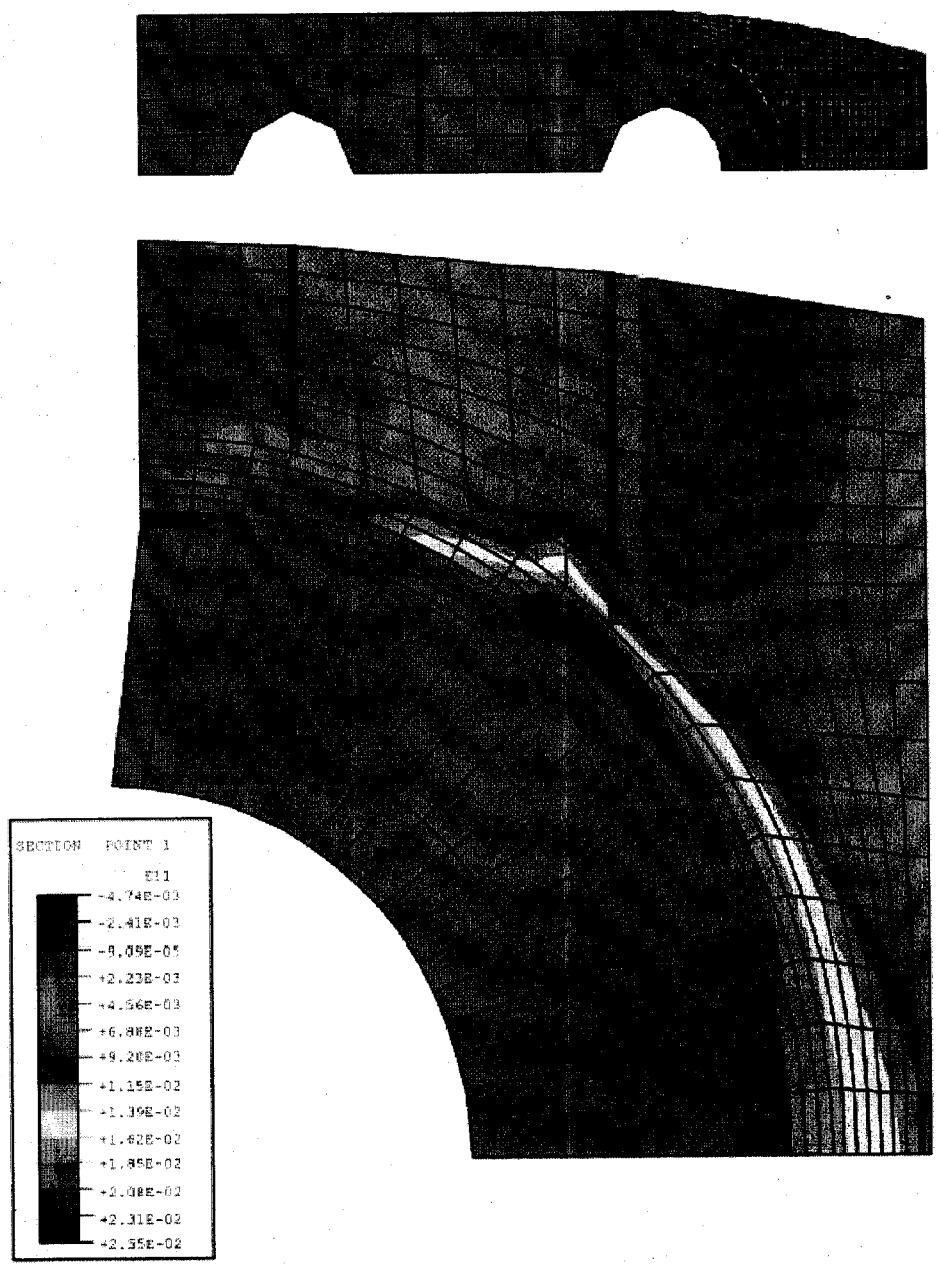

Figure 7. Hoop Strains for Posttest M/S Analysis at P=3.3P_d

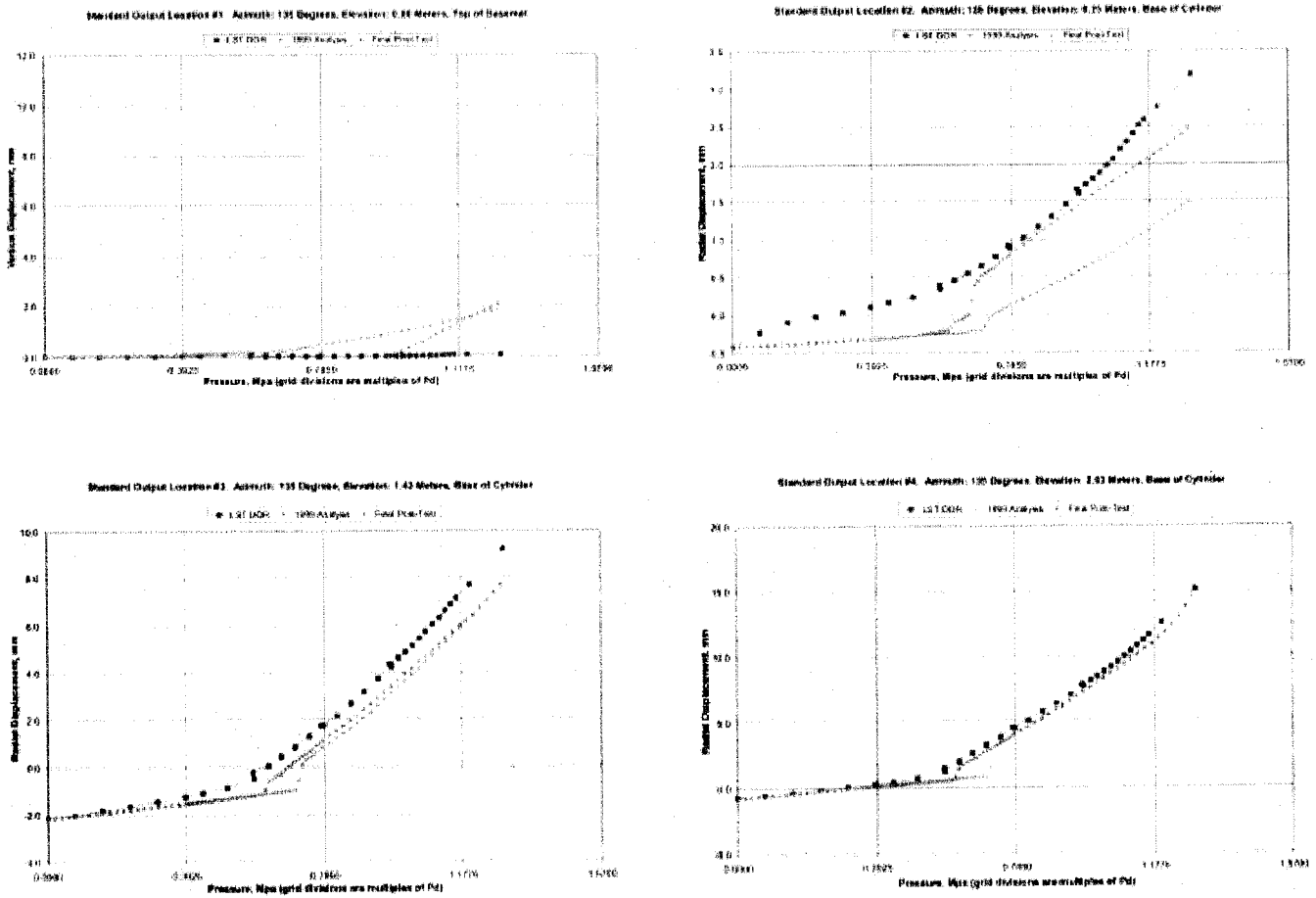

Figure 8. Comparison at Standard Output Locations 1, 2, 3 and 4

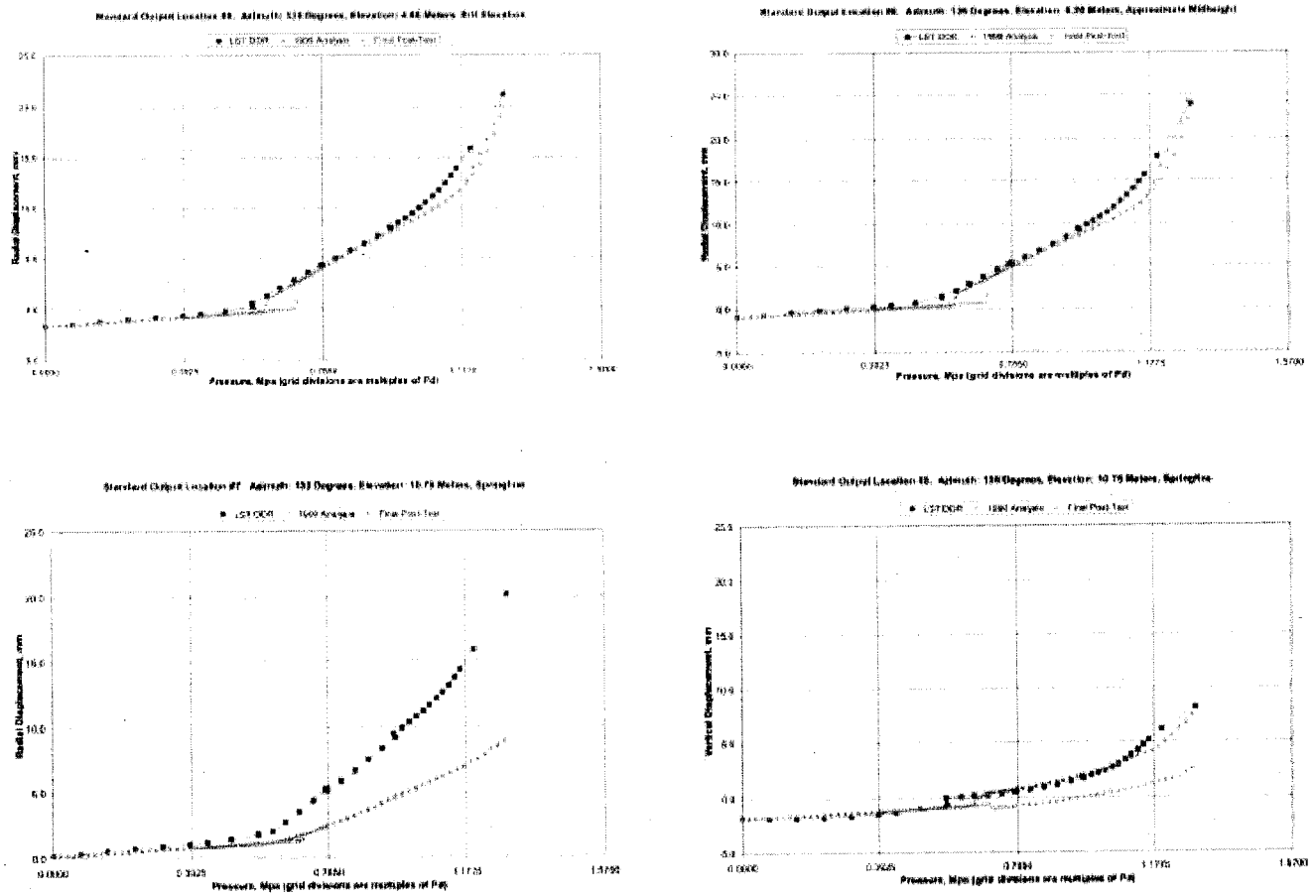

Figure 9. Comparison at Standard Output Locations 5, 6, 7 and 8

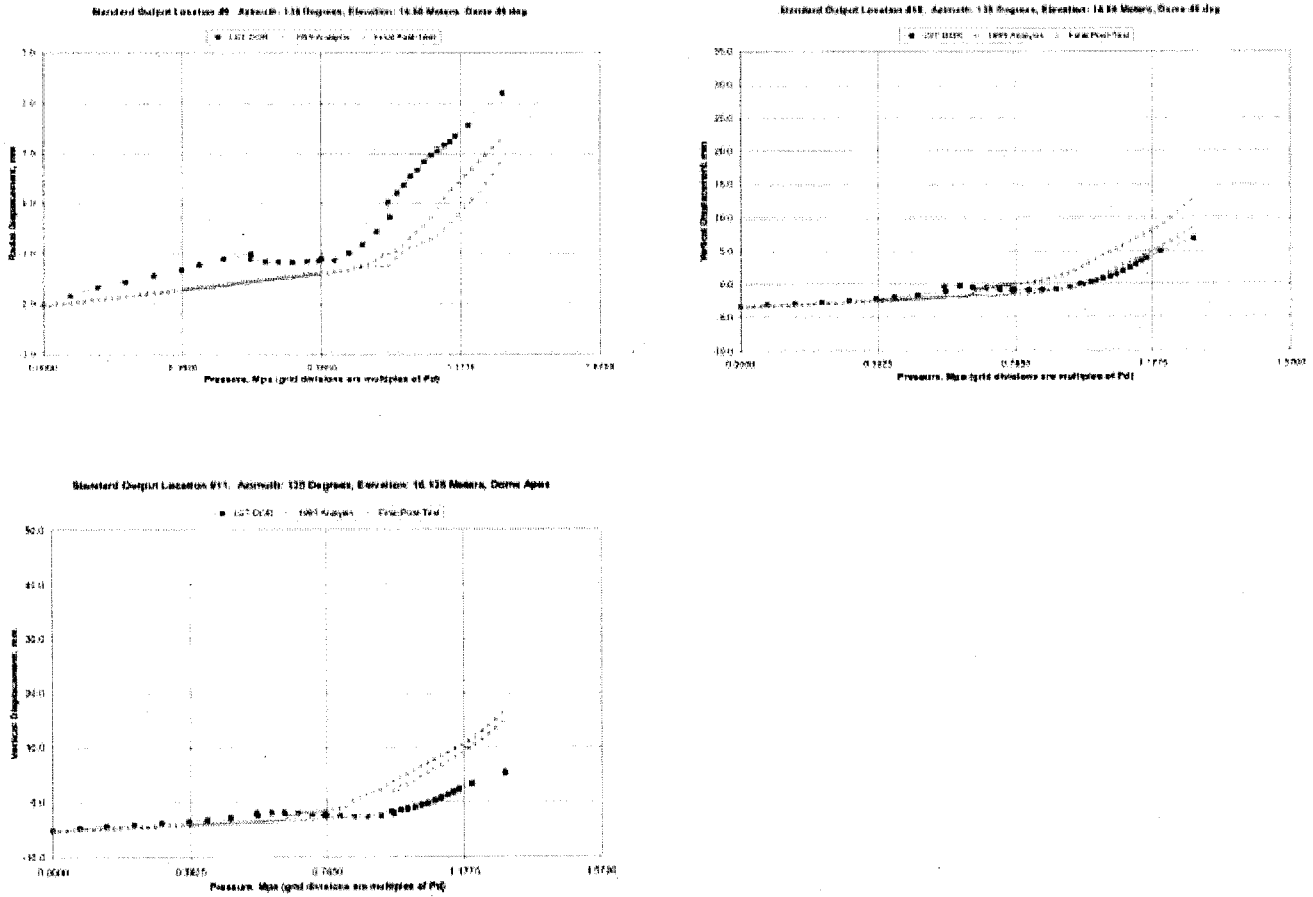

Figure 10. Comparison at Standard Output Locations 9, 10 and 11

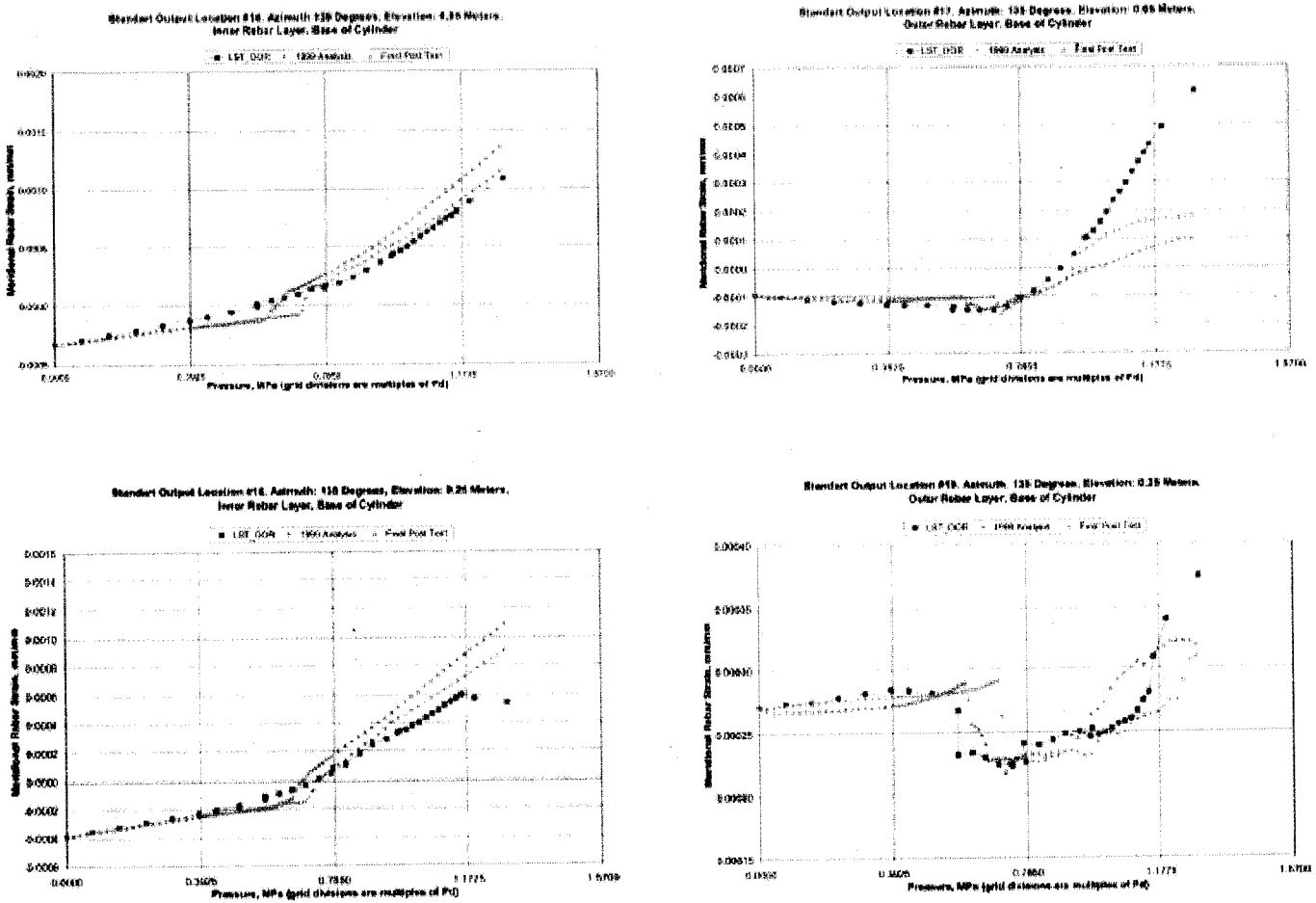

Figure 11. Comparison at Standard Output Locations 16, 17, 18 and 19

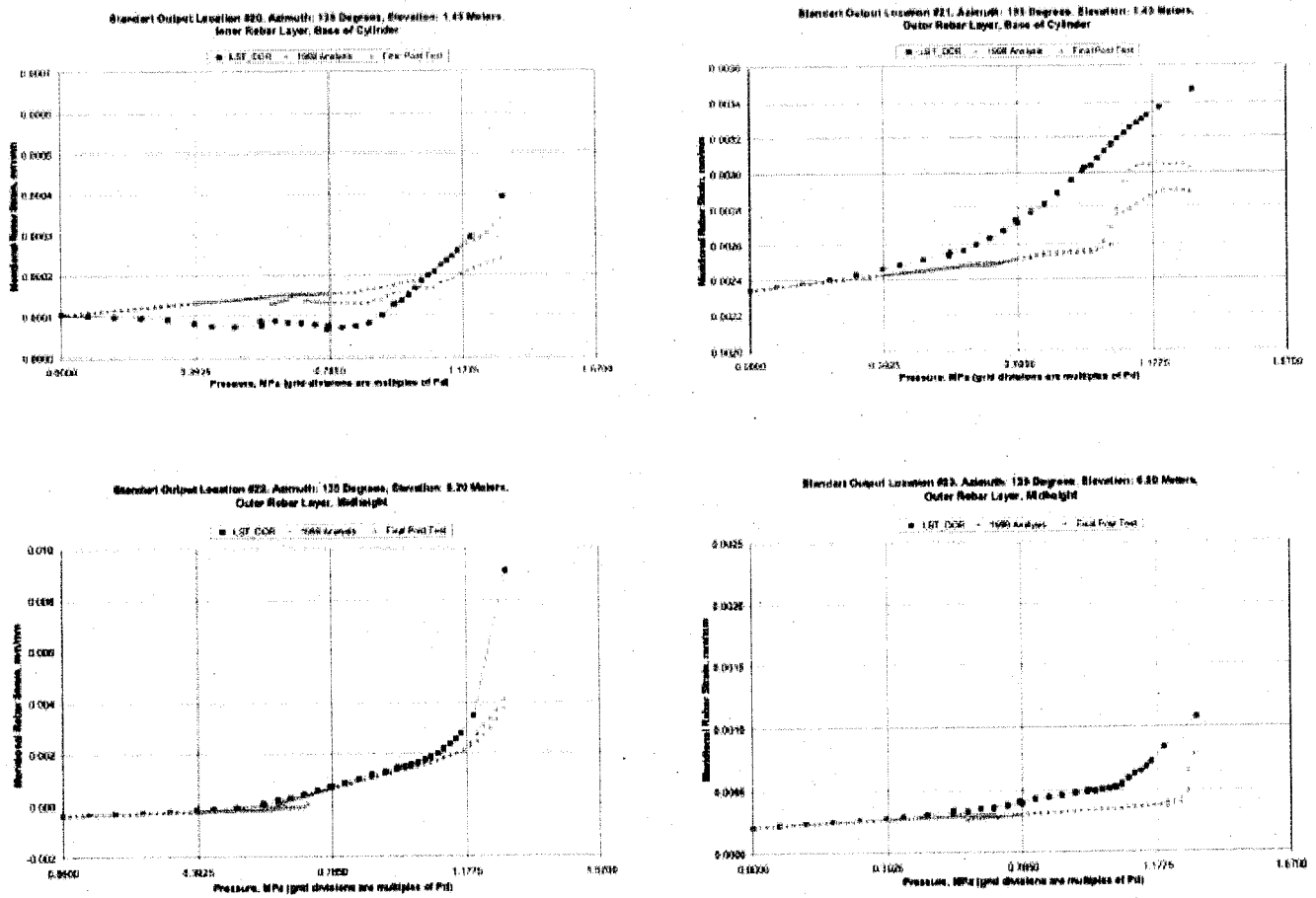

Figure 12. Comparison at Standard Output Locations 20, 21, 22 and 23

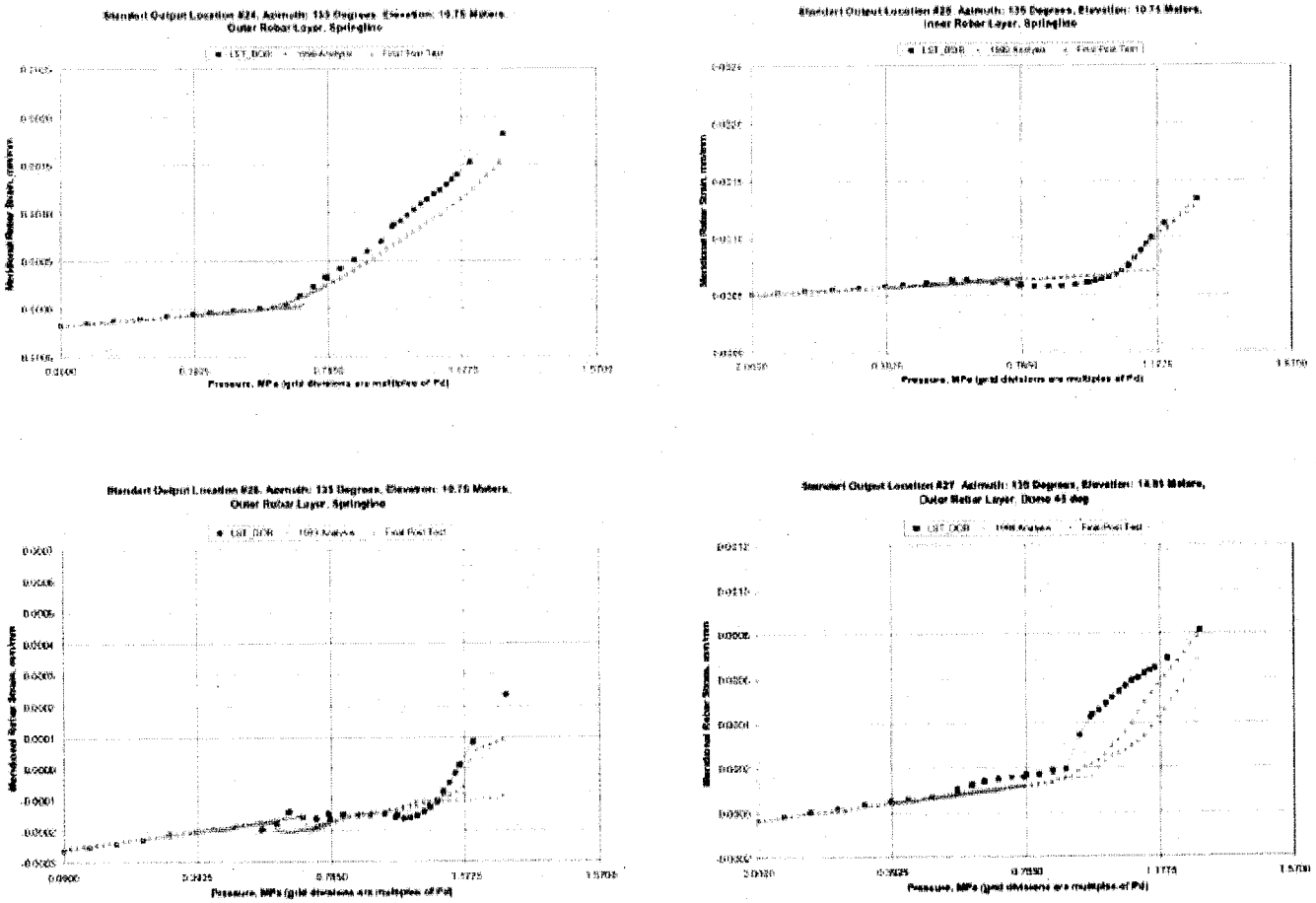

Figure 13. Comparison at Standard Output Locations 24, 25, 26 and 27

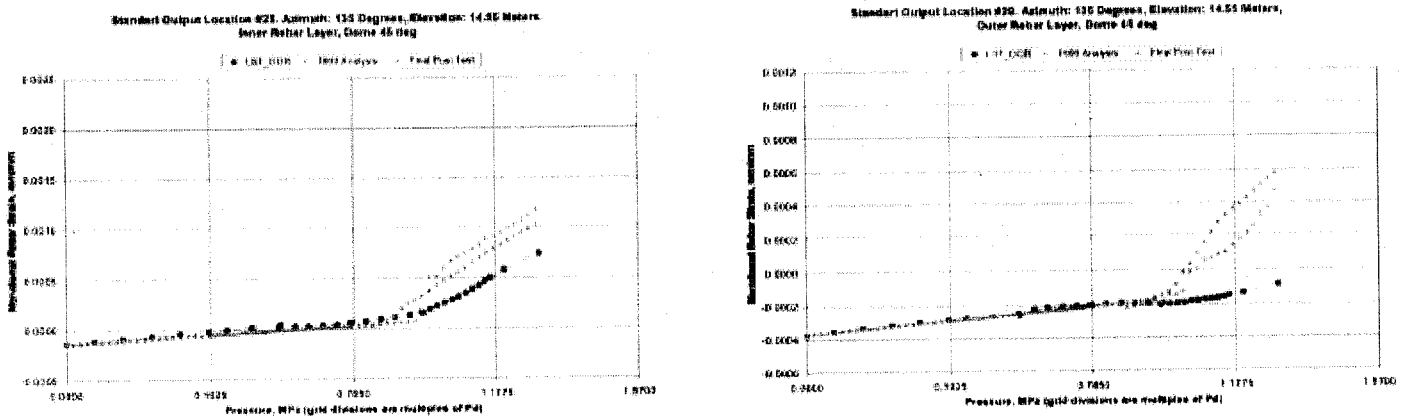

Figure 14. Comparison at Standard Output Locations 28 and 29

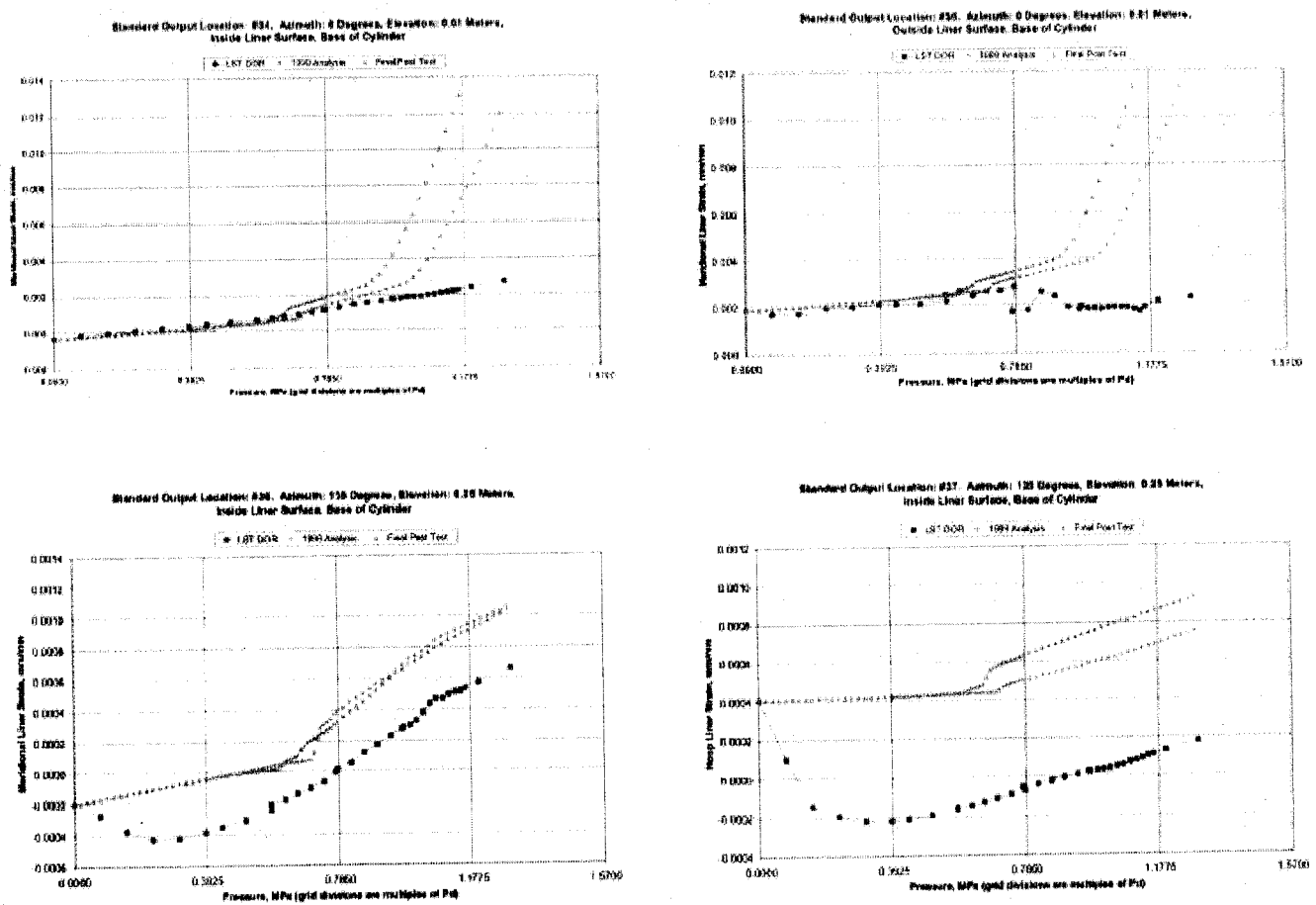

Figure 15. Comparison at Standard Output Locations 34, 35, 36 and 37

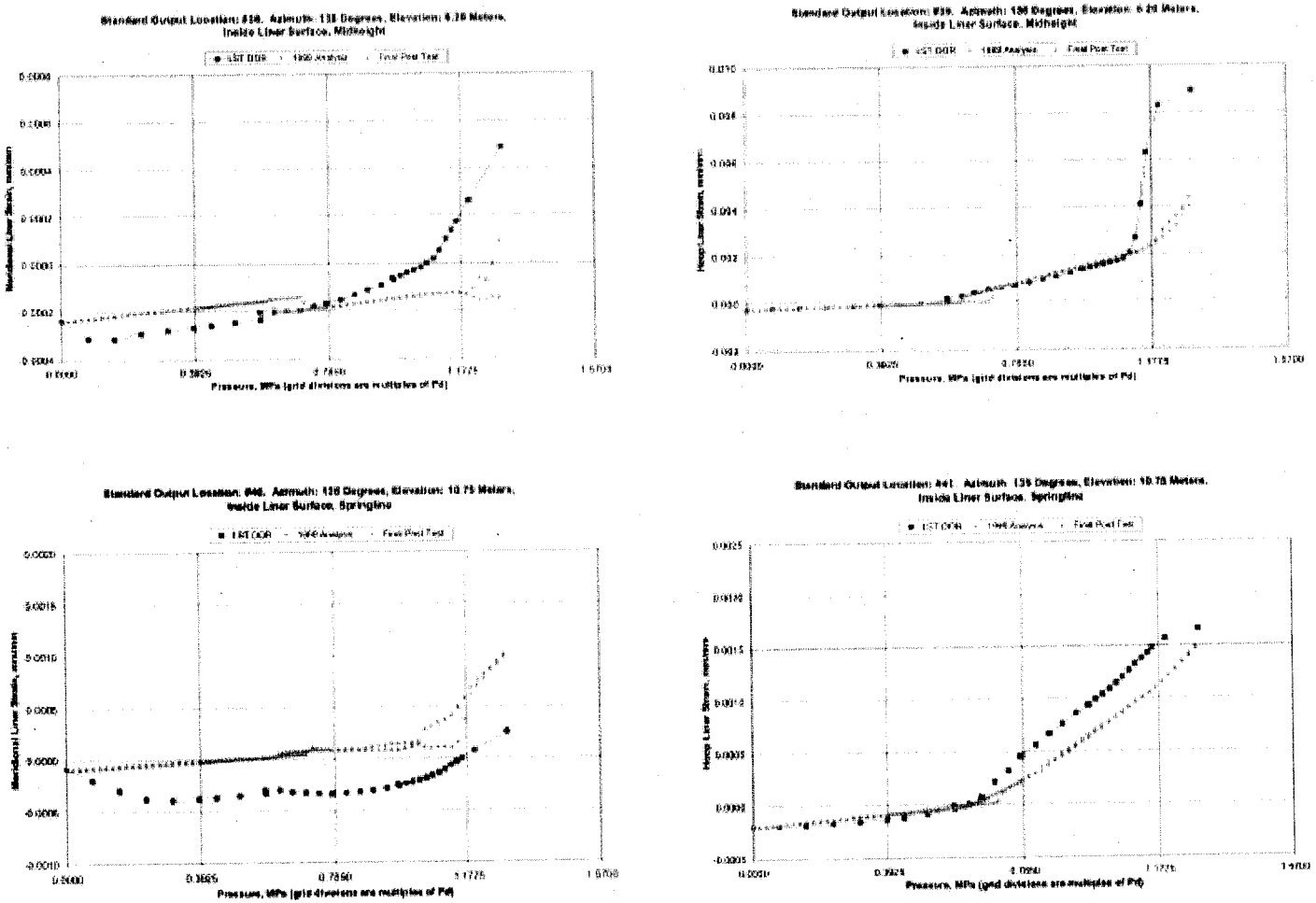

Figure 16. Comparison at Standard Output Locations 38, 39, 40 and 41

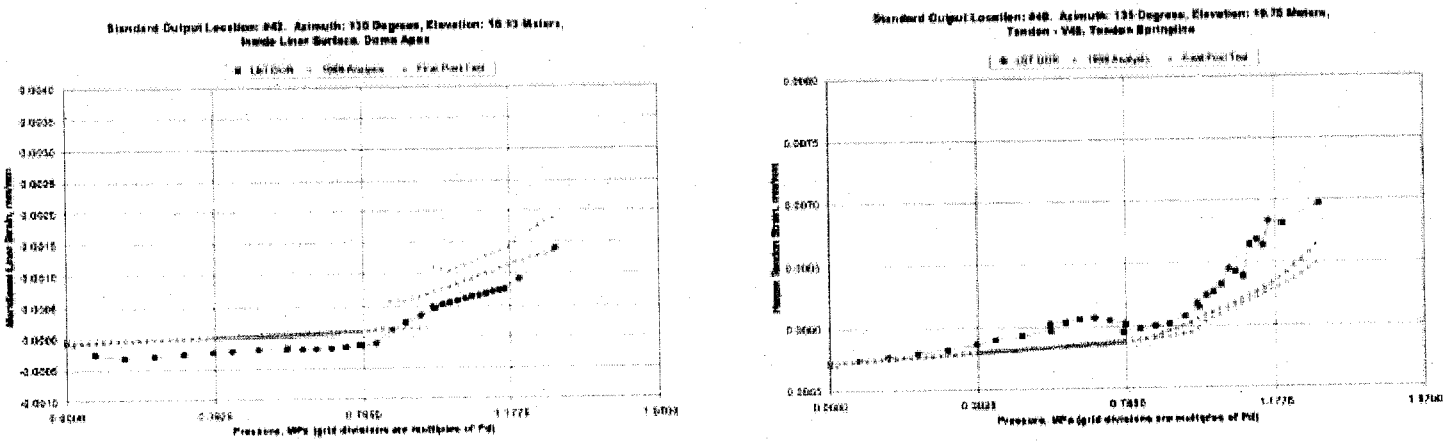

Figure 17. Comparison at Standard Output Locations 42 and 49

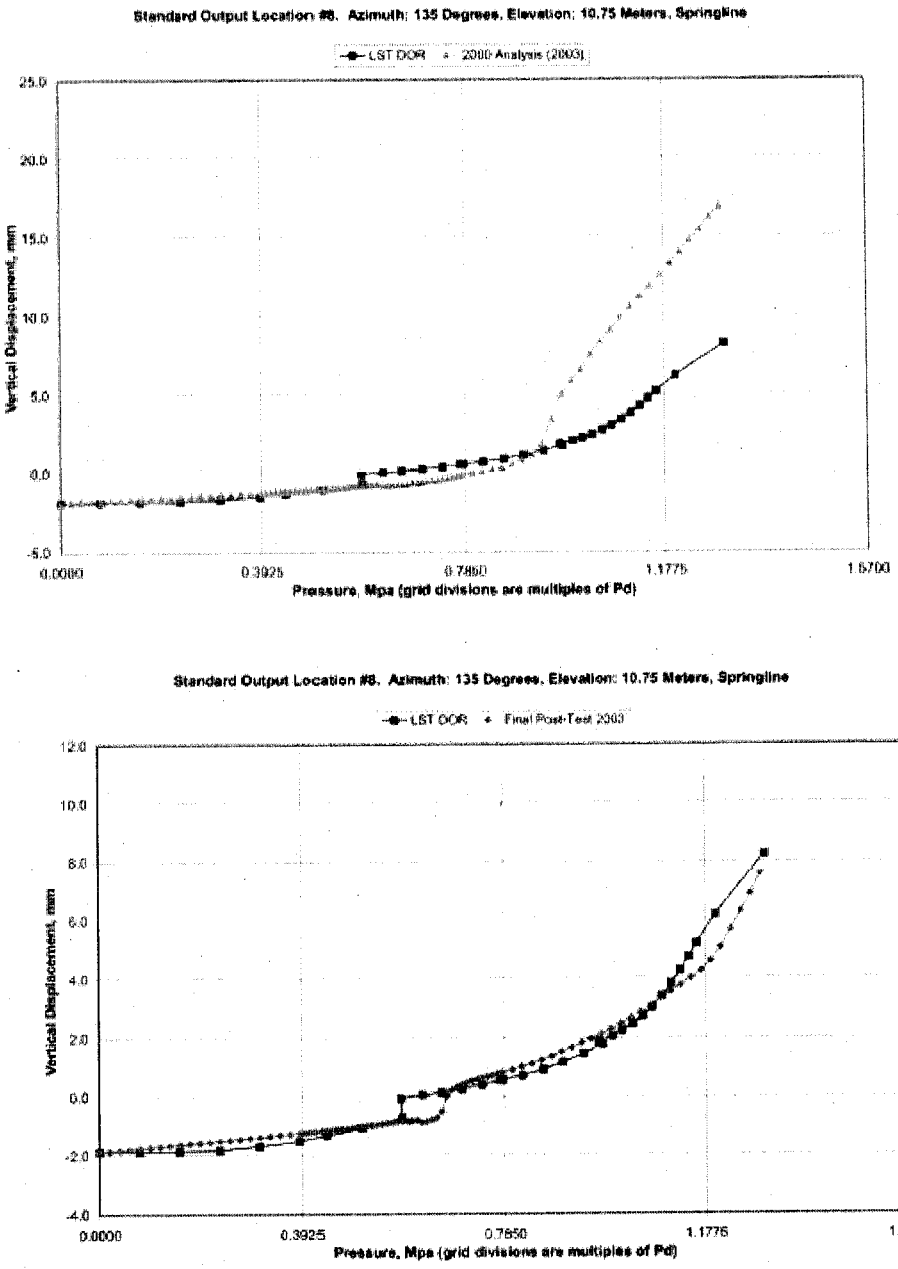

Figure 18. Comparison of Pretest (Upper) and Posttest (Lower) Analysis, Vertical Displacement of Springline to Test Data

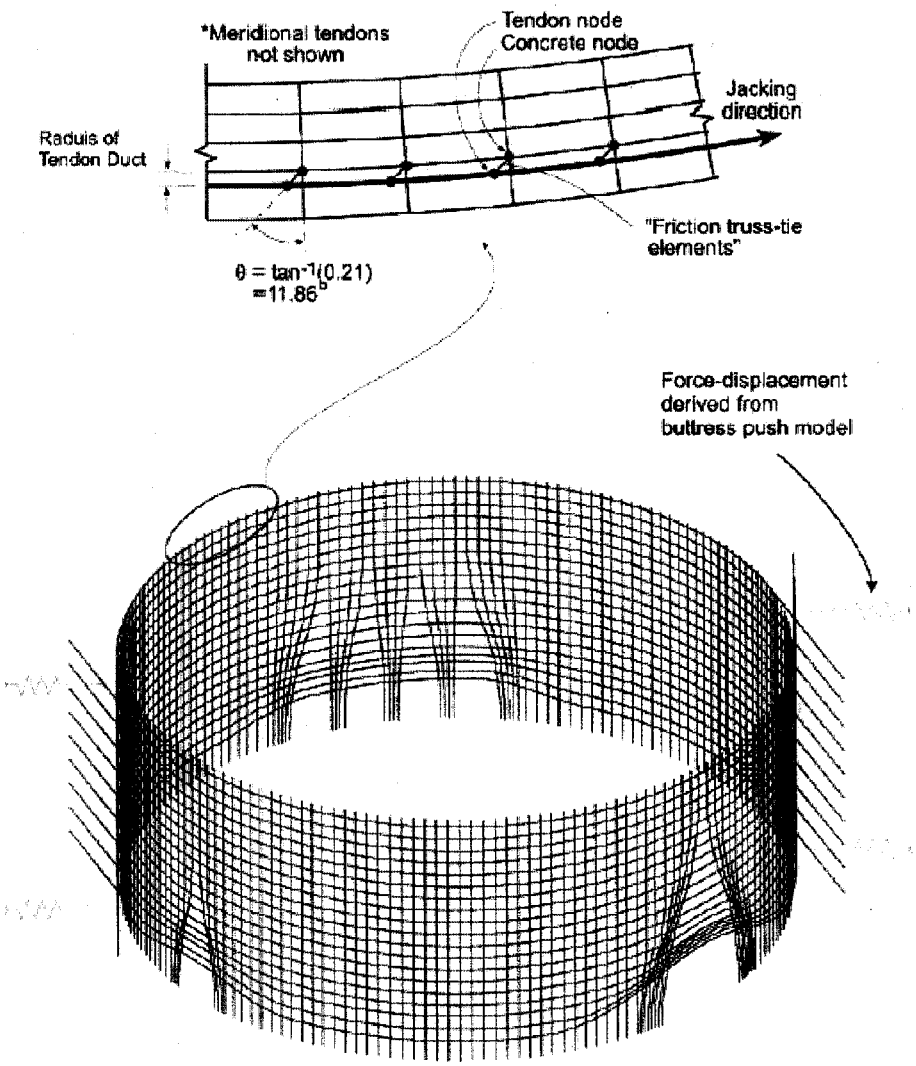

Figure 19. 3DCM Model; Added Buttress Springs; Tendon Friction Modeling

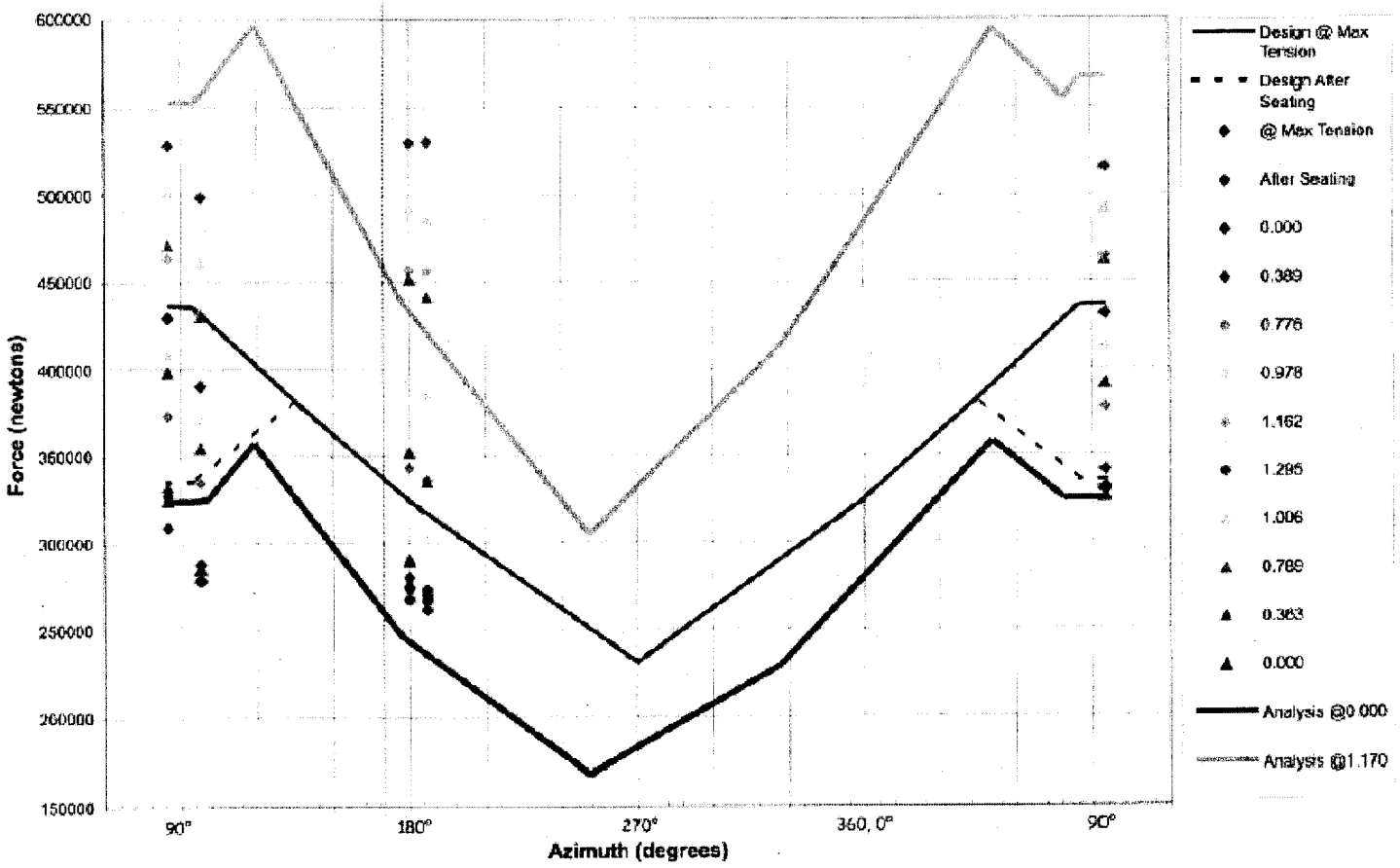

Figure 20. H35 Tendon Force Comparisons to Pretest

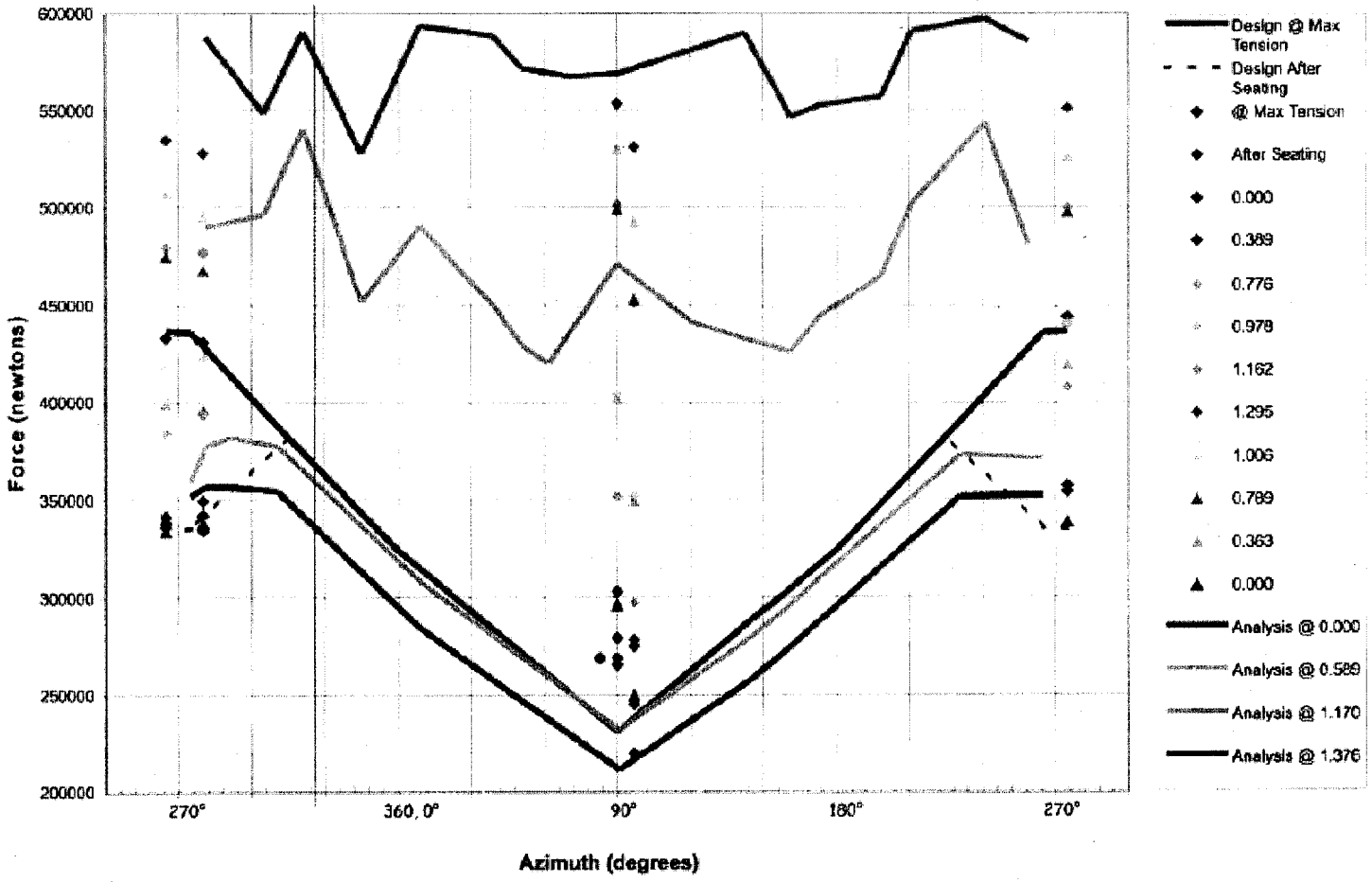

Figure 21. H53 Hoop Tendon Force Comparisons to Posttest Run #9 (with two-way friction)

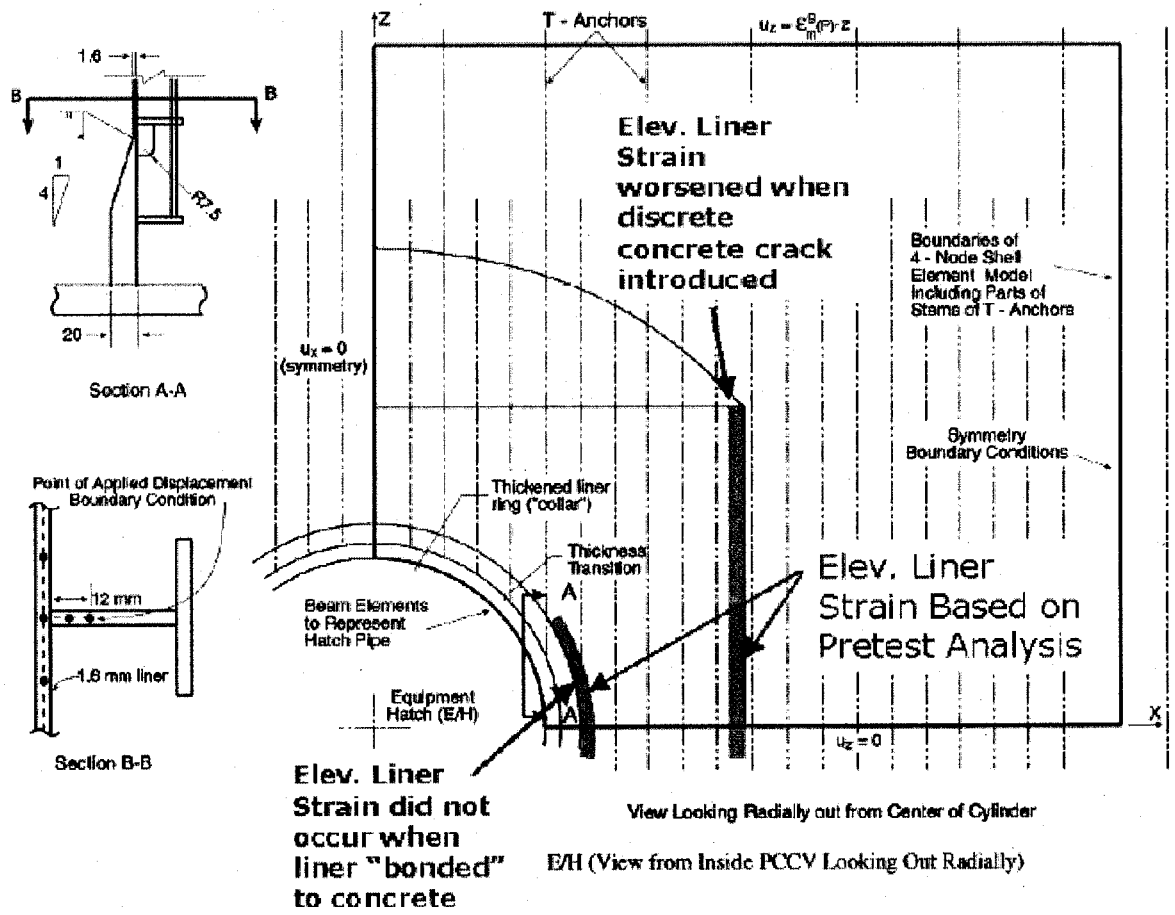

Figure 22. Details of Liner Modeling for Local E/H Model

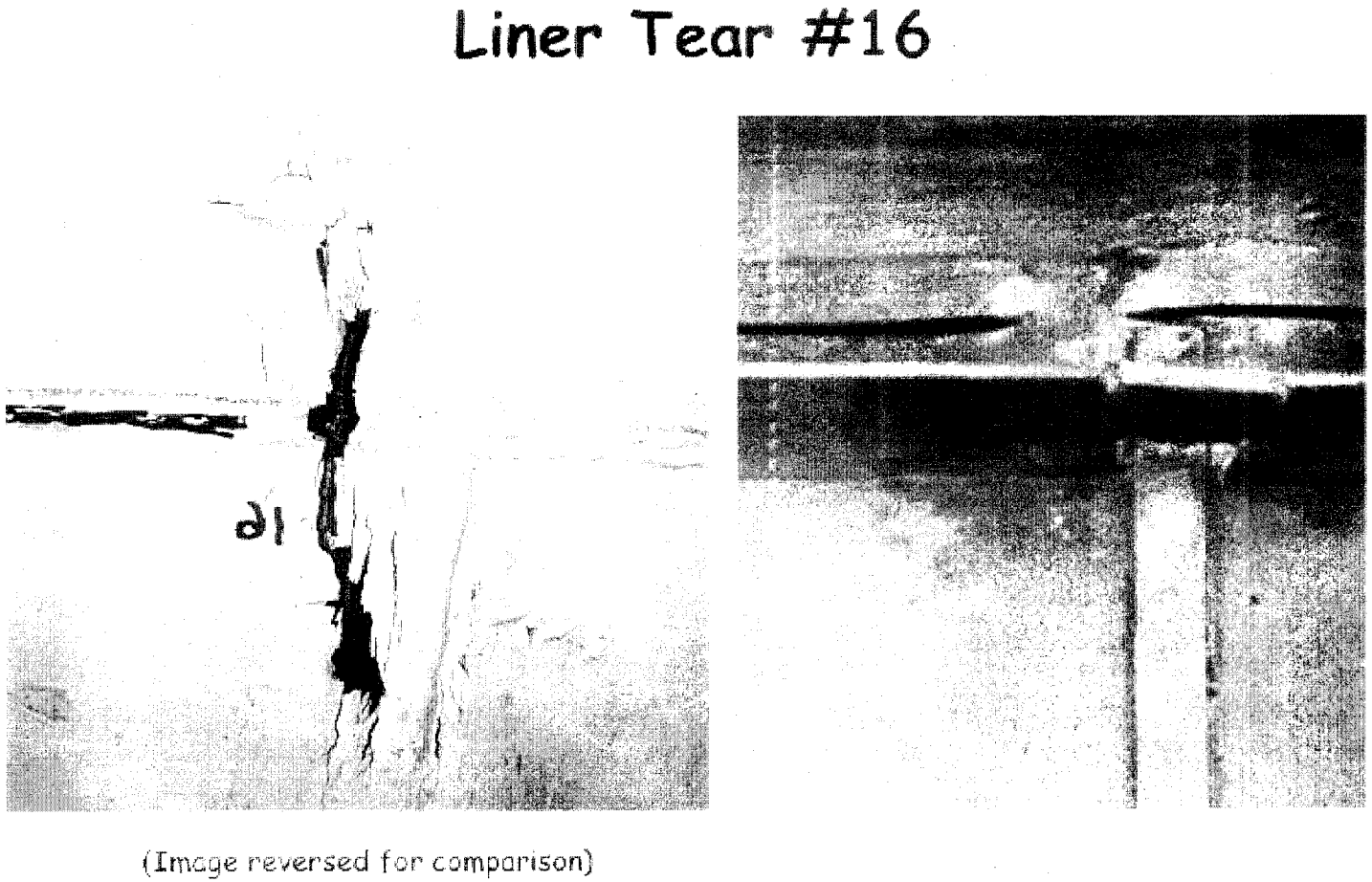

Figure 23. LST - Typical Tear Location

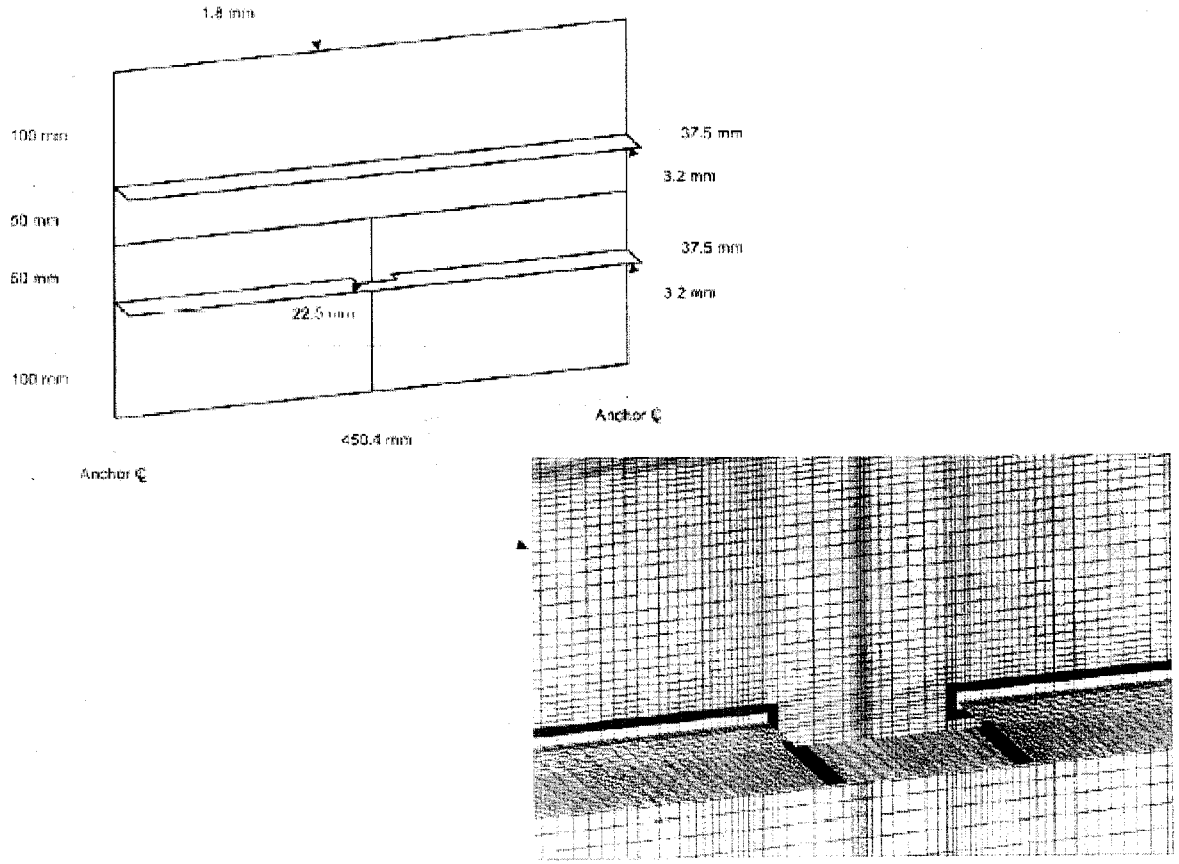

Figure 24. Liner Seam Model Geometric Details

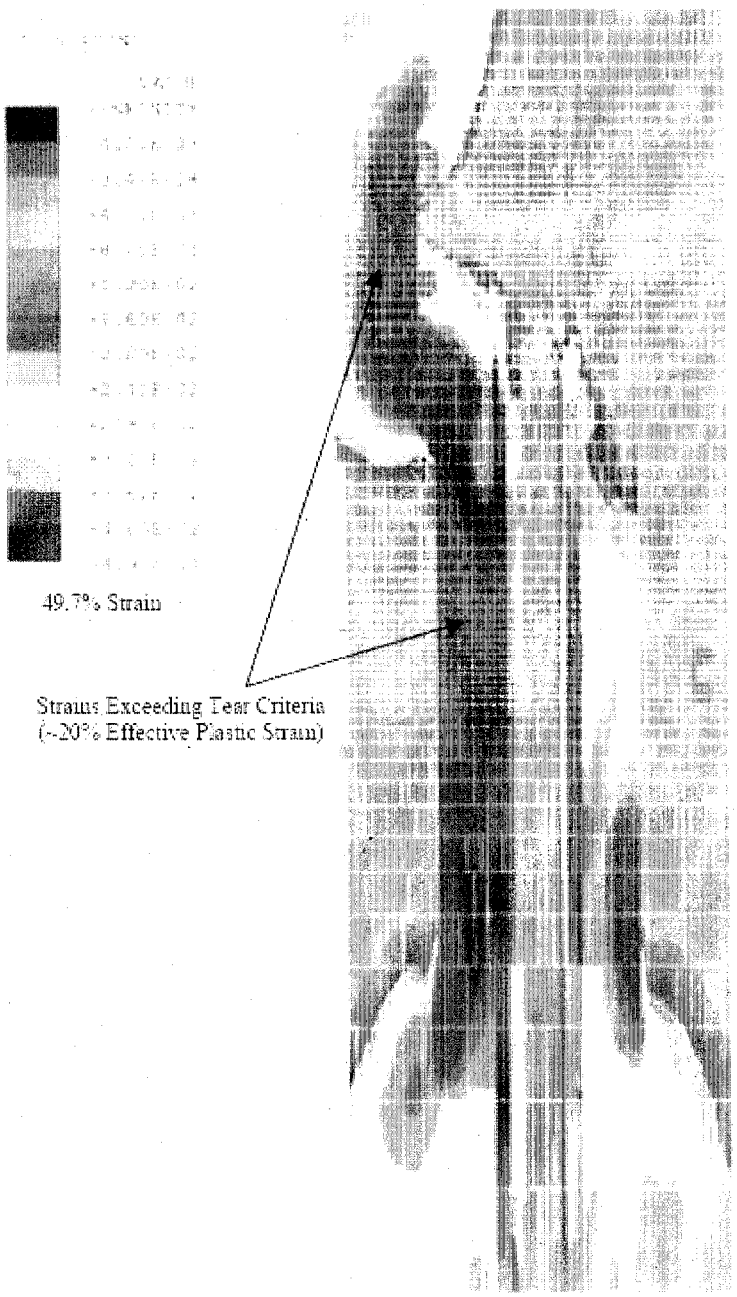

Figure 25. Local Liner Seam Analysis Model (Simulation of Tear 16)

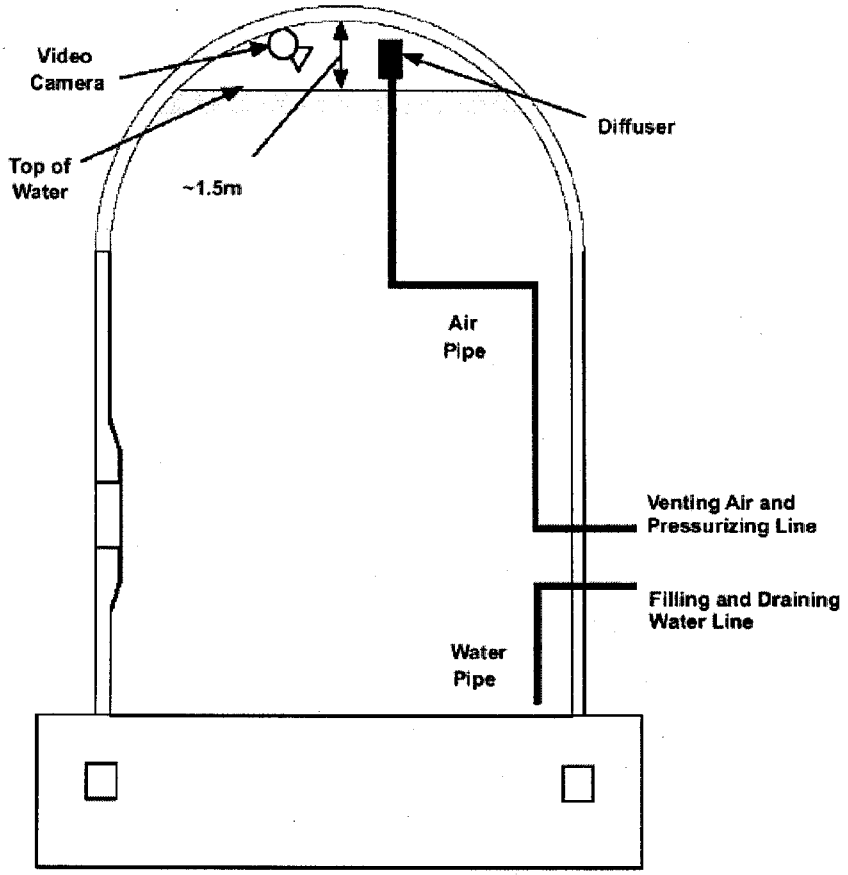

Figure 26. PCCV SFMT Pressurization Configuration

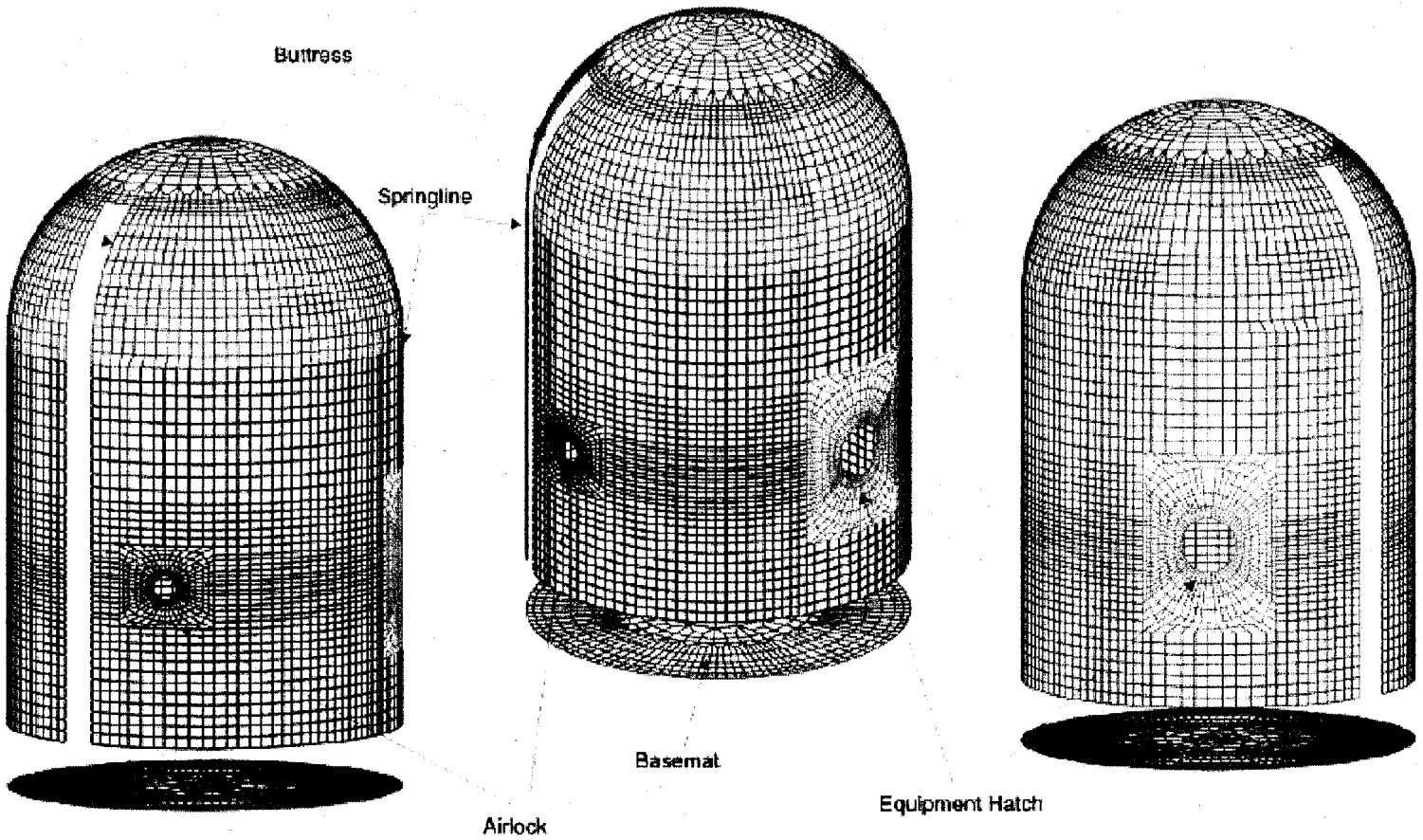

Figure 27. PCCV SFMT, 3D Global Shell Model

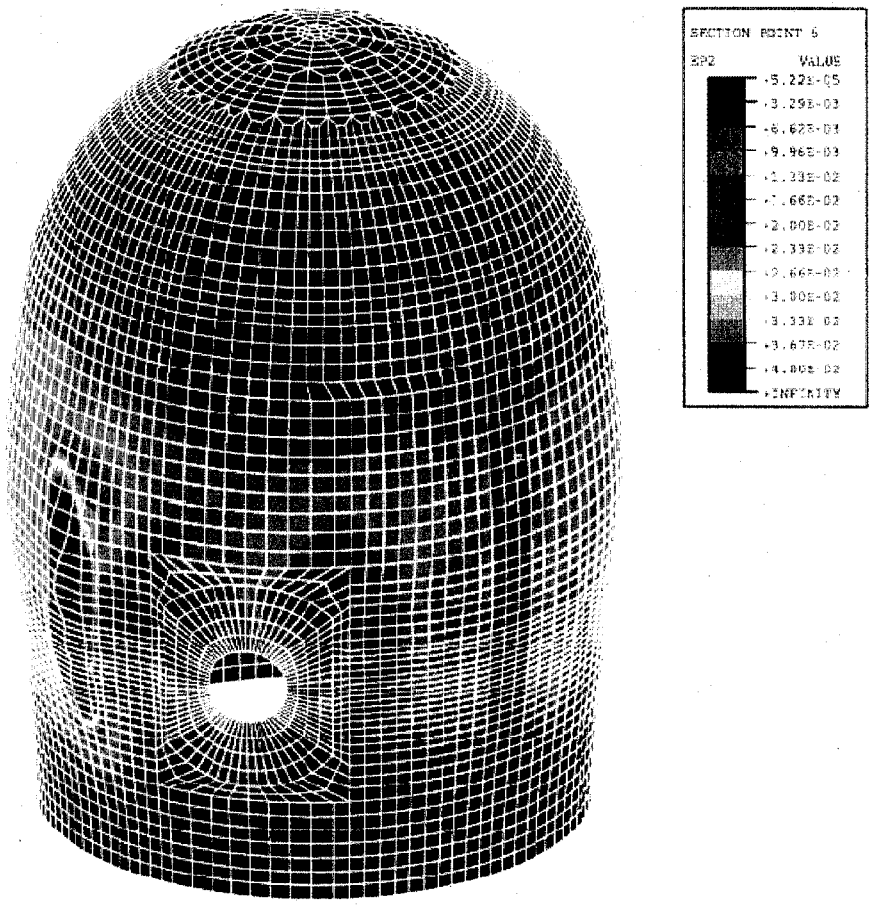

1.381 MPa

Figure 28. PCCV SFMT, 3D Global Shell Tendon Rupture Model. Concrete Maximum Principal Strain. For Pressure at 1.381 MPa (3.51P_d), Displacement x10.

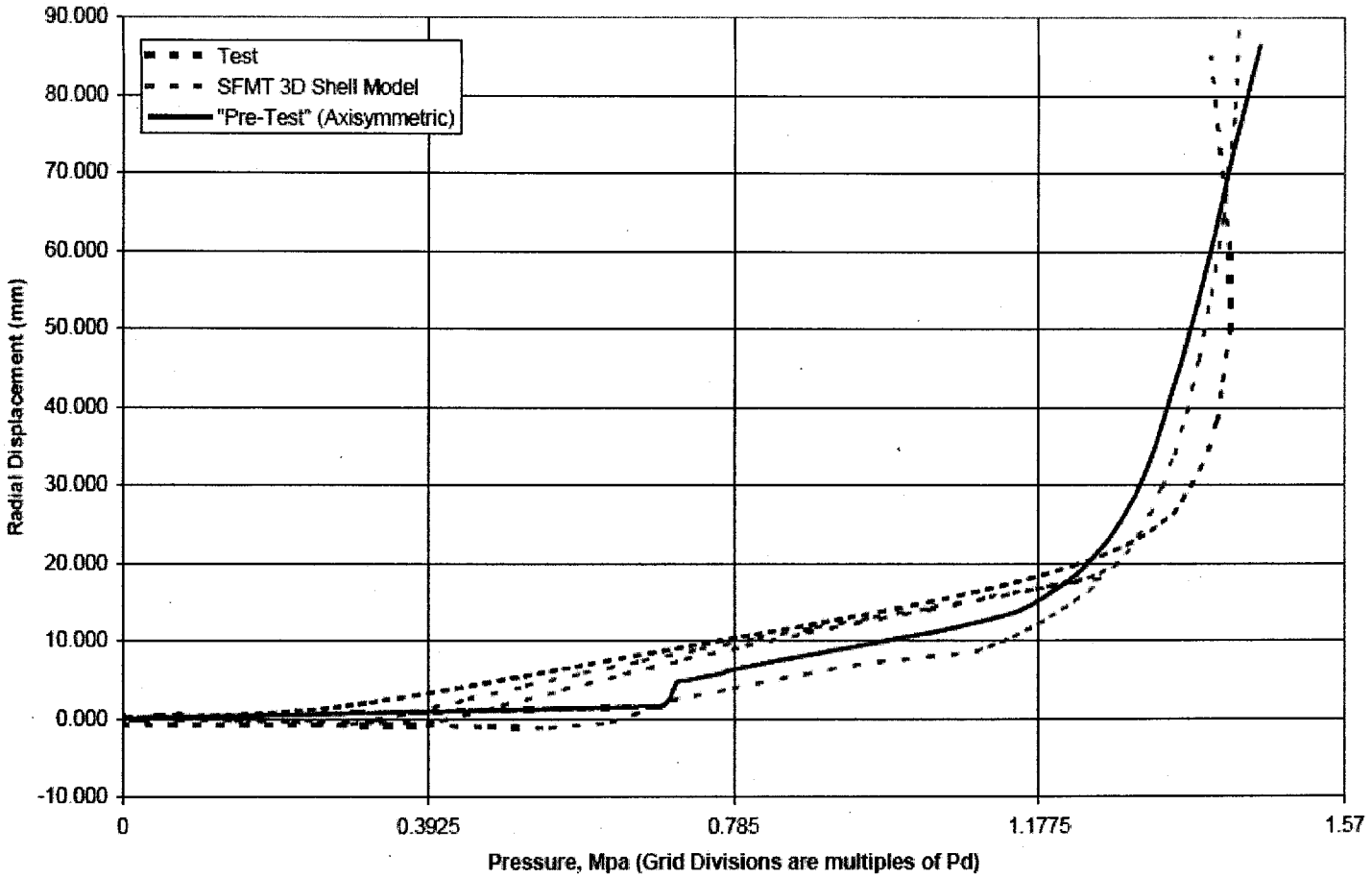

Figure 29. 3D Global Shell Model - Gage R-Z6-05 Comparison, Radial Displacement, 135 Degrees, Elevation 6.20m

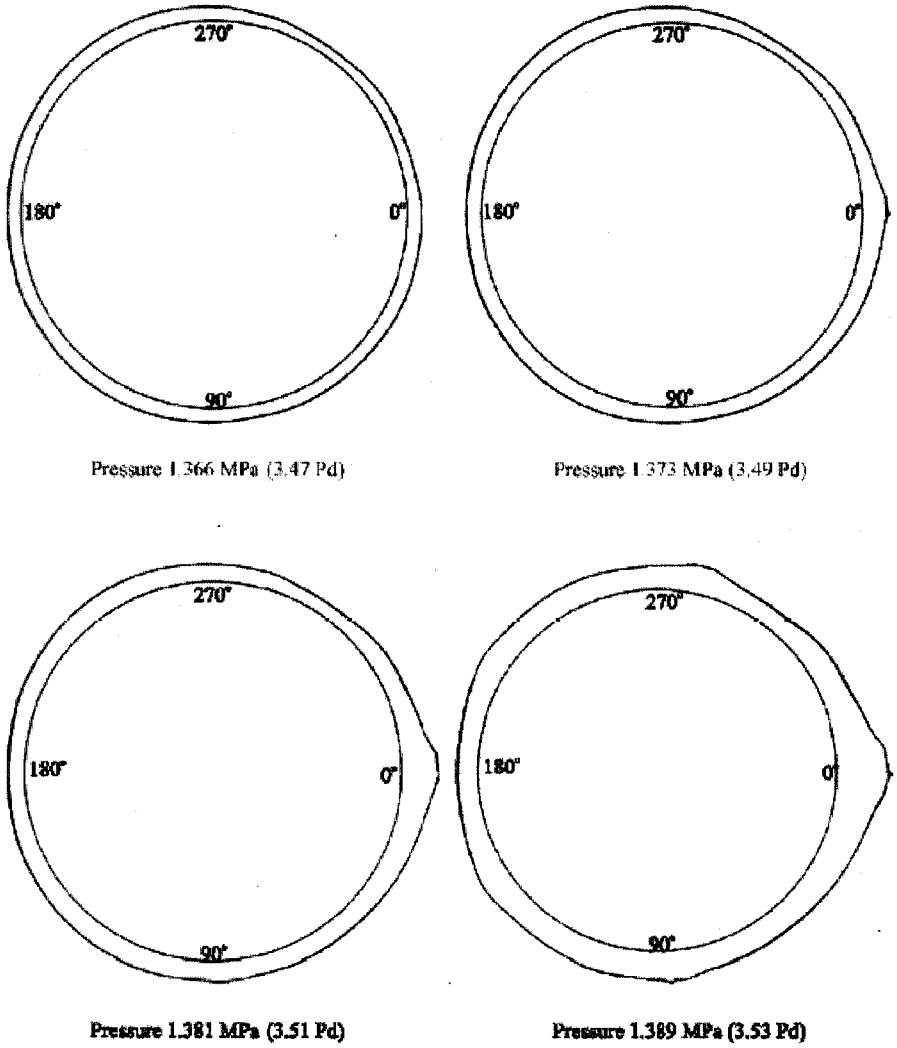

Figure 30. PCCV SFMT, 3D Global Shell Tendon Rupture Model. Deformed Shape. For Elevation of 6.5m. Displacement x10.

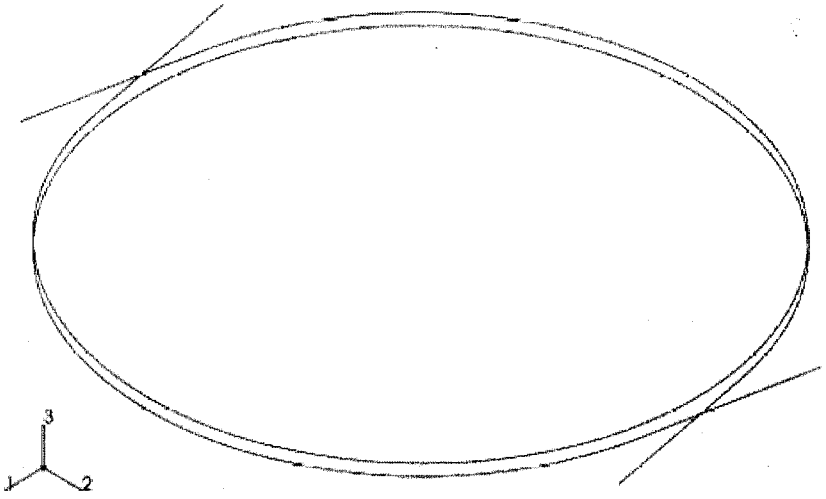

Tendon Groups H67 and H68

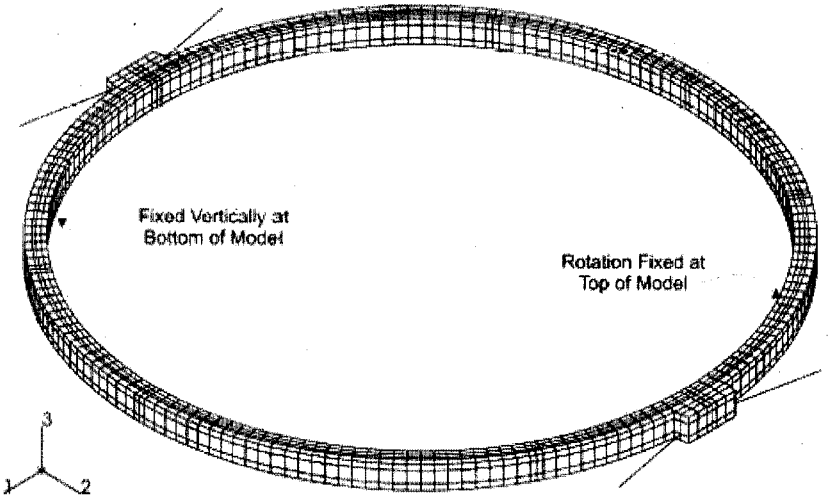

Figure 31. Ring Model Tendons and Boundary Conditions

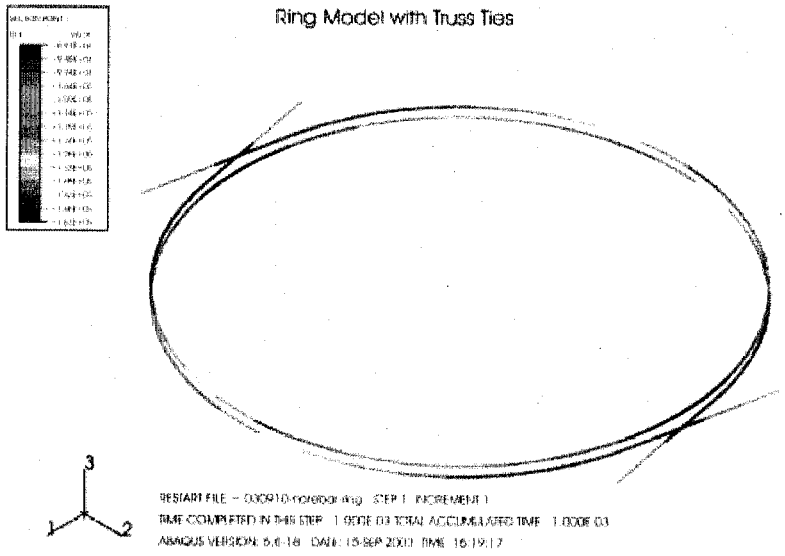

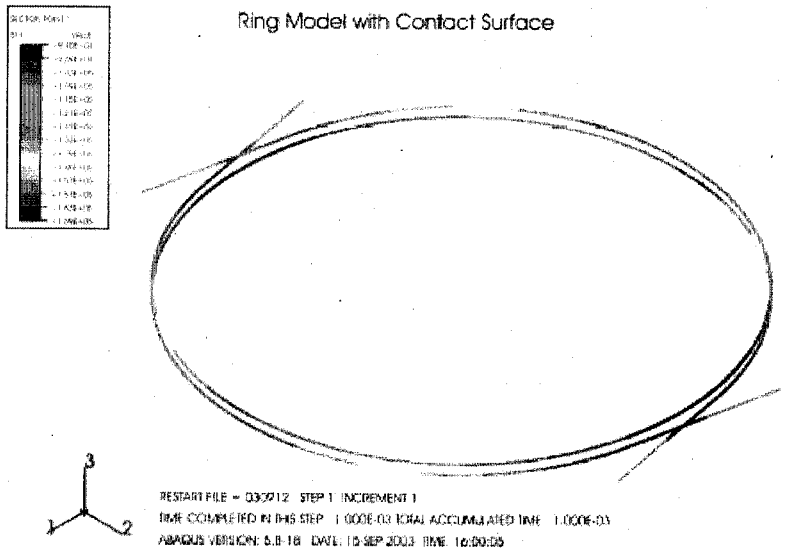

Figure 32. Tendon Stress Contour (Initial Prestress)

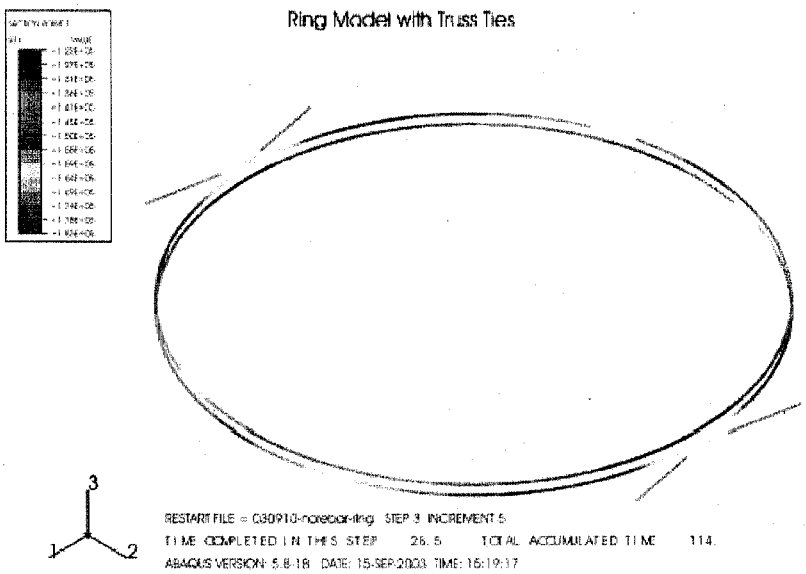

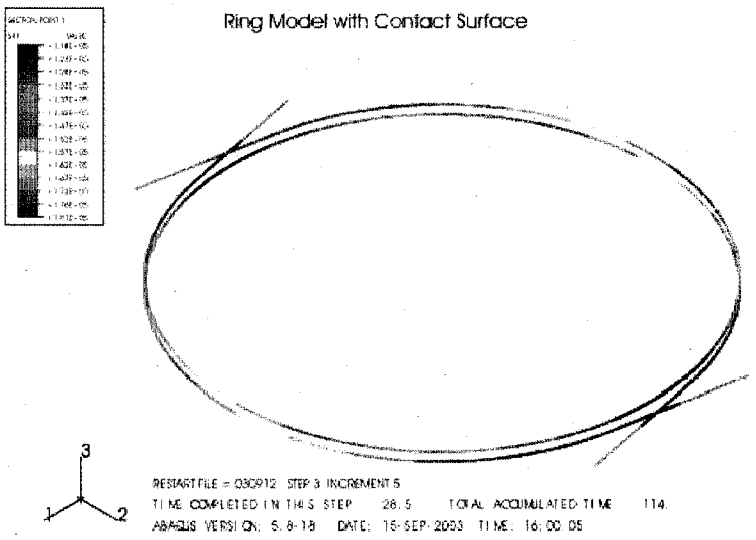

Figure 33. Tendon Stress Contour (Pressure=2.0P_d)

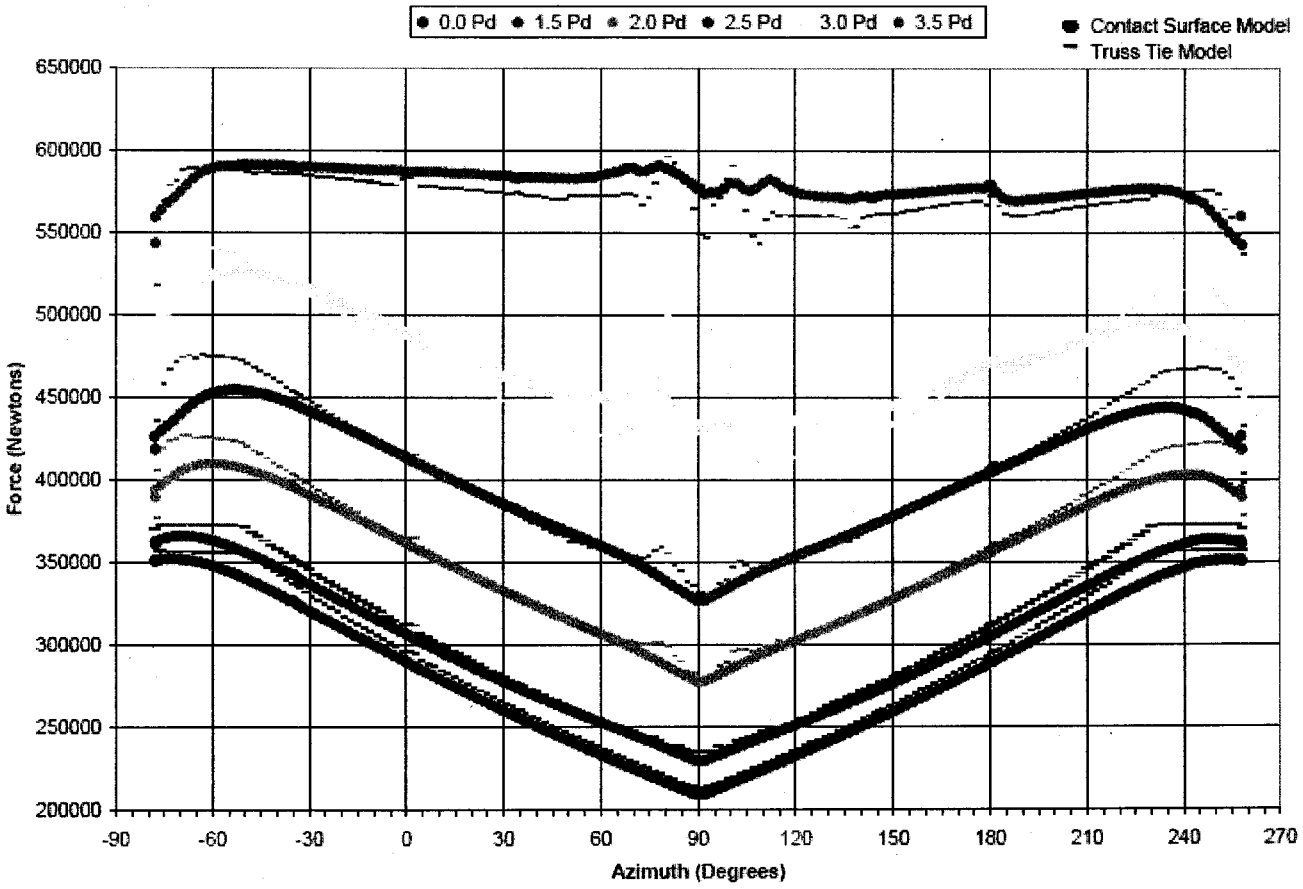

Figure 34. Comparison of Tendon Modeling in Ring Model for Tendon H68

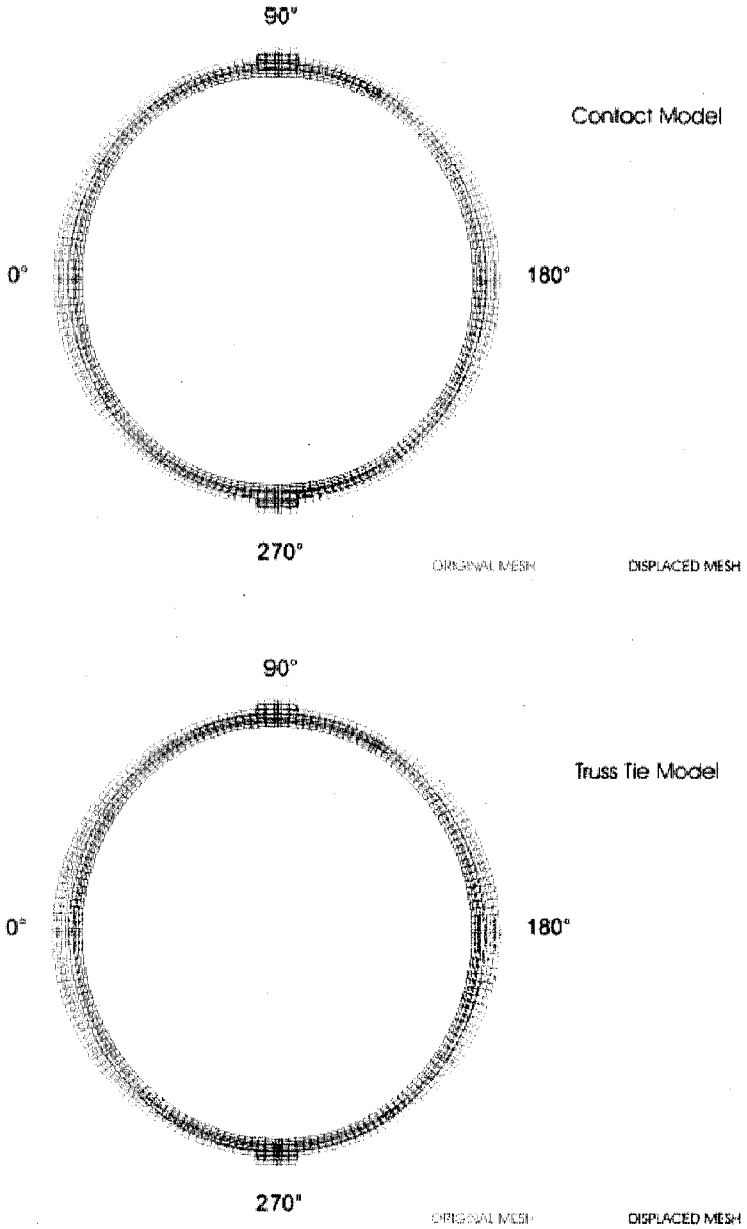

Figure 35. Comparison of Deformed Shapes (displ. x 200) Using Tendon Friction Truss Ties vs. the Contact Surface Model at P=0P_d; After Prestress

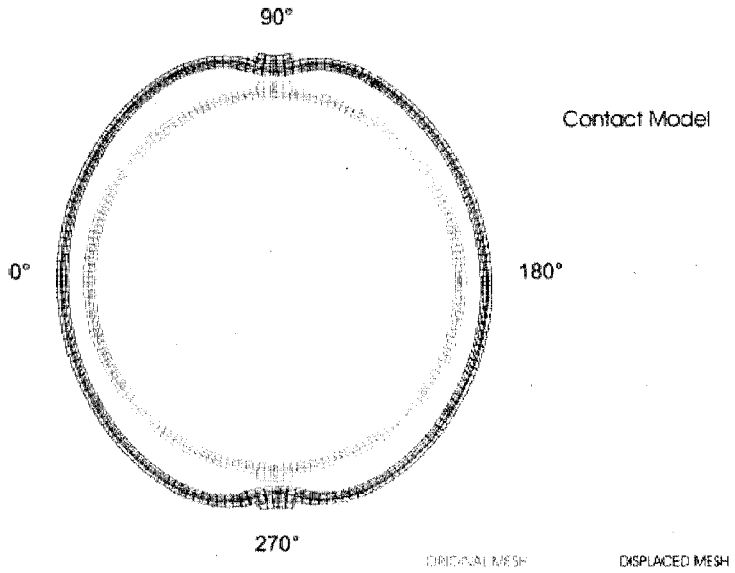

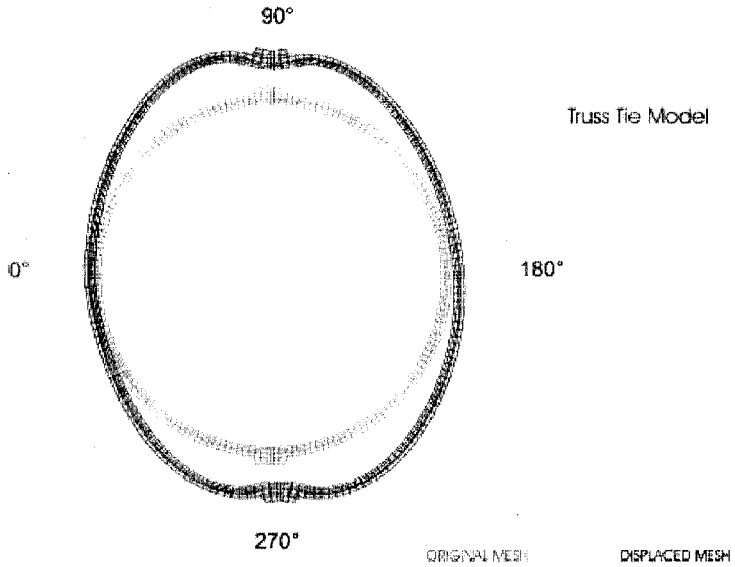

Figure 36. Comparison of Deformed Shapes (displ. x 200) Using Tendon Friction Truss Ties vs. the Contact Surface Model at P=2.0P_d

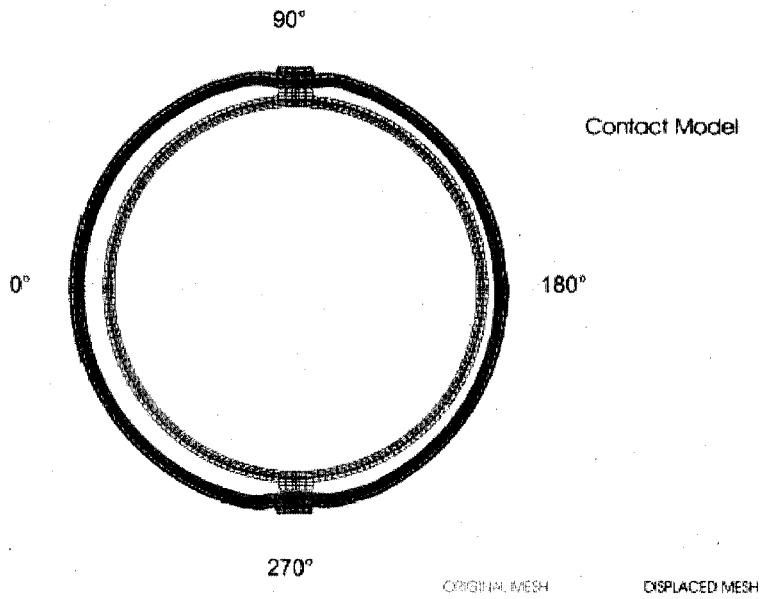

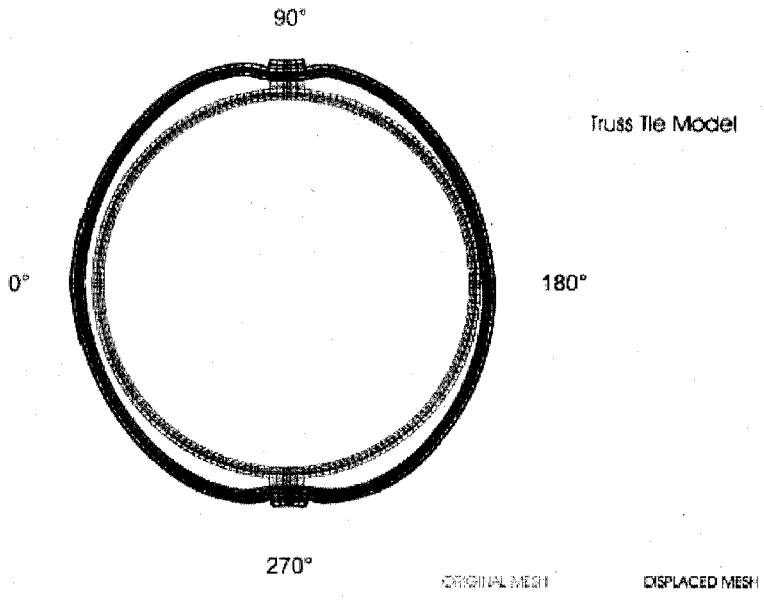

Figure 37. Comparison of Deformed Shapes (displ. x 20) Using Tendon Friction Truss Ties vs. the Contact Surface Model at P=3.5P_d

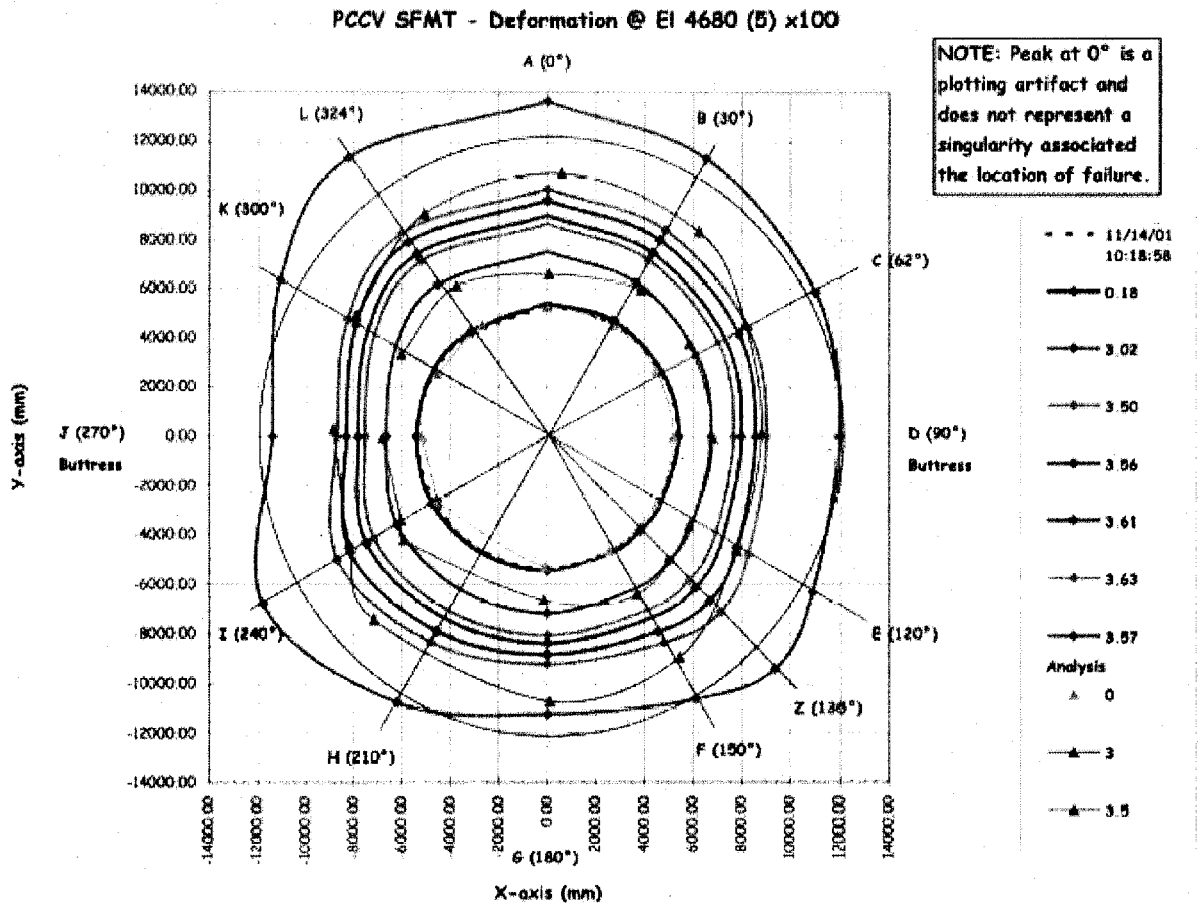

Figure 38. SFMT Deformation versus Ring Model Deformation

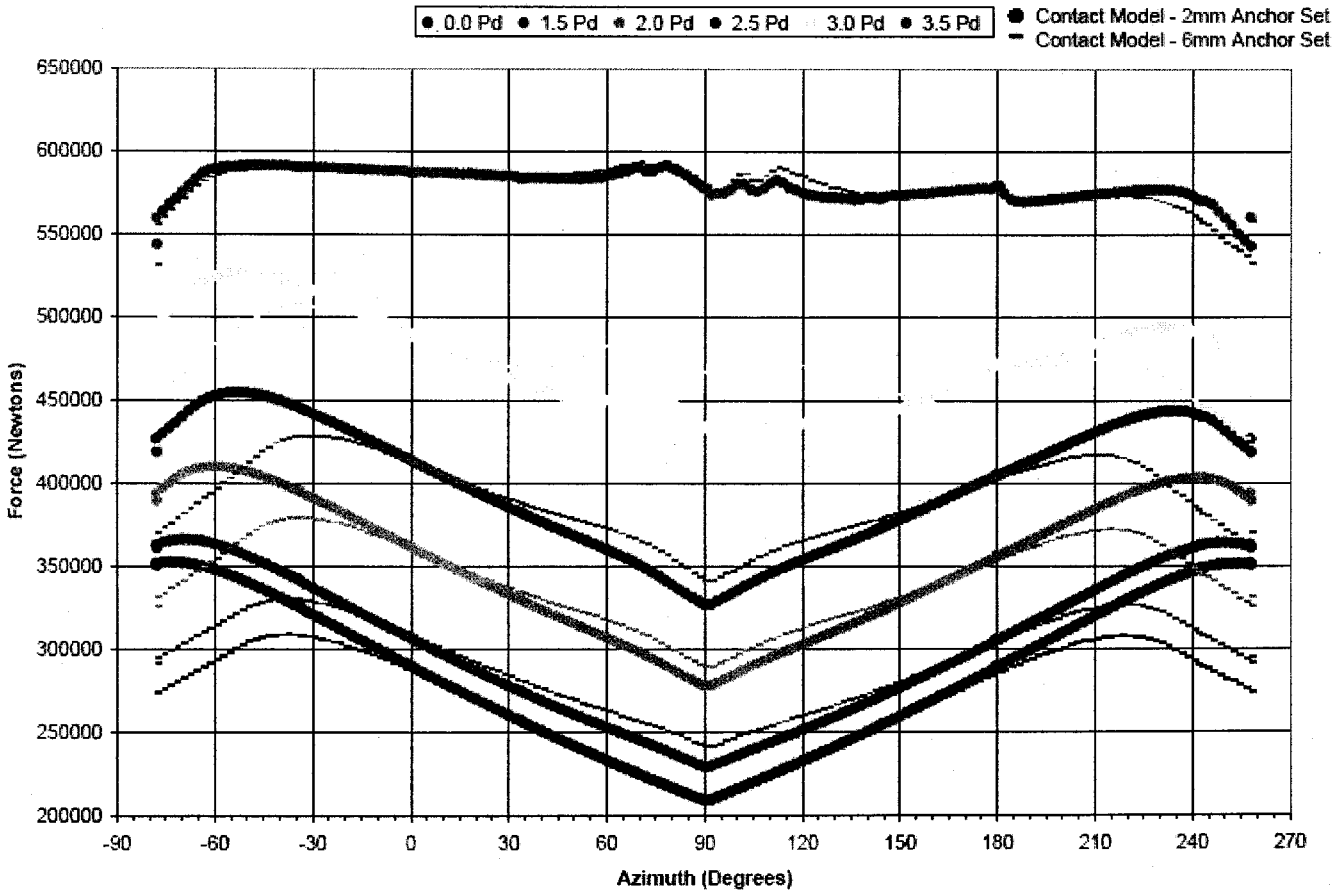

Figure 39. Comparison of Tendon Modeling in Ring Model for Tendon H68

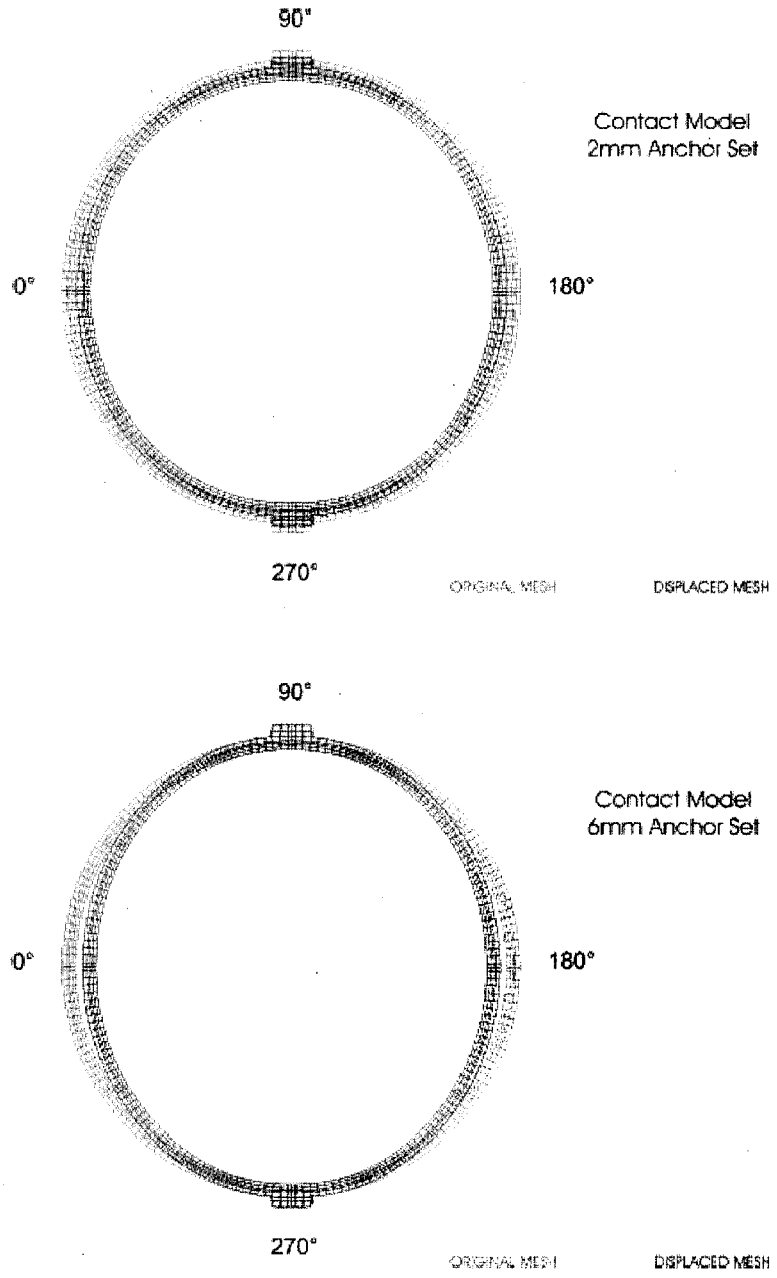

Figure 40. Comparison of Deformed Shapes (displ. x 200) Using Contact Surface Models with 2mm and 6mm of Anchor Set; After Prestress

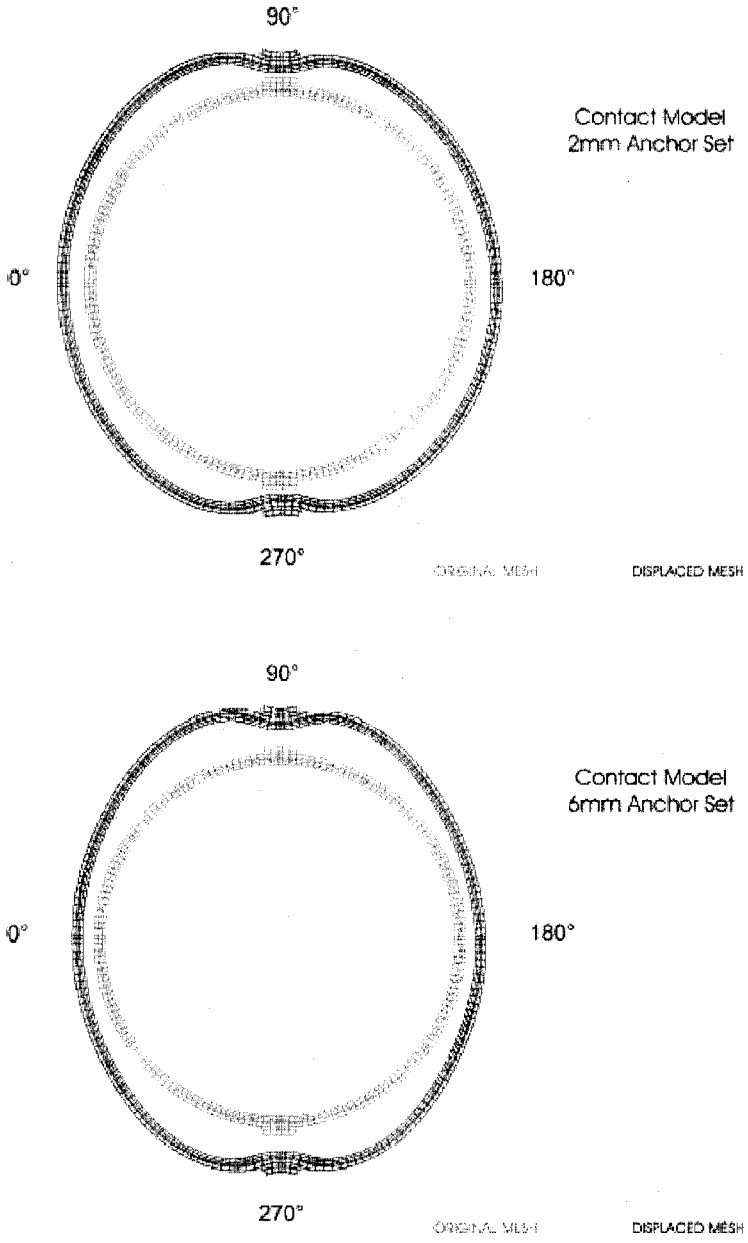

Figure 41. Comparison of Deformed Shapes (displ. x 200) Using Contact Surface Models with 2mm and 6mm of Anchor Set; P=2.0P_d

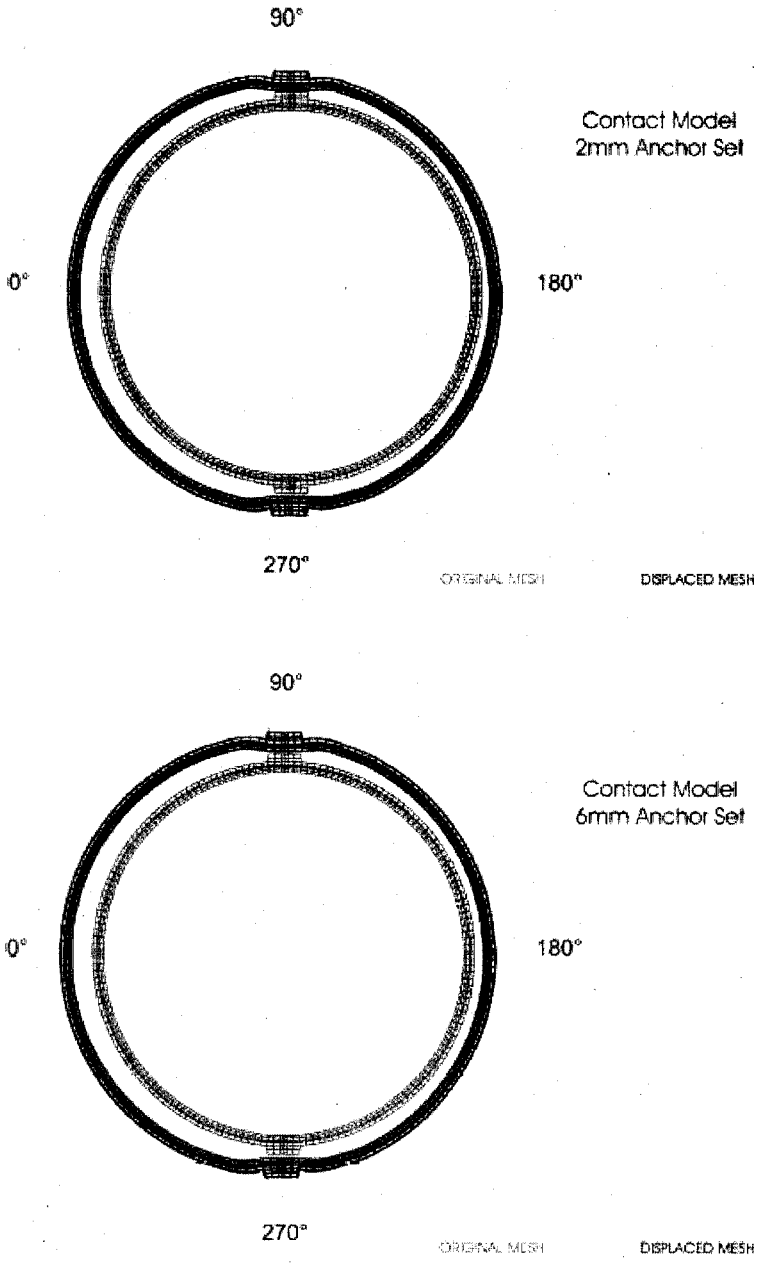

Figure 42. Comparison of Deformed Shapes (displ. x 20) Using Contact Surface Models with 2mm and 6mm of Anchor Set; P=3.5P_d

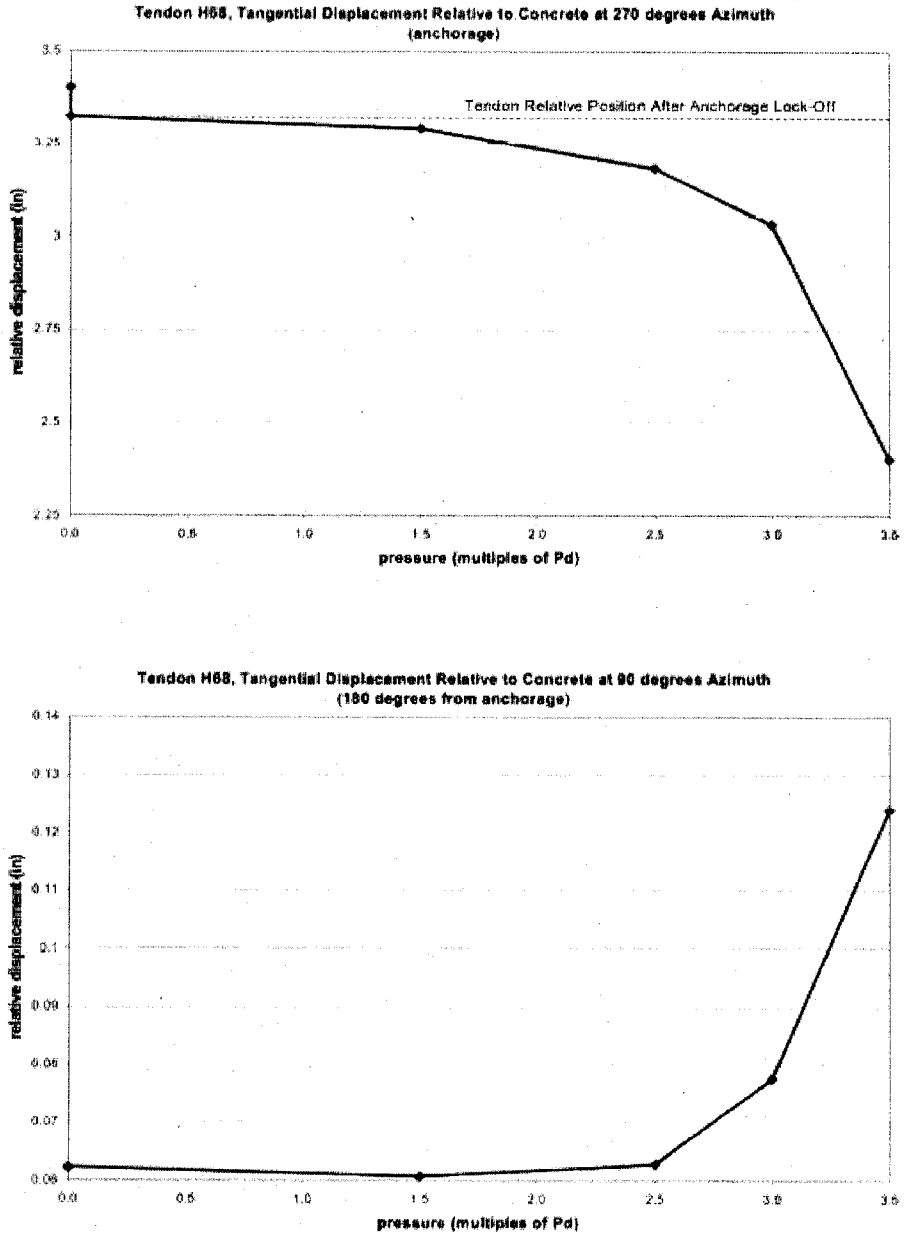

Figure 43. Tendon H68 Relative Displacement, Contact Model with 2mm Anchor Set

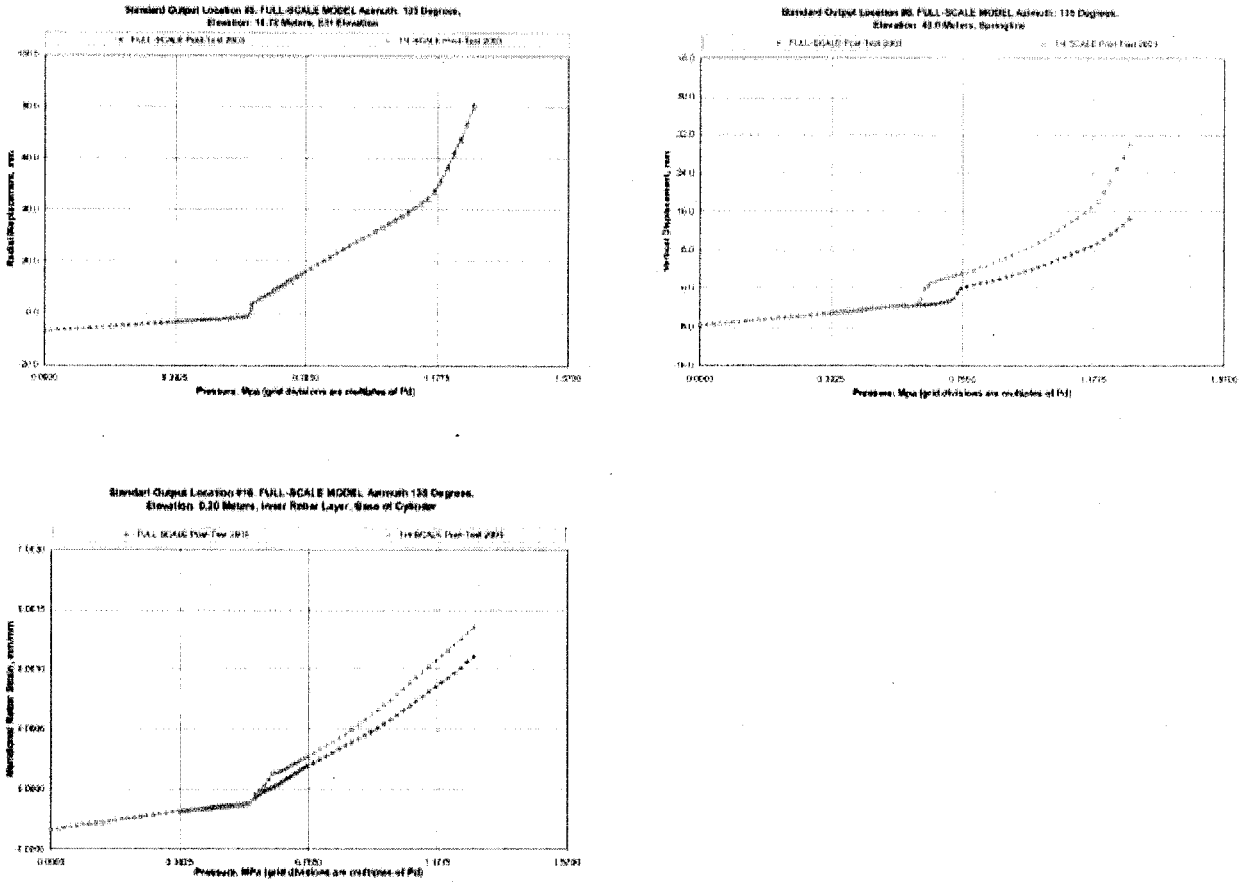

Figure 44. 1/4-Scale vs. Full-Scale Model Comparison at Standard Output Locations 5, 8 and 16

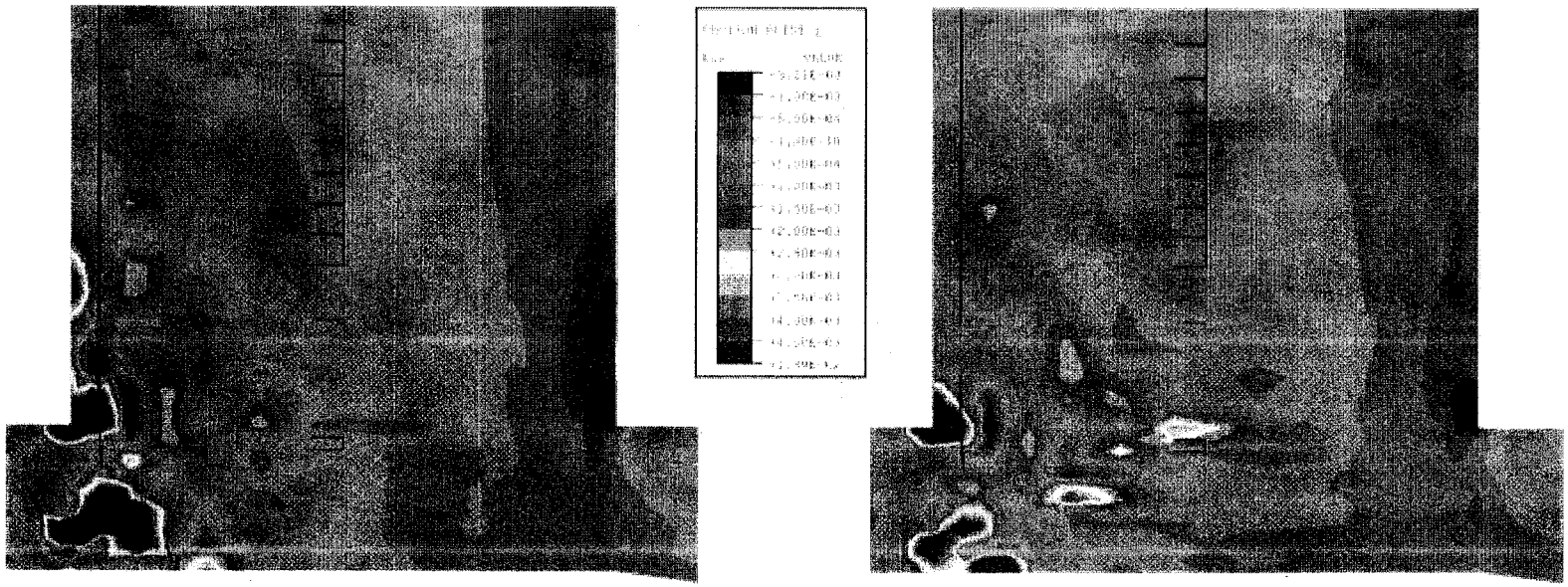

1/4-Scale

Full-Scale

Figure 45. 1/4-Scale vs. Full-Scale Vertical Strain Comparison

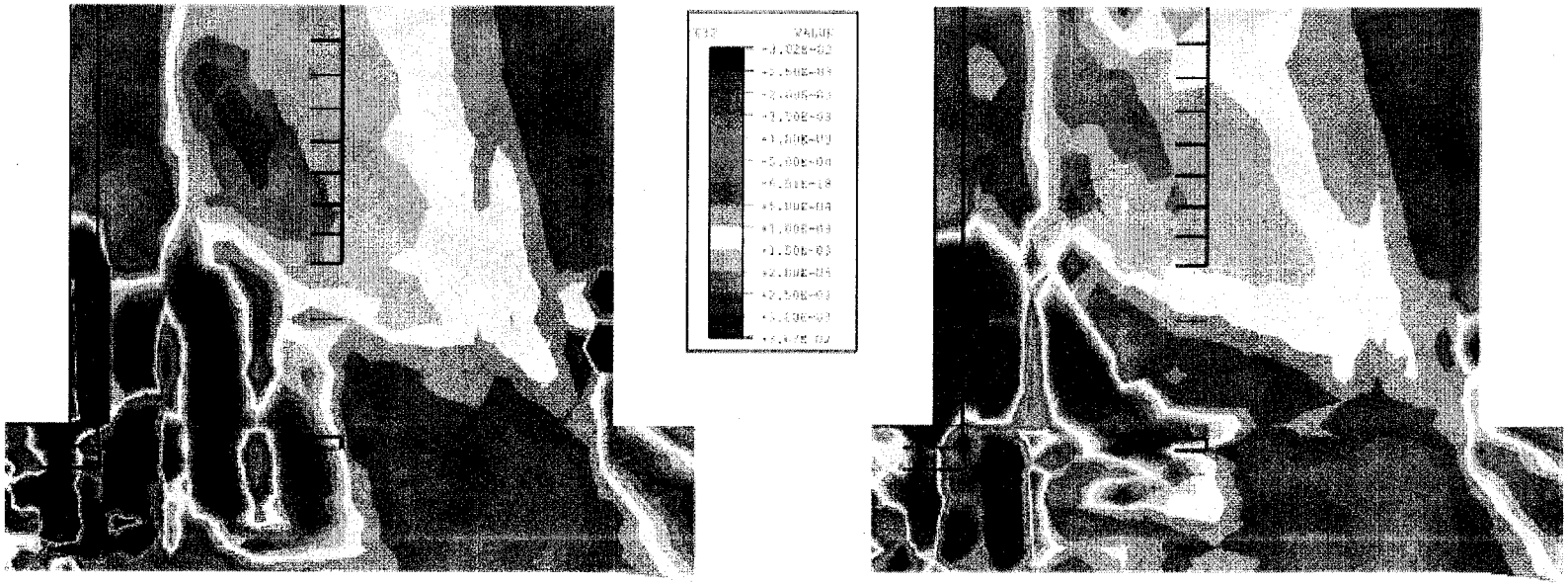

1/4-Scale

Full-Scale

Figure 46. 1/4-Scale vs. Full-Scale Shear Strain Comparison

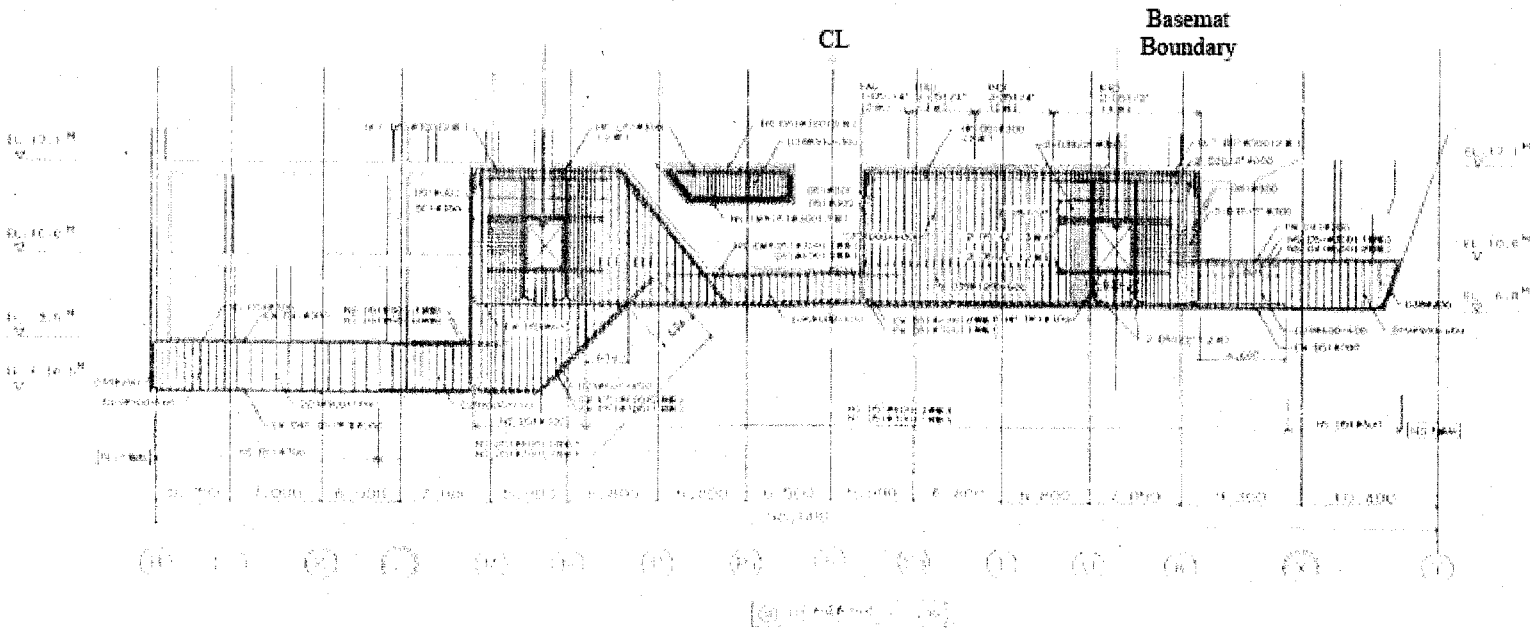

Figure 47. Reactor Pit Detail

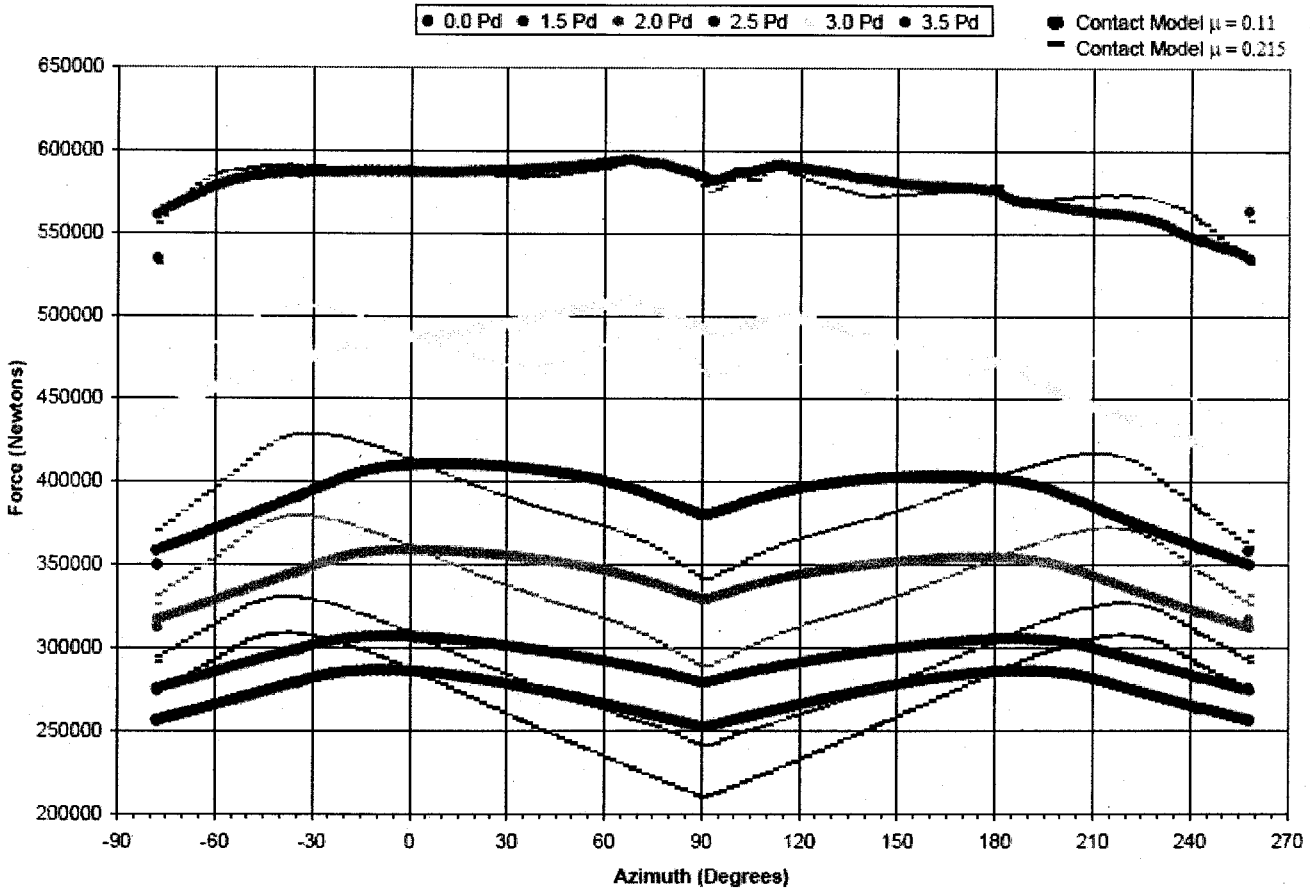

Figure 48. Comparison of Tendon Modeling in Ring Model for Tendon H68

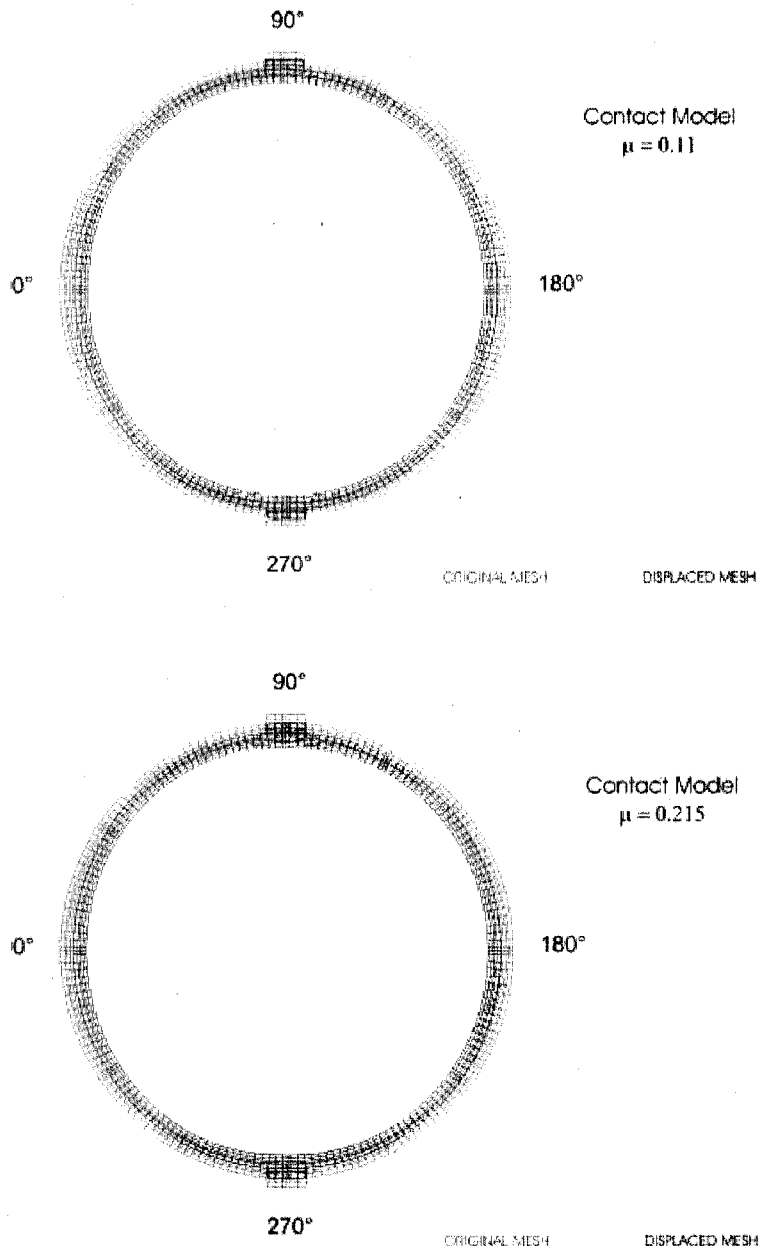

Figure 49. Comparison of Deformed Shapes (displ. x 200) Using Contact Surface Models with μ=0.11 and μ=0.215; After Prestress

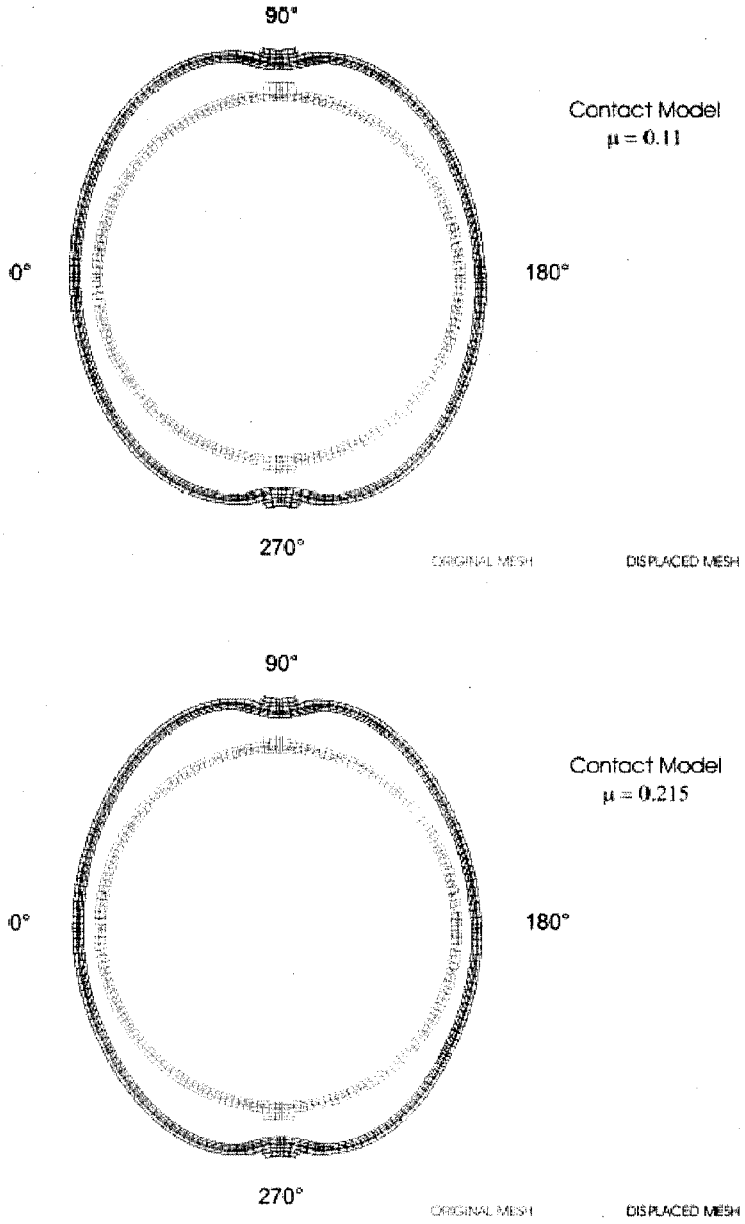

Figure 50. Comparison of Deformed Shapes (displ. x 200) Using Contact Surface Models with μ=0.11 and μ=0.215; P=2.0P_a

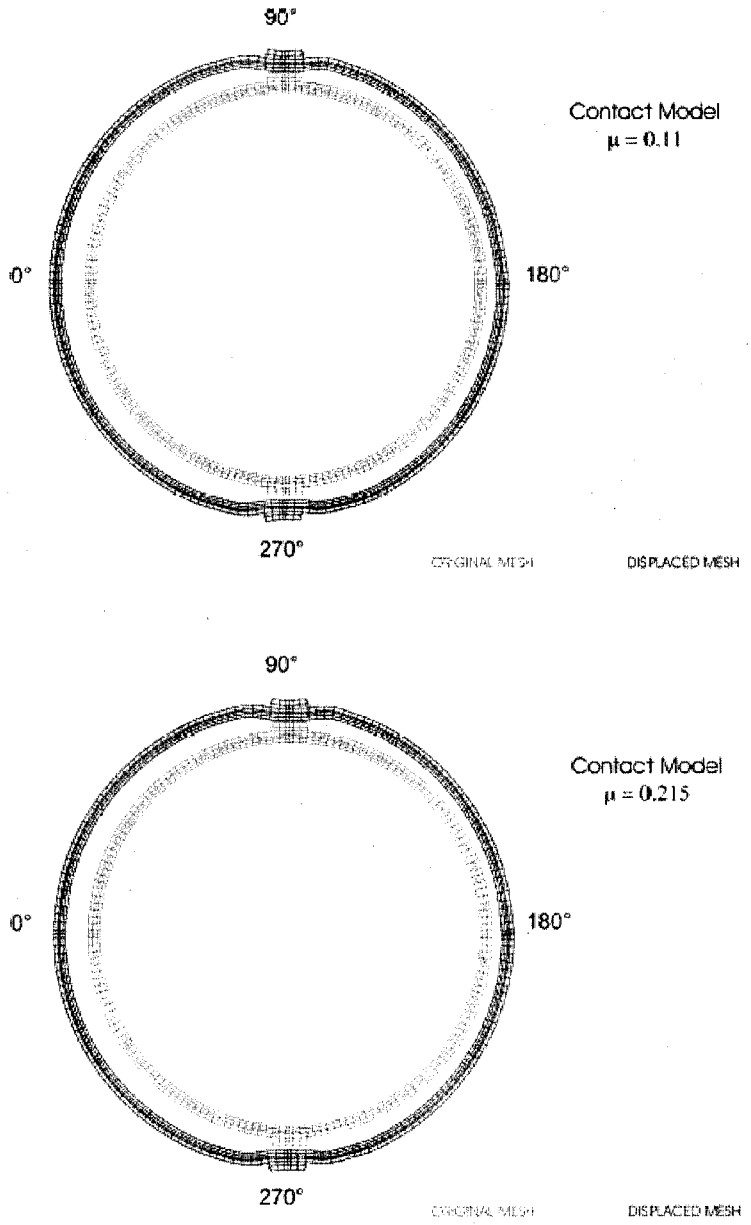

Figure 51. Comparison of Deformed Shapes (displ. x 20) Using Contact Surface Models with μ=0.11 and μ=0.215; $P=3.5P_d$

Table 1. Results Summary

Participant	Cracking		Liner Yield	Hoop Tendon Stress		Pressure	Free Field	Mode
	Hoop	Meridonal	(Rebar Yield)	Yield	2%	@ Failure	Hoop Strain	
SNL	0.62	1.14	0.85 (1.10)	1.15	-	1.26	0.35%	Liner Tear, leakage
LST	0.59-0.78	?	1.10	1.17	-	0.98 1.294	0.17% 0.42%	Liner tear, 1% mass/day leak Max. pressure @ 1000% mass/day leak

REFERENCES

1. Dameron, R. A., Rashid, Y. R., Luk, V. K. and Hessheimer, M. F. 1977. "Preliminary Analysis of a 1:4 Scale Prestressed Concrete Containment Vessel Model," in *Proceedings of the 14th International Conference on Structural Mechanics in Reactor Technology*, Vol. 5, pp 89-96, Lyon France.

2. Dameron, R. A., et al. 2000. *Pretest Analysis of a 1:4-Scale Prestressed Concrete Containment Vessel Model*, NUREG/CR-6685, SAND2000-2093. Albuquerque, NM: Sandia National Laboratories.

3. Dameron, R.A., et al. 2002. Posttest Analysis of the NUPEC/Sandia 1:4 Scale Prestressed Concrete Containment Vessell. NUREG/CR-6809, SAND2003-0839P, Albuquerque, NM: Sandia National Laboratories.

4. *ABAQUS Users Manual*, Version 5.8, 1998. Providence, RI: Hibbitt, Karlsson & Sorensen, Inc.

5. *ANACAP-U User's Manual*, Version 2.5, 1997. San Diego, CA: ANATECH Corp.

6. Luk, V. K. 2000. *Pretest Round Robin Analyses of a Prestressed Concrete Containment Vessel Model.* NUREG/CR-6678, SAND00-1535. Albuquerque, NM: Sandia National Laboratories.

7. Hessheimer, M. F., et al. 2002. *Overpressurization Test of a 1:4-Scale Prestressed Concrete Containment Vessel Model*, NUREG/CR-6810, SAND2003-0840P, Sandia National Laboratories, Albuquerque, NM.

Appendix I:

Scanscot Technology

SCANSCOT Technology

	Ref.	Edition
Technical Report	**03402/TR-01**	1

Title

ISP 48: Posttest analysis of the NUPEC/NRC 1:4-scale prestressed concrete containment vessel model

Abstract

The design events for a reactor containment usually refers to accidental loading conditions for which leak-tightness and load-bearing capacity should be verified. This involves the containment to be loaded far into the non-linear range, putting high demands on the engineering simulations. It is therefore of vital importance to ensure that the methods applied for advanced structural analysis can be verified and validated.

This report presents a method for carrying out comprehensive structural analysis of pre-stressed concrete reactor containments using the finite element technique. The method is verified and validated by comparison with test data from a large-scale overpressurization test performed on the NUPEC/NRC 1:4-scale model of a prestressed concrete containment vessel model at Sandia National Laboratory, USA. The prototype for the model is the containment building of unit 3 at the Ohi Nuclear Power Station in Japan, an 1127 MW Pressurized Water Reactor (PWR) unit.

Some different approaches on how to model unbonded pre-stressing tendons have been evaluated in the report. The chosen approach predicts pre-stressing forces very well in accordance with registred test data. This method makes it possible to take into consideration the transition from the initial uneven pre-stressing force distribution along the tendons, to a more or less even distribution along the tendons during pressurization.

The structural response predicted by applying a three-dimensional model approach agrees very well with registred test data. Pressure levels related to cracking of concrete, yielding of the steel liner, and the collapse of the containment are captured by the structural analysis, and giving results consistent with registred test data. To capture the pressure level at which rupture of the steel liner occurs, more detailed local models are needed, this is beyond the scope of this report. However, the analysis methods are capable of catching the zones where excessive yielding of the steel liner occurs, corresponding well with the first registred liner rupture position. The applied analysis methods also accuratly predict the displacements of the containment, and strains in the steel liner, the rebars and the pre-stressing tendons.

The proposed method can be used for design of new containments as well as for structural verification of existing ones. The method can be applied in case of design or evaluation against specified pressure levels and acceptance criterias according to national standards, or to calculate the leak-tightness and load-bearing capacity in order to estimate the safety margins of the structure. Furthermore, the analysis results can be used to estimate the probability of leakage or structural collapse in a probability safety assessment (PSA) of the plant.

It is also possible to utilize the method when verifying safety-related structures for other types of accidental load effects.

Edition	Date	Author	Reviewed	Approved
1	2004-04-21	O. Jovall/M. Pålsson/B. Svärd	Jan-Anders Larsson	Jan-Anders Larsson

Scanscot Technology AB
Ideon Research Park. S-223 70 Lund, Sweden
Telephone: +46 46 286 23 30, Telefax: +46 46 12 87 45

Technical Report 03402/TR-01

ISP 48: Posttest analysis of the NUPEC/NRC 1:4-scale prestressed concrete containment vessel model

TABLE OF CONTENTS

List of Revisions

Edition	Date	Revised pages	Revision refer to

0. ABSTRACT

The design events for a reactor containment usually refers to accidental loading conditions for which leak-tightness and load-bearing capacity should be verified. This involves the containment to be loaded far into the non-linear range, putting high demands on the engineering simulations. It is therefore of vital importance to ensure that the methods applied for advanced structural analysis can be verified and validated.

This report presents a method for carrying out comprehensive structural analysis of pre-stressed concrete reactor containments using the finite element technique. The method is verified and validated by comparison with test data from a large-scale overpressurization test performed on the NUPEC/NRC 1:4-scale model of a prestressed concrete containment vessel model at Sandia National Laboratory, USA. The prototype for the model is the containment building of unit 3 at the Ohi Nuclear Power Station in Japan, an 1127 MW Pressurized Water Reactor (PWR) unit.

Some different approaches on how to model unbonded pre-stressing tendons have been evaluated in the report. The chosen approach predicts pre-stressing forces very well in accordance with registred test data. This method makes it possible to take into consideration the transition from the initial uneven pre-stressing force distribution along the tendons, to a more or less even distribution along the tendons during pressurization.

The structural response predicted by applying a three-dimensional model approach agrees very well with registred test data. Pressure levels related to cracking of concrete, yielding of the steel liner, and the collapse of the containment are captured by the structural analysis, and giving results consistent with registred test data. To capture the pressure level at which rupture of the steel liner occurs, more detailed local models are needed, this is beyond the scope of this report. However, the analysis methods are capable of catching the zones where excessive yielding of the steel liner occurs, corresponding well with the first registred liner rupture position. The applied analysis methods also accuratly predict the displacements of the containment, and strains in the steel liner, the rebars and the pre-stressing tendons.

The proposed method can be used for design of new containments as well as for structural verification of existing ones. The method can be applied in case of design or evaluation against specified pressure levels and acceptance criterias according to national standards, or to calculate the leak-tightness and load-bearing capacity in order to estimate the safety margins of the structure. Furthermore, the analysis results can be used to estimate the probability of leakage or structural collapse in a probability safety assessment (PSA) of the plant.

It is also possible to utilize the method when verifying safety-related structures for other types of accidental load effects.

1. INTRODUCTION

1.1 Background

The design event for a reactor containment refers usually to accidental loading conditions for which leak-tightness and load-bearing capacity should be verified. This involves the containment to be loaded far into the non-linear range, putting high demands on the engineering simulations.

It is therefore of vital importance to ensure that the methods applied for advanced structural analysis can be verified and validated. The verification of codes for structural analyses (FEA-software) is made by the supplier, usually at the local finite element level. The codes are also usually verified with the help of experimental tests on smaller test cubes, columns, beams and slabs loaded to failure, i.e. laboratory tests. To achieve an even higher accuracy in analysis results it is necessary to compare analysis results with the measured response from tests on large-scale structures, see Figure 1.1.

In the ISP 48 project, benchmark studies are performed in order to compare structural analysis results to test data from a large-scale test of a 1:4-scale prestressed concrete containment vessel.

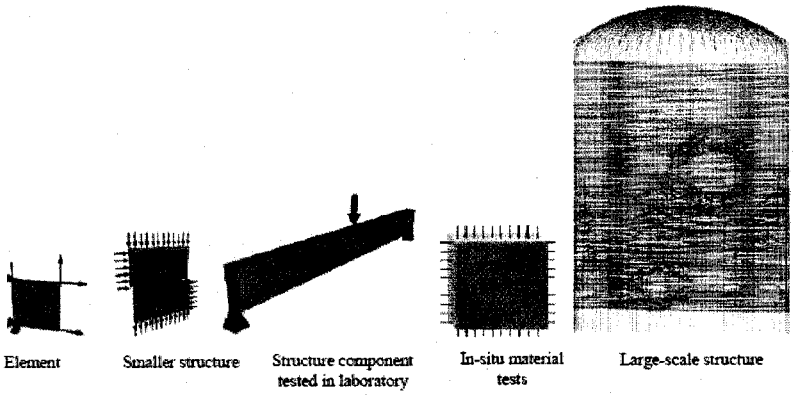

Figure 1.1 Examples of structural analysis verification.

Scanscot Technology has for more than ten years carried out reactor containment investigations for the nuclear power industry in Sweden, using advanced finite element analysis methods. The ISP 48 project gives us the possibility to validate our software by comparing analysis results with large-scale experimental test results. Another important benefit from the project is to share experience and knowledge with colleagues from other countries who are also working in this subject field

Participation in this project also provides valuable input to the ongoing EURATOM 5th framework programme project CONMOD [1], in which Scanscot Technology is one of the participants. The CONMOD project aims to

create a system which will ensure that safety requirements for concrete containment structures will be up-held during the entire planned lifetime of plants and possibly during an extended lifetime. An important part of the project is to develop the application and understanding of Non-Destructive Testing (NDT) techniques for the assessment of conformity and the condition of concrete reactor containments as well as to integrate this with state-of-the-art and developed Finite Element (FE) modelling techniques and analysis of structural behaviour. The objective being to create a diagnostic method for the evaluation of defects, ageing and degradation of concrete containments.

Our possibility to participate in ISP 48 has been made possible by financial support from the Swedish and Finnish nuclear power industry (Oskarshamn, Ringhals, Forsmark and TVO), and the Swedish Nuclear Power Inspectorate.

1.2 General

The Nuclear Power Engineering Corporation (NUPEC) of Japan and the U.S. Nuclear Regulatory Commission (NRC) cosponsored and jointly funded a Cooperative Containment Research Program at Sandia National Laboratories (SNL), USA, from July, 1991 through December, 2002.

As a part of this program, a 1:4-scale model of a pre-stressed concrete containment vessel (PCCV) was conducted and pressure tested to failure. The prototype for the model is the containment building of unit 3 at the Ohi Nuclear Power Station in Japan, an 1127 MW Pressurized Water Reactor (PWR) unit. The design accident overpressure, P_d, of both the prototype and the model containment is 0.39 MPa.

The objectives of the model containment test were to;

- simulate some aspects of the severe accident loads on containment vessels
- observe the model failure mechanisms
- obtain structural response data up to failure for comparison with analytical models

Construction of the model containment commenced January, 1997, and ended June, 2000. During September, 2000, the limit state pressurization test (LST) was carried out. At the end of 2002, the limit state test was complemented with a pressurization up to total collapse of the structure, the structural failure mode test (SFMT). During pressurization the structural response was monitored, giving information on displacements, liner, rebar, concrete and tendon strains and tendon anchor forces. In addition, acoustic monitoring, video and still photography were used to monitor the structural behaviour.

During 2002, the Nuclear Energy Agency (NEA) at OECD, decided to include the NUPEC/NRC model containment test as an International Standard Problem (ISP) on containment capacity, ISP 48. At a first meeting in Stockholm, Sweden, the objectives and schedule was set up. The ISP 48 project started up January, 2003 and will be ended June, 2005.

The objective of the ISP 48 is to extend the understanding of capacities of actual containment structures based on results of the NUPEC/NRC model containment test and other previous research. Two questions regarding full size structures arise; How to transpose to real size containment (would the onset of leakage be later and much closer to the burst pressure)? How would including the effect(s) of accident temperature change the outcome?

The ISP 48 posttest analysis of the NUPEC/NRC model containment was decided to consist of four phases;

1. Data collection and identification
2. Calculation of the limit state test (LST) – mechanical loading
3. Calculation of the response under both mechanical and thermal loadings
4. Reporting, Workshop

A detailed description of these four phases with a corresponding time-schedule is given in Appendix 1. Appendix 1 also includes a table of the names of the ISP 48 participants.

The scope of this report covers the phase 2 calculations performed by Scanscot Technology.

1.3 Over-pressurization test

The model containment was a 1:4-scale model of the prestressed concrete containment vessel (PCCV) of an actual nuclear power plant in Japan, Ohi-3 (Figure 1.2). Ohi-3 is an 1127 MW Pressurized Water Reactor (PWR) unit, one of four units comprising the Ohi Nuclear Power station located in Fukui Prefecture, owned and operated by Kansai Electric Power Company.

The prototype containment, Ohi-3, consists of a thin prestressed concrete cylindrical shell with a hemispherical dome and a continuous steel liner anchored to a reinforced concrete basemat which extends beyond the containment to support other plant structures.

The features and scale of the model containment were chosen so that the response of the model would mimic the global behavior of the prototype but also to represent local details, particularly those around penetrations. One of the primary considerations was the desire to utilize construction materials that were identical, or nearly so, to the material used in the construction of the prototype.

It was decided that the scale of the model would be a uniform 1:4, with minor exceptions to accommodate fabrication and construction concerns. This was judged to be the minimum scale that would allow the steel liner to be constructed from prototypical materials and fabricated with details and procedures that were representative of the prototype. The model containment and its overall geometry and dimensions are shown in Figure 1.3 and Figure 1.4.

It was also decided that the model containment would include representation of the major penetrations, namely the equipment hatch (E/H), the personnel air lock (A/L), the main steam (M/S) and the feed water (F/W) penetrations.

Key elements of the design philosophy of the model containment included:

- The model containment would be a uniform 1:4-scale model of the prototype or actual prestressed concrete containment vessel of Ohi Unit 3.
- Elements of the model which would affect the ultimate strength would be equivalent to the prototype. The model liner would be one-fourth the thickness of the prototype liner. Reinforcing ratios would be maintained and the number and arrangement of the prestressing tendons would, to the extent possible, be identical to the prototype.
- The model should be capable of reproducing the failure modes postulated for the prototype, including:
  a) Hoop tensile failure of the cylinder wall
  b) Bending-shear failure at the junction of the cylinder wall with the basemat
  c) Shear failure in the basemat above the tendon gallery
  d) Bearing failure at the tendon anchors
  e) Bending-shear failure at the large penetrations
  f) Bending-shear at the small penetrations
  g) Liner tearing due to strain concentrations at local discontinuities (stiffeners/anchors, thickened reinforcing plates at penetrations and embedments)
  h) Leakage at penetration seals due to ovalization or distortion of the sealing surfaces
- Avoid introduction of non-representative failure modes, as a result of scaling or other modeling artifacts

The general arrangement of the prototype and representative failure mode locations are shown in Figure 1.2.

The decision was to perform a static, pneumatic over-pressurization test at ambient temperature. The test was terminated following a functional failure, i.e. a leak in the model containment, with only limited structural damage occurring. Subsequently, it was decided to re-pressurize the model containment prior to demolition, in an attempt to observe larger inelastic response and, if possible, a global structural failure. This test was performed as a combined pneumatic-hydrostatic test.

Milestones in the construction and testing of the model containment include the following:

12 February 1997	First Basemat Pour (F1)
19 June 1997	First Liner Panel Installed
15 April 1999	Final Dome Pour (D3)
12-14 October 1999	Pretest Round Robin Meeting

8 March-3 May 2000	Prestressing
25 June 2000	Construction Completed
12-14 September 2000	Structural Integrity and Integrated Leak Rate Test
27-28 September 2000	Limit State Test
22 August 2001	Posttest Round Robin Meeting
14 November 2002	Structural Failure Mode Test
3 May 2002	Demolition and Site Restoration Completed

The model containment was not 'designed' in a conventional sense, instead its features were scaled directly from the prototype containment Ohi-3 design with some simplification to facilitate construction, but without compromising the objectives of the test. The basic design philosophies were to ensure that all elements of the containment structure respond essentially elastically (with some minor exceptions for secondary stresses) to the specified design loading conditions.

A detailed presentation of the overpressurization test is given in [2].

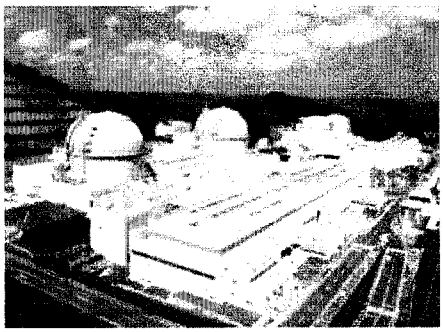

a) Plant

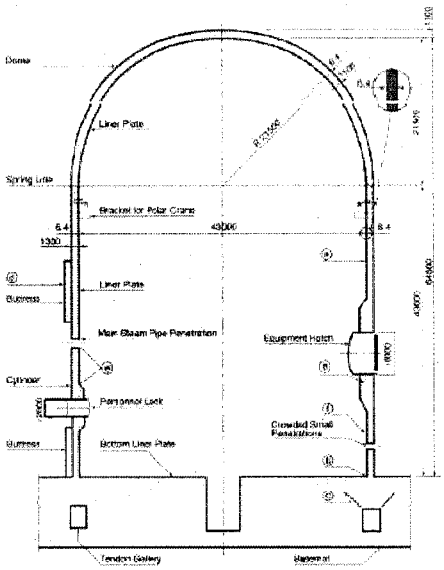

b) Geometry and potential failure locations

No.	Potential failure description
a	Hoop tensile failure of the cylinder wall
b	Bending-shear failure at the junction of the cylinder wall with the basemat
c	Shear failure in the basemat above the tendon gallery
d	Bearing failure at the tendon anchors
e	Bending-shear failure at the large penetrations
f	Bending-shear at the small penetrations
g	Liner tearing due to strain concentrations at local discontinuities (stiffeners/anchors, thickened reinforcing plates at penetrations and embedments)
h	Leakage at penetration seals due to ovalization or distortion of the sealing surfaces.

Figure 1.2 Prototype containment: Ohi Nuclear Power Station, Ohi-cho, Fukui, Japan (from [2]).

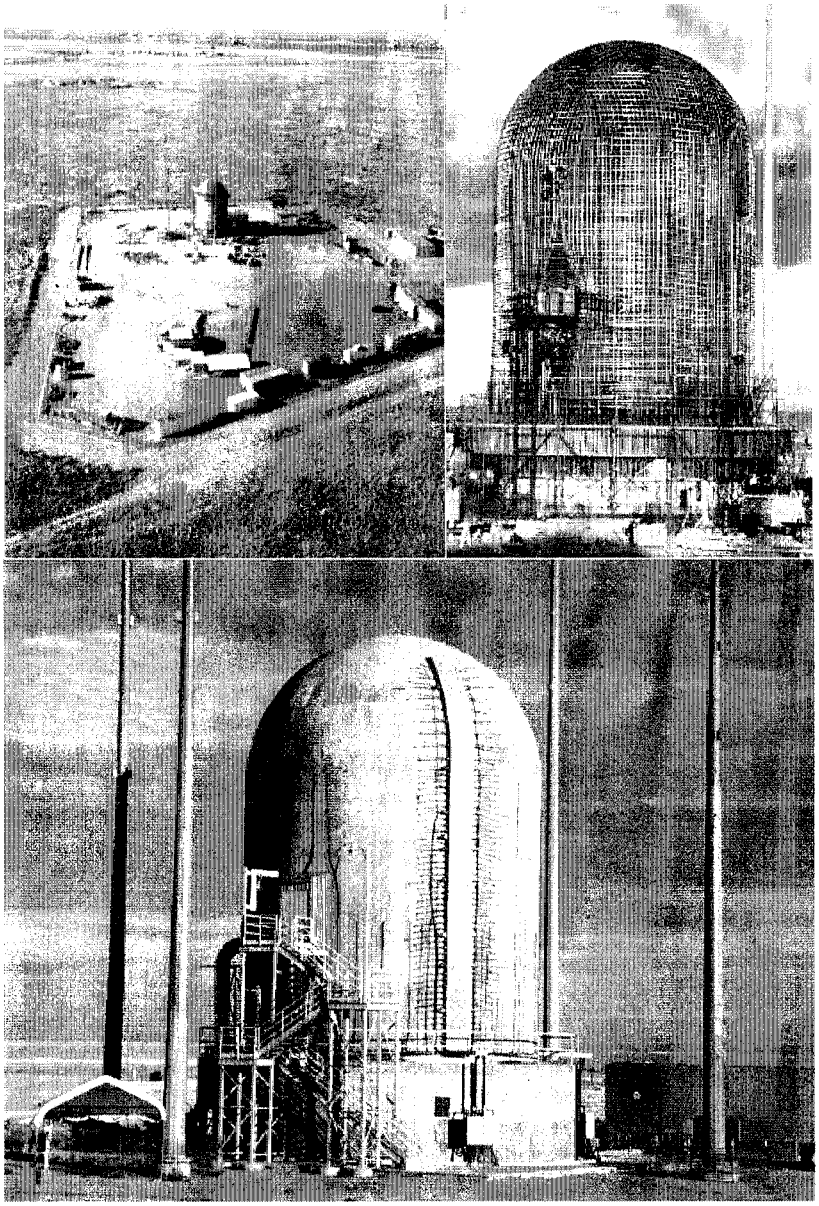

Figure 1.3 The model containment (from [2]).

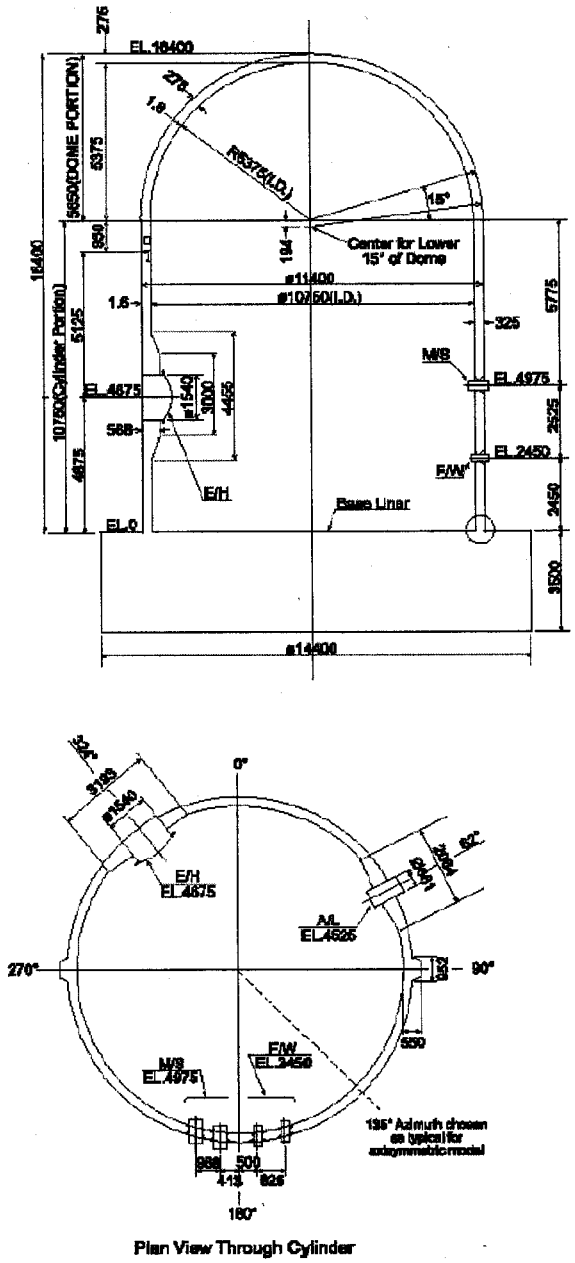

Figure 1.4 Model containment geometry (dimensions in mm), from [2].

2. METHODS OF ANALYSIS

2.1 General

In principle, four major levels of analysis approaches are applicable when utilizing the finite element technique for studying the structural behaviour of a prestressed concrete reactor containment:

1. Axi-symmetrical analysis
2. Three-dimensional global analysis
3. Local analysis at critical areas
4. Detailed studies of the leak-tightness integrity

These levels are examplified in Figure 2.1, and discussed here below.

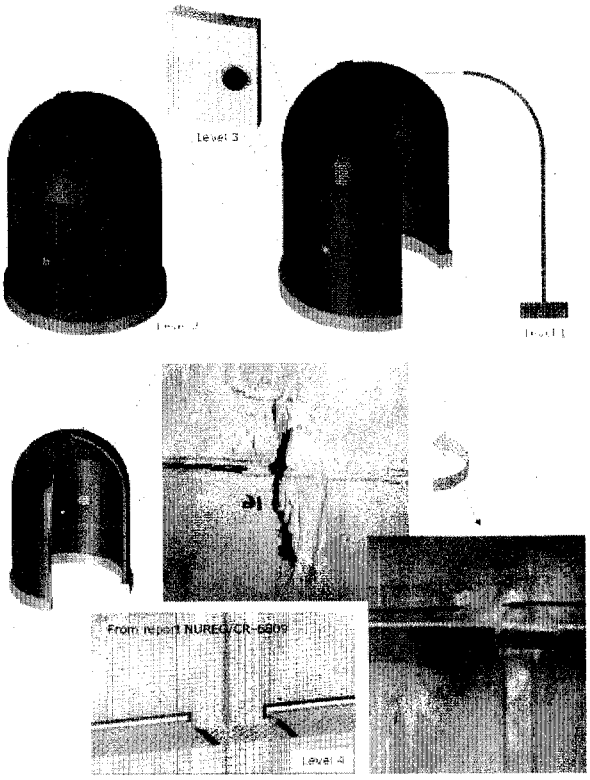

Figure 2.1 FE modeling, levels of detailing.

A reactor containment constitutes in principle a cylindrical construction and is therefore suitable to be analysed with the help of an axi-symmetrical model

when affected by globally distributed loads of the type overpressures. An axi-symmetric analysis can thus be used to understand the global behaviour of the model containment in an un-disturbed region, as a first approximation of the leak-tightness and structural capacity. The local behaviour of the wall-basemat connection can also be studied, if the model is detailed enough. Otherwise, a separate local model has to be used.

Another advantage with an axi-symmetric model is to execute parametrical studies and sensitivity analysis in an efficient way. In order to provide a good basis for defining high-quality model assumptions for the three-dimensional analysis.

The axi-symmetrical model is not capable of catching the structural effects due to major penetrations, pre-stressing buttresses, non-uniform layout of the pre-stressing tendons and reinforcement, and non-uniform and pressure-dependent pre-stressing effects. These effects will to a major extent influence the structural behaviour of the containment, including overpressure levels at leakage and collapse, as well as rupture positions. To take these matters into consideration, a fully three-dimensional model has to be used.

This is evident not only from the outcome of this report, but also from other studies, see for example Figure 2.2 from [1], illustrating the influence on the response from a containment buttress.

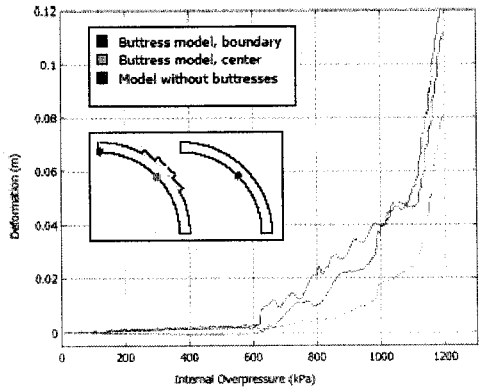

Figure 2.2 Study of influence of buttress on radial deformation (from [1]).

The need for advanced models is even more pronounced for the more complicated geometries of type BWR containments, see Figure 2.3. At the Swedish BWR containments, there is another complication in the sense that the steel liner is embedded approximatly 20-30 cm from the inside of the containment wall. The liner is not anchored to the concrete wall with any mechanical anchors, except at a few locations. Thus, the friction between the embedded liner and the surrounding concrete is an important paramater to take into consideration.

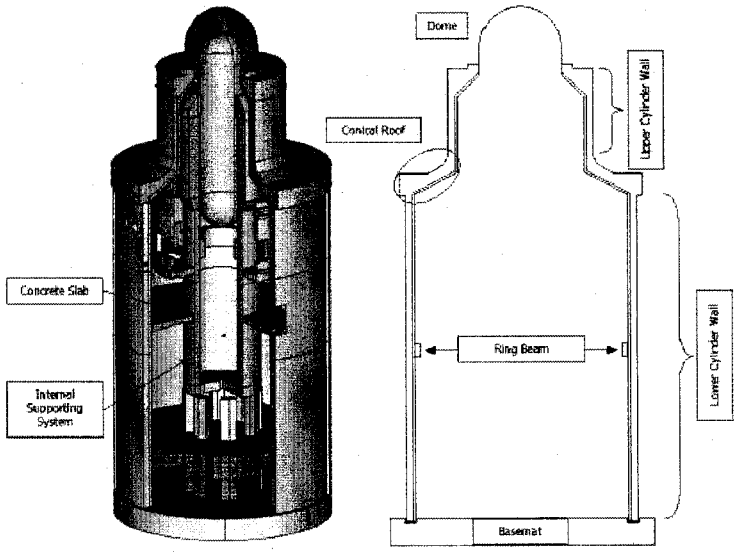

Figure 2.3 Typical Swedish BWR containment.

For some important and more complicated parts of the containment, such as the major penetrations, local detailed models can be used instead of increasing the discretization level in the global 3D-model. When using local models, submodeling can be a useful technique, where the boundary conditions of the local model is driven by the deformation calculated in the global analysis.

To fully reach the objective of this project, i.e. to determine good estimates of the pressure level and rupture position at leakage, even more detailed local models of the steel liner including welds and stiffeners etc are needed. This due to the fact that the rupture is dependent on local strain as well as workmanship of the welds.

In general, the degree of detailing to be used is dependent on the objectives of the analysis, and the different requirements to be regarded:

- Design or evaluation against specified pressure levels and acceptance criterias according to national standards.
- Analysis results to be used as input to a probabilistic safety assessment (PSA) of the plant, where input may be the probability of leakage, a specific leak-rate or structural collapse.
- Best estimate of leak-tightness and load-bearing capacity and safety margins of the structure based on nominal or measured parameters (as in the CONMOD project, see section 1.1 and [1]).

The interpretation of the acceptance criterias, or failure criterias, to be assest in the finite element analysis will of course differ depending on the objective of the analysis, but also on the modeling and analysis approaches to be applied.

2.2 Model containment

The objective of this project is to simulate the behaviour of the model containment pressurized to rupture. With the aim of describing the pressurization event as realistic as possible the analysis have been carried out using a fully three-dimensional (3D) global model applying non-linear material models.

An axi-symmetrical model has been applied for parametrical studies, in order to minimize executional runtimes. The parametrical studies have provided the basis for model assumptions for the 3D-model analysis.

In the next phase of the ISP 48 project, the above mentioned models will be complemented with local models of the major penetration.

2.3 Software

In the main analysis, the finite element program ABAQUS/Explicit version 6.4 has been used. Comparative calculations have been performed with ABAQUS/Standard version 6.4 For pre- and postprocessing both ABAQUS/CAE and Altair/HyperMesh have been used.

3. STRUCTURAL SYSTEM

3.1 General

This chapter will cover a description of the structural system of the model containment.

3.2 Description of the structural system

3.2.1 General

The model containment can be devided into three main structural parts. the basemat, the cylindrical wall and the dome, see Figure 3.1. These are briefly presented below, followed by a description of the structural elements in each part. A detailed description of the model containment is given in [2].

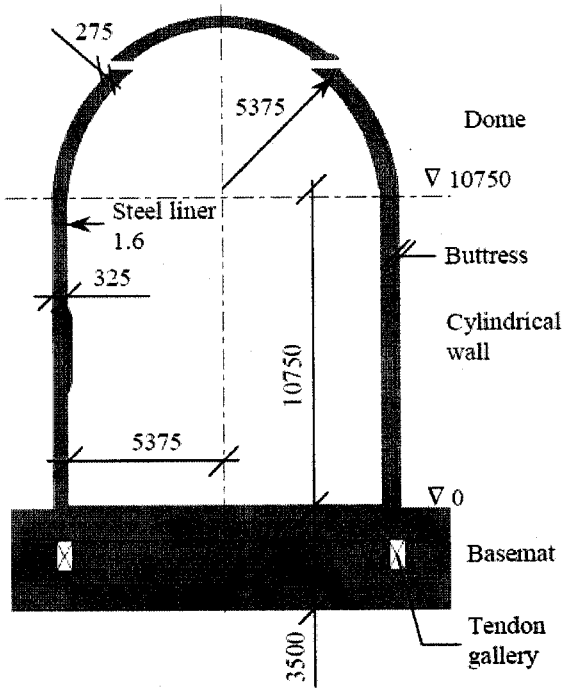

Figure 3.1 Model containment, main structural parts and dimensions [mm].

3.2.2 Basemat

The basemat consists of a 3.5 m thick reinforced concrete slab on a 0.3 m thick mudmat of concrete, cast on an approximately 8 m thick engineered backfill.

The basemat includes the tendon gallery, situated underneath the cylindrical wall, where the vertical wall tendons are tensioned and anchored.

A steel liner is placed on top of the basemat.

3.2.3 Cylindrical wall

The wall has a thickness of 0.325 m, locally thickened at the major penetrations. The wall is pre-stressed in both the vertical and horizontal directions. Two vertical pre-stressing buttresses are erected at 90 and 270 degrees, where the hoop tendons are tensioned and anchored. The buttresses start at the top of the basemat and extend halfway into the dome. The wall includes conventionally arranged reinforcement bars.

The steel liner is placed on the inside of the wall and anchored to the concrete by means of mechanical anchors, see section 3.2.5.

All penetrations through the containment are situated in the cylindrical wall, see section 3.2.6.

3.2.4 Dome

The dome thickness is 0.275 m. At the connection to the wall the thickness is gradually increased to 0.325 m, in order to match the thickness of the wall. The vertical tendons in the wall are continued throughout the dome, constituting an orthogonal pattern of tendons, see Figure 3.2 and Figure 3.6. Hoop tendons are placed in the dome except for the uppermost part. The dome also includes conventionally arranged reinforcement bars.

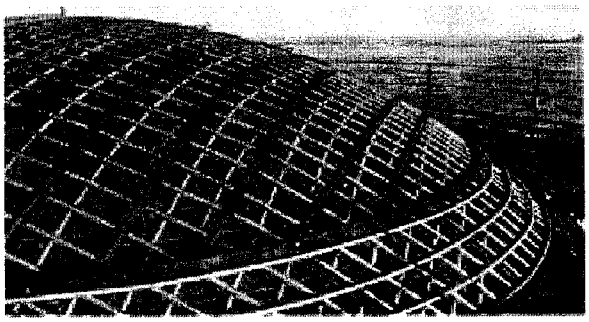

Figure 3.2 Arrangement of tendons in the dome.

The steel liner is placed on the inside of the dome and anchored to the concrete by means of mechanical anchors, see section 3.2.5.

3.2.5 Steel liner

3.2.5.1 Steel liner

The steel liner is fabricated from carbon steel and has a thickness of 1.6 mm. The as-built liner is 1.8 mm, the extra 0.2 mm providing a fabrication allowance. The liner was shop welded to liner plates approximately 3 meters square. During this construction phase the vertical anchors were also welded to the plates. Plates for the dome and around penetrations where generally smaller. To prevent buckling during erection horizontal stiffeners where welded to the plates. These stiffeners had no structural function after the model containment construction was completed. The plates were welded together at site. At penetrations, locally thickened plates were used, connected to the penetration assemblies.

3.2.5.2 Welds

The liner was shop welded into plates using computer controlled automatic welders. Also anchors and stiffeners were continuously welded to the liner during this phase. All shop welding was done without the use of back-up bars. When connecting the liner plates at site, back-up bars were used during welding.

3.2.5.3 Anchors

The steel liner was anchored to the concrete with vertical T-anchors continuously welded to the liner. They are spaced 0.45 m, except in the regions of the penetrations where they are more closely spaced, 0.15 m apart. The liner anchor layout is presented in Figure 3.3.

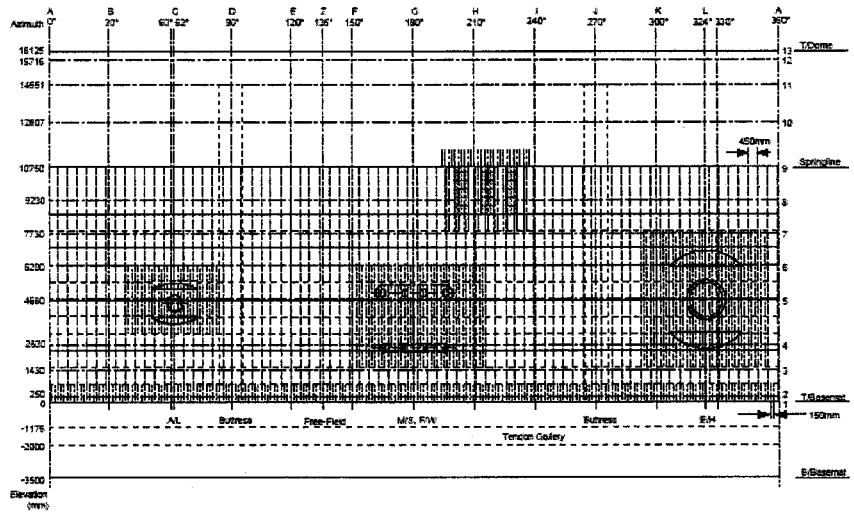

Figure 3.3 Liner anchor layout.

The vertical T-anchors are not extended into the dome. Here the liner is instead anchored to the dome with small stud-type anchors.

3.2.6 Penetrations

There are several penetrations through the model containment; the equipment hatch (E/H), the personnel airlock (A/L), the main steam (M/S) and the feedwater (F/W) penetrations. All penetrations are placed in the cylindrical wall, the layout of the penetrations is shown in Figure 3.4. The E/H and A/L penetration assemblies are 1:4-scale functional representations, while the M/S and F/#W penetrations only includes the penetration sleeve and reinforcing plates.

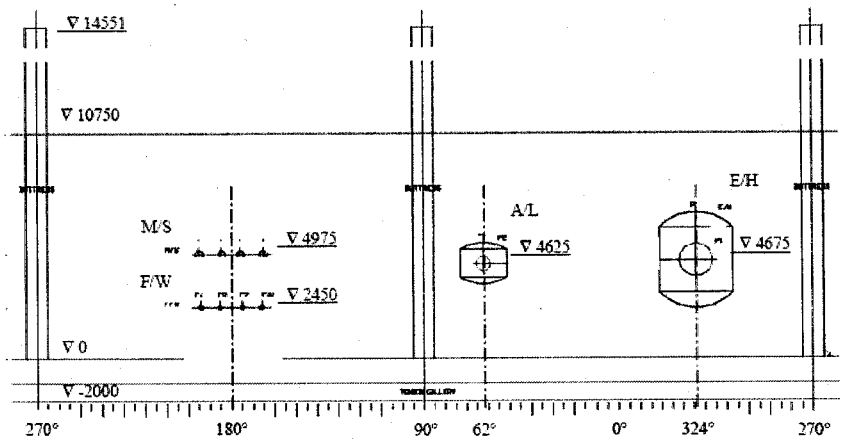

Figure 3.4 Layout of the penetrations (elevation, outside containment).

3.2.7 Pre-stressing tendons

The cylindrical wall and the dome are pre-stressed using unbonded tendons. The tendons consists of 3 pieces of 13.7 mm seven wire strands placed in metal ducts, normally 35 mm in diameter. The tendons were erected in the ducts after the concrete was cast and cured, and then tensioned.

The hoop tendons consist of 360° tendons with both ends anchored at the same vertical buttress. These tendons are tensioned from both ends. Every other tendon is anchored at the 90° buttress and 270° buttress respectively. The vertical tendons in the wall and dome are tensioned and anchored in the basemat tendon gallery. The tendon layout is shown in Figure 3.5, Figure 3.6 and Figure 3.7.

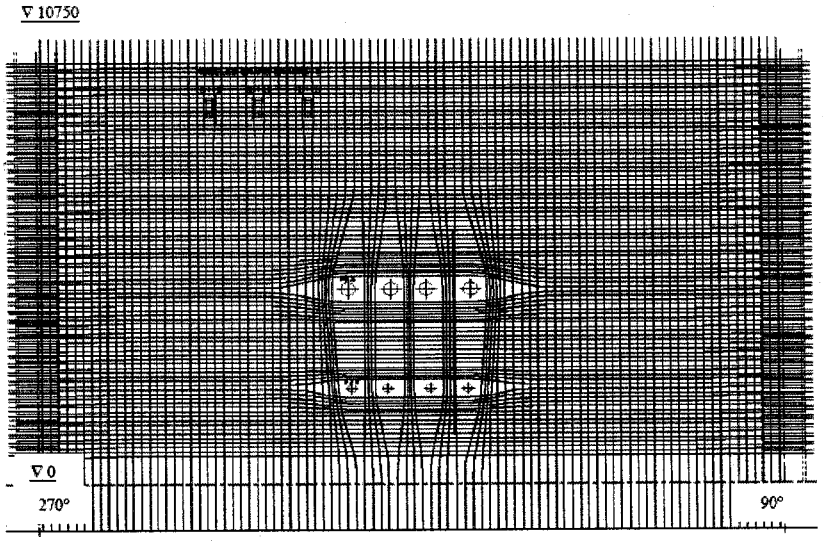

a) Pre-stressing tendon arrangement in cylindrical wall, elevation, outside containment, 270° - 90°

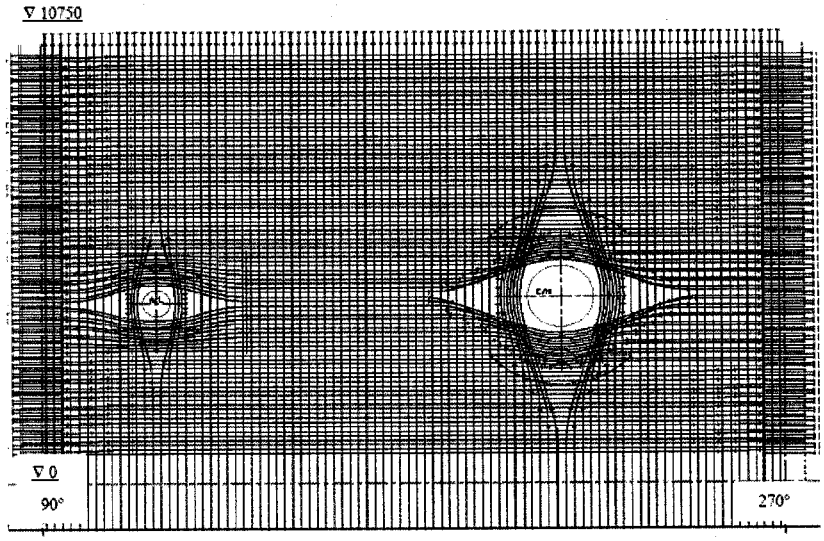

b) Pre-stressing tendon arrangement in cylindrical wall, elevation, outside containment, 90° - 270°

Figure 3.5 Pre-stressing tendon arrangement, cylindrical part (elevation).

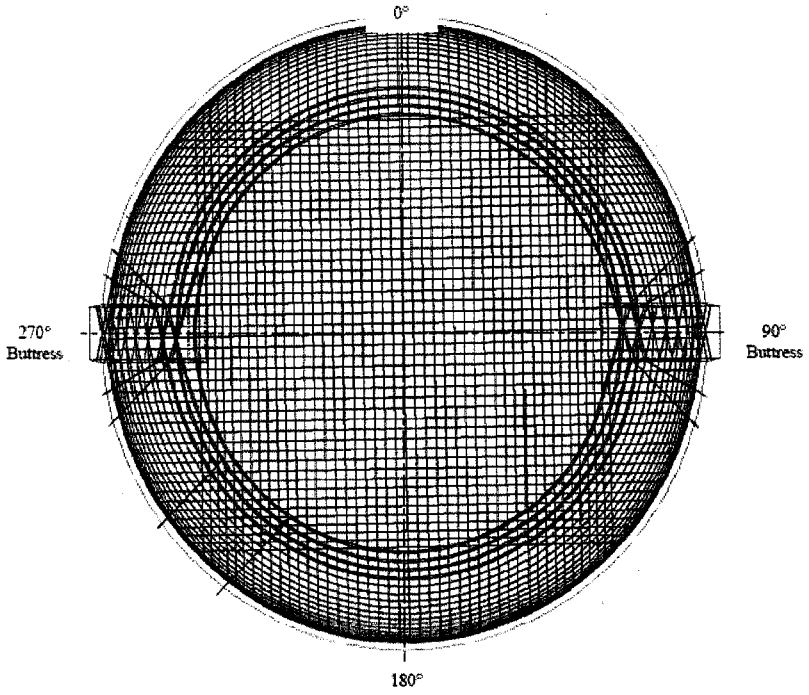

Figure 3.6 Pre-stressing tendon arrangement, dome (plan view from above).

3.2.8 Reinforcing steel

All outside and inside surfaces of the containment are conventionally reinforced with carbon steel deformed rebars. Also, all structural parts have shear reinforcement. Additional reinforcing is placed around penetrations, near the wall-basemat junction and at tendon anchoring zones, i.e. tendon gallery and buttresses. The general rebar layout is shown in Figure 3.7. The bars in the vertical direction are of diameter 10-19 mm, and the bars in the horizontal direction of diameter 10-22 mm.

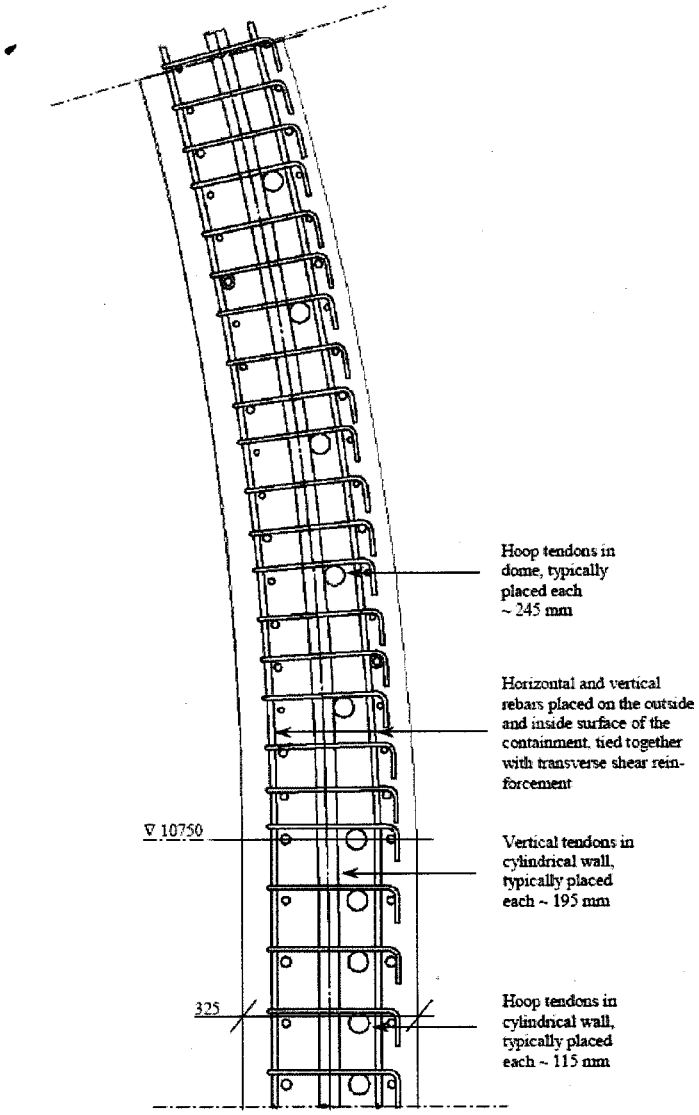

Figure 3.7 Pre-stressing tendons and rebar arrangement, section through wall/dome.

3.2.9 Concrete

A concrete mix with the same properties as for the prototype structure where used for the model containment. Two different concrete strengths where used, 30 MPa for the majority of the basemat and 45 MPa for the wall and dome as well as above the basemat tendon gallery. Concrete lifts and strengths are shown in Figure 3.8.

The concrete mix used is air-entrained and contains flyash and superplasticizer. Maximum aggregate size is 10 mm.

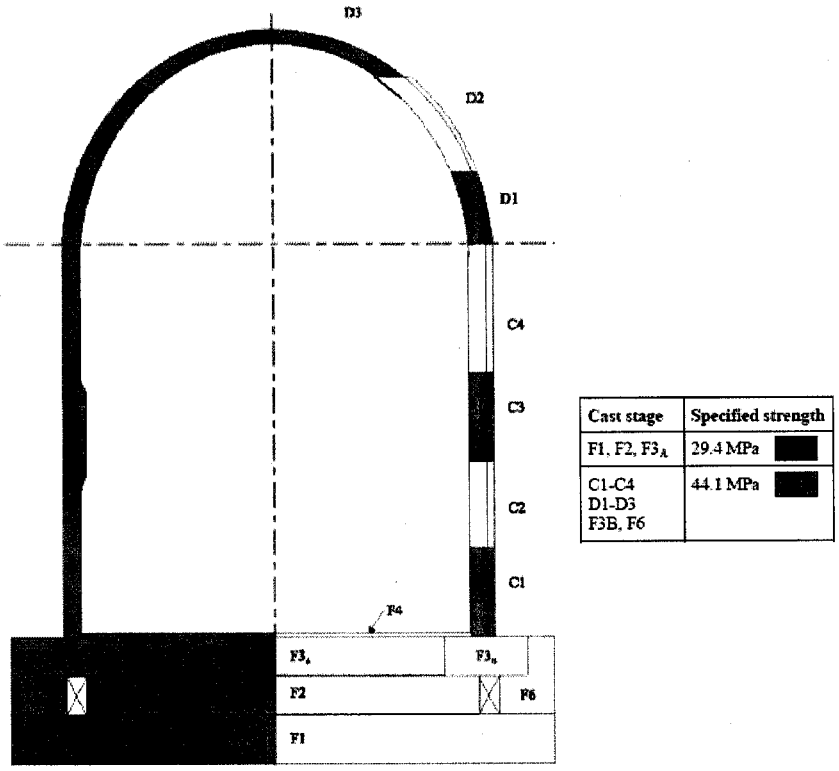

Figure 3.8 Concrete quality and cast stages.

3.3 Material

3.3.1 General

The aim of this project is to simulate the actual structural response of the model containment. The values of material parameters are therefore based on tests performed on material specimens from the model containment, and mean values are

chosen. The tension-stiffening curves are chosen as piece-wise linear curves fitting test data.

3.3.2 Stress and strain measures

In order to describe the behavior of the material on a local element level, *ABAQUS* uses true stresses and strains, even referred to as logarithmic strains. The following convention is used to translate the nominal stresses and strains to true stresses and strains for isotropic materials:

$$\sigma_{true} = \sigma_{nom} \cdot (1 + \varepsilon_{nom})$$

$$\varepsilon_{\ln}^{pl} = \ln(1 + \varepsilon_{nom}) - \frac{\sigma_{true}}{E}$$

where E is the Young's modulus.

3.3.3 Failure criteria

In *ABAQUS* it is possible to define material failure criteria. When the strains in an element reach the prescribed failure criterion that element is no longer active in the model. A failure criterion is introduced for every steel structural part when ε_{max} is reached. The concrete material failure criteria is explained in section 3.3.4 below.

3.3.4 Concrete

The following mean values for the concrete material properties at the time for the limit state test (LST) have been identified from the given test data presented in [2]:

Dome and cylinder, specified strength 44.1 MPa

$f_c^{LST} = 58.5$ MPa

$E_c^{LST} = 26.8$ GPa

Basemat, regions with specified strength 29.4 MPa

$f_c^{LST} = 49.2$ MPa

$E_c^{LST} = 26.0$ Gpa

Basemat, regions with specified strength 44.1 MPa

$f_c^{LST} = 59.4$ MPa

$E_c^{LST} = 28.0$ GPa

The strain at peak stress is chosen to 0.0026.

Tensile strength values are also provided. Since visual inspection of the model containment before the start of the LST test revealed the existence of micro-cracking throughout the cylinder, the tensile concrete strength was reduced to correspond to a cracking strain of $\varepsilon_{cr} = 40 \cdot 10^{-6}$. A typical value for Mode I fracture energy G_f^I is chosen to 120 N/m according to CEB-FIP Model Code 1990.

This value is reduced as shown in Figure 3.9. The general tension-stiffening curve for concrete exposed to tension is also presented in Figure 3.9.

The Poisson´s ratio is set to 0.2, also based on test results.

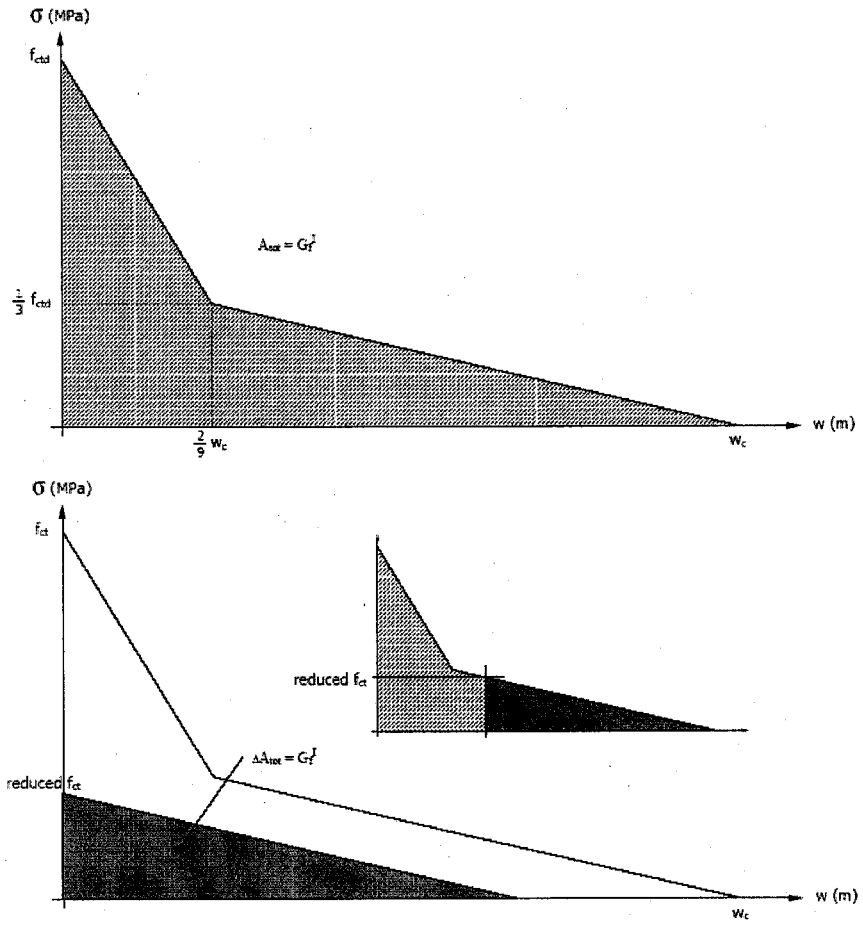

Figure 3.9 General tension-stiffening curve for concrete.
Upper diagram: Crack-free concrete.
Lower diagram: Idealization for concrete with micro-cracks, modeled with reduced strength f_{ct}.

3.3.5 Pre-stressing tendons

The following mean values for the pre-stressing tendon material parameters have been identified from the test data provided in [2]:

f_y = 1713 MPa

f_u = 1882 MPa

E_s = 191 GPa

ε_{max} = 3.83 %

These values are calculated using given test data of force-elongation and cross sectional area for the tendon system. Each tendon has an ultimate capacity of 638 kN.

The general tension-stiffening curve for pre-stressing tendons is presented in Figure 3.10.

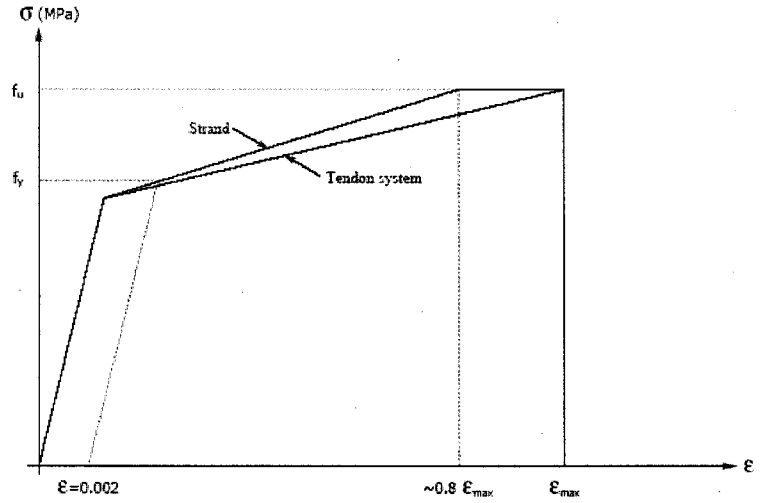

Figure 3.10 General tension-stiffening curve for pre-stressing tendons.

3.3.6 Reinforcement

The following mean values for the rebar material parameters have been identified from the test data provided in [2]:

Reinforcing steel, specified yield strength 392 MPa

f_y = 440 MPa

f_u = 610 MPa

E_s = 183 GPa

ε_2 = 0.85 %

ε_3 = 8.64 %

ε_{max} = 13 % (estimated value of strain at maximum engineering stress)

The general tension-stiffening curve for reinforcement, shell main bars, is presented in Figure 3.11.

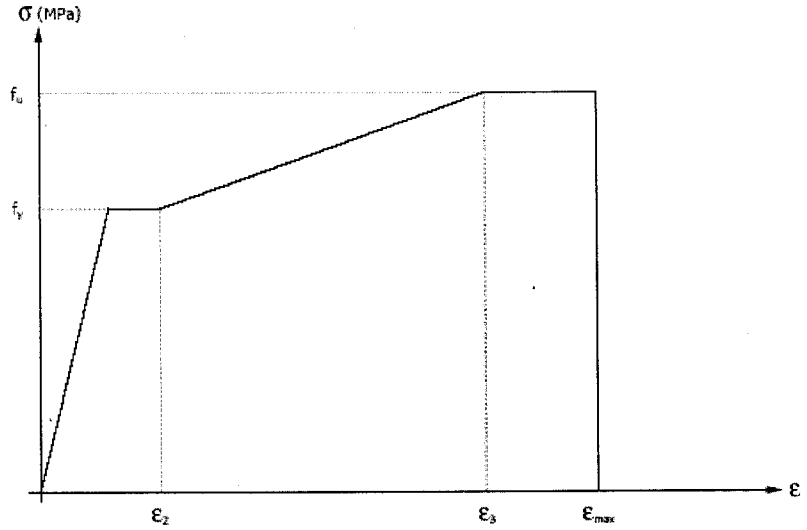

Figure 3.11 General tension-stiffening curve for reinforcement steel.

3.3.7 Steel liner

The following mean values for the steel liner material parameters, not affected by welding, have been identified from the test data provided in [2]:

$f_y = 383$ MPa

$f_u = 498$ MPa

$E_s = 219$ GPa

$\varepsilon_{max} = 20$ % (estimated value of strain at maximum engineering stress)

$\varepsilon_2 = 1.37$ %

$\varepsilon_3 = 6.77$ %

The general tension-stiffening curve for steel liner is presented in Figure 3.12.

Corresponding values for steel liner in zones affected by welding are:

$\varepsilon_{max} = 18$ % (estimated value of strain at maximum engineering stress)

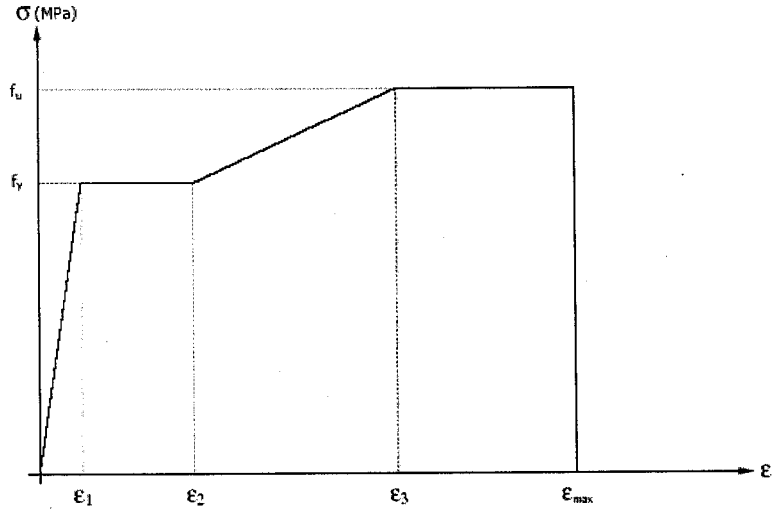

Figure 3.12 General tension-stiffening curve for steel liner.

3.4 Loads

3.4.1 General

Here below follows a presentation of the loads applied in the analyses.

3.4.2 Dead load

The dead load of the structural parts is based on the material densities specified in Table 3.1 below.

Material	Density [kN/m^3]
Concrete	21.9
Reinforcement	78
Steel liner	78
Pre-stressing tendons	78

Table 3.1 Densities for structural parts.

3.4.3 Pre-stressing load

The forces in the pre-stressing tendons prior to pressurization are chosen as the values measured at site two months after completion of the pre-stressing operation. These measurements were performed approximately two months before the start of the limit state test. No adjustments have, however, been done due to time

dependent losses for the period of time between measurement and start of the LST test. This because the tendon forces appear to be very stable, when compared to measurements performed earlier. In Table 3.2 pre-stressing data are given, as average values in the vertical and the horizontal directions respectively.

Average values	Hoop tendons	Vertical tendons
Load cell force	331 kN	435 kN
Friction coefficient	0.18	0.21
Seating loss	3.95 mm	4.95 mm
Seating loss force	95.6 kN	47.9 kN

Table 3.2 Pre-stressing data summary.

The variation of the pre-stressing force along the tendon due to friction and seating loss can be calculated using measured values of the friction coefficient and seating loss, as well as test data giving strains in discrete positions along the tendons. In Figure 3.13 and Figure 3.14 variation of pre-stressing force along the tendons valid for horizontal and vertical directions respectively are presented. These are average values supposed to be valid for all tendons not affected by penetrations. Near penetrations, tendons have increased curvature giving rise to additional losses due to friction. How the tendon force distribution during pressurization is handled is presented in section 5.

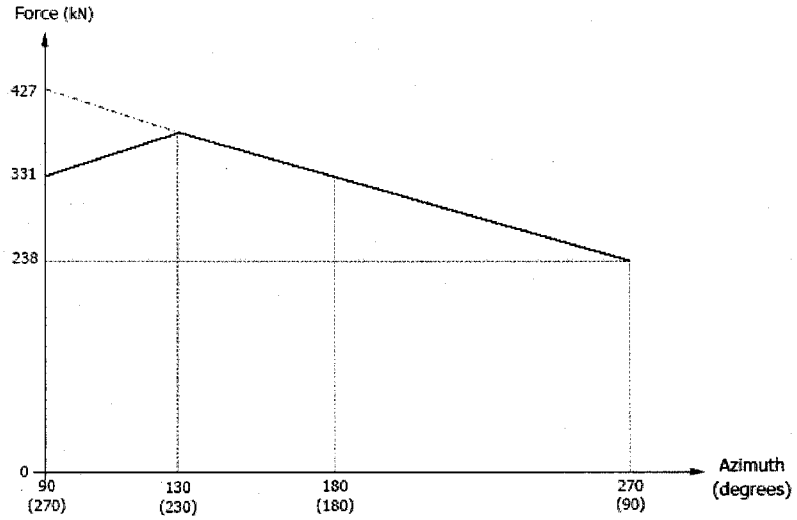

Figure 3.13 Horizontal tendon force variation.

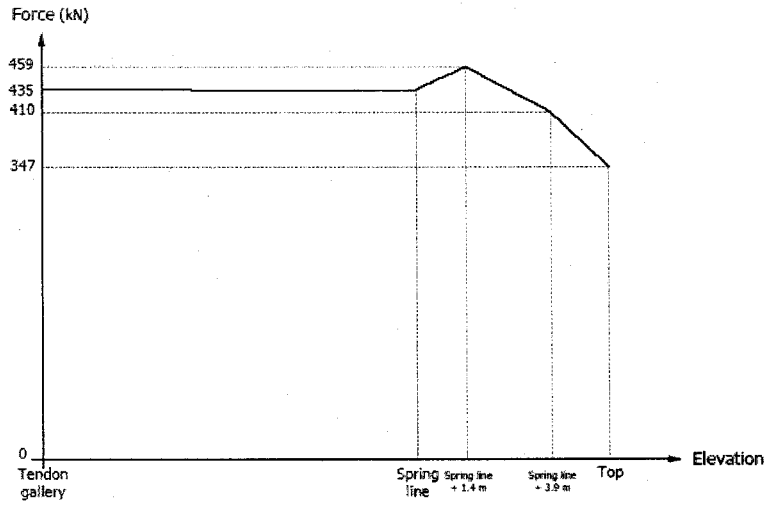

Figure 3.14 Vertical tendon force variation.

The Young´s modulus of the concrete at pre-stressing and at the start of the LST test show only a minor difference (~1-2%). The same modulus can thus be used both when simulating the tensioning of the tendons and the pressurization of the model containment during the LST test.

3.4.4 Over-pressurization

The over-pressurization studied in this report correspond to the limit state test (LST). The pressure history for all tests performed is given in Figure 3.15 below. A linear monotonic increasing internal pressure load is applied as an over-pressure in relation to normal atmosphere pressure.

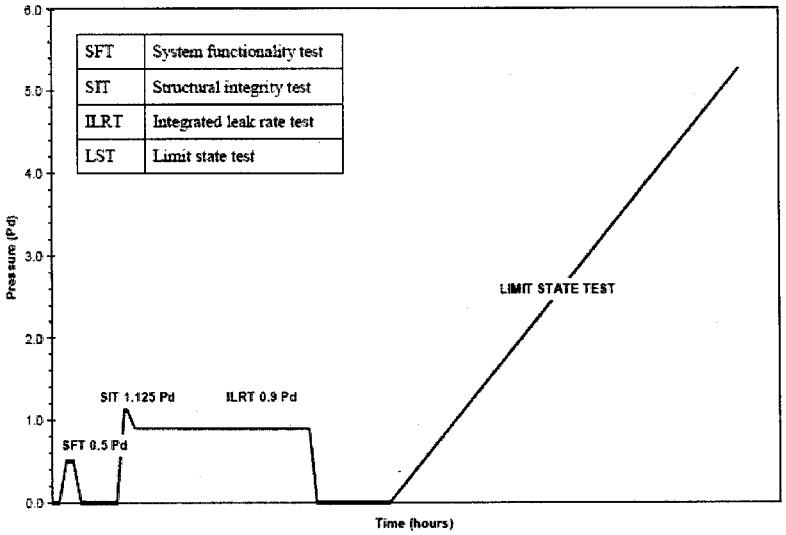

Figure 3.15 Pressurization of the model containment.

4. PARAMETRICAL STUDIES: AXI-SYMMETRICAL MODEL

4.1 General

The model containment can be reasonably well analysed with an axi-symmetrical model when studying global behaviour in the event of over-pressurization. An axi-symmetric analysis can be used to understand the global behaviour of the model containment in an un-disturbed region, i.e. as a first approximation of the leak-tightness and structural capacity.

However, the main purpose of an axi-symmetric model is to provide efficient executional runtimes in order to facilitate parametrical studies and sensitivity analysis. This to be able to define high-quality model assumptions for the three-dimensional model to be used in the main structural analysis (section 6).

Only a small part of the basemat is included in the axi-symmetric model since the local non-linear behaviour close to the wall-basemet connection is dominating over the global effects of the basemat to the containment wall, as is shown in the parametrical study presented in section 4.6. The basemat behaviour, and specially the tendon gallery zone, has then to be studied in a separate analysis.

4.2 Structural model

4.2.1 Geometry

The axi-symmetrical model has been established out of drawings provided in [2]. General dimensions are presented in section 3 above. The axi-symmetrical model is shown in Figure 4.1.

The finite element model represents the geometry of the model containment at approximately azimuth 135°, see Figure 4.1. This section is relatively free from geometrical disturbances like e.g. buttresses and penetrations. Furthermore, the force in the pre-stressing tendons is here representative.

For comparative studies, an axi-symmetric model including both the base-slab and the underground, mudmat and engineering backfill, has been built as shown in Figure 4.2. The mudmat of concrete and the engineering backfill are modeled using linear elastic material properties. Between the bottom of the base-slab and the mudmat, a contact formulation is specified, allowing uplift of the baseslab. The material properties of the underground are adjusted to correspond to a settlement of 25 mm for the dead weight of the containment, as registred on site during construction.

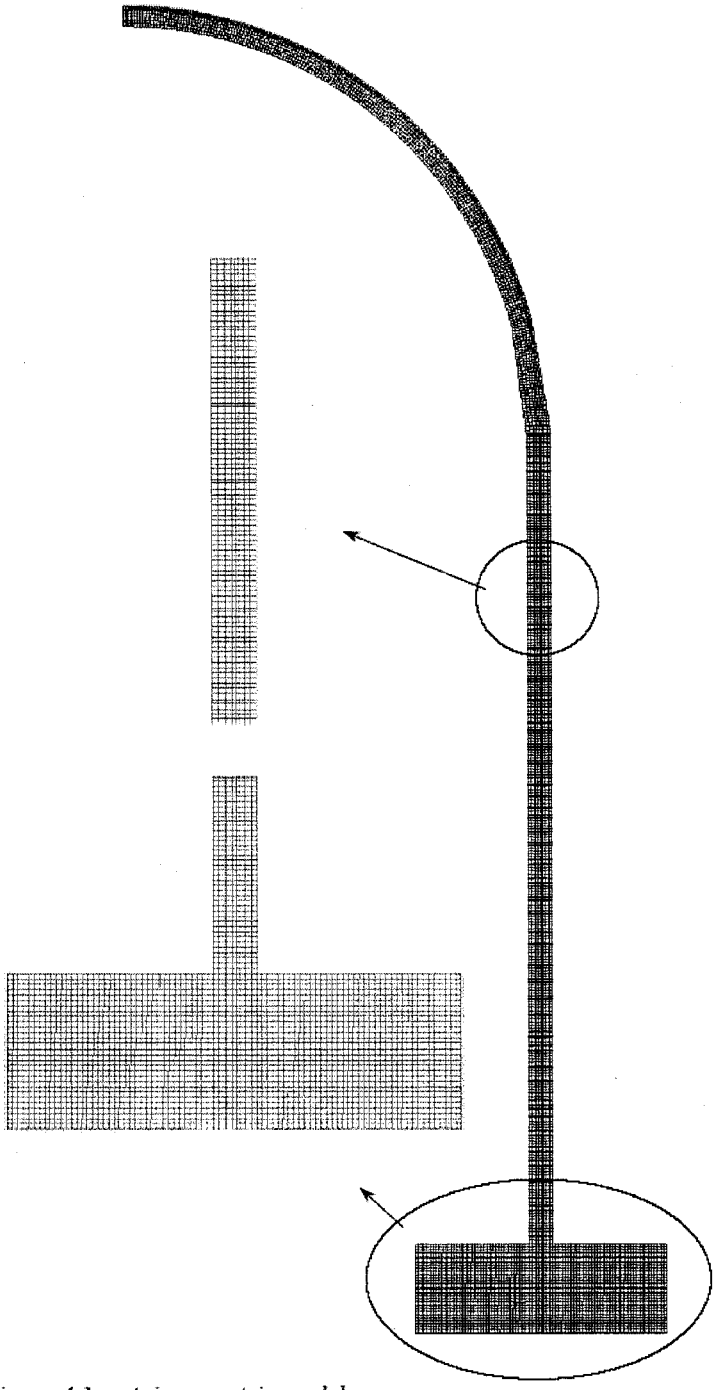

Figure 4.1 Axi-symmetric model.

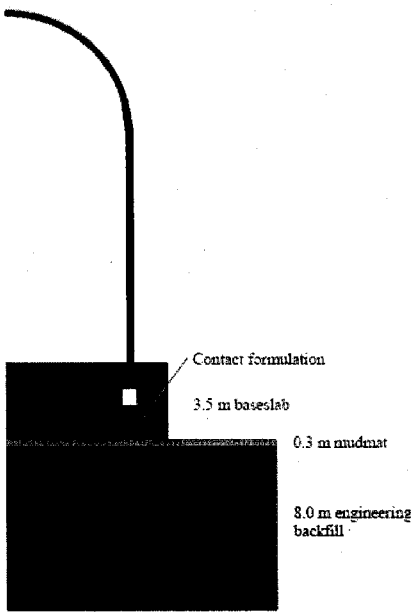

Figure 4.2 Axi-symmetric model including underground.

4.2.2 Types of finite element

The concrete parts in the FE-model are represented by axi-symmetrical continuum elements with a reduced number of integration points denominated CAX4R. The steel liner is represented by axi-symmetrical shell elements denominated SAX1. Both the pre-stressing tendons and the reinforcement are desribed by using the rebar modeling feature in ABAQUS. The reinforcement is modeled by rebars in the form of a layer inside the underlying continuum elements (concrete). The tendons are defined as single rebars in the underlying element.

4.2.3 Boundary conditions

Only a minor part of the basemat is included in the FE-model. the part between the cylindrical wall connection and the tendon gallery, i.e. approximately corresponding to the cast stage $F3_B$, see Figure 3.8 in section 3.2.9. The bottom and the vertical faces of the basemat part are constrained in both vertical and horizontal direction. No constrains are applied on the nodes situated directly above the tendon gallery. Constrained nodes are shown in Figure 4.3.

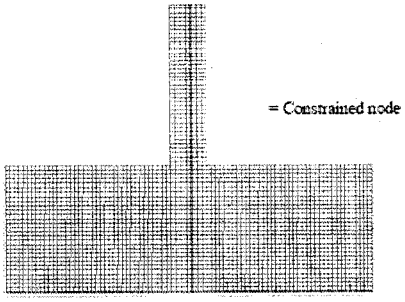

Figure 4.3 Boundary conditions applied to the basemat part.

In order to describe the symmetry conditions at the top of the dome the horizontal degree of freedom are constrained, see Figure 4.4.

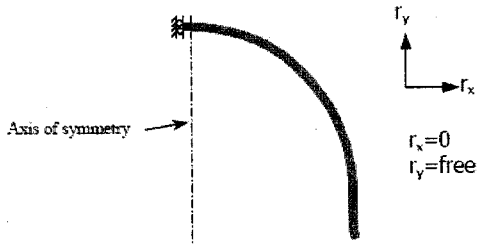

Figure 4.4 Axi-symmetric boundary conditions at the top of the dome.

4.2.4 Reinforcement

The reinforcement layout in the cylindrical wall, i.e. elements including rebar specification, is shown in Figure 4.5. The rebars are rigidly connected to the concrete.

4.2.5 Pre-stressing tendons

The tendon layout is shown in Figure 4.5. The tendons are simplified and modeled as rigidly connected to the concrete, i.e. modeled as grouted, since it is not possible to do otherwise for the hoop tendons in an axi-symmetric model. For the vertical tendon, the effect of longitudinal variation has lesser influence than for the horizontal tendons, as can be noticed when comparing the tendon force variation presented in Figure 3.13 and Figure 3.14.

The tensioning of the tendons is modeled by applying a temperature load to the tendons, giving a uniformly pre-stressing force along the length of the tendon.

The tendons in the horizontal direction are tensioned to 928 MPa, corresponding to a pre-stressing force of 320 kN, and the tendons in the vertical direction to 1300 MPa, corresponding to a force of 447 kN.

4.2.6 Steel liner

The steel liner is positioned on the inside of the containment as shown in Figure 4.5. The steel liner is rigidly connected to the concrete elements.

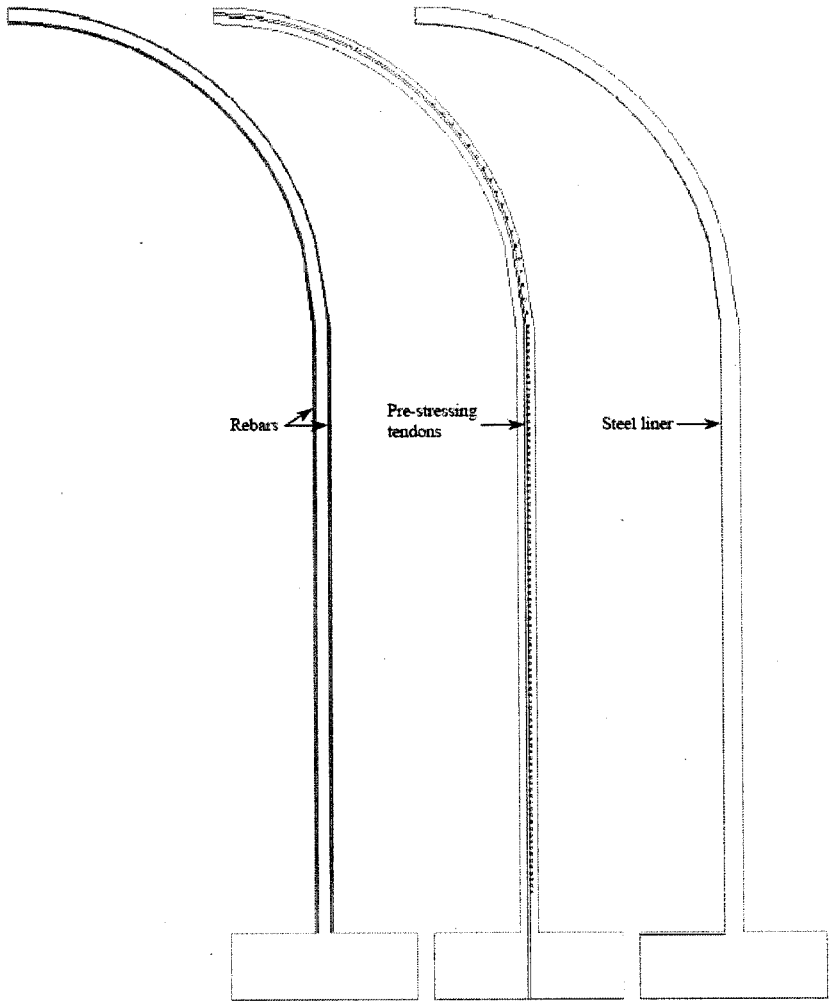

Figure 4.5 Positions of rebar, pre-stressing tendons and steel liner.

4.2.7 Application of loads

Dead weight is modeled applying a field of gravity acting downwards, using the gravitational constant 9.81 m/s^2.

The internal overpressure is applied as a linear monotonic increasing internal pressure load to the inside of the containment, i.e. to the shell element representing the steel liner.

4.3 Structural analysis

4.3.1 General

Four comparative studies regarding FE-analysis techniques have been carried out;

1. Comparison between implicit and explicit solving techniques, i.e. the analysis are executed using ABAQUS/Standard and ABAQUS/Explicit respectively.
2. Comparison between two different material models for concrete. The material models compared are the Brittle Cracking (BC) model and the Concrete Damage Plasticity (CDP) model, both included in ABAQUS to be used when modeling concrete structures. For further information see [3].
3. Comparison of the influence on results when modeling the baseslab and underground in detail. An analysis modeling only a small part of the baseslab is compared with an analysis including both the baseslab as well as the underground (mudmat and engineering backfill).
4. Loading rate and mass scaling are important issues to regard influencing the executional runtime in explicit analysis. These parameters are trimmed with the help of parametrical studies.

4.3.2 Result positions

Results are presented in the nodes of the model corresponding to test data positions. In Figure 4.6 result positions from the axi-symmetrical analysis are shown. All points correspond to azimuth 135°.

Due to the fact that the main purpose of the axi-symmetric analysis is to carry out parametrical studies, only displacement data are presented. However, the axi-symmetrical results for all output postions at azimuth 135 are presented in the result diagrams for the 3D-analysis as a comparison, see section 7.3.3.

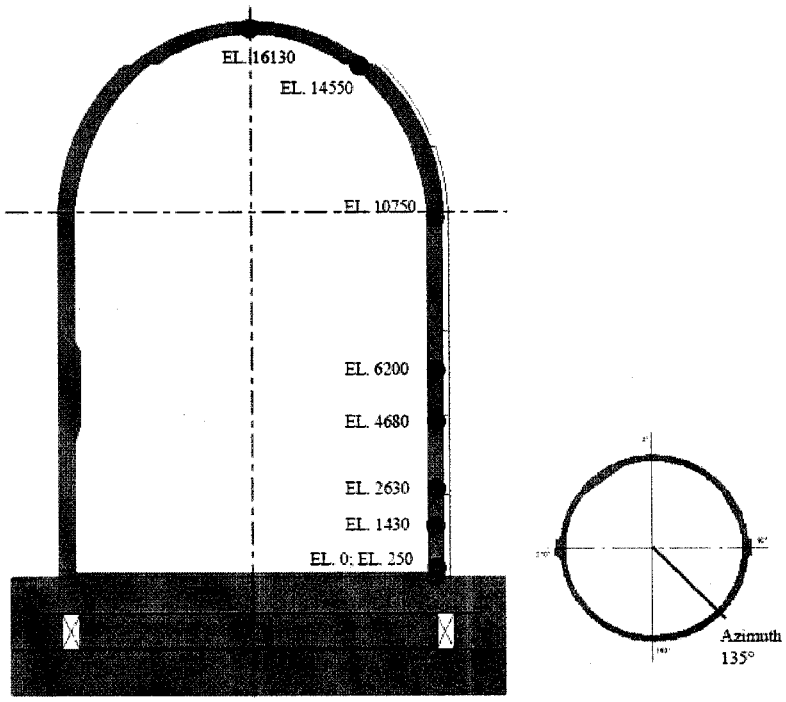

Figure 4.6 Result positions, axi-symmetric model azimuth 135° [mm].

4.4 Parametrical study 1: Solver techniques

4.4.1 General

In this section, results from parametrical studies regarding comparison between implicit and explicit solving techniques are given, i.e. the analysis are executed using ABAQUS/Standard and ABAQUS/Explicit respectively.

4.4.2 Displacements

Displacements in the radial direction are presented with the initial position of the structure before pressurization as reference. Displacements in the vertical direction are presented with the upper part of the basemat as reference, i.e. excluding any basemat uplift.

In Figure 4.7 to Figure 4.17 in the next section analysis results regarding radial and vertical displacement are presented together with measured displacements during the limit state test (LST) of the model containment.

The analysis results agree very well with corresponding test data regarding displacements in the radial direction. In the vertical direction, the results for the

dome differ from test results when using the Concrete Damage Plasticity (CDP) model as described in section 4.5.2.

As can be seen in the diagrams, there is good agreement between analysis using implicit and explicit time integration schemes, respectively.

4.4.3 Conclusions

Due to the fact that there is no difference in results between using implicit or explicit solver, the explicit solver will be used in the main three-dimensional analysis.

4.5 Parametrical study 2: Constitutive models for concrete

4.5.1 General

Results from a comparison between two different material models for concrete is presented in this section. The material models compared are the Brittle Cracking (BC) model and the Concrete Damage Plasticity (CDP) model, both included in ABAQUS to be used when modeling concrete structures. For further information see [3].

4.5.2 Displacements

Displacements in the radial direction are presented with the initial position of the structure before pressurization as reference. Displacements in the vertical direction are presented with the upper part of the basemat as reference, i.e. excluding any basemat uplift.

In Figure 4.7 to Figure 4.17 analysis results regarding radial and vertical displacement are presented together with measured displacements during the limit state test (LST) of the model containment.

The analysis results agree very well with corresponding test data regarding displacements in the radial direction. In the vertical direction, the results for the dome differ from test results when using the Concrete Damage Plasticity (CDP) model. When the concrete starts to crack, the analysis result using the CDP model shows a decrease in vertical displacement, not registered during the test. This can be explained by the fact that in the CDP model no consideration is taken to the direction of the concrete cracks. Instead, the stiffness in the concrete is decreased in all directions, not only in the principal tension direction. Therefore, even if the concrete is cracked only due to hoop stresses, the stiffness in the vertical direction drops as well. When the pressure level is reached cracking in the hoop direction occurs, there are compression stresses in the vertical direction due to the pre-stressing force. This will give rise to a displacement directed downwards due to the aritifical decrease in stiffness. In the Brittle Cracking model, crack direction is taken into consideration, thus giving a much better estimation of the displacement in the vertical direction.

There is a good agreement between the two different concrete material models used, except in the vertical direction as explained above.

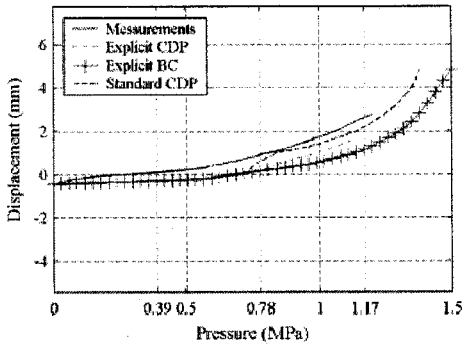

Figure 4.7 Displacement in the radial direction at elevation 250

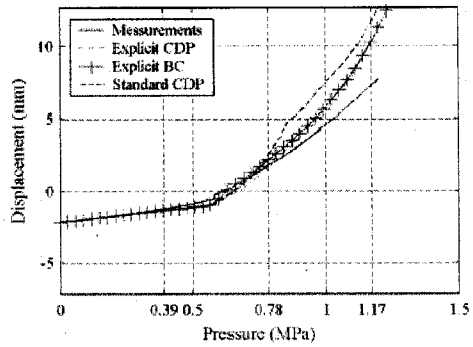

Figure 4.8 Displacement in the radial direction at elevation 1430

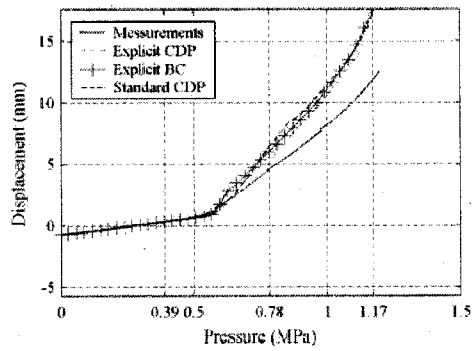

Figure 4.9 Displacement in the radial direction at elevation 2630

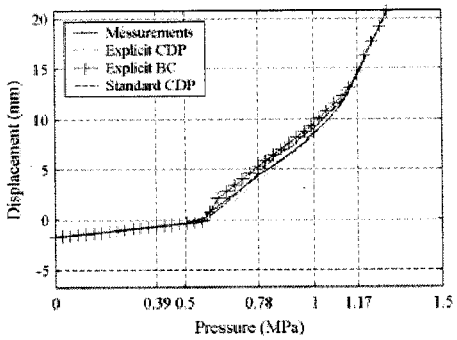

Figure 4.10 Displacement in the radial direction at elevation 4680

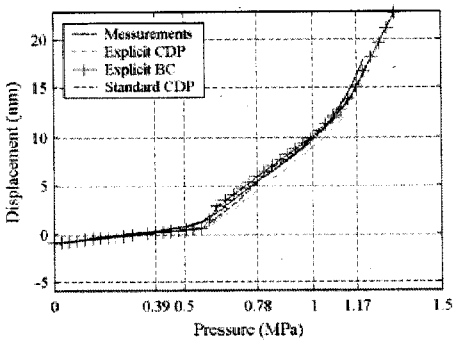

Figure 4.11 Displacement in the radial direction at elevation 6200

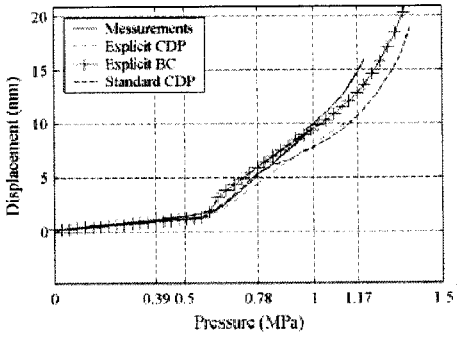

Figure 4.12 Displacement in the radial direction at elevation 10750

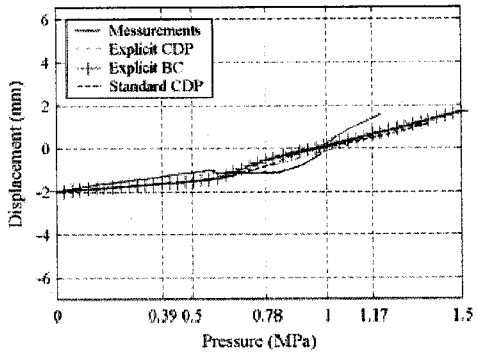

Figure 4.13 Displacement in the horizontal direction at elevation 14550

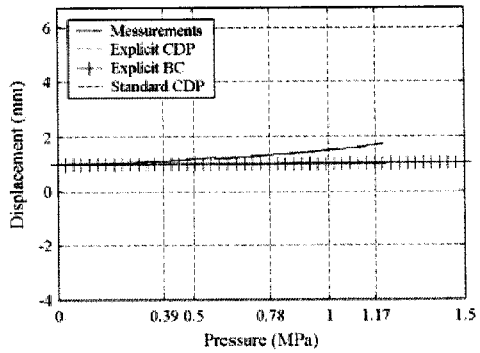

Figure 4.14 Displacement in the vertical direction at elevation 0

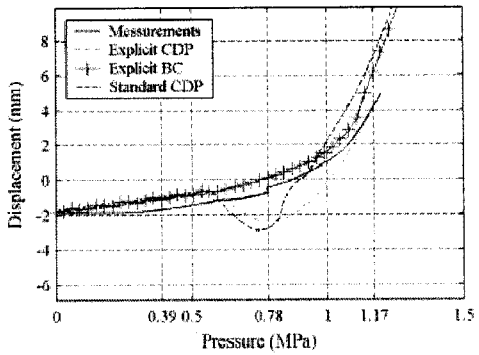

Figure 4.15 Displacement in the vertical direction at elevation 10750

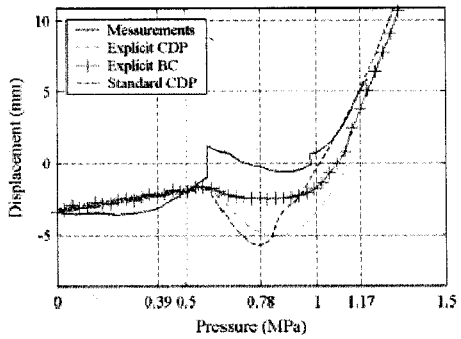

Figure 4.16 Displacement in the vertical direction at elevation 14550

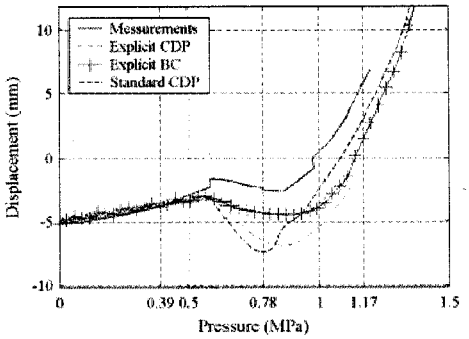

Figure 4.17 Displacement in the vertical direction at elevation 16130

4.5.3 Conclusions

Because the Concrete Damage Plasticity model gives some non-accurate results for the typical stress state prevalent in the containment, the Brittle Cracking model is chosen for the main analysis.

4.6 Parametrical study 3: Basemat and underground

4.6.1 General

To be able to minimize the model size for the three-dimensional model, it would be conveniant if most of the basemat and the underground could be neglected. Therefore, in the third parametrical study a comparison between modeling the baseslab and underground in detail with modeling only a small part of the baseslab is done.

4.6.2 Displacements

The radial displacement is in principal equal for both analysis. The vertical deformation also agrees well.

4.6.3 Conclusions

Due to the fact that the results from the the two comparative analysis do not differ, the central part of the basemat and the underground can be neglected when creating the three-dimensional model.

4.7 Parametrical study 4: Loading rate and mass scaling

In an explicit dynamic analysis the load has to be applied quasi-statically during a sufficiently long period of time, in order not to introduce any dynamical effects on the structure, i.e. inertia forces and kinetic energy can be regarded as negligible. A loading rate well below the critical value has to be chosen.

To minimize the executional runtime, mass-scaling can be used. Mass-scaling is only to be used during the linear elastic response phase of the analysis, that is up to an overpressure of 600 kPa. Mass-scaling increases the effect of inertia forces so care must be taken not to introduce any dynamical effects in the quasi-static analysis. The benefits of using mass-scaling is explained below.

An estimate of the stability limit in explicit dynamics procedure can be expressed as

$$\Delta t = \frac{L^e}{c_d}$$

where Δt is the stable time increment, L^e is the smallest characteristic element length and c_d is the dilatational wave speed of the material. The dilatational wave speed in a linear elastic material (with Poisson´s ratio equal to zero) is

$$c_d = \sqrt{\frac{E}{\rho}}$$

where E is the elastic modulus and ρ is the material density.

If we artificially increase the material density by a factor of f^2, the wave speed decreases by a factor of f, and therefore the stable time increment increases by a factor of f. This increase in stable time increment will give rise to a corresponding reduction in executional runtime.

The mass-scaling chosen in the presented analysis has reduced the executional runtime with approximately 40 percent. This reduction is of great importance when analyzing large FE-models, or in the case of performing comprehensive sensitivity studies.

5. MODELING OF PRE-STRESSING TENDONS

5.1 Overview

One of the most important modeling issues is the modeling of the pre-stressing tendons. The tendons in the model containment are non-grouted, i.e. unbonded. These types of tendons can be modeled at different levels of sophistication;

Level 1 Taking into consideration the actual friction between the tendon and the concrete, not only during the tensioning and seating procedure, but also during the pressurization of the containment.

Level 2 The tendon force is specified by taking the variation of tendon force along the tendon into consideration during tensioning due to friction and seat losses etc. During the pressurization process the tendon is modeled as fully bonded to the concrete.

Level 3 The tendon force is specified as a constant force along the tendon, initially specified as a mean value taking friction and seat losses etc into consideration. During the pressurization process the tendon is modeled as fully bonded to the concrete.

The test results show, as expected, that the force distribution along the tendon is un-evenly distributed due to friction and seating losses during the tensioning procedure. This force distribution, however, will gradually change to a more or less evenly distributed force along the tendon when the internal pressure in the containment rises. The change of force distribution starts to appear when the hoop forces equilibrate the pre-stressing force and the distribution will then gradually approach an even distribution for further increase in pressure load. In this phase the tendon force increases as expected as a consequence of elongation due to the radial deformation of the containment.

Due to this tendon behaviour, it is an advantage if the modeling method is in accordance with the level 1 approach described above.

5.2 Test of level 1 modeling methods

We have used ABAQUS in order to test four different level 1 methods to enable to take into consideration the friction and slip between the unbonded tendon and the concrete during both construction, i.e tensioning and seating, and during pressurization. These methods are briefly presented in sections 5.2.1 – 5.2.4 below. A comparision of results is also made using the level 2 approach, i.e. to model the tendons fully bonded to the concrete during pressurization.

The test is carried out as a basis for choosing modeling methods to be used in the 3D FE-analysis of the model containment. Three main areas are evaluated in the test;

- Simulation capabilities, i.e. the possibility to simulate the true tendon forces along the tendon.

- Computational runtime.
- Modeling effort.

The evaluation of the modeling effort is a subjective matter and to some extent dependent on the pre-processor available, however a relative comparison will be presented. Computational runtimes will be presented as relative values because the absolute values are of course dependent on the computer capacity at hand.

The test calculations are carried out using a horizontal 180° segment of an 0.3 meter high un-disturbed part of the model containment wall including 3 pre-stressing tendons, see Figure 5.1. The loading sequence of the model is tensioning, seating and finaly pressurization. Geometry, loading conditions and material parameters are the same as for the analysis of the model containment.

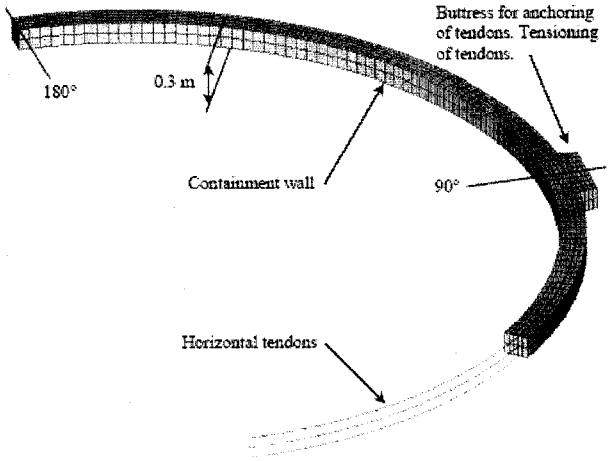

Figure 5.1 Horizontal 180° segment model including three pre-stressing tendons.

5.2.1 Contact formulation between tendon and concrete (truss elements)

The tendons are modeled with truss elements and the concrete with solid elements. The interaction between the truss elements and the solid elements is modeled with a contact formulation. A friction coefficient is specified between the tendon and the concrete.

Using this method the force distribution along the tendon during tensioning and seating is automatically calculated. Also, the re-distribution of tendon force and increase in friction force during pressurization is automatically taken into consideration in the analysis.

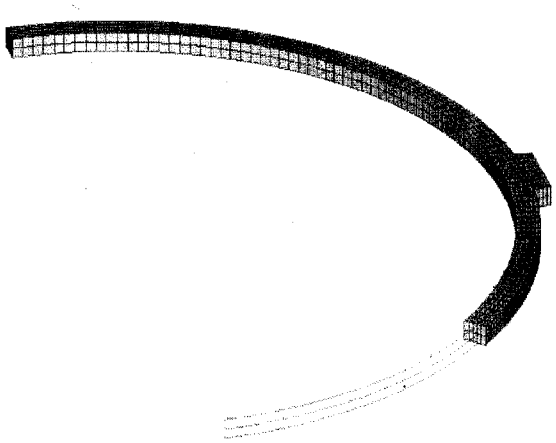

Figure 5.2 Horizontal tendons modeled with trusses, interaction between tendon and concrete modeled with a contact formulation.

The element and node positions for truss and solid elements respectively can be specified independently of each other making the modeling work straightforward.

The contact formulation increases the computational runtime in comparison to the other methods using coupling elements between the tendon and concrete nodes, i.e. friction connectors and friction trusses.

5.2.2 Contact formulation between tendon and concrete (membrane elements)

This method is identical to the one specified in section 5.2.1 above, except that the tendons are modeled using membrane elements instead of truss elements, see Figure 5.3. Using this method it is not necessary to explicitly model each tendon.

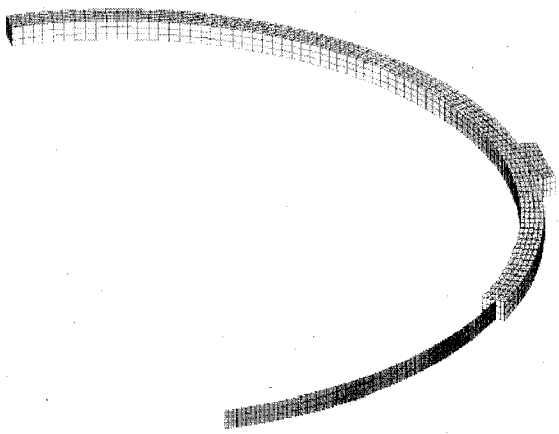

Figure 5.3 Horizontal tendons modeled with membrane, interaction between tendon and concrete modeled with a contact formulation.

This method is favourable when the tendon curvature is only in one plane, and the tendons are evenly distributed at rather small distances. It is possible to use the method also for curvature in more than one plane by using rotated material directions, see Figure 5.4. However, this increases the modeling effort, and therfore modeling tendons explicitly with truss elements would in this case be an equal or even better alternative.

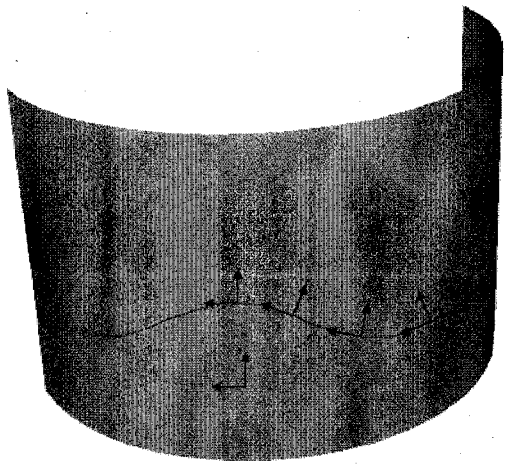

Figure 5.4 Rotating material directions (upper tendon) for tendon curvature in more than one direction, when using membrane elements modeling the tendons.

5.2.3 Friction connectors between tendon and concrete

The tendons are modeled with truss elements and the concrete with solid elements. The interaction between the truss elements and the solid elements is modeled with friction connectors. A friction force is specified and this force will be activated in the correct direction based on the relative motion between the coupled nodes.

Using this method the force distribution along the tendon during tensioning and seating is automatically calculated. Also, the re-distribution of tendon force during pressurization is automatically taken into consideration in the analysis. During pressurization, the friction force will increase. Therefore the friction force specified with the connector element has to be a function of the pressure load. This dependency has to be calculated before the finite element analysis starts and is given as input data.

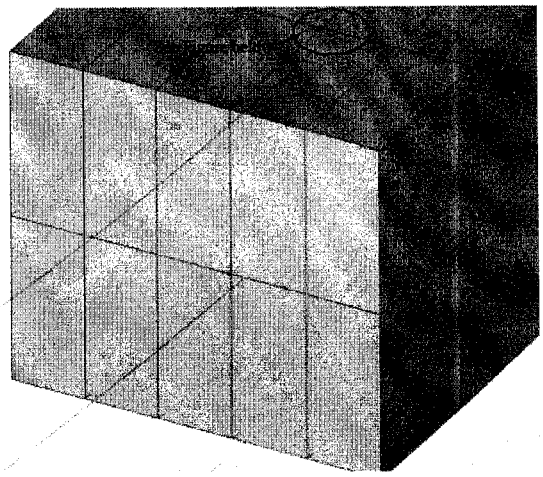

Figure 5.5 Interaction between tendon and concrete modeled with friction connectors.

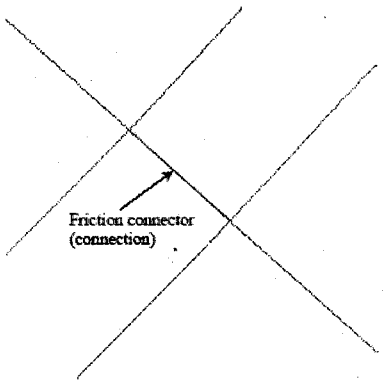

Figure 5.6 Interaction between tendon and concrete modeled with friction connectors.

In this method the truss nodes are connected to the nearest solid element node. Therefore the node positions for truss and solid elements respectively can not be specified to far away from each other, putting some constraints on the modeling work. However, this will often be easily handled by using approximatly the same element size for truss elements and solid elements and due to the fact that the element size has to be rather small in any case.

5.2.4 Friction trusses between tendon and concrete

The tendons are modeled with truss elements and the concrete with solid elements. The interaction between the truss elements and the solid elements is modeled with friction trusses. This method is presented in [4]. The direction of the friction trusses have to coincide with the angle of friction. Therefore the direction of the friction trusses have to be adjusted when the direction of slip is changed. This is the case when going from tensioning to seating, but also in some areas during pressurization, see Figure 5.14.

Using this method the force distribution along the tendon during tensioning and seating is calculated. Also, the re-distribution of tendon force and increase in friction force during pressurization is taken into consideration in the analysis. However, this is only true as long as the friction force doesn't change direction. When a direction change is at hand the model has to be changed by adjusting the direction of the friction trusses, see Figure 5.8.

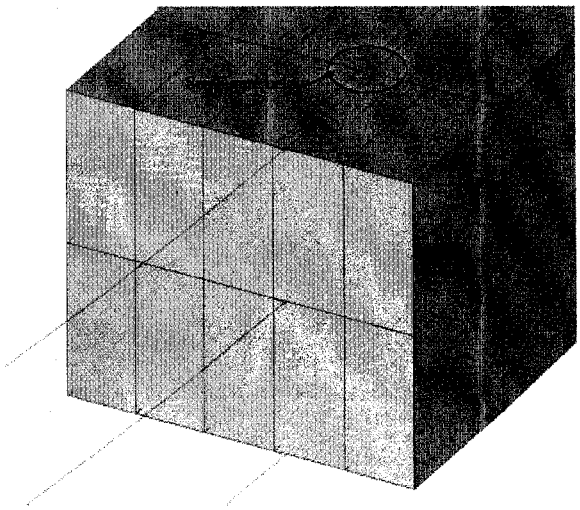

Figure 5.7 Interaction between tendon and concrete modeled with friction trusses.

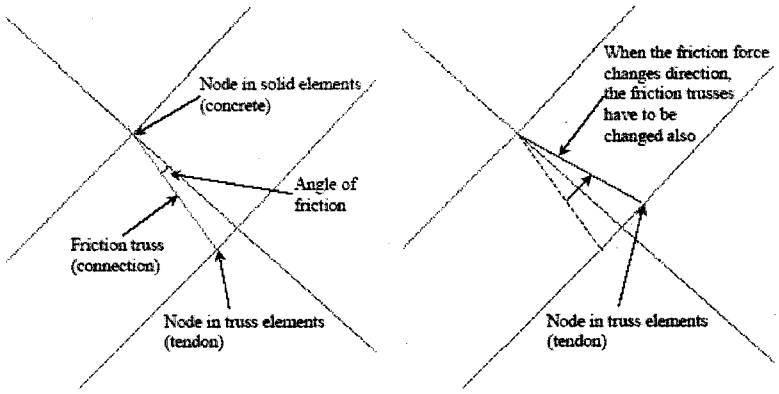

Figure 5.8 Interaction between tendon and concrete modeled with friction trusses, plan view.

To receive the correct direction of the friction trusses when connecting the truss elements with the solid elements, the spatial positioning of the nodes have to be very exact. Also, in zones were the friction force changes direction two nodes have to be specified for the truss element for each solid element connecting node. The demands on spatial positioning of nodes will increase the time to build the model to a great extent, if an automated process is not available, i.e through a specially tailored pre-processor or script.

5.2.5 Results

All methods provide accurate results when modeling tensioning and seating, as can be seen in Figure 5.9. In this figure the curve named Contact represents both the method using trusses and membranes for modeling the tendons.

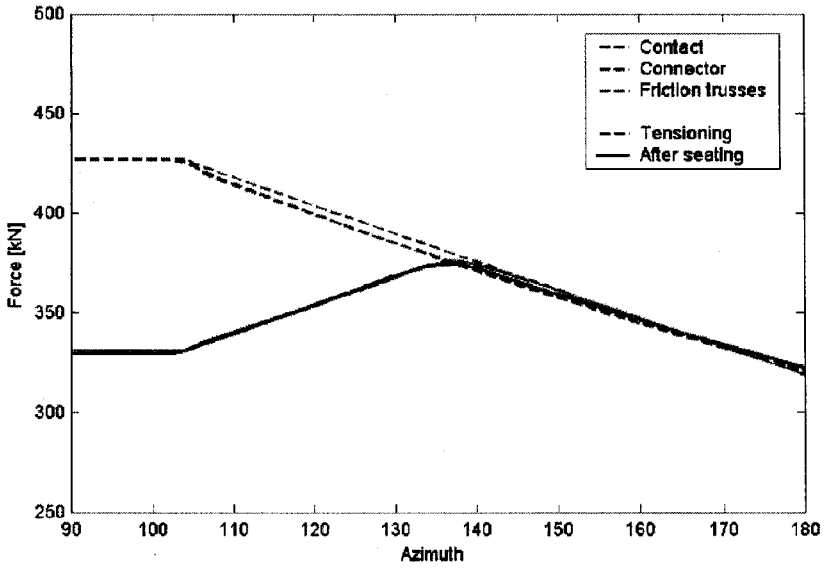

Figure 5.9 Distribution of pre-stressing force for unbonded tendons at tensioning using different modeling techniques.

During pressurization the method using friction trusses has been excluded due to the fact that the direction of the friction trusses has to be modified when the friction force changes direction. The direction of the friction force changes several times, see Figure 5.14. The three remaining methods can in an accurate way capture the changes in tendon force distribution along the tendon during pressurization.

Figure 5.10 and Figure 5.11 present the tendon stresses after tensioning and after seating respectively. In Figure 5.12 tendon forces along the tendon at different loading levels are shown.

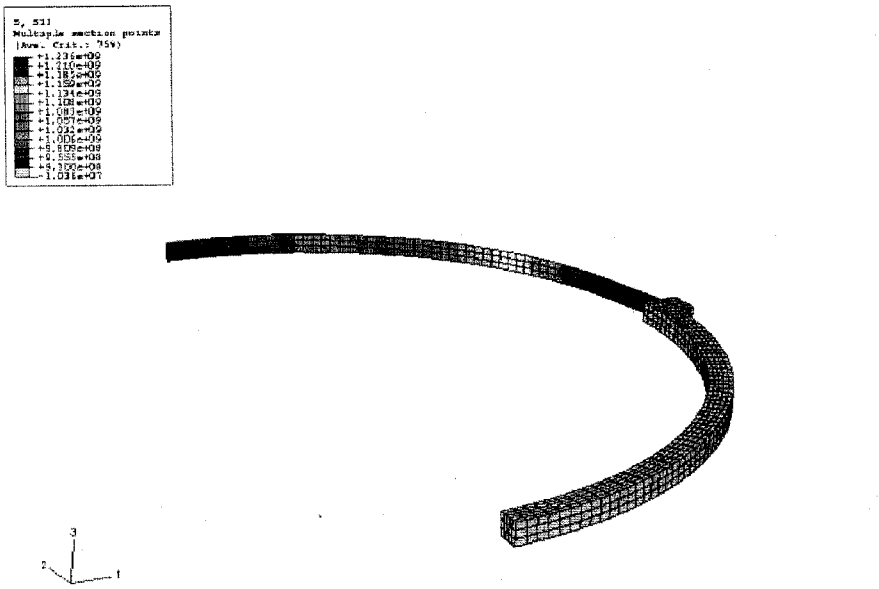

Figure 5.10 Pre-stressing tendons modeled with membrane elements/contact formulation, tensioned using translatory connectors: tensioning phase.

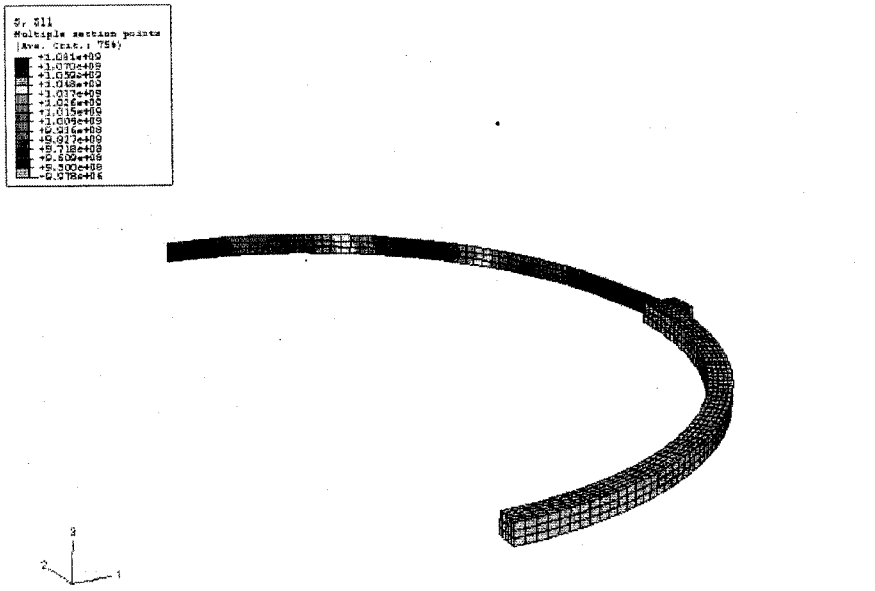

Figure 5.11 Pre-stressing tendons modeled with membrane elements/contact formulation, tensioned using translatory connectors: after seating.

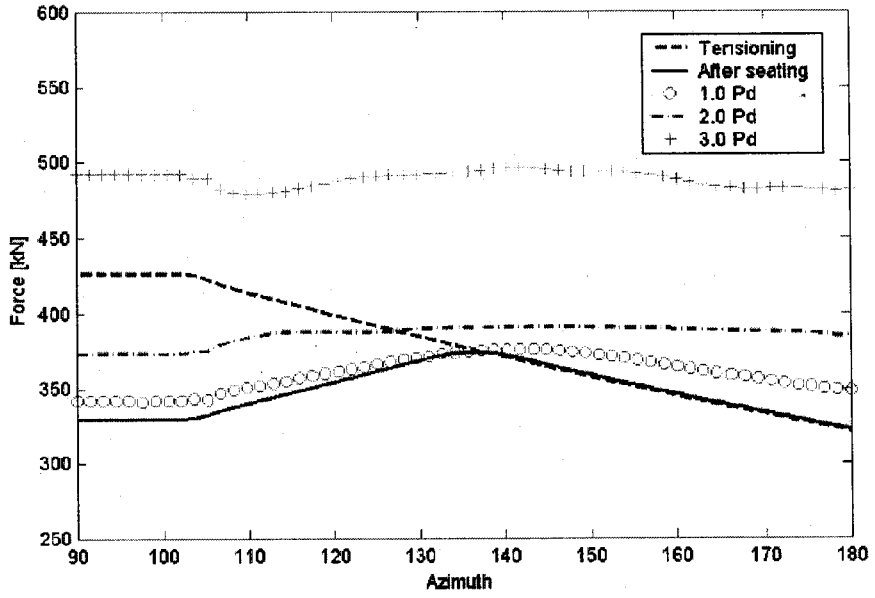

Figure 5.12 Pre-stressing tendons modeled with truss or membrane elements/contact formulation: distribution of pre-stressing force for unbonded tendon at different loading stages.

A comparison with level 2 methods, i.e. modeling the tendons as fully bonded to the concrete during pressurization, is made in Figure 5.13. Here we see that the force in the tendons differ to a great extent in some regions. If these regions coincide with critical areas regarding leak-tightness, the difference has a non-negligible effect.

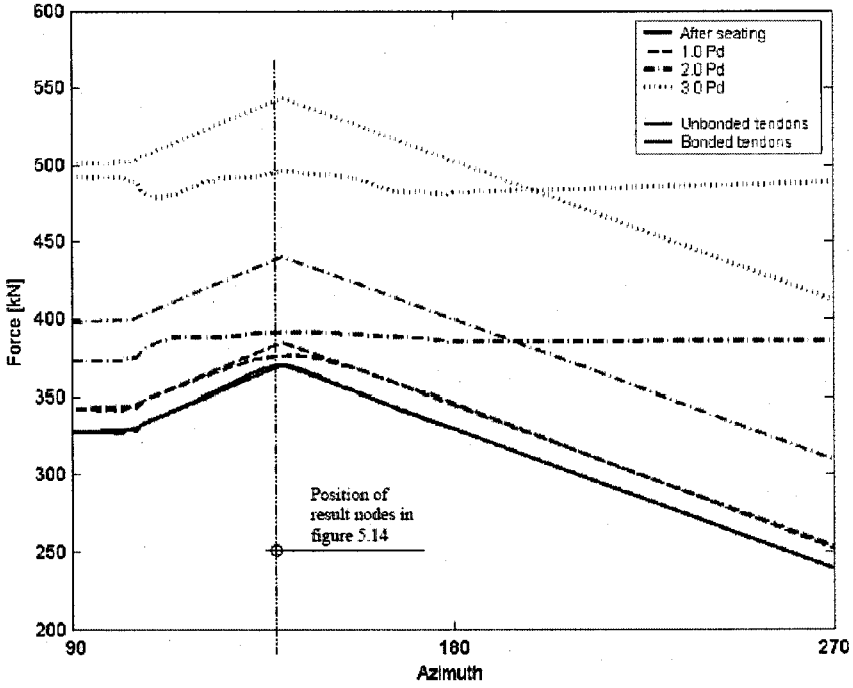

Figure 5.13 Pre-stressing tendons modeled with truss or membrane elements/contact formulation: distribution of pre-stressing force for unbonded tendon at different loading stages. As comparison, theoretically determined force distribution for fully bonded tendon, and uniform strain along the tendon, are shown.

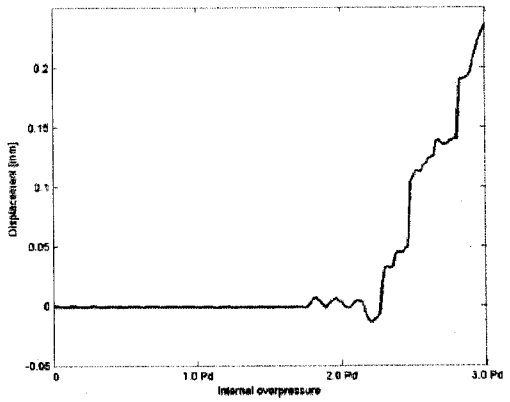

Figure 5.14 Differential displacement between a concretre node and a tendon node due to slippage during pressurization. The node is positioned at approximatly azimuth 120, see figure 5.13.

5.2.6 Conclusions

In Table 5.1 a short summary of the different modeling techniques is given.

As can be seen in Figure 5.13, the re-distribution of the tendon force along the tendon occurs between the overpressurization levels $1*P_d$ and $2*P_d$. Due to the fact that the yielding and rupture of the liner occurs at pressure levels well above this, we have decided to take this phenomena into consideraiton in the 3D-model analysis.

In the 3D-model of the model containment a combination of trusses and membranes have been chosen for the modeling of the tendons together with the contact formulation/friction coefficient to simulate the interaction between tendons and concrete, see section 5.2.1 and 5.2.2.

Method Area	Contact (sections 5.2.1, 5.2.2)	Friction connector (section 5.2.3)	Friction trusses (section 5.2.4)
Simulation capabilities	Tendon force distribution along the tendon during tensioning and seating automatically calculated. Friction coefficient has to be specified as input data. Re-distribution of tendon force during pressurization automatically calculated. Increase in friction force during pressurization automatically calculated. Can be used both for implicit and explicit codes, but convergence problems can occur when using implicit codes.	Tendon force distribution along the tendon during tensioning and seating automatically calculated. Friction forces has to specified as input data. Re-distribution of tendon force during pressurization automatically calculated. Increase in friction force during pressurization has to be specificed as a function of the pressure load and given as input data. Can be used both for implicit and explicit codes.	Tendon force distribution along the tendon during tensioning and seating calculated. Change of model necessary when friction force changes direction, i.e between the tensioning and the seating phase. Angle of friction implicitly specified when defining geometry. Re-distribution of tendon force during pressurization automatically calculated only as long as the direction of the friction forces not change, otherwise the model has to be changed as stated above. Increase in friction force during pressurization automatically calculated. Cannot be used with explicit codes or using large deformation theory with implicit codes.
Computational runtime	1	~ 0.5	~ 0.5
Modeling effort	1 (tendons modeled with trusses) ~ 0.75 (tendons modeled with membranes)	~ 2	~ 4
Comments	Modeling technique selected to be used in the 3D-model (section 6).		

Table 5.1 Comparison between friction modeling methods when modeling unbonded pre-stressing tendons.

6. MAIN ANALYSIS: GLOBAL THREE-DIMENSIONAL MODEL

6.1 General

The axi-symmetrical approach applied in the parametrical studies (section 4) provides a first estimate regarding the global response of the structure. However, the axi-symmetrical model is not capable of catching effects due to for example major penetrations, pre-stressing buttresses, non-uniform layout of the pre-stressing tendons and reinforcement, and the non-uniform and pressure-dependent pre-stressing effects. These effects will to a major extent influence the structural behaviour of the containment, including overpressure levels at leakage and collapse, as well as rupture positions. To take into consideration all these matters, a fully three-dimensional model has to be used.

Modeling assumptions are based on the parametrical studies carried out in section 4, and the investigation regarding modeling techniques for unbonded tendons presented in section 5.

6.2 Structural model

6.2.1 Geometry

The global three-dimensional model has been established out of drawings provided in [2]. General dimensions are presented in section 3 above. The model is shown in Figure 6.1, Figure 6.2 and Figure 6.3.

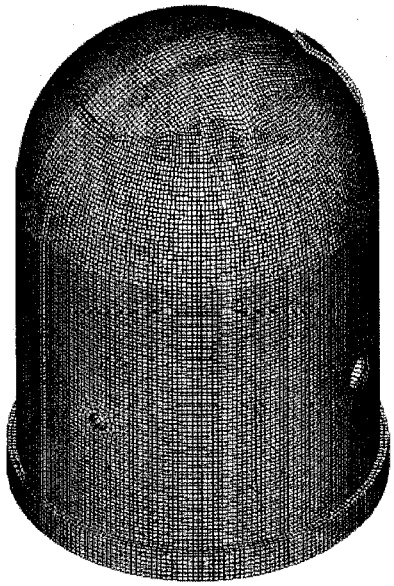

Figure 6.1 Global three-dimensional model.

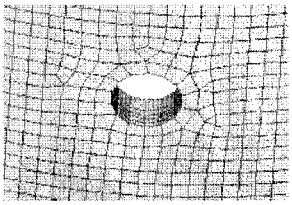

Figure 6.2 Global three-dimensional model, modeling of A/L.

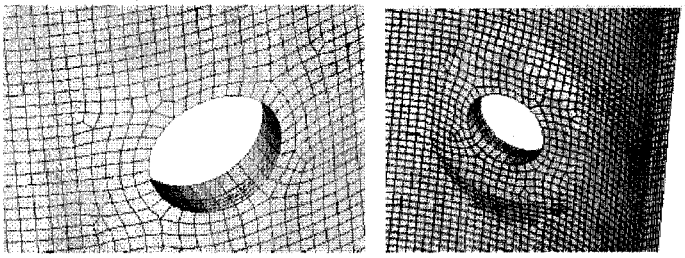

Figure 6.3 Global three-dimensional model, modeling of E/H, outside (left) and inside (right).

6.2.2 Types of element

The concrete parts are in the FE-model represented by rectangular solid continuum elements with a reduced number of integration points denominated C3D8R. The steel liner is represented by rectangular shell elements denominated S4R. A very limited number of the elements are triangle elements denominated C3D6R and S3R respectively. The pre-stressing tendons are modeled by using both truss and membrane elements. The reinforcement are described by using the rebar modeling feature in ABAQUS. The reinforcement are then modeled by rebars in form of a layer inside the underlying continuum elements (concrete).

6.2.3 Boundary conditions

Only a minor part of the basemat is included in the FE-model, the part between the cylindrical wall connection and the tendon gallery, i.e. approximately corresponding to the cast stage $F3_B$, see Figure 3.8 in section 3. The bottom and the vertical faces of the basemet part are constrained in both the vertical and the horizontal direction. No constrains are applied on the nodes situated directly above the tendon gallery. Constrained nodes are shown in Figure 4.3.

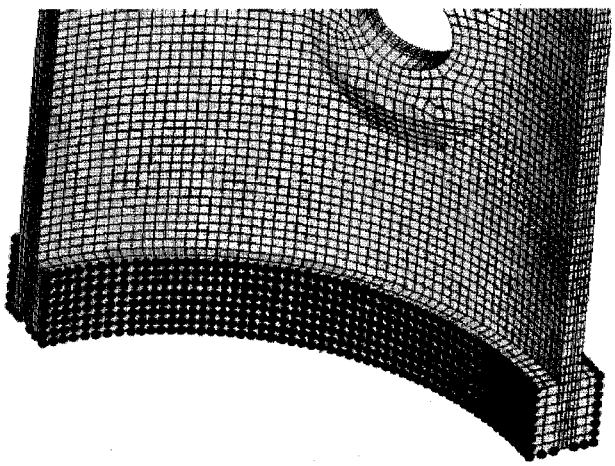

Figure 6.4 Boundary conditions applied to the basemat part.

6.2.4 Contact

In order to get a realistic interaction between the pre-stressing tendons and the concrete, contact definitions have been introduced in the model. In the contact definition the coefficient of friction between the structural parts has to be defined. The coefficients of friction controls the amount of transferable shear force between the tendon and the concrete due to compressive stress over the contact surface. When tensile stresses occur over the contact surface, neither normal stresses or shear stresses can be transferred.

In Figure 6.5 the principles of contact definition between the pre-stressing tendons and the concrete are presented.

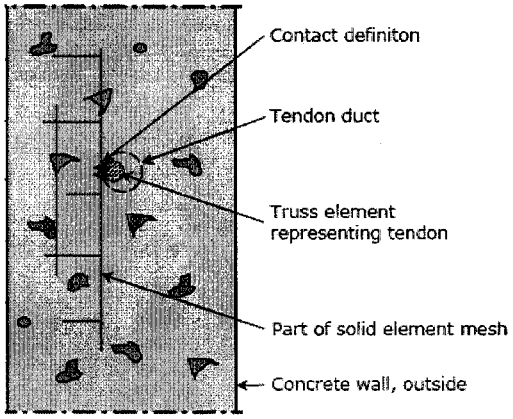

Figure 6.5 Contact definition between pre-stressing tendon and concrete.

6.2.5 Pre-stressing tendons

The tendons are connected to the concrete by applying a contact definition, see section 6.2.4 above, i.e. they are modeled as un-grouted (unbonded). The tensioning of the tendons is modeled by using translator connector elements, connecting the end of the tendons to a steel anchorplate. The anchorplate is connected to the buttress concrete. The tensioning and seating process are then simulated in the analysis, stretching the tendons with the help of the connector element to the same amount as done with the jack during construction, see Figure 6.6.

This procedure gives rise to an un-evenly distributed tendon force along the length of the tendon, due to the friction specified in the contact definition, thus matching the actual tendon force variation.

With the method chosen for the modeling of the tendons, during pressurization, the pre-stressing force along the tendon is automatically changed from an un-even distribution to a more or less evenly distributed force, see section 5.2.1 and Table 5.1.

The tendons in the horizontal direction are tensioned to a maximum stress after seating of 1120 MPa, corresponding to a pre-stressing force of 380 kN, and the tendons in the vertical direction to 1280 MPa, corresponding to a force of 435 kN. The modeling of the tendons is shown in Figure 6.7 and Figure 6.8.

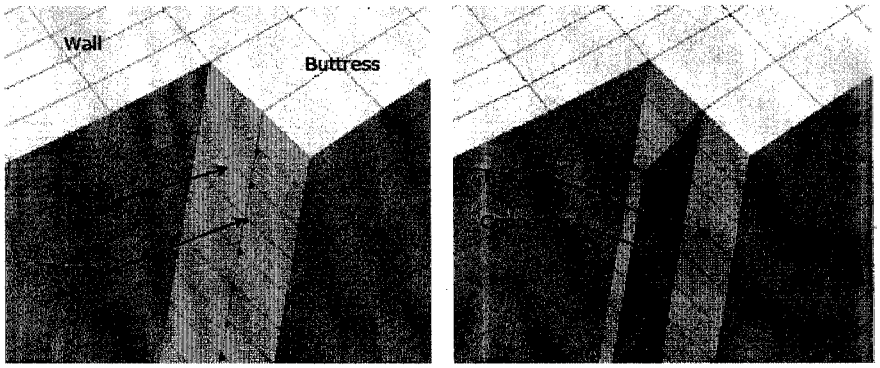

Figure 6.6 Tensioning of cables using Connector elements: before tensioning (left) and after tensioning (right) respectively.

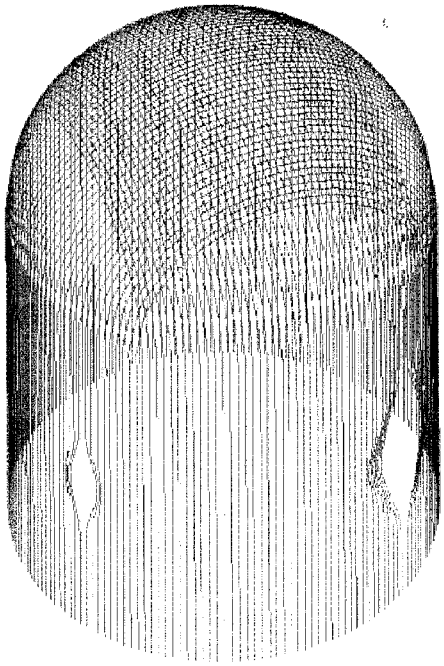

Figure 6.7 Vertical pre-stressing tendons.

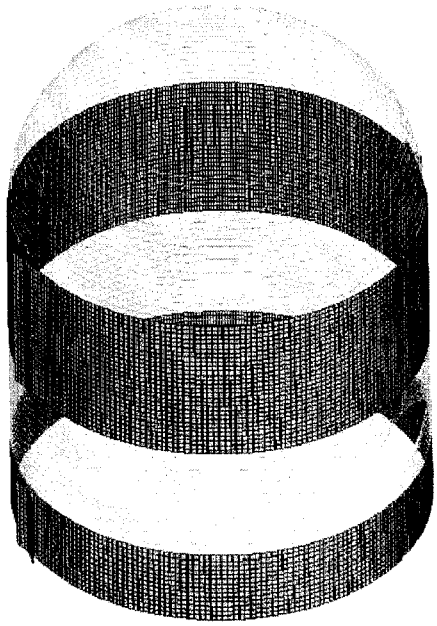

Figure 6.8 Horizontal pre-stressing tendons.

6.2.6 Reinforcement

The reinforcement bars at the inner and outer surface of the model containment are in principle modeled as shown in Figure 6.9 and Figure 6.10. The different colours represent regions with different reinforcement content. The rebars are rigidly connected to the concrete as described in section 6.2.2 above.

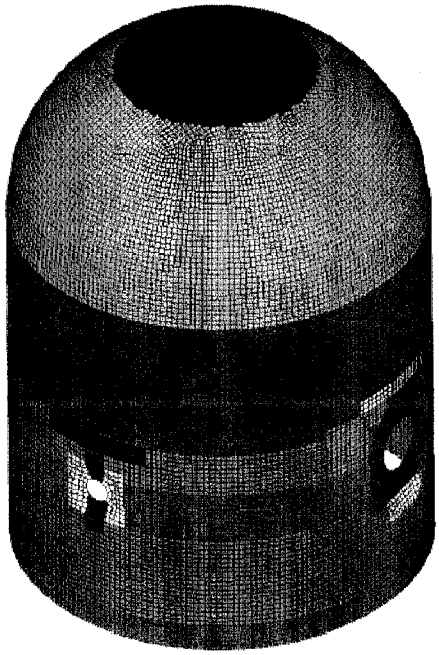

Figure 6.9 Reinforcement regions, inner surface.

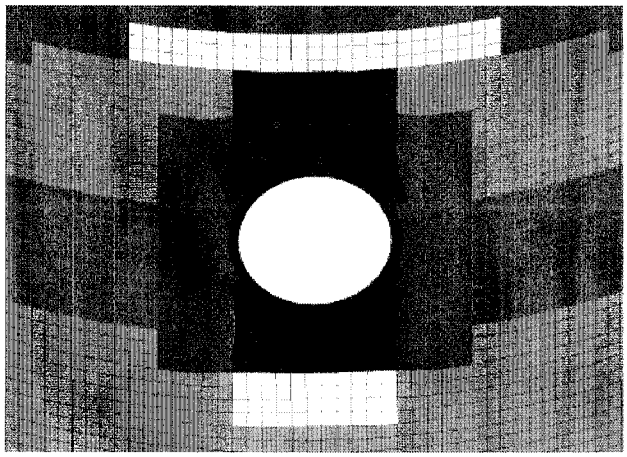

Figure 6.10 Reinforcement regions, inner surface, around E/H.

6.2.7 Steel liner

The steel liner is positioned on the inside of the containment and is rigidly connected to the concrete elements.

6.2.8 Application of loads

Dead weight is modeled applying a field of gravity acting downwards, using the gravitational constant 9.81 m/s^2.

The internal overpressure is applied as a linear monotonic increasing pressure load at the inner face of the containment, i.e. to the shell element representing the steel liner.

Since an explicit dynamic analysis has been executed the load has been applied quasi-statically during a sufficient long period of time, in order not to introduce any dynamical effects on the structure, i.e. inertia forces and kinetic energy can be regarded as negligible. This means for the 3D-model a loading-rate of 1000 kPa/s according to Figure 6.11. The internal overpressure in the containment has been limited to 2000 kPa, which is well above the ultimate load bearing capacity of the containment model.

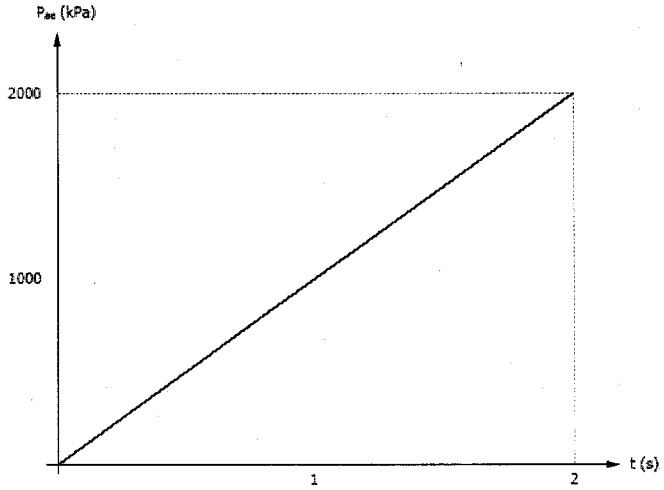

Figure 6.11 Load-time history of the internal overpressure in the explicit dynamic analysis.

7. STRUCTURAL ANALYSIS AND RESULTS

7.1 General

In this chapter the results from the structural analysis are compared to test data at pre-defined positions. In addition, pressure-levels corresponding to important characteristic events, i.e. cracking of concrete, yielding of the steel liner, and tendon rupture leading to burst of the structure, are estimated. An estimation of pressure-level at first leakage, i.e. liner rupture, is somewhat cumbersome to carry out because of the large rupture strain of the liner given by material tests, even for the welded zones. The load level at leakage has in principle to be estimated using more detailed models (modeling approach level 3 and 4 according to Figure 2.1) taking into consideration major penetrations, localized strains, construction details and workmanship etc. Therefore, no prediction of these pressure levels has been made within the scope of this report. Instead, the maximum steel liner strain in the analysis is provided at the test pressure levels corresponding to first leakage and excessive leakage respectively.

In addition to the pressure levels, factors of the design pressure P_d (0.39 MPa internal overpressure) are shown in tables and in result diagrams to facilitate the result interpretation.

All results presented, if not otherwise stated, are taken from the main analysis using the global three-dimensional model.

7.2 Result summary of important events and output parameters

7.2.1 General

Major characteristic events of interest are;

- Start of non-linear structural response, i.e. cracking of concrete.
- Risk of leakage, i.e. yielding of steel liner.
- Excessive leakage, i.e failure of steel liner.
- Collapse of the structure, i.e. failure of tendons.

In Table 7.1 overpressure levels, when these events occur during the experimental tests, are presented and compared with estimated values from the three-dimensional model and the axi-symmetrical model analysis. The events are then discussed in more detail in section 7.2.2 – 7.2.5.

In section 7.2.6, a summary of the outcome of overpressure histories at pre-defined positions for several output parameters is presented. Detailed output parameter results are presented in section 7.3.

Model	Concrete	Steel liner			Hoop tendons			Unit
	Cracking	Yield	First failure	Excessive leakage	Yield	2%	Failure	
Test	**0.59-0.78** 1.5-2.0	- [1]	**0.98** 2.5 0.17 %[2]	**1.29** 3.31 0.42 %[3]	**1.17** 3.0	-	**1.4** 3.59	MPa *P_d
3D	**0.55-0.7** 1.41-1.79	**0.8** 2.05	- - 0.9 %[3]	- - 2.4 %[3]	**1.12** 2.87	**1.35** 3.46	**1.38** 3.54	MPa *P_d
Axi	0.52-0.62 1.33-1.59	1.02 2.62	- - 0.17 %[3]	- - 0.42 %[3]	1.29 3.31	1.47 3.78	~1.75 4.49	MPa *P_d

1) A test value of 1.1 MPa is specified. However, the strain gauges were not placed in the position of first yielding.
2) Free field hoop strain given as test result.
3) Maximum strain in the steel liner obtained in the structural analysis at overpressure levels corresponding to first leakage (0.98 MPa) and to excessive leakage (1.29 MPa), respectively. Failure strain of the liner is of the order of 10-20 %. See section 7.1 for discussion.

Table 7.1 Result summary of important events.

7.2.2 Cracking of concrete

In Figure 7.1 predicted initial cracking of the concrete is shown. As can be seen the first cracking occurs at the major penetrations and near the buttresses.

The major cracking of concrete occurs at overpressure levels of 0.59-0.78 MPa. By analysis predicted overpressure at cracking of concrete is 0.55-0.7 MPa, i.e. that is in good agreement with test results.

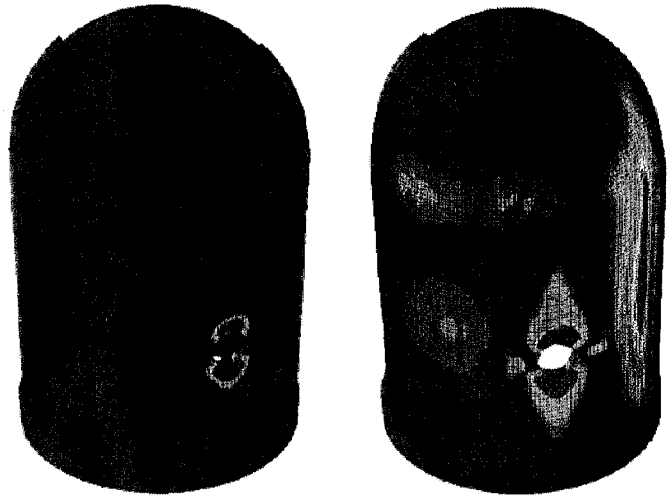

Figure 7.1 Cracking of concrete (red colour indicates the largest cracking).

7.2.3 Steel liner

In Figure 7.2 predicted yielding of the steel liner is shown, and in Figure 7.3 the position of predicted yielding is compared with steel liner rupture positions mapped after completion of the overpresurization test. The analysis results and test results agree well.

As can bee seen in Figure 7.3, the position of first yielding near the equipment hatch (E/H) predicted by the analysis (position I) differ to a small extent from the actual rupture position during test. This is due to the fact that the rupture of the liner during the test occurs at a position where the thickness of the steel liner changes. This sectional change is not included in the model used, giving a rupture position placed underneath the E/H instead of at the side of the hatch.

The first yielding of the steel liner during test is registred for an overpressure of 1.1 MPa. However, the strain gauges measuring the strains in the steel liner are not placed at the position for first yielding, i.e first yielding has to occur at an lower overpressure level. By analysis, predicted first yielding of the steel liner occurs at an overpressure of 0.8 MPa, which is in agreement with the conclusions stated above.

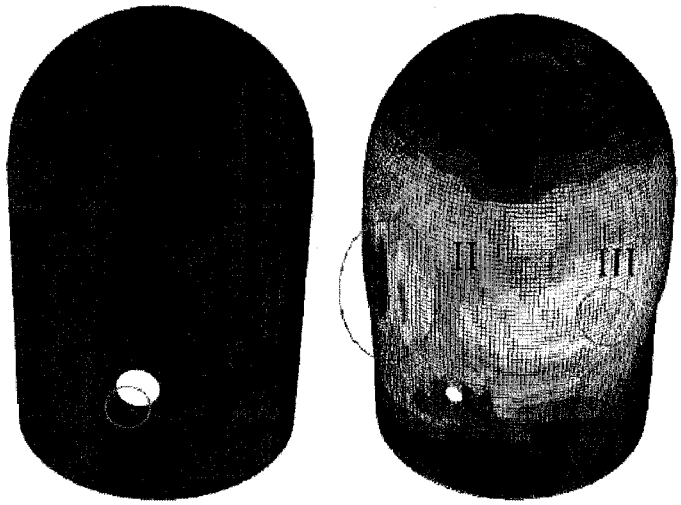

Figure 7.2 Yielding of steel liner (red colour indicates maximum yielding).

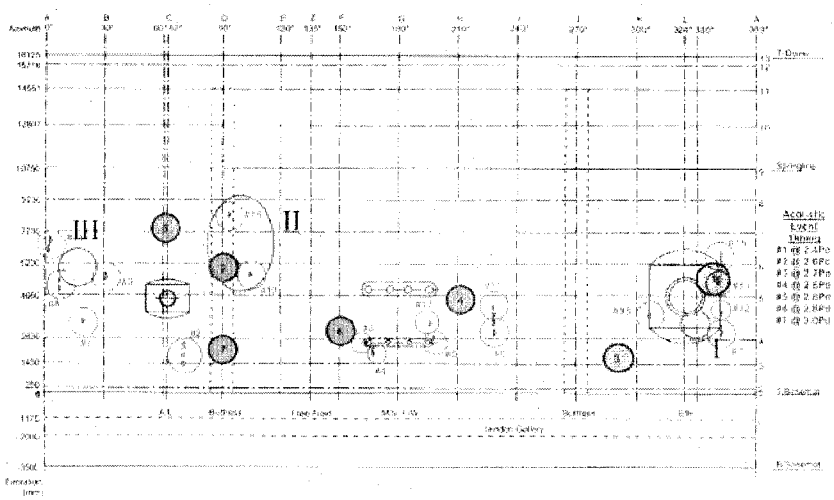

Figure 7.3 Liner rupture positions from test compared with analysis results.

7.2.4 Collapse of structure

In Figure 7.4 (left) the predicted position of rupture of the containment during structural collapse is shown. The predicted position agrees very well with the actual rupture (burst) position during test, as can be seen in Figure 7.4 (right).

Collapse of the model containment during the test occurred at an overpressure level of 1.4 MPa. By analysis, using the 3D-model, collapse was predicted to occurre at an overpressure of 1.38 MPa, in good agreement with test data. The axi-symmetrical model, however, overestimate the load-bearing capacity of the containment, predicting a collapse pressure of more than 1.75 MPa.

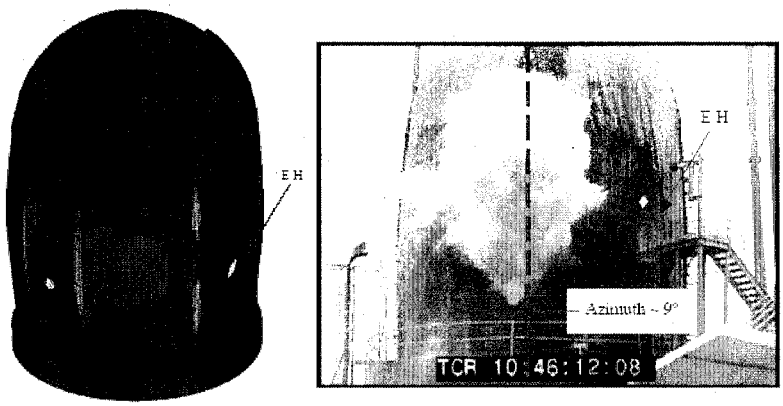

Figure 7.4 Rupture position (red colour).

7.2.5 Results at pre-defined positions

Results for several output parameters as a function of overpressure are presented in section 7.3 for different pre-defined positions in the structure, in total 55 diagrams. These result outputs correspond to experimental test data positions. In Table 7.2 below, a summary and evaluation of the analysis results is presented.

The most important result parameters are the radial deformation, strains in the steel liner and strains in the tendons. This is due to the fact that the radial stresses and strains governs the capacity of the model containment, not the stresses/strains in the vertical direction. Further more, the strain in the liner is the most important parameter to determine the leak-tightness capacity, and the strains in the tendons, the corresponding parameter to govern the load-bearing capacity. For these parameters there is good agreement between measured test data and calculated analysis results. The same applies for vertical deformation and rebar strain.

Result component	Result evaluation
Displacements	
Radial:	Good – very good
Vertical:	Accurate - good
Rebar strain	
Hoop:	Accurate - good
Meridional:	Accurate - good
Liner strain	
Hoop:	Accurate – very good
Meridional:	Accurate – very good
Tendon strain	
Hoop:	Very good
Vertical:	Very good

Table 7.2 Evaluation summary of results for the 55 output locations.

For azimuth 135, the axi-symmetrical model also gives good results regarding displacements. However, due to the fact that the radial displacement varies a lot depending on the circumferential position (azimuth), as can be seen in Table 7.3, it is evident that the axi-symmetrical model is not quite capable of capturing the true behaviour of the containment. For rebar strain the axi-symmetrical model gives poor results, while the three-dimensional models gives good results. Correspondingly for liner strains the 3D-model gives more accurate results than the axi-symmetrical model.

Level	Azimuth	Displacement	
		Measured test data	Results from axi-symmetrical model (azimuth 135)
4.6	66	9 mm	-
	135	8 mm	10 mm
	334	13 mm	-
6.2	90	6 mm	-
	135	10 mm	10 mm

Table 7.3 Comparison between during the test measured radial displacement, at overpressure 1 MPa, in different circumferential positions with displacement calculated using the axi-symmetrical model.

7.3 3D-model analysis

7.3.1 General

The main analysis of the model containment is carried out using a three-dimensional model as discussed in section 2.

In this section analysis results from the 3D-model analysis are compared to test data. For results at azimuth 135 degrees, corresponding results from the axi-symmetrical analysis are also shown for comparison.

7.3.2 Result positions

Results are presented in 55 pre-defined positions corresponding to test data positions. In Figure 7.5 and Figure 7.6 result positions used for presentation are shown. Most of the positions correspond to azimuth 135°, but results are also presented at azimuth 0, 58, 66, 90, 180, 241, 275, 280 and 334 respectively, as indicated in the figures.

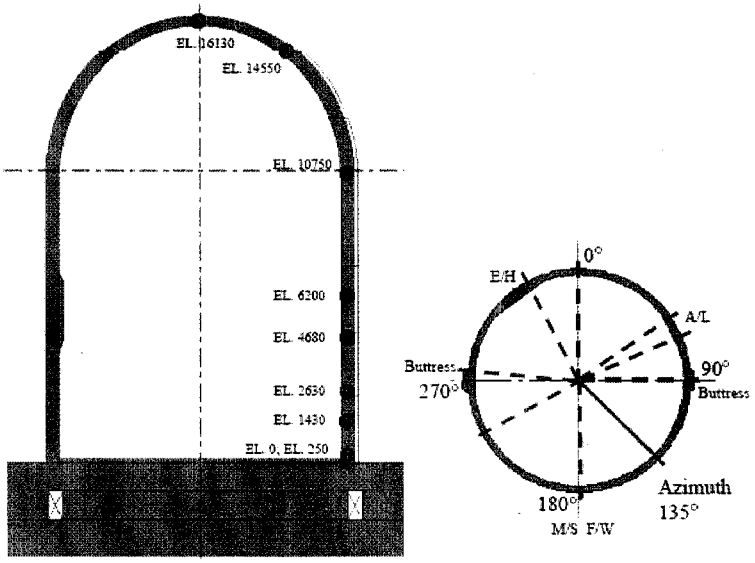

Figure 7.5 Result positions for 3D-model.

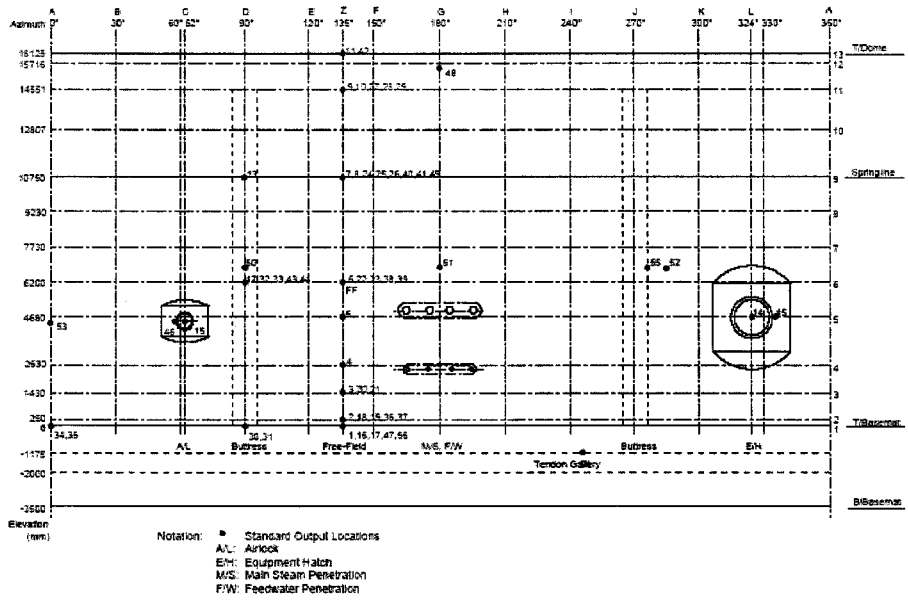

Figure 7.6 Result positions for 3D-model (elevation of inside surface).

7.3.3 Result presentation

7.3.3.1 Displacements

Displacements in the radial direction are presented, using the initial position of the structure before pressurization as reference position. Displacement in the vertical direction are presented with the upper part of the basemat as reference, i.e. excluding any basemat uplift.

In Figure 7.7 to Figure 7.21 analysis results regarding radial and vertical displacement are presented together with measured displacements during the limit state test (LST) of the model containment.

The analysis results agree very well to corresponding test data regarding displacements in the radial direction. The results in the vertical direction also agree well to corresponding test data.

7.3.3.2 Rebar strain

In Figure 7.22 to Figure 7.39 analysis results regarding rebar strain are shown. For the main analysis using the 3D-model the results agree well with test data. However for the axi-symmetrical analysis, a large deviation from test data occurs.

7.3.3.3 Liner strain

In Figure 7.40 to Figure 7.51 analysis results regarding liner strain are shown. The results agree well to corresponding test data.

7.3.3.4 Tendon strain

In Figure 7.52 to Figure 7.58 analysis results regarding tendon strain are shown. The results agree very well to corresponding test data.

7.3.3.5 Result diagrams

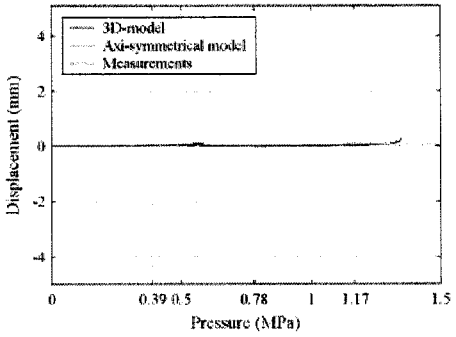

Figure 7.7 Pos. 1-Displacement in vertical direction for el 0.0 and az 135.

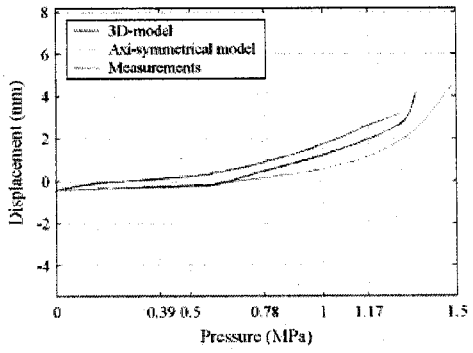

Figure 7.8 Pos. 2-Displacement in radial direction for el 0.25 and az 135.

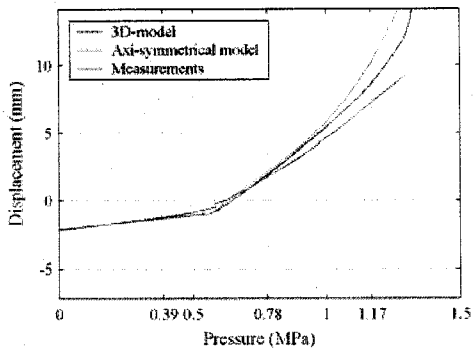

Figure 7.9 Pos. 3-Displacement in radial direction for el 1.43 and az 135.

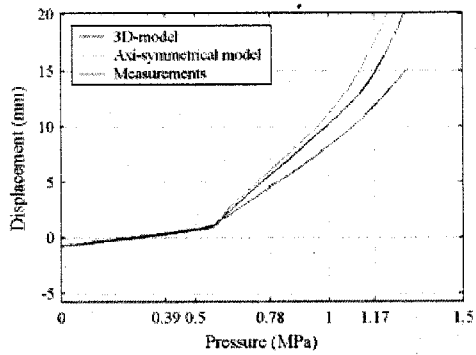

Figure 7.10 Pos. 4-Displacement in radial direction for el 2.63 and az 135.

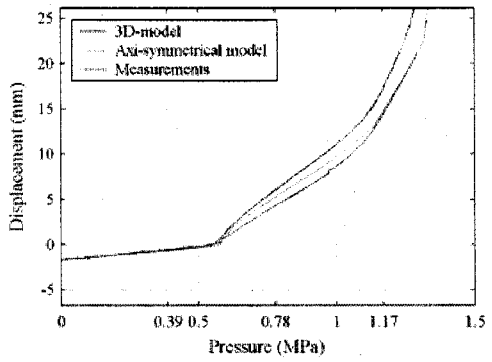

Figure 7.11 Pos. 5-Displacement in radial direction for el 4.68 and az 135.

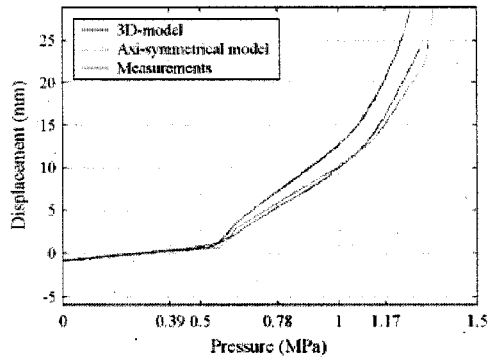

Figure 7.12 Pos. 6-Displacement in radial direction for el 6.2 and az 135.

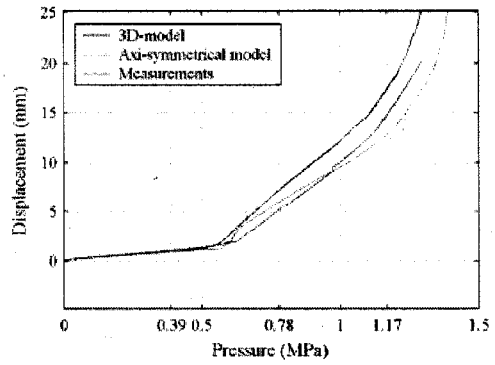

Figure 7.13 Pos. 7-Displacement in radial direction for el 10.75 and az 135.

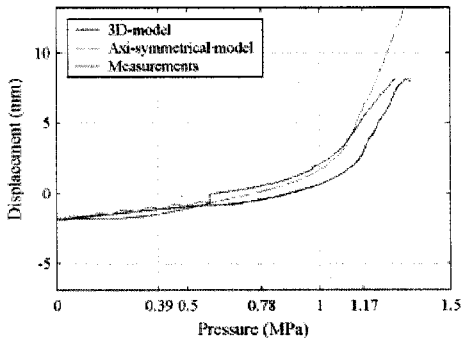

Figure 7.14 Pos. 8-Displacement in vertical direction for el 10.75 and az 135.

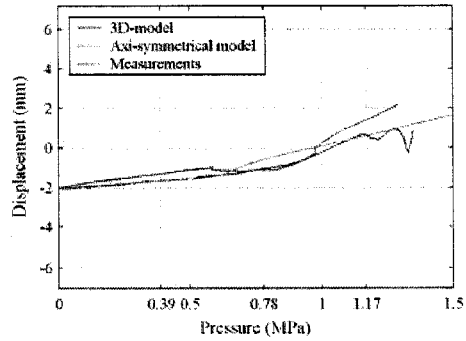

Figure 7.15 Pos. 9-Displacement in radial direction for el 14.55 and az 135.

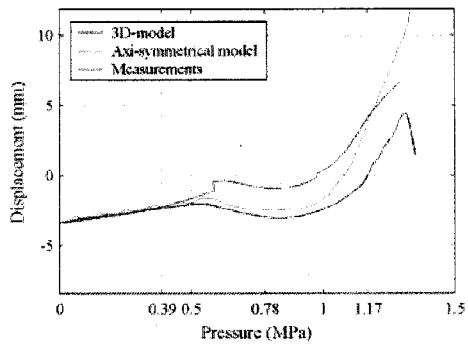

Figure 7.16 Pos. 10-Displacement in vertical direction for el 14.55 and az 135.

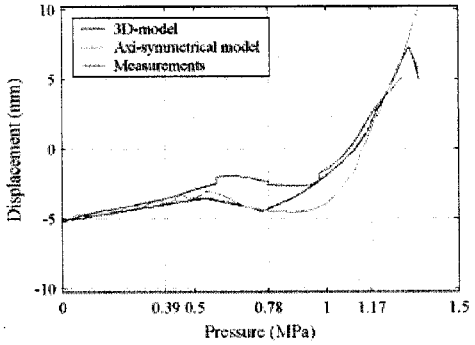

Figure 7.17 Pos. 11-Displacement in vertical direction for el 16.13 and az 135.

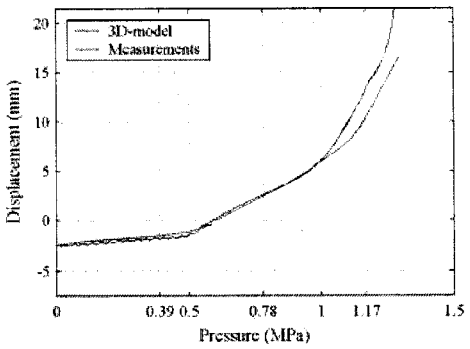

Figure 7.18 Pos. 12-Displacement in radial direction for el 6.2 and az 90.

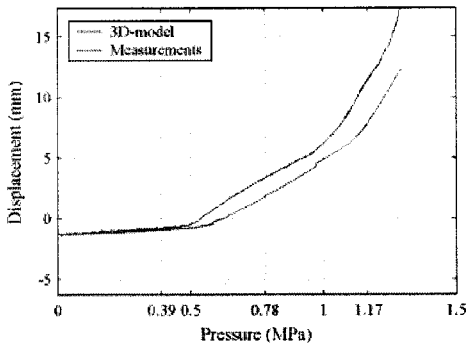

Figure 7.19 Pos. 13-Displacement in radial direction for el 10.7 and az 90.

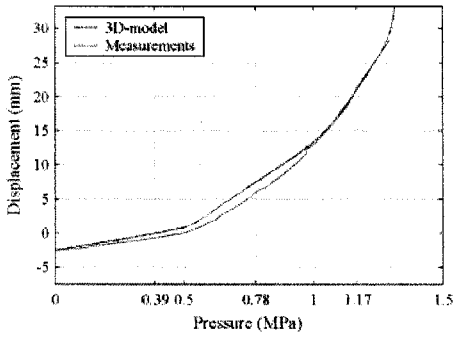

Figure 7.20 Pos. 14-Displacement in radial direction for el 4.675 and az 334.

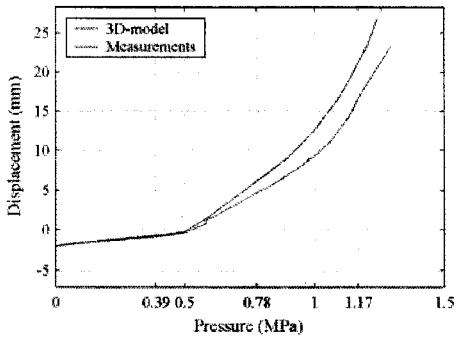

Figure 7.21 Pos. 15-Displacement in radial direction for el 4.525 and az 66.

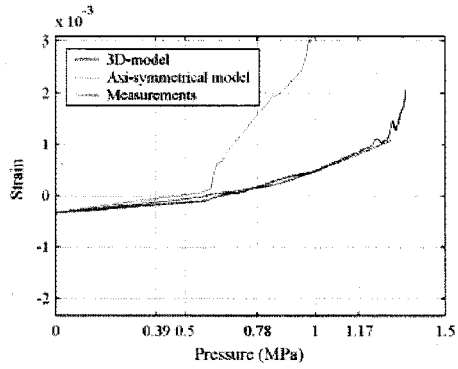

Figure 7.22 Pos. 16-Rebar strain inside layer in meridional direction for el 0.05 and az 135.

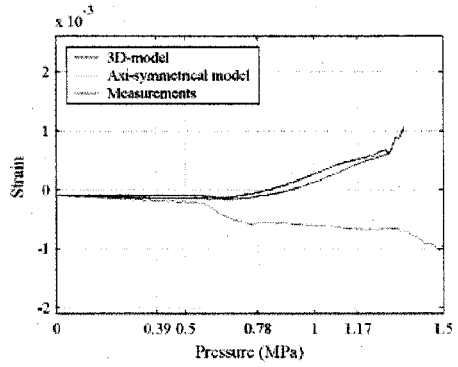

Figure 7.23 Pos. 17-Rebar strain outside layer in meridional direction for el 0.05 and az 135.

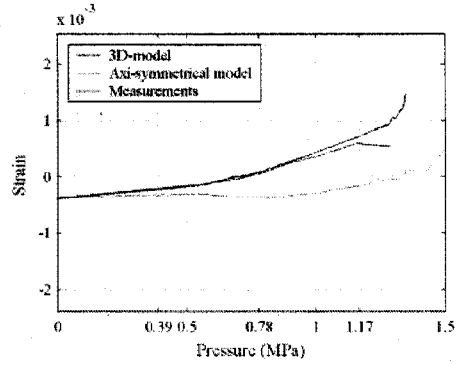

Figure 7.24 Pos. 18-Rebar strain inside layer in meridional direction for el 0.25 and az 135.

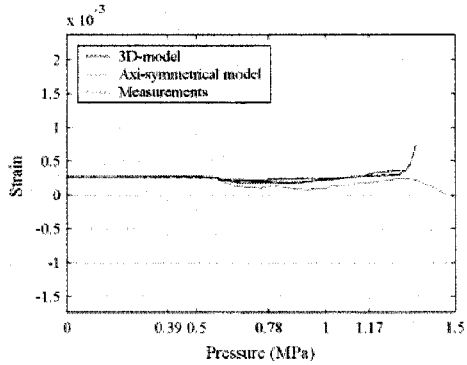

Figure 7.25 Pos. 19-Rebar strain outside layer in meridional direction for el 0.25 and az 135.

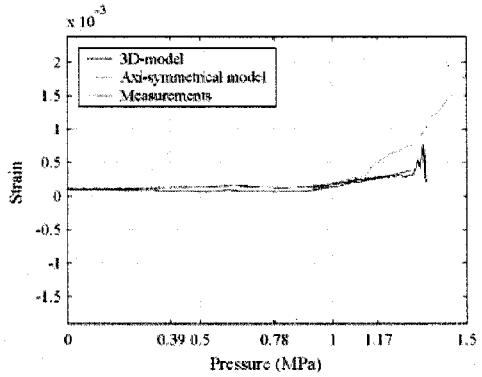

Figure 7.26 Pos. 20-Rebar strain inside layer in meridional direction for el 1.43 and az 135.

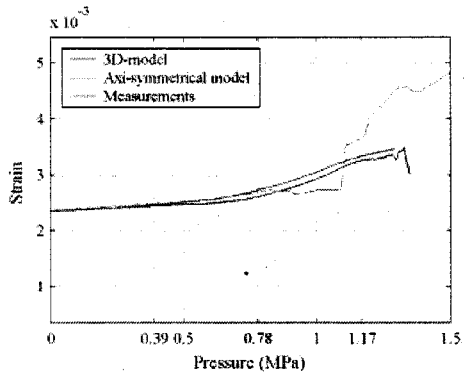

Figure 7.27 Pos. 21-Rebar strain outside layer in meridional direction for el 1.43 and az 135.

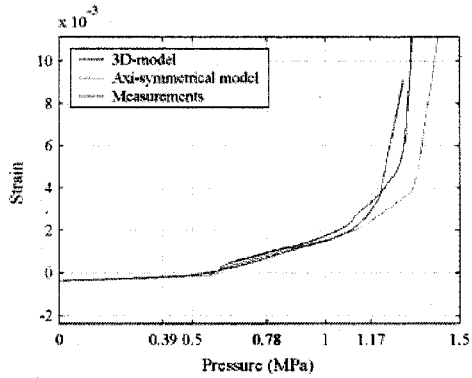

Figure 7.28 Pos. 22-Rebar strain outside layer in hoop direction for el 6.2 and az 135.

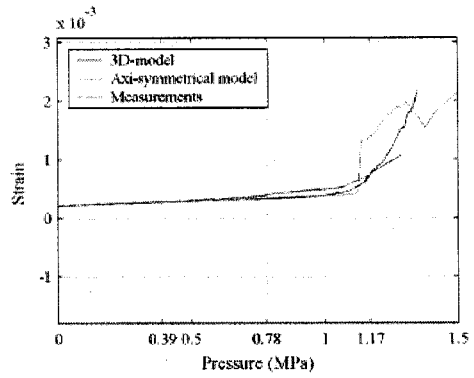

Figure 7.29 Pos. 23-Rebar strain outside layer in meridional direction for el 6.2 and az 135.

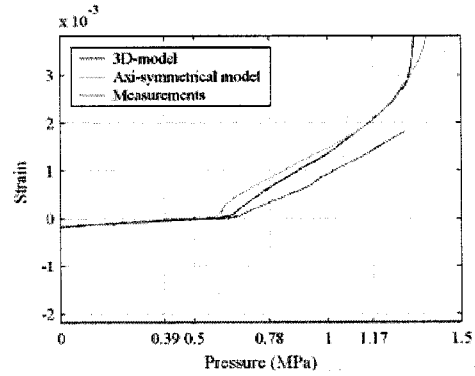

Figure 7.30 Pos. 24-Rebar strain outside layer in hoop direction for el 10.75 and az 135.

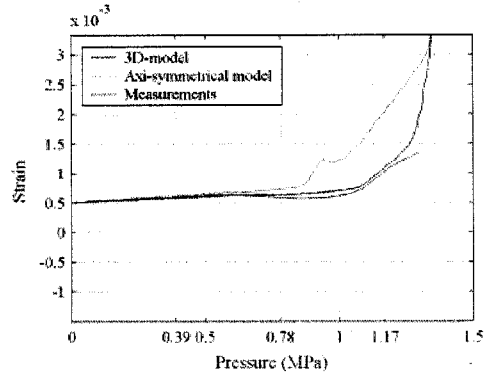

Figure 7.31 Pos. 25-Rebar strain inside layer in meridional direction for el 10.75 and az 135.

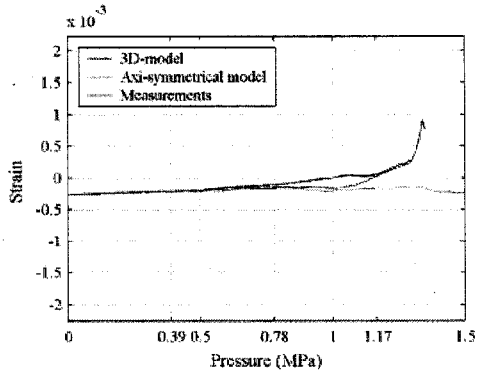

Figure 7.32 Pos. 26-Rebar strain outside layer in meridional direction for el 10.75 and az 135.

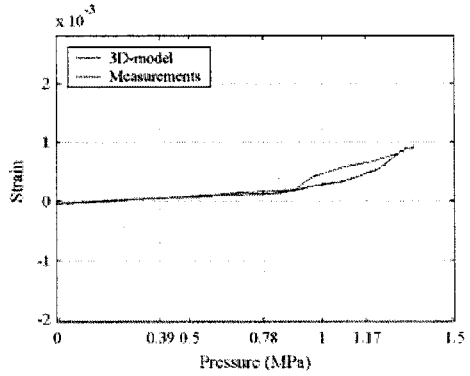

Figure 7.33 Pos. 27-Rebar strain outside layer in hoop direction for el 14.55 and az 135.

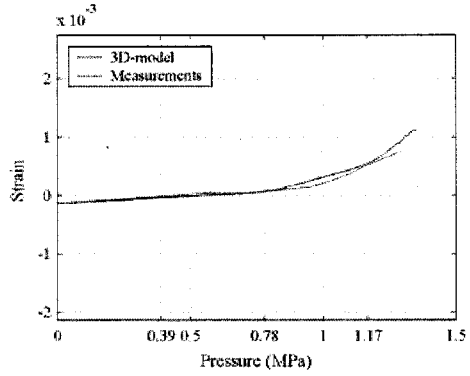

Figure 7.34 Pos. 28-Rebar strain inside layer in meridional direction for el 10.75 and az 135.

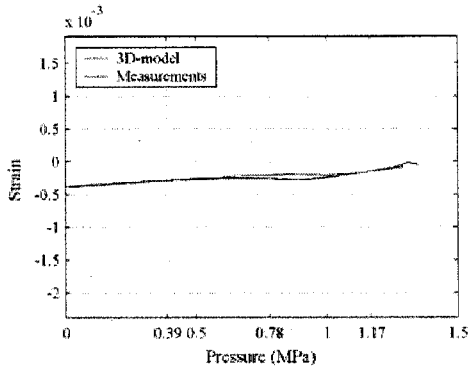

Figure 7.35 Pos. 29-Rebar strain outside layer in meridional direction for el 10.75 and az 135.

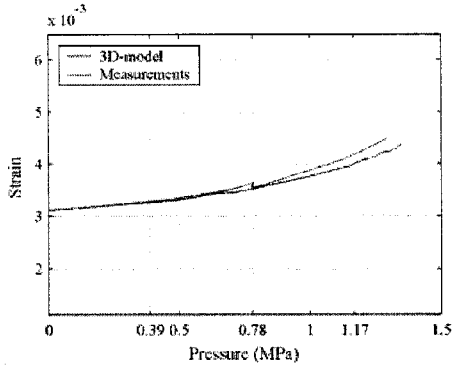

Figure 7.36 Pos. 30-Rebar strain inside layer in meridional direction for el 0.05 and az 90.

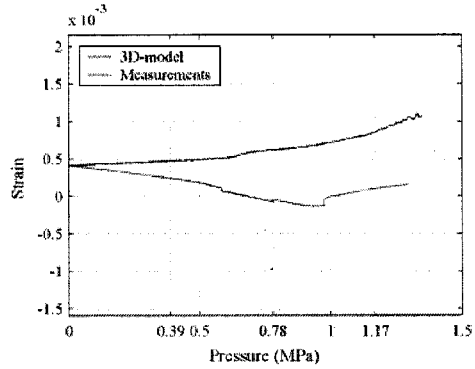

Figure 7.37 Pos. 31-Rebar strain outside layer in meridional direction for el 0.05 and az 90.

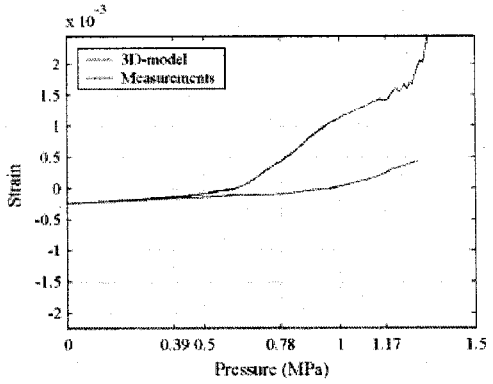

Figure 7.38 Pos. 32-Rebar strain outside layer in hoop direction for el 6.2 and az 90.

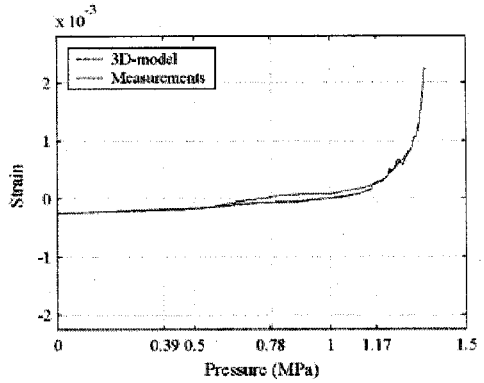

Figure 7.39 Pos. 33-Rebar strain outside layer in meridional direction for el 6.2 and az 90.

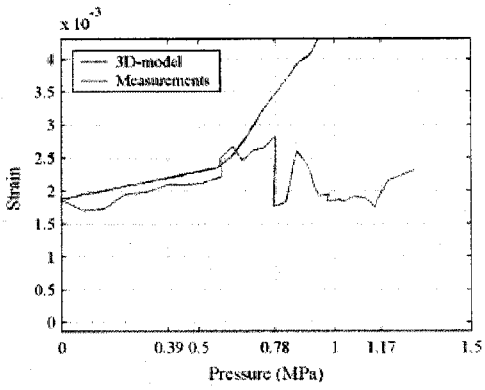

Figure 7.40 Pos. 35-Liner strain in meridional direction for el 0.01 and az 0.

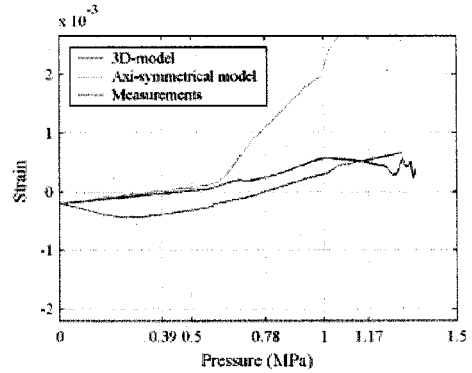

Figure 7.41 Pos. 36-Liner strain in meridional direction for el 0.25 and az 135.

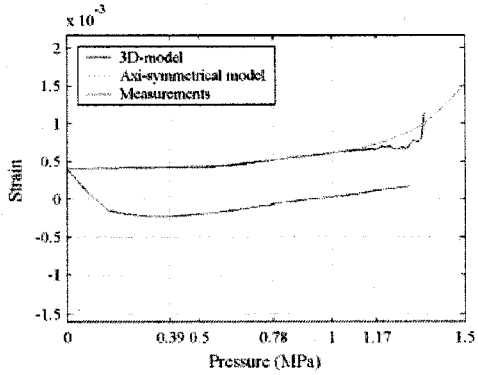

Figure 7.42 Pos. 37-Liner strain in hoop direction for el 0.25 and az 135.

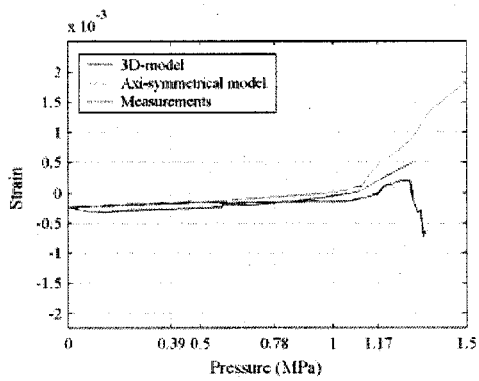

Figure 7.43 Pos. 38-Liner strain in meridional direction for el 6.2 and az 135.

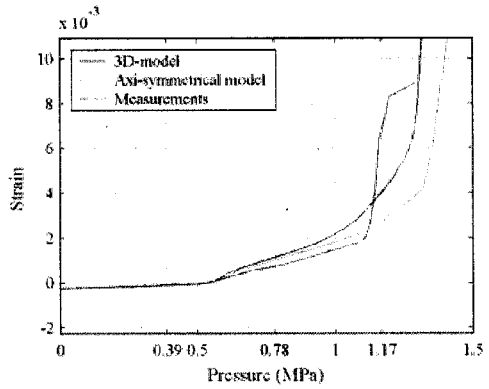

Figure 7.44 Pos. 39-Liner strain in hoop direction for el 6.2 and az 135.

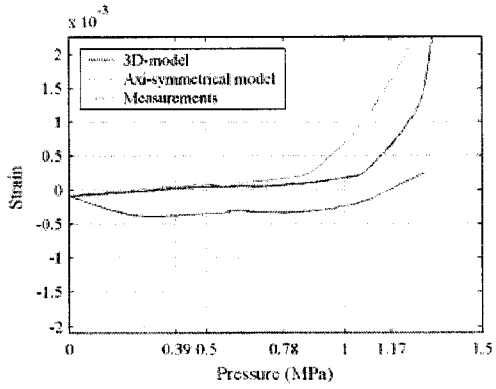

Figure 7.45 Pos. 40-Liner strain in meridional direction for el 10.75 and az 135.

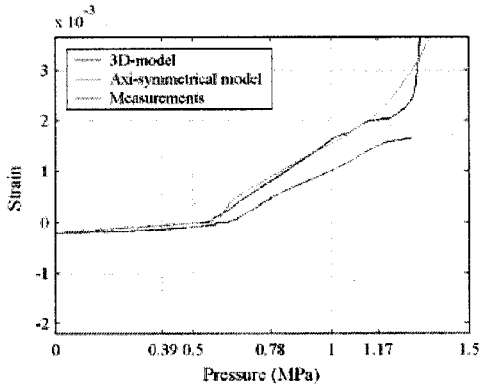

Figure 7.46 Pos. 41-Liner strain in hoop direction for el 10.75 and az 135.

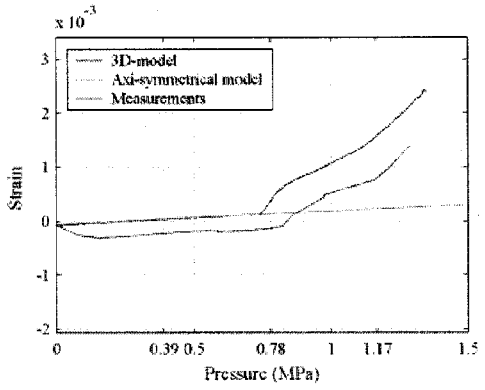

Figure 7.47 Pos. 42-Liner strain in meridional direction for el 16.13 and az 135.

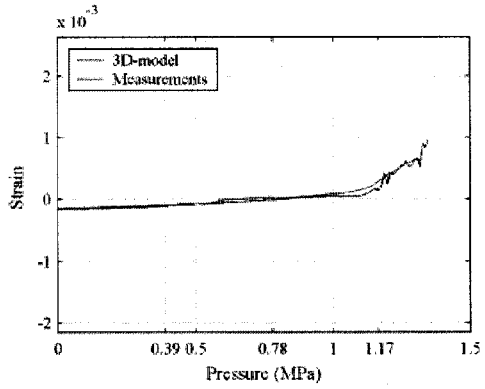

Figure 7.48 Pos. 43-Liner strain in meridional direction for el 6.2 and az 90.

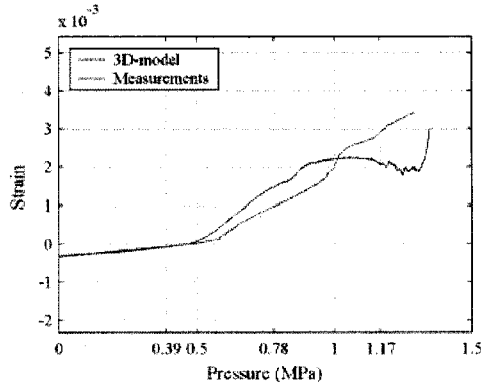

Figure 7.49 Pos. 44-Liner strain in hoop direction for el 6.2 and az 90.

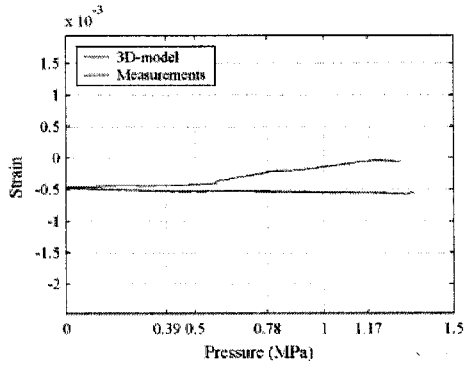

Figure 7.50 Pos. 45-Liner strain in hoop direction for el 4.675 and az 334.

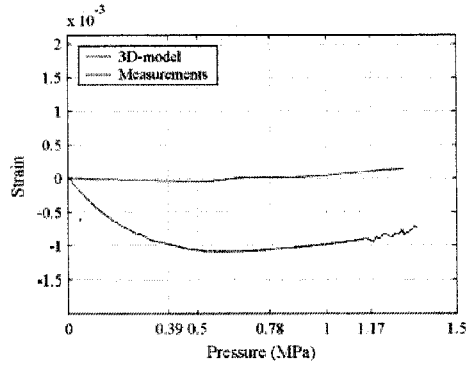

Figure 7.51 Pos. 46-Liner strain in hoop direction for el 4.525 and az 58.

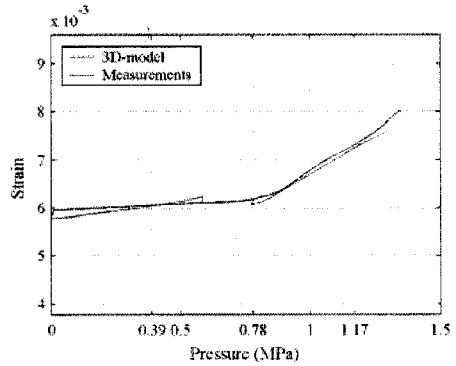

Figure 7.52 Pos. 48-Tendon strain in vertical direction for el 15.6 and az 180.

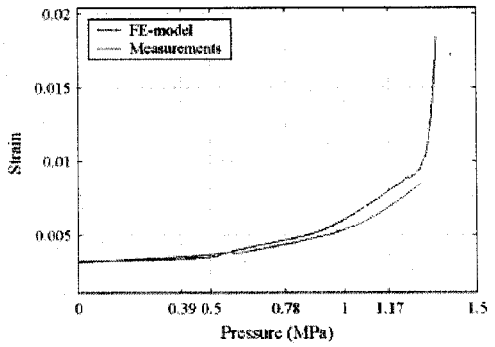

Figure 7.53 Pos. 50-Tendon strain in hoop direction for el 6.58.6 and az 90.

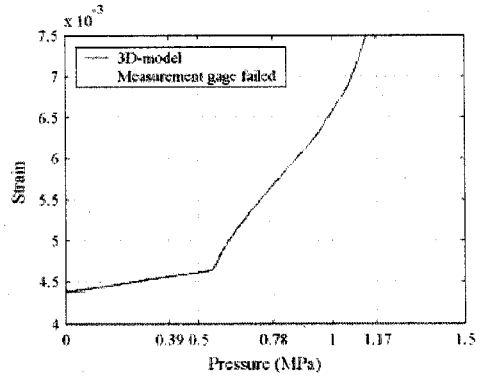

Figure 7.54 Pos. 51-Tendon strain in hoop direction for el 6.58 and az 180.

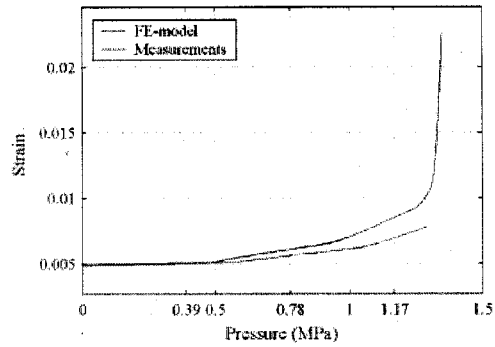

Figure 7.55 Pos. 52-Tendon strain in hoop direction for el 6.58 and az 280.

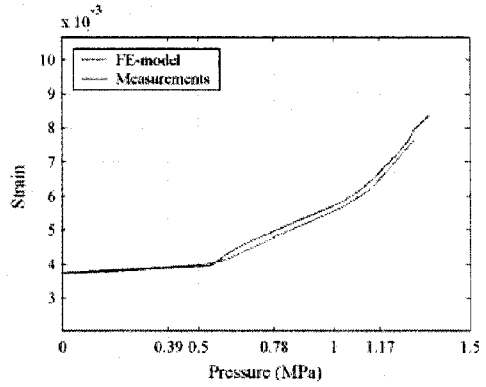

Figure 7.56 Pos. 53-Tendon strain in hoop direction for el 4.57 and az 0.

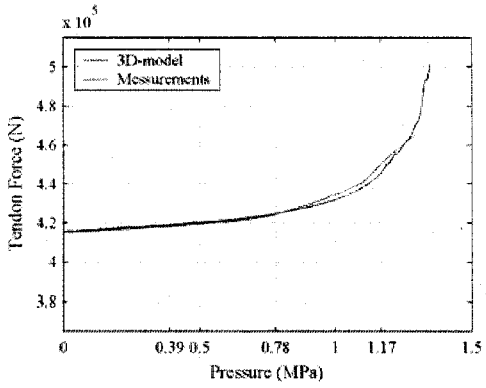

Figure 7.57 Pos. 54-Tendon force in hairpin direction for el-1.16 and az 241.

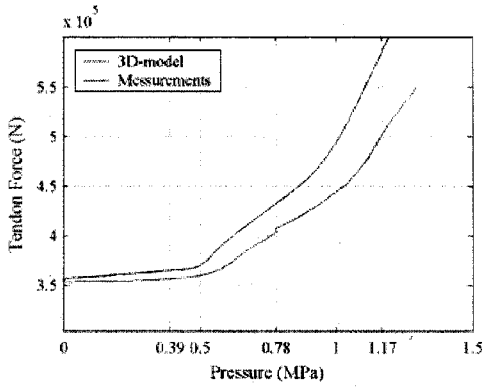

Figure 7.58 Pos. 55-Tendon force in hoop direction for el 6,58 and az 275.

8. REFERENCES

[1] Jovall O. et al, *Concrete containment management and modeling, CONMOD*, in Proceedings of the 17th International Conference on Structural Mechanics in Reactor Technology, SMiRT, Prague, 2003.

[2] Hessheimer M.F. et al, *Overpressurization test of a 1:4-scale prestressed concrete containment vessel model*, NUREG/CR-6810, SAND2003-0840P, Sandia National Laboratories, Albuquerque, 2003.

[3] *ABAQUS Analysis Users Manual*, version 6.4, ABAQUS Inc., Providence 2002.

[4] Dameron R.A. et al, *Posttest analysis of the 1:4-scale prestressed concrete containment vessel model*, NUREG/CR-6809, SAND2003-0839P, Sandia National Laboratories, Albuquerque, 2003.

APPENDIX 1: ISP 48

Phase 1: Data collection and identification

The group of members in ISP 48 agreed on the following basic principles: all participants should use the same data, calculate the same structure, and report on the same positions for comparison. It was also agreed that the most representative data should be used.

It was decided that

- The chairman would send the list of requests for completion to all participants within a week for all of them to comment within one week. The list will then be sent to SNL.
- SNL would provide the list of available data taking into account the list mentioned above to the extent possible. Deadline is Jan 15.
- Considering that participants may use different models, data needed may be different. Consequently, participants would review SNL's list and see if data fitted. Comments would have to be sent to SNL by end of February.
- SNL would deliver the data in a format appropriate with the use of computer codes and standard softwares.

With regard to the location of measurements, the group agreed that it would be easier to use the locations as for the round robin (displacement, strain, rebars strain, etc). The group would check if it was complete enough and make suggestion with regard to possible addition by Jan 15.

Phase 2: Calculation of the LST test (Limit State Test) performed at Sandia - Mechanical loading

Phase 2 will start on April 1, 2003 and delivery of individual reports is expected by the end of Dec 2003.

The following items were agreed upon:

- Computation up to leakage. It was nevertheless recognized that assessment of the time and the value of the leakage was very complicated.
- Displacements and stresses would be compared with test results.
- Concrete cracking, liner tearing and cable rupture would be compared with test results
- Individual reports would be issued by Dec 31, 2003 to SNL and circulated through participants in January 2004.

With regard to Phase 2 synthesis report by SNL, it was agreed that it would include:

- Comparison of all results including sensitivity of the results to models

- Proposals for transposition to real size containments.

With regard to the completion of Phase 2, it was agreed that a meeting would be held in Feb 2004 with the following preliminary agenda:

- Presentation of Phase 2 synthesis report
- Individual presentations on phase 2 calculations
- Conclusions by the group including thoughts on transposition to real size containments
- Definition of Phase 3 exercise including the data and thermal hypothesis to be used for the exercise

Phase 3: Calculation of the response under both mechanical and thermal loadings.

Considering that models would have been checked out against the test under mechanical loading after Phase 2, the objective of Phase 3 is to study the effect of temperature on the global behavior of the structure.

Although there was no test supporting this calculation, the group agreed that an increase in temperature was better and more realistic than a constant temperature. They thus approved the proposal made by IRSN to use the pressure and thermal loadings as defined in WASH1400. IRSN will provide the group with the evolution of temperature and pressure versus time by the end of March 2003.

As said before, the group decided to discuss thoroughly thermal hypothesis and data to be used during the phase 2 meeting. Nevertheless, the following were agreed upon:

- Temperature will be applied on the surface of the liner;
- Contact (i.e. no air gap) will be assumed between the liner and the concrete. The transfer coefficient will be specified;
- Boundary conditions will be the same for all participants and will be specified;
- Calculation should be performed up to 24 hours or up to rupture whichever comes first;
- As to results, it was decided to compare, at several times to be defined:
    - the temperature profile through the thickness;
    - tendon, liner stresses (to be determined);
    - displacements (less points that in phase 2 will be selected based on phase 2 results);
    - crack patterns;
    - etc

Individual reports will be delivered at the end of phase 3.

The duration of Phase 3 is still under discussion. This item is discussed under Phase 4 below.

Phase 4: Reporting, Workshop

The group decided that the ISP should be completed and presented at the June 2005 CSNI meeting.

Based on that, it was agreed that:

- a Workshop would be held in April 2005 to allow time for conclusions and recommendations to be written;
- the individual phase 3 reports should be delivered to SNL, copy to all, about 6 months before (i.e Nov 2004);
- between those dates, SNL would draft the phase 3 synthesis report and the outline of the draft final synthesis report with inputs from all participants.

ISP 48 time-schedule

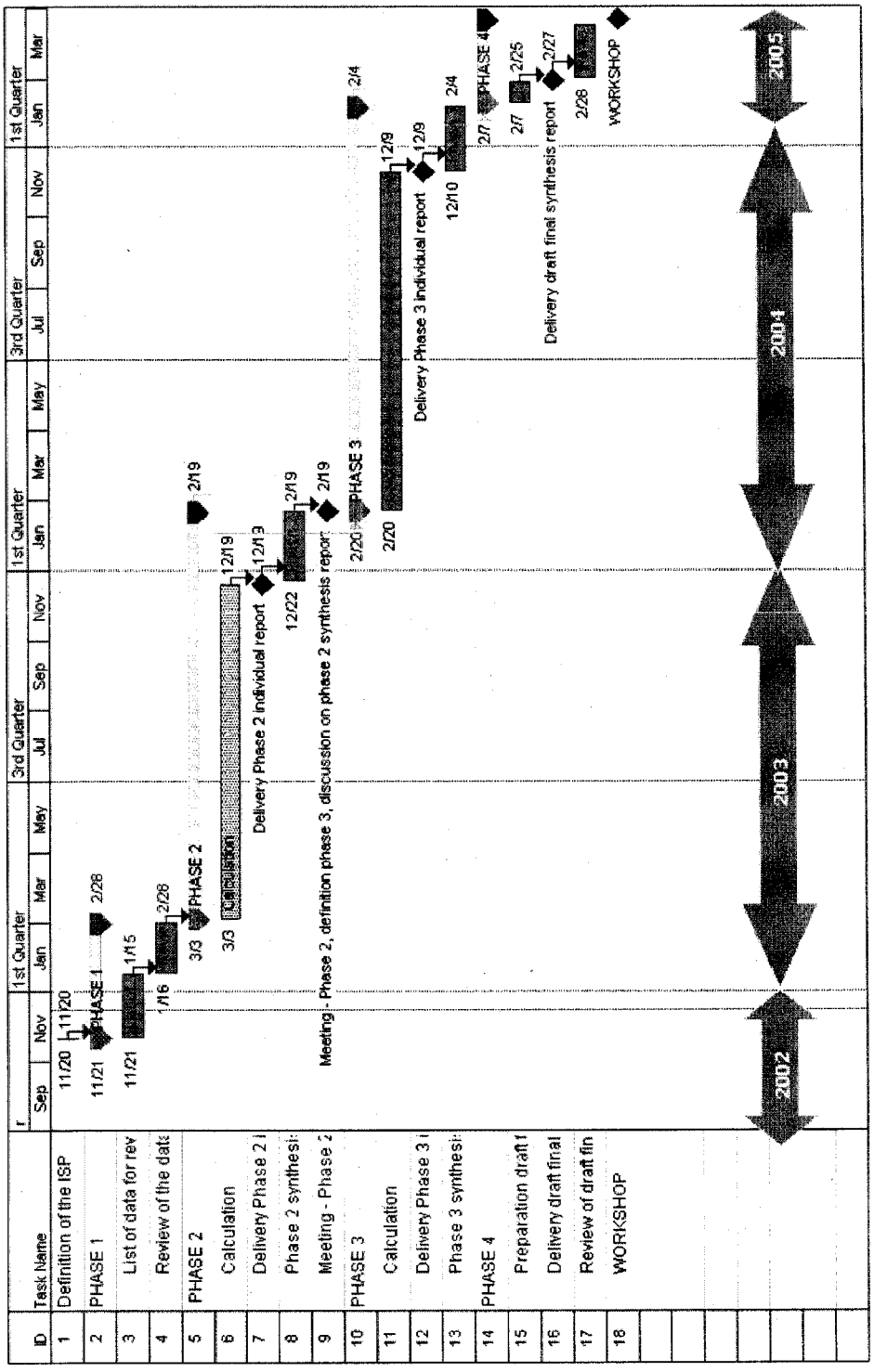

ISP 48 participants

Name	City	Est
CZECH REPUBLIC		
Mr. Jan MALY	Prague	ENERGOPROJ
FRANCE		
Mr. Georges NAHAS	Fontenay-aux-Roses	IRSN
Mr. Jean-Pierre TOURET	Villeurbanne	EDF VILLEUR
GERMANY		
Dr. Hans GREBNER	Koeln	GRS KOLN
Mr. Christoph NIKLASCH	Karlsruhe	UKARLIBM
Dr. Jurgen SIEVERS	Koeln	GRS KOLN
JAPAN		
Mr S. SHIBATA		MISJPN
Dr. Mikio YAMAMOTO	Tokyo	NUPEC
KOREA (REPUBLIC OF)		
Dr. Nam-Ho LEE	Taejon	KOPEC
Dr Sangjin LEE	Taejon	KAERI
SLOVAK REPUBLIC		
Mr. Milan PRANDORFY		MISSL
SWEDEN		
Mr. Ola JOVALL	Lund	SCANSCOT
UNITED KINGDOM		
Mr. Michael W. JOHNSTON	East Kilbride	BEG
Mr. David SHEPHERD	Bootle (nr. Liverpool)	HSE BOOTLE
UNITED STATES OF AMERICA		
Dr. James F. COSTELLO	Washington	NRC
Mr. Michael F. HESSHEIMER	Albuquerque	SANDIA